COLLEGE OF ENGINEERING

VPI-Aero-108

CURVED FLOW WIND TUNNEL TEST

OF F18 AIRCRAFT

Frederick H. Lutze

April 1980

VIRGINIA POLYTECHNIC INSTITUTE AND STATE UNIVERSITY

BLACKSBURG, VIRGINIA

VPI-Aero-108

CURVED FLOW WIND TUNNEL TEST OF F18 AIRCRAFT

Frederick H. Lutze

April 1980

NAS1-15080

CURVED FLOW WIND TUNNEL TEST OF F-18 AIRCRAFT

Frederick H. Lutze

ABSTRACT

The curved flow capability of the Virginia Tech Stability Wind Tunnel was used to investigate the lateral-directional characteristics of an F-18 aircraft. This report deals with a description of the model, the procedures used to obtain and correct the data and a graphical presentation of the results. The results include graphs of lateral-directional derivatives versus sideslip or static plots, the lateral directional static stability derivatives versus angle of attack, and finally the lateral-directional derivatives versus non dimensional yaw rate for different angles of attack and sideslip. Results are presented for several configurations including complete, complete without vertical tails, complete without horizontal tails, fuselage-wing and fuselage alone. Each of these were tested with and without wing leading edge extensions. In addition results of deflecting the basic control surfaces were investigated. A brief discussion of the results is included highlighting unusual characteristics.

ACKNOWLEDGEMENTS

The compilation of the large amount of data associated with this project could not be done without the aid of several assistants. Special mention should be given Don DeGutz, Richard Goff, Howard Gofus, Diane Liebenow, Sandra Merritt, and Tom Trimbath. Without their committment to the program and long hours of work, aquisition of the data required for this report would have been impossible. The funds for this research were provided by NASA Langley Research Center under Contract NAS1-15080 Task Authorization Number 8.

TABLE OF CONTENTS

LIST OF TABLES

LIST OF FIGURES

LIST OF SYMBOLS

A_F	Projected frontal area of model perpendicular to wind tunnel axis (m^2)
A_x	Projected area perpendicular to x body axis (m^2)
A_y	Projected area perpendicular to y body axis (m^2)
A_z	Projected area perpendicular to z body axis (m^2)
b	Wing span (m)
$\bar{c}$	Wing mean aerodynamic chord (m)
C_1, C_2, C_3	Shape constants given in Table 2
$C_D = D/\bar{q}S$	Drag coefficient
$C_L = L/\bar{q}S$	Lift coefficient
$C_\ell = L/\bar{q}Sb$	Roll moment coefficient
$C_m = M/\bar{q}S\bar{c}$	Pitch moment coefficient
$C_n = N/\bar{q}Sb$	Yaw moment coefficient
$C_y = Y/\bar{q}S$	Side force coefficient
D	Drag (N)
F	Fuselage
F_n	Parameter defined on page 8
H	Horizontal Tail
L	Lift (N), roll moment
LEX	Wing leading edge extensions
M	Pitch moment (Nm)
N	Yaw moment (Nm)
p	Pressure (N/m^2)
$\bar{q}$	Dynamic pressure (N/m^2)

R	Radius of tunnel calibrated curvature (N)
r	Yaw rate (rad/sec)
$\hat{r} = rb/2V$	Non-dimensional yaw rate
S	Wing area (m^2)
V	Speed (m/sec)
V	Vertical tails
W	Wing
X_{CB}	Distance from reference point to center of volume (m)
Y	Side force (N)
α	Angle of attack (deg)
β	Angle of sideslip (deg)
ε	Blockage correction factor
δ_a	Aileron deflection, positive right aileron down (deg)
δ_d	Horizontal tail differential deflection, positive right tail trailing edge down (deg)
$\delta_{f,\ell e}$	Wing leading edge flap deflection (deg)
$\delta_{f,te}$	Wing trailing edge slap deflection (deg)
δ_h	Horizontal tail deflection, positive trailing edge down (deg)
δ_r	Rudder deflection, positive trailing edge left (deg)
ρ	Air density (kg/m^3)

INTRODUCTION

Currently there is a strong interest in the dynamic stability of aerospace vehicles. In order to obtain a better understanding of this phenomena, many types of wind tunnel, free flight, and flight tests have been devised. A recent AGARD conference, devoted solely to this aspect of flight mechanics, summarizes the current work being done in this area.[1] Reference 1 cites several research topics related to this problem which need further investigation. Included in these topics are the need for separation of rotary and unsteady aerodynamic derivatives and the need for determining dynamic cross coupling derivatives. These effects seem to be of particular interest for vehicles at high angle of attack. Consequently a considerable amount of research has been concentrated in the range of high angle of attack studies.[2]

Several methods of testing have been used in an attempt to provide the required data. Included in these techniques are oscillating and free flight tests,[3] and rotary balance methods.[4] Another method, developed at NASA Langley and now implimented at V.P.I., is that of curved flow. In this method the model is immersed in a curved flow with the appropriate velocity profile necessary to simulate flight in a curved path.[5,6,7] From this type of test the pure rotary derivatives can be obtained in a steady state environment. Furthermore standard wind tunnel procedures can be used for data aquisition and blockage corrections. In addition the steady state environment permits ease of implimenting flow visualization techniques. The range of angles of attack that can be tested is limited only by the method used for support. A description of the wind tunnel, its calibration and necessary corrections for reducing data are discussed in reference 8.

This report presents the results of testing an F-18 fighter aircraft model in the curved flow test section in the VPI&SU Stability Wind Tunnel. Lateral data are presented for four curvatures associated with four yaw rates as well as for straight flow. For each curvature data are presented for several configurations allowing the contributions of each appendage to be assessed and allowing the interaction of the curved flow on the various appendages to be observed. A brief discussion of the results is presented emphasizing the salient aerodynamic characteristics obtained.

APPARATUS, MODEL, TEST TECHNIQUE

Wind Tunnel

The tests were conducted in the square 1.83 x 1.83 m (6 x 6 ft.) test section of the Virginia Tech Stability Wind Tunnel located in the Department of Aerospace and Ocean Engineering. The nominally square test section has vertical walls which are designed to have enough flexibility so that they may be deflected into a curve, creating a curved air flow past the model. Jack-screws positioned at regular intervals along each wall allow the curvature to be set at prescribed values. In order to complete the simulation of flight in a curved path it is necessary to redistribute the velocity profile in the radial direction. This is done by installing wire screens, varying in mesh across the wind tunnel, upstream of the test section. The mesh size varies so that the densest portion is located toward the center of curvature. A sketch showing a typical curved flow test arrangement is presented in Figure 1. Details of curved flow theory, calibration and tunnel operation are given in Reference 8.

Balance

The forces and moments were measured by the use of an internally mounted strain gage balance. Two separate balances were used, one for the longitudinal measurements, Langley balance #FF05, (normal and axial forces, and pitch moment) and another for the lateral measurements, Langley balance #FF06, (roll and yaw moments, and side force). The balances were supplied by NASA Langley Research Center and were compatible with the model. A nominal five volt power supply was used to supply power to the balances.

Calibration of the balances to account for system dependent variations such as voltage supply and cable length differences was accomplished using a span check. Basically this check consists of applying the same load to the balance (via a precision resistor) in the local system as was used in the calibrating system and observing the system readout. An appropriate correction factor can then be determined and a calibration determined. The calibrations used throughout the tests were as follows:

Normal force	56.3879 N/mV	(12.6765 lbs/mV
Axial force	39.2244 N/mV	(8.8180 lbs/mV)
Pitch moment	5.9187 Nm/mV	(4.3654 ft lbs/mV)
Roll moment	1.8175 Nm/mV	(1.3405 ft lbs/mV)
Yaw moment	11.7105 Nm/mV	(8.6372 ft lbs/mV)
Side force	32.4391 N/mV	(7.2926 lbs/mV)

Data Aquisition System

Data was obtained using a Hewlett Packard (HP) 3052 Data Aquisition

System. This system includes an HP 3455 digital voltmeter, an HP 3495 forty channel Scanner and an HP 9825 Calculator. Data was obtained according to the procedures described below, reduced and stored on tape. Subsequently it was transferred to the University's IBM 370/168 computer where it was sorted for the purposes of plotting the results.

Model

The investigation was conducted with a 0.07 scale model of the F-18 aircraft. The model, supplied by the Langley Research Center was specially built for these tests and was constructed to be compatible with the above balances and sting support system. A three view sketch showing the general layout of the model is shown in Figure 2.

The model was constructed in a manner that allowed various parts to be easily removed to permit build-up tests of several configurations to be performed. In addition several control surfaces could be set in deflected positions. These included wing leading and trailing edge flaps, ailerons, rudders on the twin vertical tails. In addition the horizontal tail surfaces could be deflected together or in a different manner. The configurations tested along with their identifying numbers are given in Table 1. It should be noted that the base configuration (#1) was the full configuration with the wing leading edge flaps deflected down 25 degrees. Unless otherwise stated, the leading edge flaps were in the deflected position for all configurations.

In order to reduce the data to account for blockage effects, and in curved flow, to account for pressure gradient effects,[8] it is necessary to know the front, planform, and profile areas as well as the model volume for each configuration. These quantities along with the basic reference geometry are given in Table 2.

Test Procedure

The model was mounted in the wind tunnel using a pylon supporting sting mount. By using a double dog-leg arrangement as shown in Figure 1, it was possible to obtain angles of attack from 0 to 45 degrees. The pylon support was mounted on a turntable and slide arrangement to allow sideslip angles of $\pm$ 10 degrees while maintaining the model location in the center of the tunnel. (See Figure 1) As the walls were curved for simulating increased yaw rates, the limited travel of the slide mechanism prevented obtaining positive side slip angles greater than 5 degrees. In fact at the largest curvature tested, the model had to be displaced 0.102 m (4 in.) off the centerline (toward the inner wall) to obtain the desired 5 degrees angle of sideslip. Corrections in mean velocity were made to account for this shift.

The matrix of tests were completed by first selecting the curvature or yaw rate, then selecting the configuration, sideslip and angle of attack. Hence angle of attack sweeps were done for each sideslip angle which in turn were swept for each configuration. Data for these tests were taken in the following manner. For each new configuration wind off as well as wind on readings were taken for each angle of attack at the first sideslip angle selected. The wind off valves were stored to be used for the same configuration at corresponding angles of attack for the remaining sideslip angles. Consequently the data taken at these remaining sideslip angles were taken without shutting the tunnel down as the angle of attack sweeps were made.

At each test point curvature, configuration, pitch angle and yaw angle were observed and entered into the data aquisition system. The static

pressure, temperature, tunnel dynamic pressure (see below), and the six components of the strain gage balance were read on command by the data aquisition system. These latter readings were obtained by taking the average of 15 samples taken over an 8 second time interval.

The test conditions in the wind tunnel were set by calibrating the pressure drop across the upstream contraction with the dynamic pressure in the empty test section for straight flow. The same pressure drop was used for the straight and curved flow tests. The values used for this test were a pressure drop of 0.044 m (1.71 in) of water which corresponds to a dynamic pressure of $\bar{q}$ = 766.08 N/m^2 (16 lbs/ft^2) in the unoccupied test section. This speed corresponds to a Reynolds number of approximately 6 x 10^5 based on the mean aerodynamic chord.

TESTS

Tests using the longitudinal balance were carried out for the straight flow or non-yawing case only. Eight configurations were examined corresponding to the following numbers from Table 1; configurations 1,2,3,9,10,13,14 and 15. Tests were carried out for three sideslip angles of β = - 5, 0, and 5 degrees and for 10 angles of attack from 0 to 45 degrees in 5 degree increments.

Lateral tests were performed for four different calibrated yaw rates in addition to straight flow. The four non-dimensional yaw rates rb/2V = -0.0253, -0.0380, -0.0515, and -0.0707. Lateral tests were carried out for all configurations shown in Table 2 for all curvatures. Tests were run for all angles of attack from 0 to 45 degrees in 5 degree increments at sideslips from -10 to +10 degrees sideslip in 5 degree increments. As noted previously

sideslip angles only up to +5 degrees could be tested at the two highest yaw rates, rb/2V = - 0.0380 and -0.0707. Exceptions to the above test schedule occurred for configurations 5, 16, 17, and 18. Configuration 5 was tested only in straight flow for full range of sideslip while configurations 16, 17 and 18 were tested at all yaw rates but only at zero sideslip.

DATA REDUCTION

Data recorded for each test included run number, curvature, configuration, pitch angle, yaw angle, local pressure, temperature, contraction ratio pressure drop, and six components of strain gage data with wind on and wind off (stored data). This data was reduced and printed out in the form of run number, configuration number, curvature, angle of attack, sideslip angle, corrected tunnel dynamic pressure, speed, Reynolds number, and the nondimensional force and moment coefficients in both body and stability axes. Included in this reduction are corrections in the tunnel dynamic pressure due to blockage effects and corrections for the lateral pressure gradient which occurs when the walls are curved. A brief discussion of these corrections is given below. More details can be found in References 8 and 9.

The blockage correction used is empirical but has been shown in the past to be adequate at the high angle of attack range and in addition is simple to apply.[6,9] The correction in the dynamic pressure is given by

$$\bar{q}_c = \bar{q} \, (1 + 2\varepsilon)$$

where

$$\varepsilon = 1/4 \frac{\text{frontal area}}{\text{tunnel area}}$$

The frontal area depends upon angle of attack and sideslip and is given by

$$A_F = (A_x \cos \alpha + A_z \sin\alpha) \cos \beta + A_y \ |\sin \beta|$$

where A_x, A_y and A_z are the projected areas perpendicular to the x,y, and z body axes and are given in Table 2.

The correction for the lateral pressure gradient caused by curving the flow depends on the model volume and shape. Details involved in the development of these corrections are given in Reference 8. Important in these corrections are the model volume, approximating ellipsoid shape factors, and the value of the lateral pressure gradient. These values were established by direct measurements from the model and from tunnel calibration data and are given in Tables 2 and 3. The corrections used are defined as(corrected value) - (tunnel value) = Δvalue and given by the following:

$$\Delta\text{Axial} = [(1 + 2C_2) \sin \beta \cos \alpha - F_n \cos \beta \cos \alpha] \cdot \frac{\partial p}{\partial R} \cdot (\text{Vol})$$

$$\Delta Y = [(1 + 2C_1 \cos^2 \alpha + 2C_3 \sin^2 \alpha) \cos \beta + F_n \sin \beta] \cdot \frac{\partial p}{\partial R} \cdot (\text{Vol})$$

$$\Delta\text{Norm} = [(1 + 2C_2) \sin \beta \sin \alpha - F_n \cos \beta \sin \alpha] \cdot \frac{\partial p}{\partial R} \cdot (\text{Vol})$$

where $F_n = [(C_3-C_1) \cos^2 \alpha + (C_2-C_3)] \sin 2 \beta$

and C_1, C_2, C_3 are the shape parameters in Table 2. An additional correction associated with the lateral pressure gradient must be made if the center

of volume of the model does not coincide with the moment reference point under these circumstances a correction must be made to the yawing moment. The change in apparent yawing moment is given by

$$\Delta N = \Delta y \cdot X_{CB}$$

where X_{CB} is the position of the center of buoyancy (center of volume) with respect to moment reference point. For this test this distance was assumed to be zero.

One final correction was made for the case of tests run with the largest curvature at + 5 degrees sideslip. As discussed previously physical limitations of the tunnel prevented the model from being centered. Because of the velocity gradient, a small correction for the nominal dynamic pressure had to be included. In this case the dynamic pressure was 0.95 the dynamic pressure at the centerline and such a correction was included in the data reduction.

The final reduced data was obtained by taking the difference between wind on and wind off strain gage readings, applying the balance calibration factors, correcting the resulting forces for pressure gradient effects and dividing the corrected force and moment readings by the corrected dynamic pressure and appropriate geometric constrants to yield the proper force and moment coefficients.

RESULTS AND DISCUSSION

The results of the curved flow tests are presented graphically in Figures 3 thru 32. These figures include the standard static tests results as well as

the results observed in the steady state curved flow. All results unless otherwise noted are presented in stability axes since the yaw rate simulated in the tunnel is about the Z stability axis. In the following discussion the significance of each figure will be discussed and the highlight associated with it pointed out. Possible phenomena associated with these highlights will be briefly discussed.

Figures 3, 4 and 5 present the longitudinal data of lift, drag and pitching moment coefficient for several configurations; Figure 3 for configurations 1, 9, and 10, Figure 4 for configurations 13, 14 and 15 and Figure 5 for configurations 1, 2 and 3. Each figure contains results for -5, 0, and 5 degrees sideslip.

Figure 3 shows that for the full configuration the vehicle shows gentle stall characteristics with the stall not occurring until 40 degrees angle of attack (AOA). These characteristics are the same for all configurations including the leading edge extensions (LEX). A considerable amount of lift (20%) is generated by the horizontal tail at AOA above 20 degrees. The pitching moment for the complete configuration shows a negative slope with an increase in AOA up to about 30 degrees after which the slope is zero. The tailless configuration shows a marked positive slope after 5 degrees AOA remaining positive at a lesser amount above 20 degrees. There is virtually no effect of sideslip on any of the properties discussed above.

Figure 4 shows the effects of the LEX on fuselage-wing characteristics. Of importance is the fact that without the LEX the wing-fuselage combination shows an abrupt stall at 20 degrees AOA. This would indicate that the smooth flow over the wing is probably disrupted and stall occurs at this AOA. The

effect of the LEX on this flow pattern can only be conjectured. One suspects that not only do the LEX contribute to the lift at high AOA but that the abrupt separation of flow over the wing is alleviated due to the LEX trailing vortices since no break in the lift curve with LEX is observed. However it must be assumed that some character of the flow changes at 20 degrees angle of attack if only at the wing tips.

Figure 5 shows the result of a 12 degree trailing edge up deflection of the horizontal tail as well as the effect of the wing leading edge flaps moved to a zero degree deflection. The elevator deflection shifts the moment and lift coefficient curves as expected. The positioning the leading edge flaps to the undeflected position reduces the lift coefficient considerably (5-10%) for AOA above 20 degrees and increases the lift coefficient slightly (1 - 5%) for AOA below 20 degrees. Again there seems to be little effect due to sideslip on these nominal results.

Figures 6 thru 9 are graphs of the lateral force and moment coefficients versus sideslip angle for AOA from 1 to 45 degrees in 5 degree increments. Figures 6 and 7 are basically build up plots which show the effects of adding or removing various appendages while Figure 8 shows the effect of deflecting various surfaces.

Figure 6 shows the effects of removing the vertical tails and/or the leading edge extensions from the full configuration. At the low angles of attack it is apparent that the LEX have little effect on roll, yaw or side-force change with sideslip angle. At 5 deg AOA the roll moment seems to be slightly effected by the presence or absence of the LEX, while yaw and side-force remain unaffected. Such behavior suggests asymmetric lift caused directly by the LEX or indirectly by their wake vortices flowing over the

wing. Without additional evidence it is probably the direct lift contribution. This choice is supported by noting that the pitch moment becomes more positive with the LEX than without (See Figure 4).

At 10 degrees AOA the effects of the LEX start to show up in yaw and sideforce as well as in roll. Here the vehicle shows a little more weathercock stability ($C_{n_\beta} > 0$) with the LEX than without. The roll moment exhibits unusual behavior with sideslip. It appears the vertical fins have little effect on the roll moment, the curves with and without the vertical tails falling nearly on top of each other, for each case, with and without LEX. At 15 degrees AOA the roll characteristics remain the same, showing little effect due to the vertical tails. The side force and yaw moment however show strong effects due to the vertical tails as exhibited at lower AOA. For the full configuration the yaw moment changes significantly when the LEX are removed. This effect is not observed when the vertical tails are absent indicating that interaction of the flow field generated by the LEX and the vertical tails is occurring. In this case the interaction is favorable with respect to stability in yaw.

The first significantly different behavior with and without the LEX occurs at 20 degrees AOA in the yaw moment. Here between 5 and 10 degrees sideslip, the curve without the LEX changes its slope to negative while with the LEX in place the slope remains positive and nearly constant. We would expect significant differences between with and without LEX behavior to appear at this AOA since we observed the wing without the LEX to stall at this point. These same trends carry over to the 25 degree AOA case. Here the vehicle is marginally stable in yaw without LEX but stable with them.

The roll moment characteristics show some changes from the previous patterns at lower AOA. Here adding the vertical tails and LEX decrease the effective dihedral ($C_{\ell_\beta} < 0$) the largest increment occurring when the LEX are added but an almost equivalent increment when the tails are added. Including both LEX and tails adds very little to the original increment of LEX or tails.

At AOA of 30 and 35 degrees, the vertical tails have virtually no effect on the rolling moment but enter into the yaw moment effects. The interaction of the LEX and the vertical tail can be observed in the yaw moment graphs, without the LEX the tails show significant contribution to yaw moment leading to a more positive slope with sideslip with the tails in place than without the tails in place. With the LEX in place however this slope is decreased for the case of the full configuration and increased for the configuration without the tail so that the two curves nearly coincide.

Figure 7 presents the results for the fuselage, fuselage-wing, and fuselage-wing and vertical tail, the latter two with and without LEX. The results for low angles of attack are similar to those in the previous figure indicating, as expected that the horizontal tail does not effect the lateral force and moments at low AOA. At 10 degrees AOA, however the effective dihedral is improved without the horizontal tail both with and without LEX. This phenomena does not occur at 15 or 20 degrees AOA. In fact these curves are very similar to the corresponding curves in the previous figure. At 30 degree AOA the effect of the vertical tails on the roll moment is virtually non-existant without LEX and remains small with the LEX as in the previous figure. The results for the remaining AOA are similar to those in the previous figure.

Figure 8 shows the effects of deflecting the leading and trailing edge flaps on the wing as well as a horizontal tail deflection. Significant effects

start to appear at 15 degrees AOA. Here both the roll and yaw moments show some decrease in stability when the leading edge flaps are not deflected. The LEX reduce this effect somewhat. At 25 degrees AOA the behavior in roll and yaw are completely different for the non-deflected leading edge with and without LEX indicating a strong interaction between the LEX and the flow over the wing as observed previously. At AOA above 35 degrees the effects of flap and horizontal tail deflections are reduced.

Figure 9 shows how the aerodynamic properties change with control surface deflections. At low AOA the curves are shifted as expected with rudder deflection producing a yaw moment with a slight roll moment and aileron deflection producing a roll moment with a slight yaw moment. The differential tail produces only a small roll moment since the deflection is small ($\pm$ 5 degrees) and the surfaces are close to the roll line. As the AOA increases the aileron effectiveness is reduced until about 35 degrees AOA where the aileron produces about the same amount of roll as the rudder deflection. The differential tail deflection produces a roll moment in the opposite direction at 45 degrees AOA and at all sideslip angles.

Figure 10 is a summary plot of the β-sweep curves. The slopes were calculated by taking the difference between the coefficients at $\pm$ 5 degrees angle of sideslip and dividing the result by 10. Hence the units are "per degree." In general it can be observed that the LEX have little effect on stability at the low AOA. At about 10 deg AOA the configurations with the LEX show considerable differences from the configuration without the LEX. The most notable differences occur in the roll stability graph. The full configuration with the LEX shows a stronger dihedral stability until about 25 degrees AOA where

the full configuration without the LEX shows increased stability. This trend holds for all configurations compared with and without LEX. An extreme example of this type of behavior is shown for the configuration with the wing leading edge flaps up. Here at 25 degrees AOA, the roll stability is unstable with the LEX on and strongly stable with them off indicating an important interaction among the LEX shed vortices, their position on the wing, and the sideslip angle. As might be expected Figure 10 shows little effect on lateral-directional stability due to control surface deflections.

Figures 11, 12, 13 and 14 show the same curves as Figure 10 for the various tunnel curvature settings or equivalent yaw rates. The general trends for all curvatures is the same as that for zero curvature. The effects of the LEX on yaw stability are to improve the stability up to about 20 degrees AOA and destabilizing for AOA above 20 degrees. For the full configuration this trend occurs at all curvatures but the angle at which the switch takes place tends to increase with curvature with the switch taking place at 30 degrees AOA for the largest curvature. Without the vertical tails the switching point is more strongly defined and occurs at virtually the same AOA, 25 degrees, for all curvatures. The dihedral effect shows the same trends with the configuration with the LEX showing a marked improvement in stability up to about 25 degrees AOA and large reduction in stability above this AOA. The switching point is sharply defined for both the full configuration and the full configuration without vertical tails, with latter occurring slightly earlier (23 degrees AOA) than for the full configuration. These same trends are observed for the fuselage-wing and fuselage-wing and vertical tail configurations with and without LEX. Curvature effects on the wing leading edge

flaps undeflected appear to be minimal, the same trends as discussed earlier occurring at all curvatures.

Figures 15 thru 19 are non-traditional stability derivative plots. The purpose of these plots is to show the effect of curvature and sideslip on the lateral-directional stability derivatives. Each figure contains the information for all configurations at one curvature or yaw rate. Any one graph contains the stability derivative information for one configuration calculated by three different methods. The three methods used as numbered in the figures are:

1. The standard method used in the previous figures where the derivative is obtained by evaluating the force or moment coefficient at $\pm$ 5 degrees sideslip, taking the difference and dividing by 10, e.g. $(C_X(5) - C_X(-5))/10$
2. The use of just the positive sideslip and zero sideslip quantities to give $(C_X(5) - C_X(0))/5$
3. The use of just the negative sideslip and zero sideslip quantities to give $(C_X(0) - C_X(-5))/5$

It is clear that the first method is an average of the last two and always falls in the middle. In general at low angles of attack the three methods provide the same result. At high angles of attack this is no longer true in all cases. The cause for the difference has been shown in the past[7] to be associated with the asymmetric vortex shedding from the nose area coupled with the interaction of these vortices with wing and tail structures. The additional capability to curve the flow accentuates asymmetric flow either on the forebody or tail surfaces enabling one to isolate these effects.

In viewing these graphs the key features to observe are the spreading apart of the lines for any given coefficient. This spreading signals strong dependence of the stability derivative on sideslip angle. Furthermore if this spread straddles the zero line, then the static stability itself depends upon the sideslip angle. For the purposes of discussion we will refer to such a situation as being bistable. That is a vehicle is statically bistable if sideslips in one direction yield statically stable derivatives and sideslips in the opposite direction yield statically unstable derivatives. For convenience we will refer to a vehicle as having even bistable behavior if positive sideslip gives stable stability derivatives or positive stability, and having odd bistable behavior if positive sideslip gives unstable stability derivatives or negative stability. Finally it should be pointed out that these definitions only hold for the $\pm$ 5 degree sideslip range used in these plots. As observed in previous figures and to be observed in later figures the sign of a stability derivative can change from that in the 0 to 5 degree sideslip range to a different sign in the 5 to 10 degree sideslip range. With these preliminaries we can examine the highlights of Figures 15 thru 19.

In Figure 15 straight flow results are shown. For the full configuration with LEX virtually no effects of sideslip are observed until just below 30 degrees AOA at which time slightly even bistable behavior occurs in roll with no effect on yaw. In the 30-45 degree AOA region sideslip dependence appears in both roll and yaw stability derivatives. Here, however, the roll stability is maintained for all sideslip angles while the yaw moment shows strong even bistable behavior between 33 and 43 degrees AOA. For the full configuration without the LEX a region of odd bistable behavior in yaw exists from 25 to 35

degrees AOA. Furthermore from 40 to 45 degrees AOA the full configuration without LEX displays some even bistable behavior in yaw. In roll, on the otherhand no bistable behavior is observed although strong sideslip dependence is observed from 15 to 45 degrees AOA. This dependence appears to be opposite that for the case with the LEX on in the 35 degree AOA region.

The remaining graphs in Figure 15 show the asymmetric properties for the remaining configurations with and without LEX in straight flow. The general trend is that the LEX greatly reduce the asymmetric effects and postpone those that do occur to higher angles of attack. With the LEX on rolling moment generally shows little sideslip effects compared to the same configuration without LEX. With respect to yaw, the LEX postpone the effects due to sideslip. Furthermore there is a suggestion, but certainly not a rule. that the effects are reversed at the higher AOA. The fuselage alone results are of interest since they indicate that asymmetric effects occur in the AOA region from 20 to 35 AOA in yaw and roll and from 20 to 45 degrees AOA in sideforce. It would be expected that some asymmetric nose vortices might occur for this fuselage shape and these results indicate they probably do occur. Finally the full configuration with undeflected leading edge flaps shows a considerable difference in asymmetric effects with LEX on or off. With the LEX significant asymmetric effects do not occur until 25 degrees AOE while without LEX they begin as early as 10 degrees AOA. It appears from the above observations that separated flow over the wings has a large contribution to the sideslip effects observed.

The effect of curvature on the lateral stability derivatives can be examined by comparing Figures 15 thru 19. If we initially look at the full

configuration with LEX at the lowest curvature we can observe initial curvature effects. For a small amount of curvature the yaw and rolling moment curves show consistent effects in that the values computed by the three methods don't cross as much as they did in straight flow. In particular the yaw moment stability derivative tends toward odd bistable behavior at 10 degrees AOA and actually achieves this behavior in the neighborhood of 25 degrees AOA and above 35 degrees AOA. This means that a sideslip producing a nose in toward the center of the turn or positive sideslip (recall the simulated turn in the tunnel is to the left) is destabilizing in yaw while a nose out attitude is stabilizing. The rolling moment stability derivative has this same odd bistable behavior for AOA between 30 and 40 degrees. At lower AOA the vehicle is stable in roll but has a trend toward even bistability at AOA between 15 and 27 degrees. For the roll moment this same trend is maintained for all the curvatures, only the details of where the odd bistability starts and how strong it is change slightly. The yaw moment stability derivative on the otherhand is not so well behaved with curvature. As curvature increases the odd bistable behavior at the lower yaw rates shifts to even bistable behavior at the higher yaw rates. The region of this type of behavior is always above 35 degrees AOE.

For the full configuration without LEX similar effects are observed but generally starting at a lower AOA. For the roll stability the extreme values occur at 25 degrees AOA rather than 40 degrees. At the maximum curvature no bistable behavior is observed although the trend is still present. Furthermore the trend with or without LEX for all curvatures is toward odd bistable

behavior in roll. For the case of yaw stability some differences are observed for LEX on or off. With the LEX on we previously observed a change in the bistable behavior as curvature increased. Without LEX the trend is always toward even bistable behavior in yaw except at 45 degrees where it switches to odd bistable behavior for LEX on or off.

Without the vertical tails, the effect of curvature on the asymmetric yaw moment stability properties is small. All the curves show instability no matter how they were calculated. In addition, other than the cases for straight flow and the smallest curvature, asymmetric effects on yaw stability were small. The roll moment stability curves exhibit similar behavior as shown for the full configuration. The extreme effects occur at 35 degrees AOA for the lowest curvature and at 40 degrees for the larger curvatures. The bistable behavior is in the same sense as the full configuration. At the largest curvature the effect seems to be diminished somewhat from that with the vertical tails present. The same configuration without the LEX show limited asymmetric effects except at 25 degrees AOA in roll for the larger curvatures, and at 35 degrees AOA for the smallest curvature.

The most dramatic effects of curvature on asymmetry properties occurs when comparing the fuselage-wing and vertical tail with and without LEX. With the LEX in place the stability curves for straight flow are well behaved for both yaw and roll moments. The introduction of curvature causes increased asymmetric effects in both the roll and yaw moments. The extreme differences for positive and negative sideslip occur at 35 degrees AOA for the roll moment and 40 degrees for the yaw moment. When the LEX are removed

the asymmetric effects become more pronounced at lower AOA. In particular the effects occur at 15 degree AOA for the yaw moment and at 20 degrees AOA for the roll moment. Similar trends are displayed for the fuselage-wing configuration. At the greater curvatures the effects are somewhat diminished over those at lower curvatures.

The fuselage alone indicates some asymmetric properties at zero curvature with little change at the lowest curvature. However increasing the curvature further shows large asymmetric effects in both roll and yaw moment stability. Also the fuselage alone case shows large asymmetric effects on the side force which have not shown up in previous configurations.

The trends observed for the full configuration with flaps up for straight flow with LEX on and off are observed in the curved flow situation. The curvature tends to reduce the angle of attack at which the asymmetric effects start to occur. Finally if the trailing edge flaps are deflected down, there is little change from the undeflected case. Again large effects are noticed in roll at 40 degrees AOA. For yaw moment the curves are so close to zero at large AOA that even small asymmetric effects can lead to a bistable situation. For the larger curvatures even bistability behavior is observed in yaw.

Figure 20 presents the lateral directional stability derivatives in body axes for straight flow only. These are included since a considerable amount of data in the literature is presented in body axes. Consequently these plots would make quick comparison of data possible.

Figures 21 thru 32 are curvature or yaw rate sweeps for different configurations. Here the lateral forces and moments are plotted versus the non-dimensional yaw rate for the various sideslip angles. A considerable

amount of information can be obtained from these plots including much of the material presented in Figures 15 thru 19. Lines that appear parallel on the graphs indicate that the yaw rate derivatives, C_{X_r}, are not dependent on sideslip angle. Lines that are equally spaced indicate that the sideslip derivatives C_{X_β} are not dependent on yaw rate. If the lines are straight, this indicates that the yaw rate derivatives C_{X_r} are independent of yaw rate. If the lines on the graph cross, this indicates that the sideslip derivative, C_{X_β} most likely changes sign with sideslip. The distance between the lines indicates the magnitude of the sideslip derivatives. With these rules we can examine the curve sweep plots.

Figure 21 presents the results for the full configuration. As expected at the low AOA the curves are parallel, equally spaced and nominally straight indicating little cross dependence on yaw rate or sideslip angle. This same pattern holds until about 15 degrees AOA where some irregularities can be observed in the roll moment curves. These irregularities are increased at 20 degrees AOA. The roll moment curves are equally spaced and parallel but are not straight. In fact the slope of the lines and hence the roll due to yaw derivative changes sign. At 25 degrees AOA the yaw moment curves start to become closer together indicating a reduction of C_{n_β}. The asymmetric effects discussed previously can be observed here also since for positive sideslip the curves are closer together (almost zero for $\hat{r} = -.02$) then for negative sideslip. At 30 degrees and small sideslip angles and yaw rates C_{n_β} is positive. At the larger sideslip angles C_{n_β} changes sign for positive sideslip and is greatly reduced, but still positive for negative sideslip. For this AOA small negative sideslip yields the same positive C_{n_β} for the two lowest yaw rates diminishing to zero at the highest yaw rate.

For small positive sideslip the value of C_{n_β} starts positive, goes negative and shifts strongly positive again as the curvature increases. For negative sideslips above 5 degrees, C_{n_β} is a constant negative value for all yaw rates. For positive sideslips above 5 degrees C_{n_β} is negative at the small yaw rates and approaches zero at $\hat{r} = -.04$. In roll for small sideslip angles there is little or no dihedral effect. However at $\pm$ degrees sideslip there is a strong dihedral effect which is maintained for all yaw rates.

At 35 degrees AOA the yaw moment coefficient has the following characteristics. For small positive and negative sideslip C_{n_β} remains positive for all curvatures. For sideslips above $\pm$ 5 degrees C_{n_β} remains negative for all curvatures. In roll the positive 5 degrees sideslip curve is not parallel to the remaining curves causing changes in sign in C_{ℓ_β} from stable to unstable to and back again at each curvature increment. At 40 degrees AOA the value of C_{n_β} is seen to change signs not only between 5 and 10 degrees sideslip but also with yaw rate and direction of sideslip. At zero yaw rate C_{n_β} based on the $\pm$ 5 degree sideslip increments is positive for positive sideslips (nose in toward turn center) and negative for negative sideslips, i.e. even bistable behavior. At the increments from $\pm$ 5 to $\pm$ 10 degrees sideslip the signs are reversed giving odd bistable behavior. At yaw rates between $\hat{r} = -0.02$ and -0.04 C_{n_β} is positive for all positive sideslip angles and negative for all negative sideslip angles. This situation is reversed at yaw rates past $\hat{r} = -0.045$. The roll moment shows consistent negative C_{n_β} but with a changing magnitude with yaw rate. Finally at 45 degrees AOA the roll moment curves remain in correct sequence with only the magnitude of C_{ℓ_β} changing with yaw rate. The yaw moment coefficient exhibits complex behavior. At zero yaw

rate C_{n_β} is negative or near zero for both directions of sideslip. At first curvature C_{n_β} becomes uniformly negative for all sideslips and remains so at the next yaw rate with the exception of large negative β for which C_{n_β} is slightly positive. For yaw rates past $\hat{r} = -0.045$ C_{n_β} exhibits odd bistable behavior just the opposite of the situation at 40 degrees.

Figure 22 presents the same results for the case of the full configuration without LEX. Here we will try to highlight the differences. The differences at the two lowest AOA are minimal. At 15 degrees AOA the configuration without the LEX starts to show a significantly reduced spacing between curves indicating a reduction in C_{n_β} and C_{ℓ_β} over the full configuration. At 20 degrees AOA the yaw moment curves show irregular behavior at zero yaw rate and cross with increasing yaw rate. In detail we have at zero yaw rate a positive C_{n_β} for small sideslip angles and a negative C_{n_β} for large sideslip angles. At $\hat{r} = -0.03$ the situation for large positive sideslip changes sign. For the higher yaw rates the value of C_{n_β} becomes even more negative for negative sideslip. At 25 degrees AOA the above properties continue. At 30 degrees AOA C_{n_β} is positive for negative sideslip at zero yaw rate and is positive for small positive sideslip angles and negative for larger sideslip angles. As the curvature increases C_{n_β} becomes negative for positive sideslip. With LEX this trend is reversed at this AOA. For the higher AOA the roll moment is well behaved but the yaw moment shows mixed activity at the low and intermediate curvatures, finally setting on a pattern at the higher yaw rates. At 45 degrees this pattern is odd bistable behavior of C_{n_β} which is the same for the configuration with the LEX.

Figures 23 and 24 present results for the fuselage, wing and horizontal tail with and without the LEX. In both cases the rolling moment is better behaved then in the full configuration with little crossing of curves except at 35 and 40 degrees AOA with LEX on. Yaw moment curves cross at 40 degrees AOA with LEX on and 35 degrees with LEX off. The resulting effects are different for the two configurations with the configuration with LEX showing weathercock stability at 40 degrees AOA for all curvatures and small sideslip angles with some negative stability at large negative sideslip at intermediate yaw rates. With the LEX off yaw stability virtually disappears at high yaw rates.

As might be expected Figures 25 and 26 for the fuselage, wing and vertical tails show more dramatic results indicating interaction between the vertical tails and the nose or LEX vortices. For AOA of 15 degrees and negative sideslip, nose away from the turn, an interchange of sign in C_{n_β} occurs for the large side slip angles and maximum curvature for the configuration without the LEX. No hint of crossover is exhibited by the vehicle with the LEX. At 20 degrees AOA without LEX large sideslip angles greatly reduce the yawing moment and cause C_{n_β} to change sign for the larger sideslip angles. The curvature enhances this diminished effectiveness for large negative sideslip angles. Such behavior is not observed in the configuration with the LEX.

At 25 degrees AOA both configurations show a reduced C_{n_β} with the LEX the curves basically staying in order. Without the LEX there is a switching in the sign of C_{n_β} going from small to large sideslips at all curvatures but a considerable difference in the magnitudes involved with different curvatures. At 30 degrees AOA the configuration with LEX keeps the curves in order with

little distance between them for both roll and yaw moment. Without LEX the yaw moment displays an even bistable behavior. At the higher AOA the curves are mixed for both configurations in yaw but are well spaced apart for the roll moment.

The Fuselage-Wing-LEX interactions are displayed in Figures 27 and 28. Most of the activity here occurs at 30-40 degrees AOA. At 30 degrees roll moment is sensitive to sideslip for the configuration without the LEX while it is considerably less sensitive with the LEX in place. The opposite is true in the case of yaw moment.

Figure 29 displays results for the fuselage alone configuration. At 20-35 degrees AOA the sign of C_{n_β} depends upon the sideslip angle at the larger yaw rates. In particular nose in toward the center of the turn is stable while nose out is not. These results are typical of long nosed vehicles.[7] The situation returns to normal at 45 degrees AOA.

Figures 30 and 31 show the results of tests on the full configuration with the leading edge flaps up with and without the LEX. Difficulties are first encountered at 15 degrees AOA for the configuration without the LEX and at 20 degrees AOA for the configuration with the LEX. In both cases a considerable reduction in the sensitivity of yaw moment with respect to sideslip is encountered. For the case of no LEX this condition leads to an odd bistable behavior at 25 degrees AOA. Such a condition does not develop with the LEX on.

Figure 32 shows the effect of trailing edge flaps on the full configuration with LEX. The overall results are similar to those for the full configuration without trailing edge flaps.

The above discussion details the observed effects of curvature on the lateral-directional stability derivatives. The mechanism of the flow field which produces these results has not been discussed since a considerably more detailed study of the figures must be made. It is speculated that many of the characteristics observed above are caused by interaction of the nose or LEX vortices interacting with separated flow over the wing and with the two vertical tails. The exact interaction has yet to be determined.

REFERENCES

1. AGARD Conference Proceedings No. 235, Dynamic Stability Parameters, November, 1978.

2. Chambers, J. R. and Grafton, S. B., Aerodynamic Characteristics of Airplanes of High Angles of Attack," NASA TM 74097, December 1977.

3. Grafton, S. B., Chambers, J. R. and Coe, P. L., Jr., "Wind Tunnel Free-Flight Investigation of a Model of a Spin-Resistant Fighter Configuration," NASA TN D-7716, June 1974.

4. Malcolm, G. N., "New Rotation-Balance Apparatus for Measuring Airplane Spin Aerodynamics in the Wind Tunnel," Journal of Aircraft, Vol. 16, No. 4, April, 1979, pp. 264-268.

5. Queijo, M. J., "Methods of Obtaining Stability Derivatives," NASA SP-258, pp. 71-101, 1971.

6. Lutze, F. H., "Curved Flow Wind Tunnel Test of a Spin-Resistant Aircraft Configuration," Dept. of Aerospace and Ocean Engr.Report, VPI-Aero. 067, August 1977.

7. Lutze, F. H., "Experimental Determination of Pure Rotary Stability Derivatives Using a Curved and Rolling Flow Wind Tunnel," AIAA-80-0309, 18th Aerospace Sciences Meeting, Pasadena, Calif.

8. Lutze, F. H., "New Calibration and Corrections for the VPI Stability Wind Tunnel Curved Flow Test Section," Dept. of Aerospace and Ocean Engr. Report VPI-Aero-069, August 1977.

9. Pope, A. and Harper, J., Low Speed Wind Tunnel Testing, John Wiley, 1966.

TABLE 1 Configurations

Number	Symbol	Number	Symbol
1	FWVHL	10	FWVL
2	FWVHL $\delta_h = -12$	11	FWH
3	FWVHL $\delta_f, \ell_e = 0$	12	FWV
4	FWVHL $\delta_f, t_e = 20$	13	FWL
5	FWVHL $\delta_h = -24$	14	FW
6	FWVH	15	F
7	FWVH $\delta_f, \ell_e = 0$	16	FWVHL $\delta_r = 30$
8	-	17	FWVHL $\delta_a = 25$
9	FWHL	18	FWVHL $\delta_d = 10$

where the following symbols are defined

F = fuselage
W = wing
V = vertical fins
H = horizontal tail
L = leading edge extensions (LEX)
δ_h = horizontal tail deflection (positive trailing edge down)
δ_f, ℓ_e = wing leading edge flap (nominally down 25 deg.)
δ_f, t_e = wing trailing edge flap
δ_r = rudder deflection (positive trailing edge left)
δ_a = aileron deflection (positive right aileron down = δ_a)
δ_d = differential tail deflection (positive right horizontal tail down $\delta_d/2$)

TABLE 2 Model Geometry

Reference Geometry	Wing Span = 0.798m (2.619 ft.)			Wing chord (MAC) = 0.245m (0.805 ft.)		
	Wing Area = 0.597m (1.960 ft.)			Center of Mass = 0.24 MAC		
Configurations	1,2,3,4,5,16,17,18		6,7		9	
Frontal area	0.028m^2	(0.300 ft^2)	0.028m^2	(0.300 ft^2)	0.028m^2	(0.300 ft^2)
Planform area	0.322m^2	(3.464 ft^2)	0.300m^2	(3.234 ft^2)	0.313m^2	(3.374 ft^2)
Profile area	0.120m^2	(1.294 ft^2)	0.120m^2	(1.294 ft^2)	0.097m^2	(1.040 ft^2)
Volume	0.013m^3	(0.476 ft^3)	0.013m^3	(0.476 ft^3)	0.013 m^3	(0.476 ft^3)
Configurations	10		11		12	
Frontal area	0.028m^2	(0.300 ft^2)	0.028m^2	(0.300 ft^2)	0.028m^2	(0.300 ft^2)
Planform area	0.284m^2	(3.058 ft^2)	0.292m^2	(3.144 ft^2)	0.263m^2	(2.828 ft^2)
Profile area	0.120m^2	(1.294 ft^2)	0.097m^2	(1.040 ft^2)	0.120m^2	(1.294 ft^2)
Volume	0.013m^3	(0.476 ft^3)	0.013m^3	(0.476 ft^3)	0.013m^2	(0.476 ft^3)
Configurations	13		14		15	
Frontal area	0.028m^2	(0.300 ft^2)	0.028m^2	(0.300 ft^2)	0.020m^2	(0.210 ft^2)
Planform area	0.276m^2	(2.968 ft^2)	0.254m^2	(2.738 ft^2)	0.112m^2	(1.210 ft^2)
Profile area	0.097m^2	(1.040 ft^2)	0.097m^2	(1.040 ft^2)	0.097m^2	(1.040 ft^2)
Volume	0.013m^3	(0.476 ft^3)	0.013m^3	(0.476 ft^3)	0.013m^3	(0.459 ft^2)

TABLE 3 Curved Flow Parameters

Curvature #	rb/2V	$\frac{\partial p}{\partial R}$ N/m^3 (lbs/ft^3)
0	0	0
1	-0.0253	8.771 (0.601)
2	-0.0380	13.835 (0.964)
3	-0.0515	18.242 (1.250)
4	-0.0707	24.226 (1.600)

Configurations	Shape factors
All	$C_1 = 0.03$ $C_2 = 1.20$ $C_3 = 0.83$

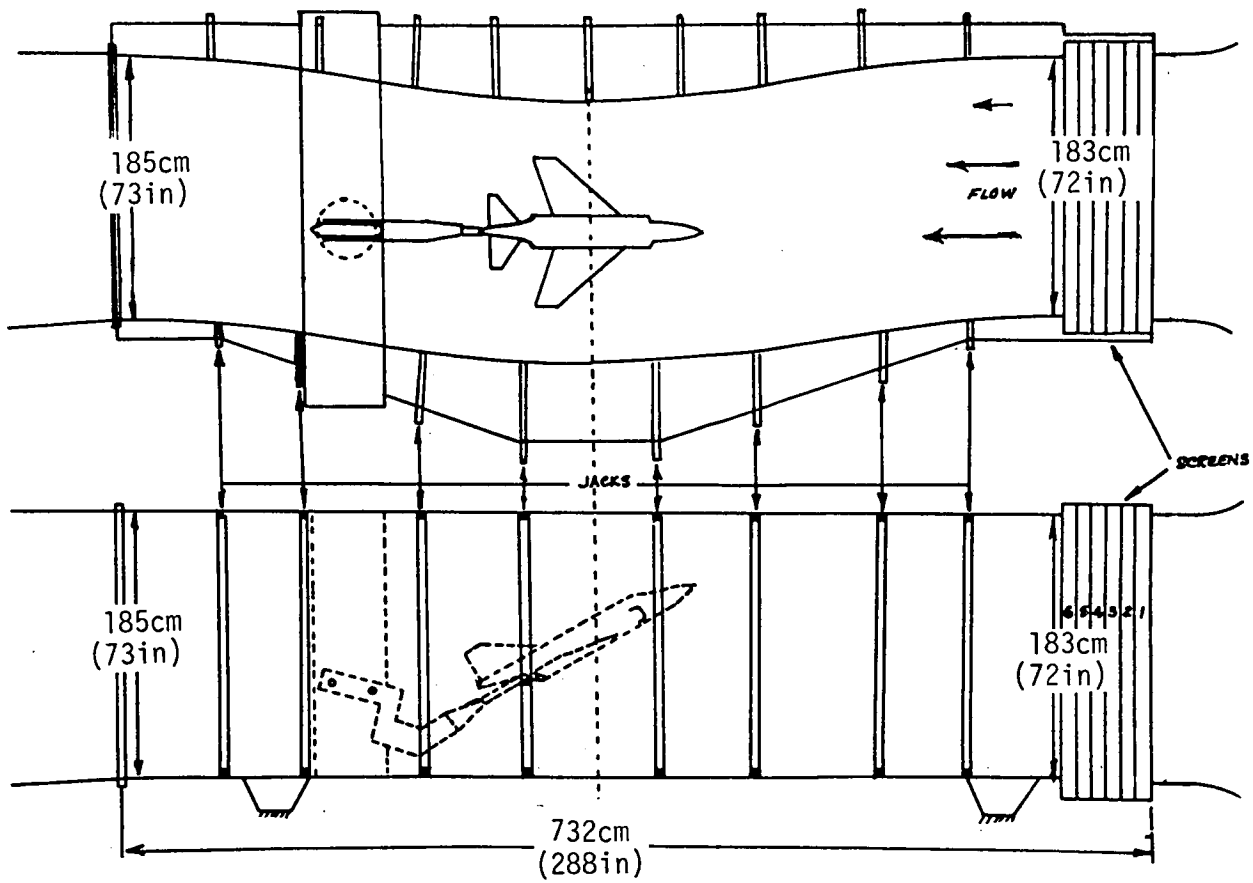

Figure 1 Curved Flow Test Section

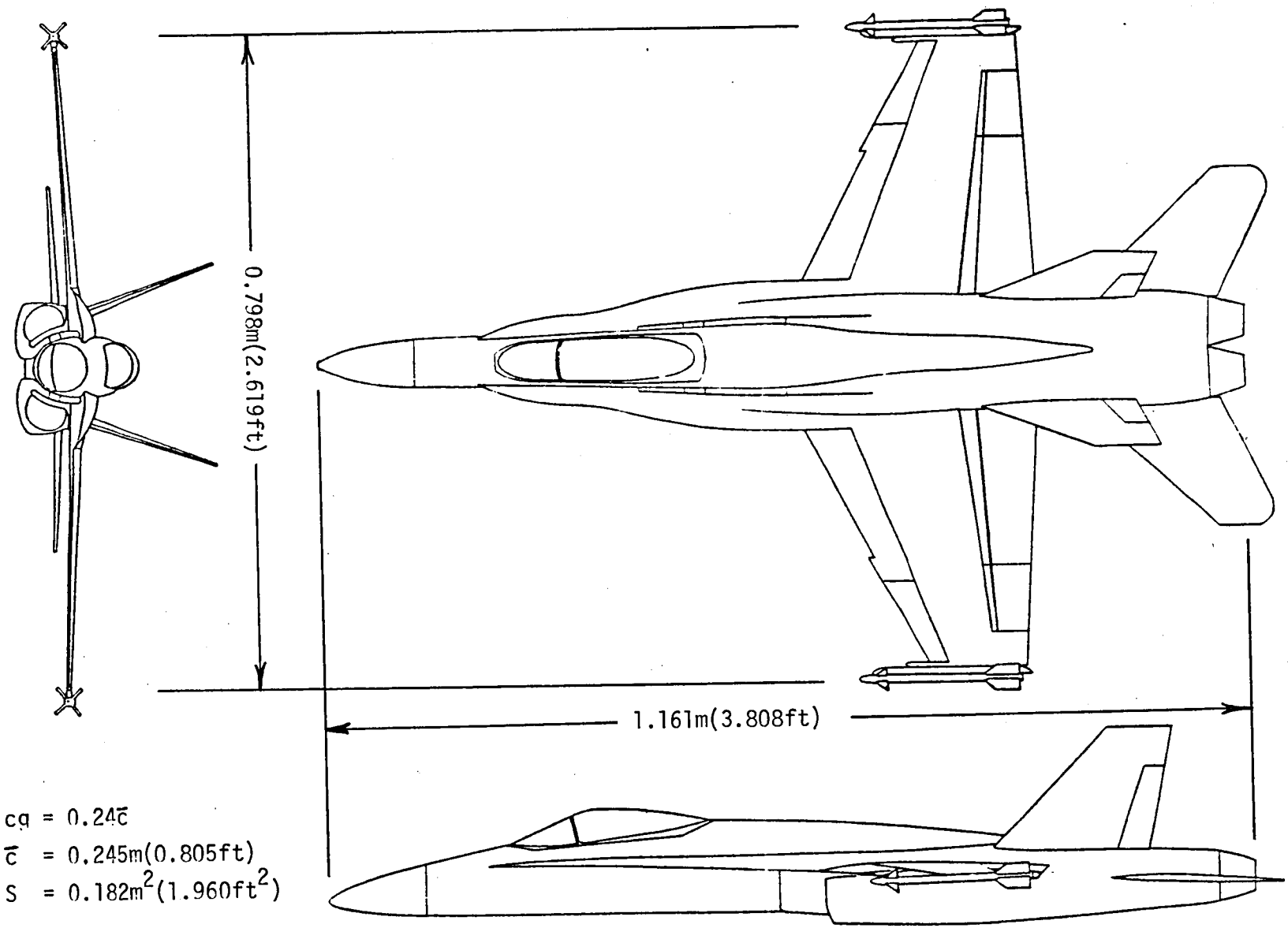

Figure 2 Sketch of Basic Model

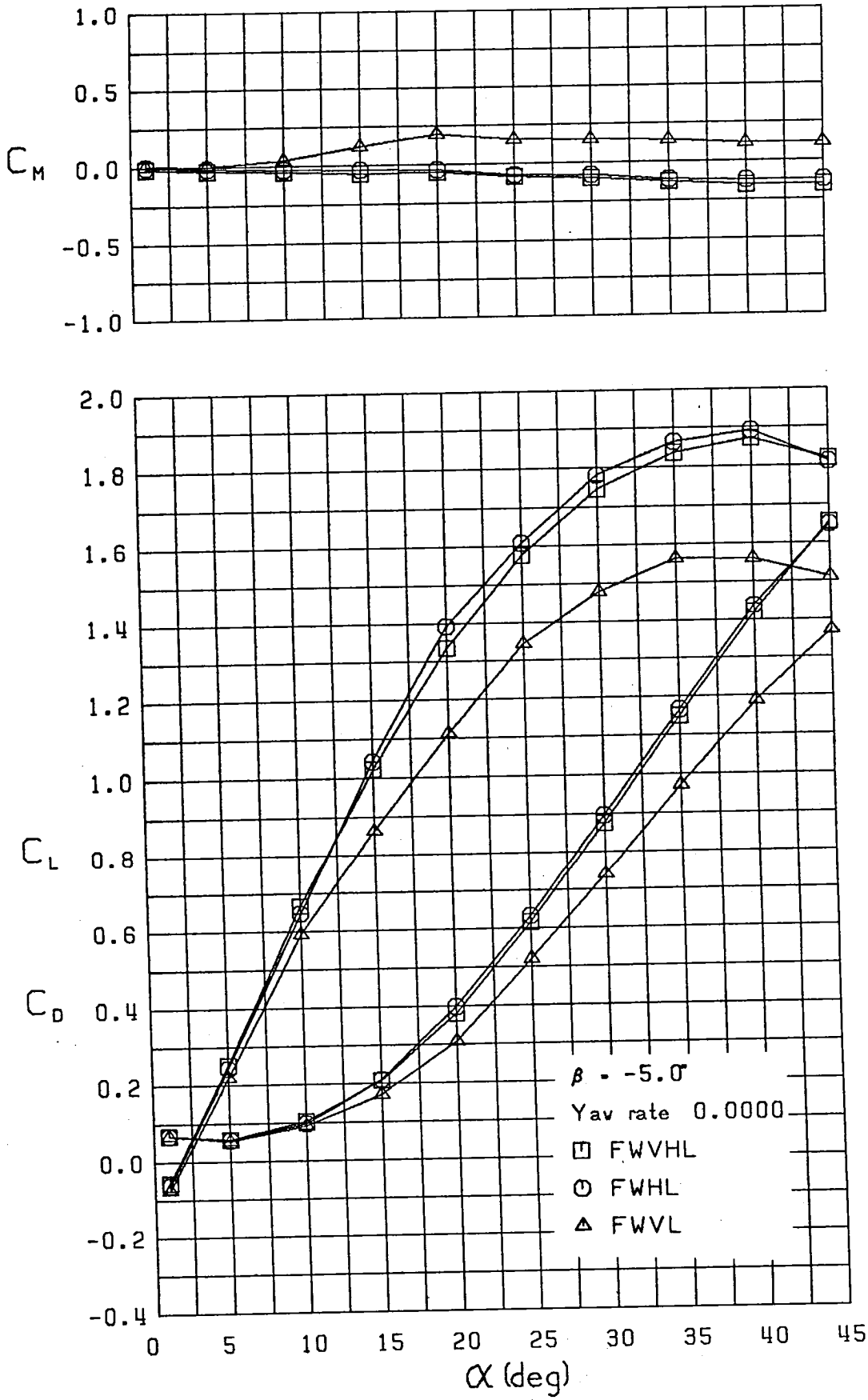

Figure 3 Longitudinal Characteristics - Configurations 1,9,10

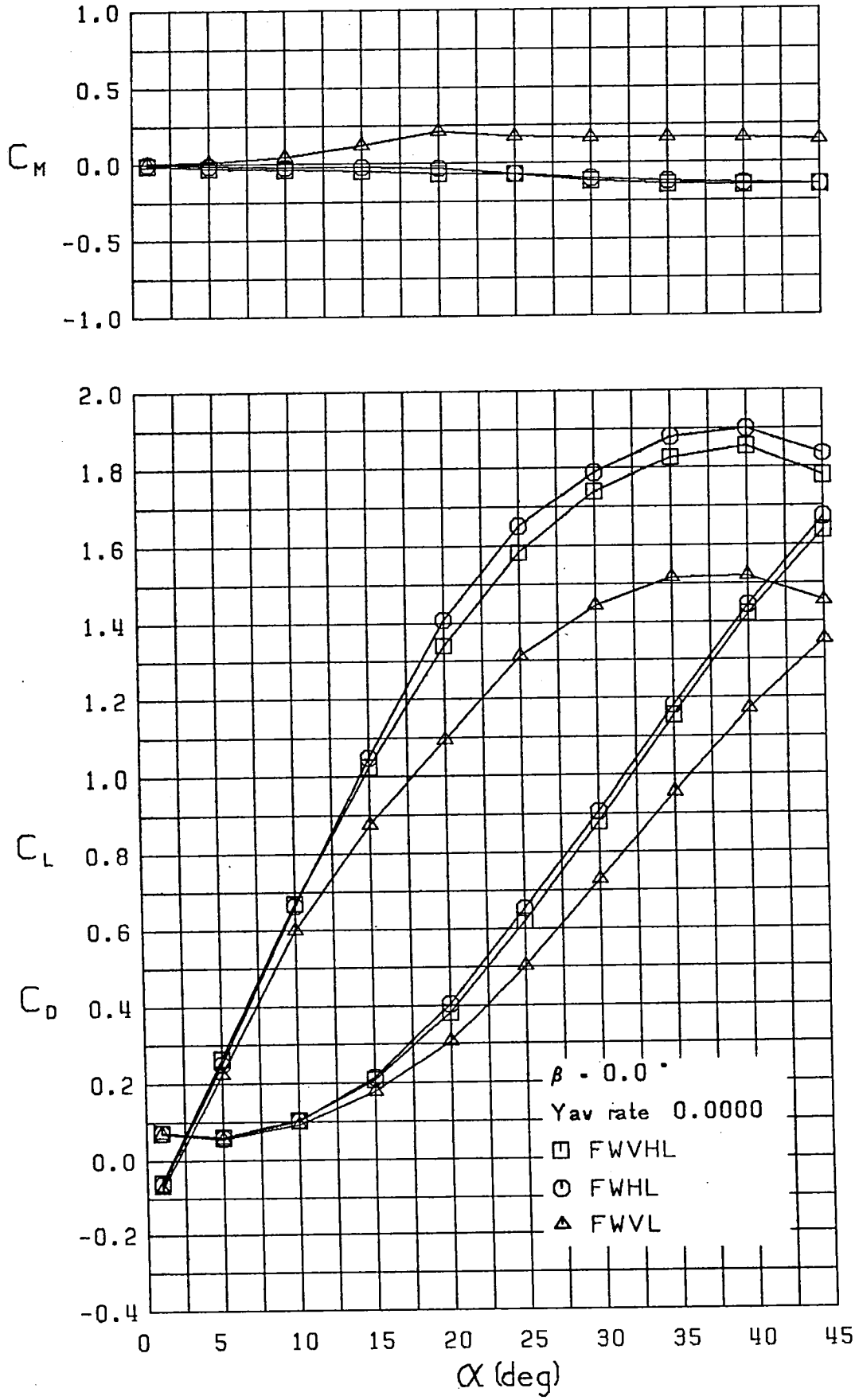

Figure 3 (Continued)

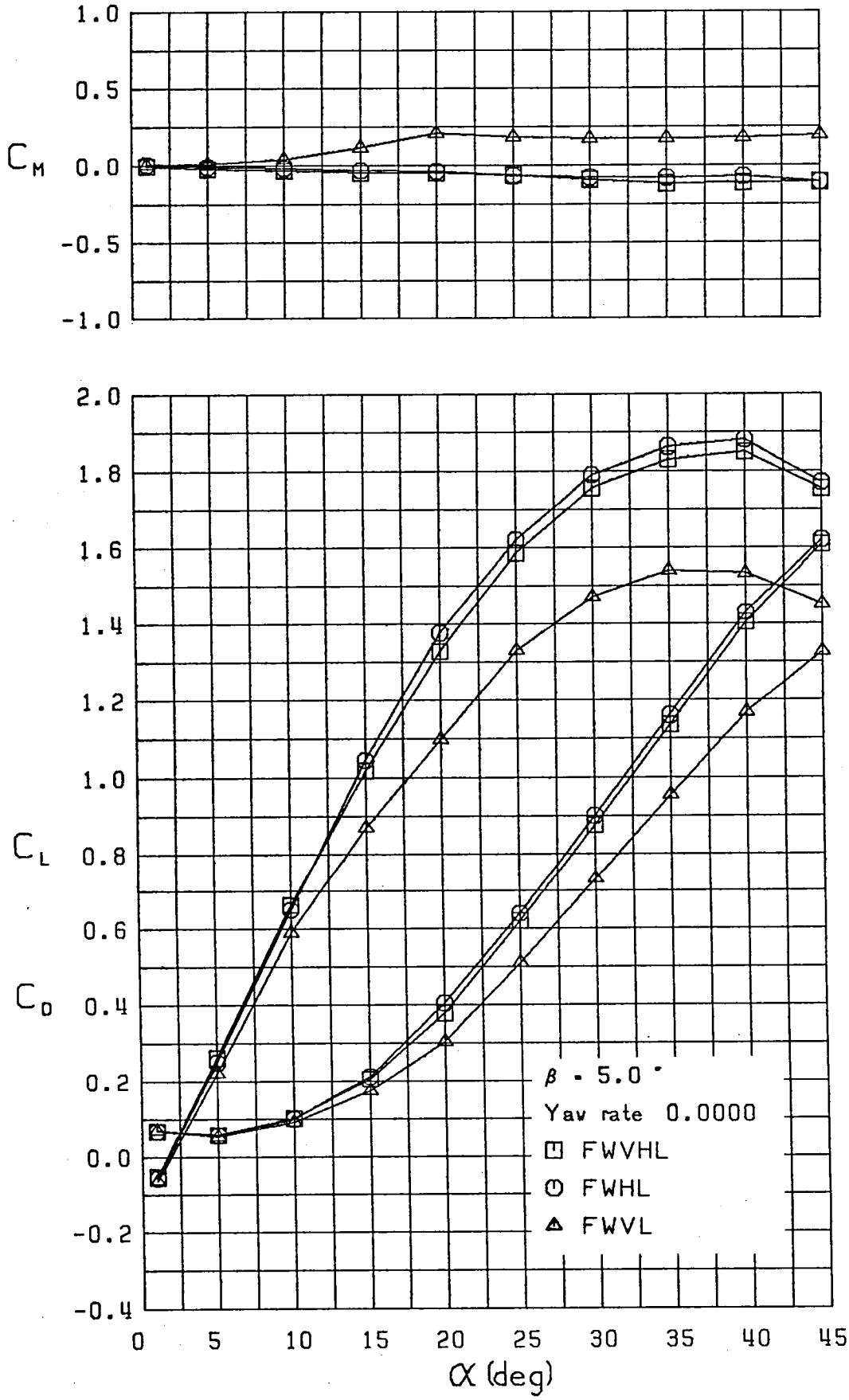

Figure 3 (Continued)

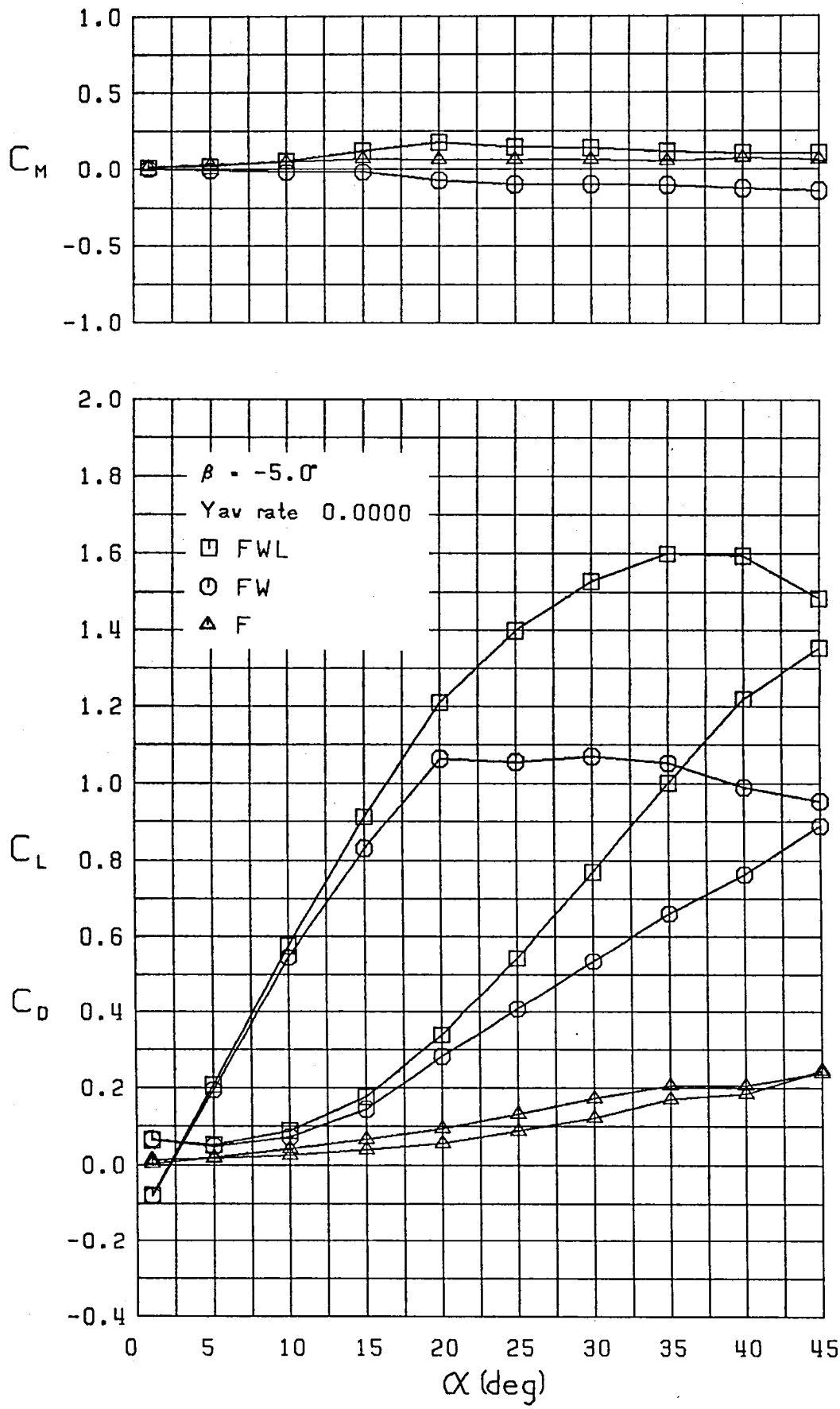

Figure 4 Longitudinal Characteristics - Configurations 13,14,15

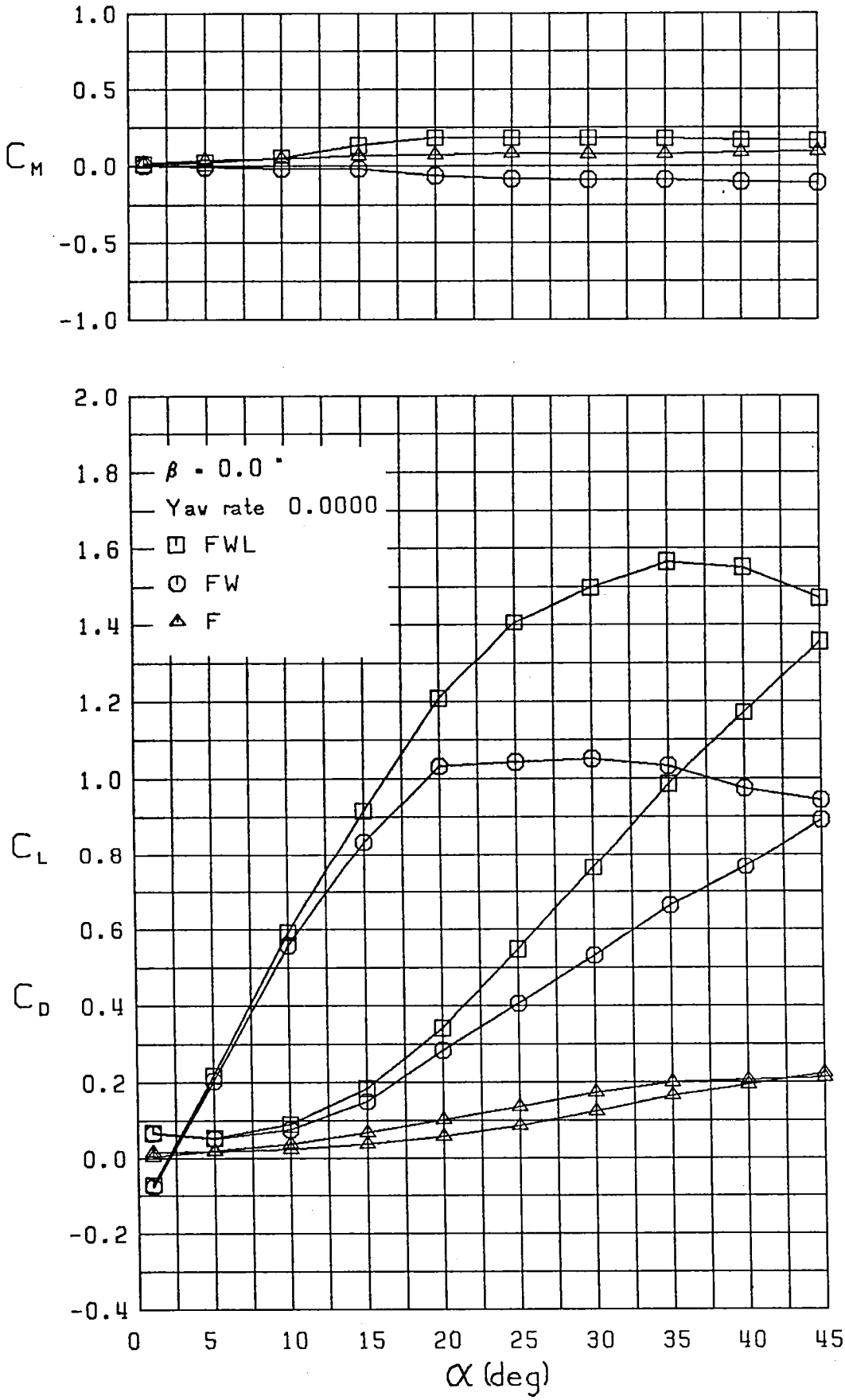

Figure 4 (Continued)

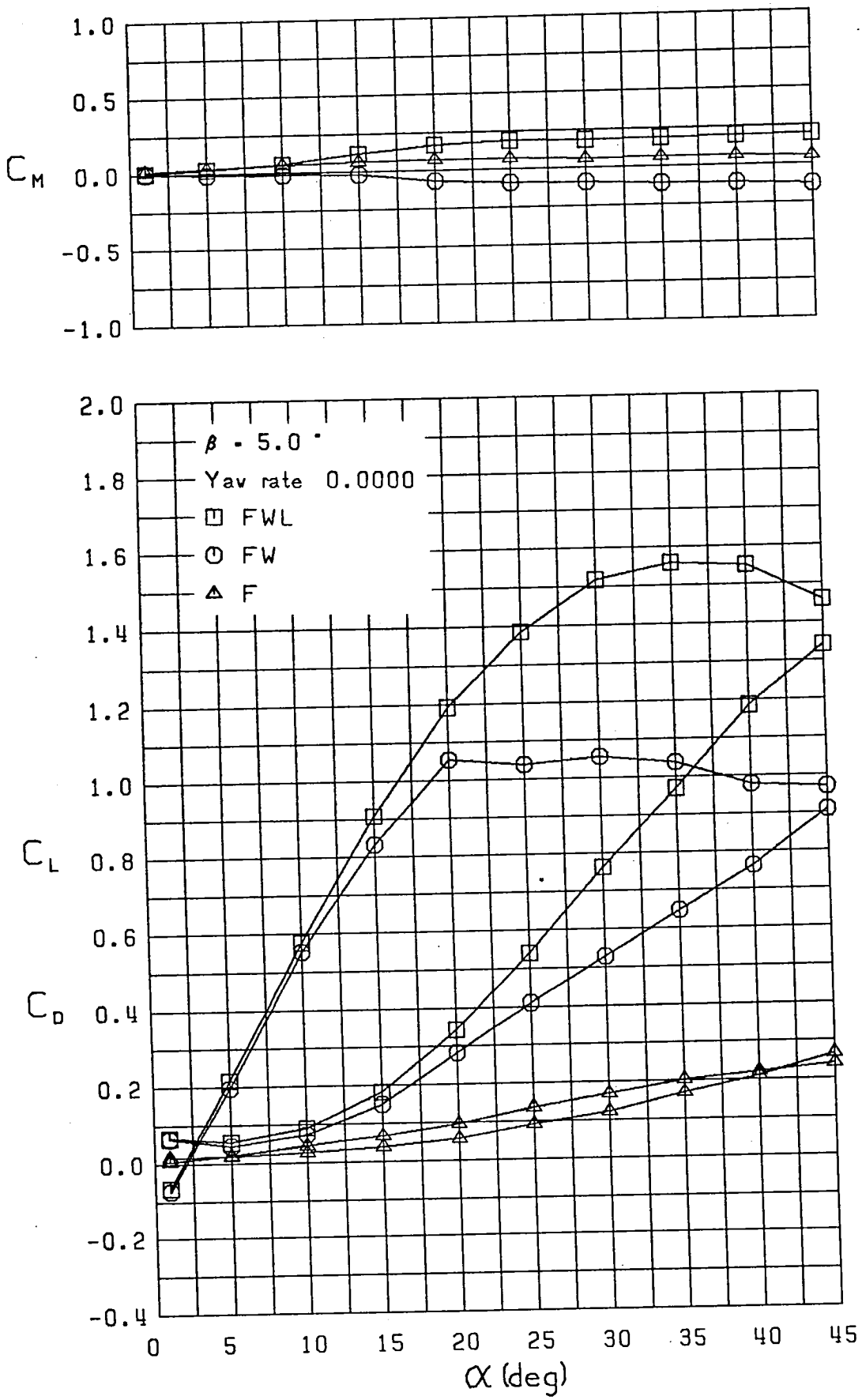

Figure 4 (Continued)

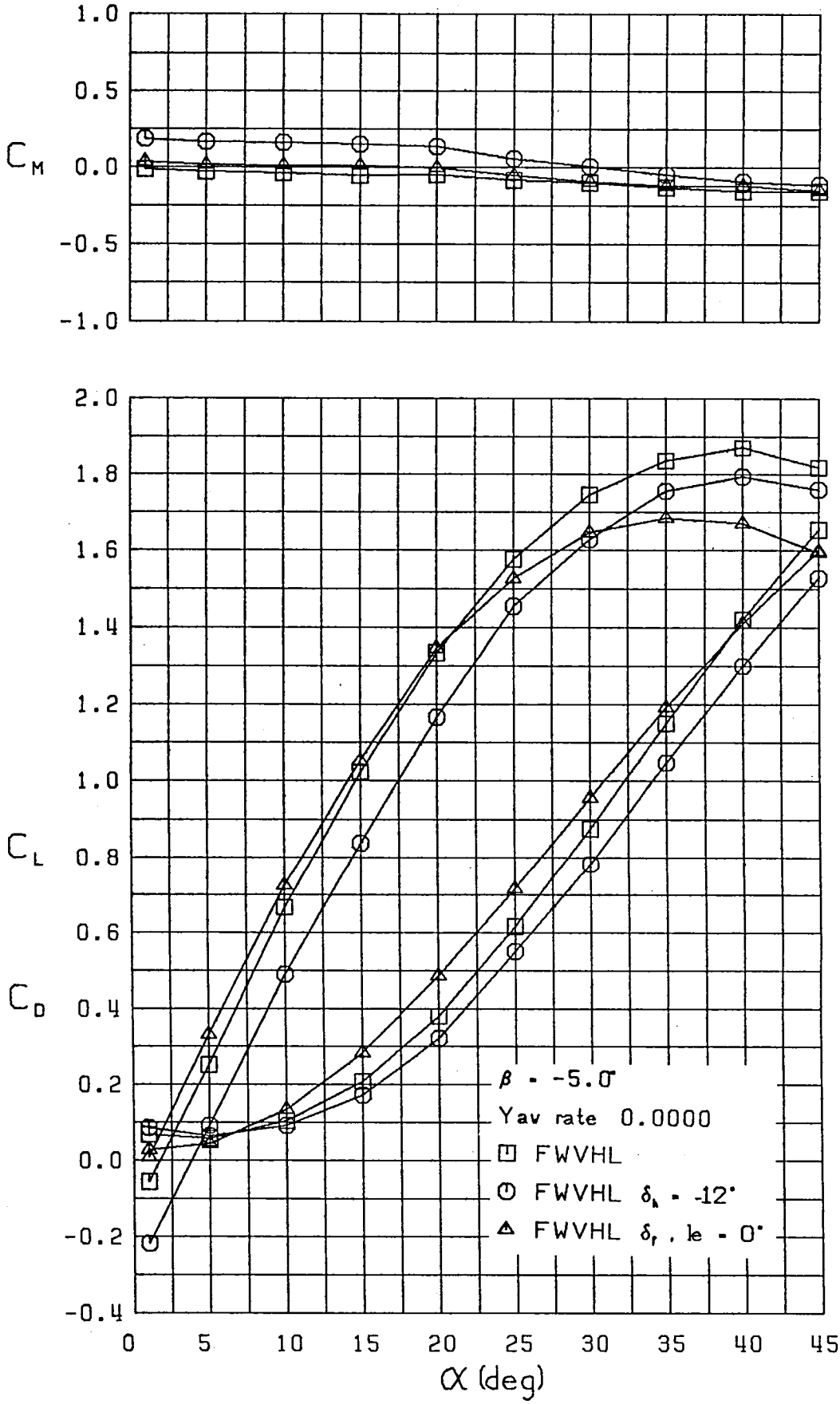

Figure 5 Longitudinal Characteristics - Configurations 1,2,3

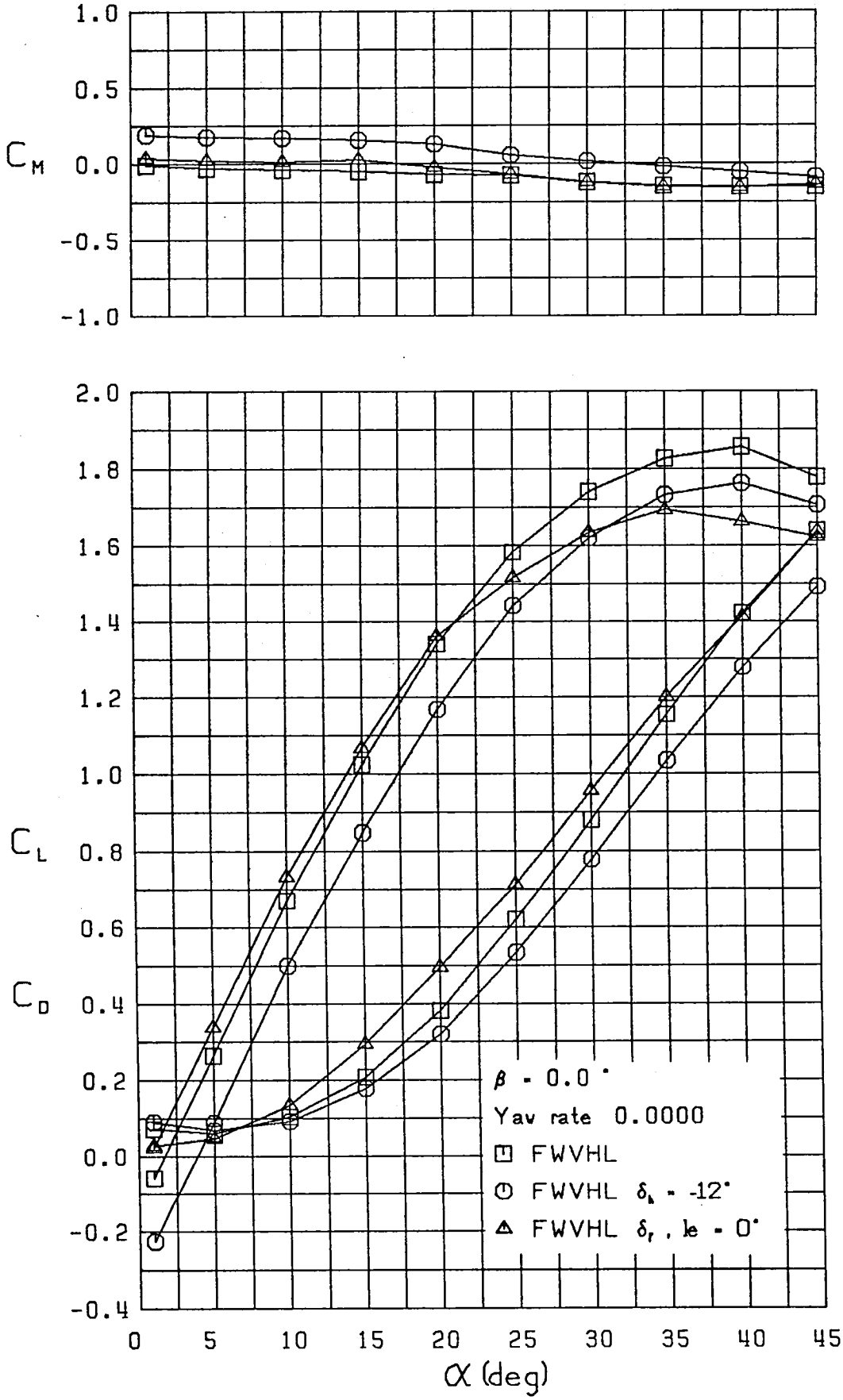

Figure 5 (Continued)

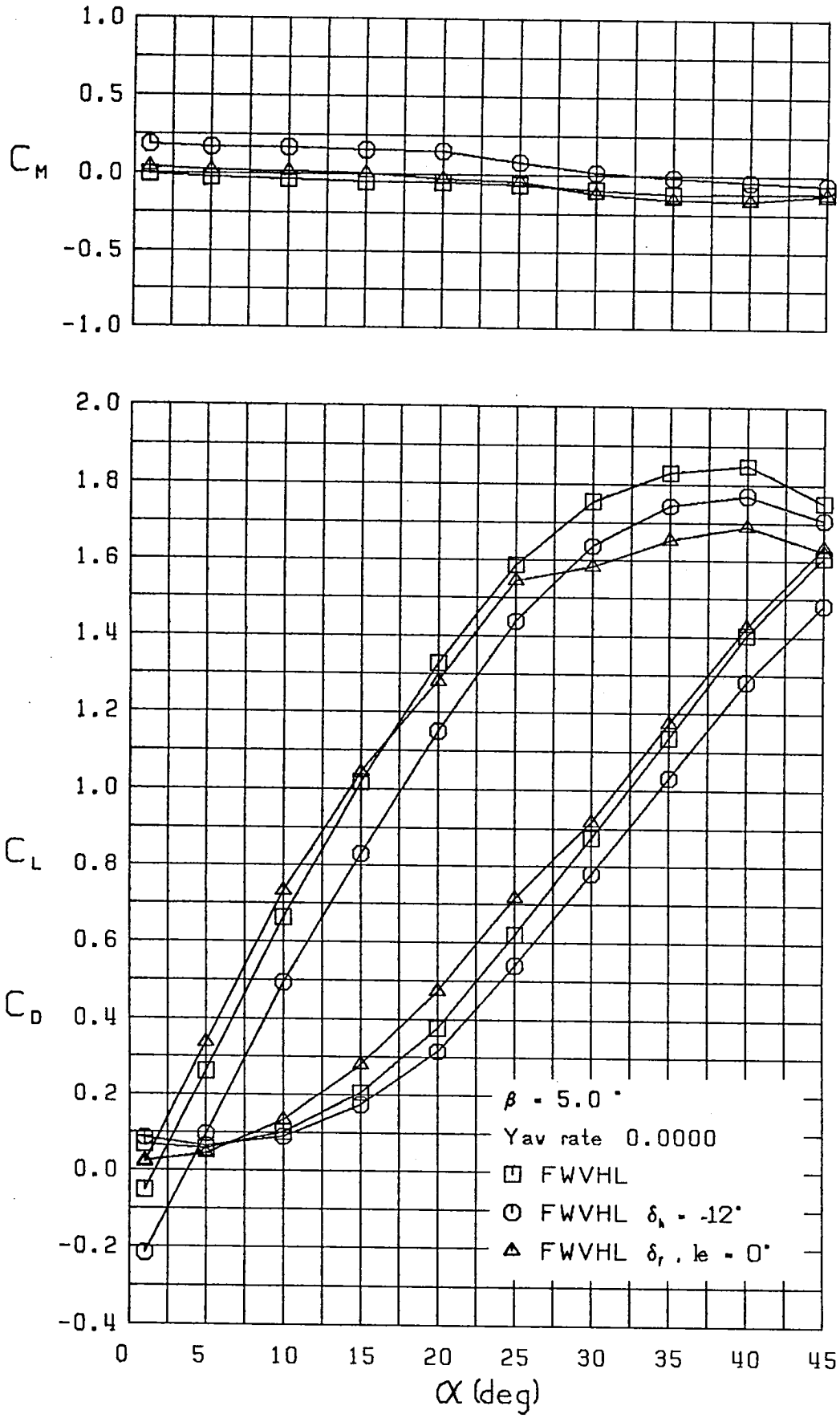

Figure 5 (Continued)

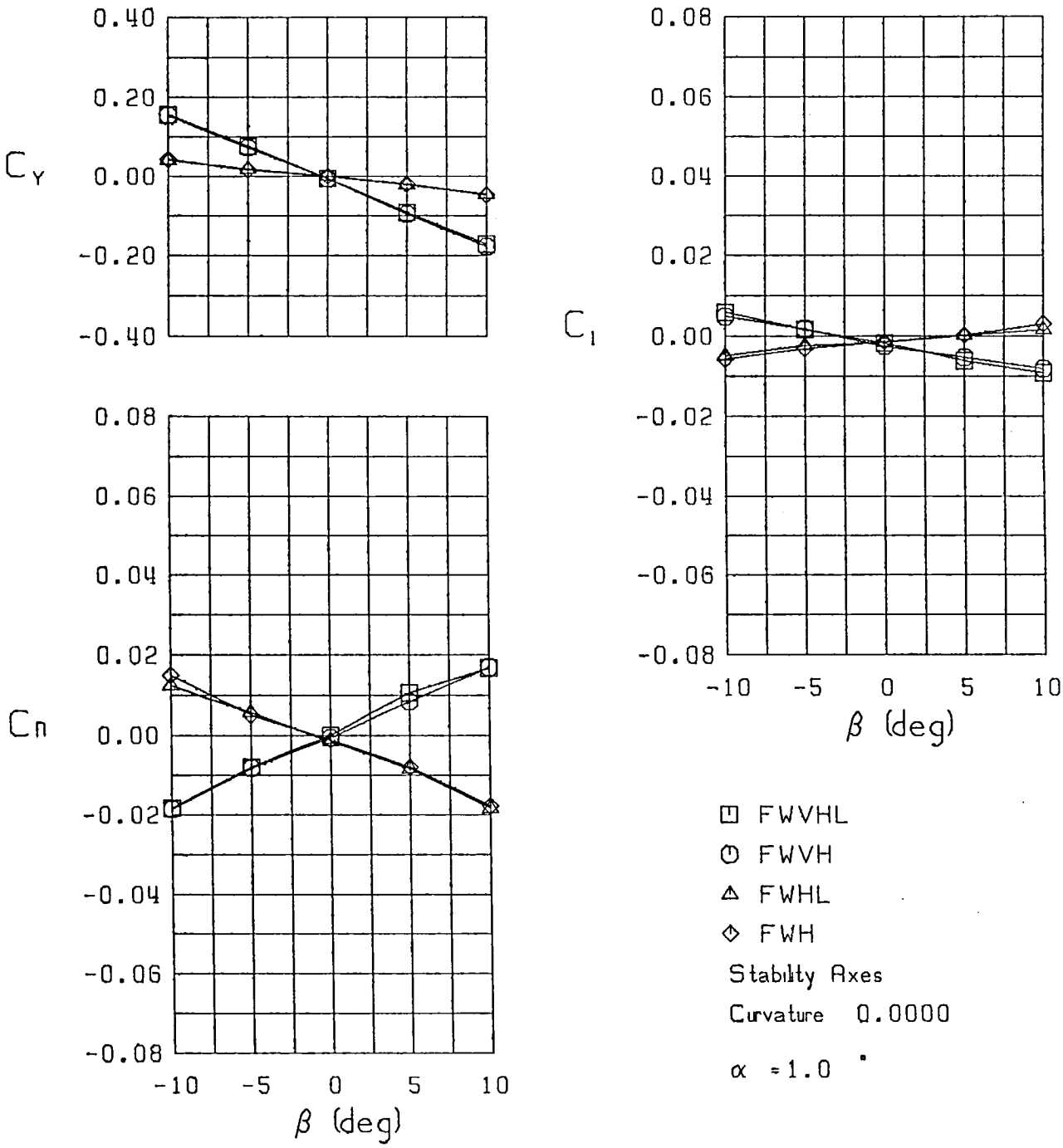

Figure 6 Variation of Static Lateral-Directional Characteristics With Angle of Sideslip - Configurations 1,6,9,11

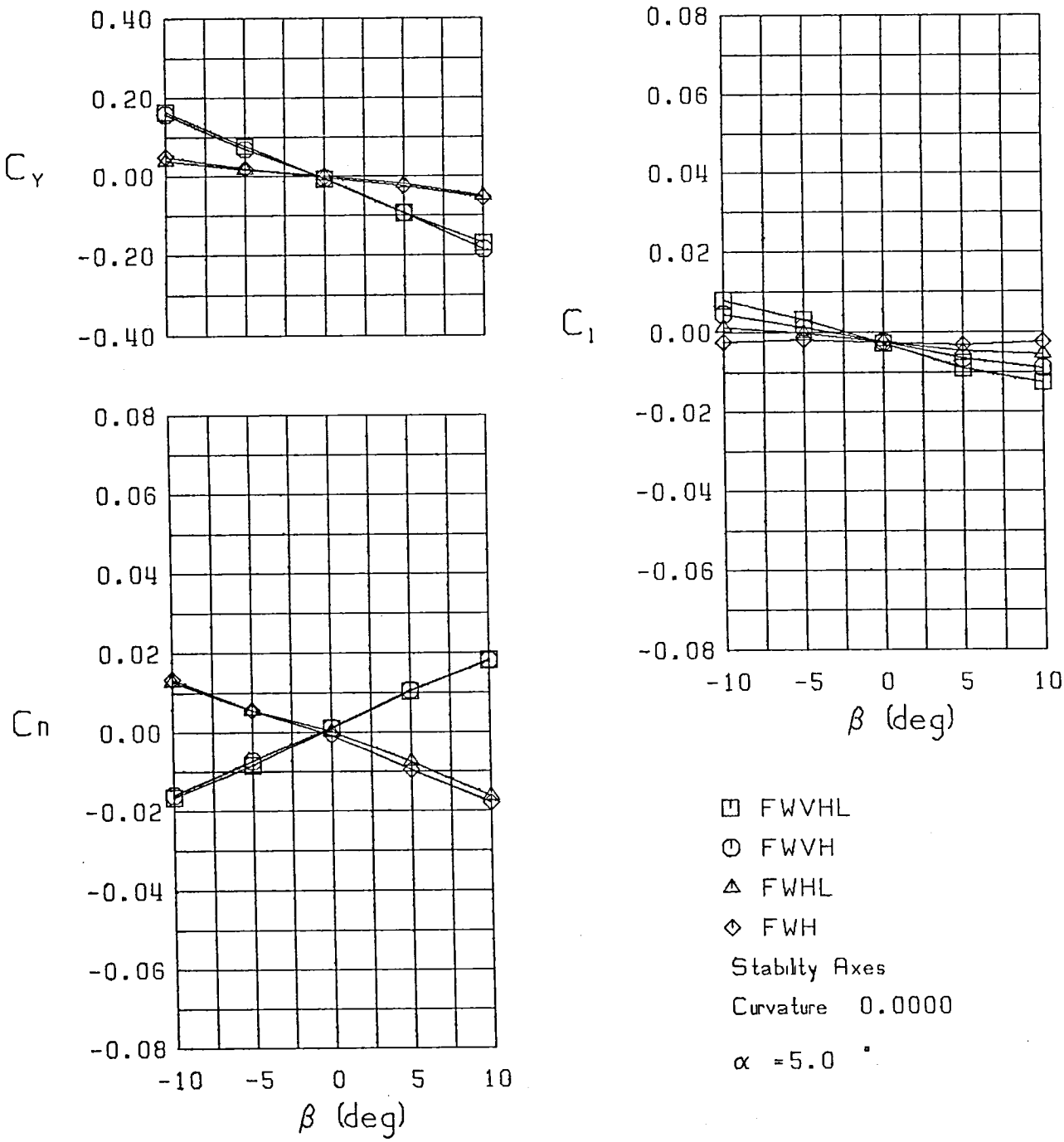

Figure 6 (Continued)

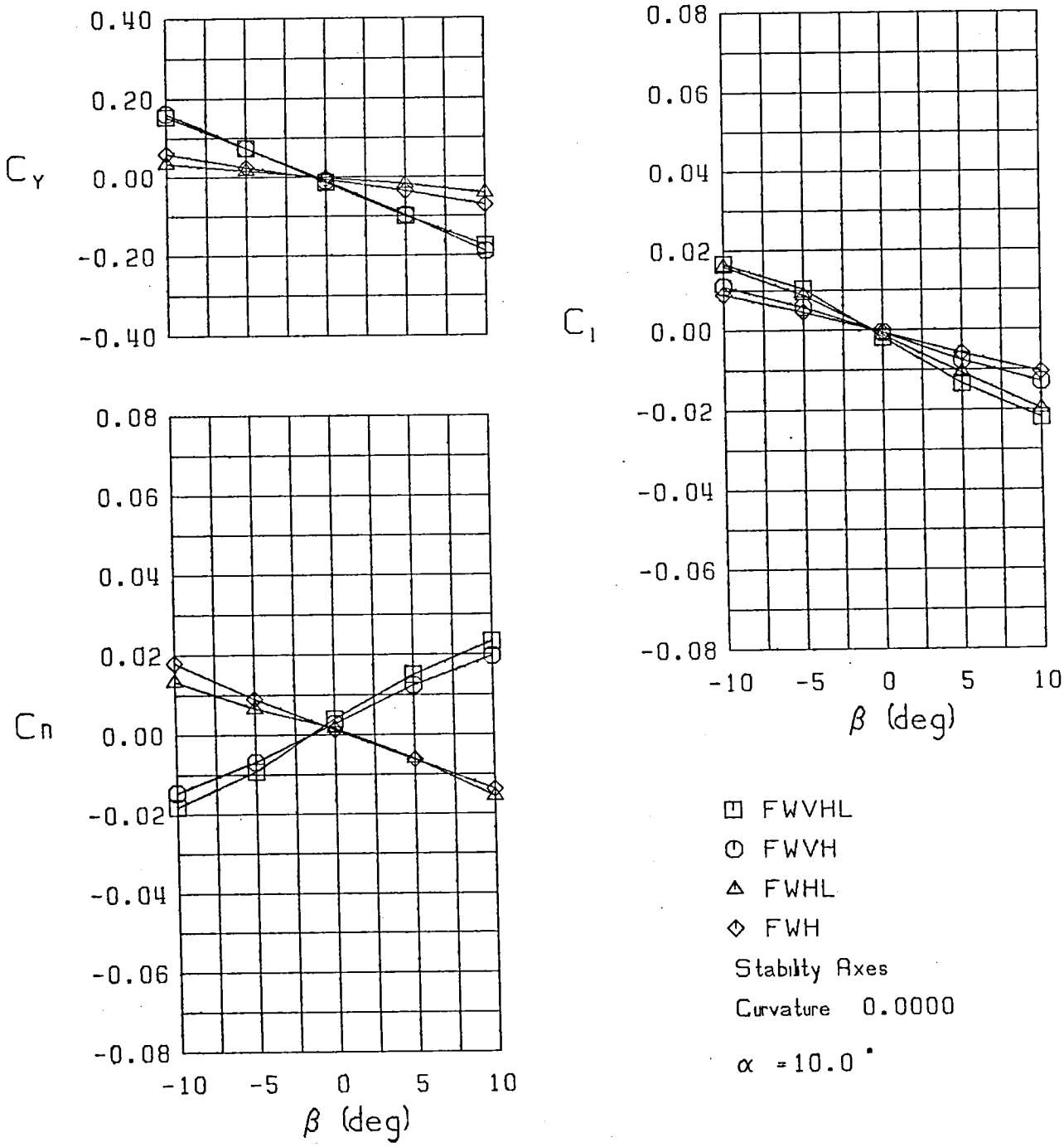

Figure 6 (Continued)

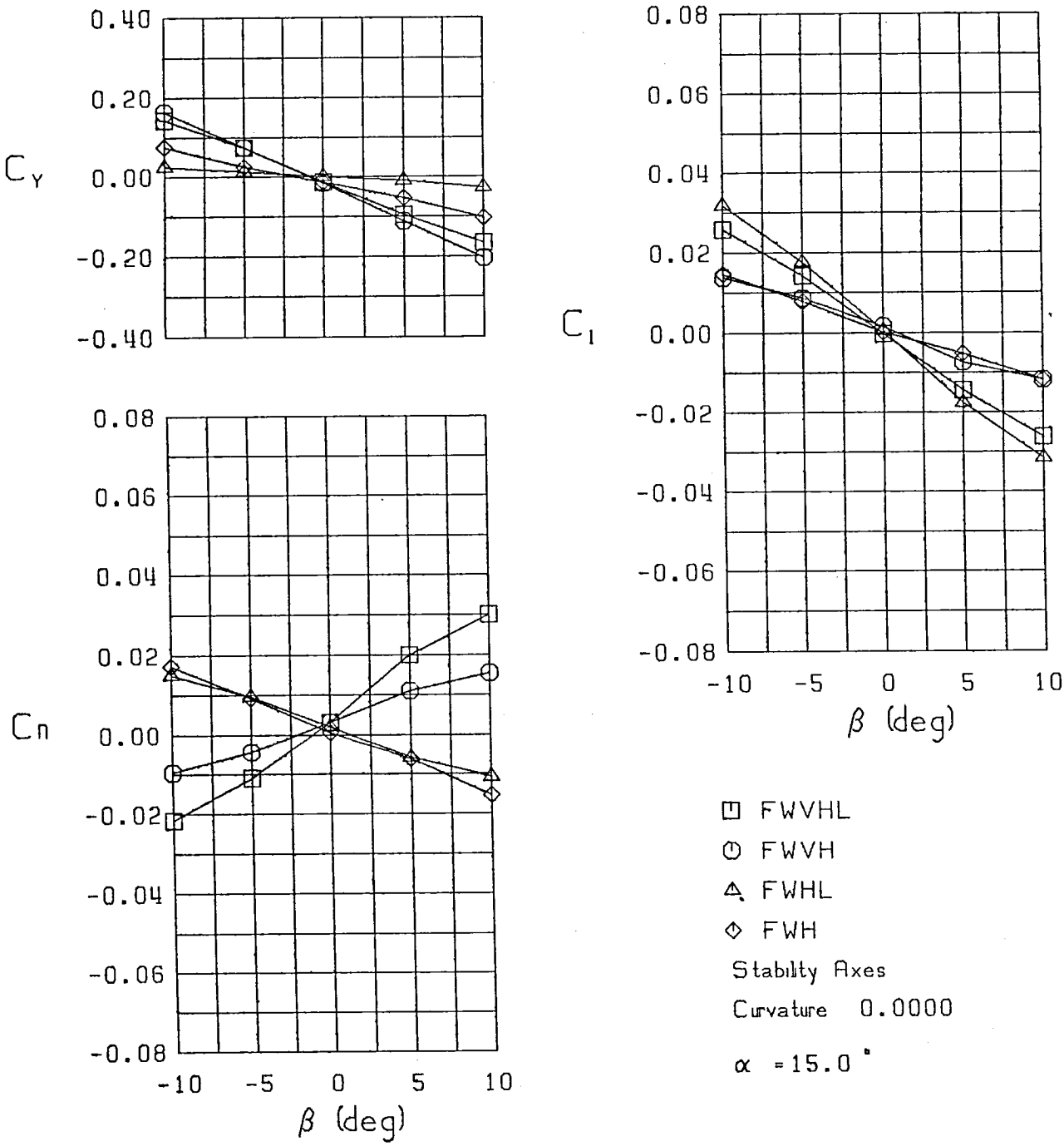

Figure 6 (Continued)

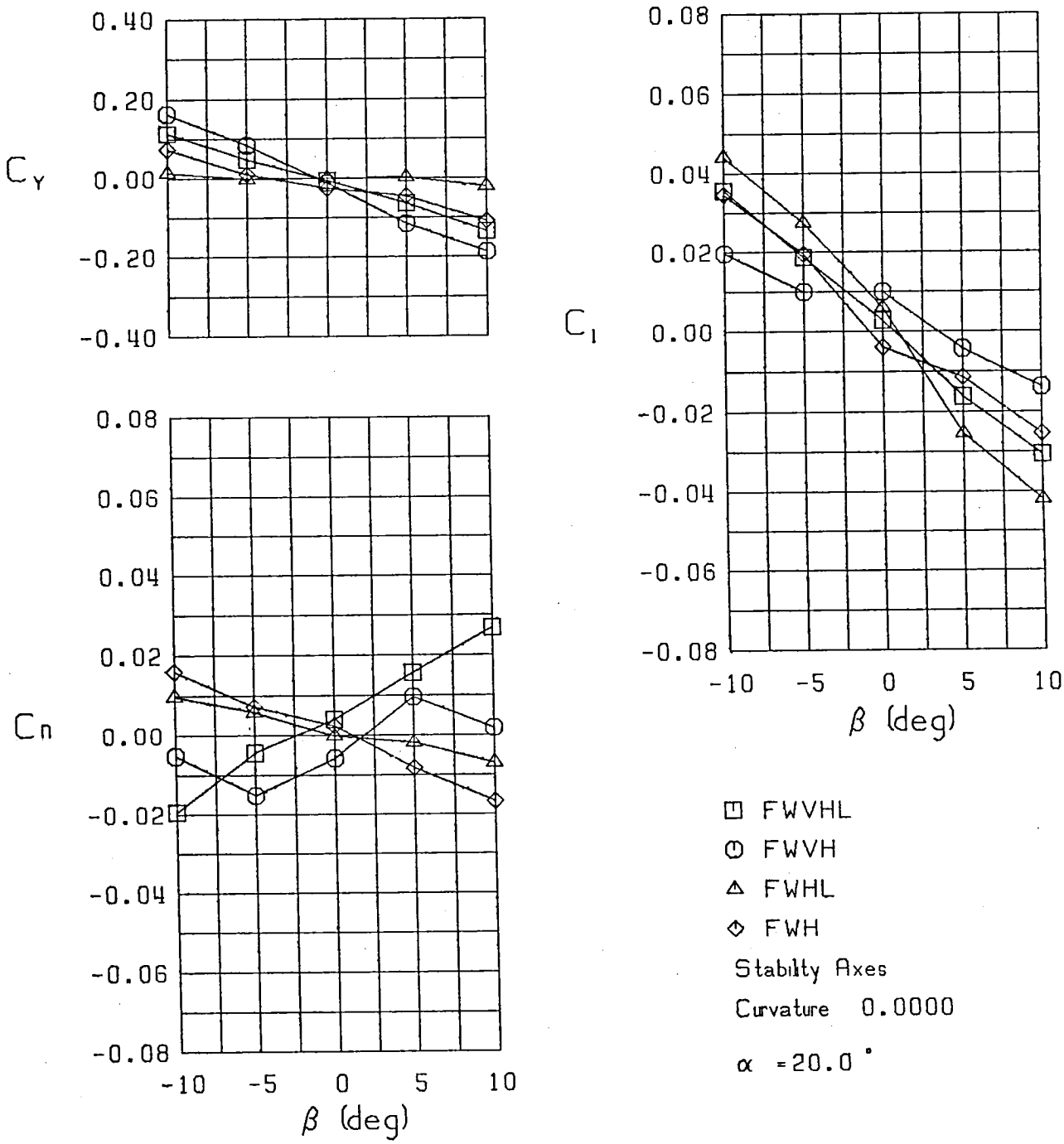

Figure 6 (Continued)

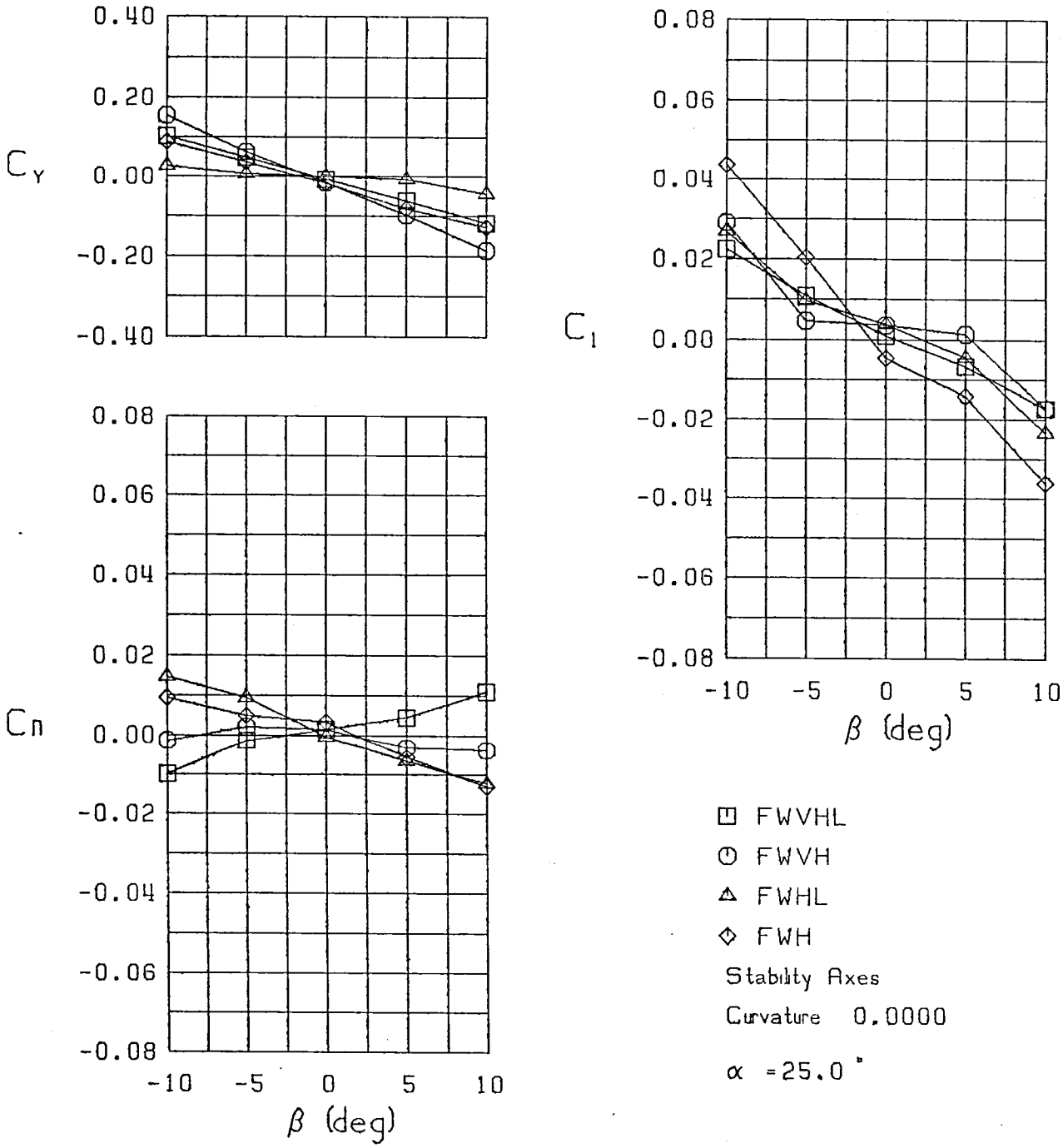

Figure 6 (Continued)

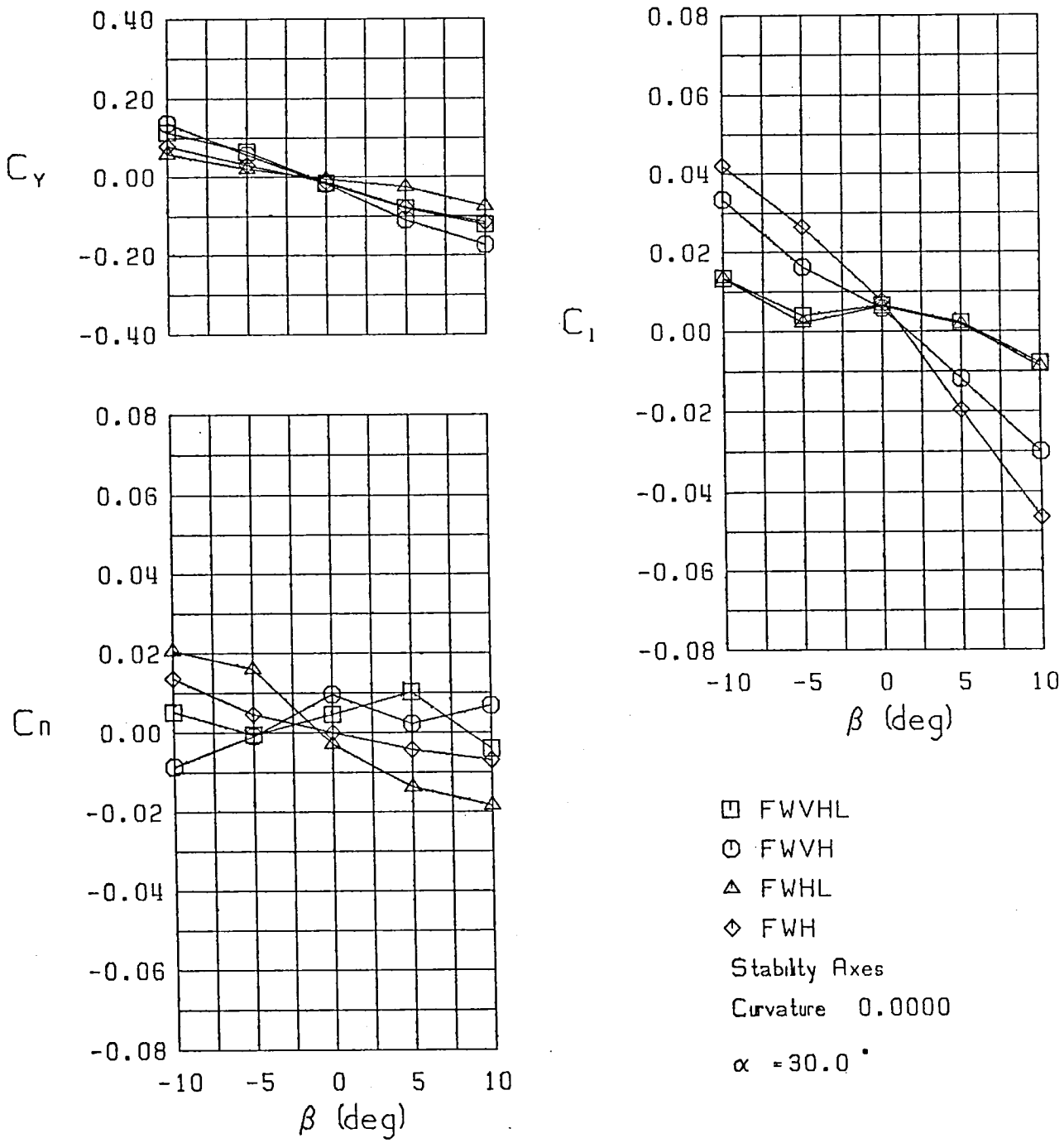

Figure 6 (Continued)

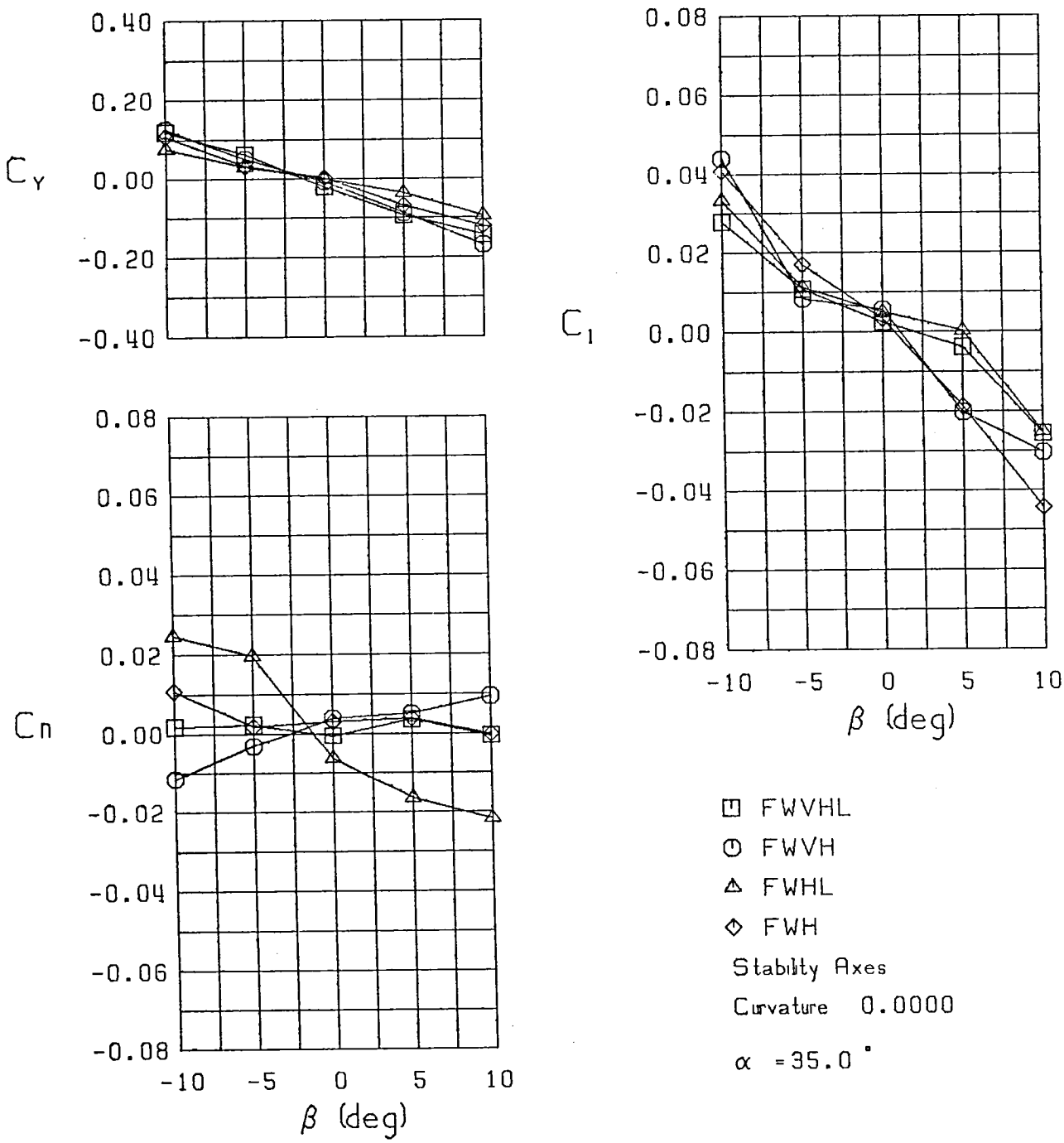

Figure 6 (Continued)

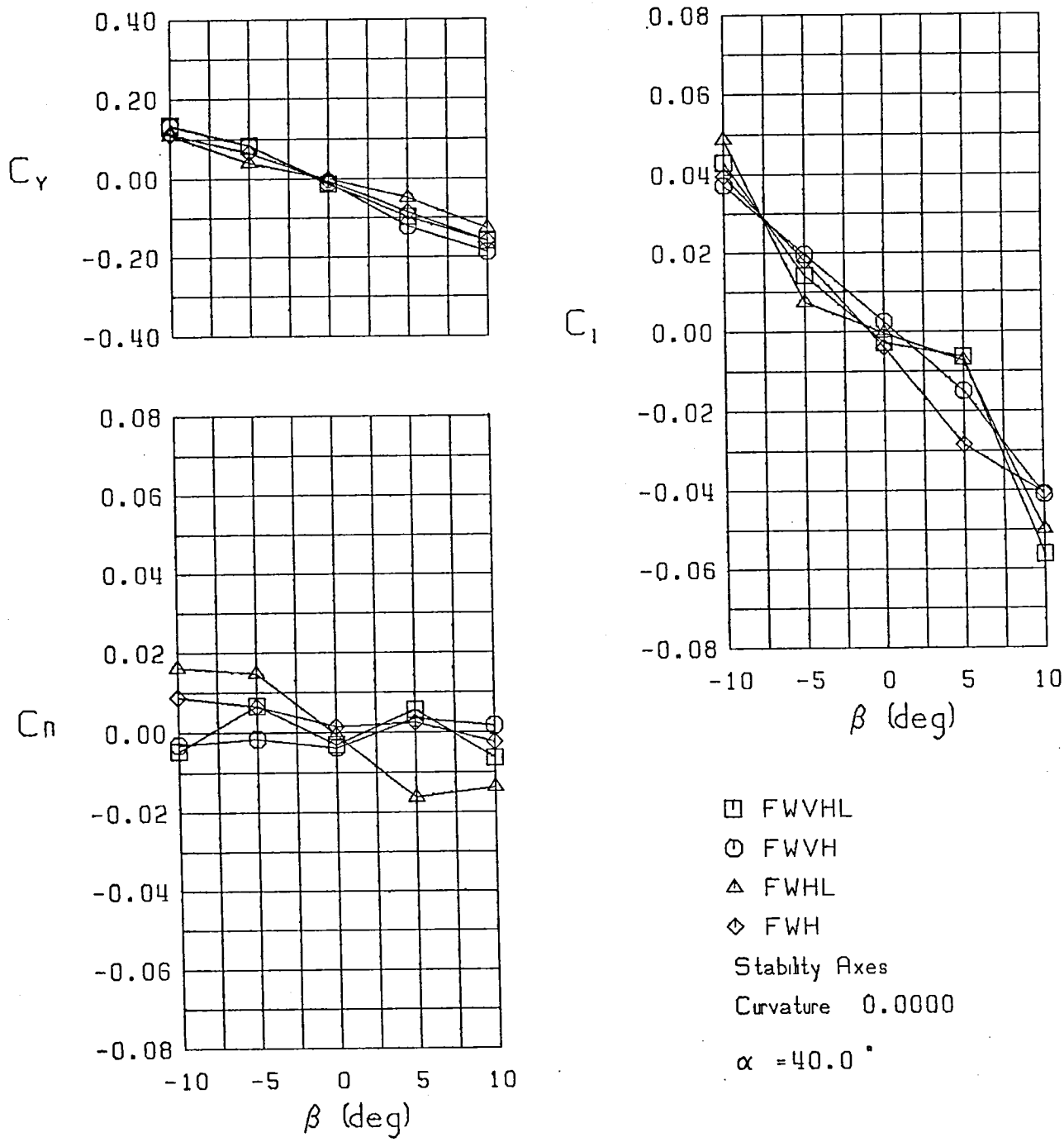

Figure 6 (Continued)

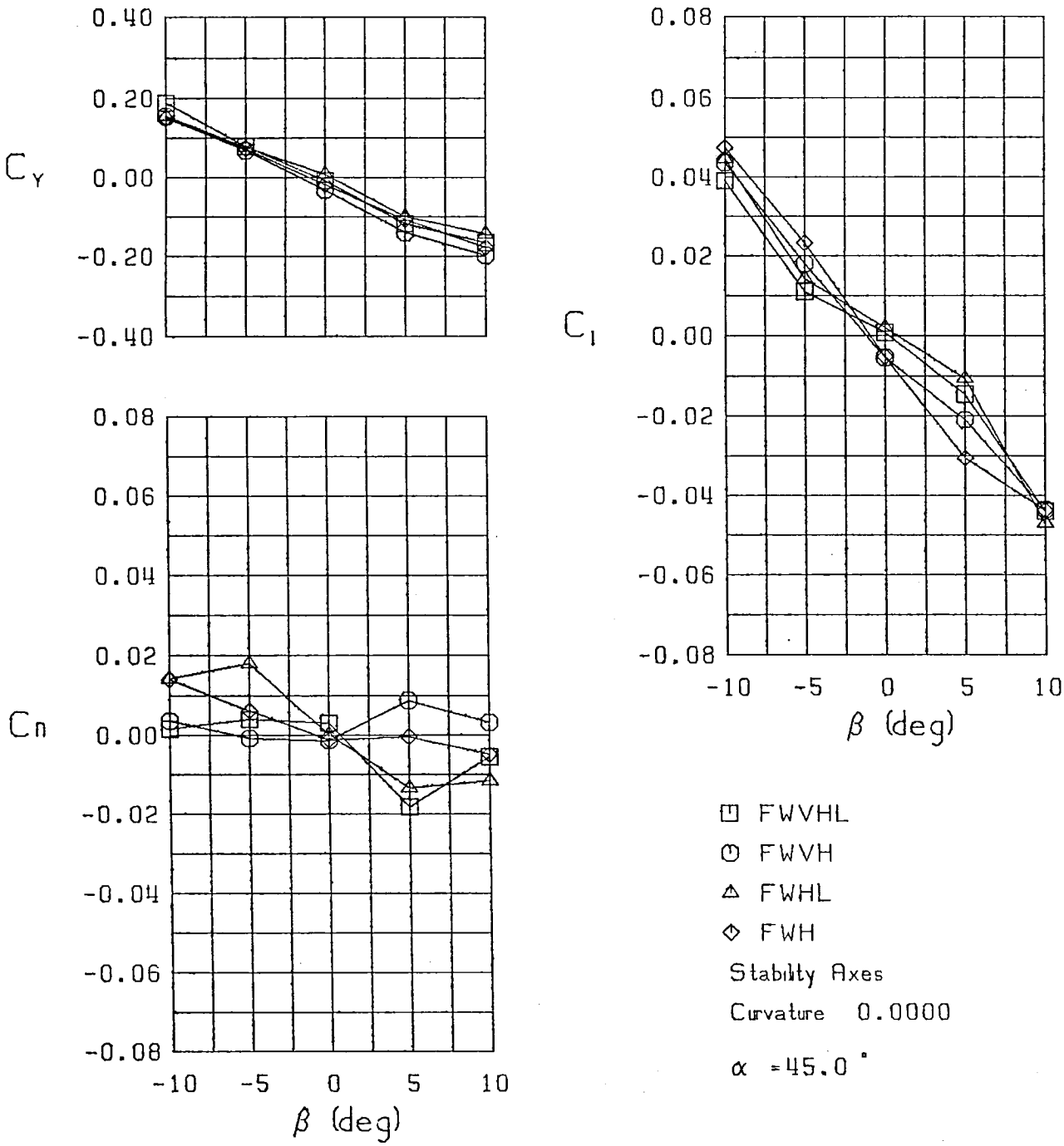

Figure 6 (Continued)

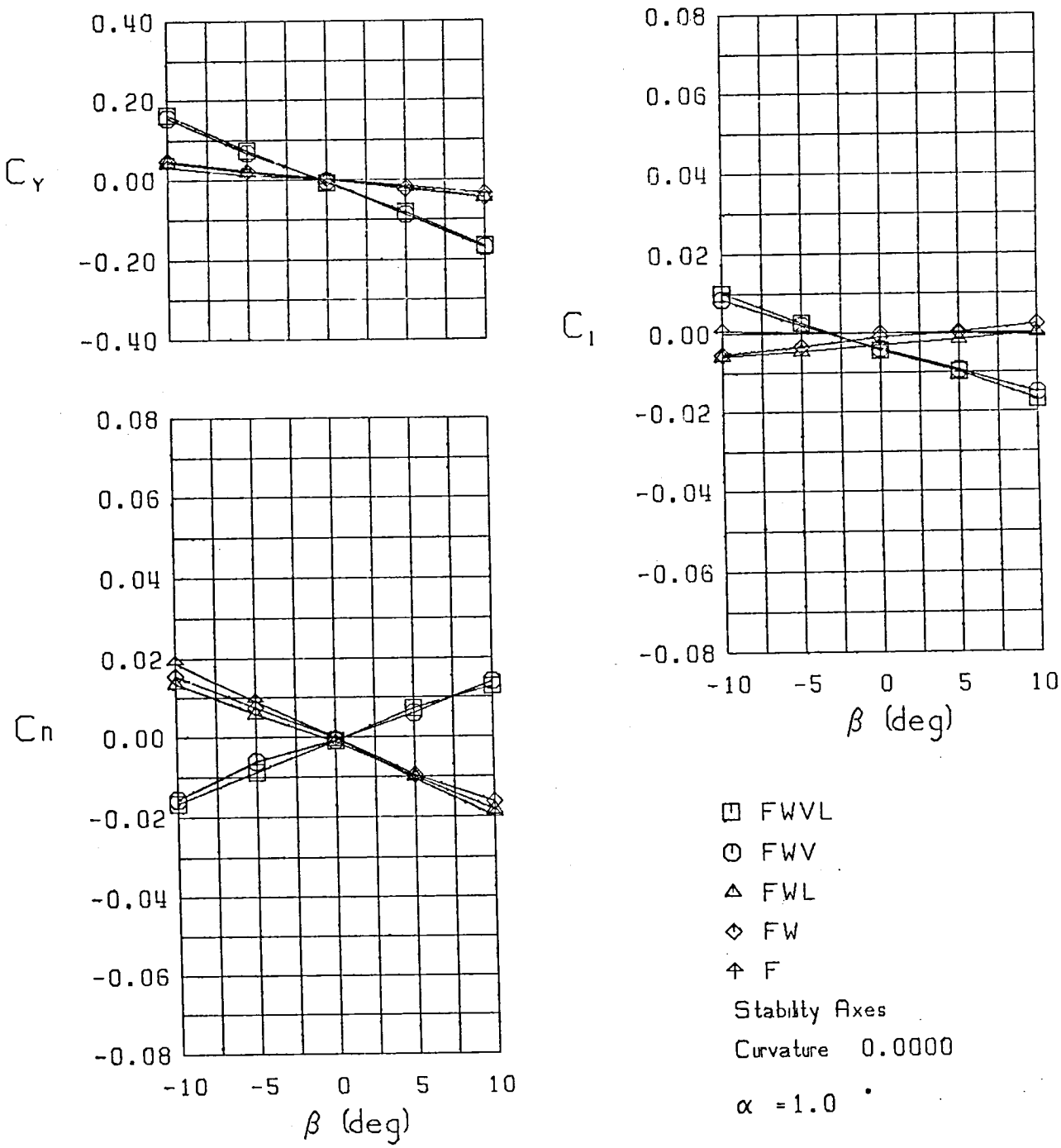

Figure 7 Variation of Static Lateral-Directional Characteristics With Angle of Sideslip - Configurations 10,12,13,14,15

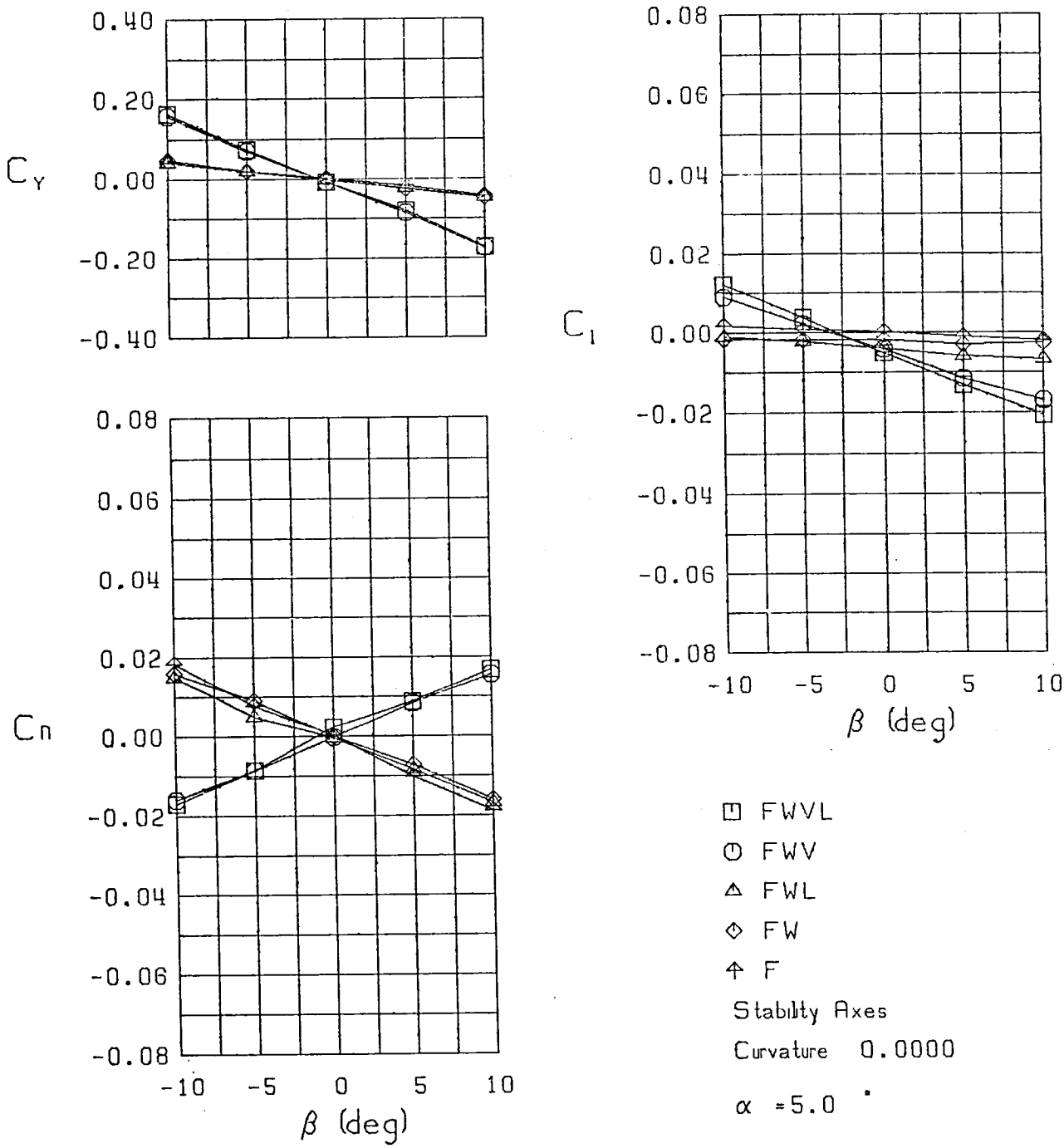

Figure 7 (Continued)

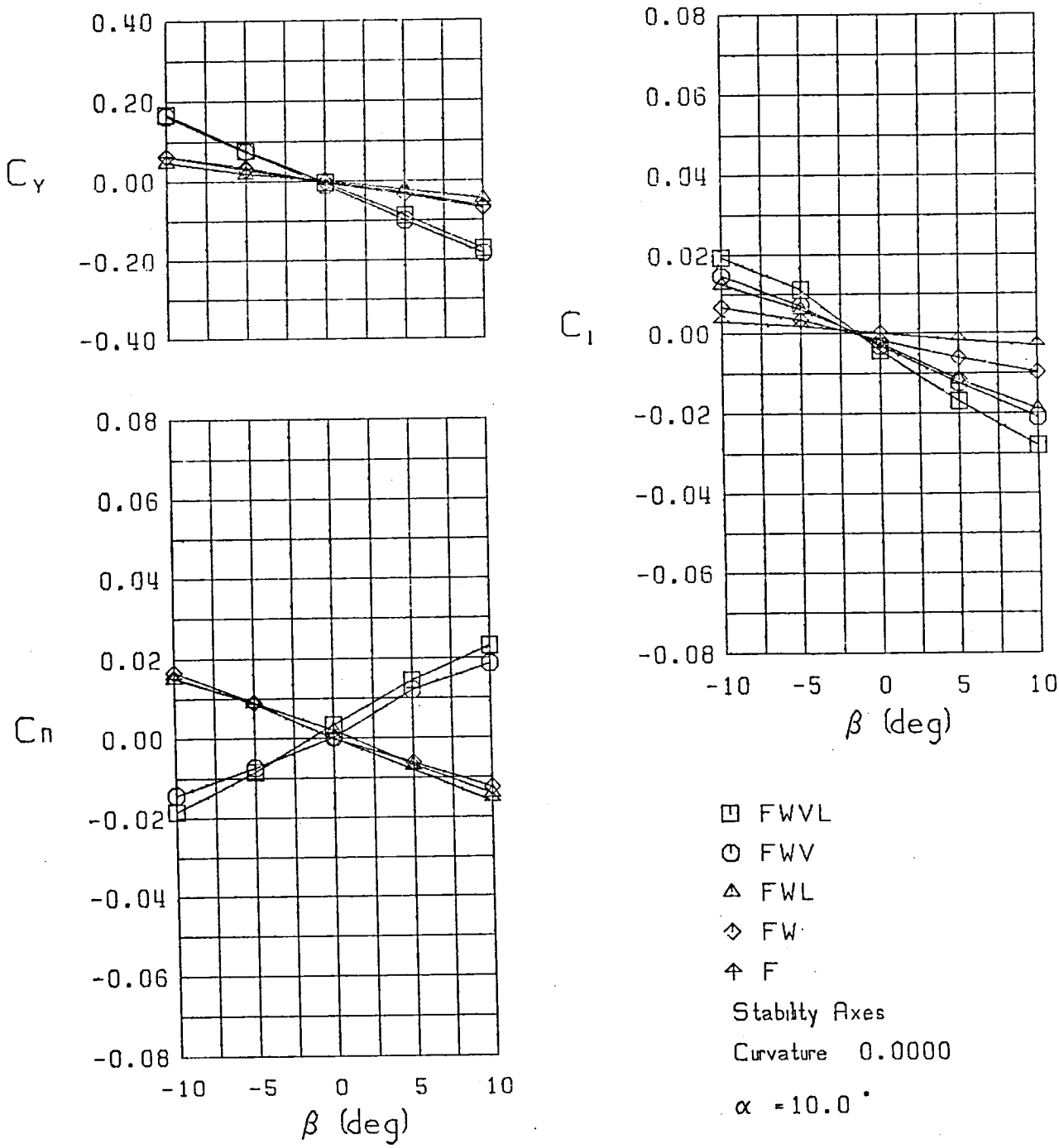

Figure 7 (Continued)

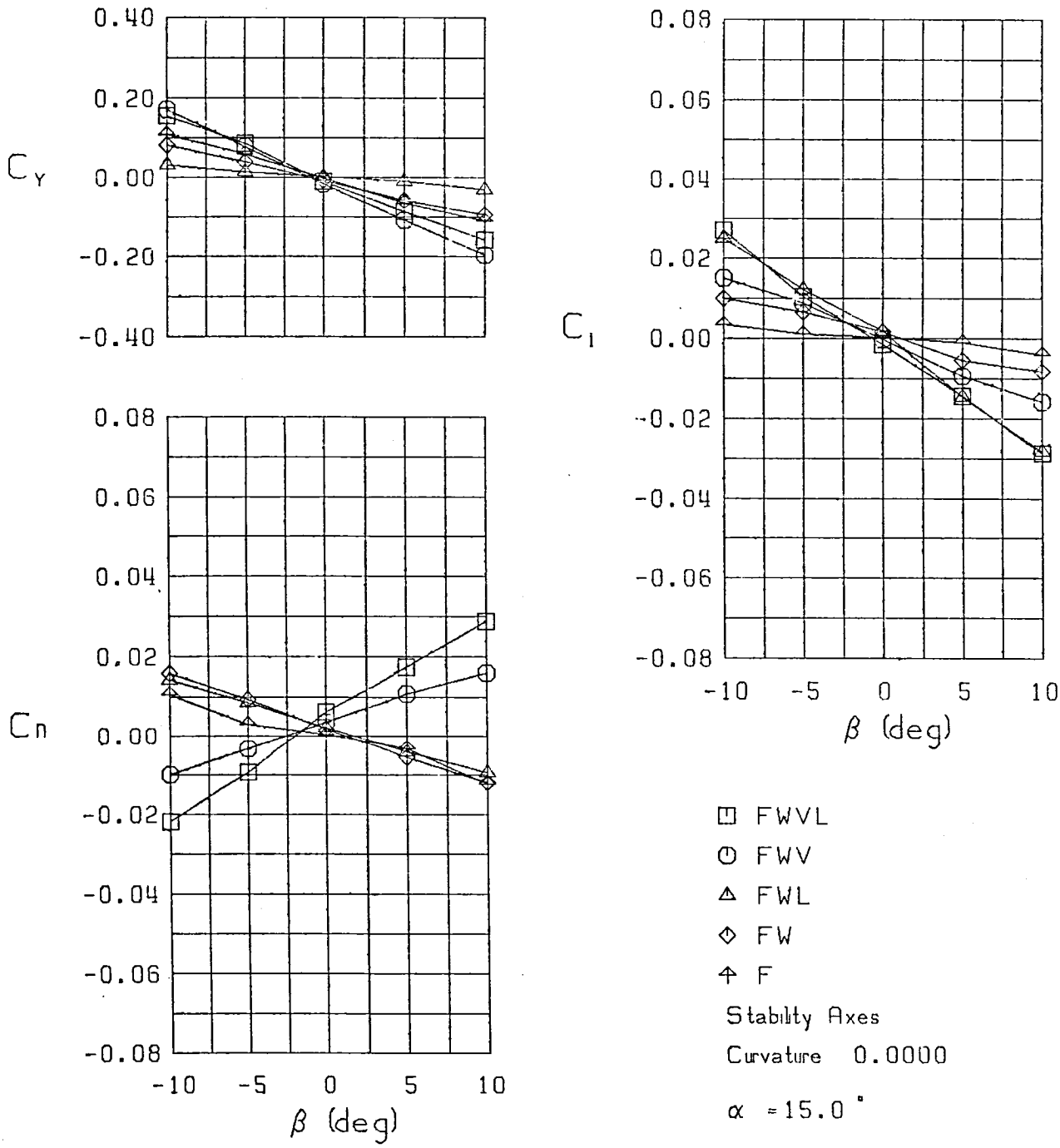

Figure 7 (Continued)

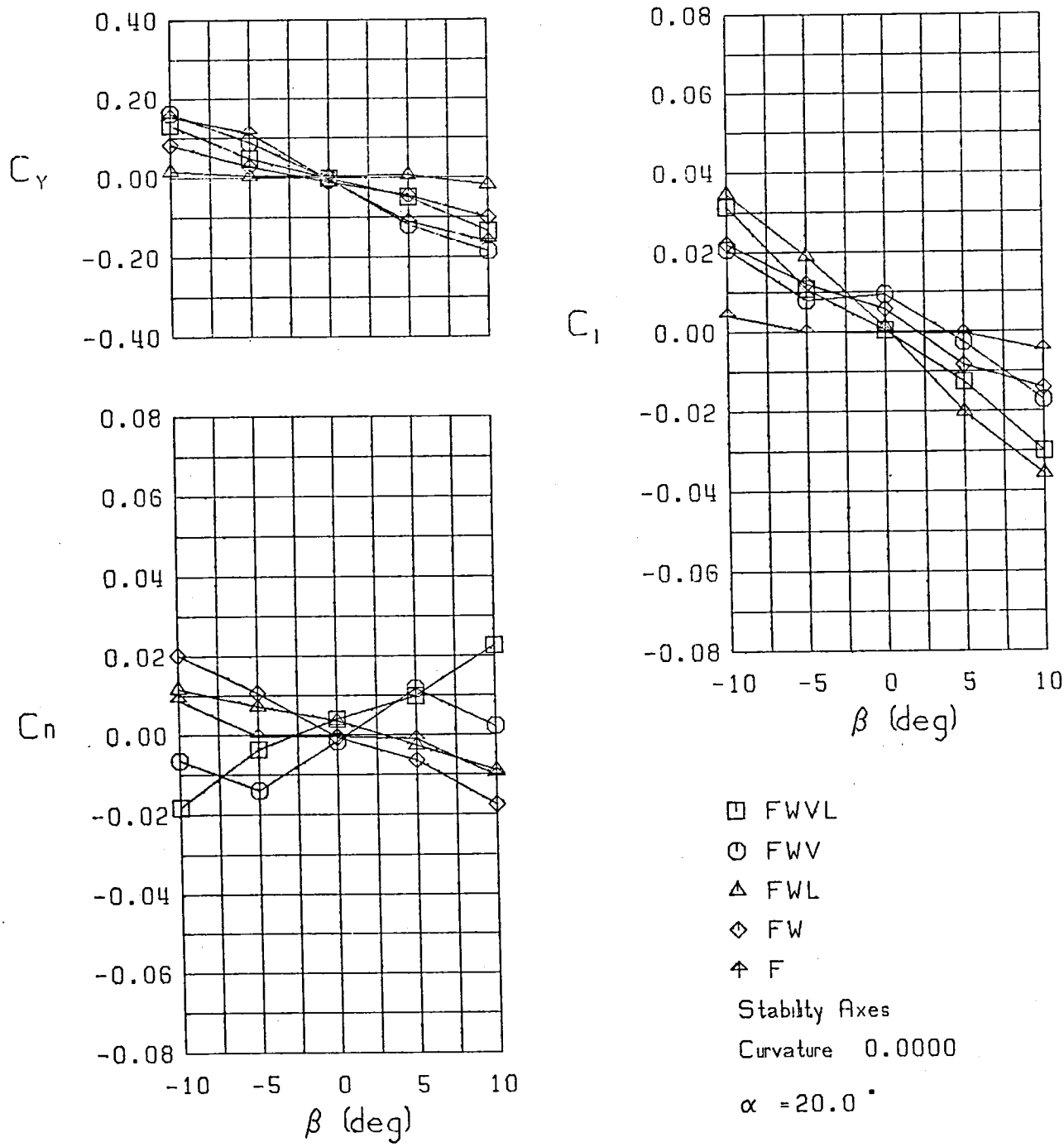

Figure 7 (Continued)

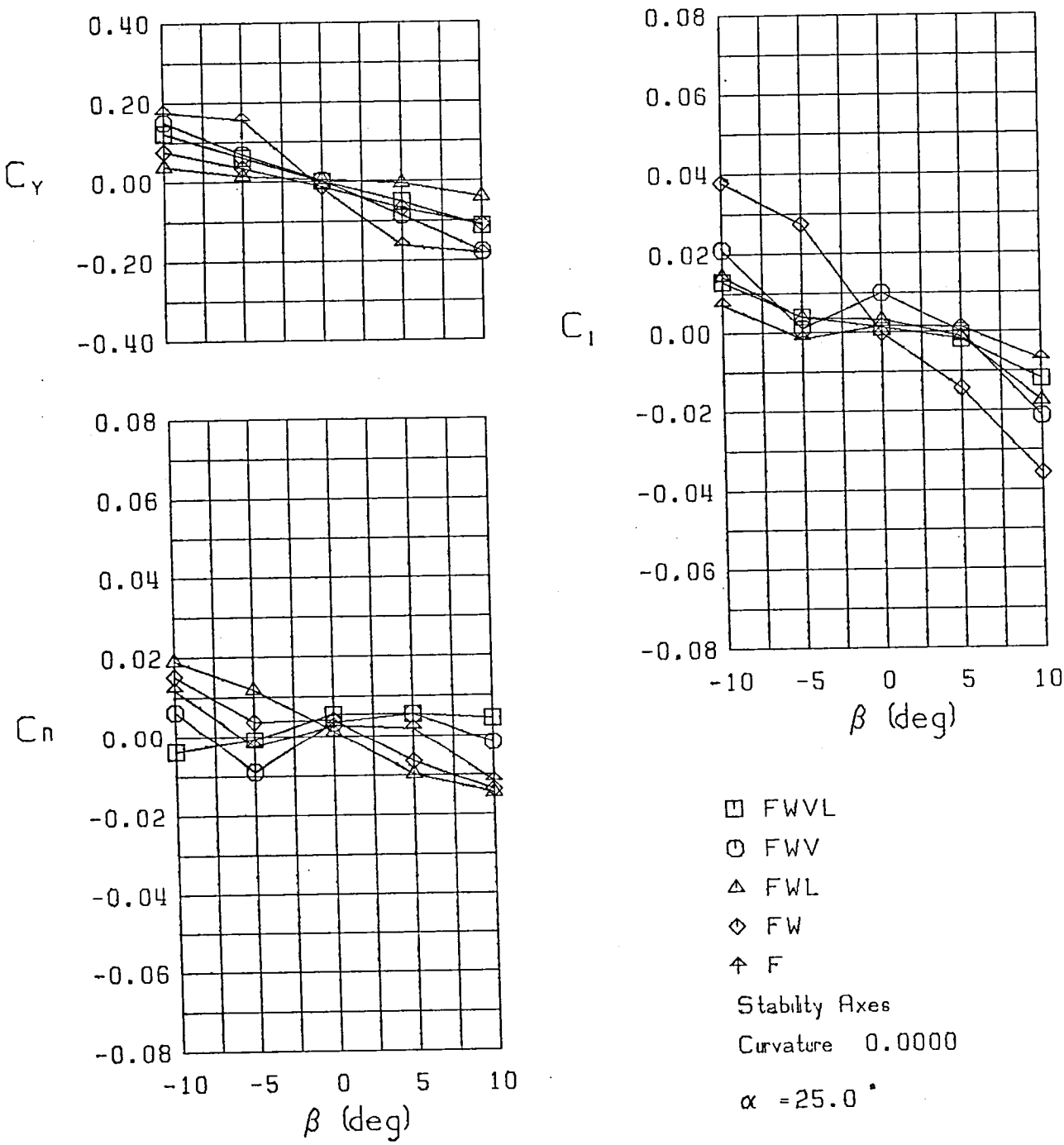

Figure 7 (Continued)

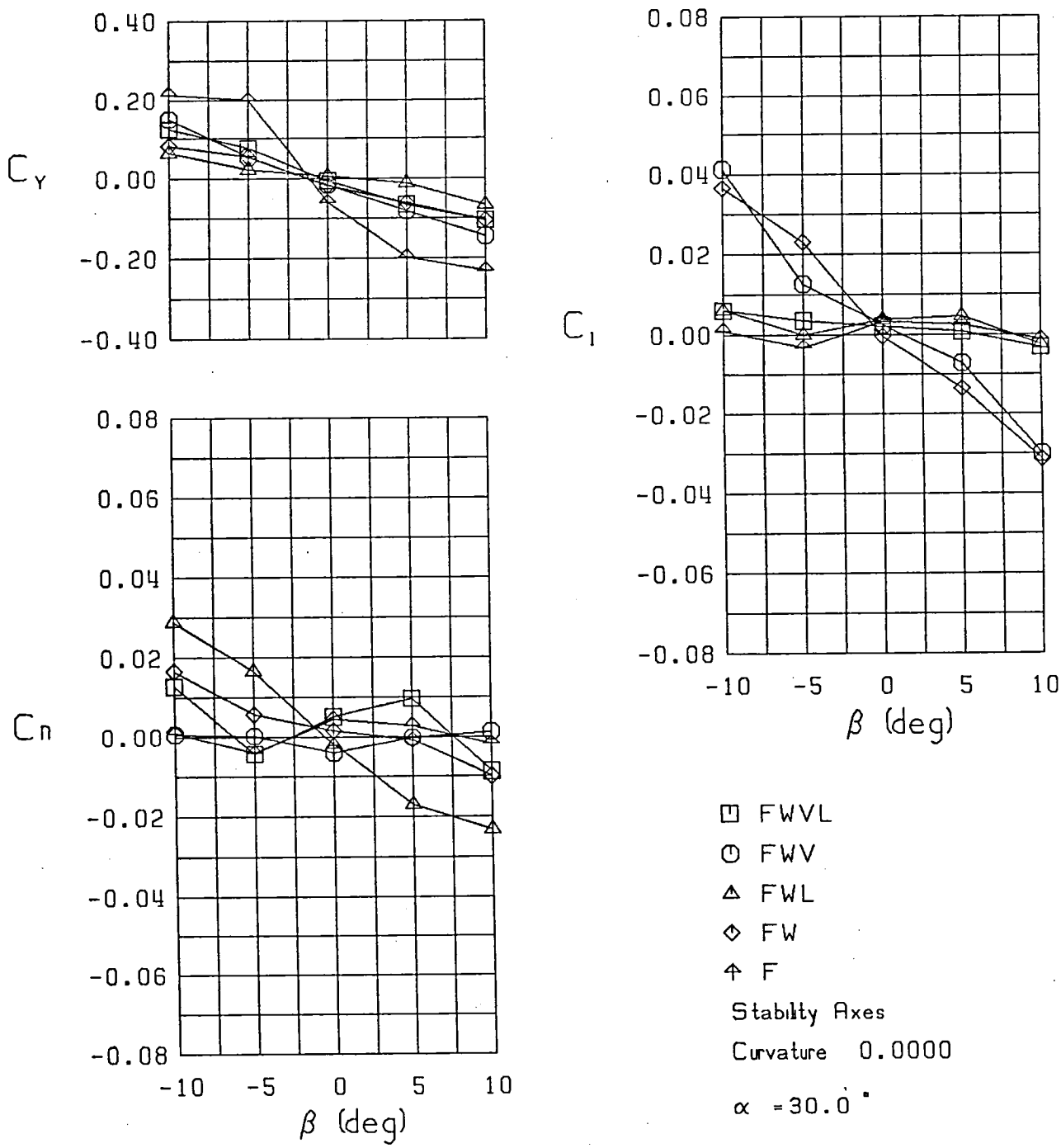

Figure 7 (Continued)

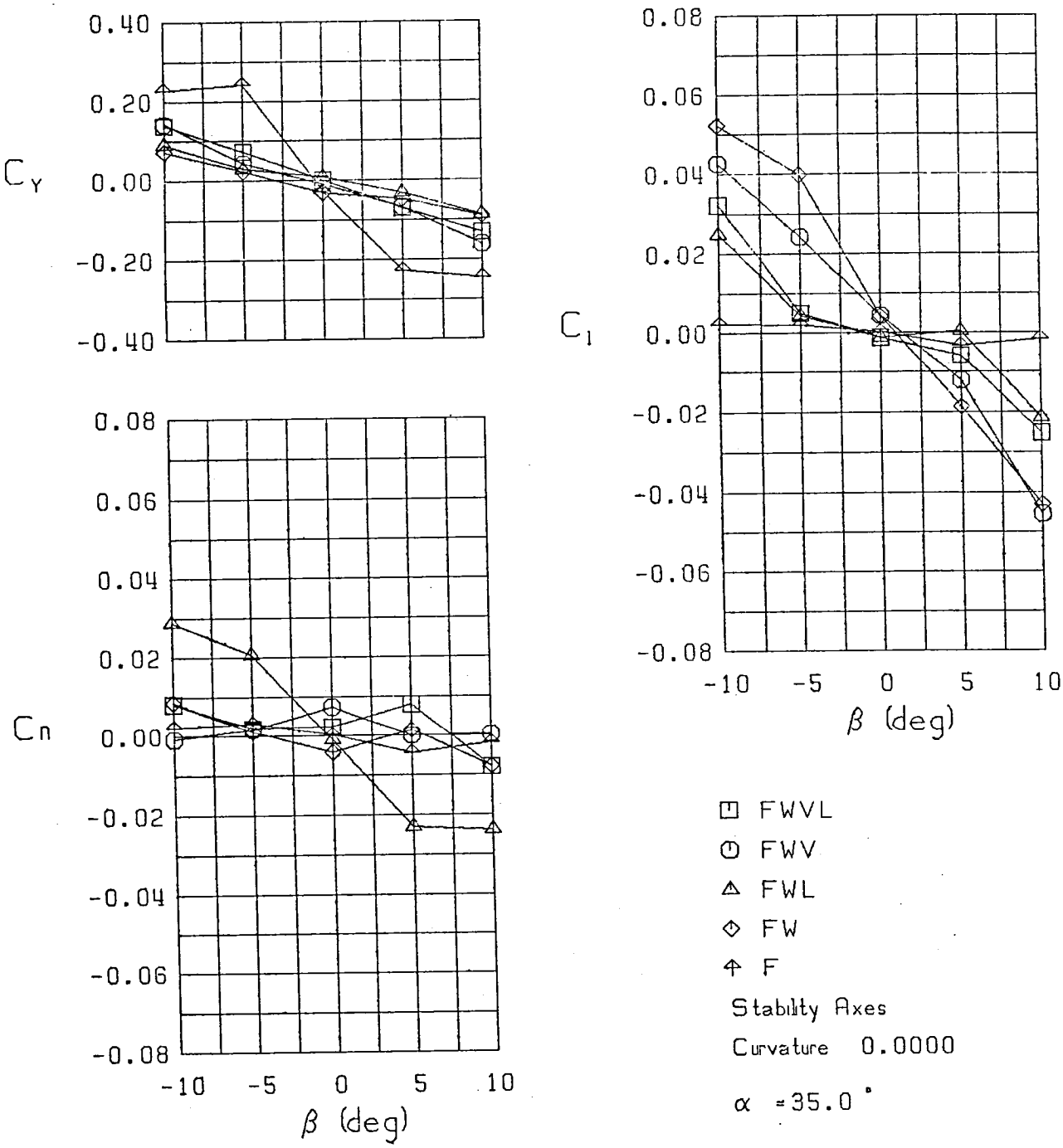

Figure 7 (Continued)

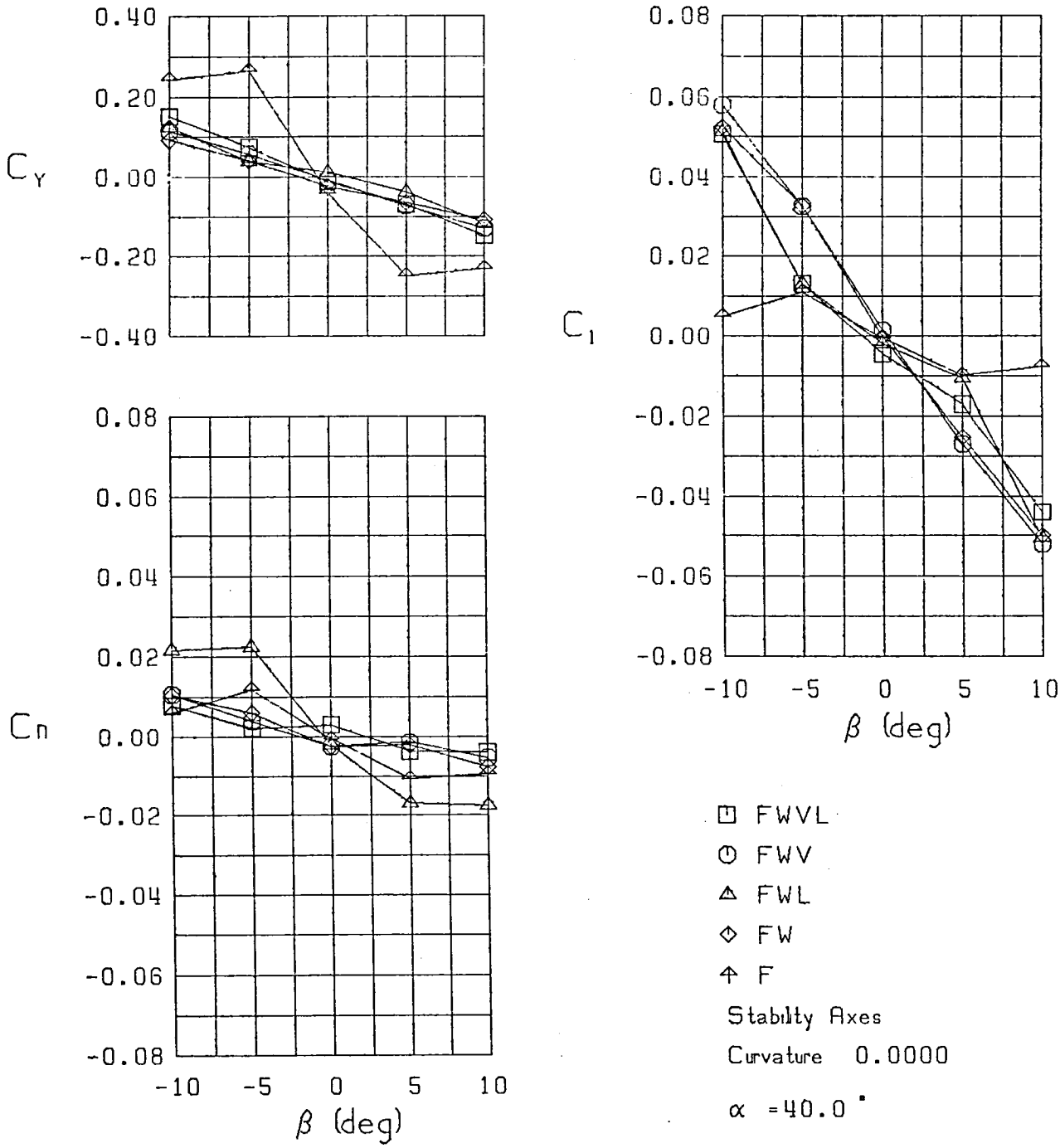

Figure 7 (Continued)

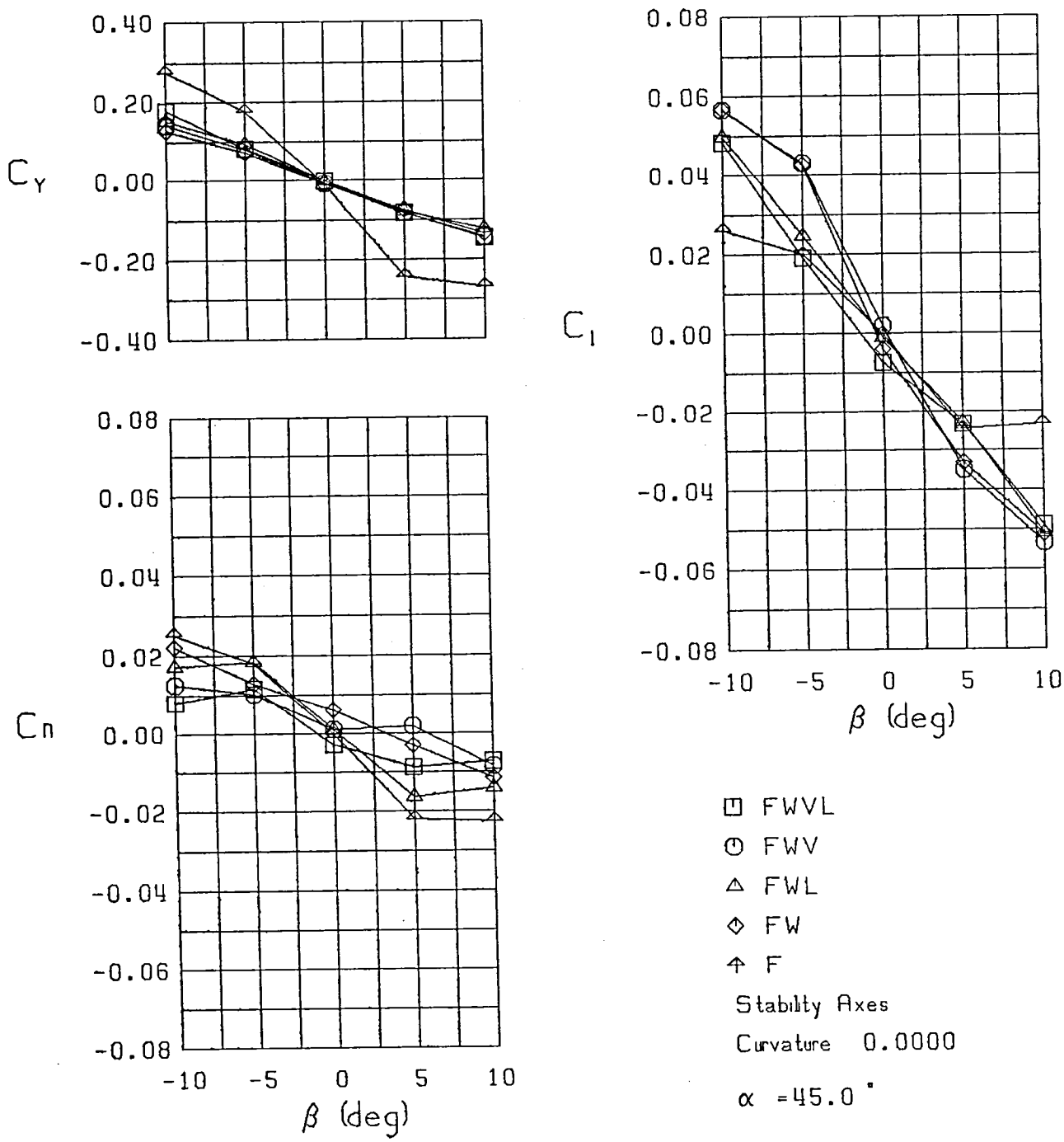

Figure 7 (Continued)

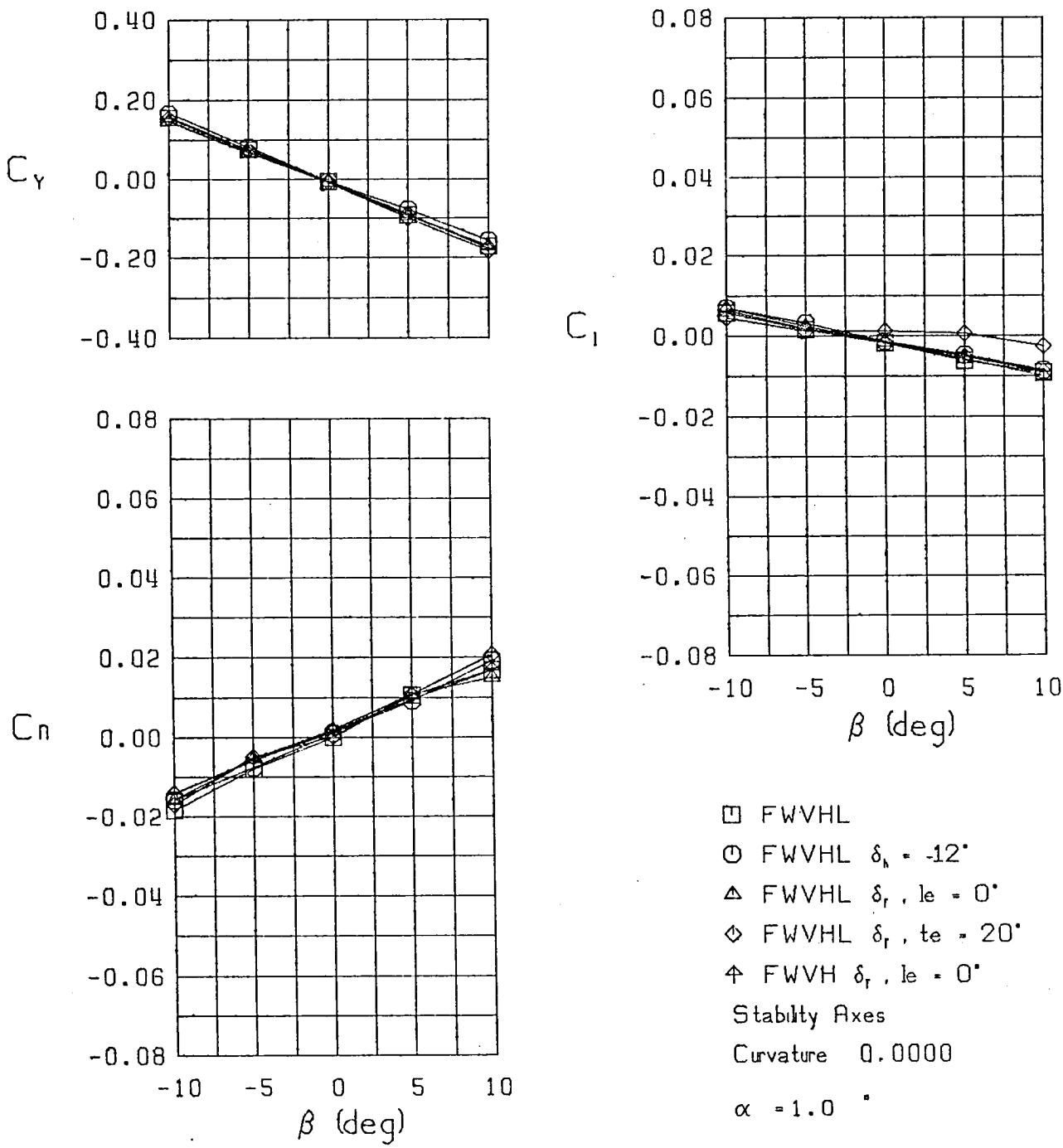

Figure 8 Variation of Static Lateral-Directional Characteristics With Angle of Sideslip - Configurations 1,2,3,4,7

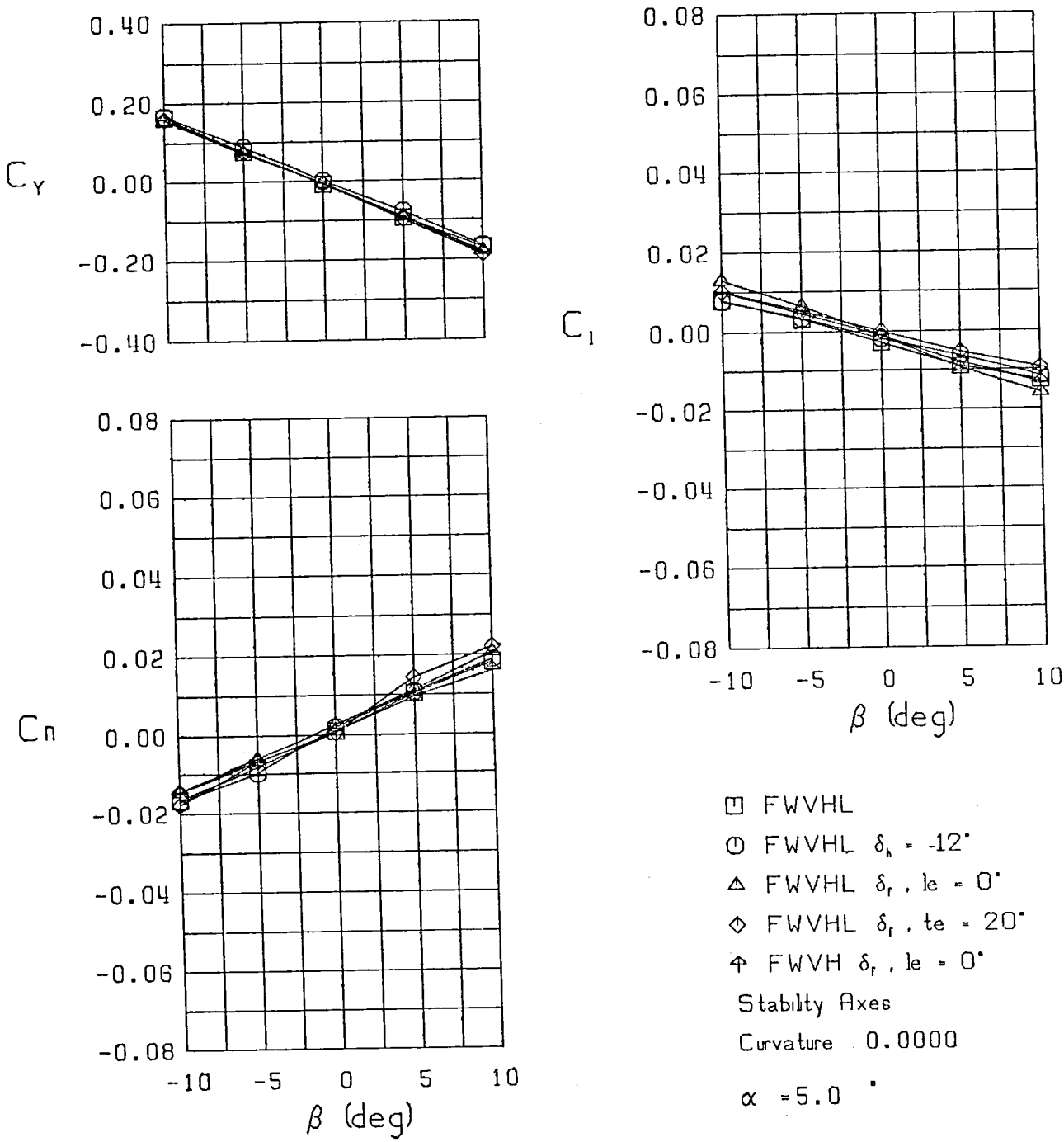

Figure 8 (Continued)

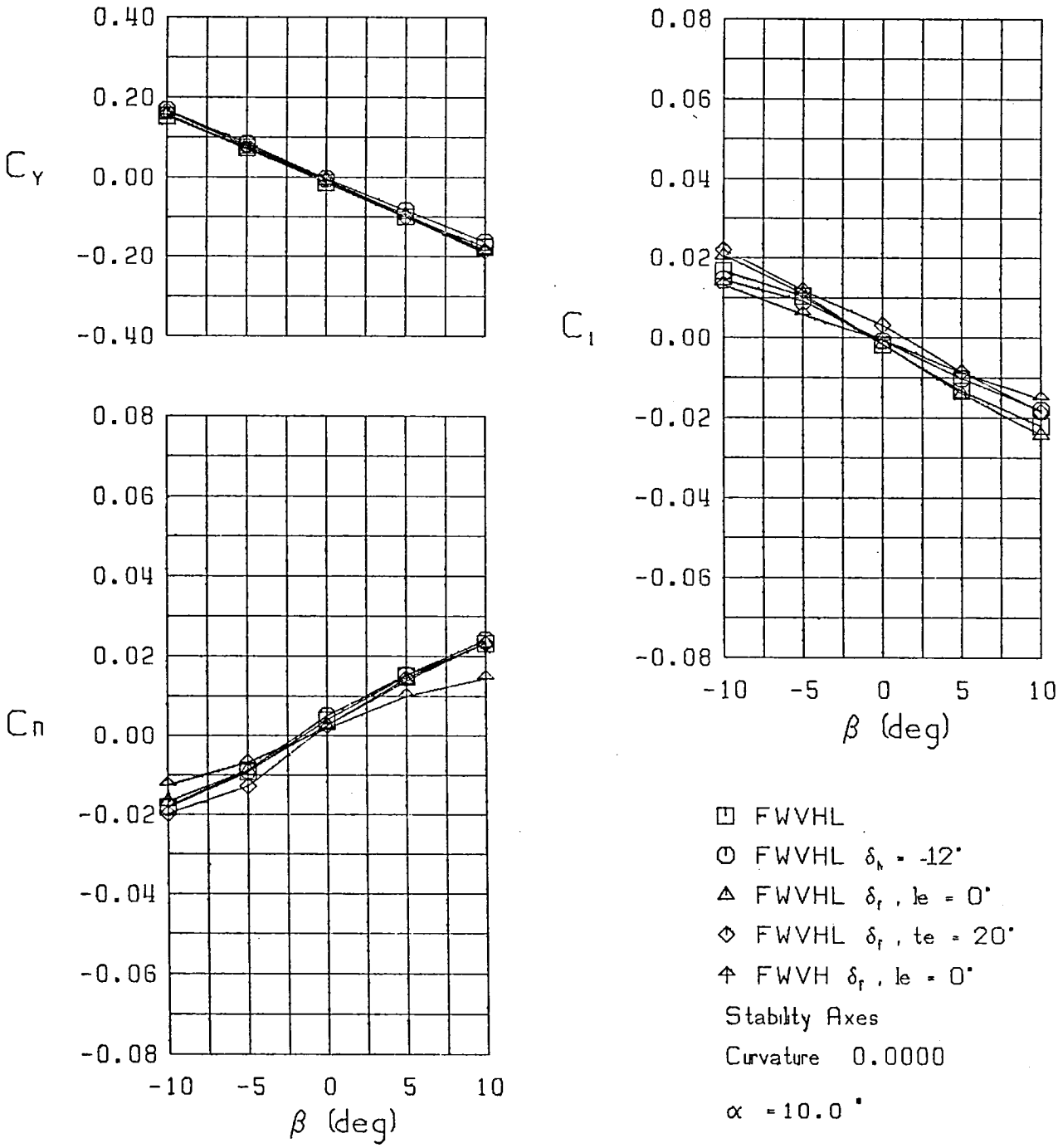

Figure 8 (Continued)

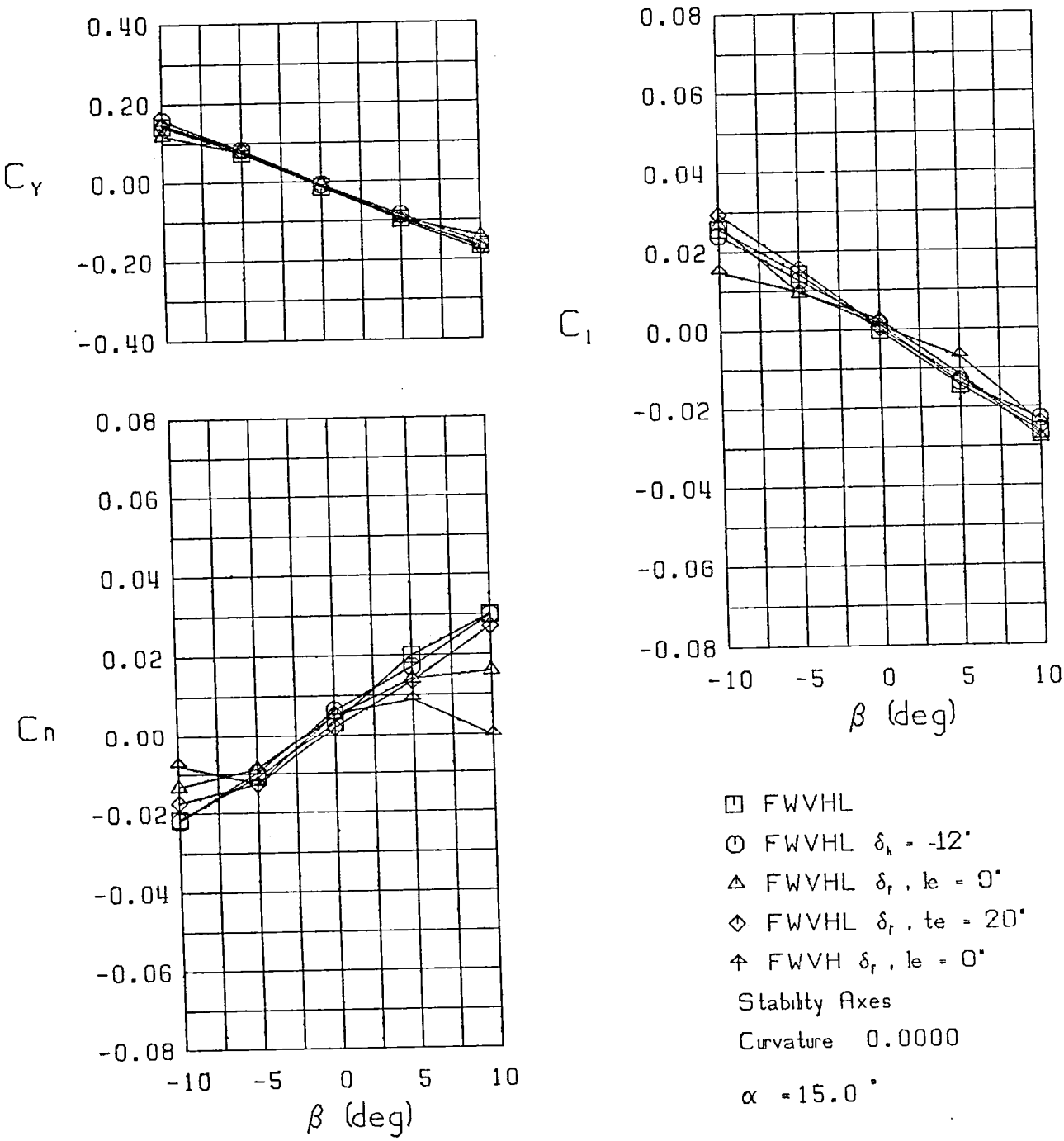

Figure 8 (Continued)

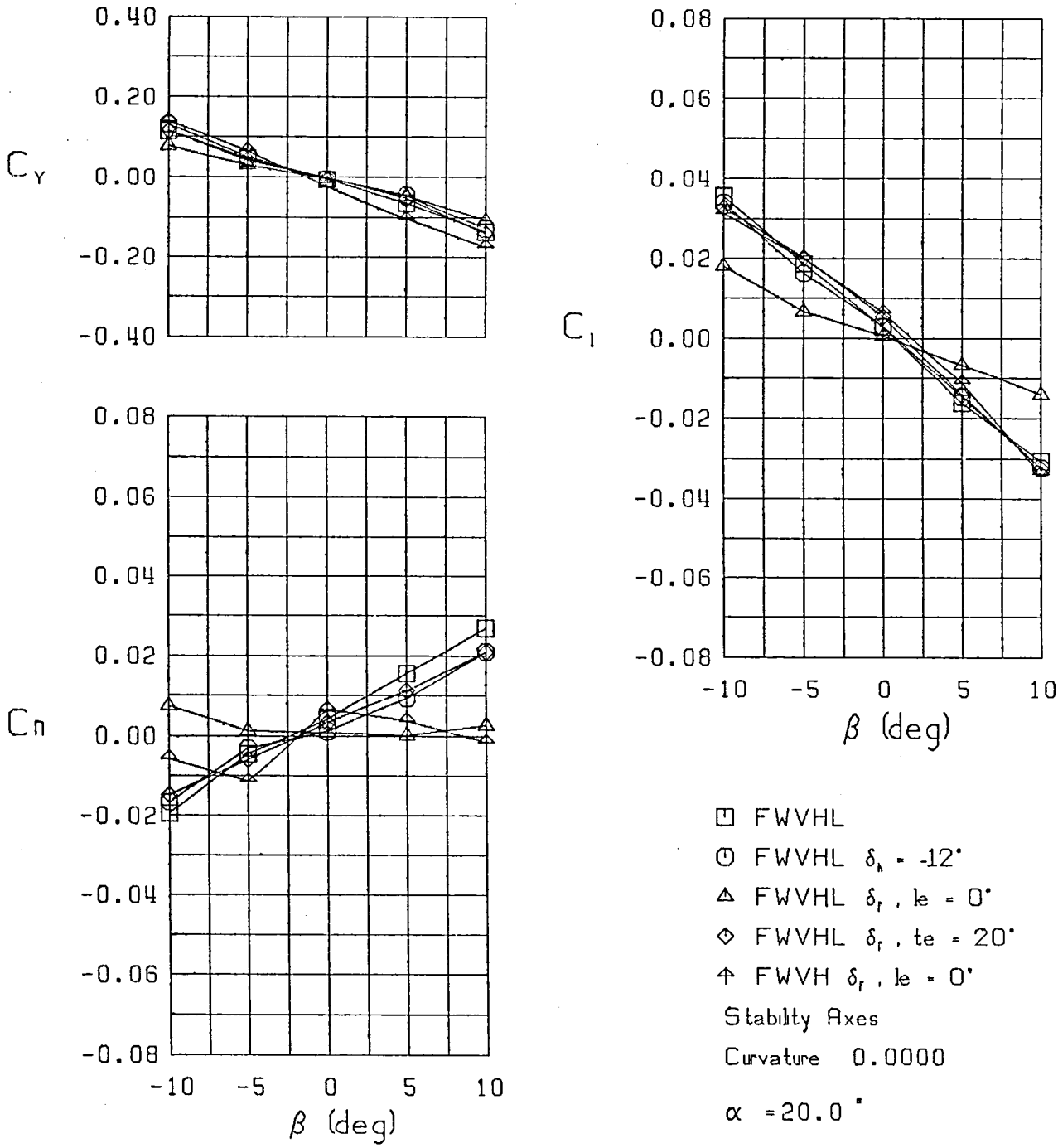

Figure 8 (Continued)

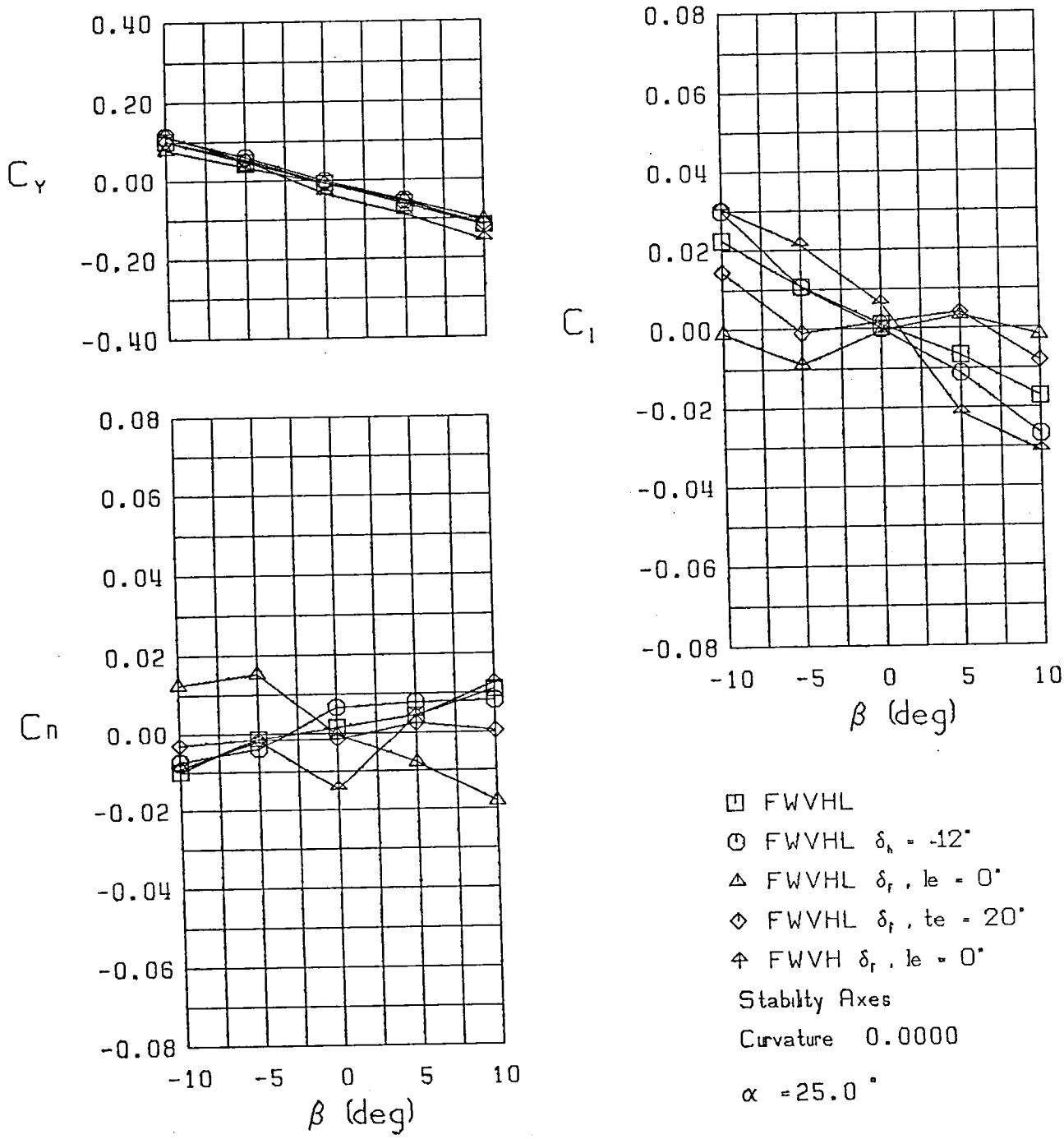

Figure 8 (Continued)

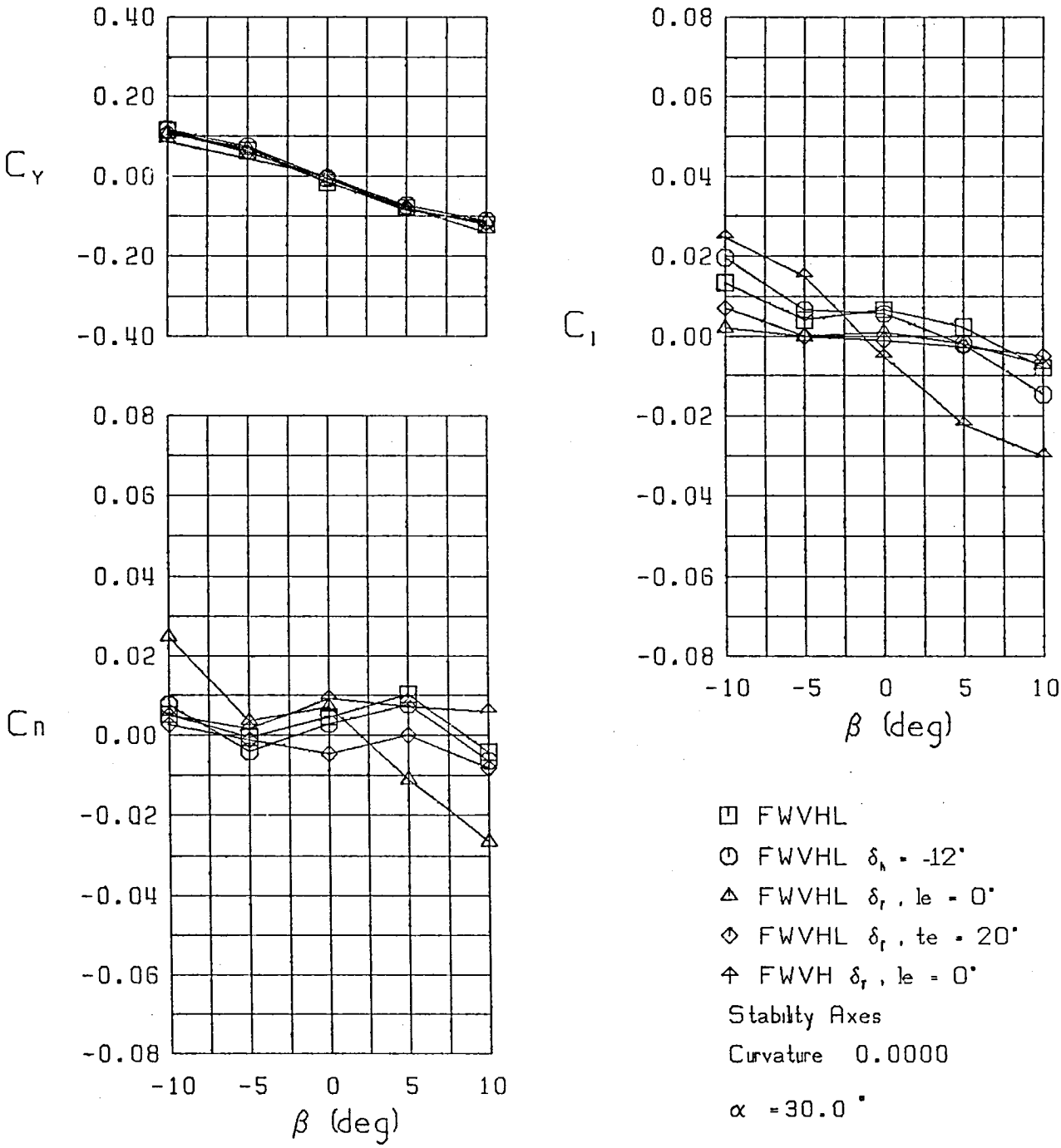

Figure 8 (Continued)

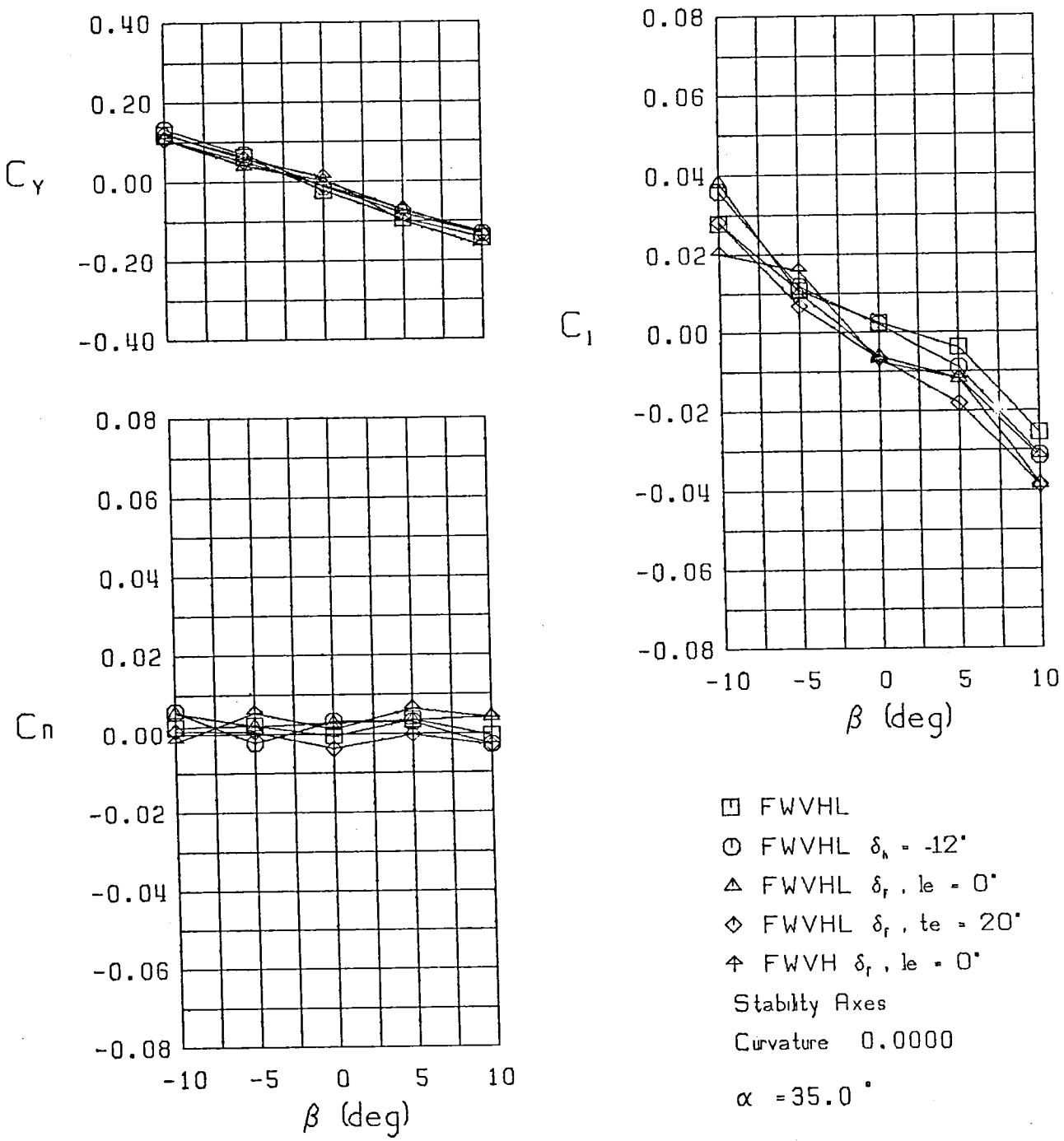

Figure 8 (Continued)

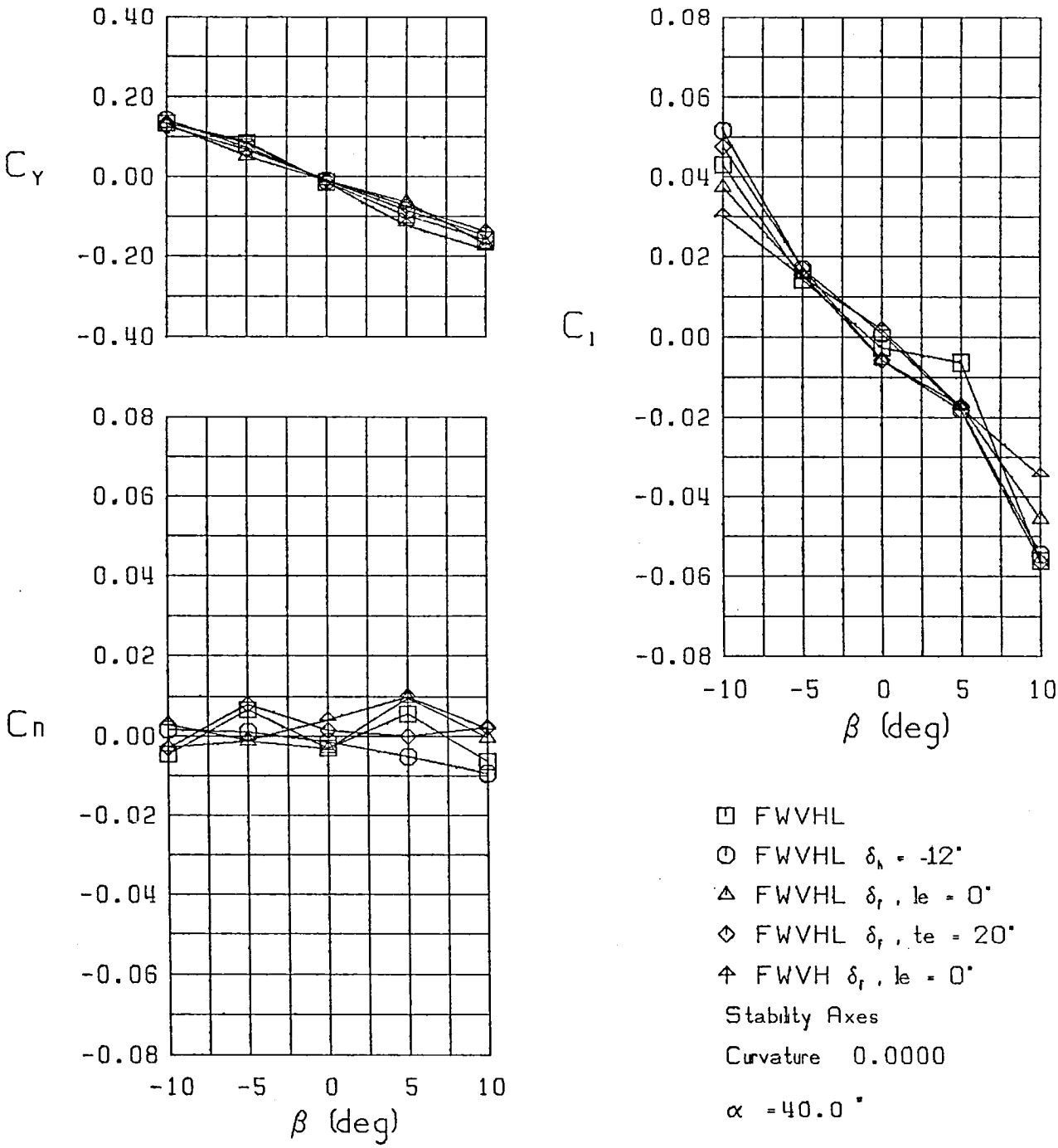

Figure 8 (Continued)

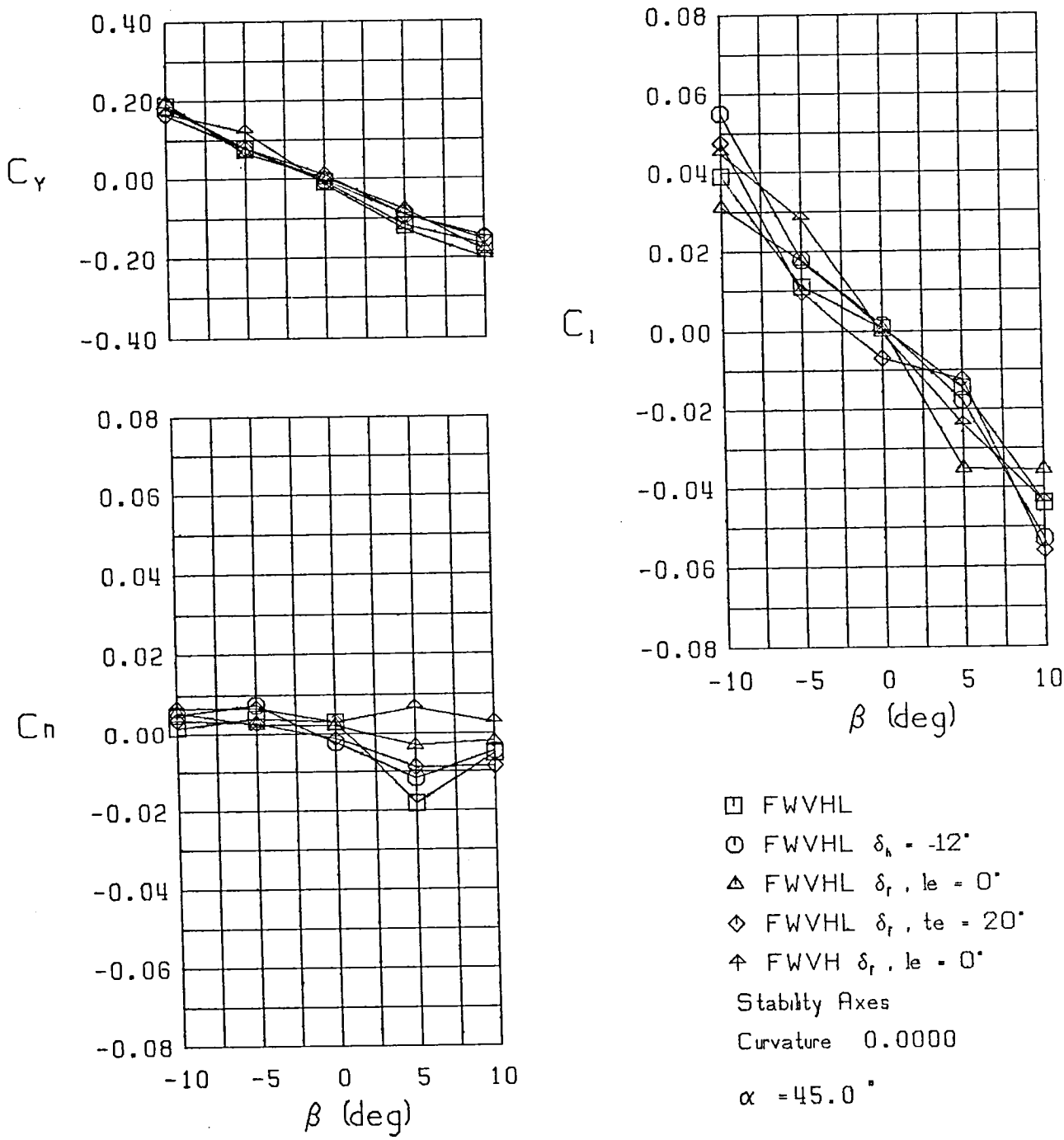

Figure 8 (Continued)

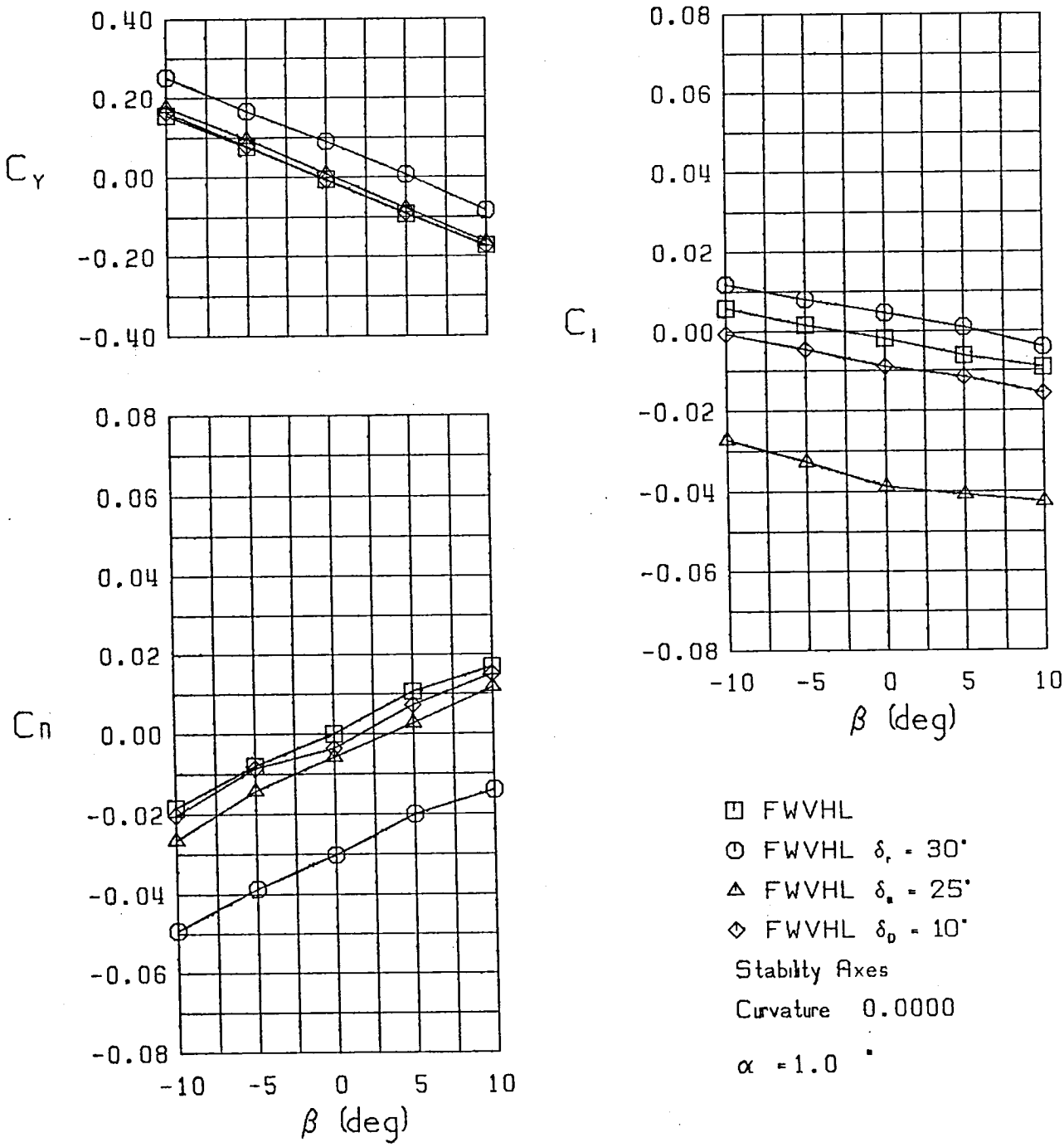

Figure 9 Variation of Static Lateral-Directional Characteristics With Angle of Sideslip - Configurations 1,16,17,18

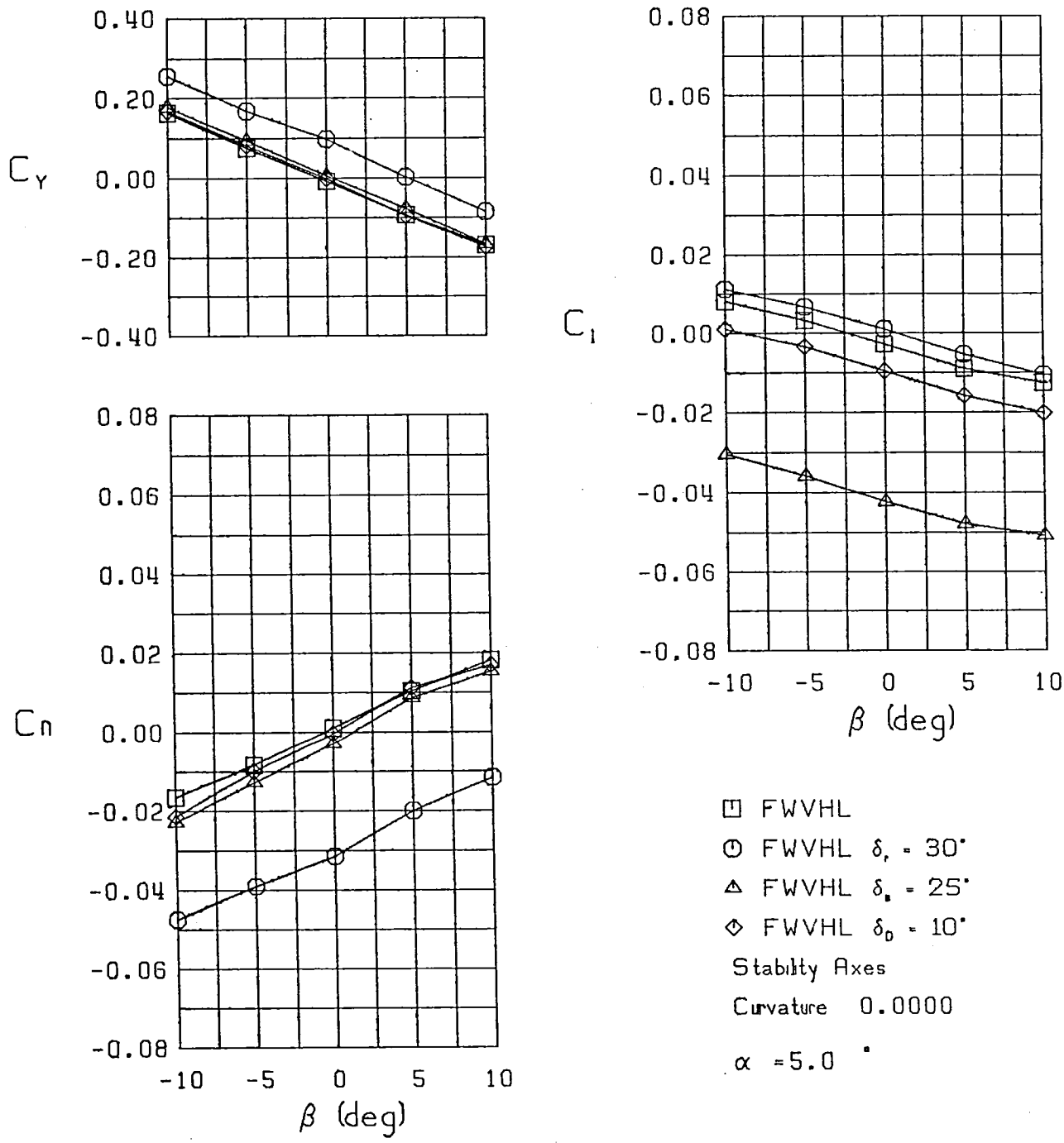

Figure 9 (Continued)

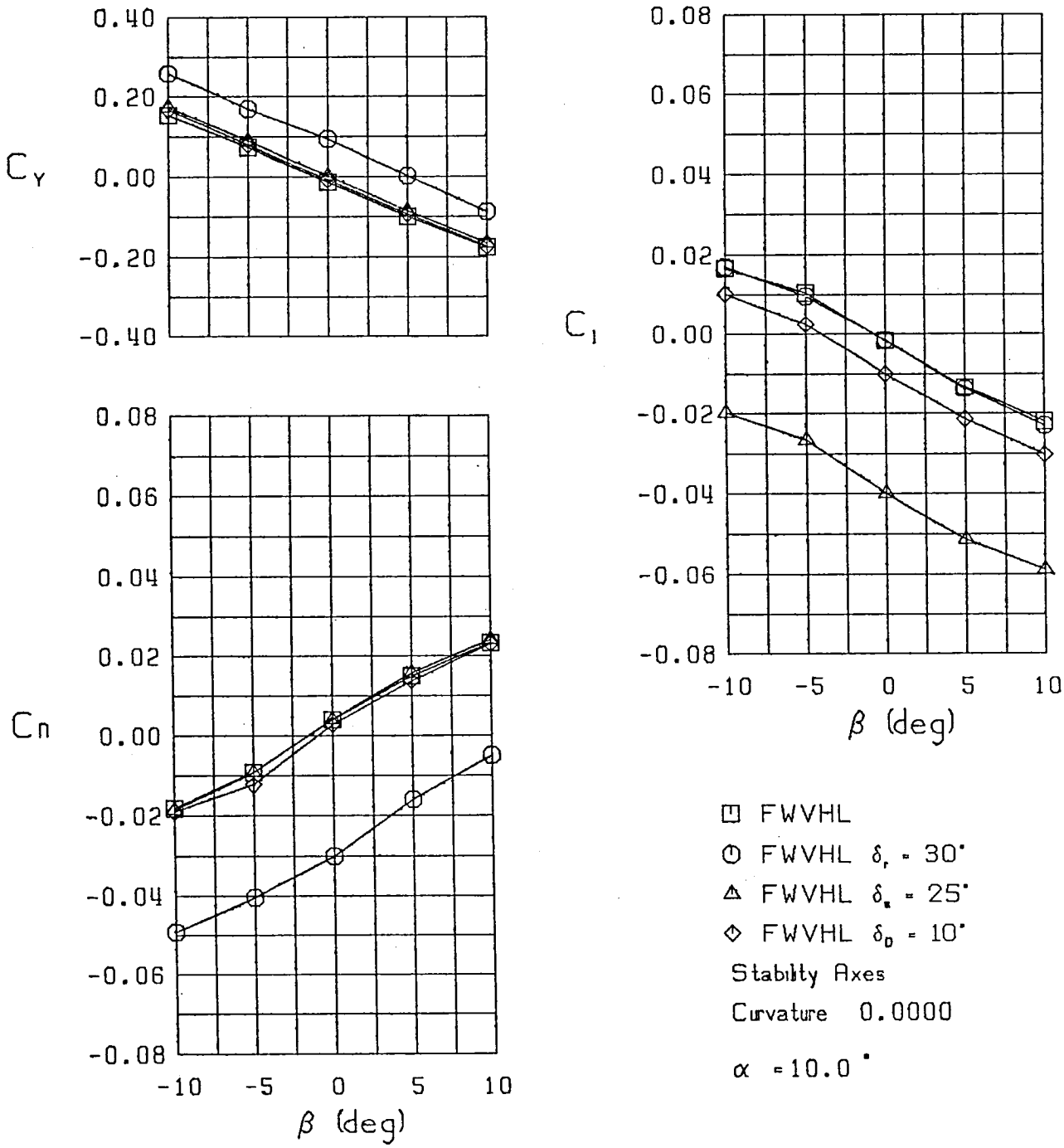

Figure 9 (Continued)

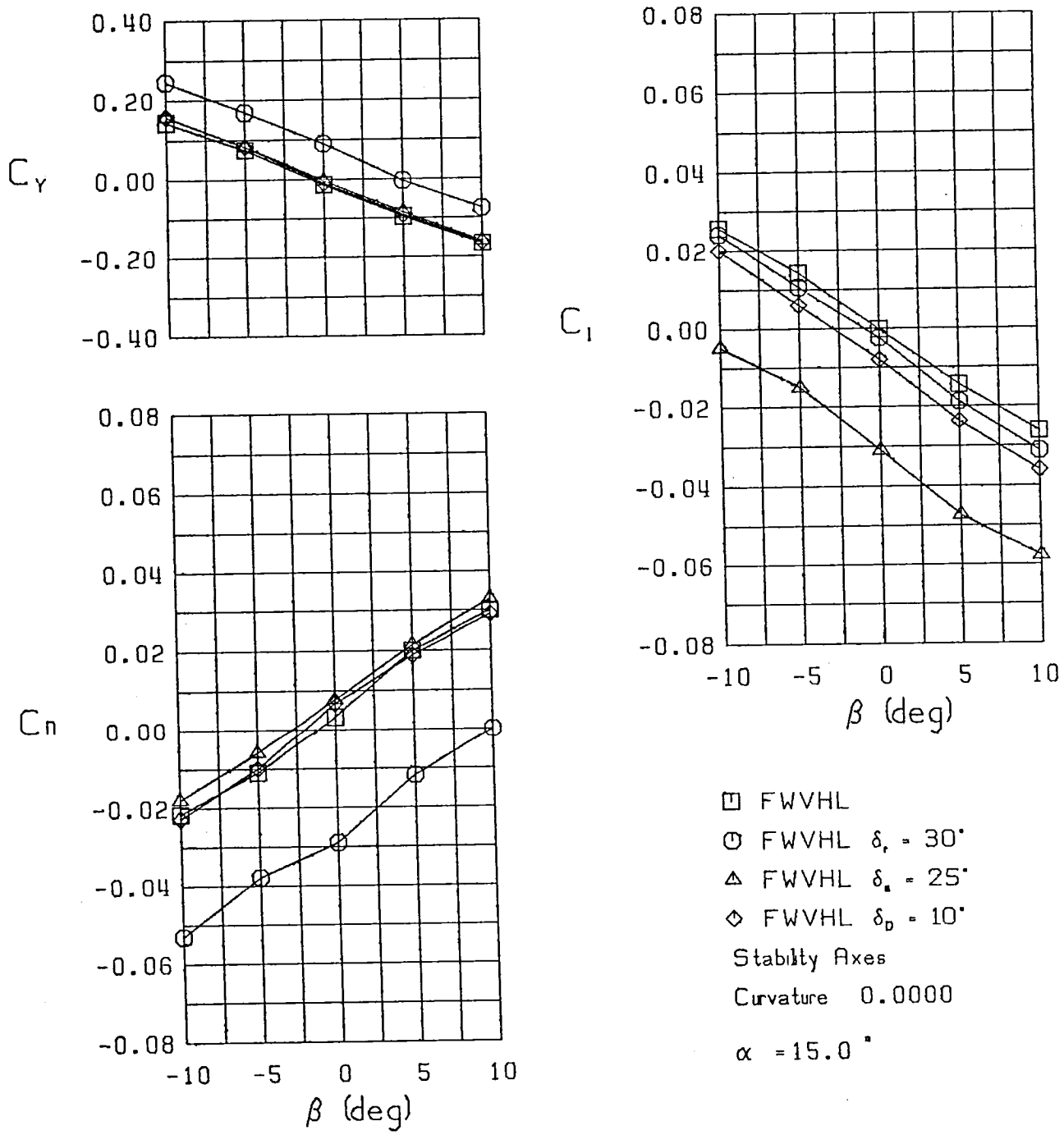

Figure 9 (Continued)

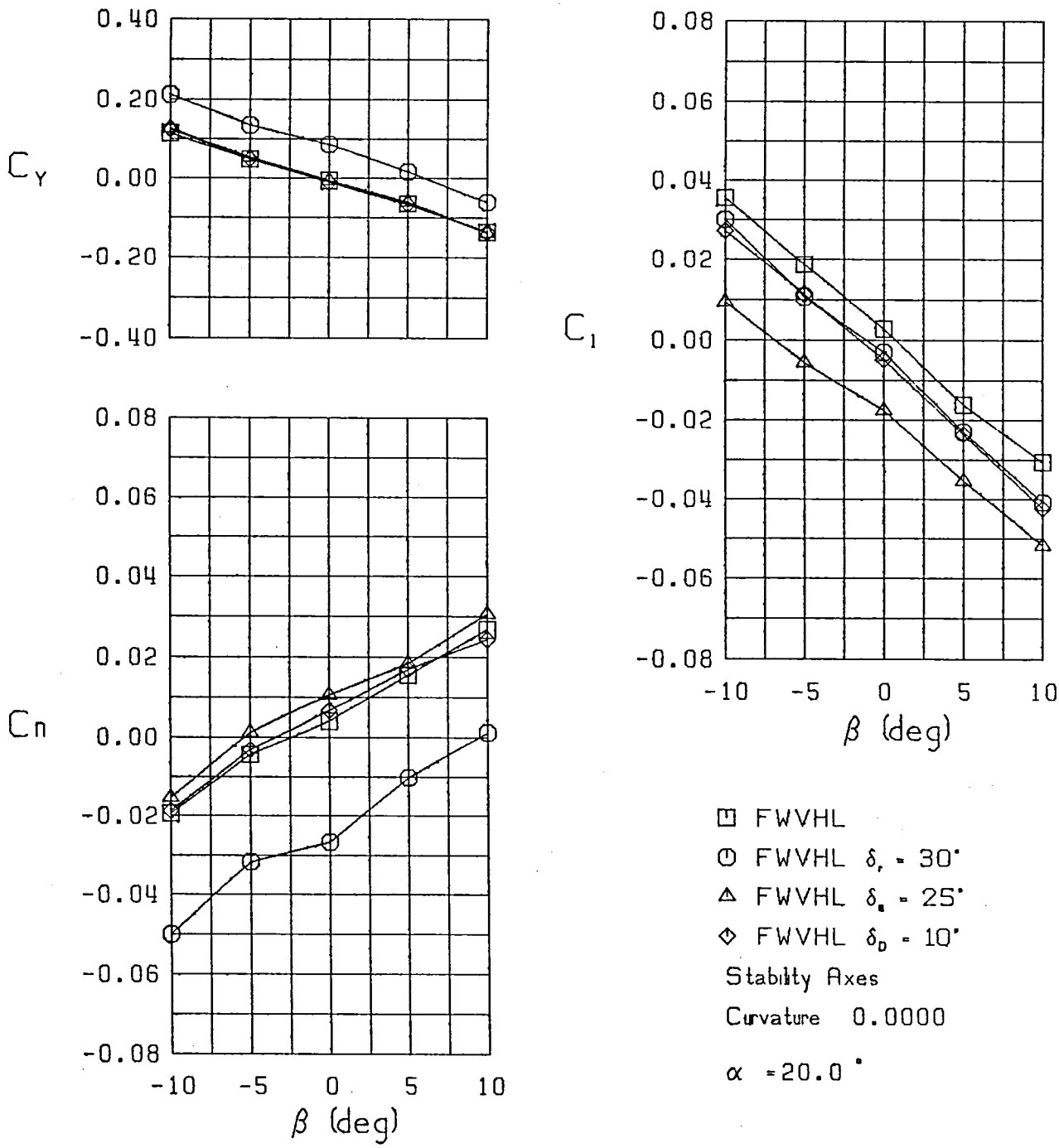

Figure 9 (Continued)

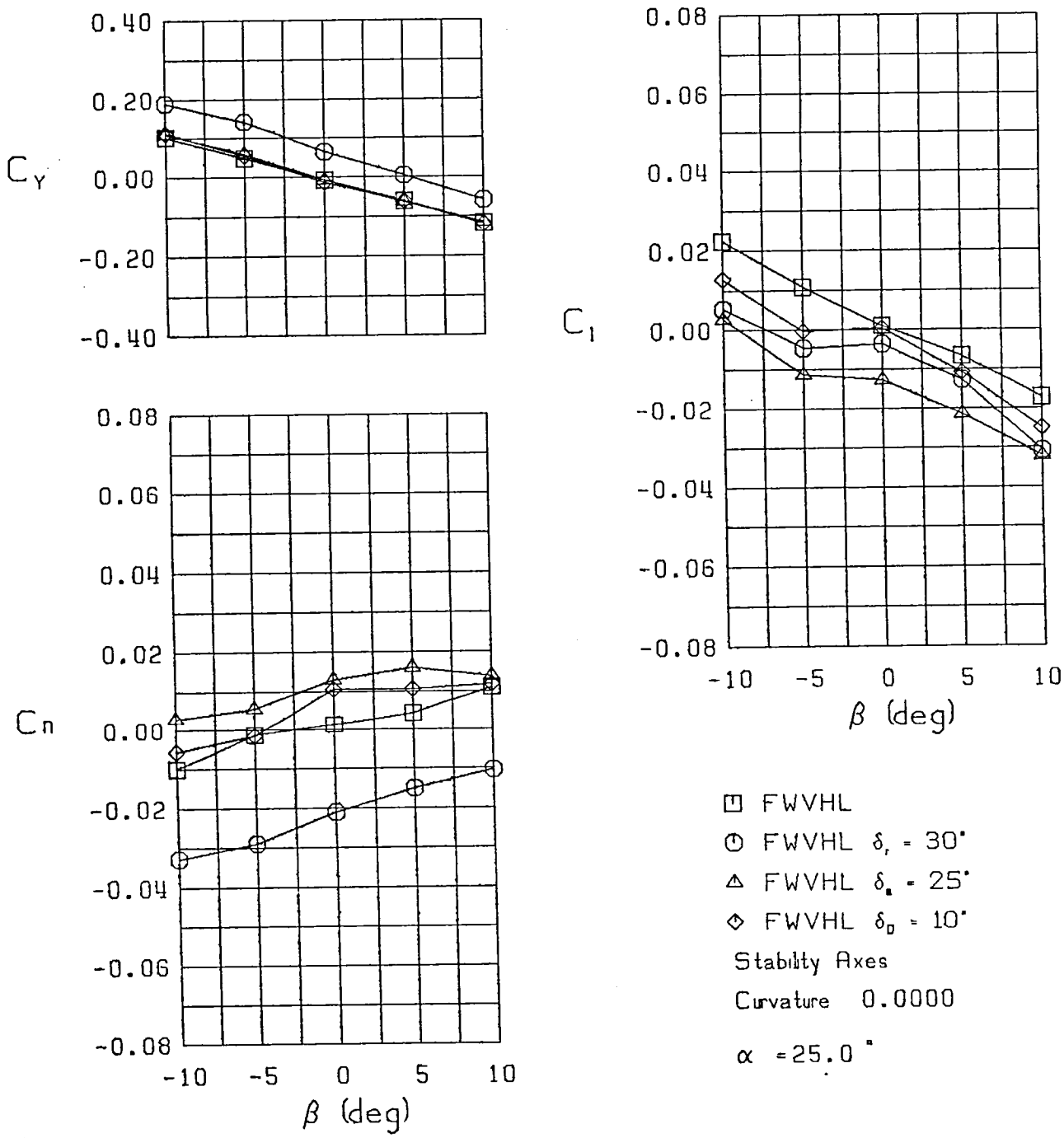

Figure 9 (Continued)

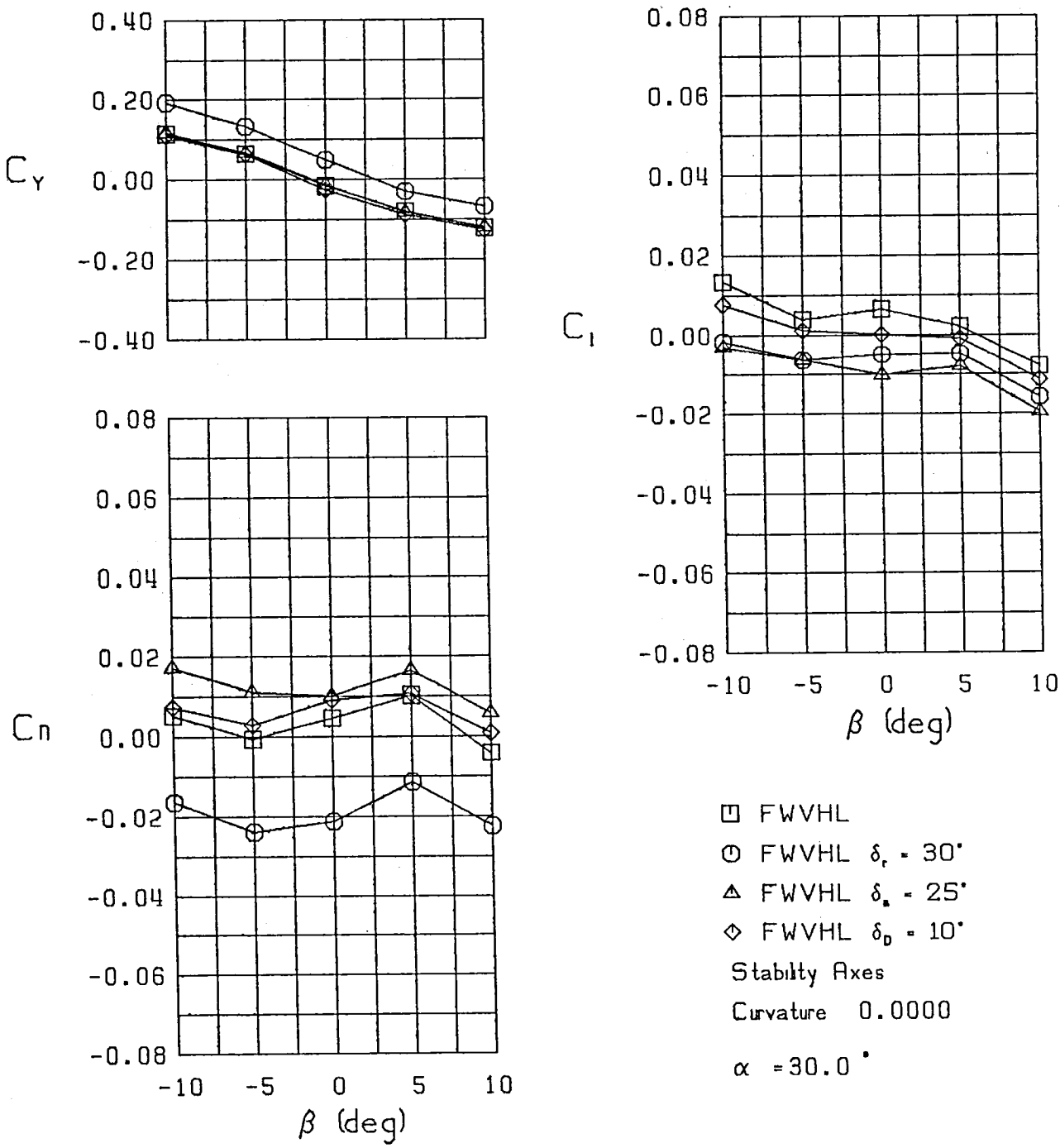

Figure 9 (Continued)

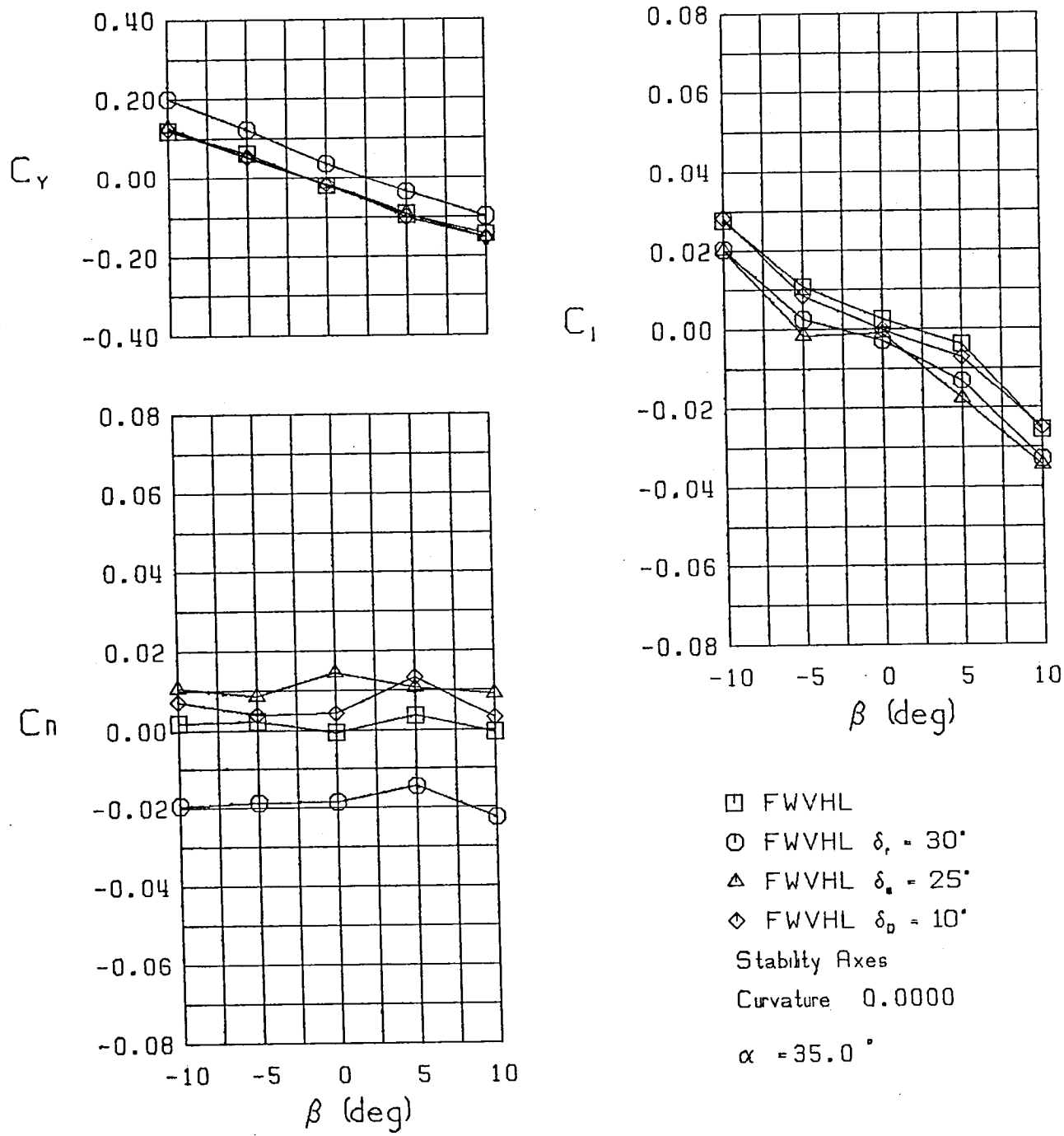

Figure 9 (Continued)

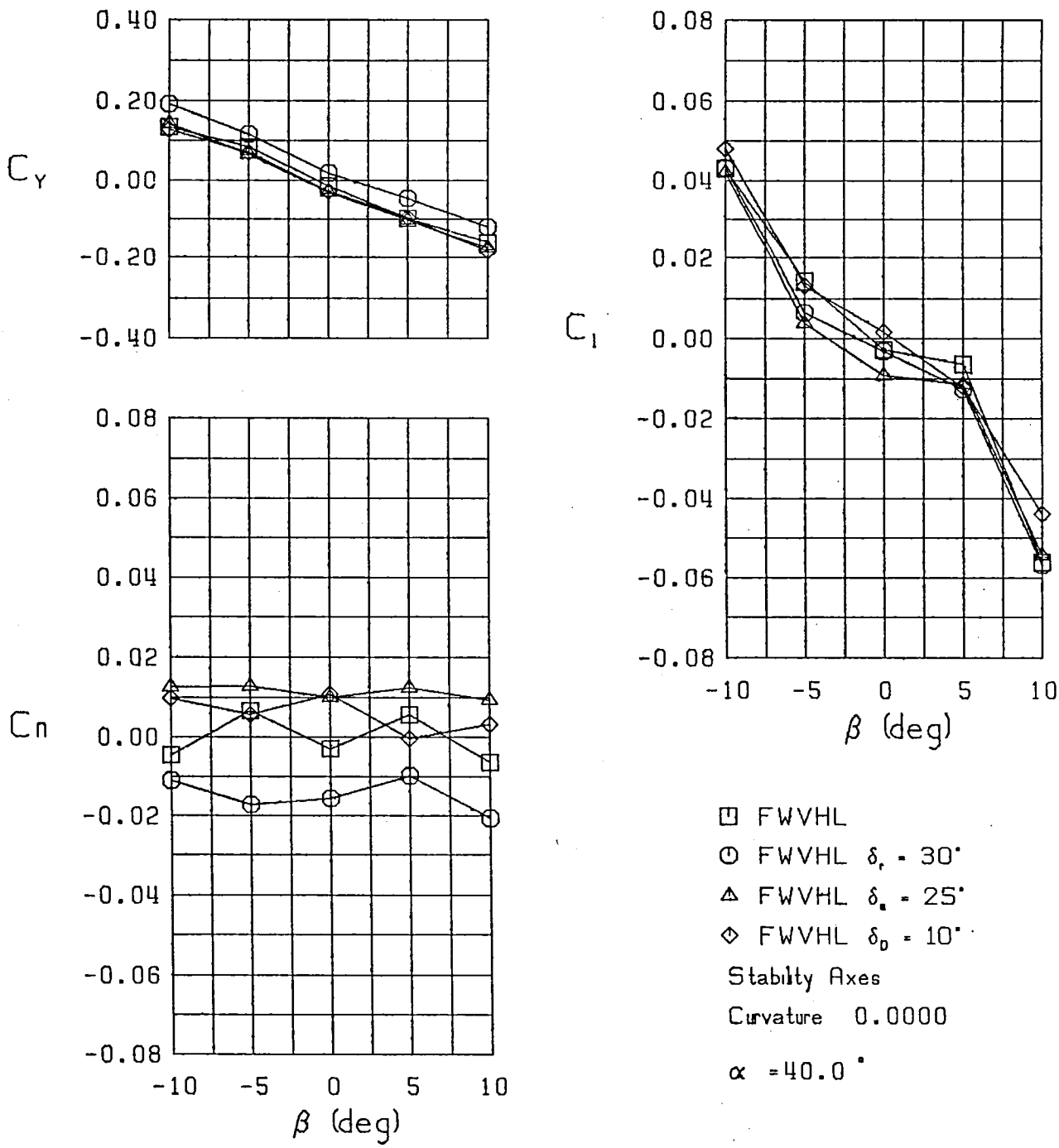

Figure 9 (Continued)

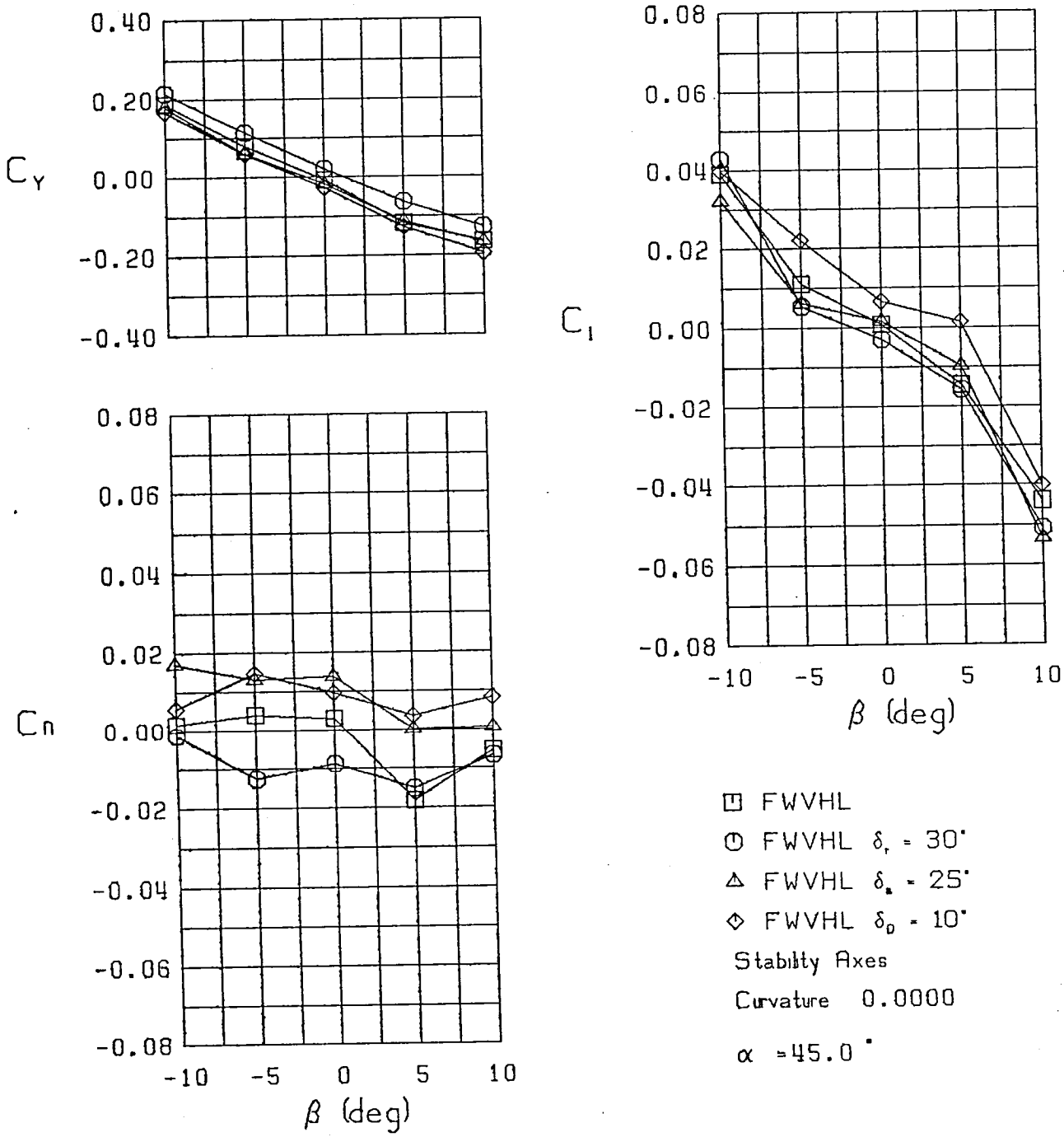

Figure 9 (Continued)

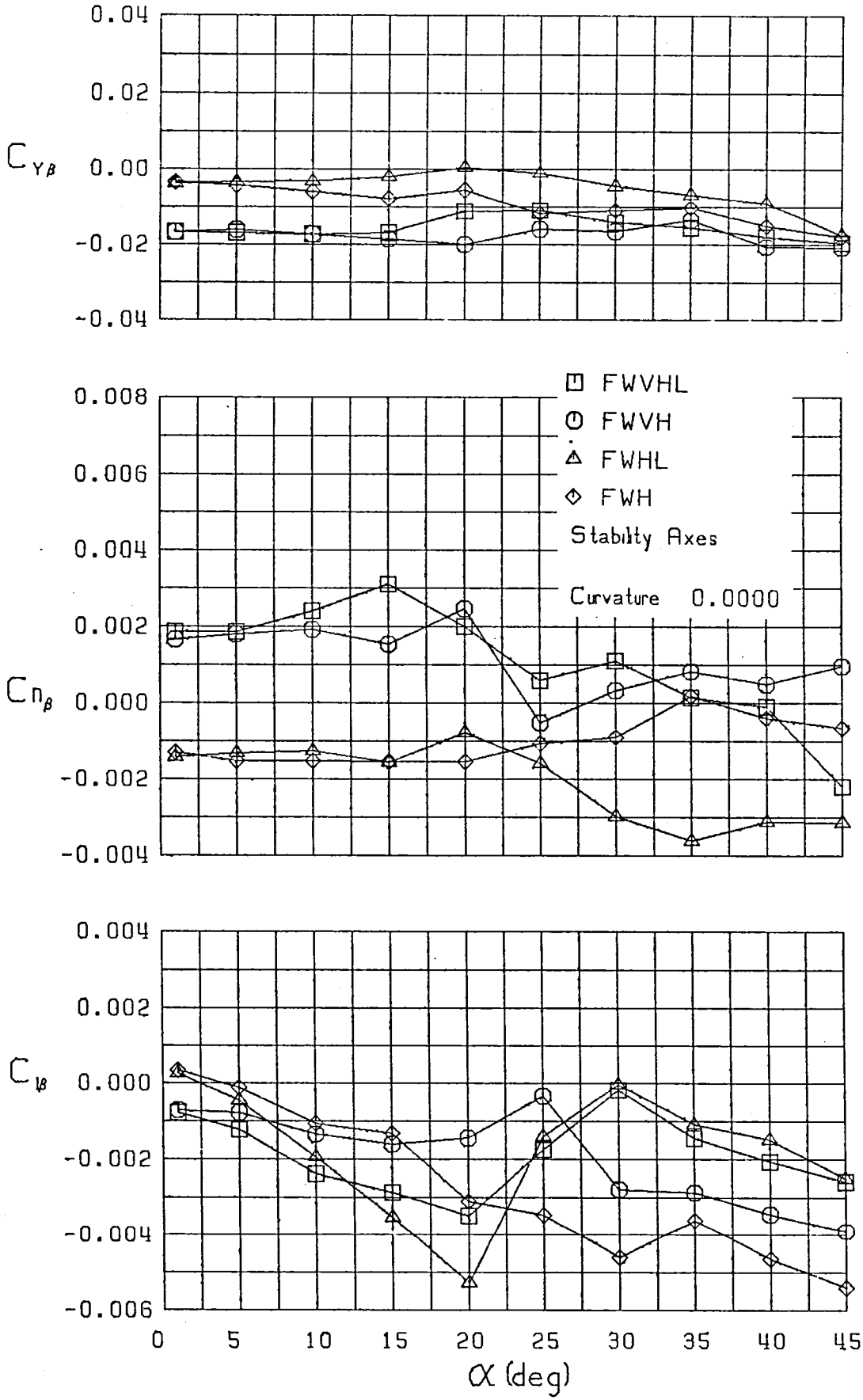

Figure 10 Variation of Lateral-Directional Static Stability Derivatives with Angle of Attack, $\hat{r} = 0$

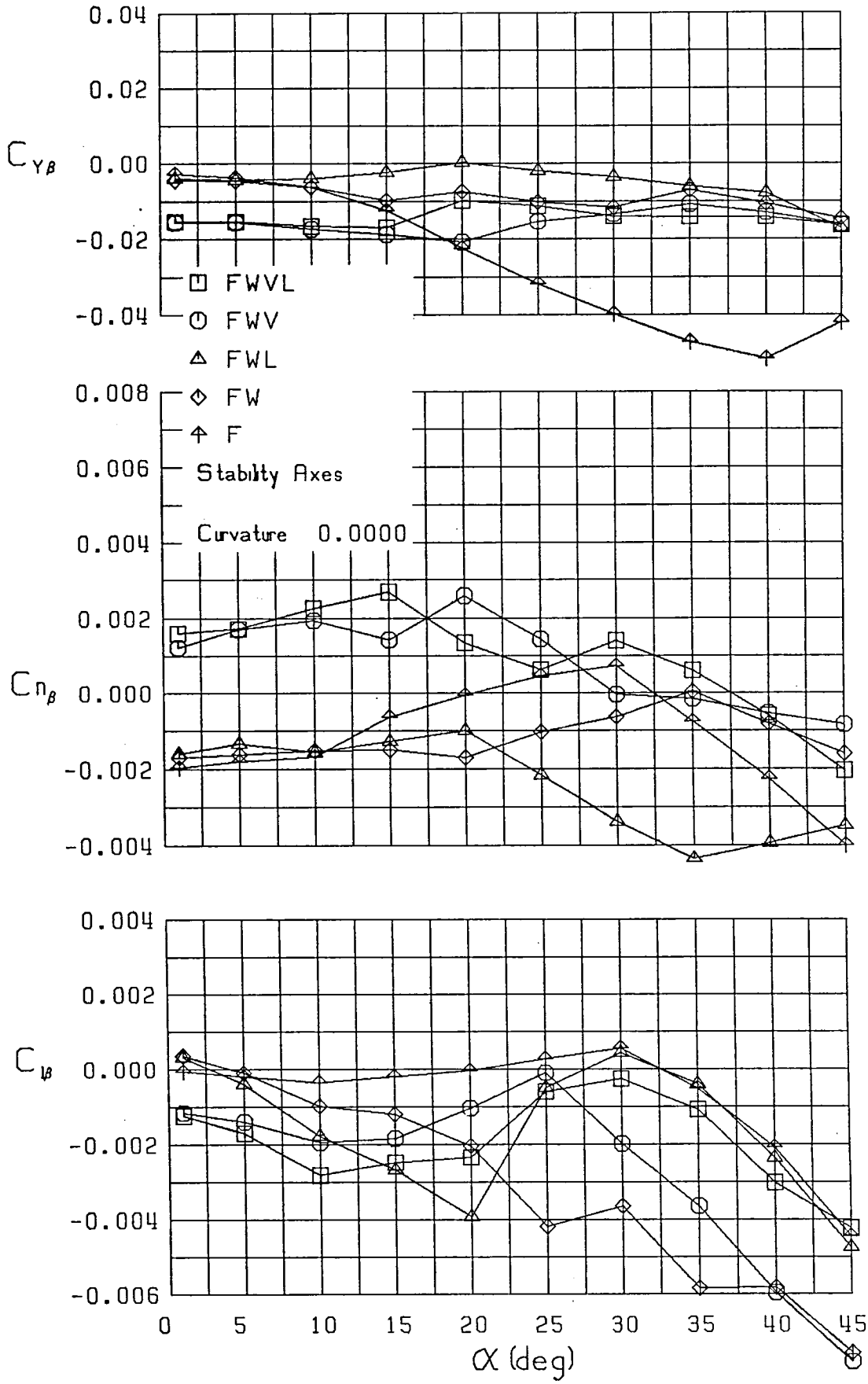

Figure 10 (Continued)

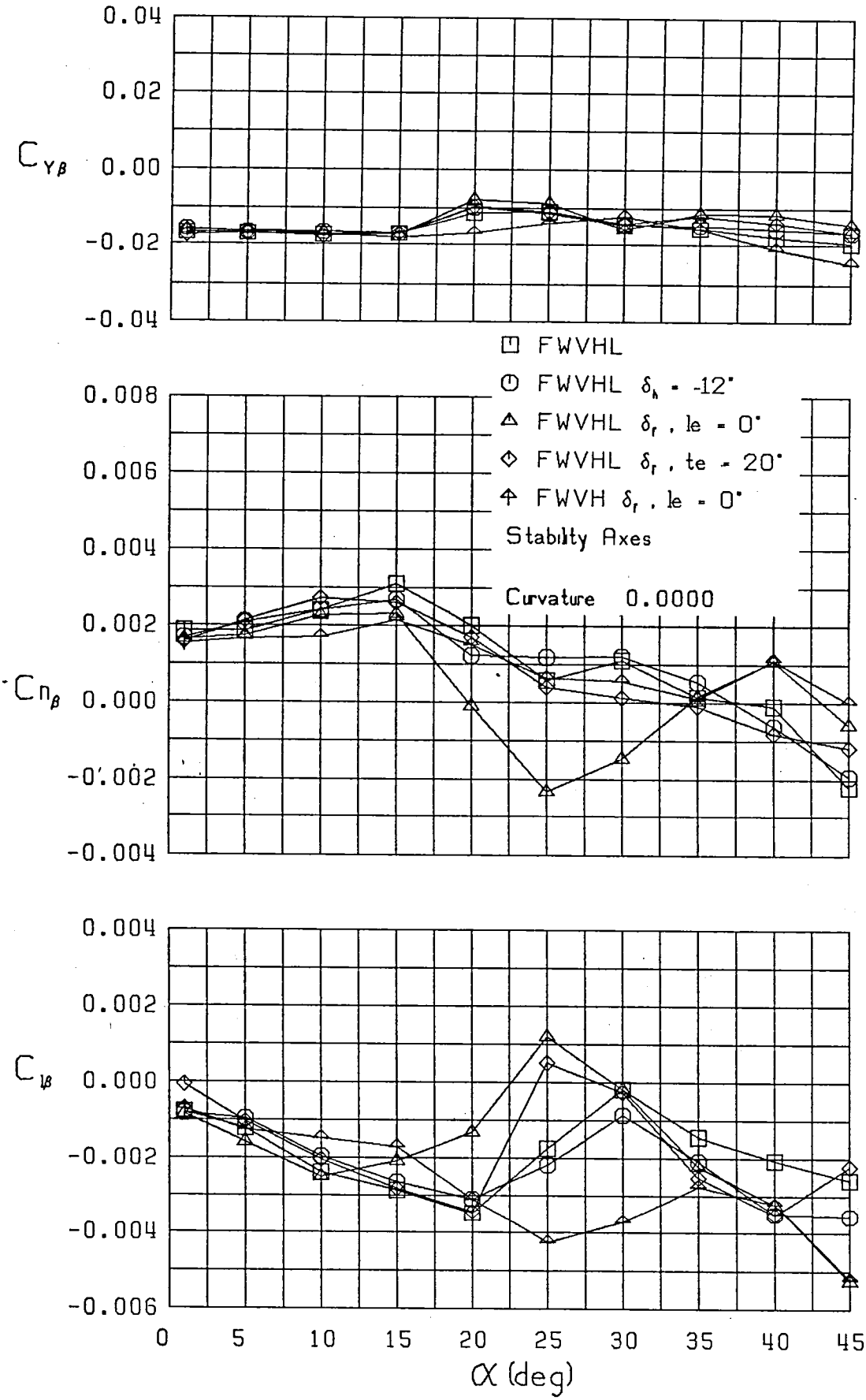

Figure 10 (Continued)

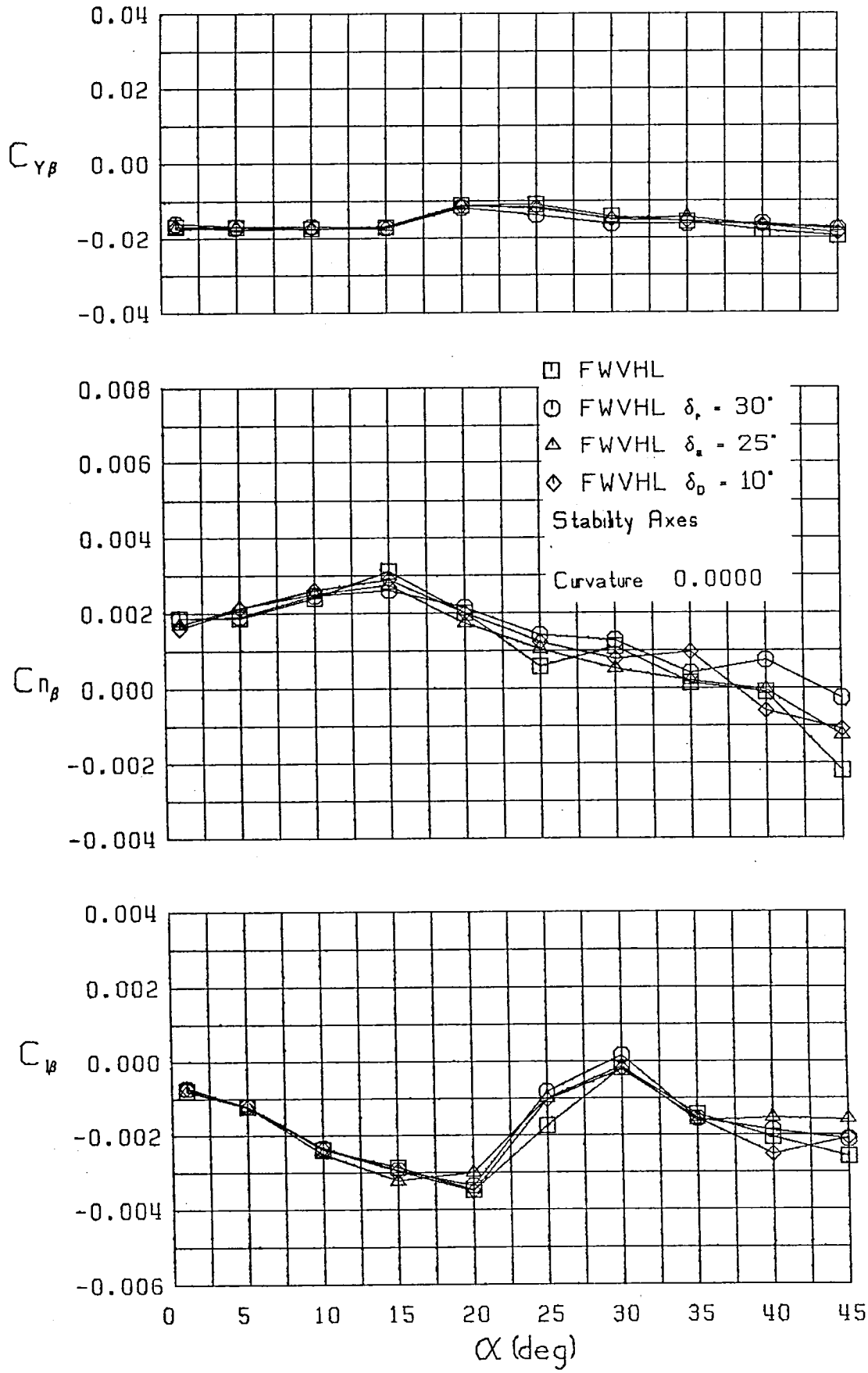

Figure 10 (Continued)

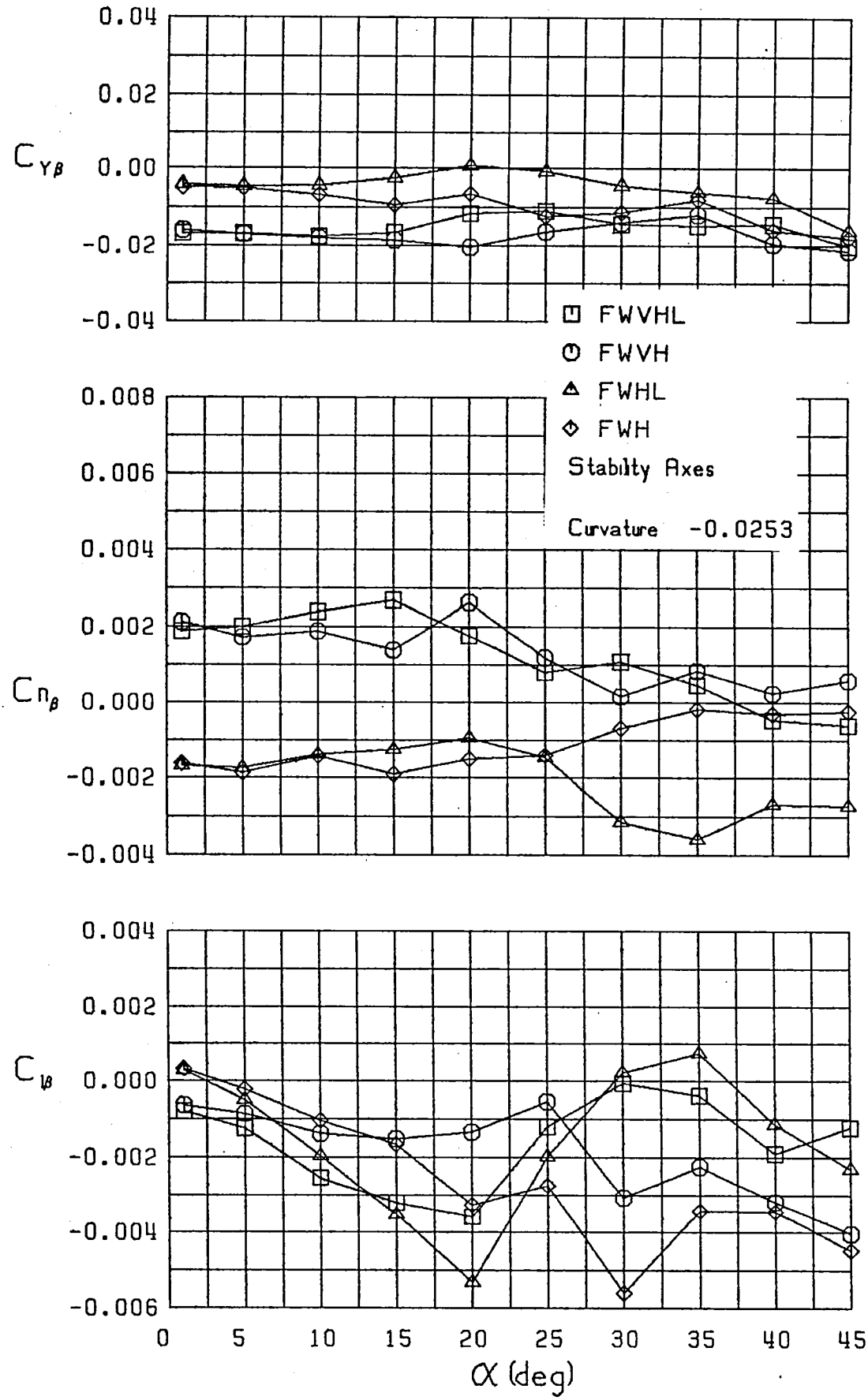

Figure 11 Variation of Lateral-Directional Static Stability Derivatives with Angle of Attack, $\hat{r}$ = - 0.0253

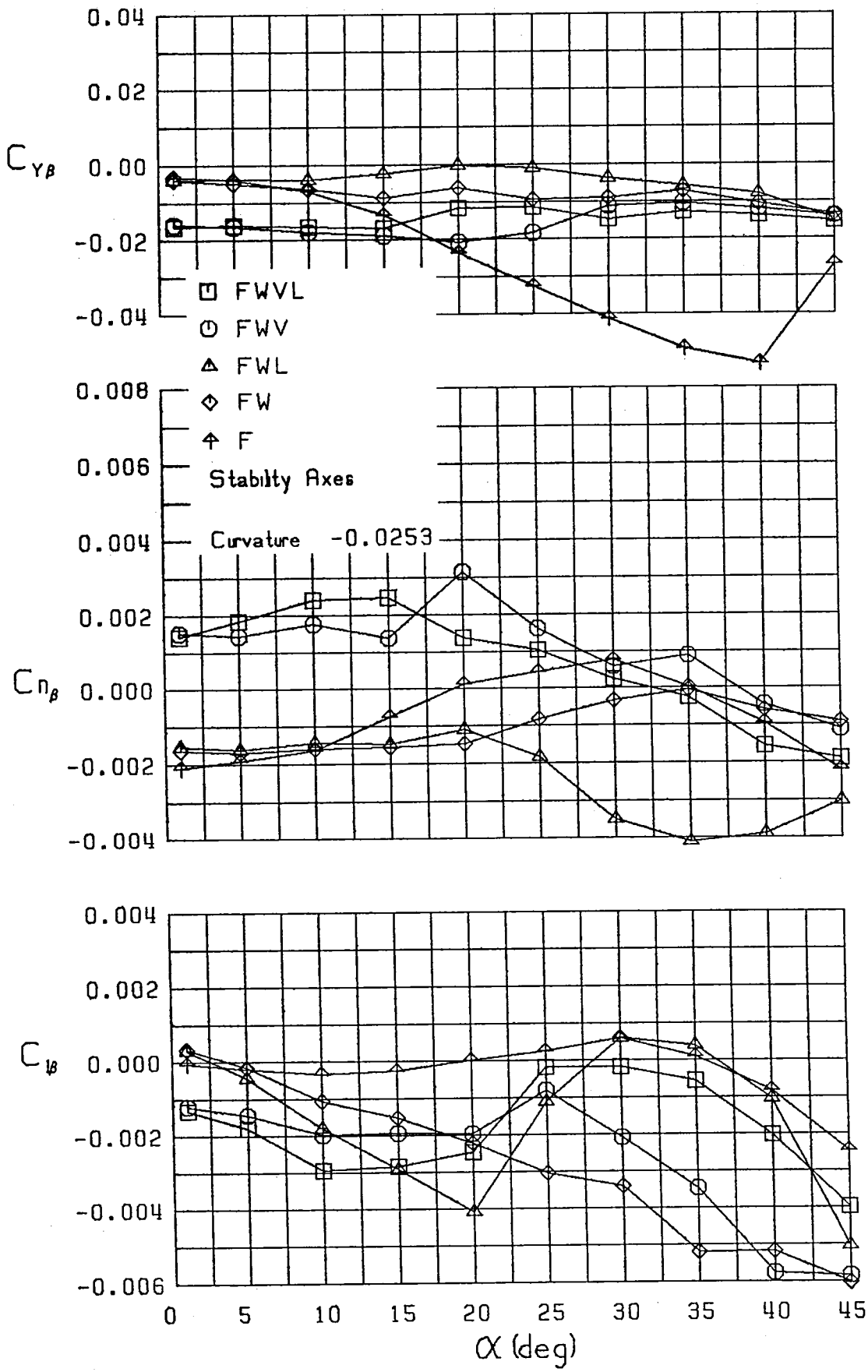

Figure 11 (Continued)

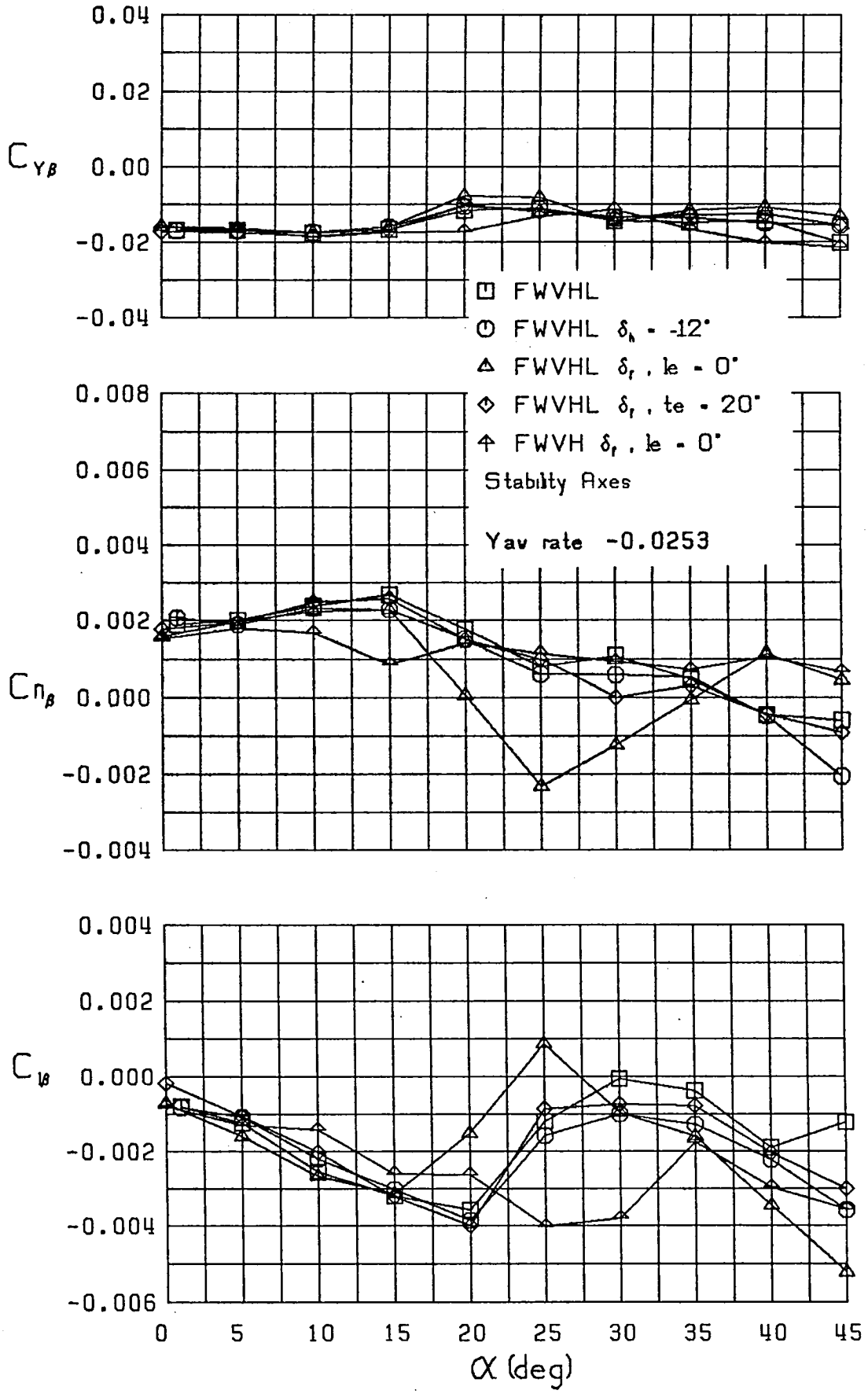

Figure 11 (Continued)

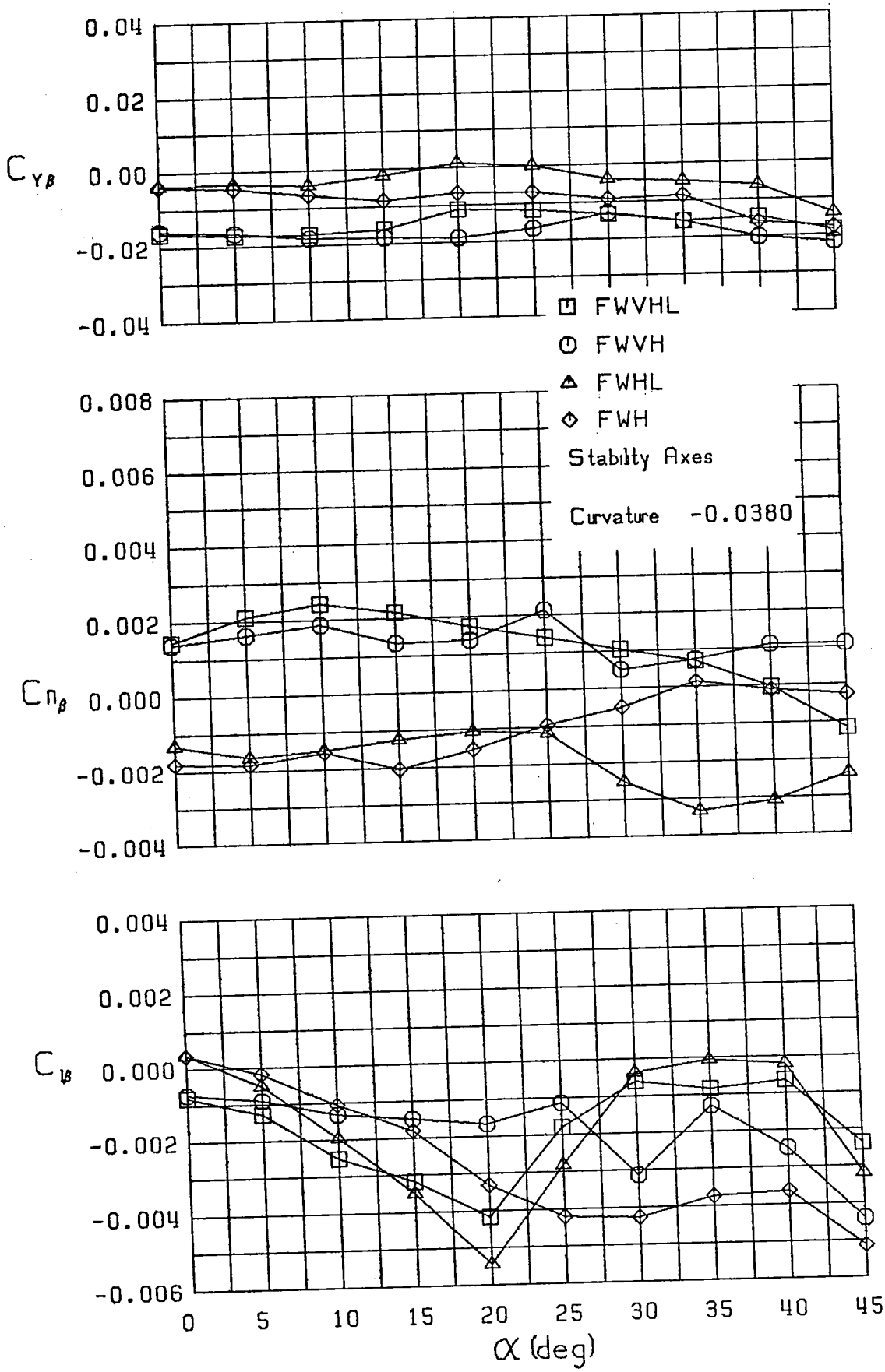

Figure 12 Variation of Lateral-Directional Static Stability Derivatives with Angle of Attack, $\hat{r}$ = - 0.0380

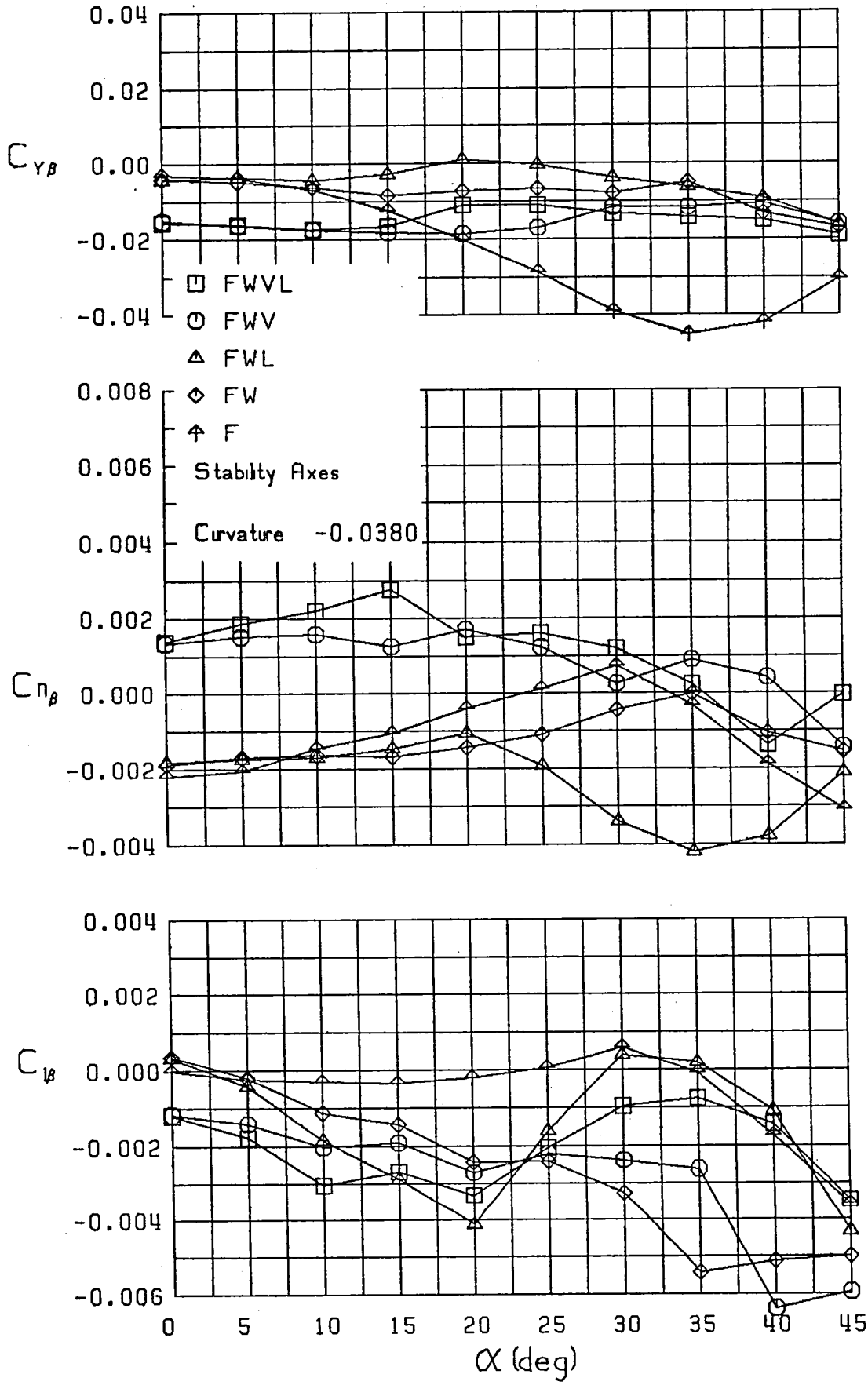

Figure 12 (Continued)

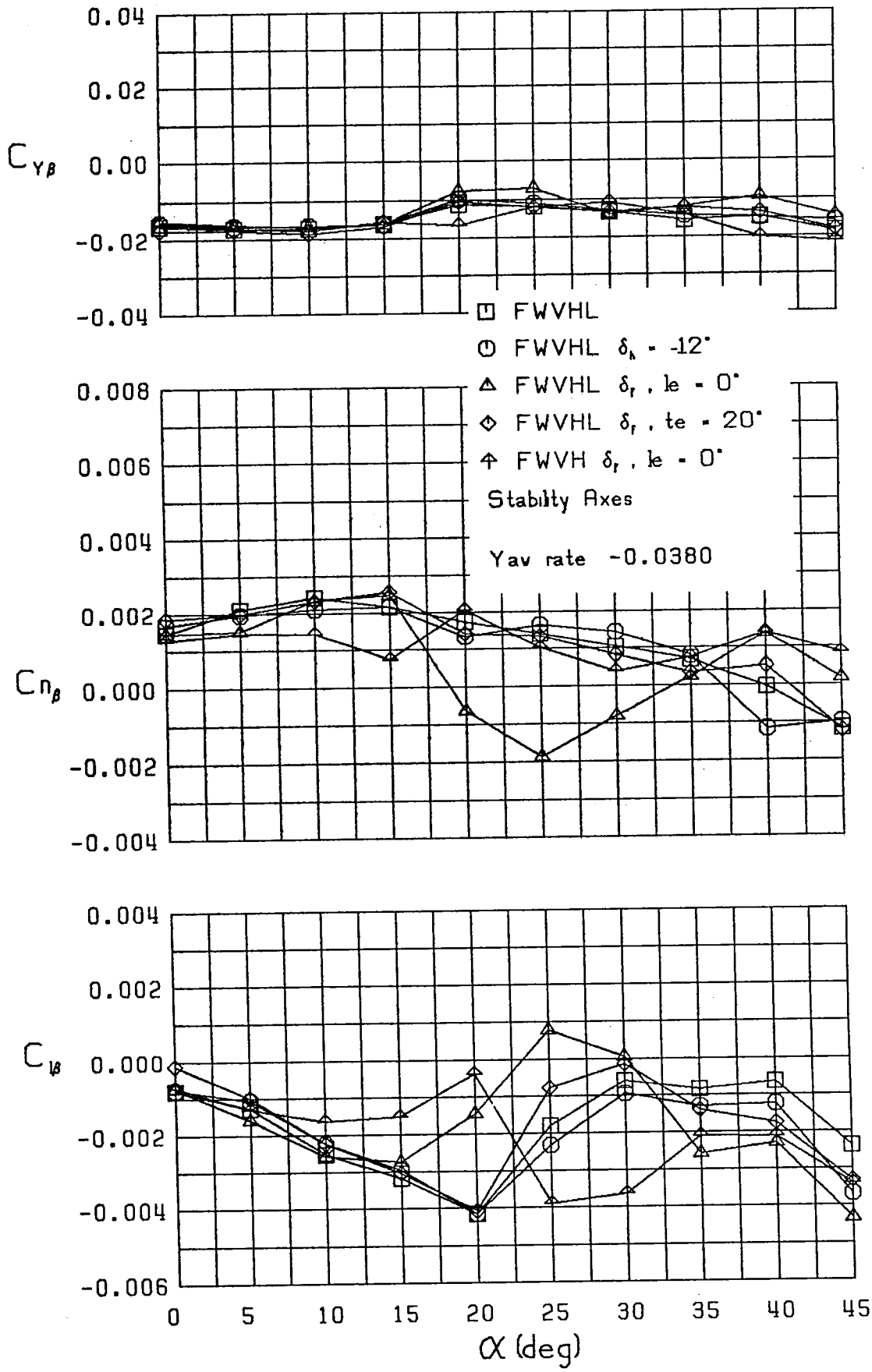

Figure 12 (Continued)

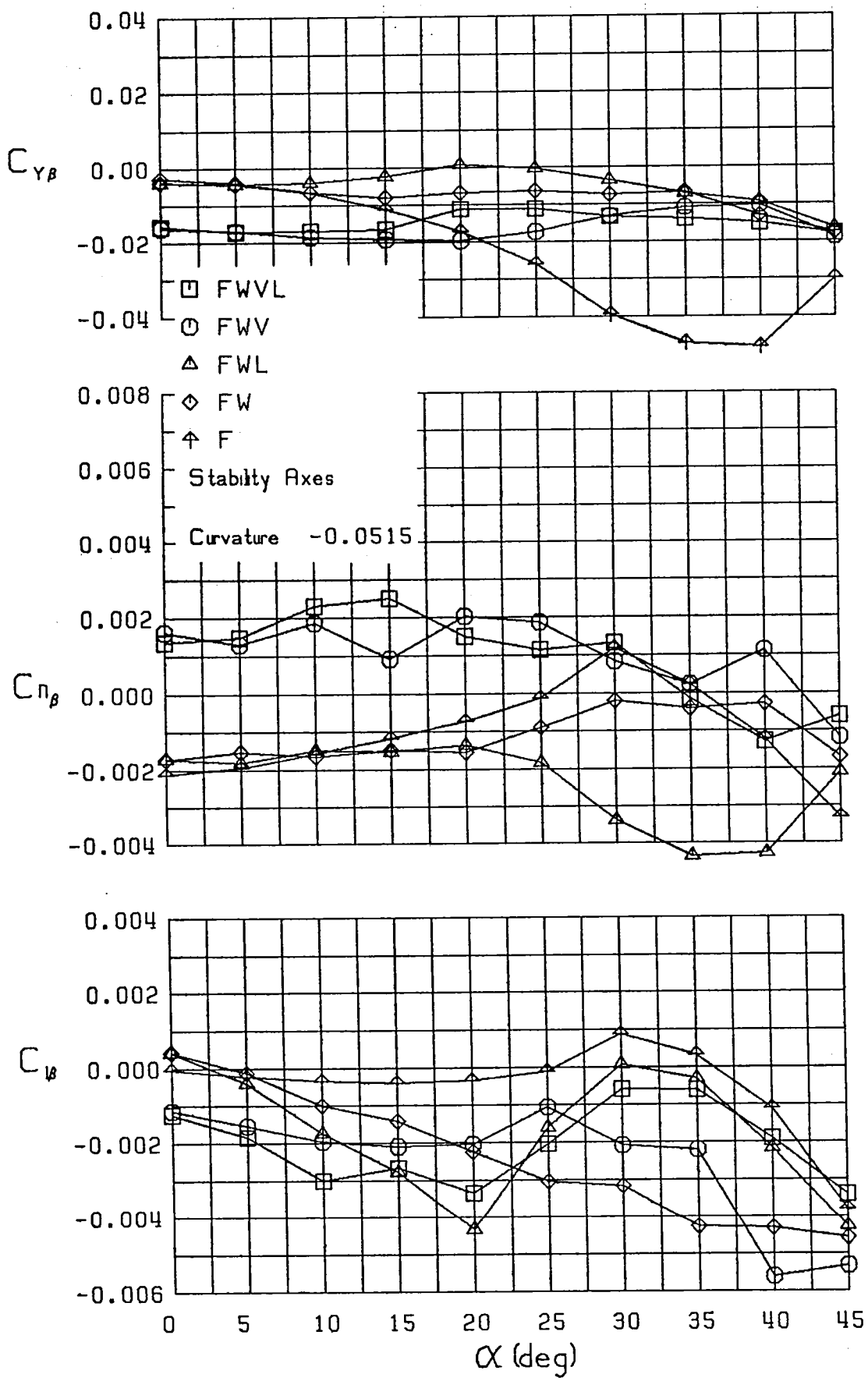

Figure 13 Variation of Lateral-Directional Static Stability Derivatives with Angle of Attack, $\hat{r}$ = - 0.0515

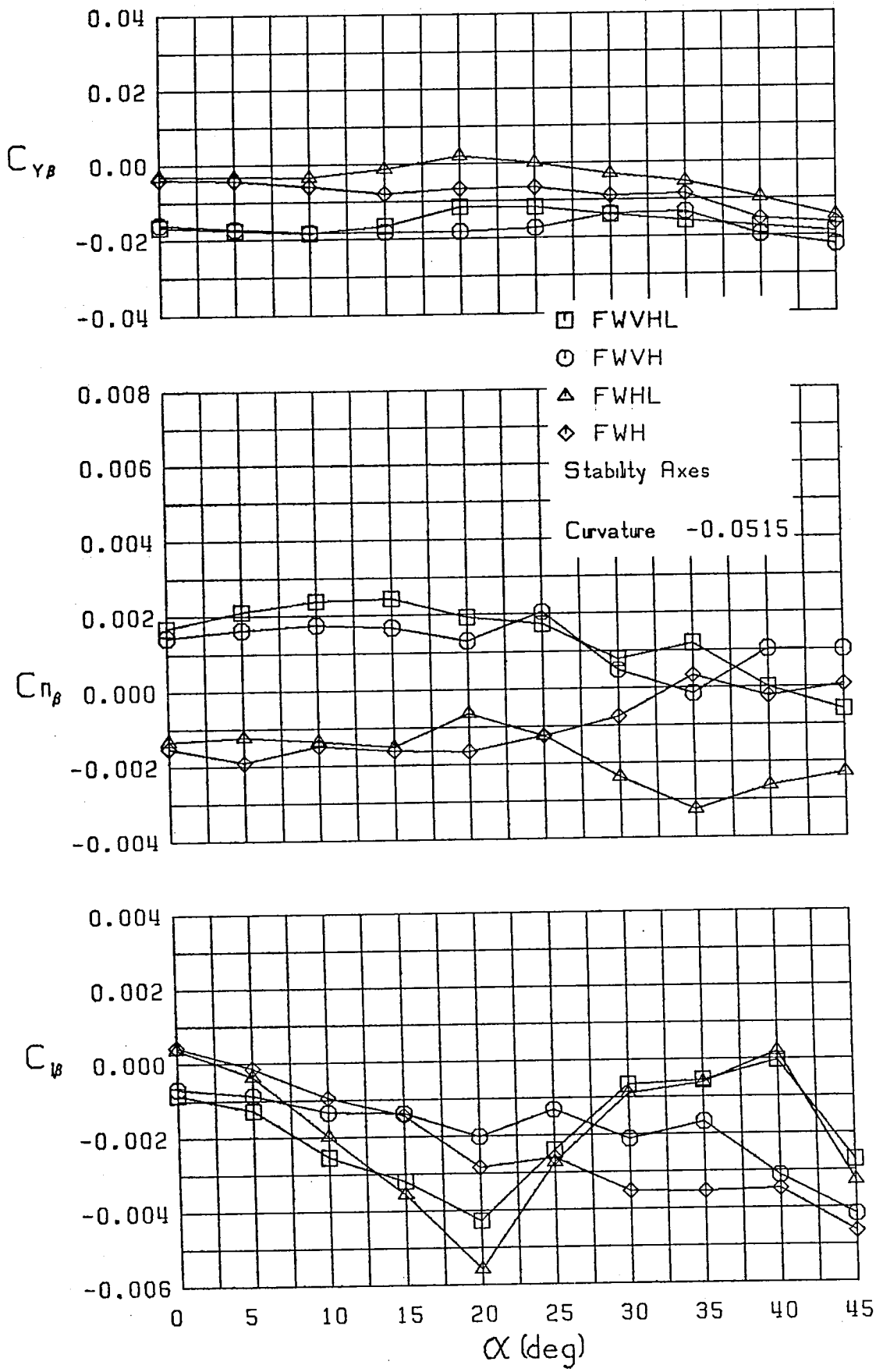

Figure 12 (Continued)

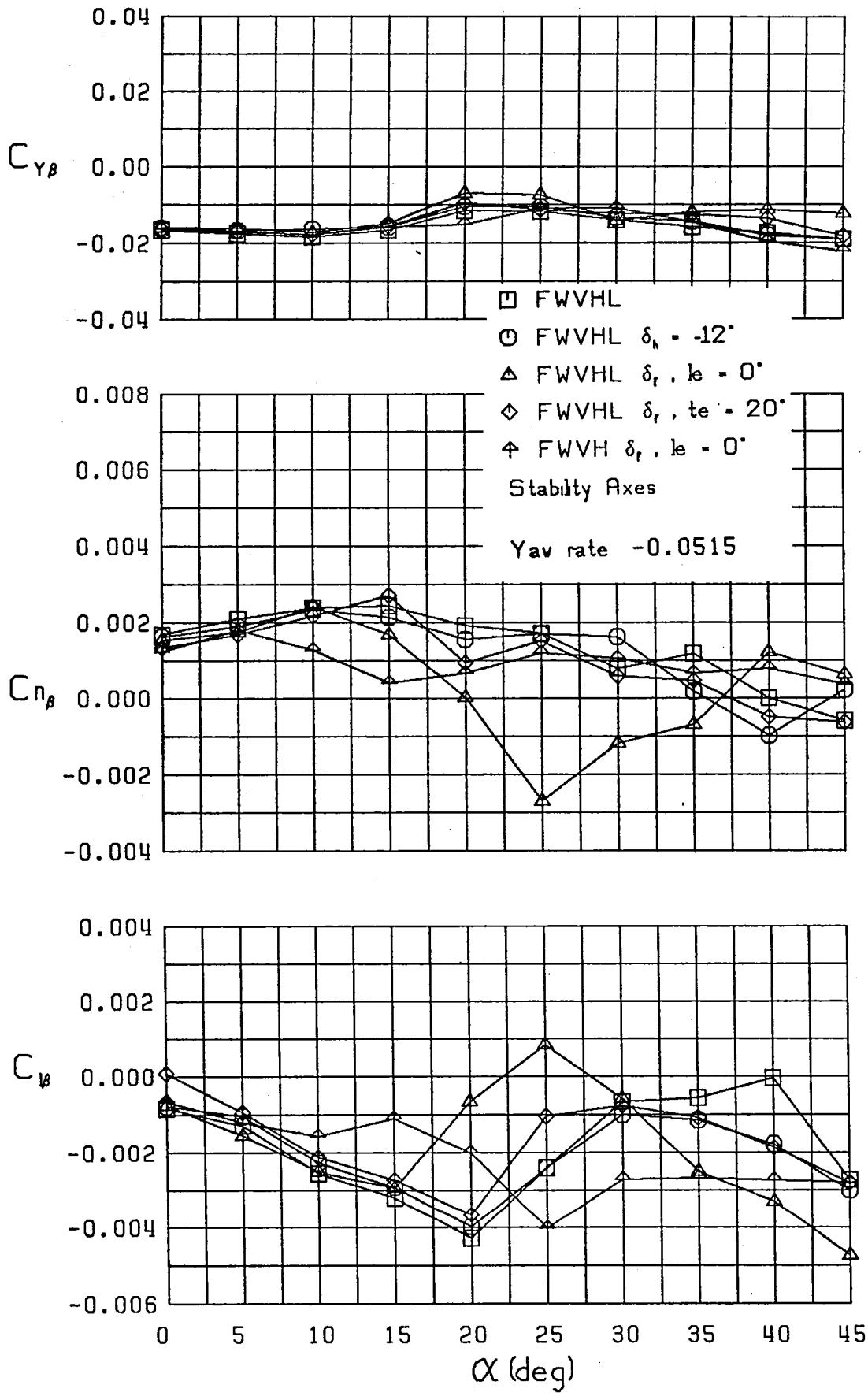

Figure 13 (Continued)

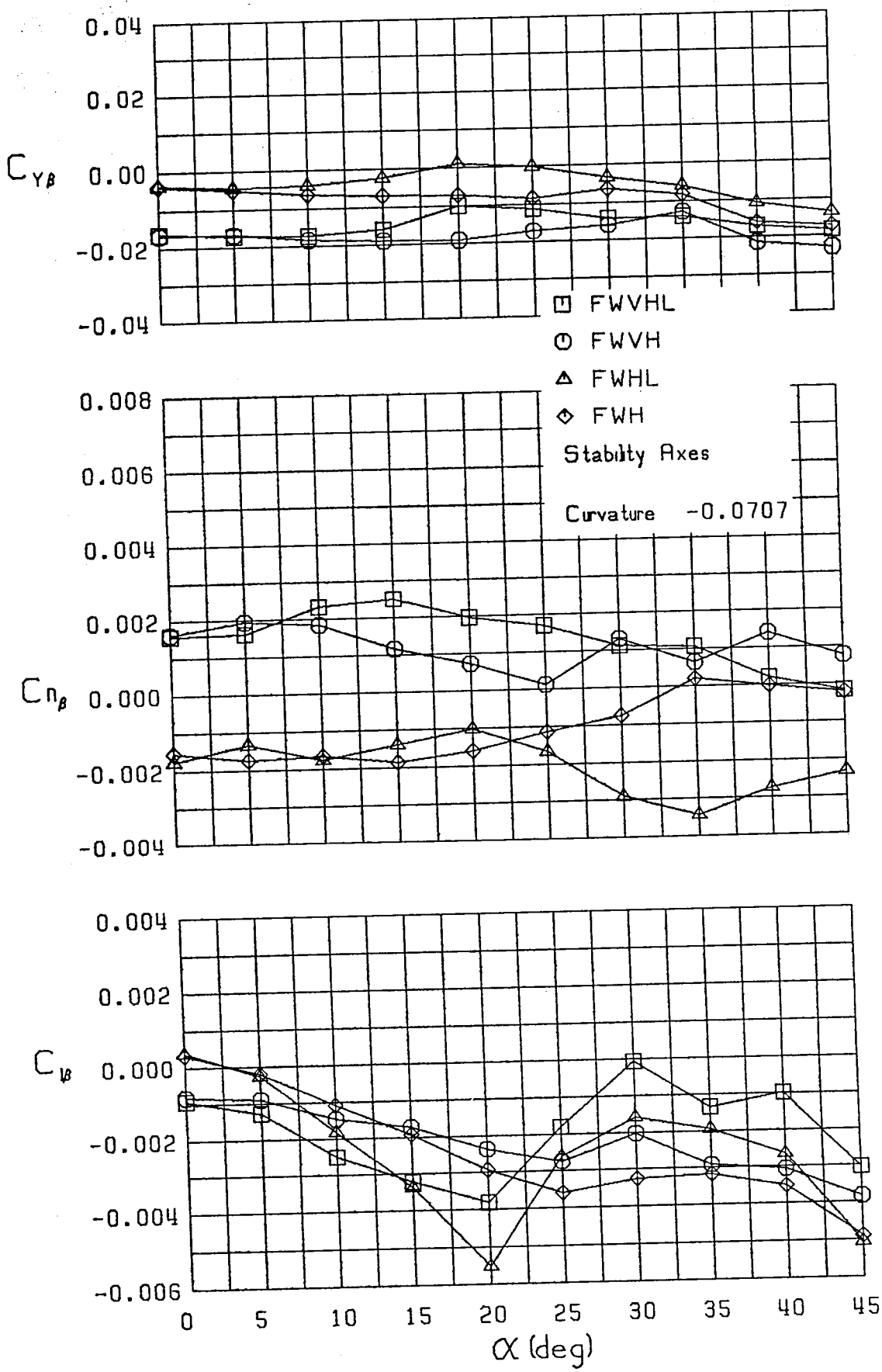

Figure 14 Variation of Lateral-Directional Static Stability Derivatives with Angle of Attack, $\hat{r}$ = - 0.0707

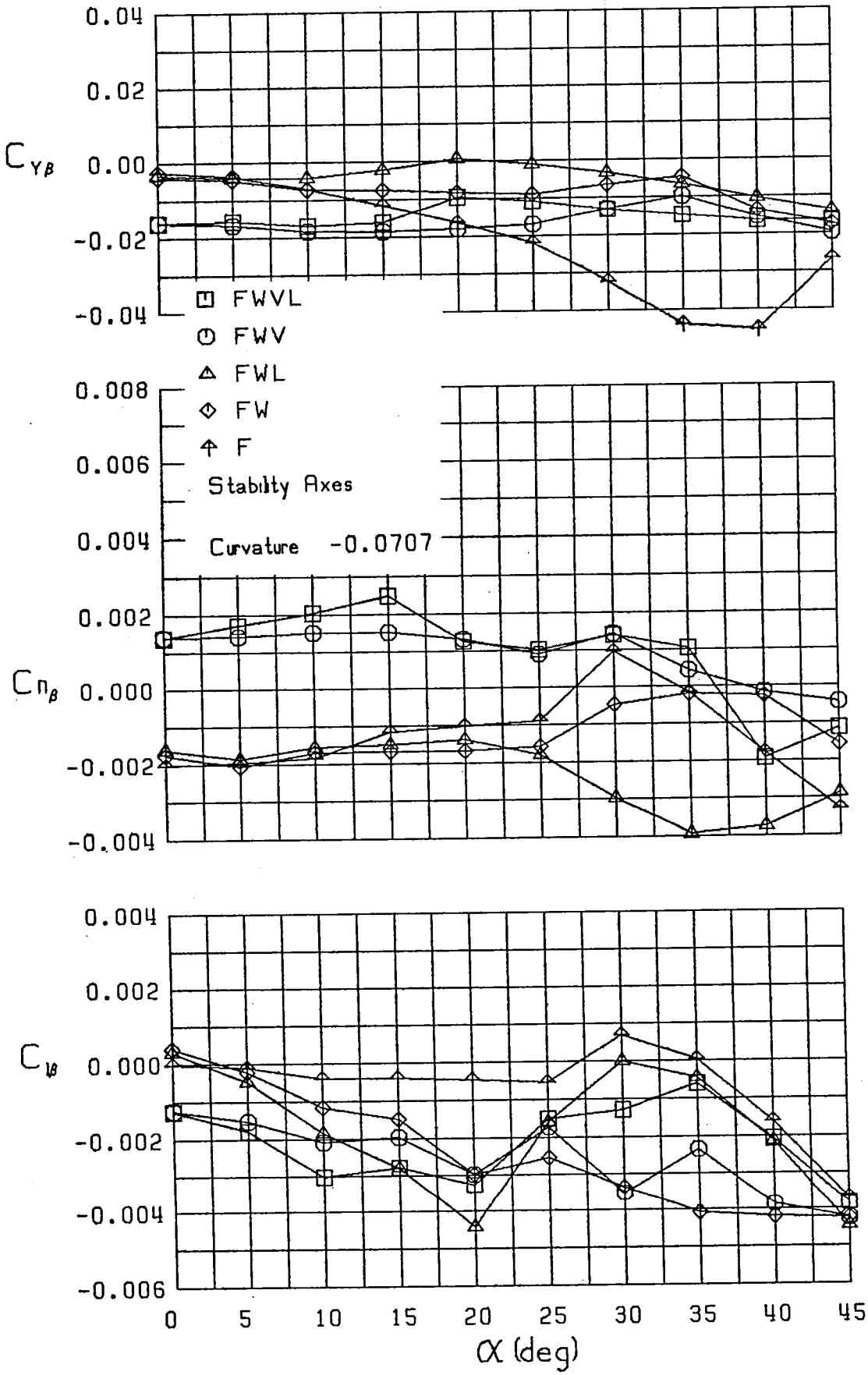

Figure 14 (Continued)

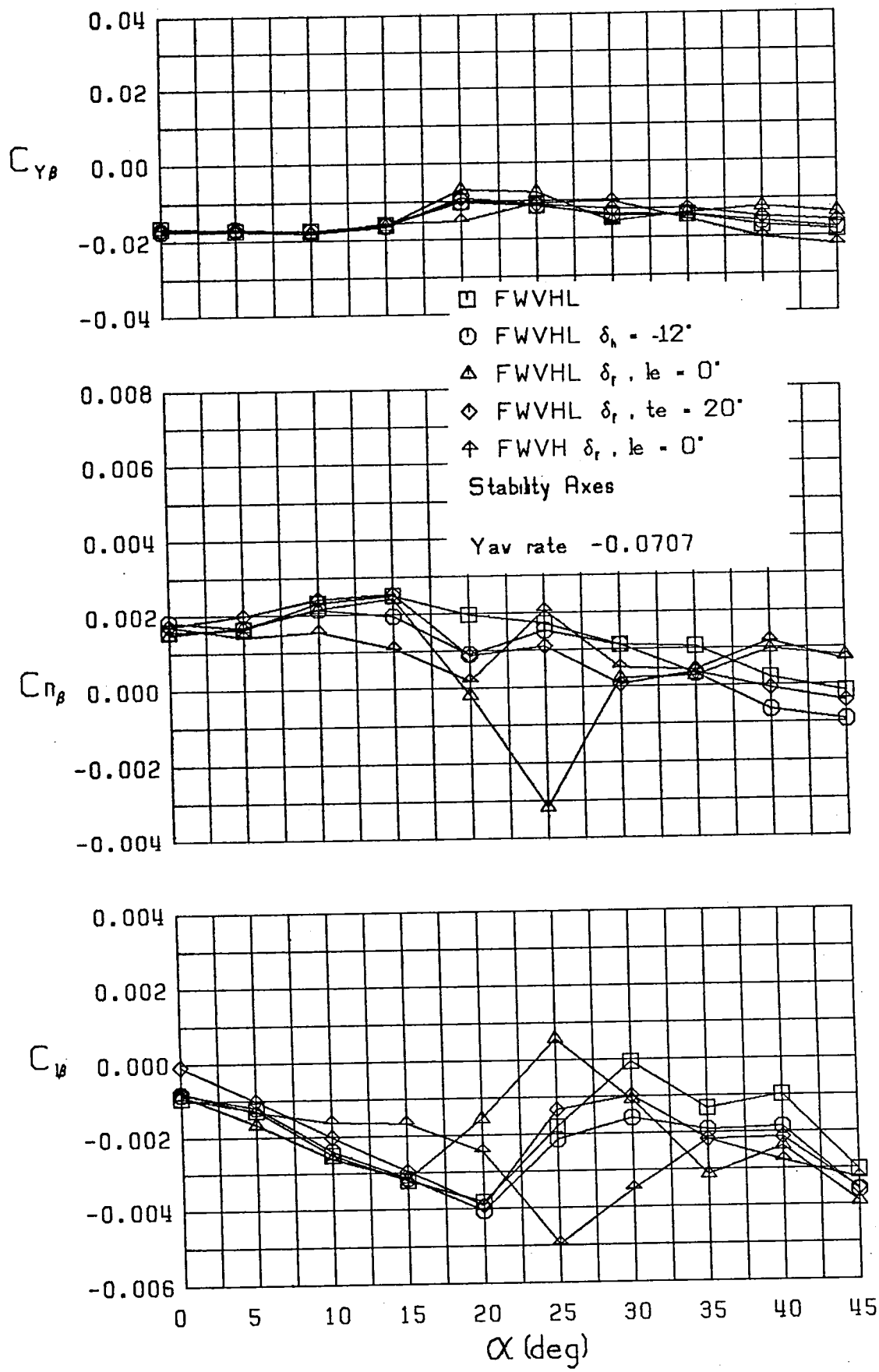

Figure 14 (Continued)

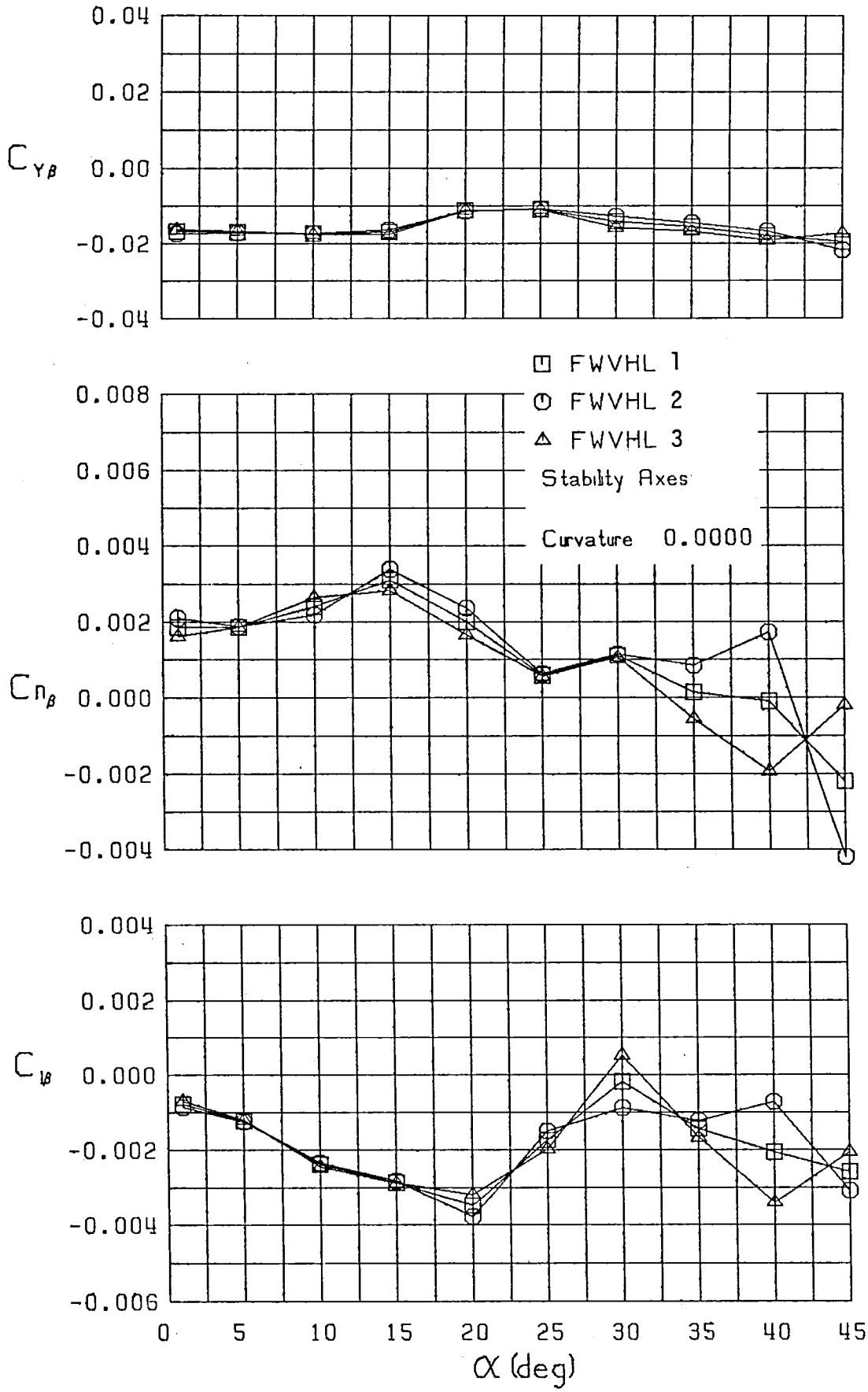

Figure 15 Variation of Lateral-Directional Static Stability Derivatives with Angle of Attack and Sideslip, $\hat{r} = 0$

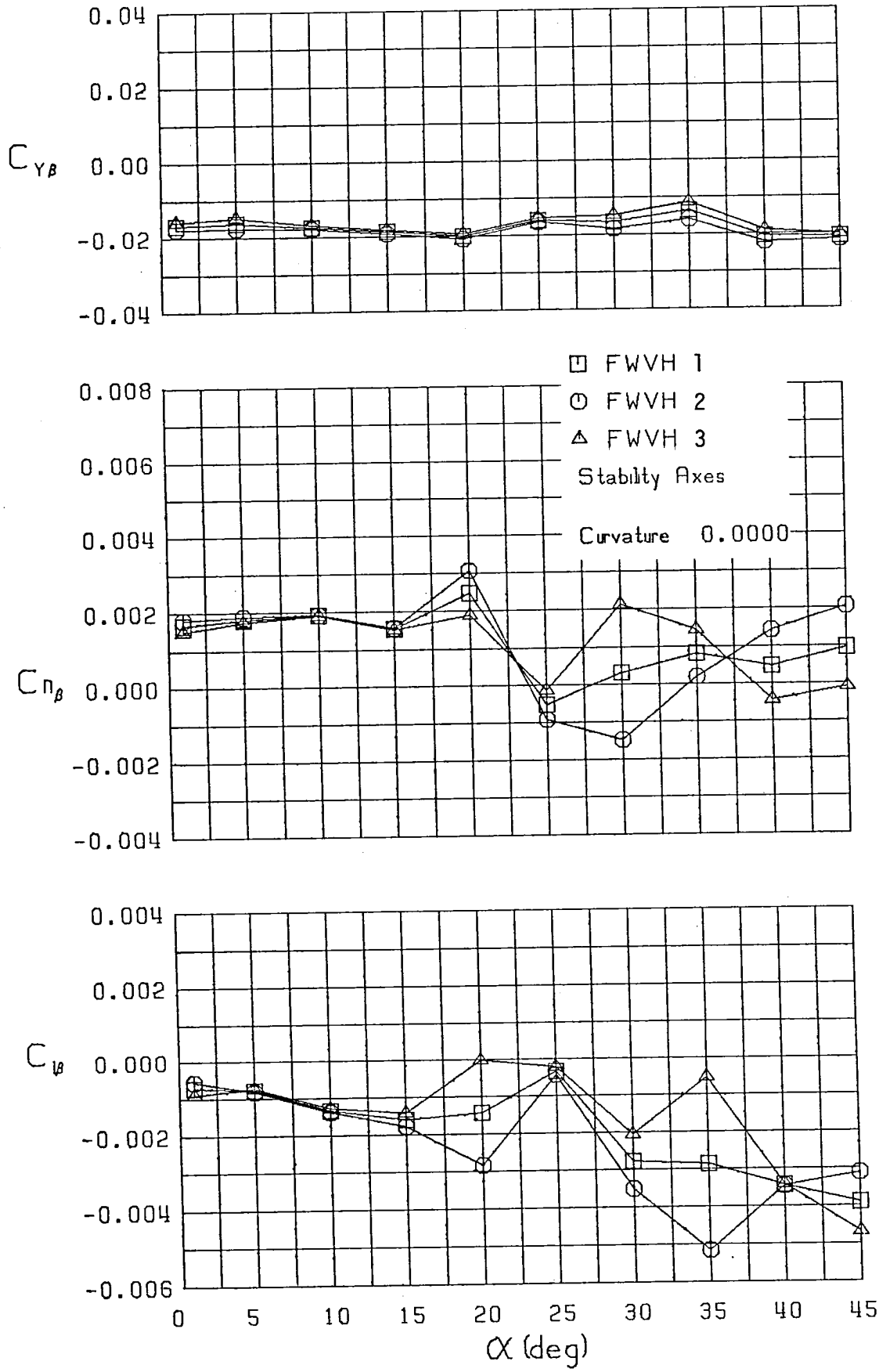

Figure 15 (Continued)

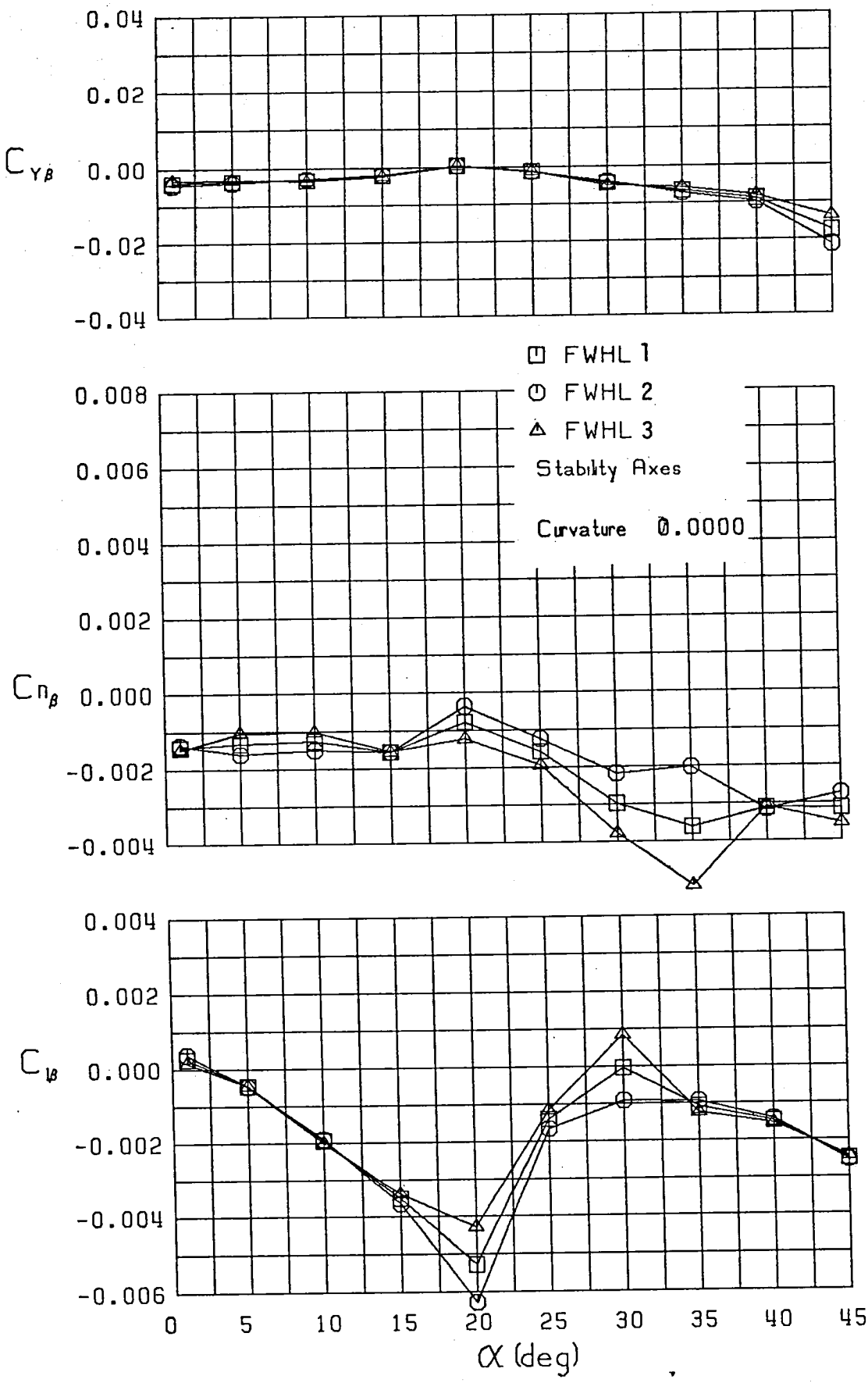

Figure 15 (Continued)

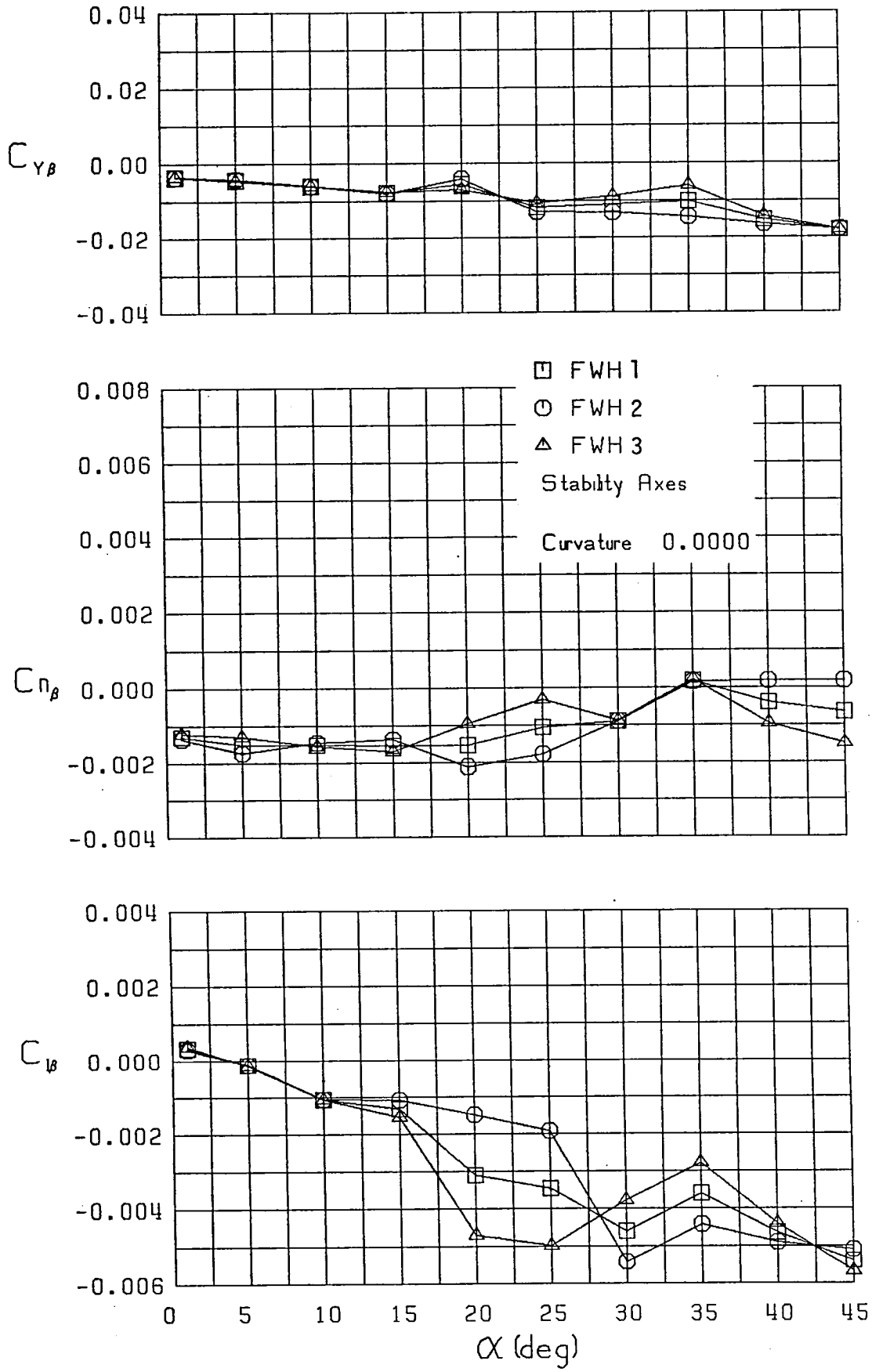

Figure 15 (Continued)

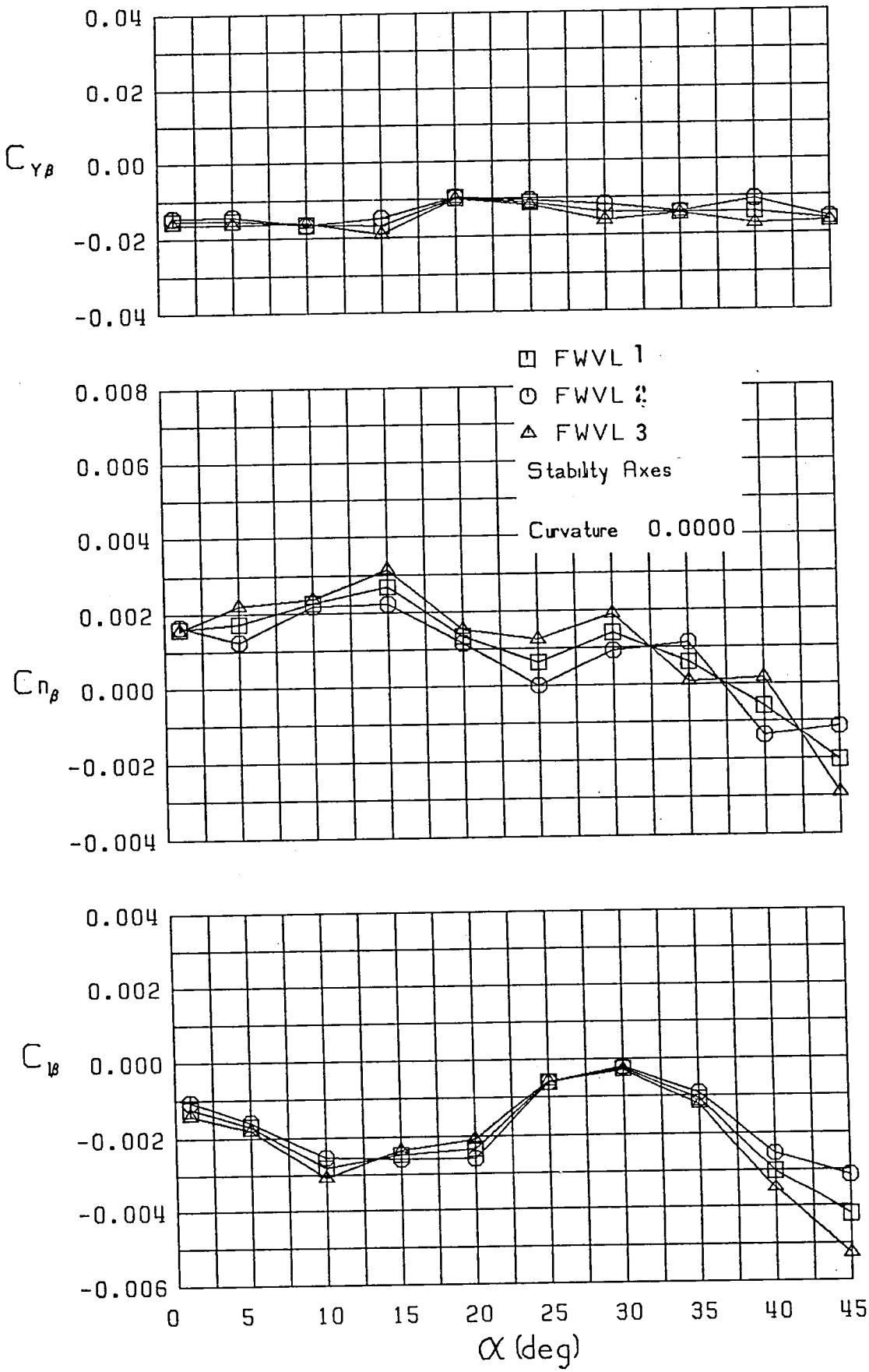

Figure 15 (Continued)

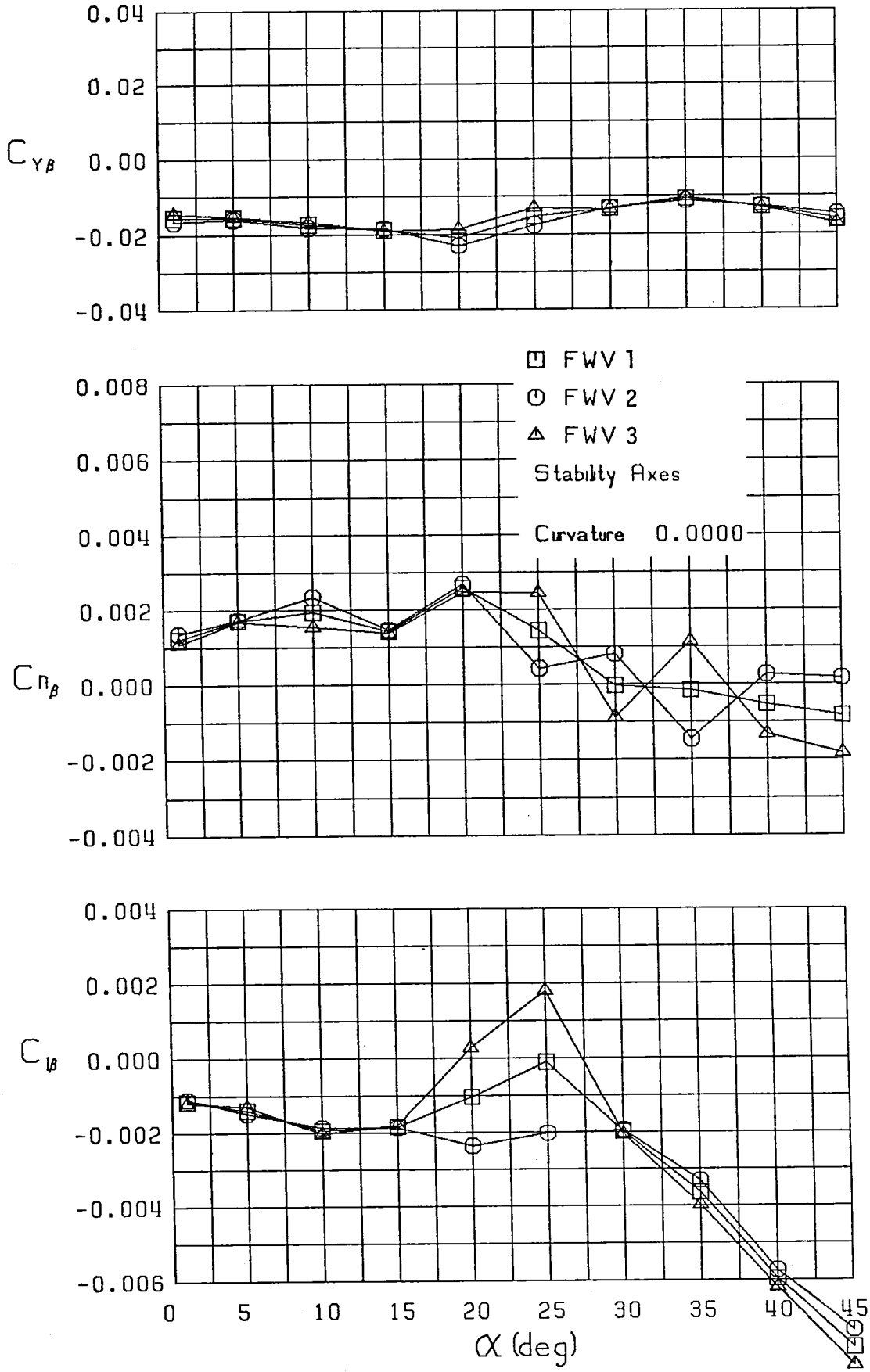

Figure 15 (Continued)

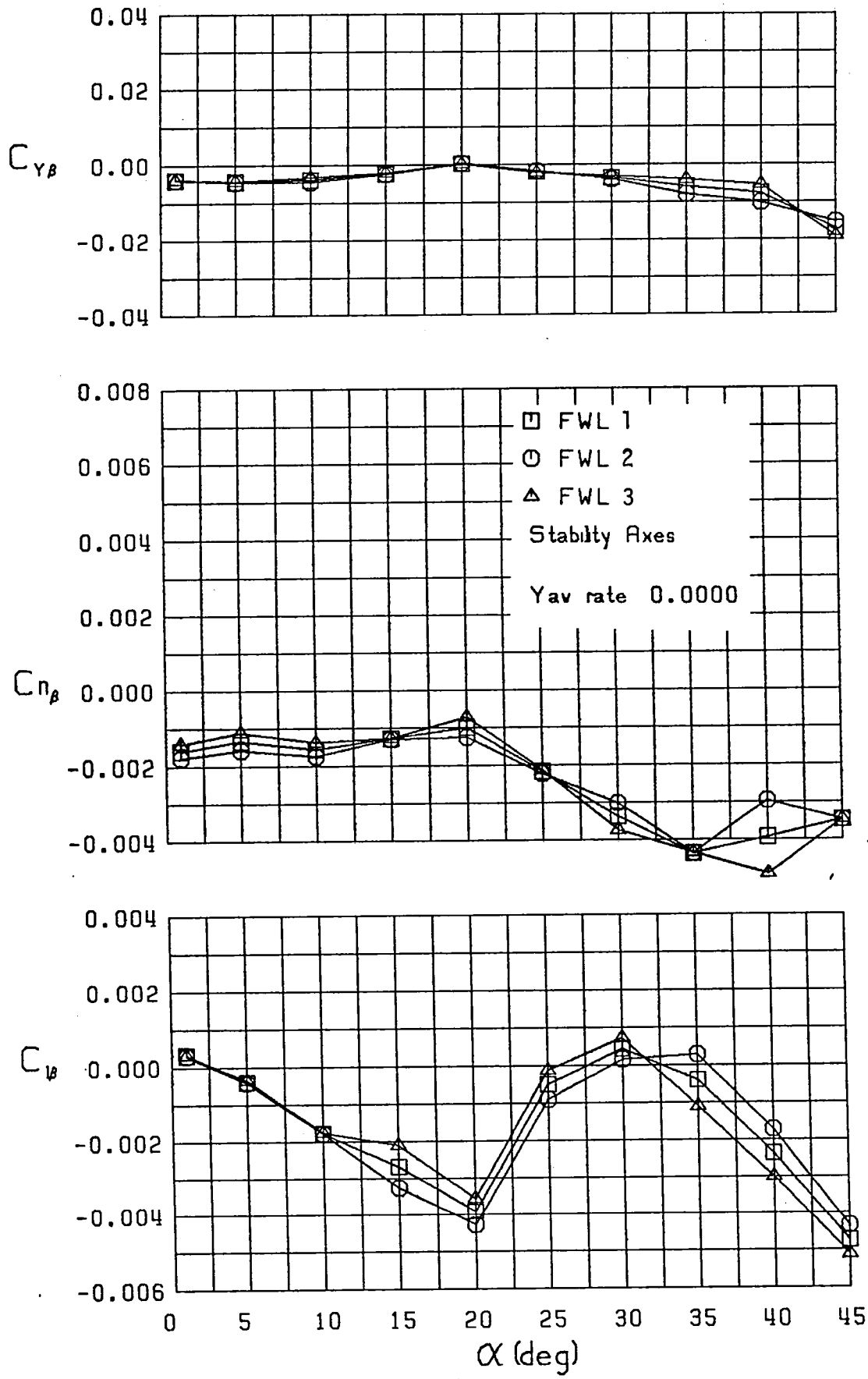

Figure 15 (Continued)

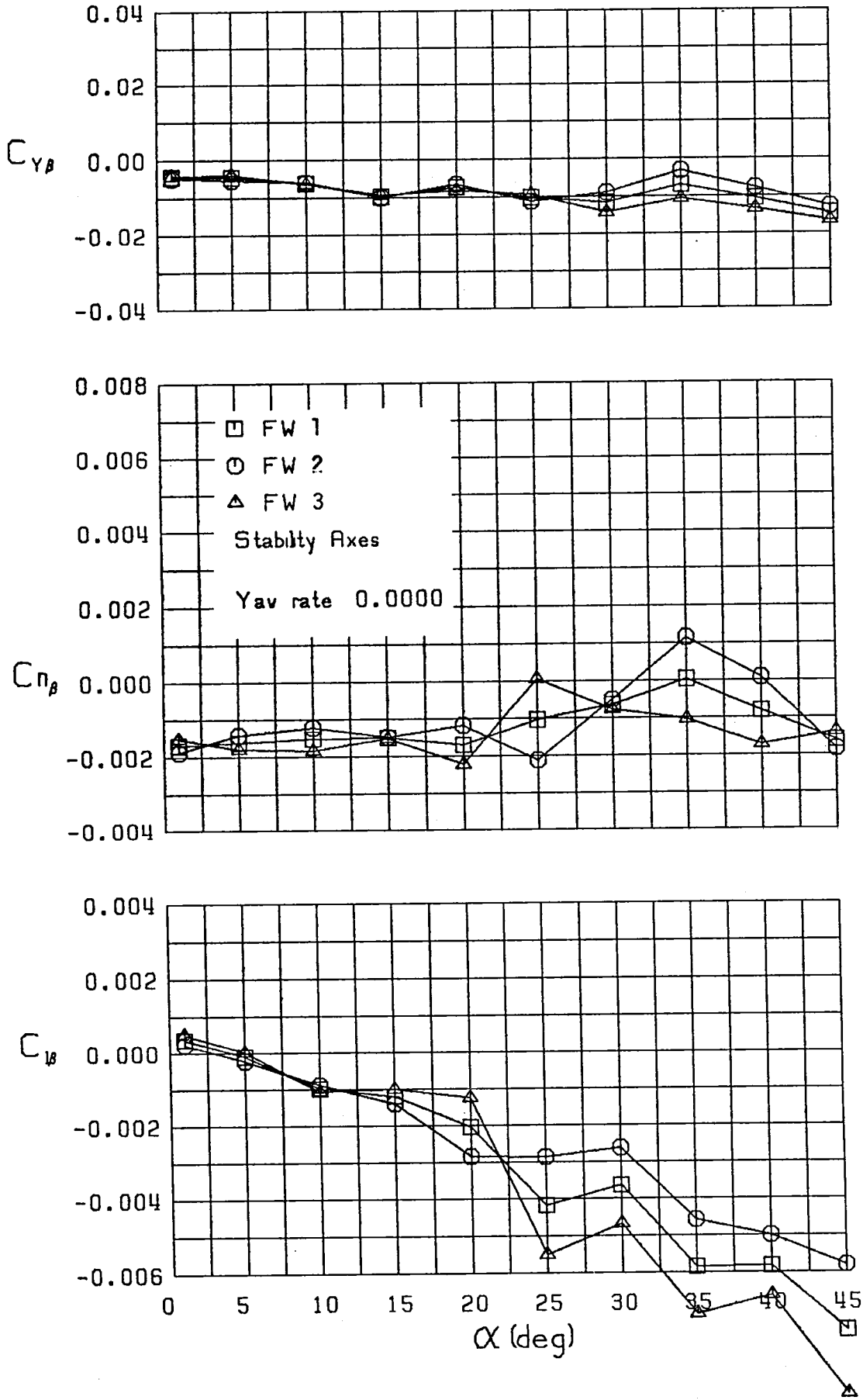

Figure 15 (Continued)

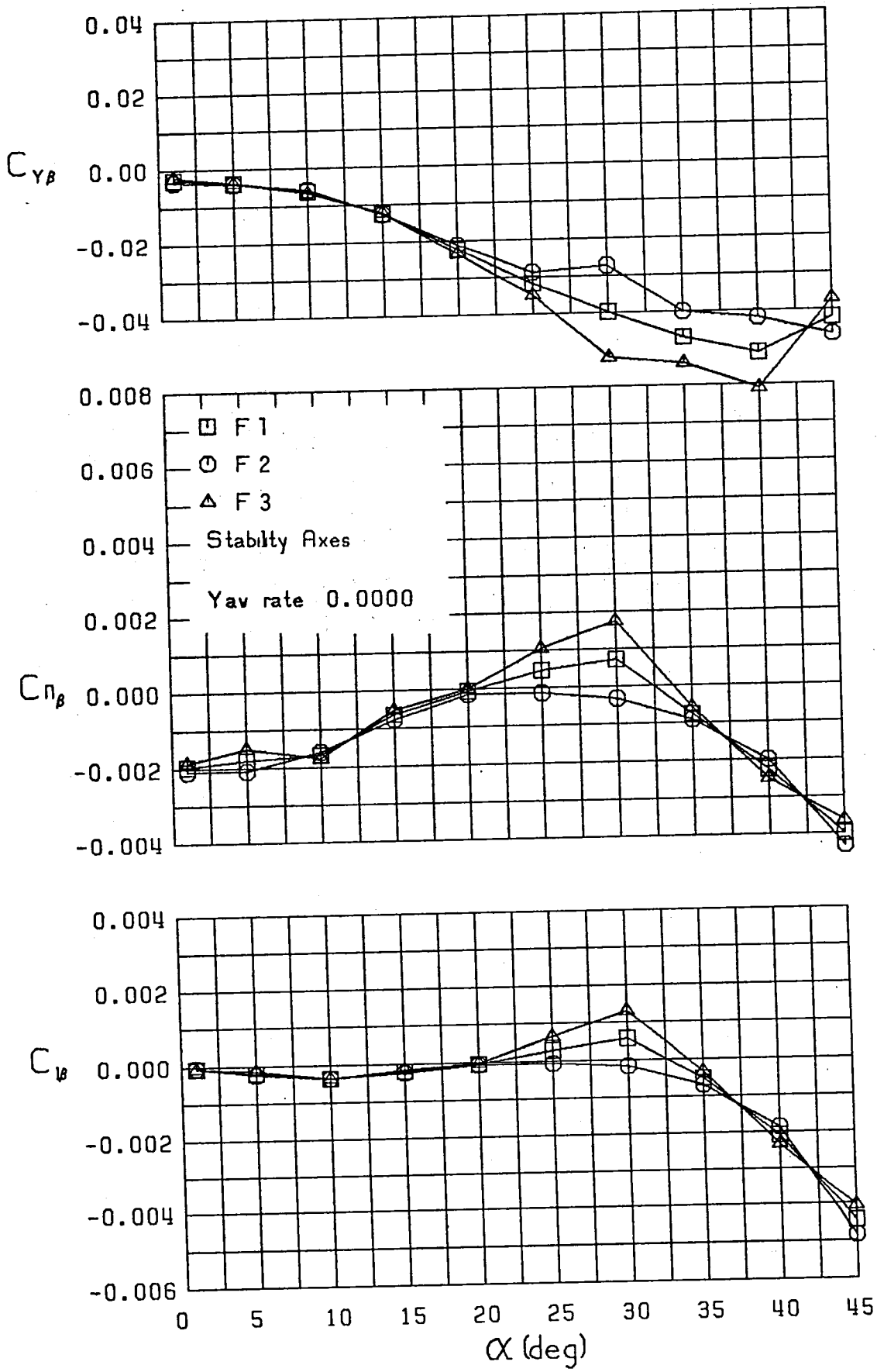

Figure 15 (Continued)

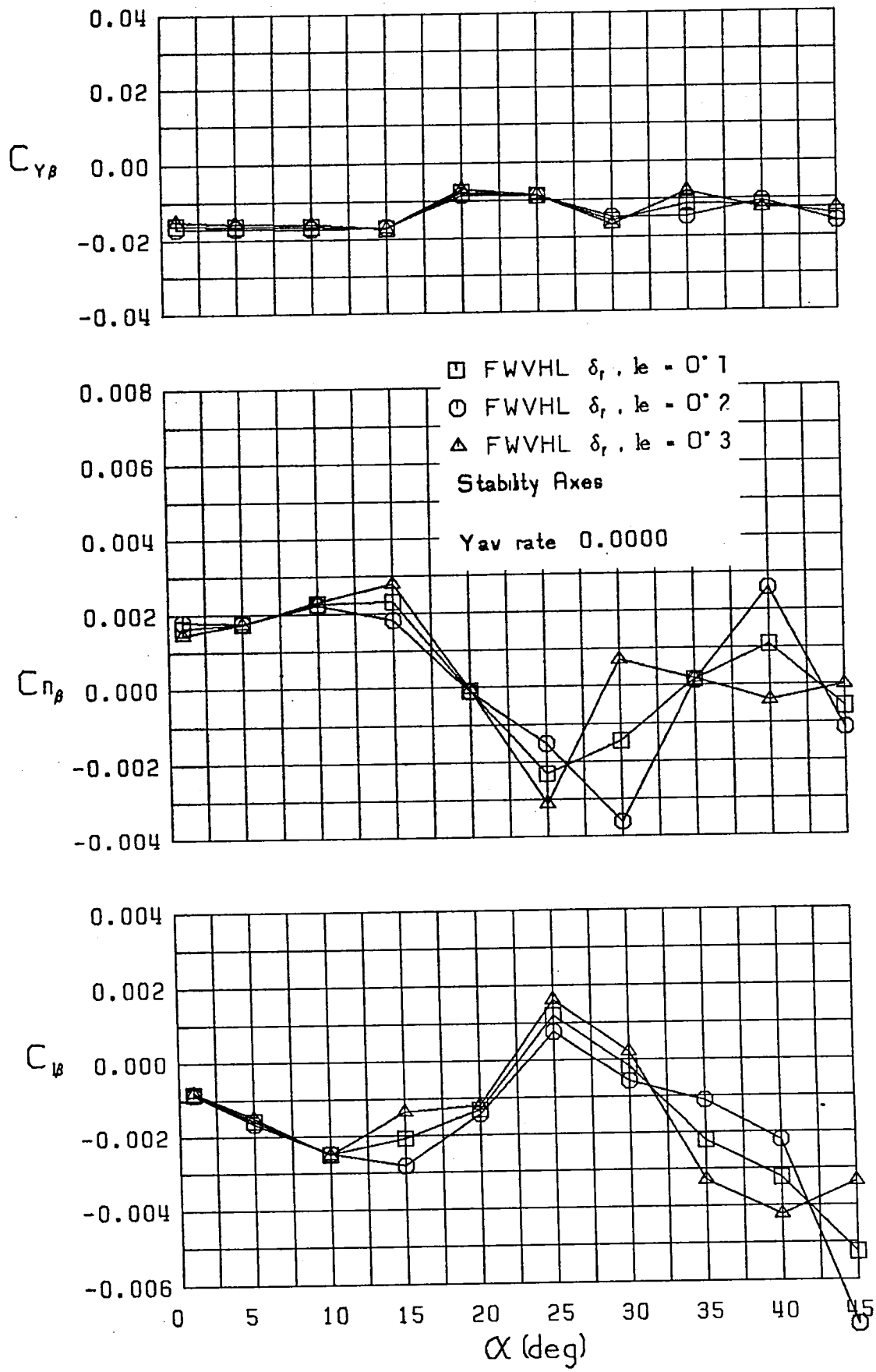

Figure 15 (Continued)

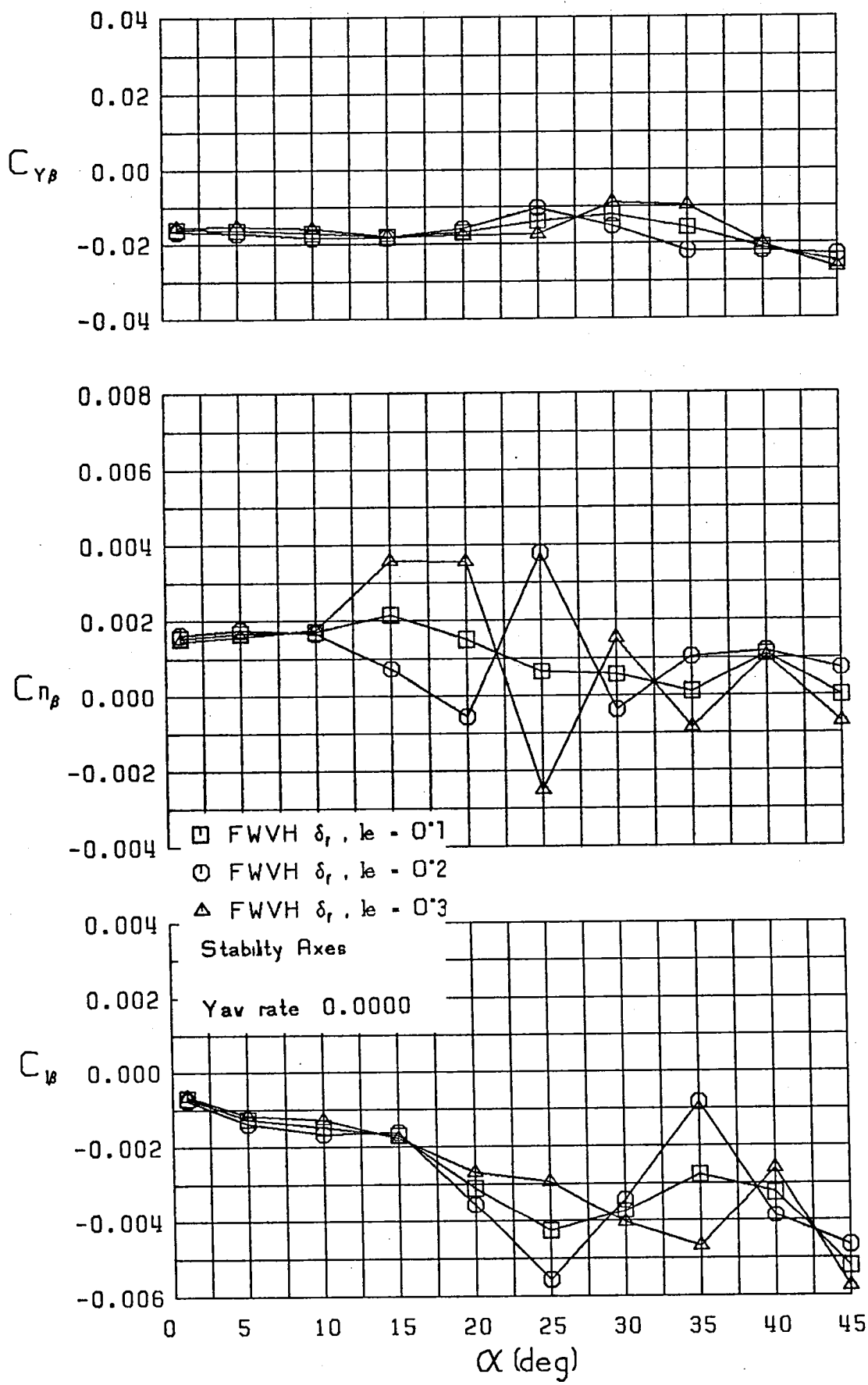

Figure 15 (Continued)

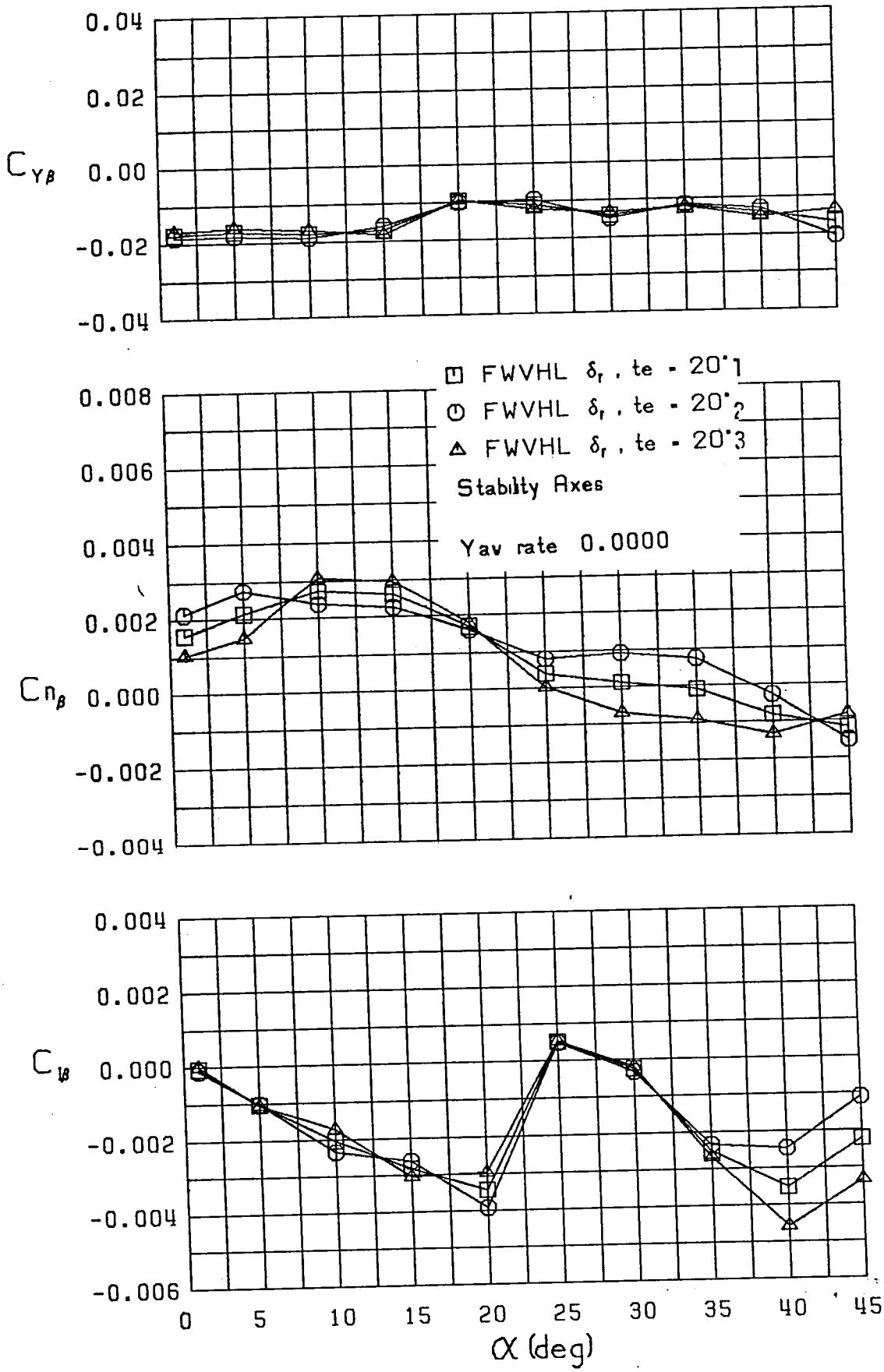

Figure 15 (Continued)

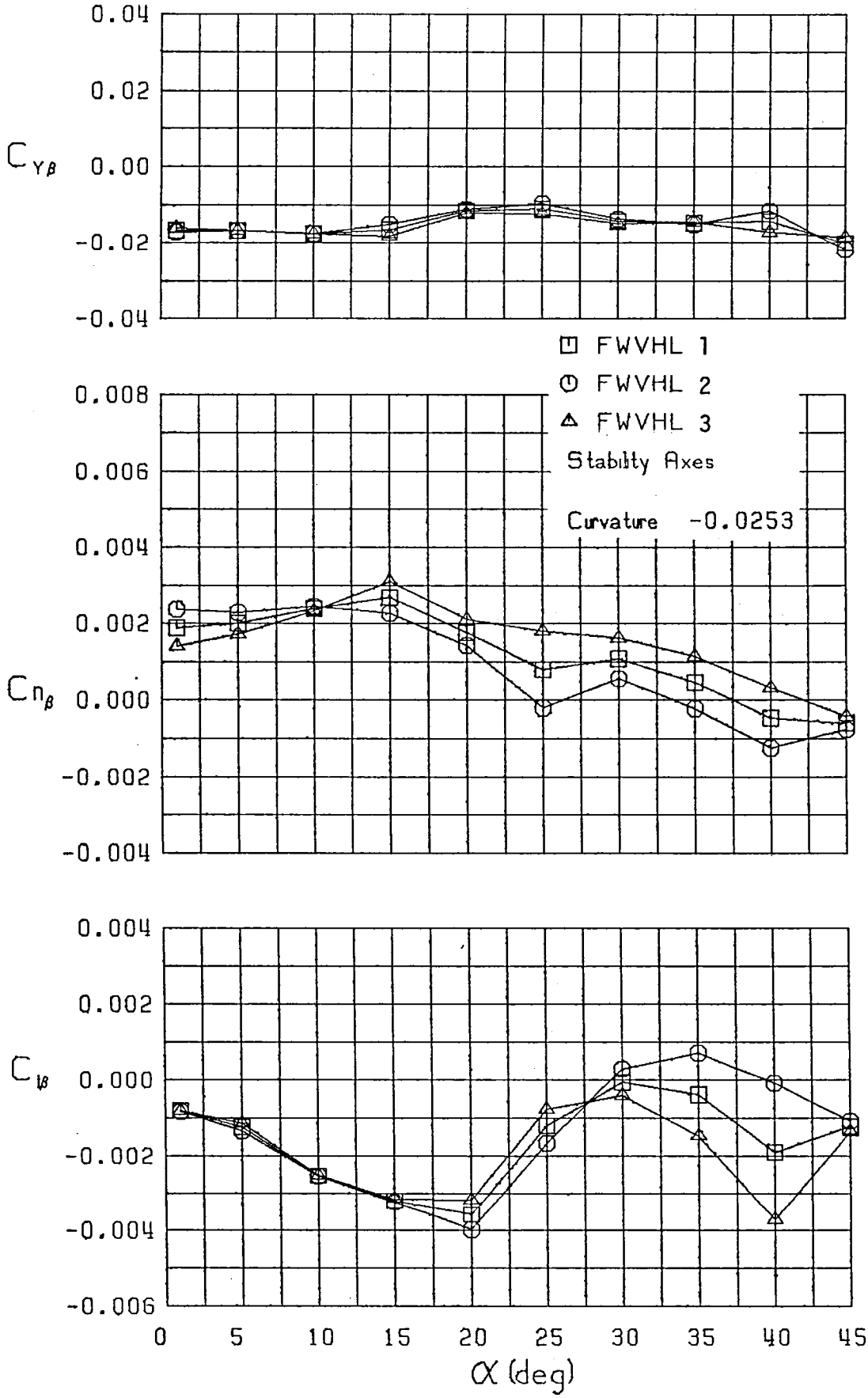

Figure 16 Variation of Lateral-Directional Static Stability Derivatives with Angle of Attack and Sideslip, $\hat{r}$ = - 0.0253

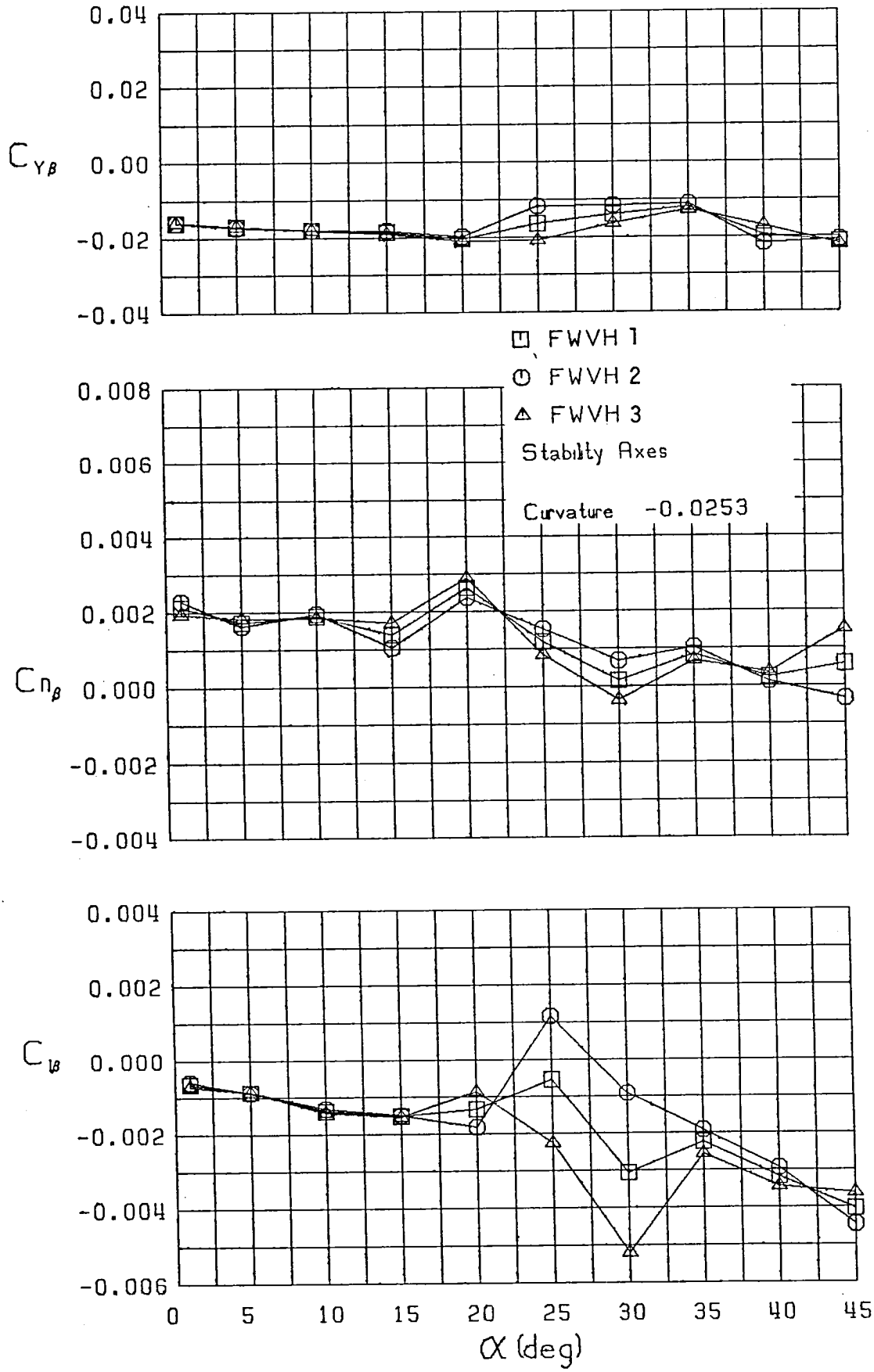

Figure 16 (Continued)

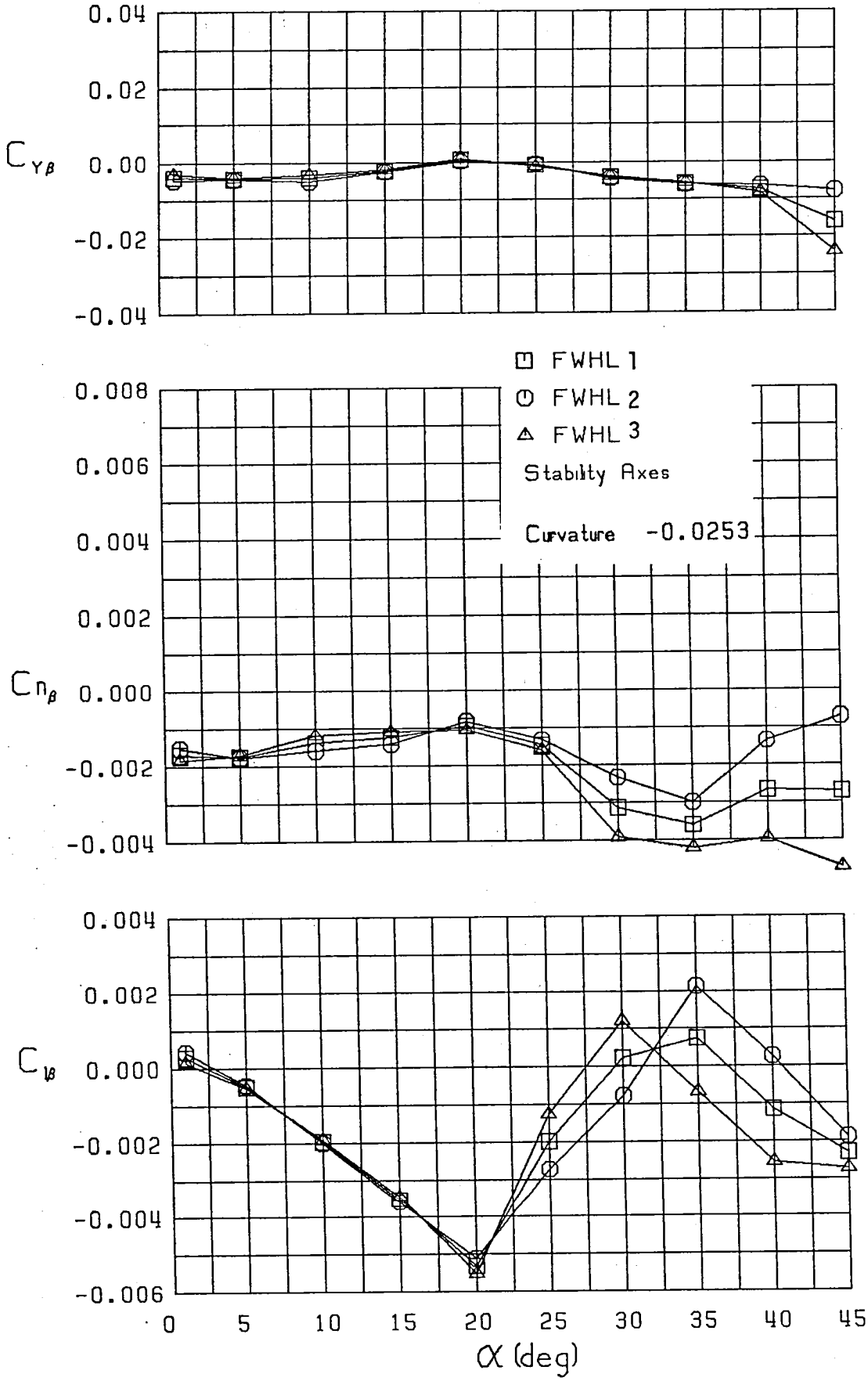

Figure 16 (Continued)

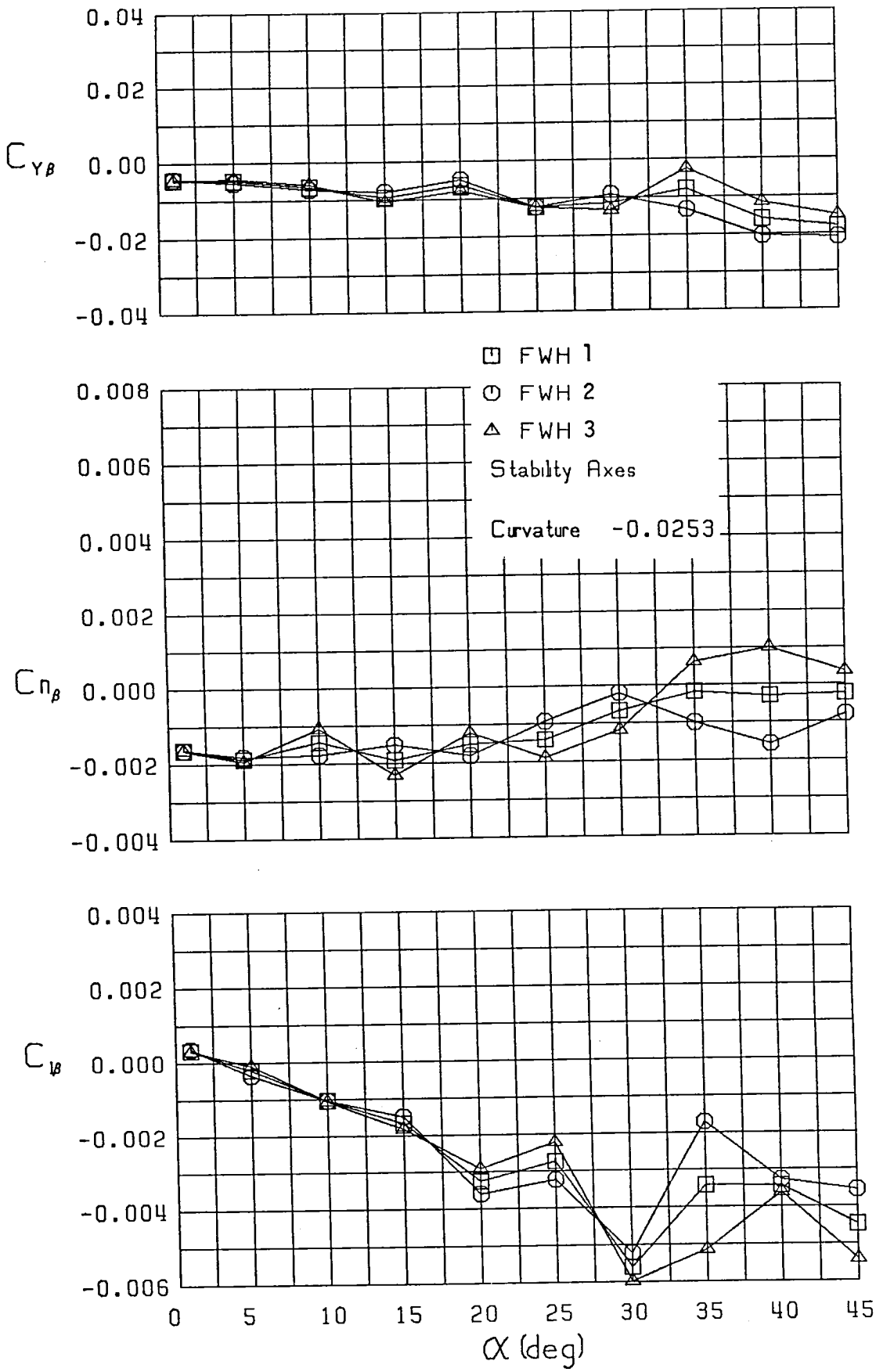

Figure 16 (Continued)

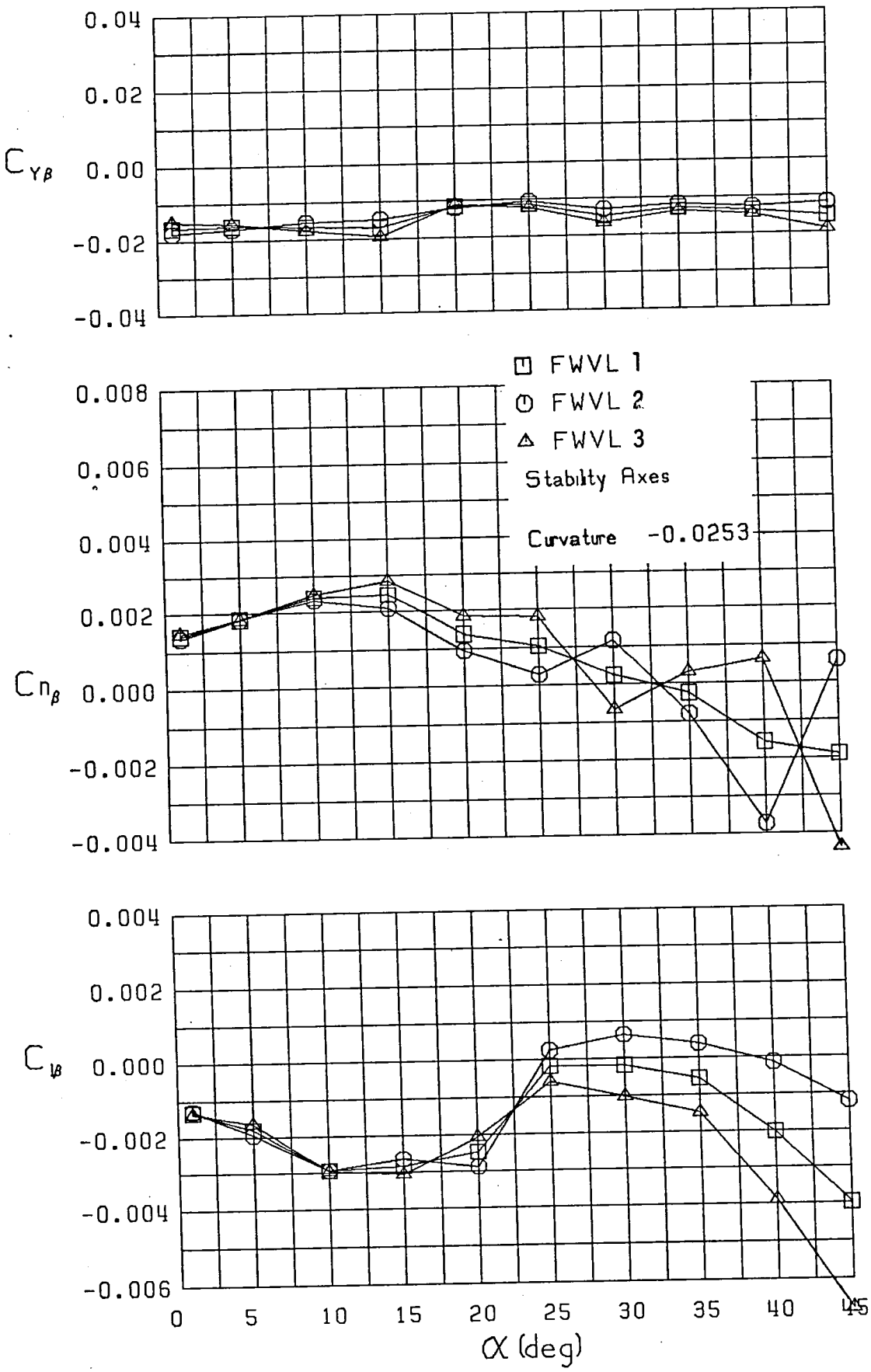

Figure 16 (Continued)

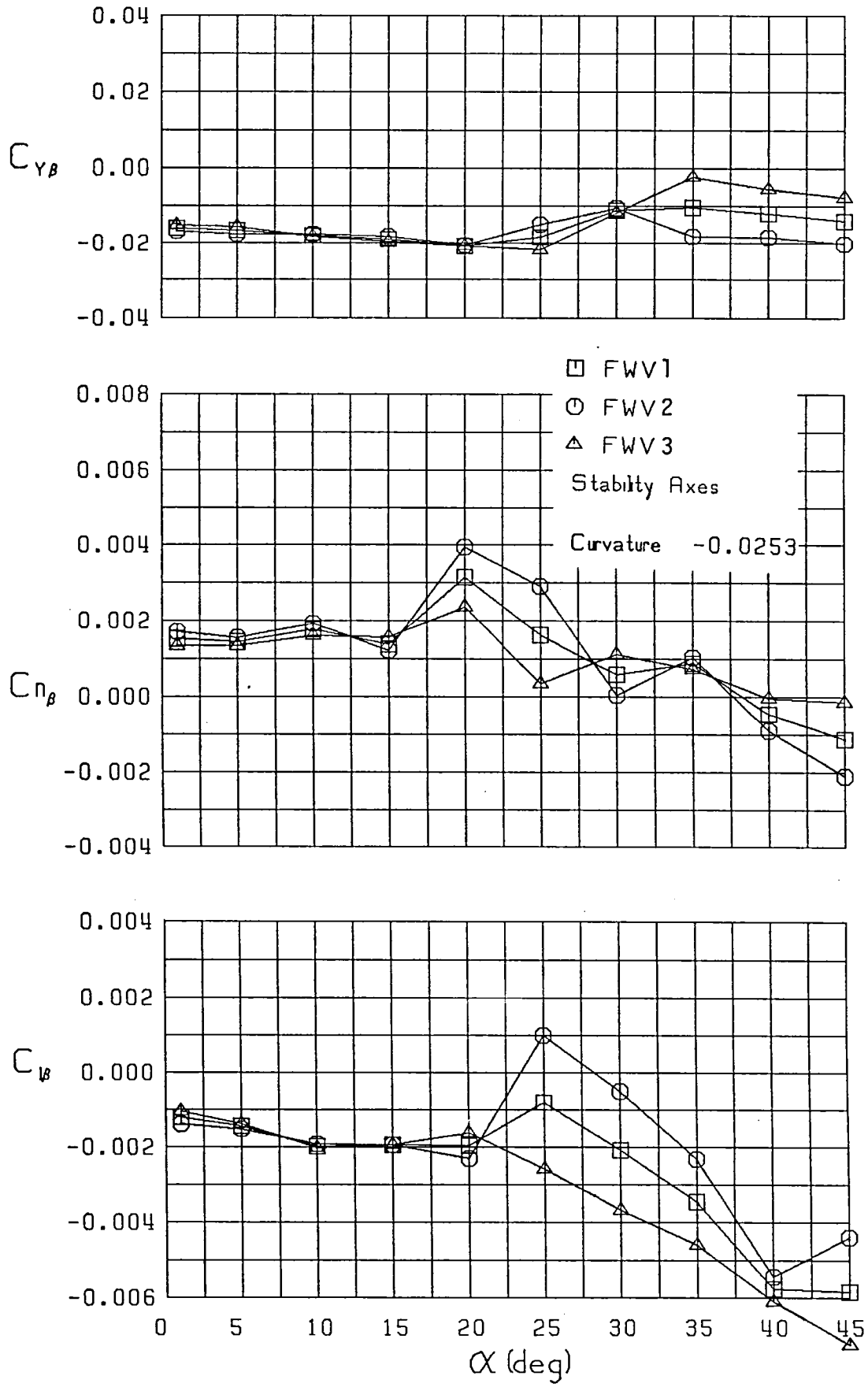

Figure 16. (Continued)

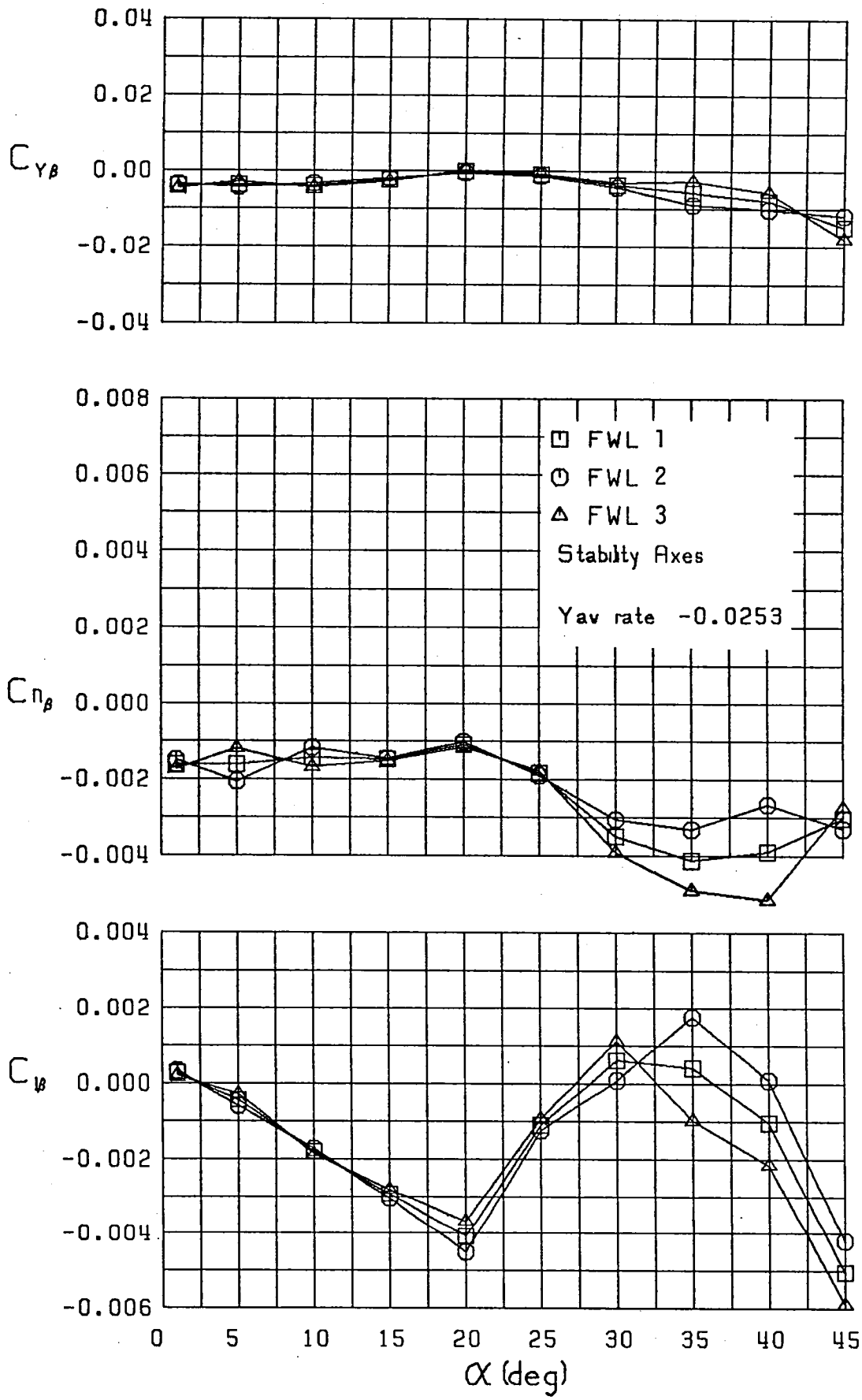

Figure 16 (Continued)

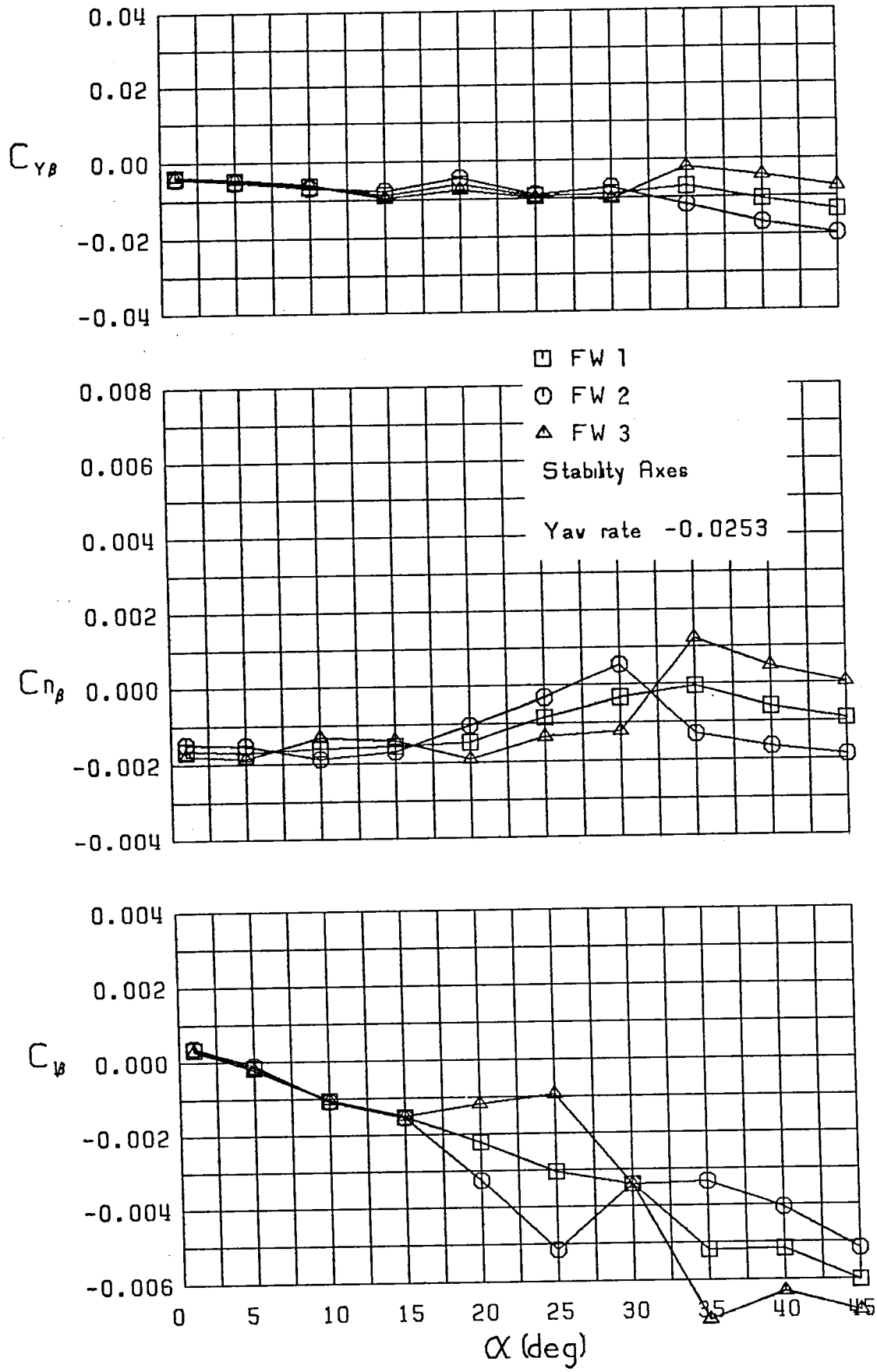

Figure 16 (Continued)

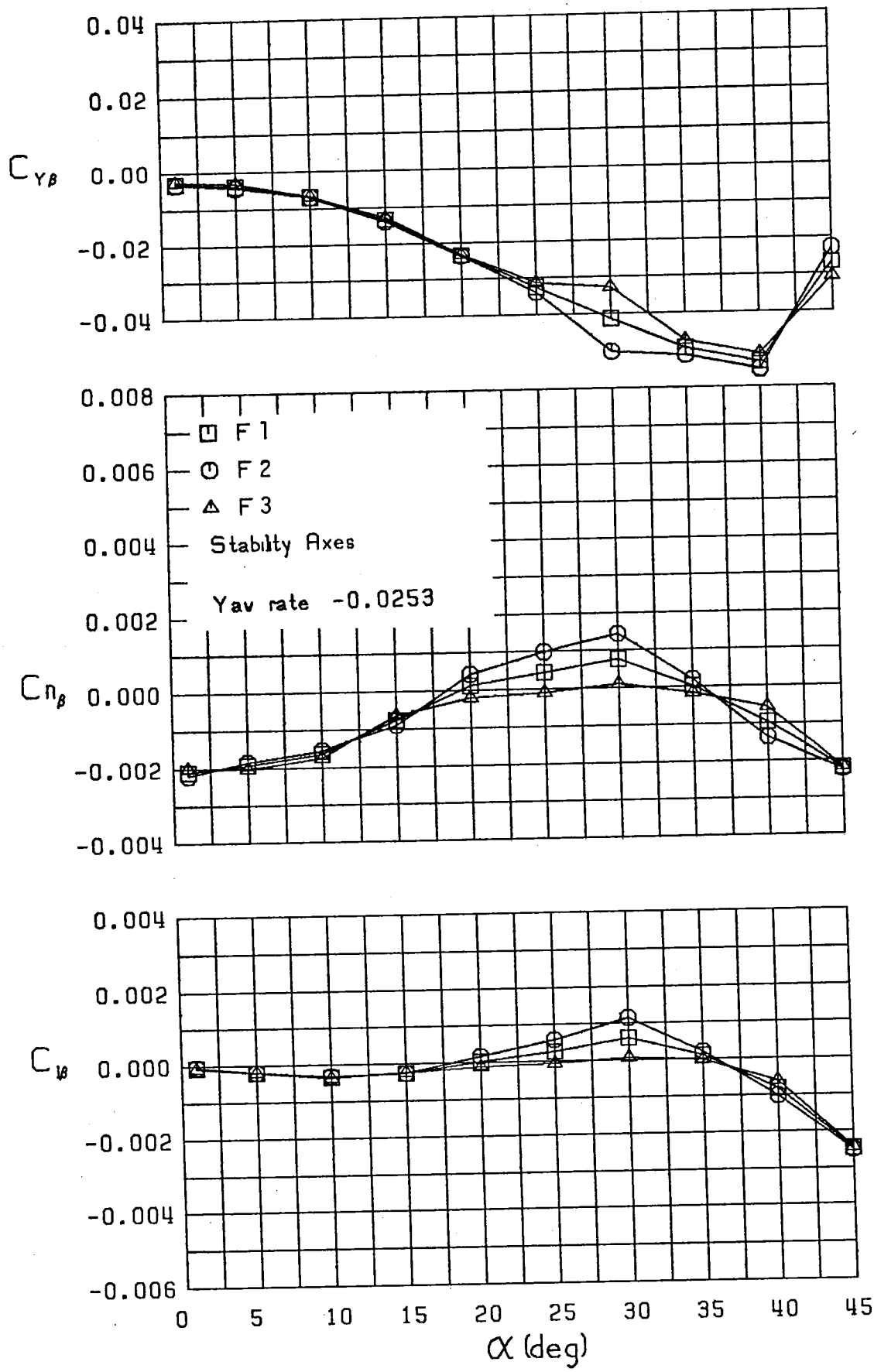

Figure 16 (Continued)

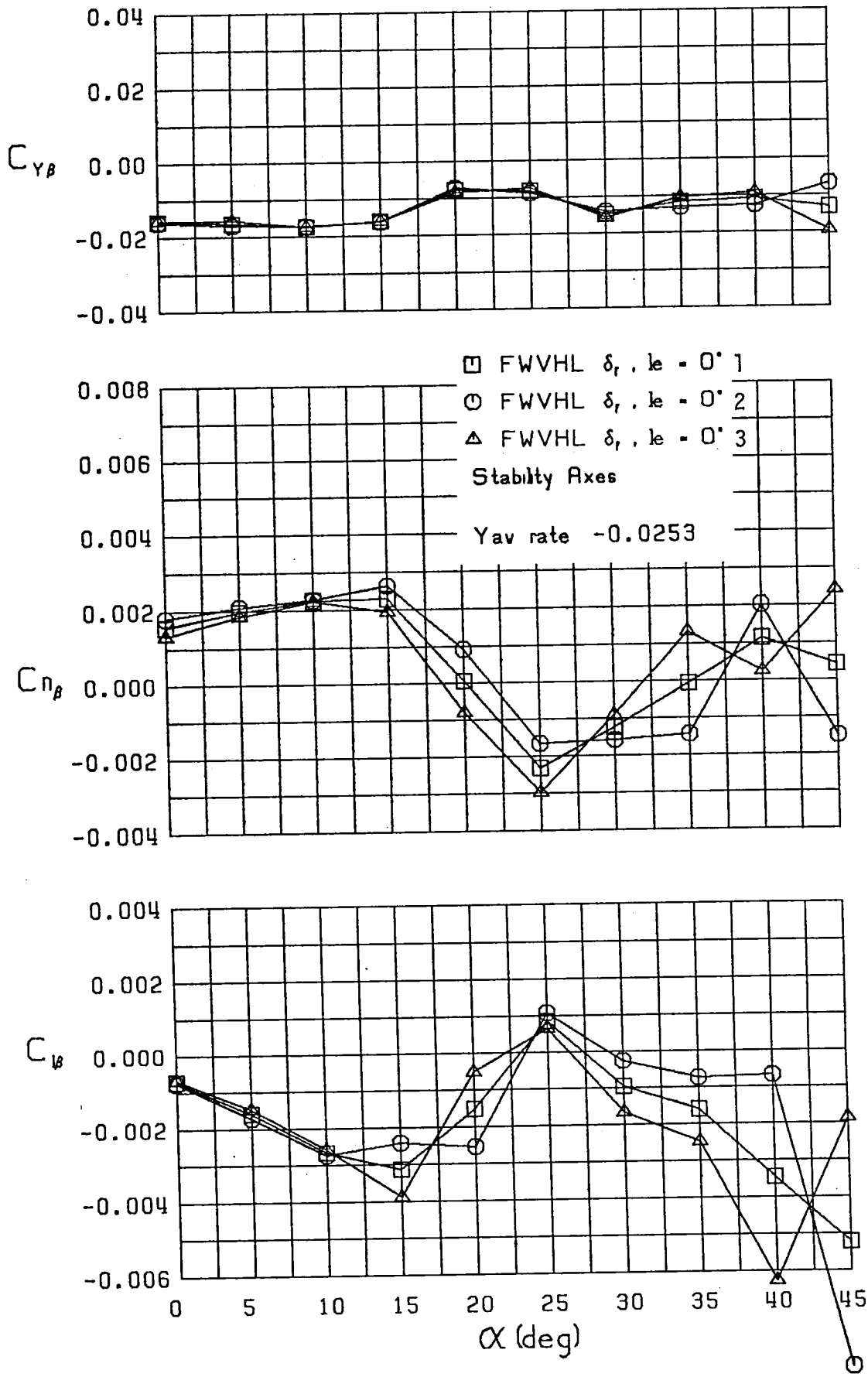

Figure 16 (Continued)

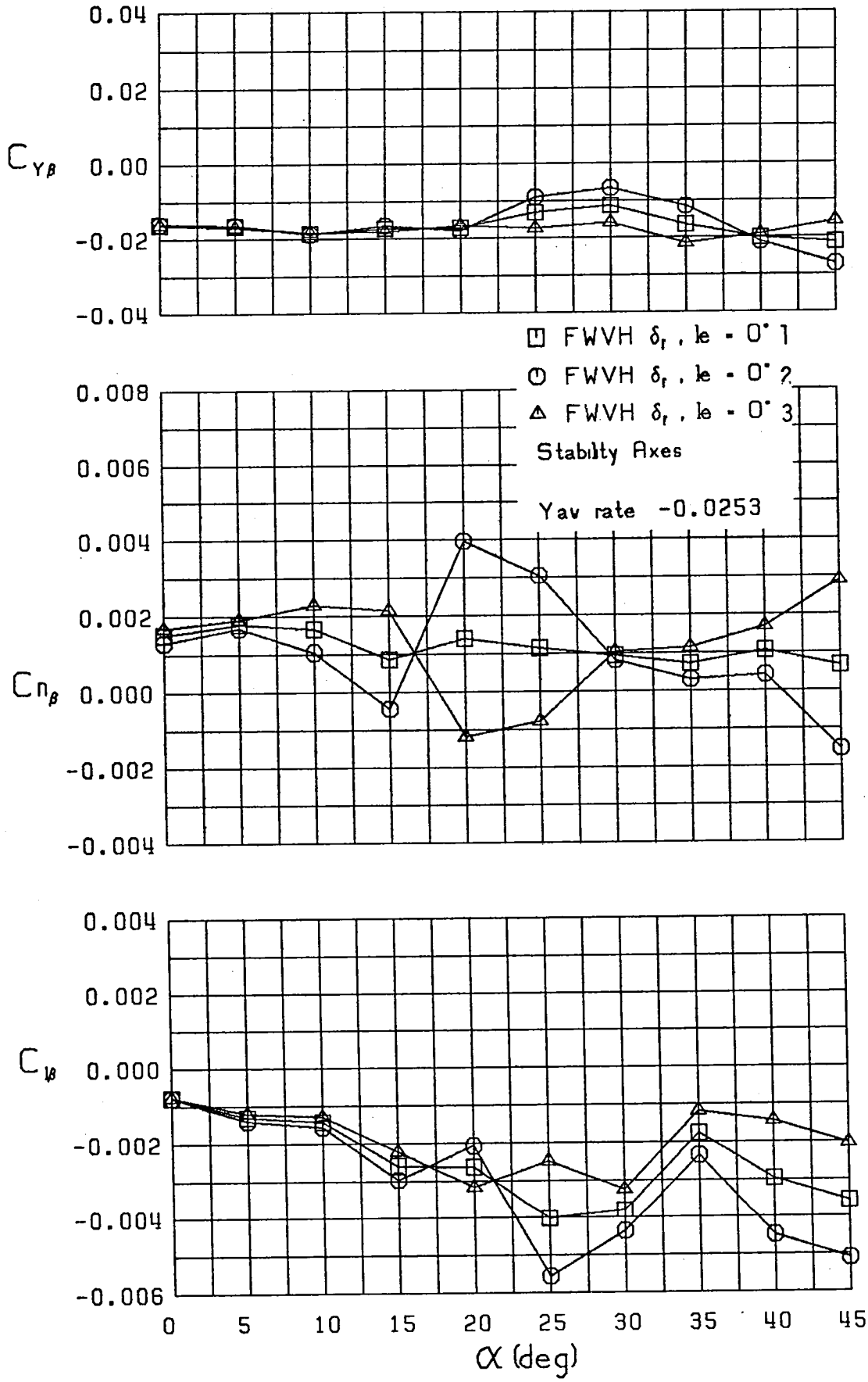

Figure 16 (Continued)

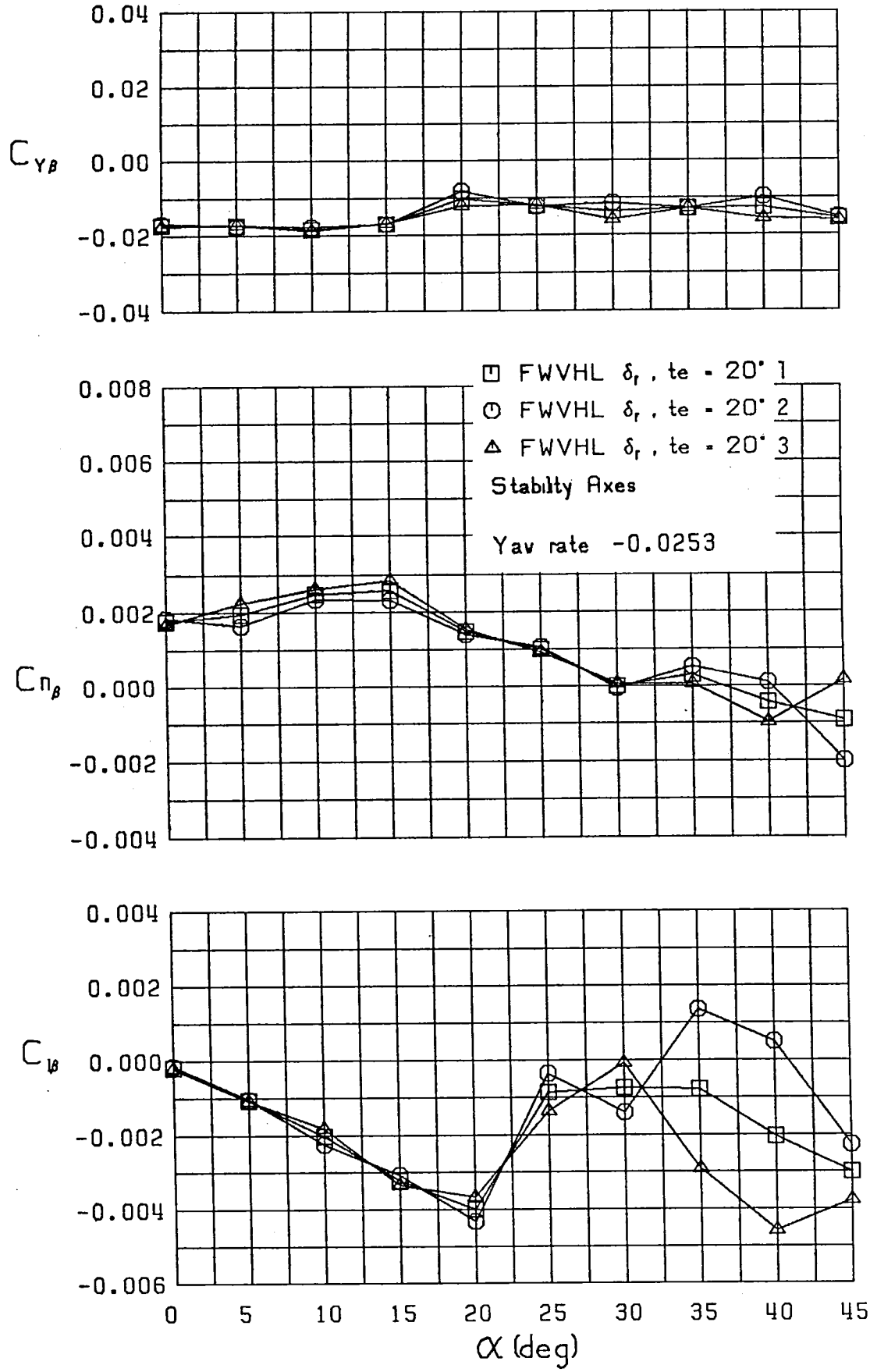

Figure 16 (Continued)

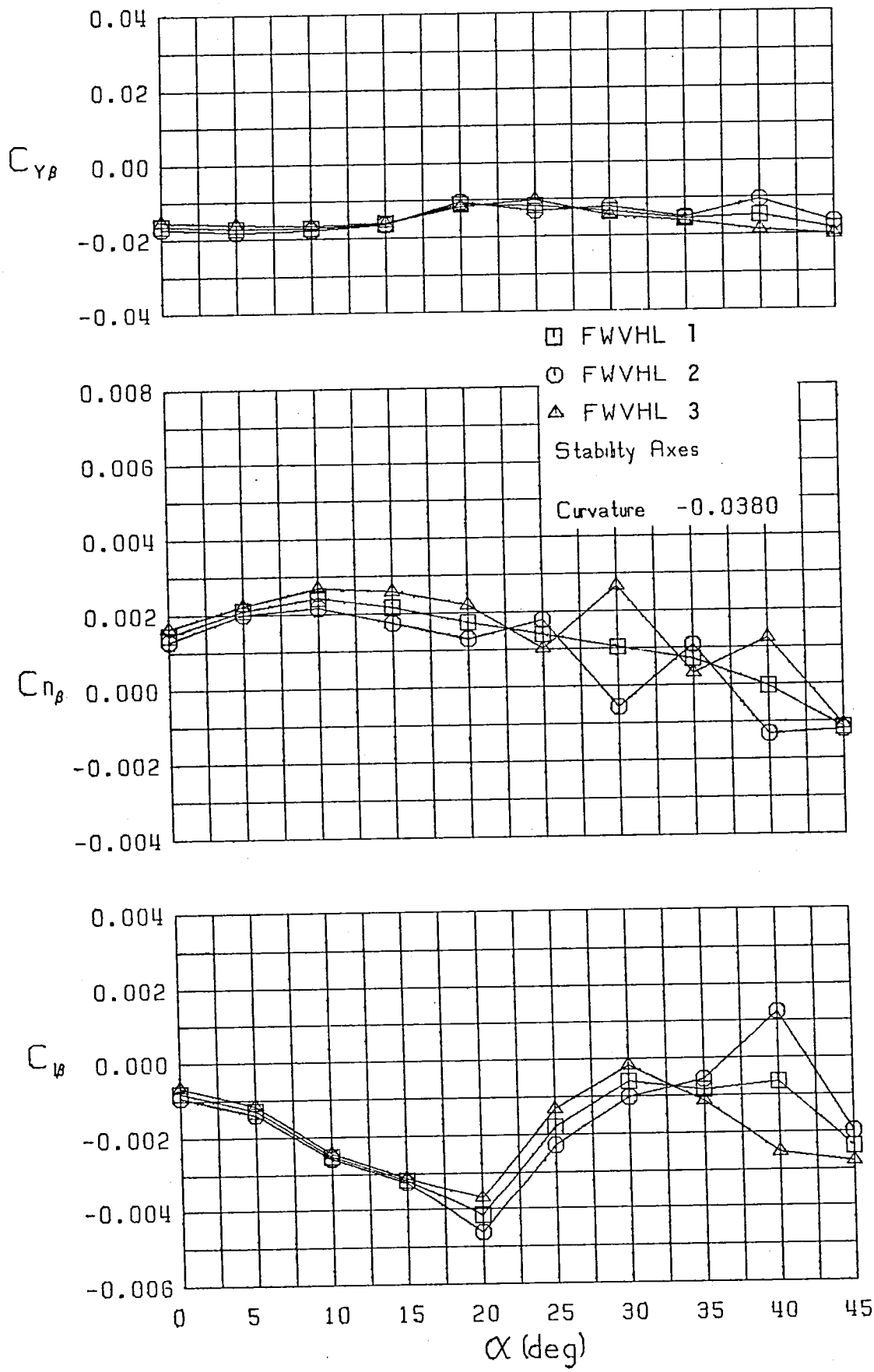

Figure 17 Variation of Lateral-Directional Static Stability Derivatives with Angle of Attack and Sideslip, $\hat{r}$ = - 0.0380

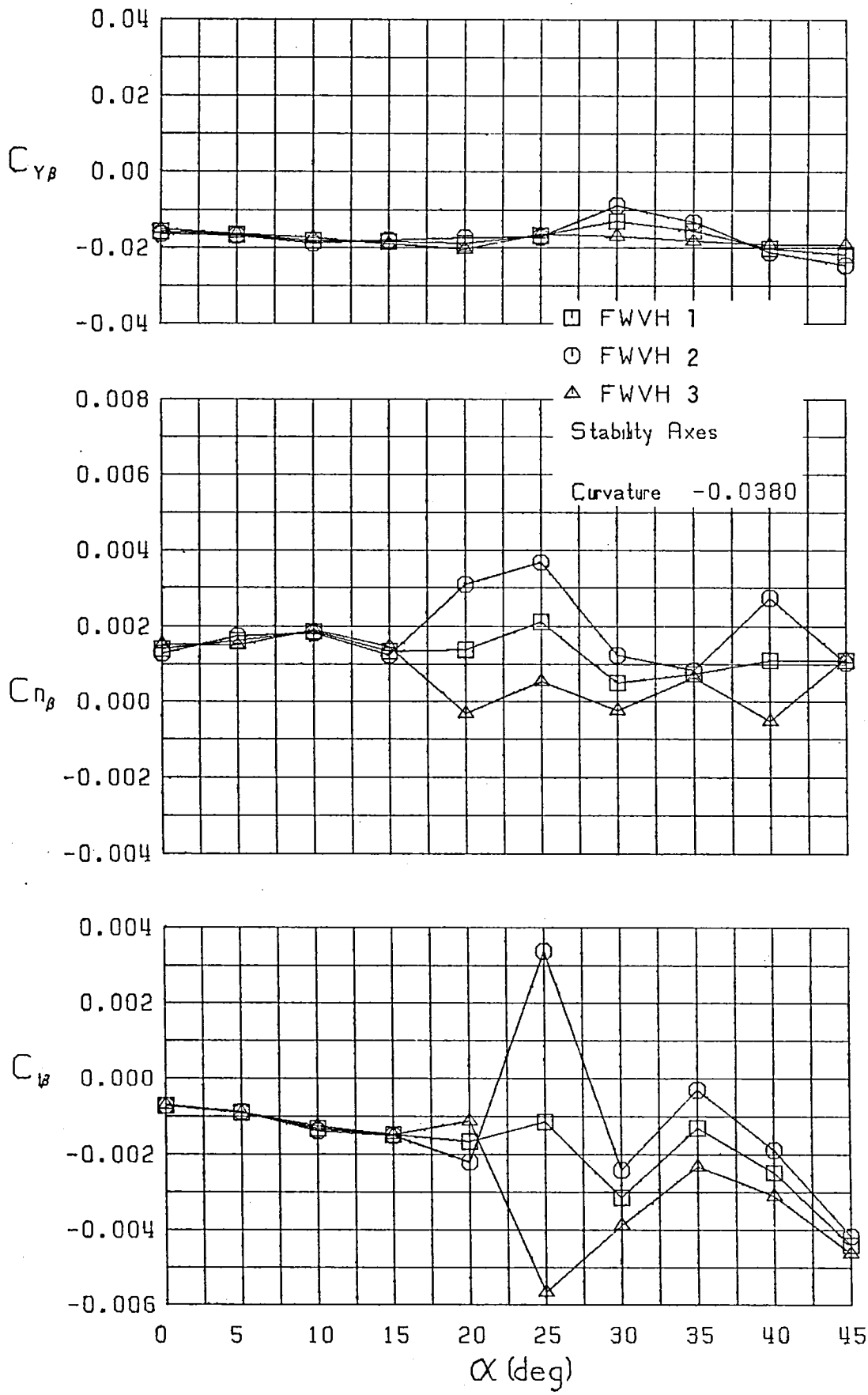

Figure 17 (Continued)

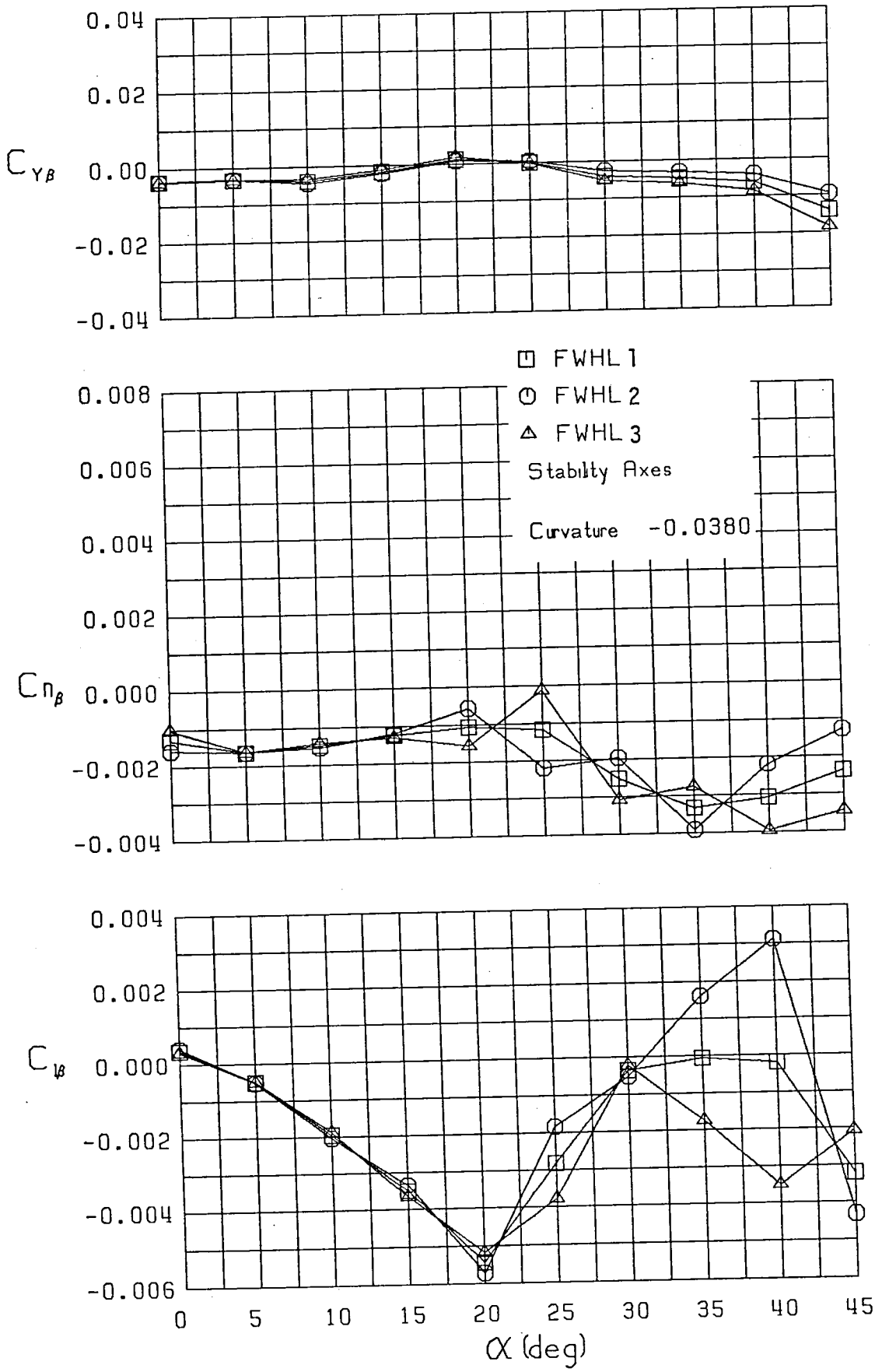

Figure 17 (Continued)

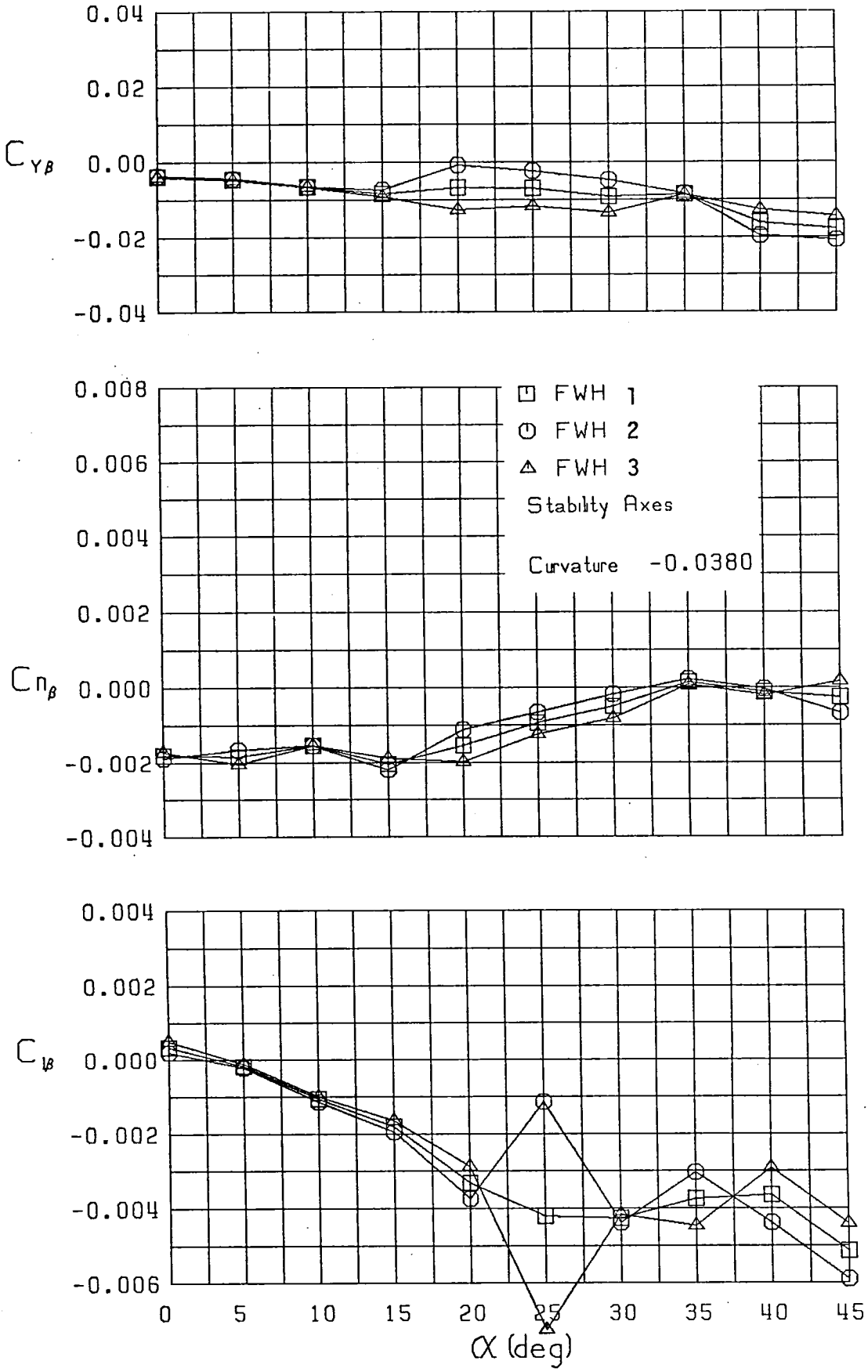

Figure 17 (Continued)

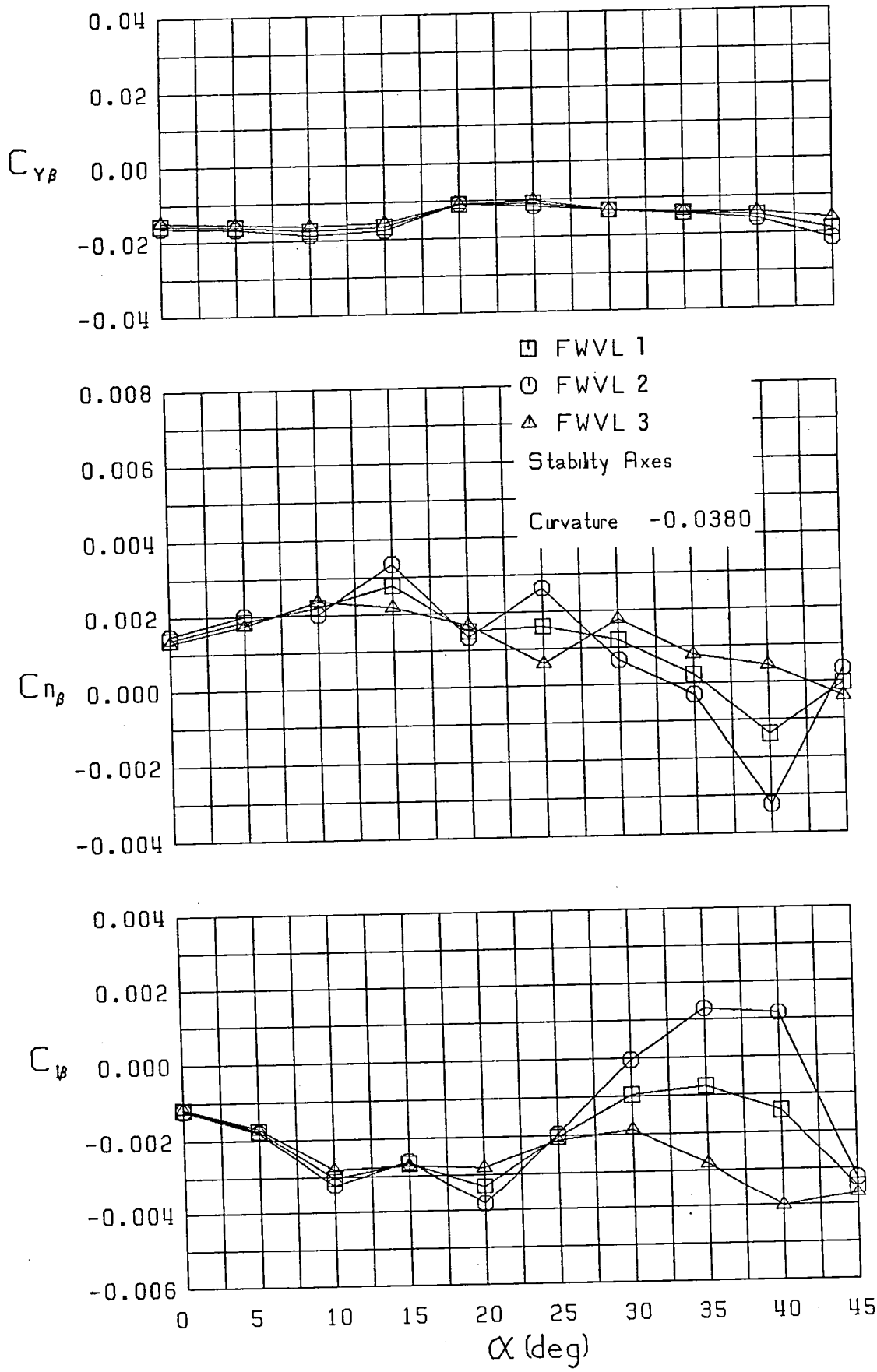

Figure 17 (Continued)

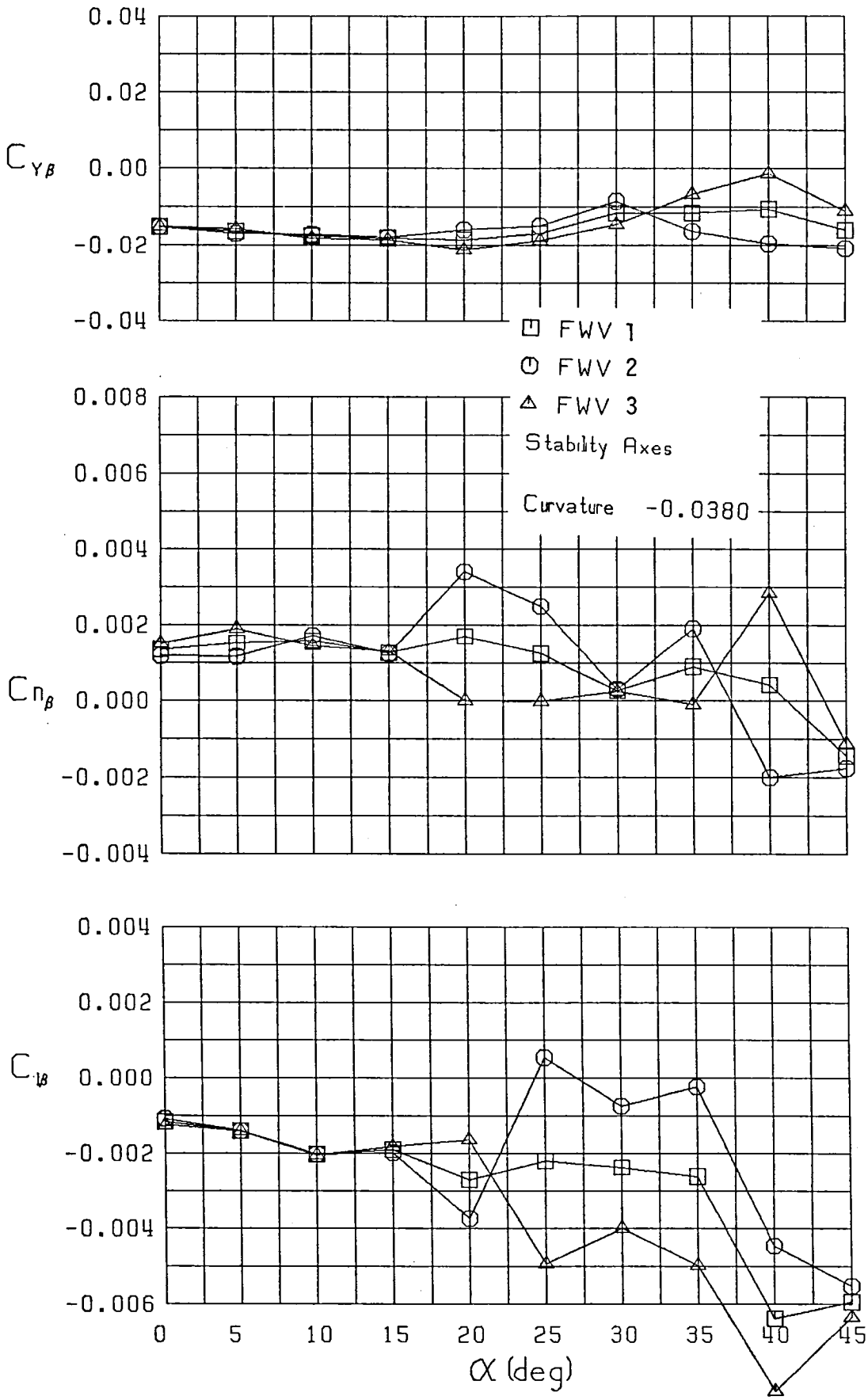

Figure 17 (Continued)

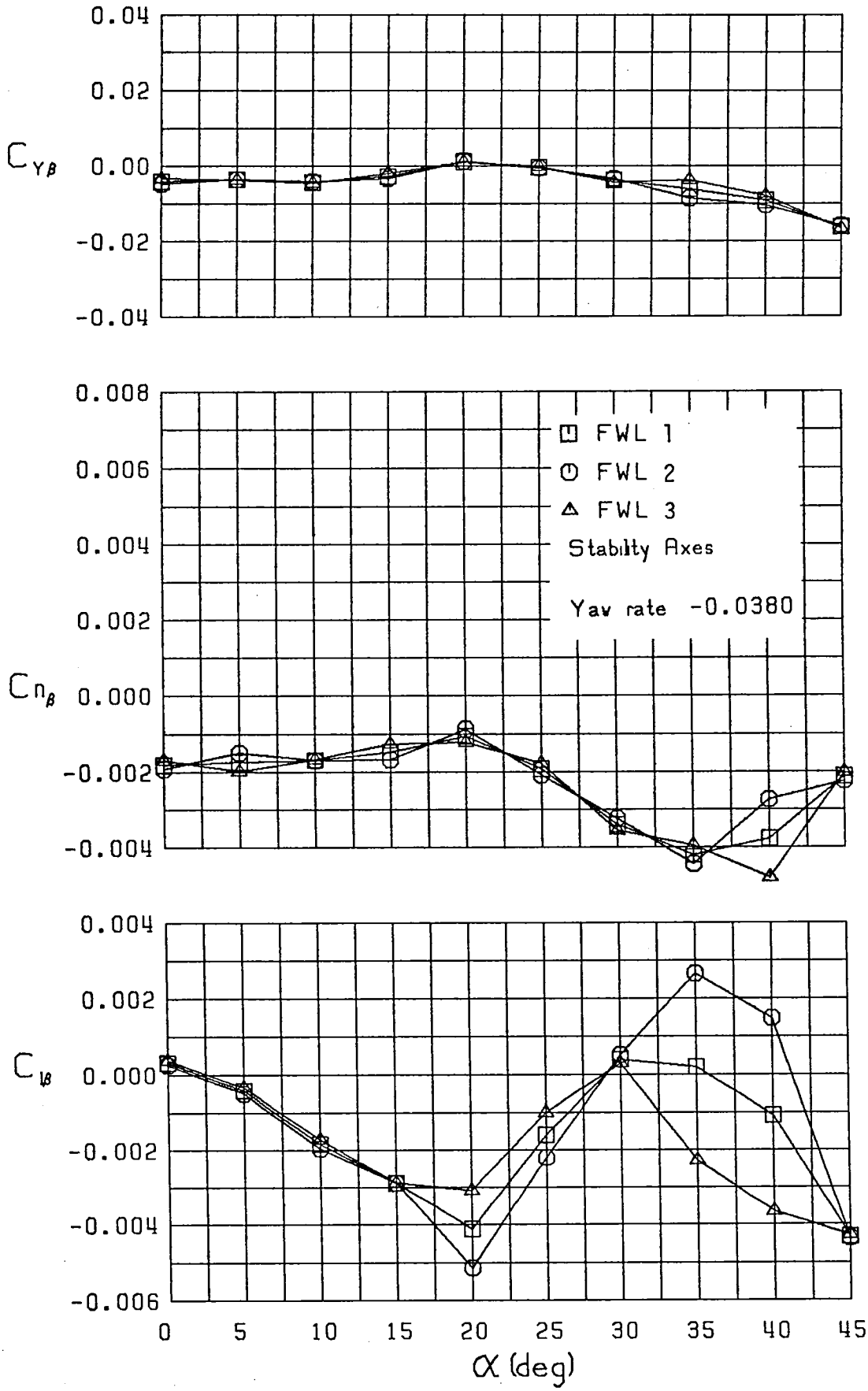

Figure 17 (Continued)

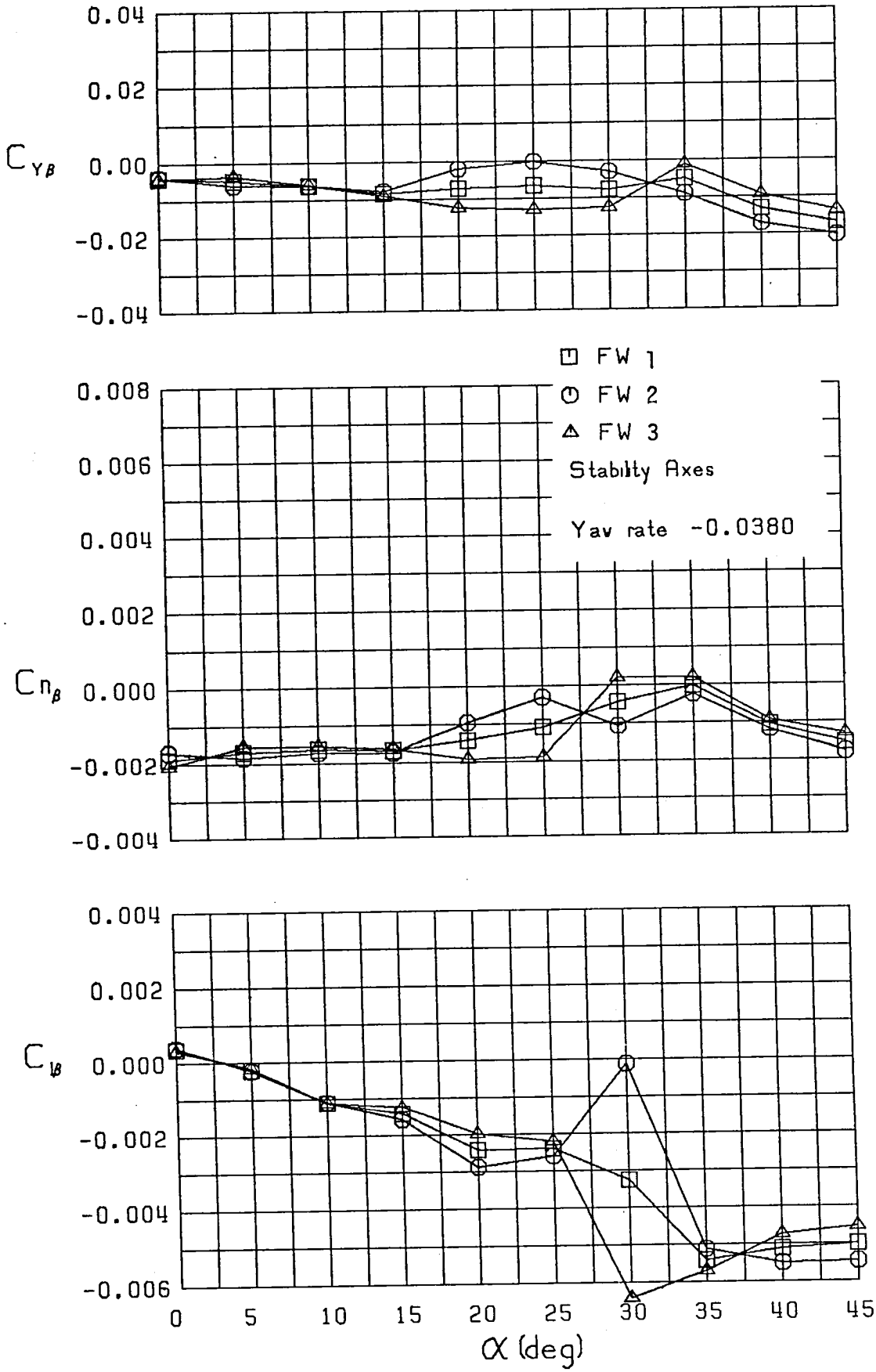

Figure 17 (Continued)

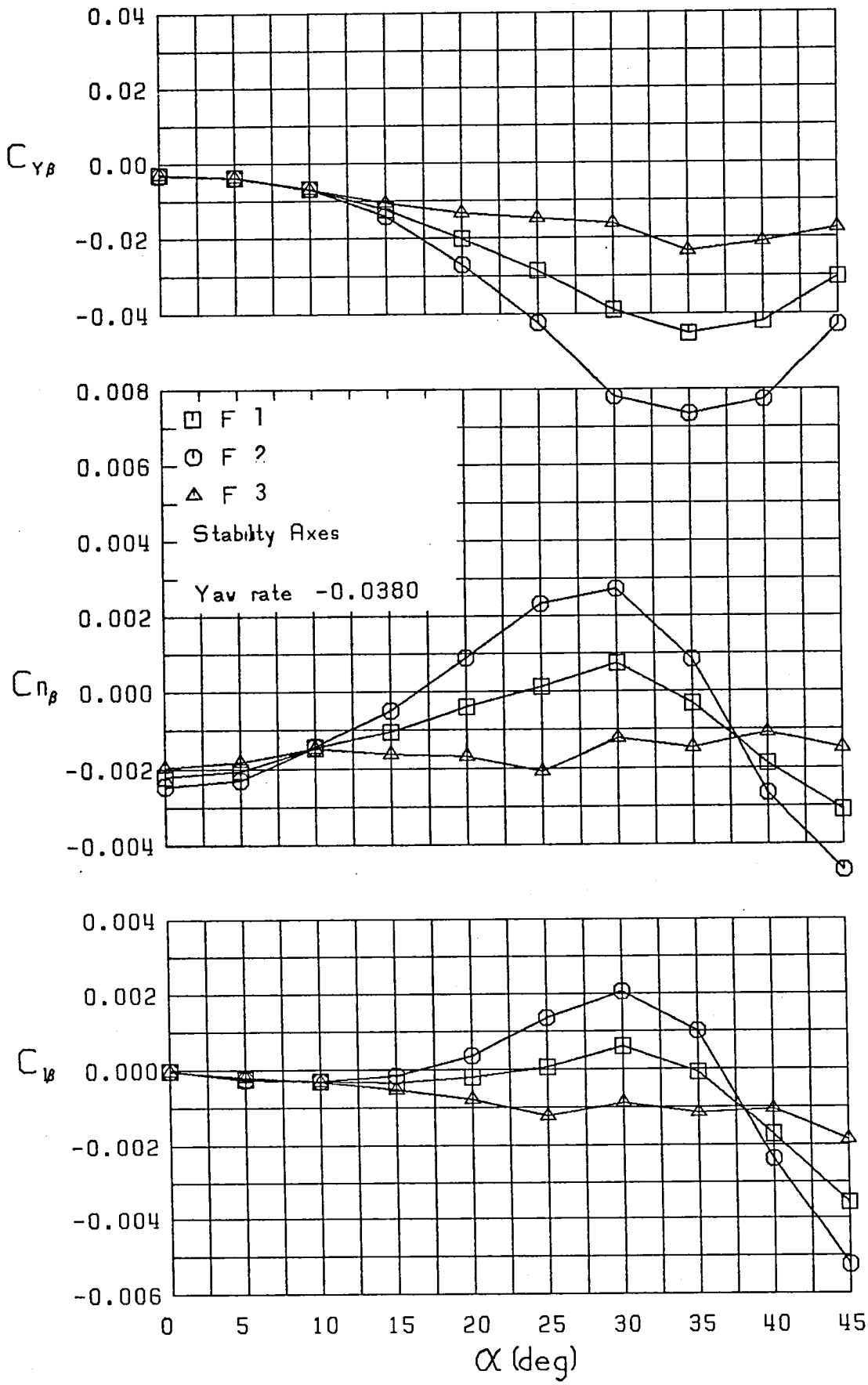

Figure 17 (Continued)

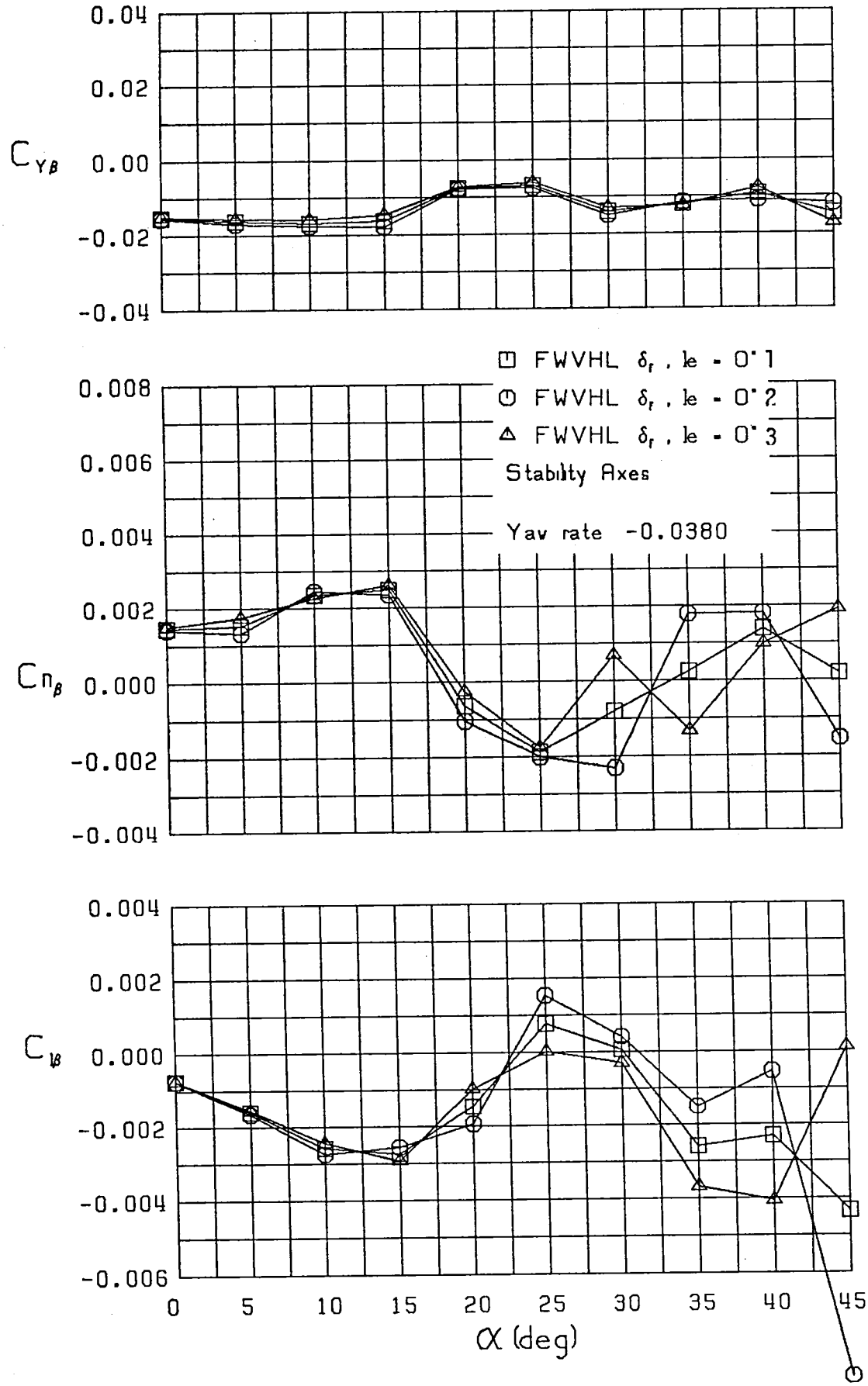

Figure 17 (Continued)

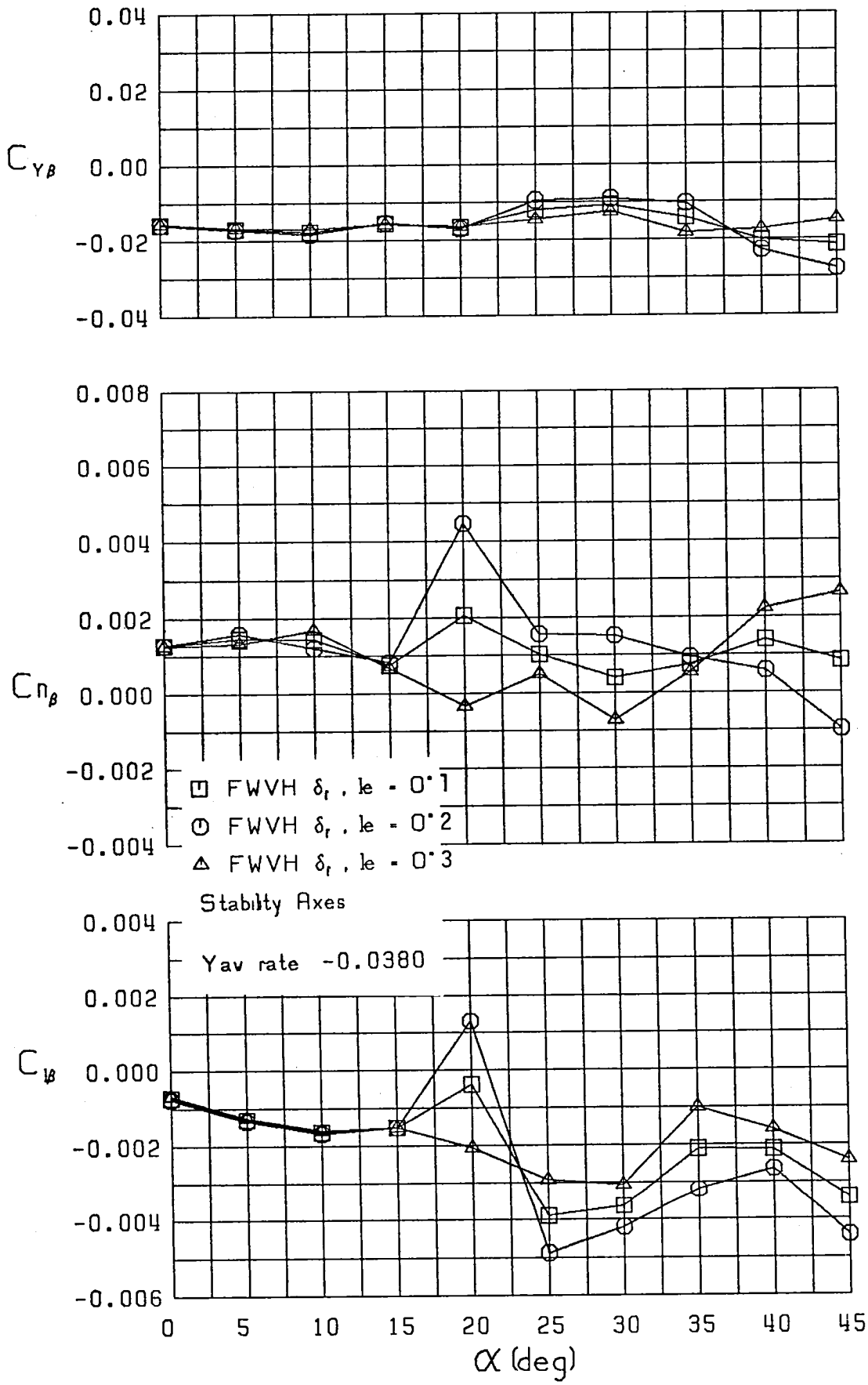

Figure 17 (Continued)

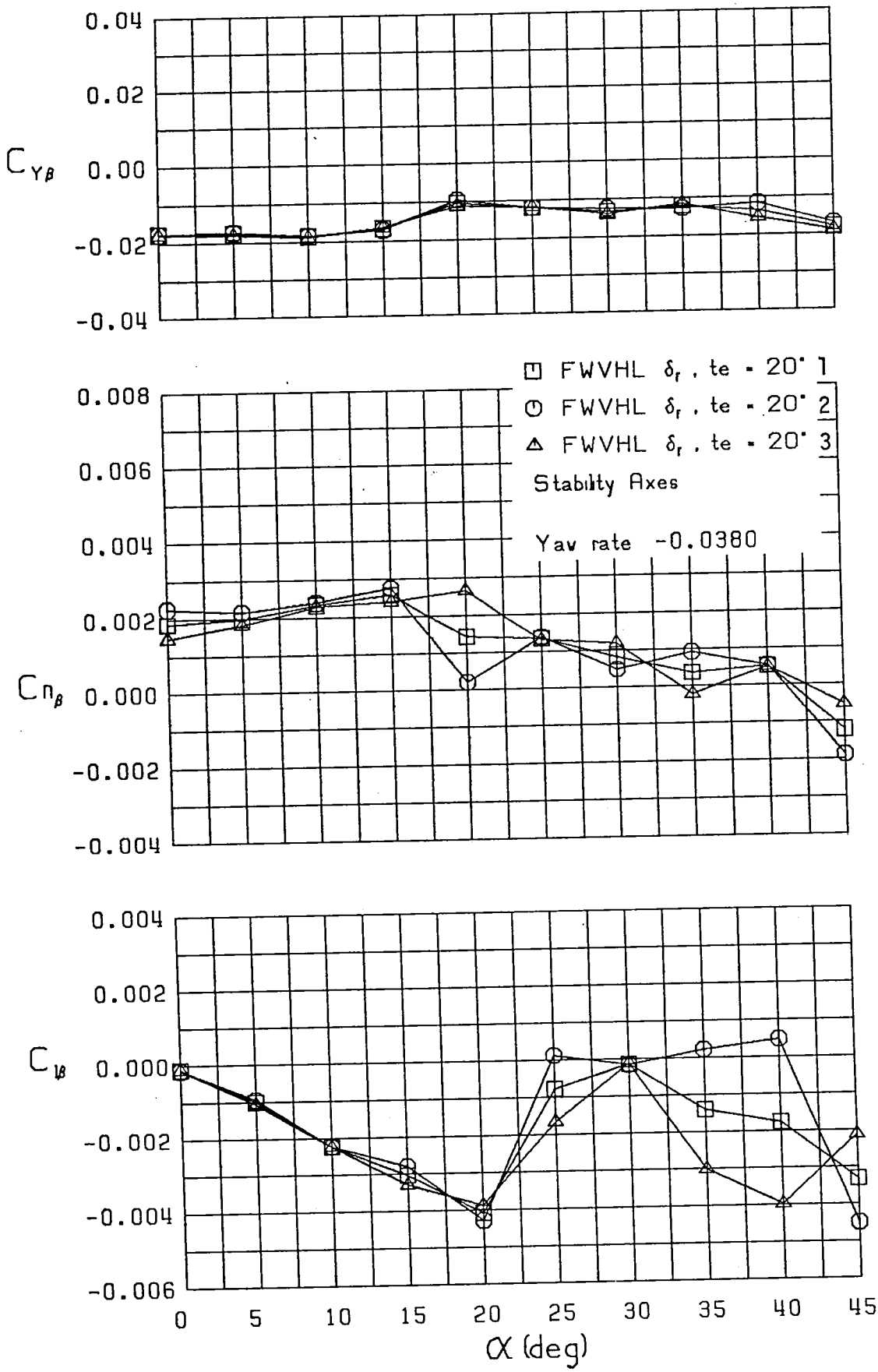

Figure 17 (Continued)

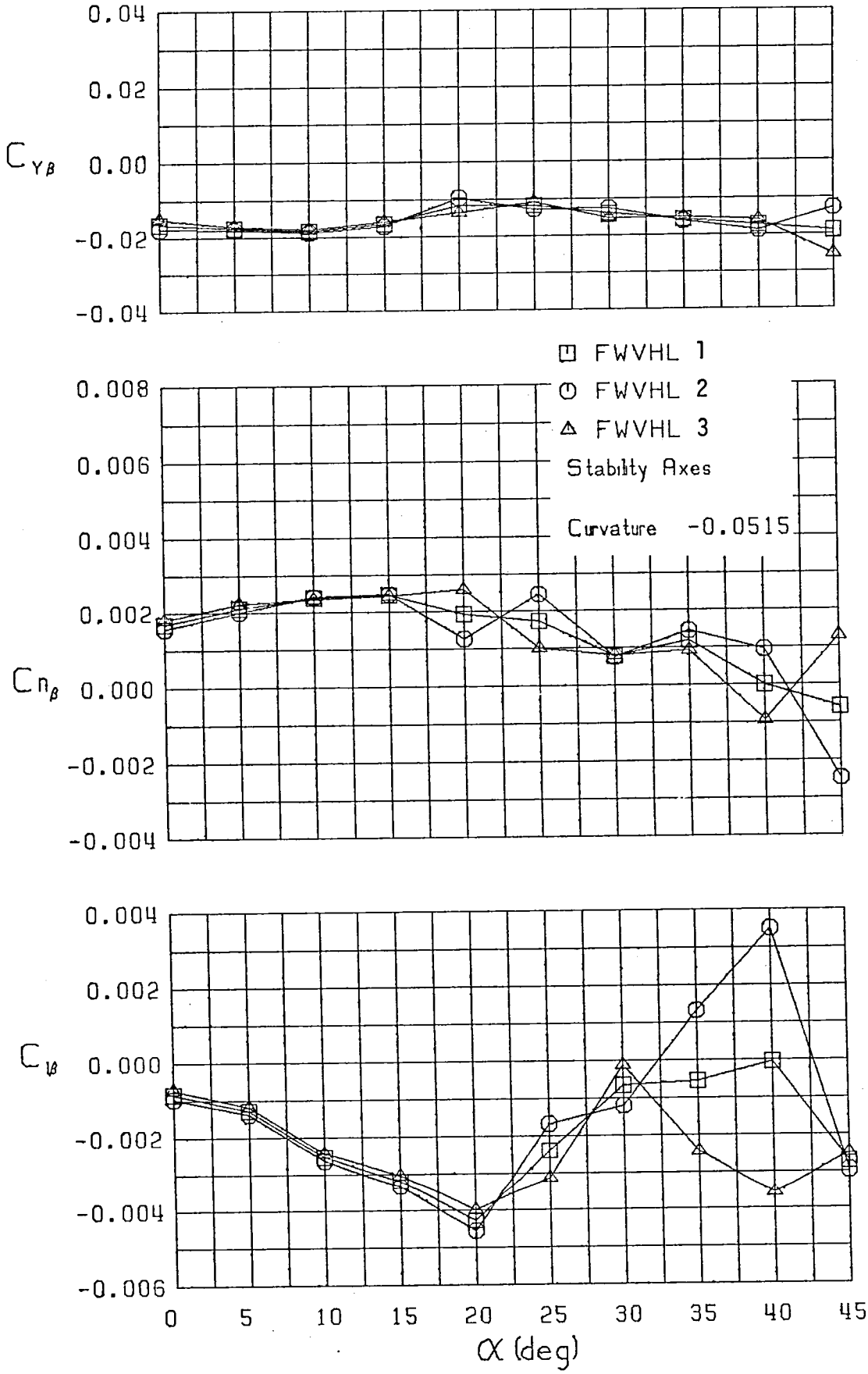

Figure 18 Variation of Lateral-Directional Static Stability Derivatives with Angle of Attack and Sideslip, $\hat{r}$ = - 0.0515

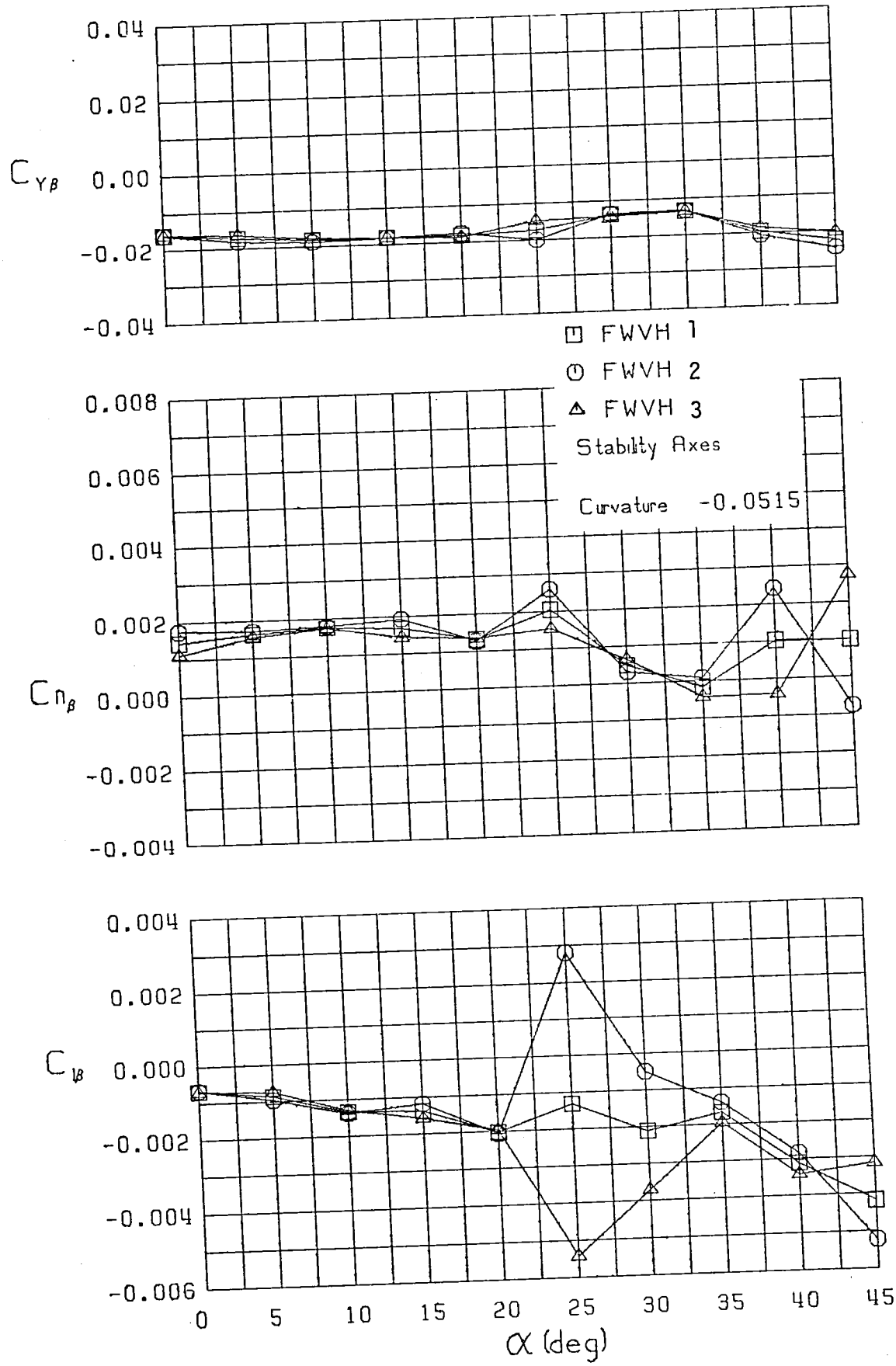

Figure 18 (Continued)

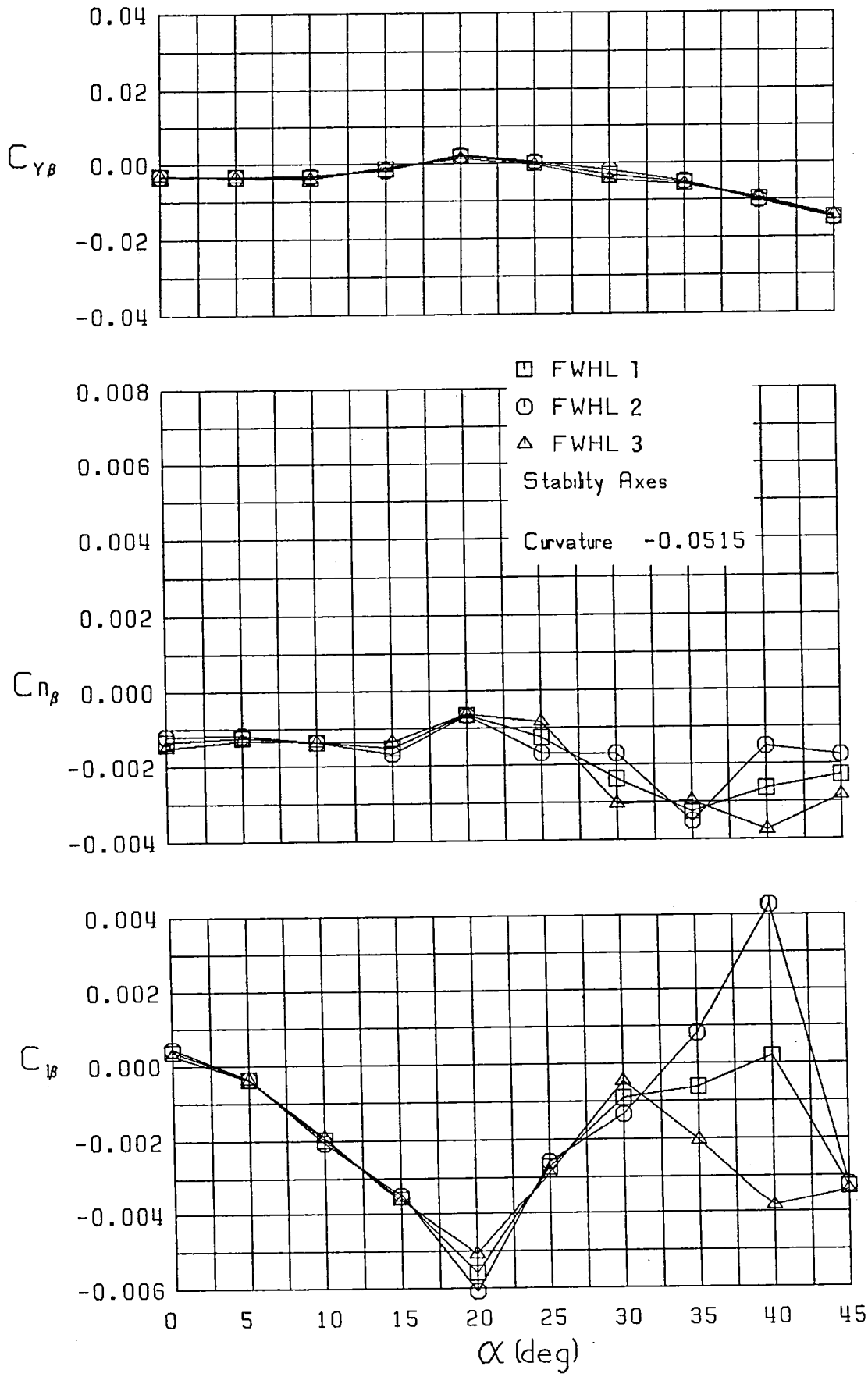

Figure 18 (Continued)

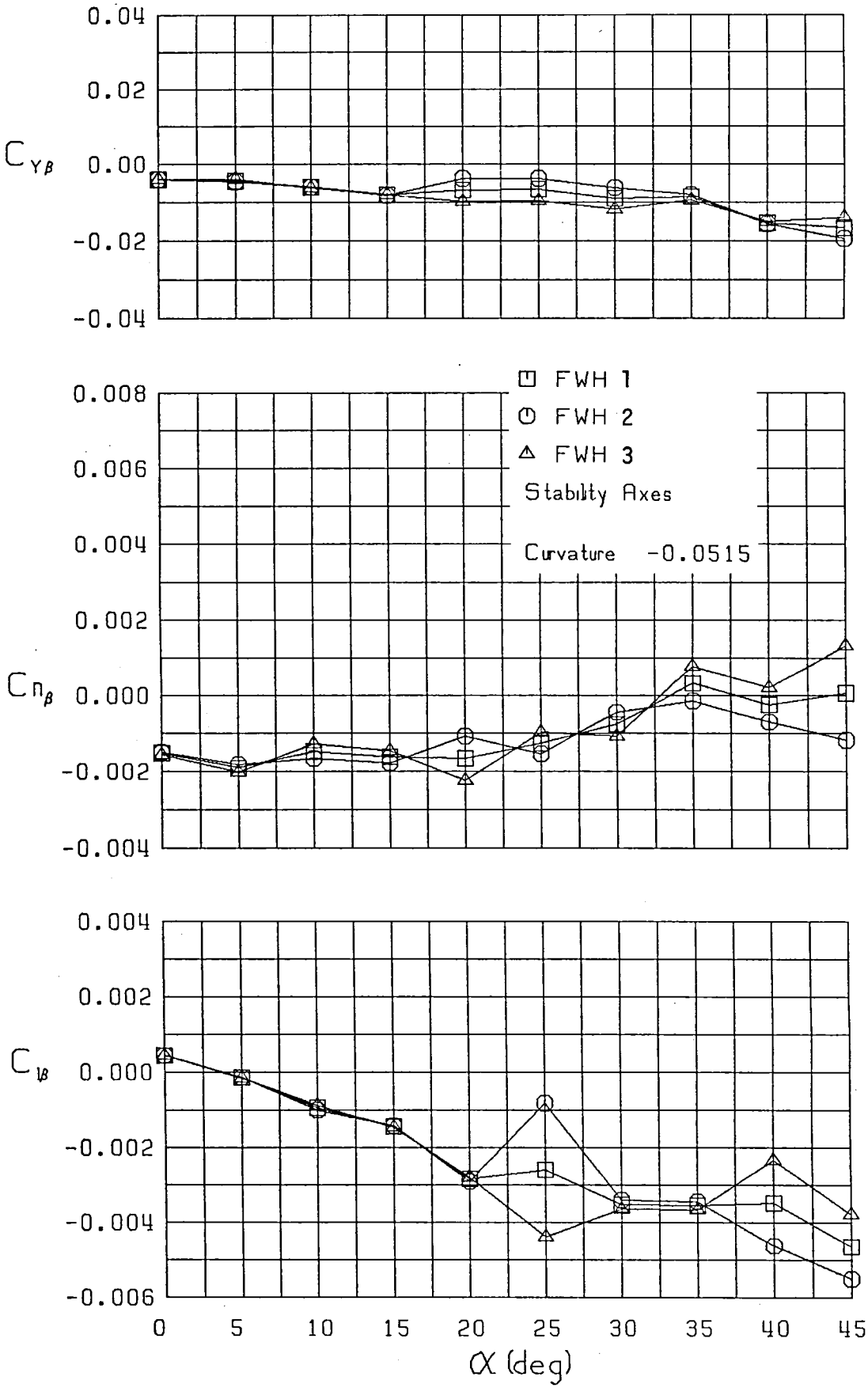

Figure 18 (Continued)

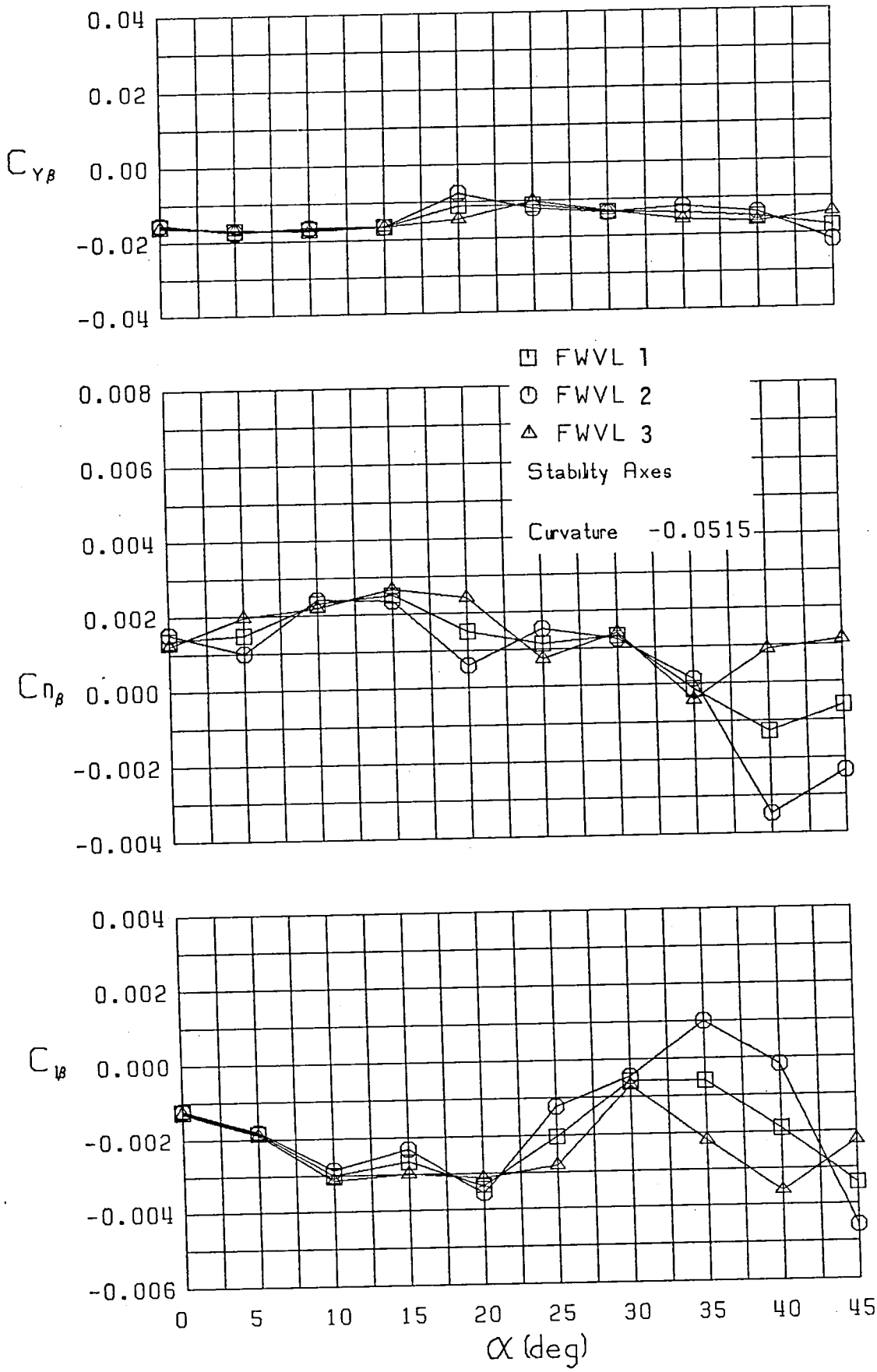

Figure 18 (Continued)

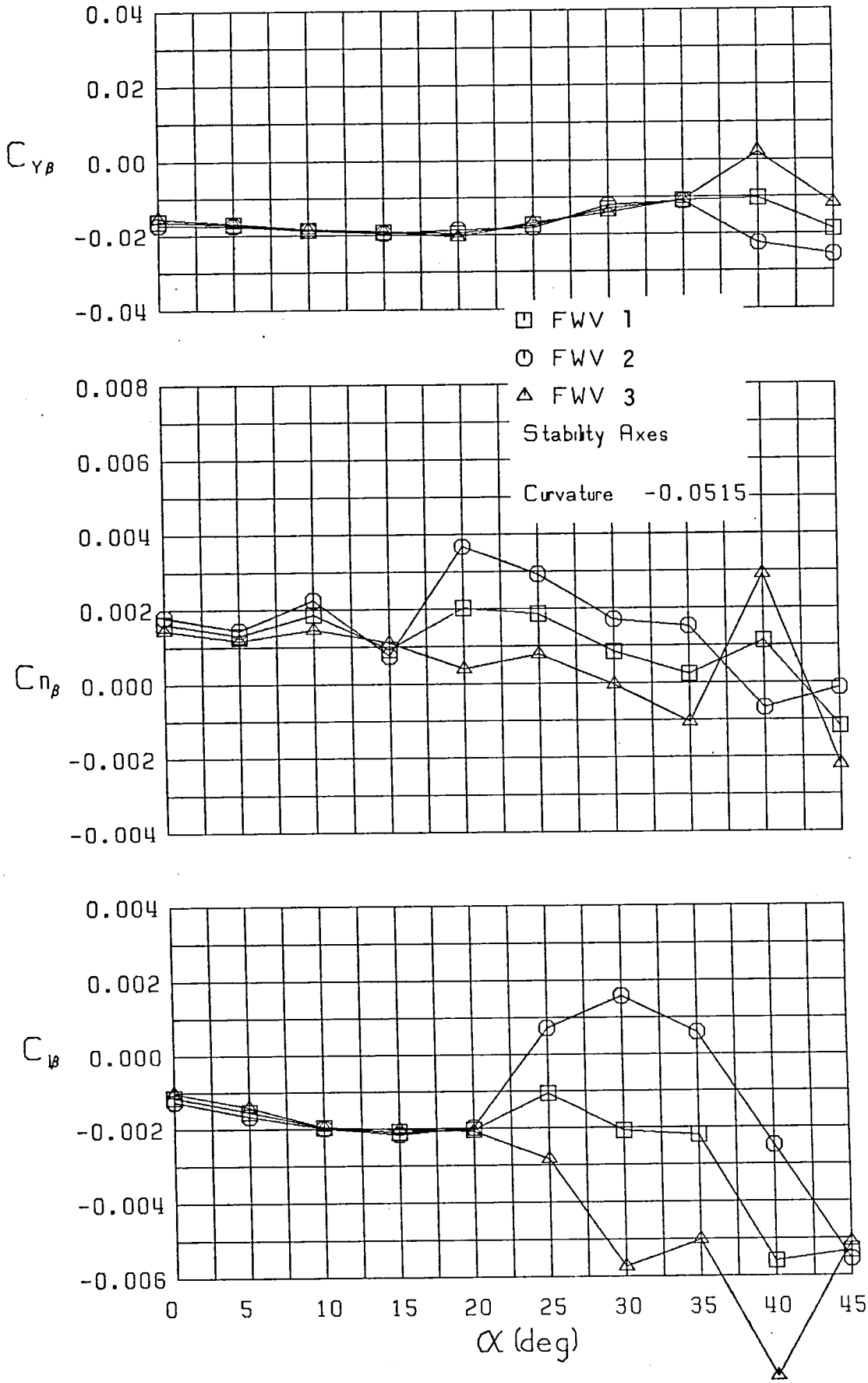

Figure 18 (Continued)

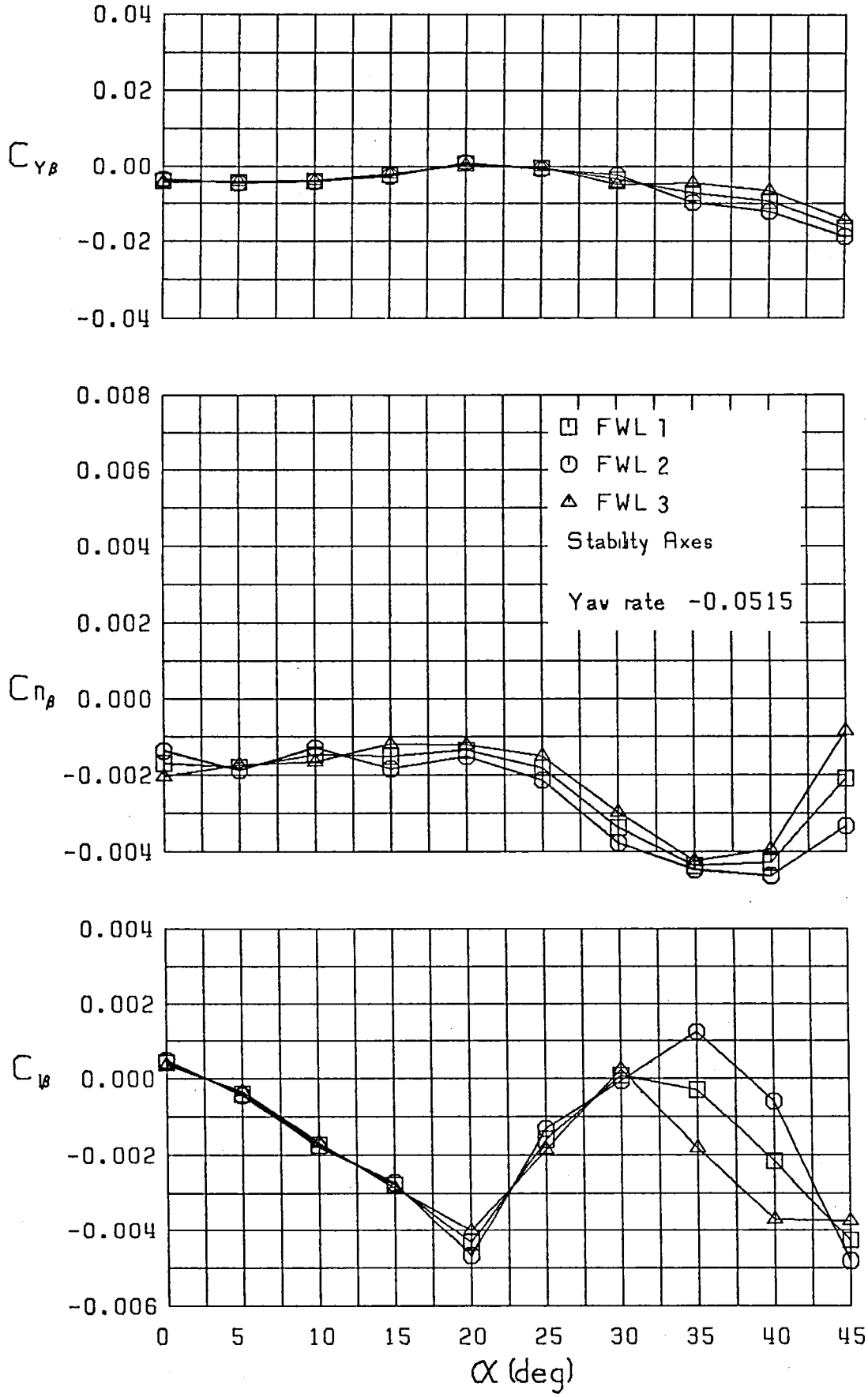

Figure 18 (Continued)

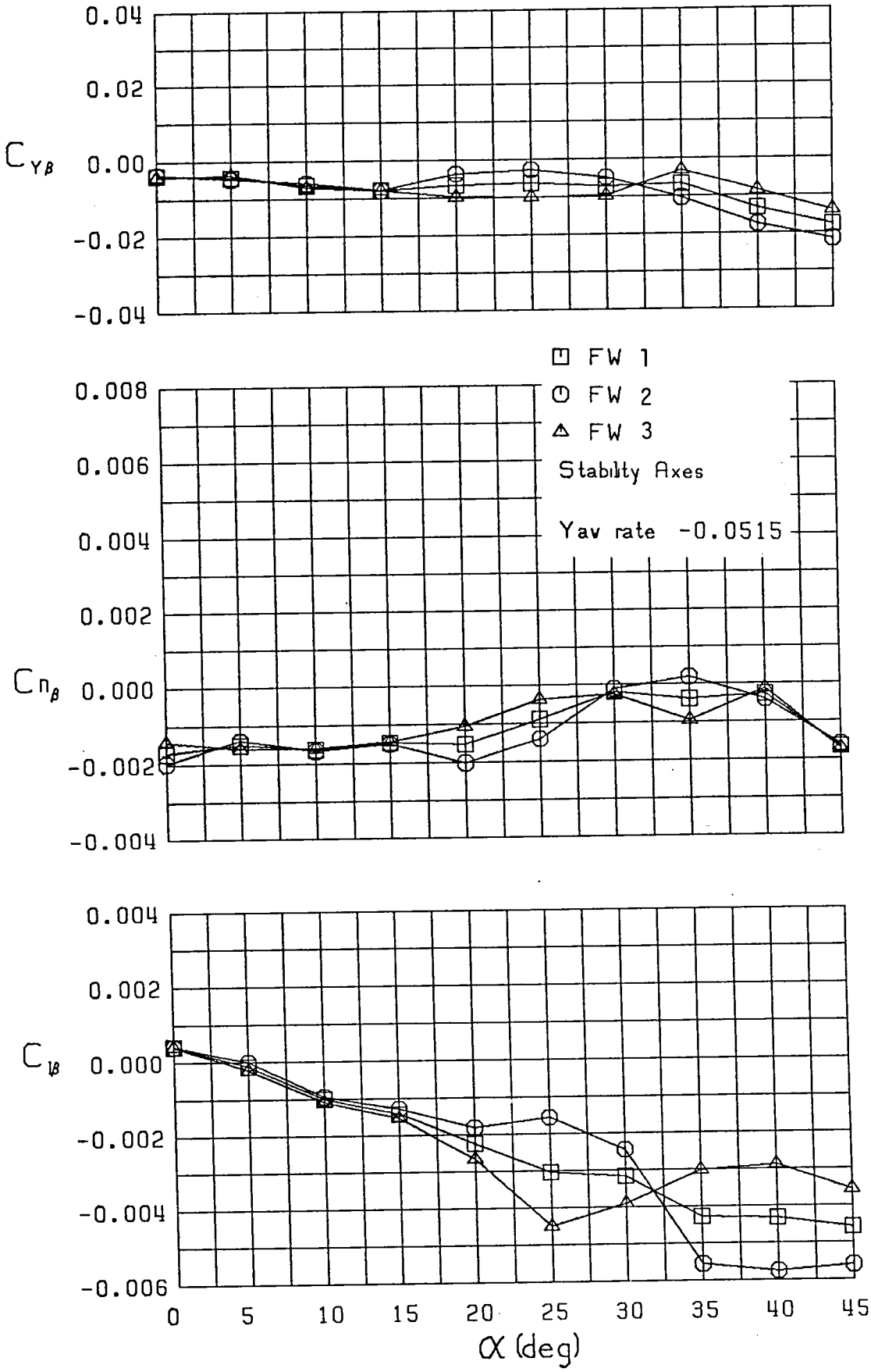

Figure 18 (Continued)

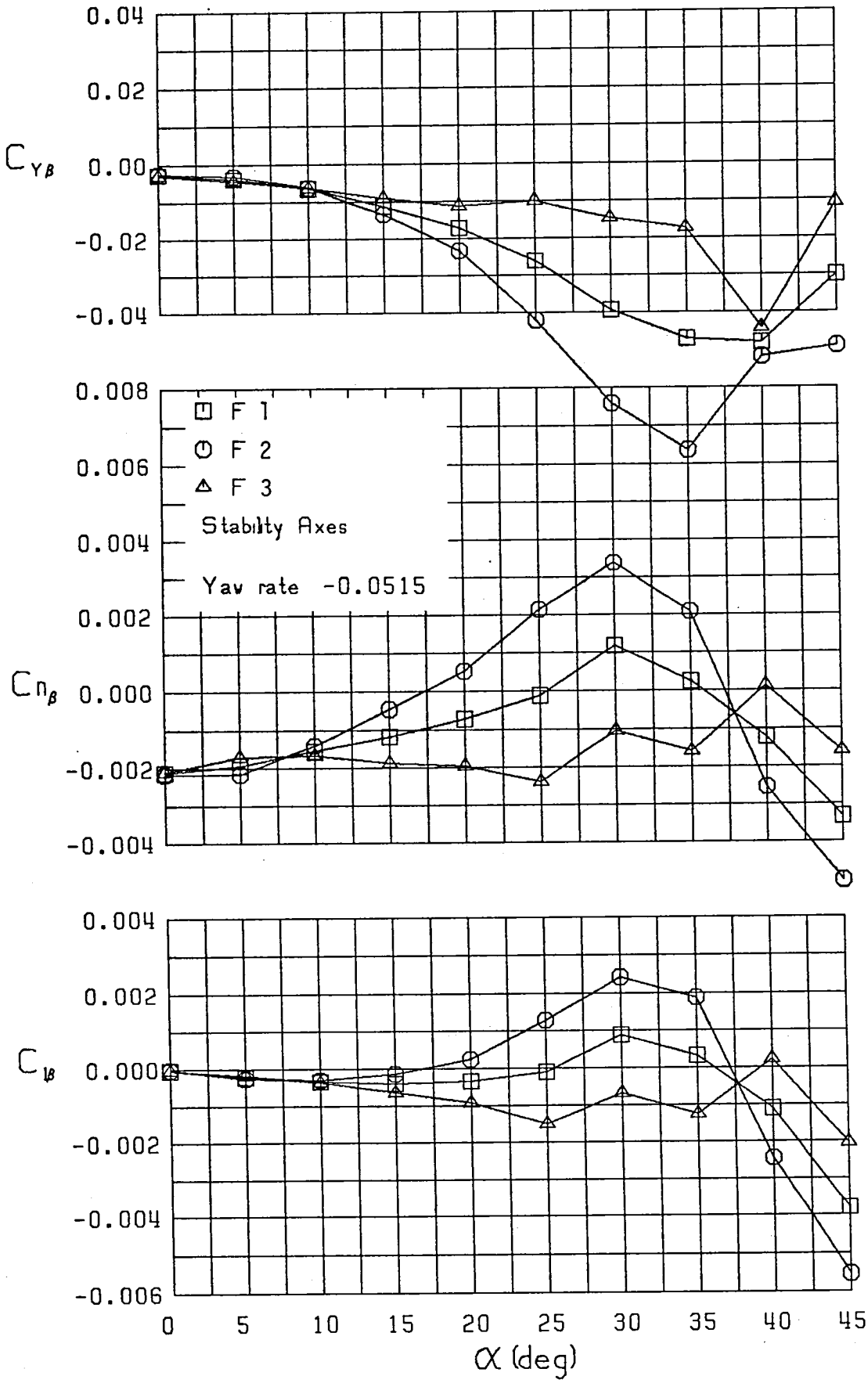

Figure 18 (Continued)

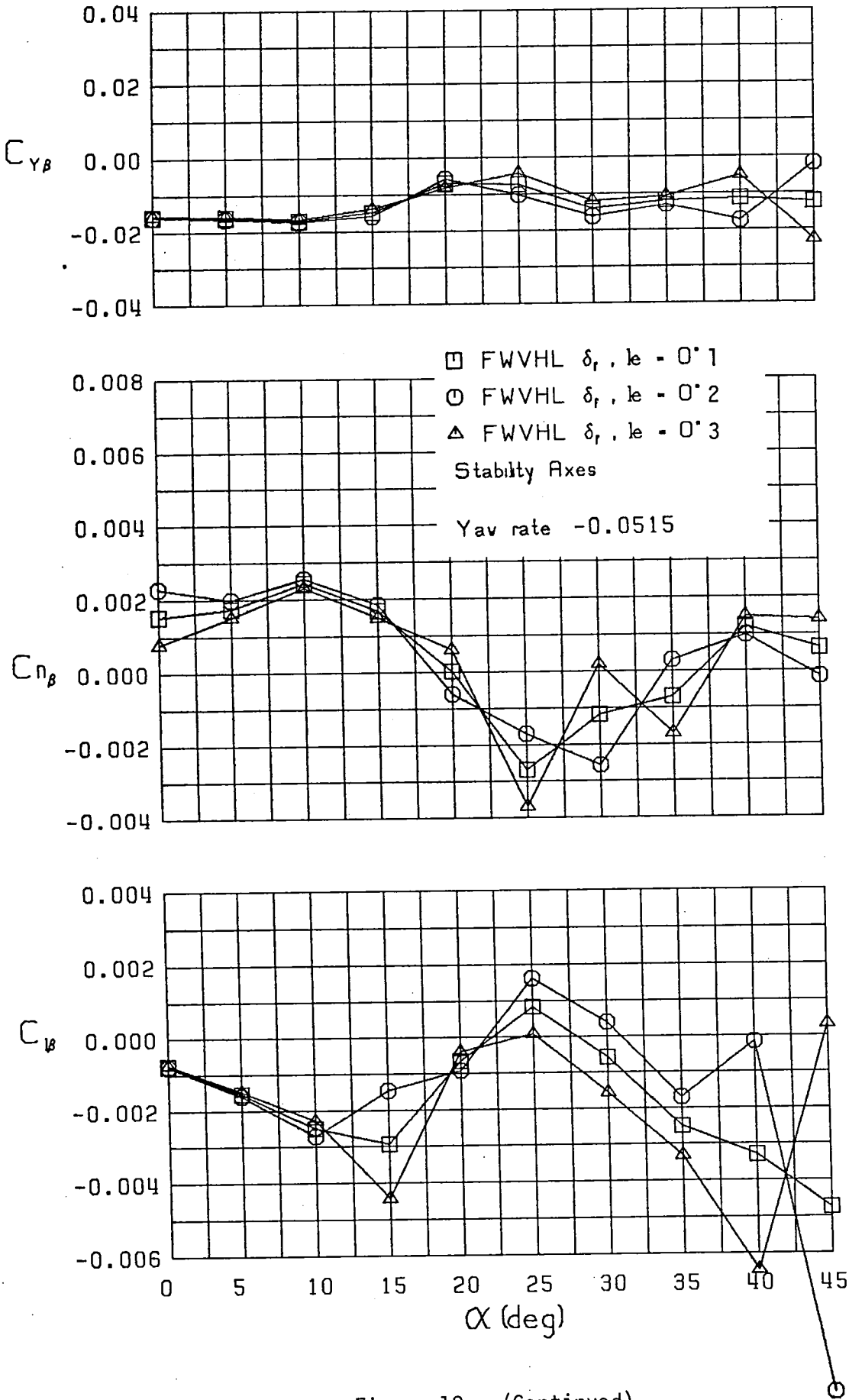

Figure 18 (Continued)

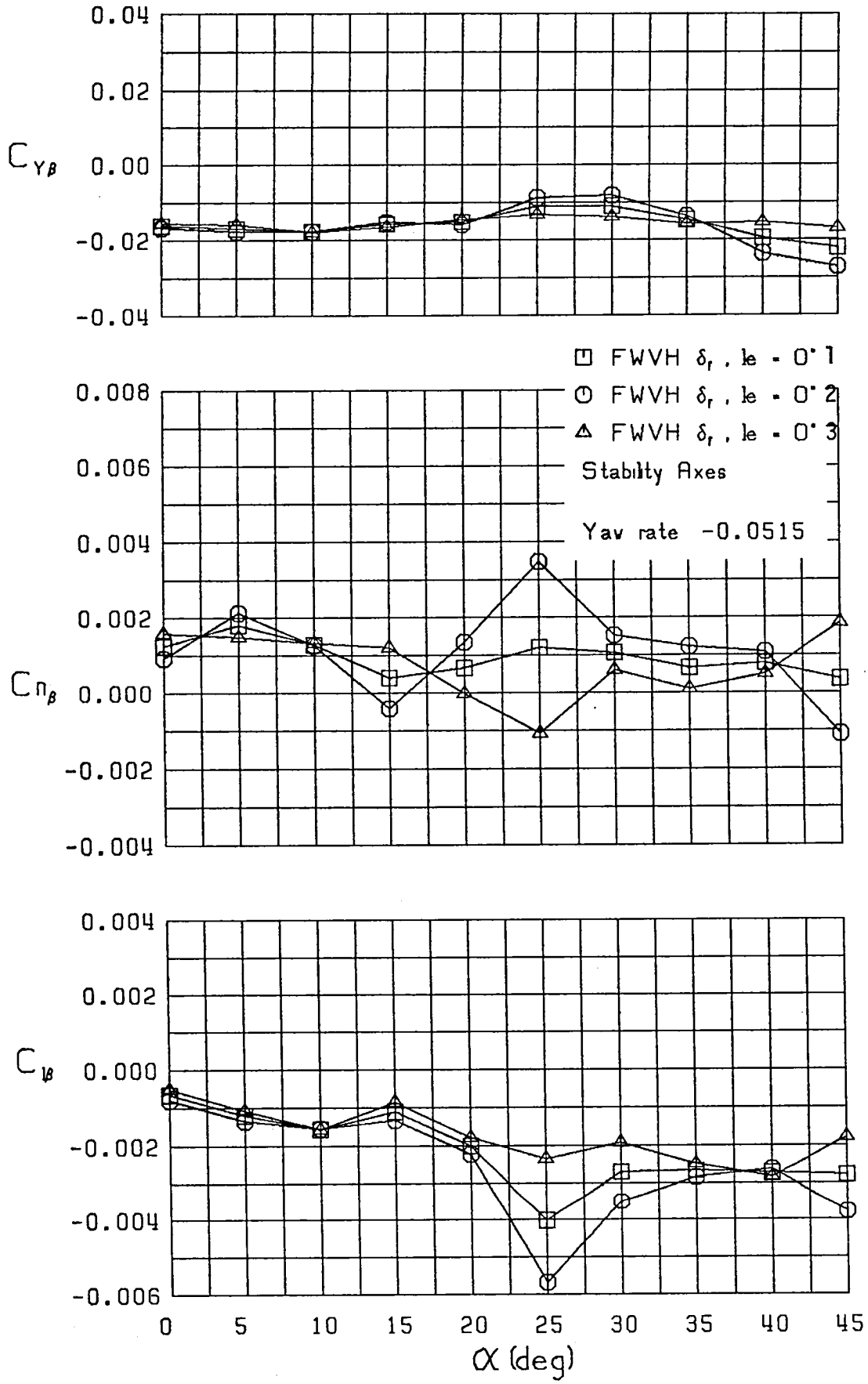

Figure 18 (Continued)

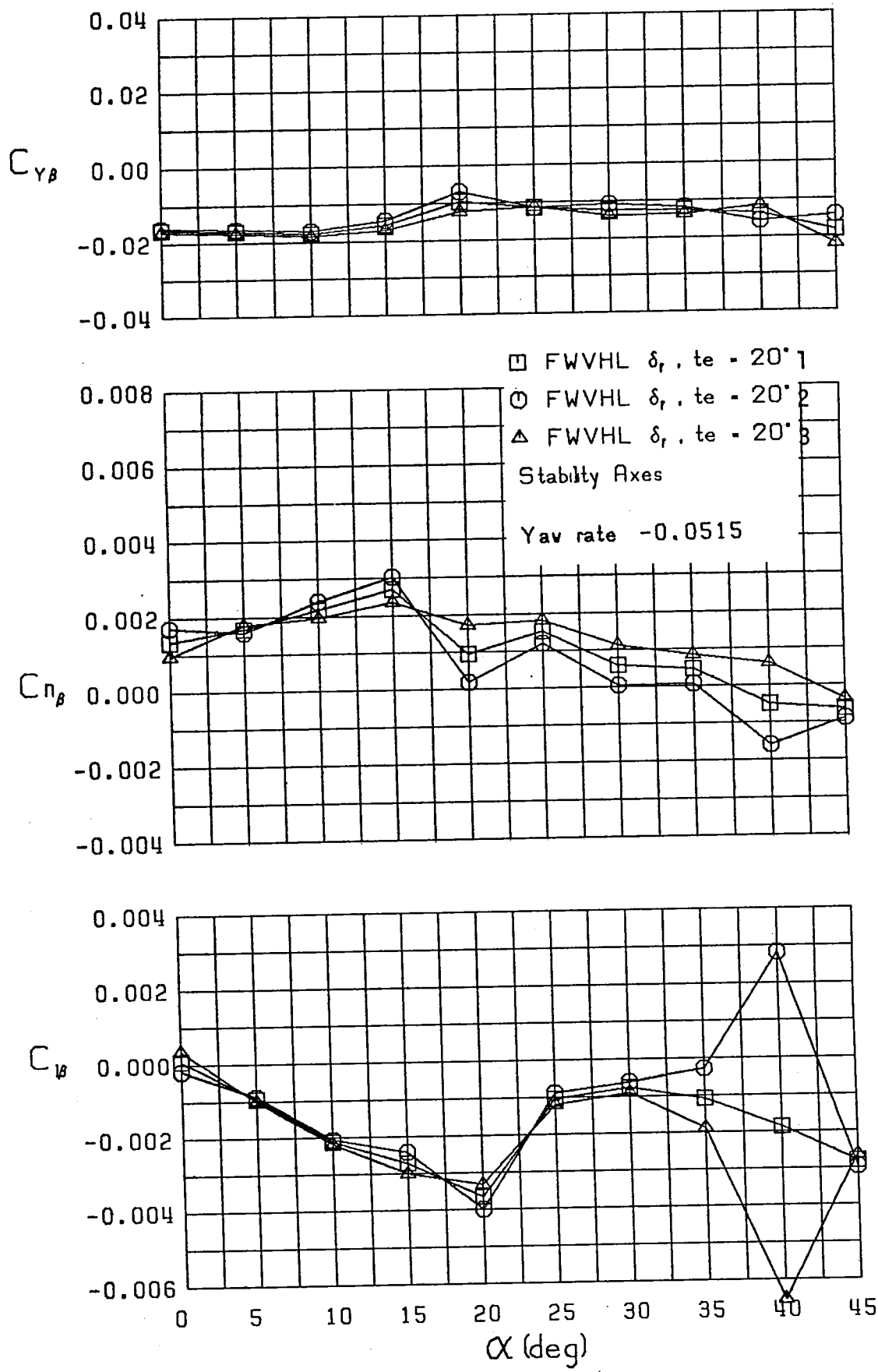

Figure 18 (Continued)

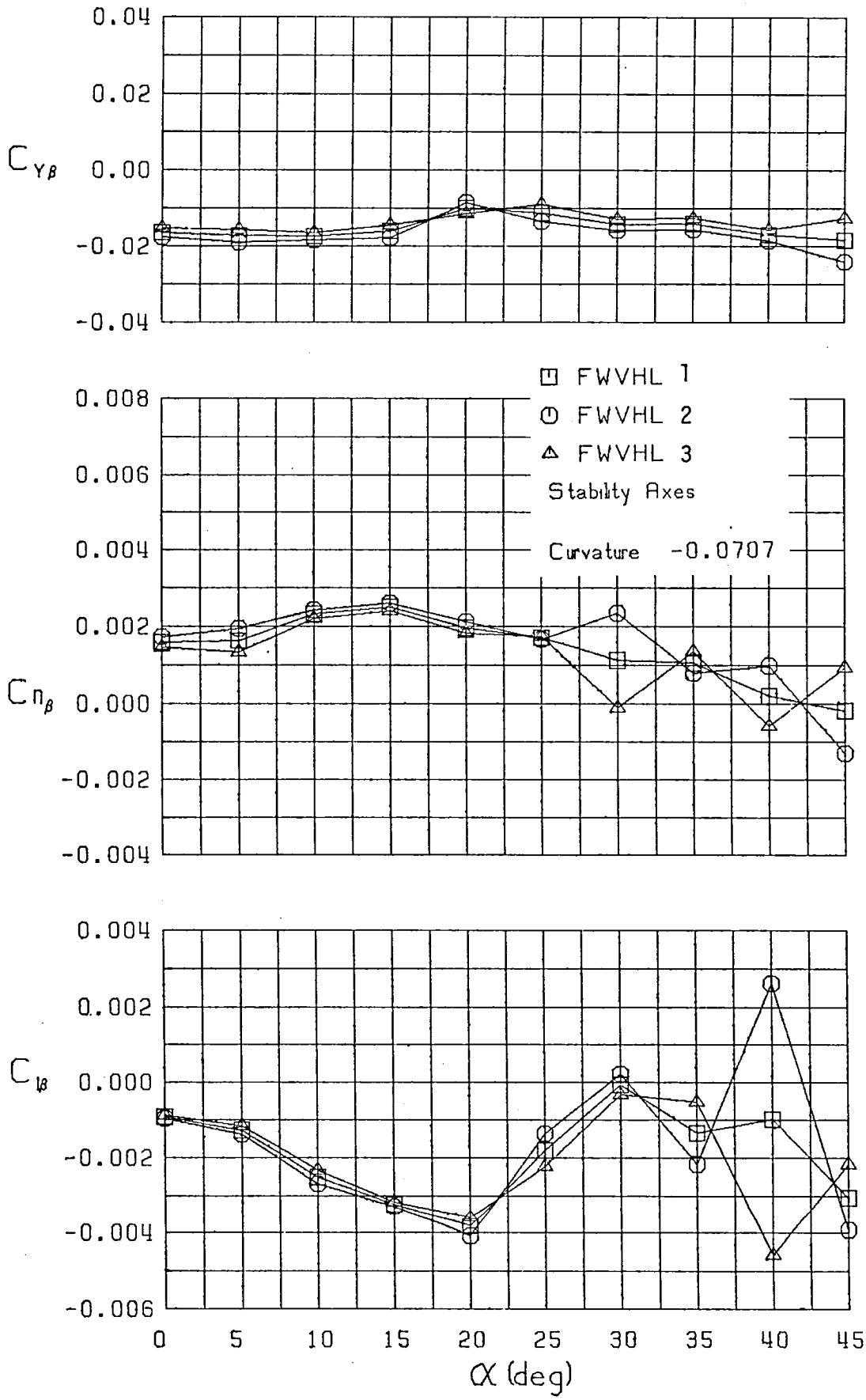

Figure 19 Variation of Lateral-Directional Static Stability Derivatives with Angle of Attack and Sideslip, $\hat{r}$ = - 0.0707

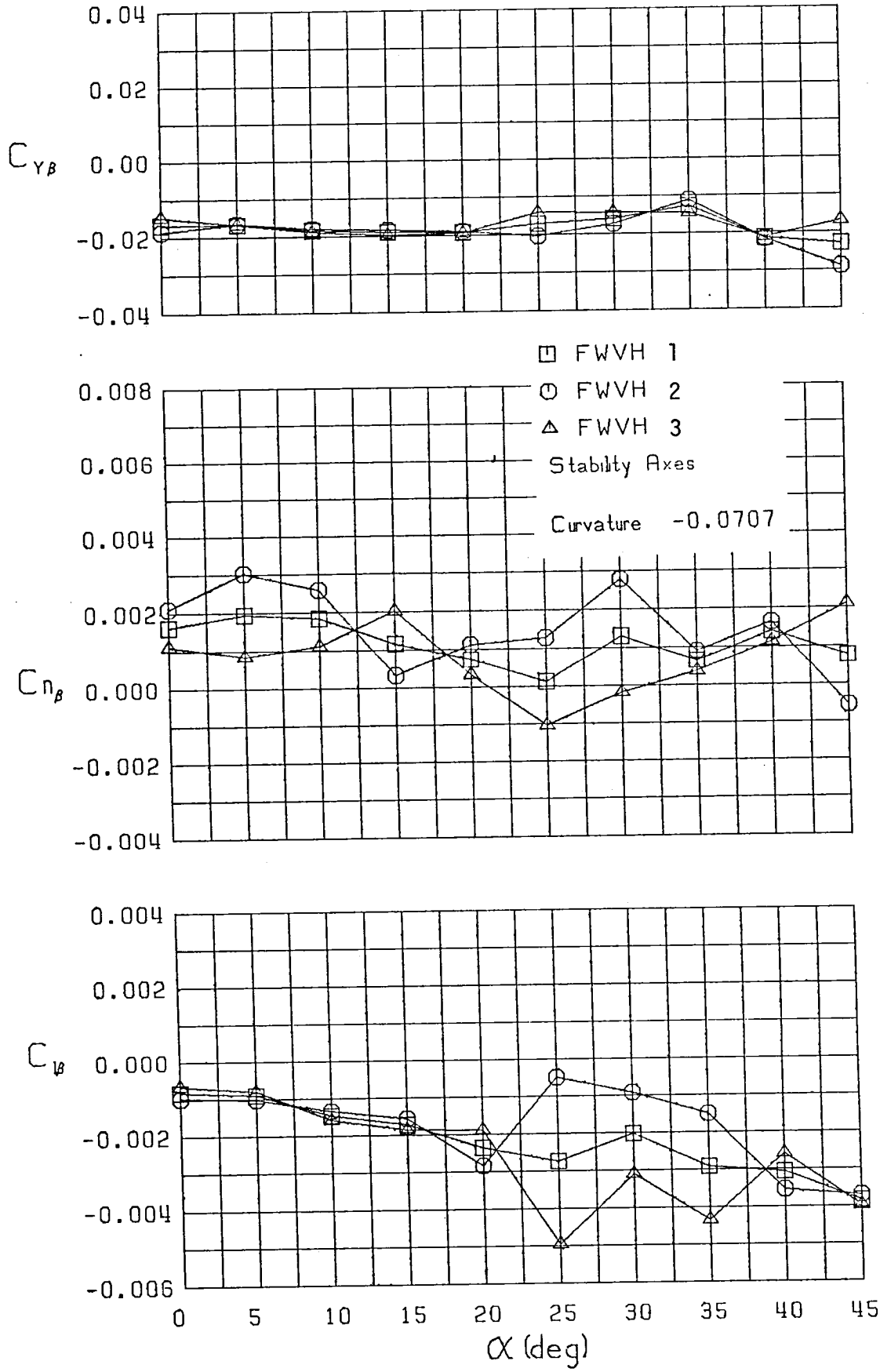

Figure 19 (Continued)

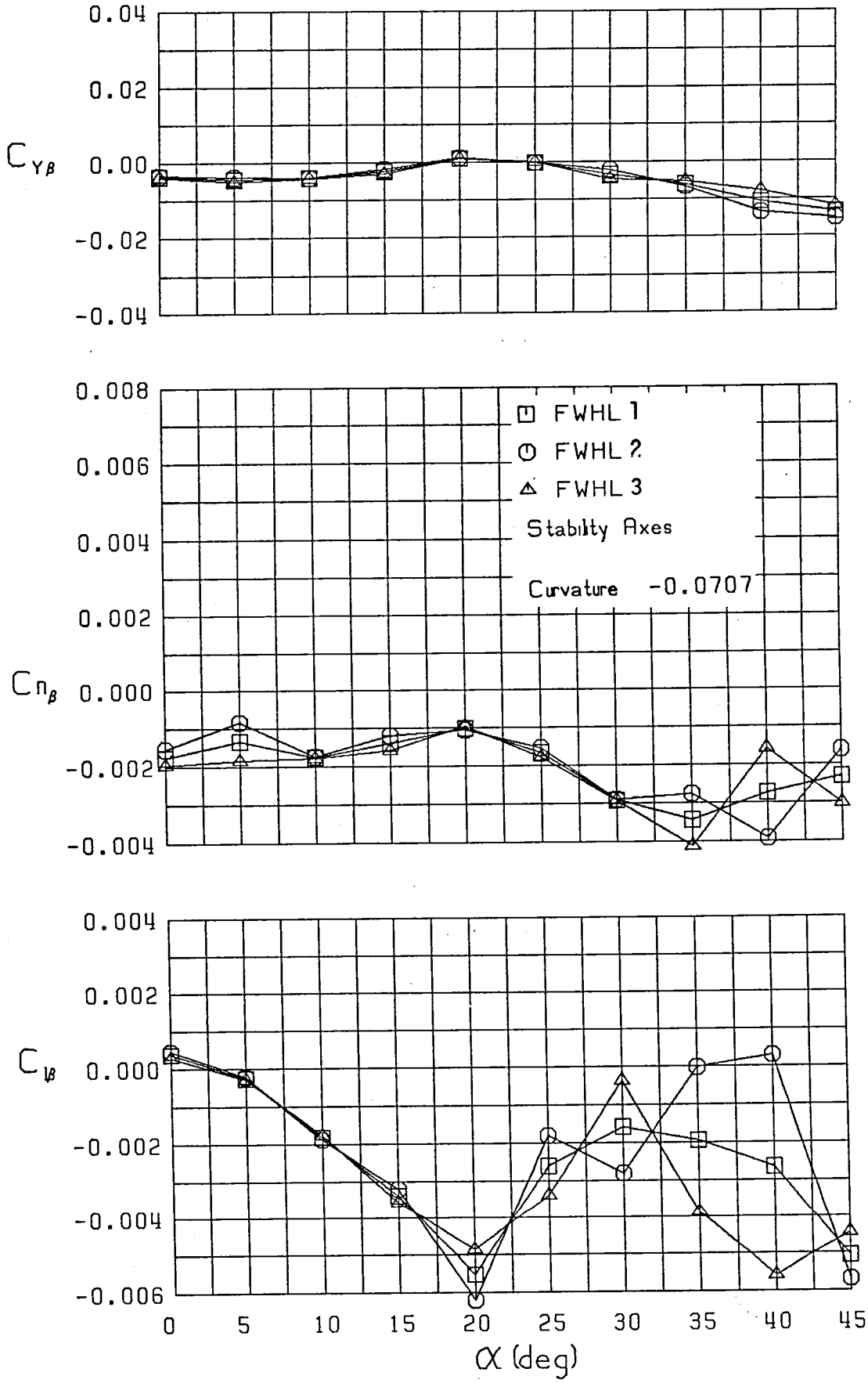

Figure 19 (Continued)

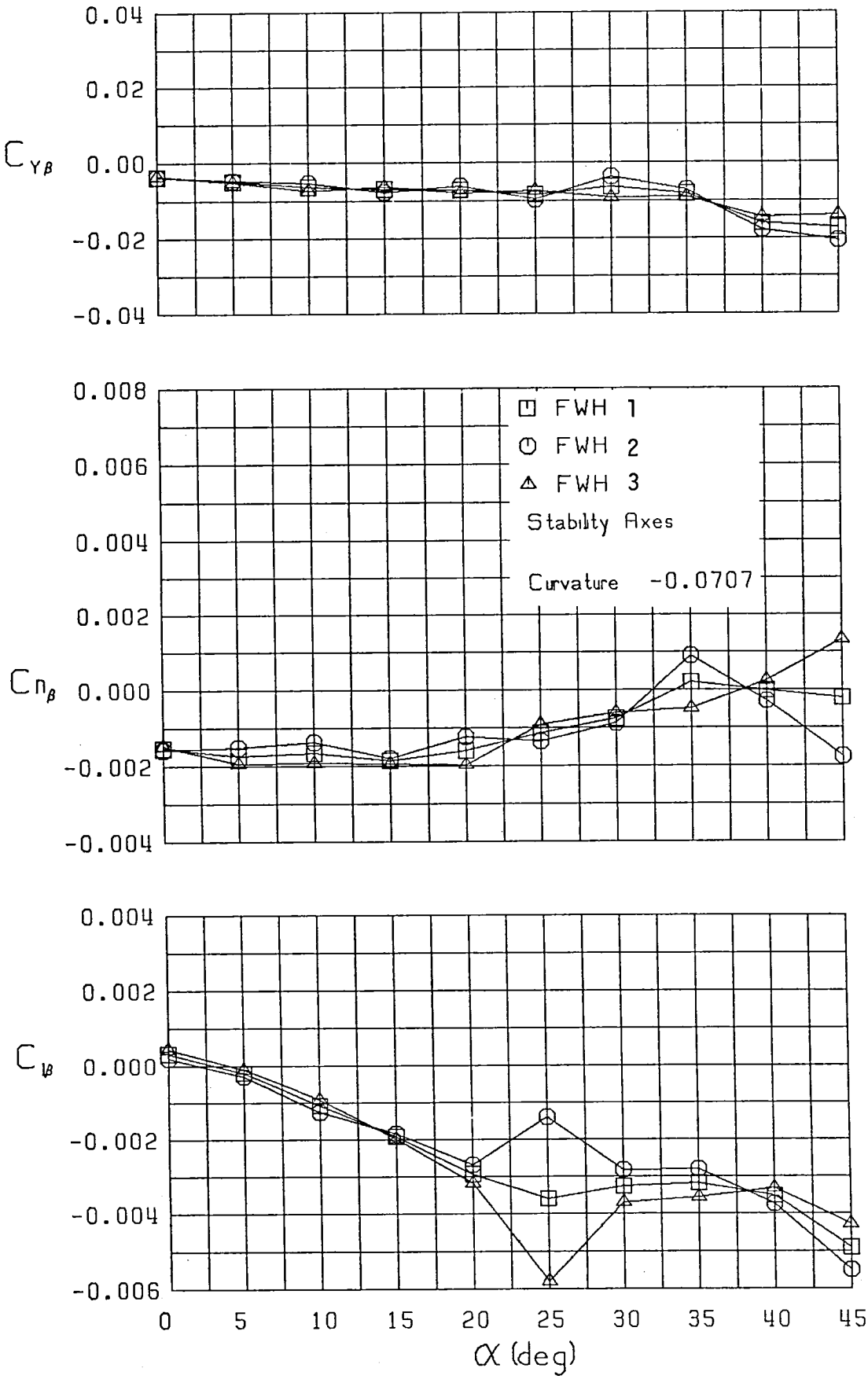

Figure 19 (Continued)

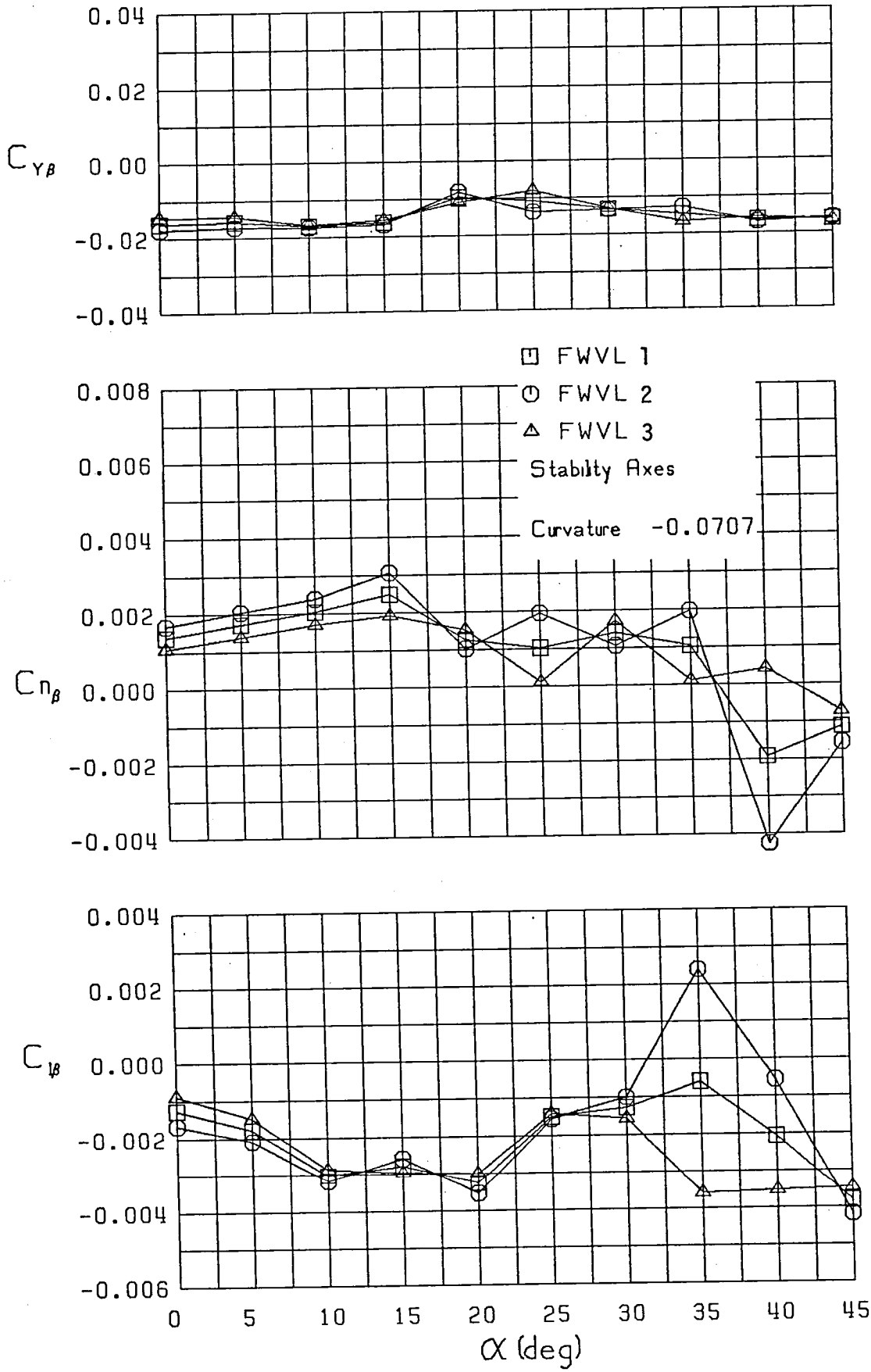

Figure 19 (Continued)

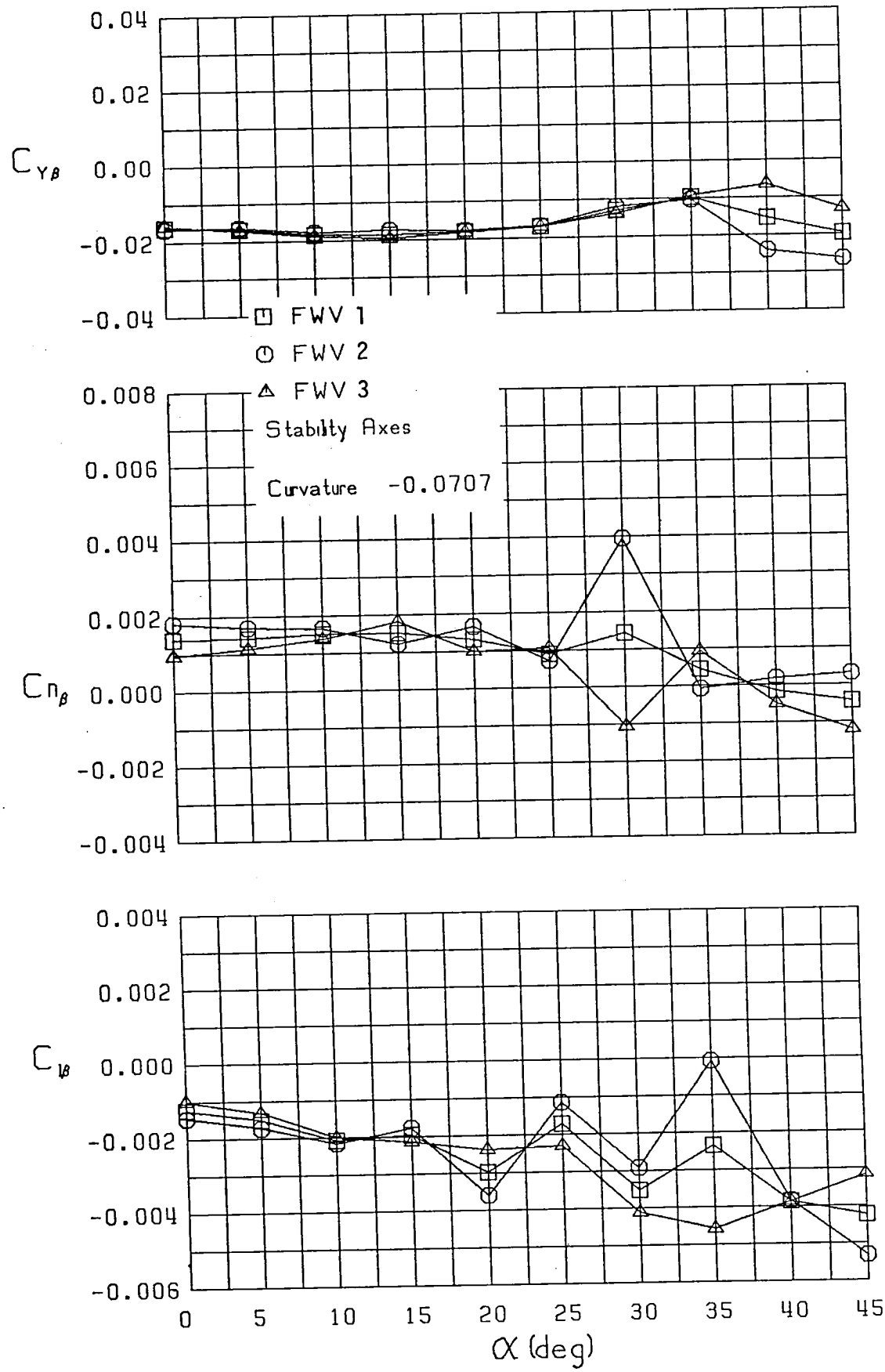

Figure 19 (Continued)

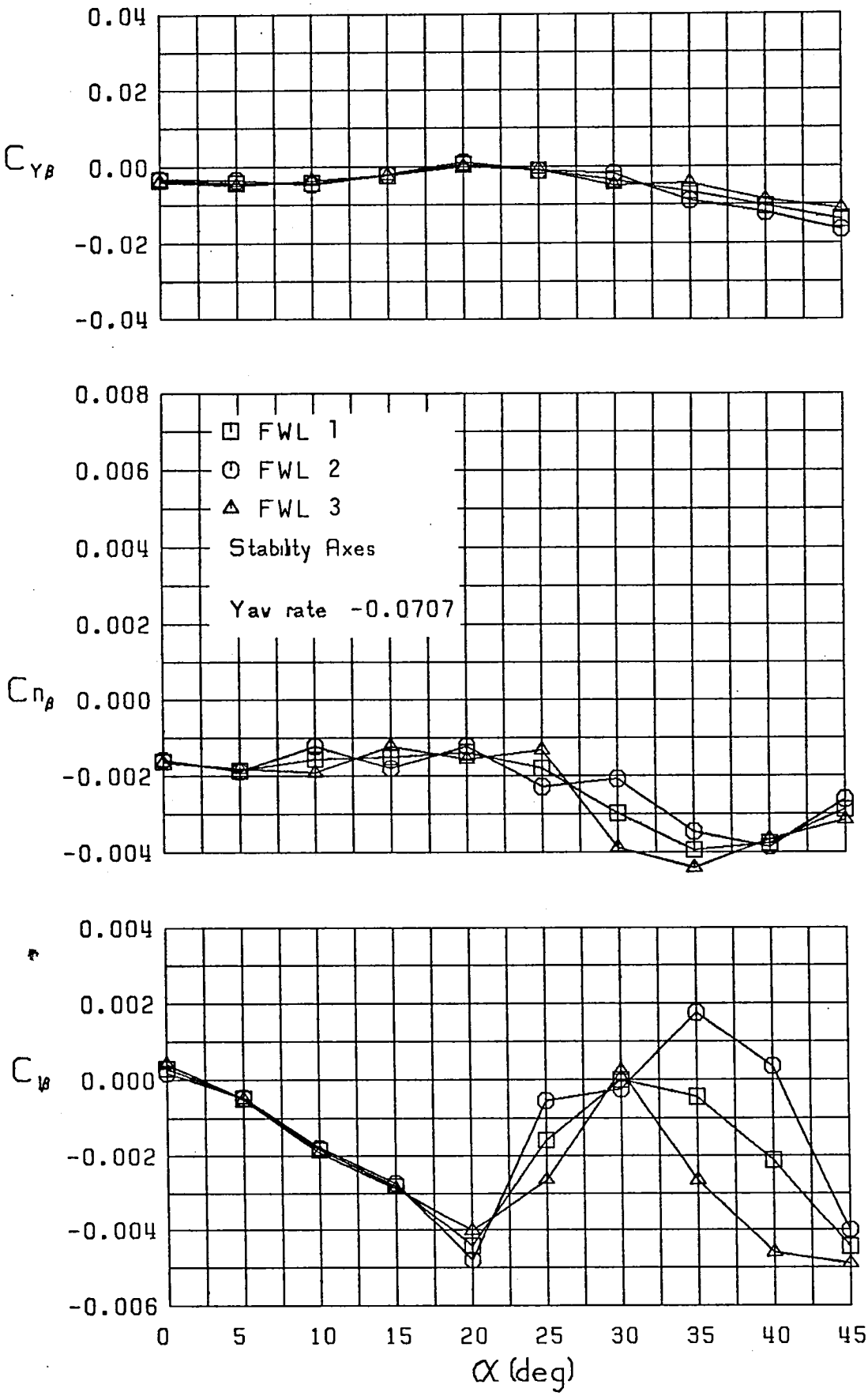

Figure 19 (Continued)

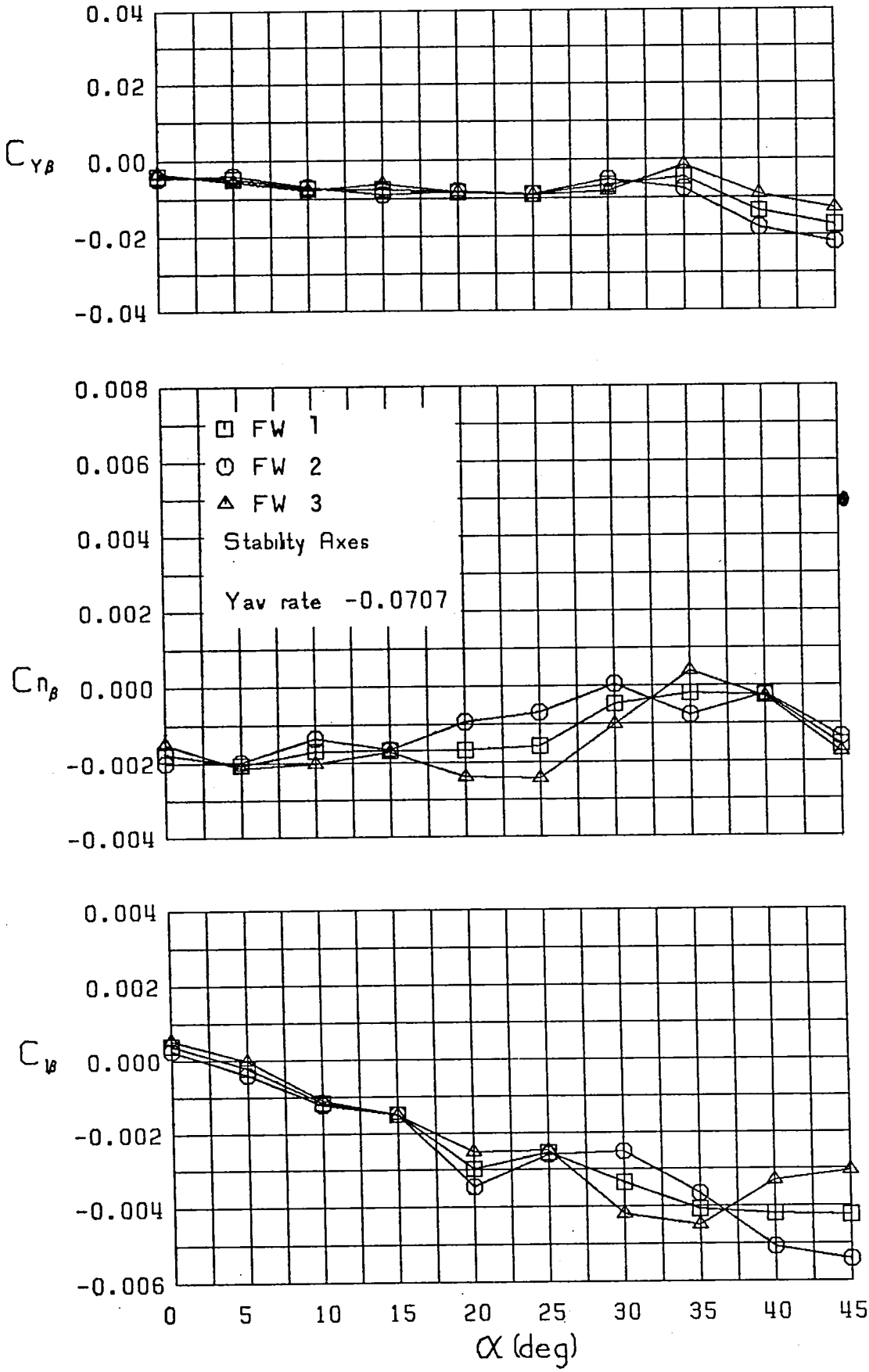

Figure 19 (Continued)

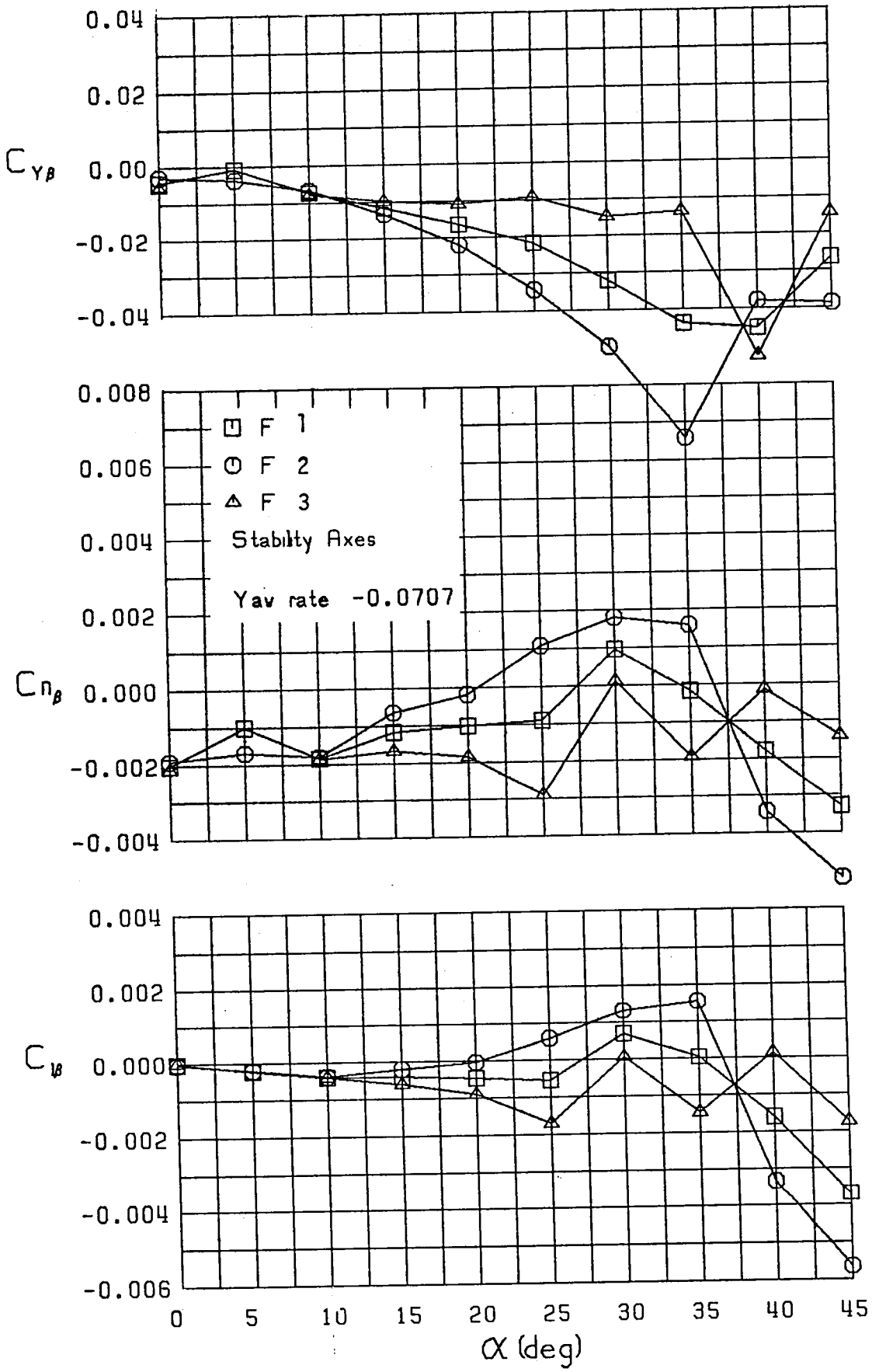

Figure 19 (Continued)

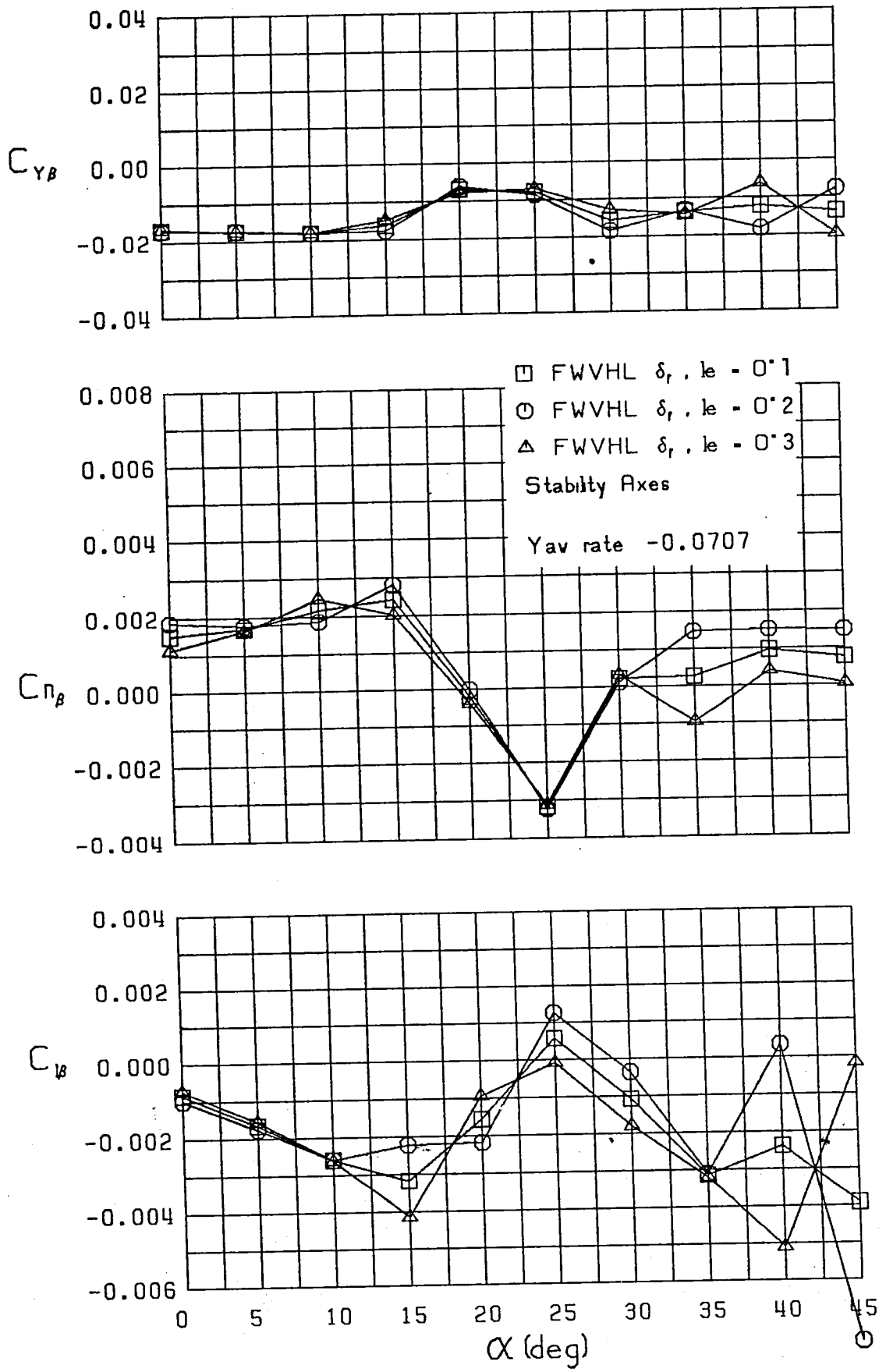

Figure 19 (Continued)

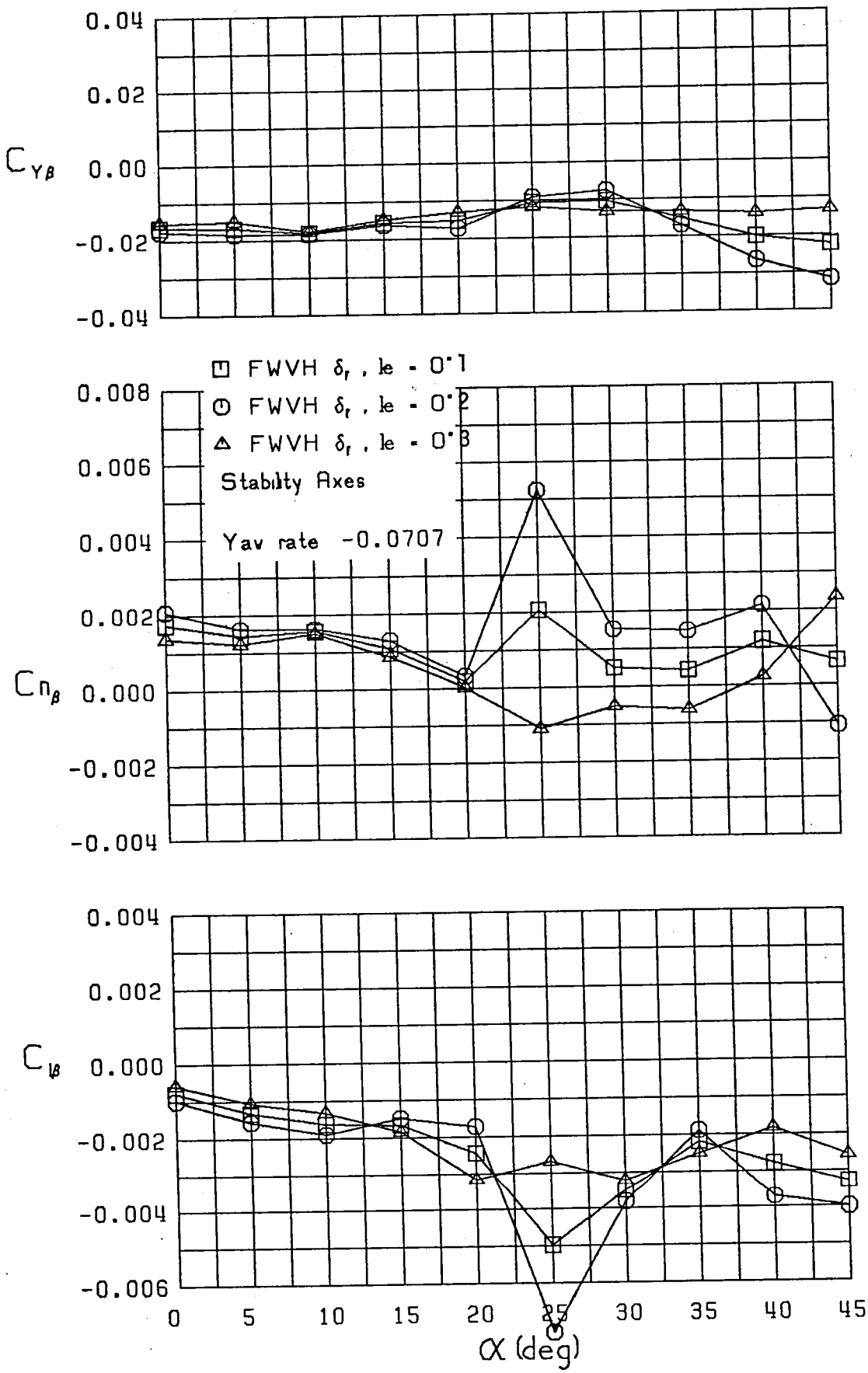

Figure 19 (Continued)

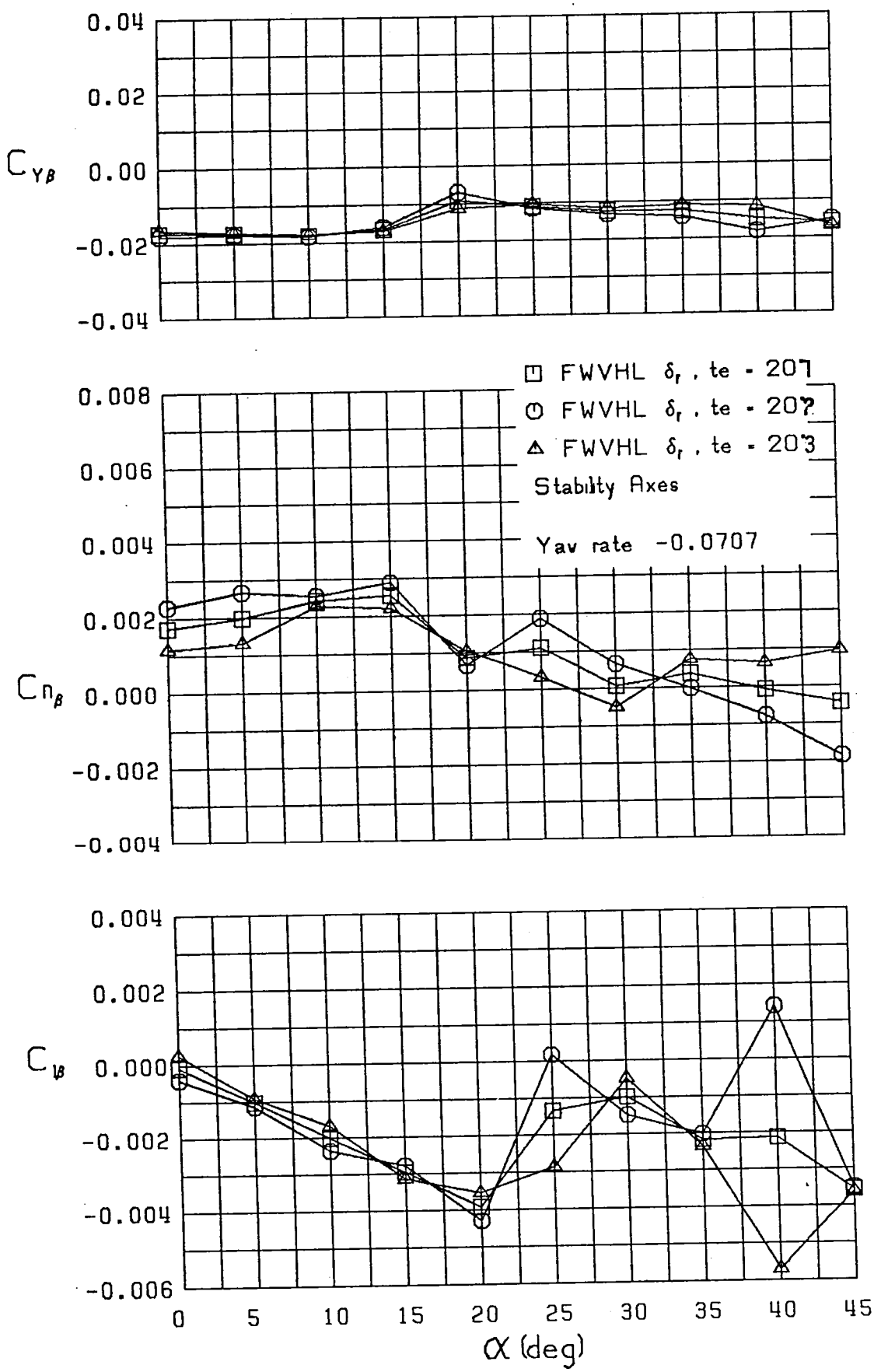

Figure 19 (Continued)

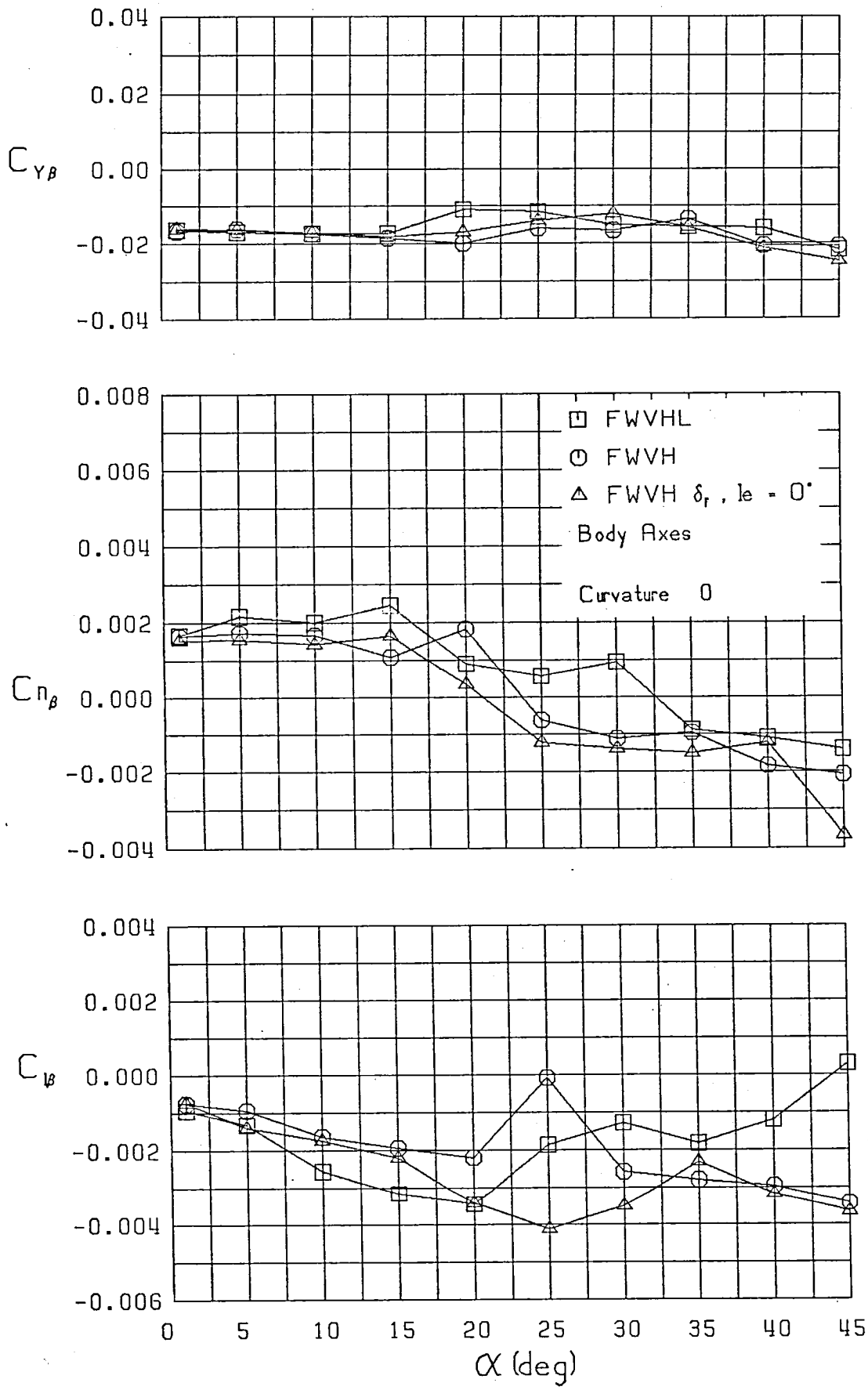

Figure 20 Variation of Lateral-Directional Static Stability Derivatives with Angle of Attack, Body Axes

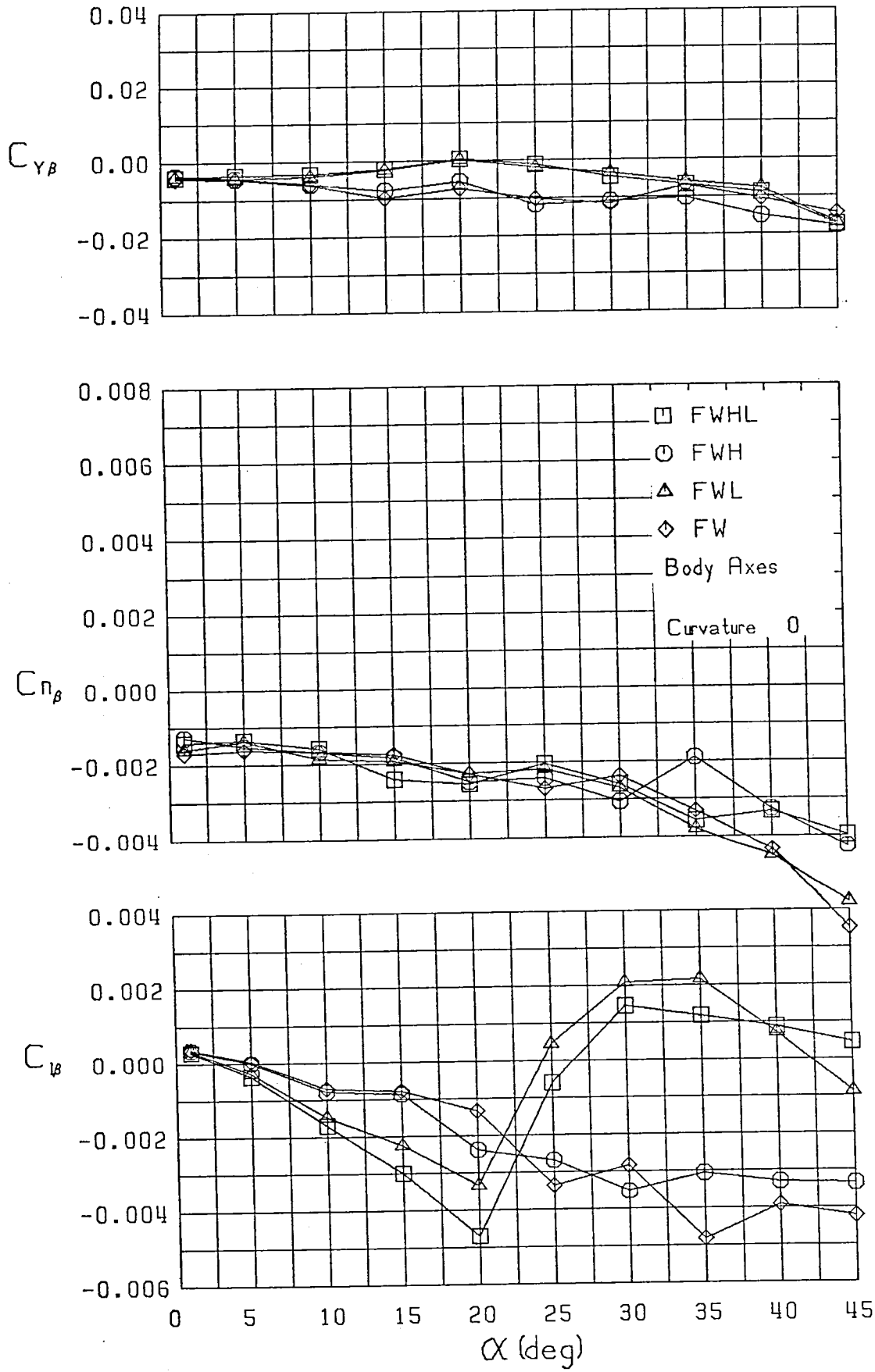

Figure 20 (Continued)

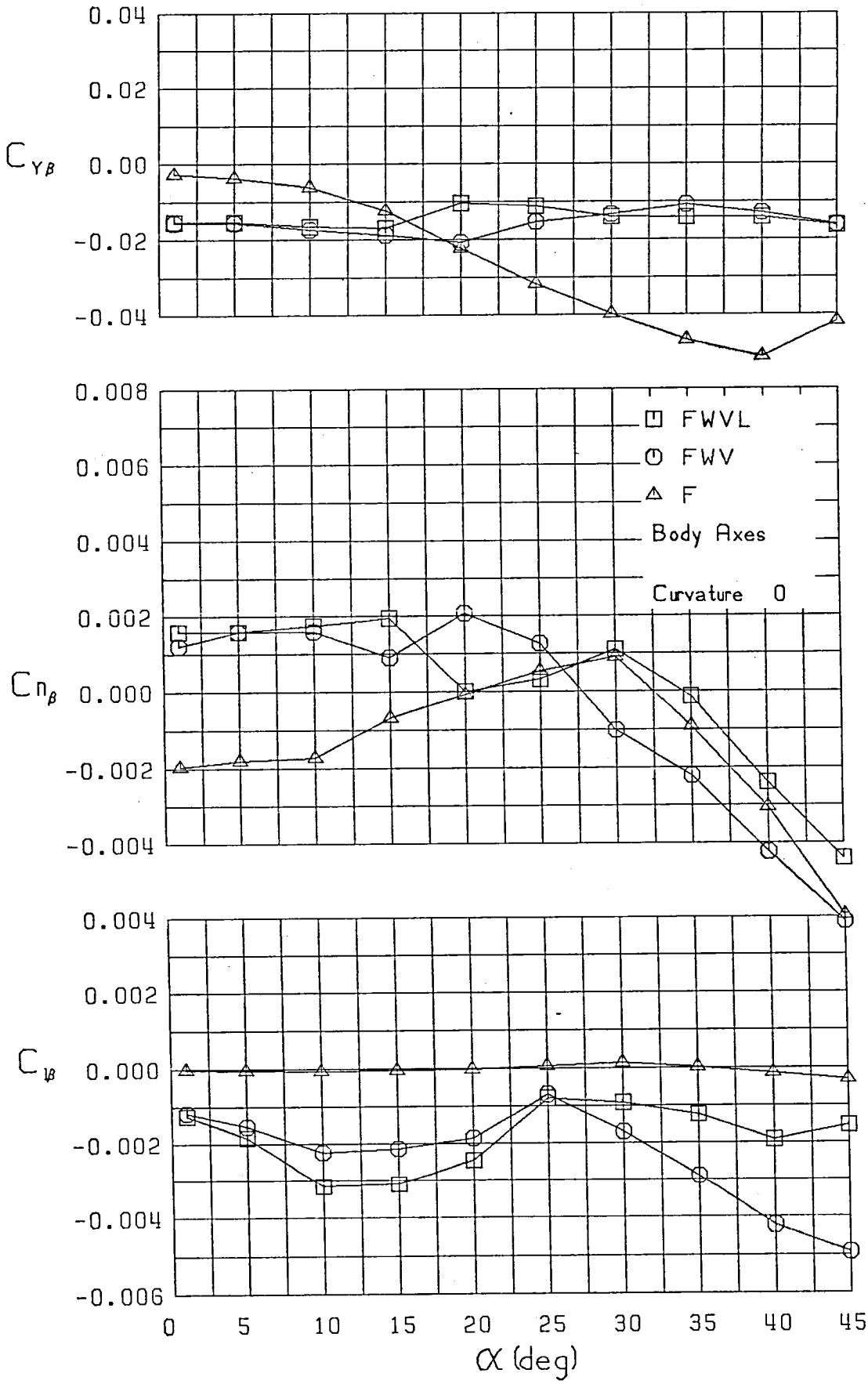

Figure 20 (Continued)

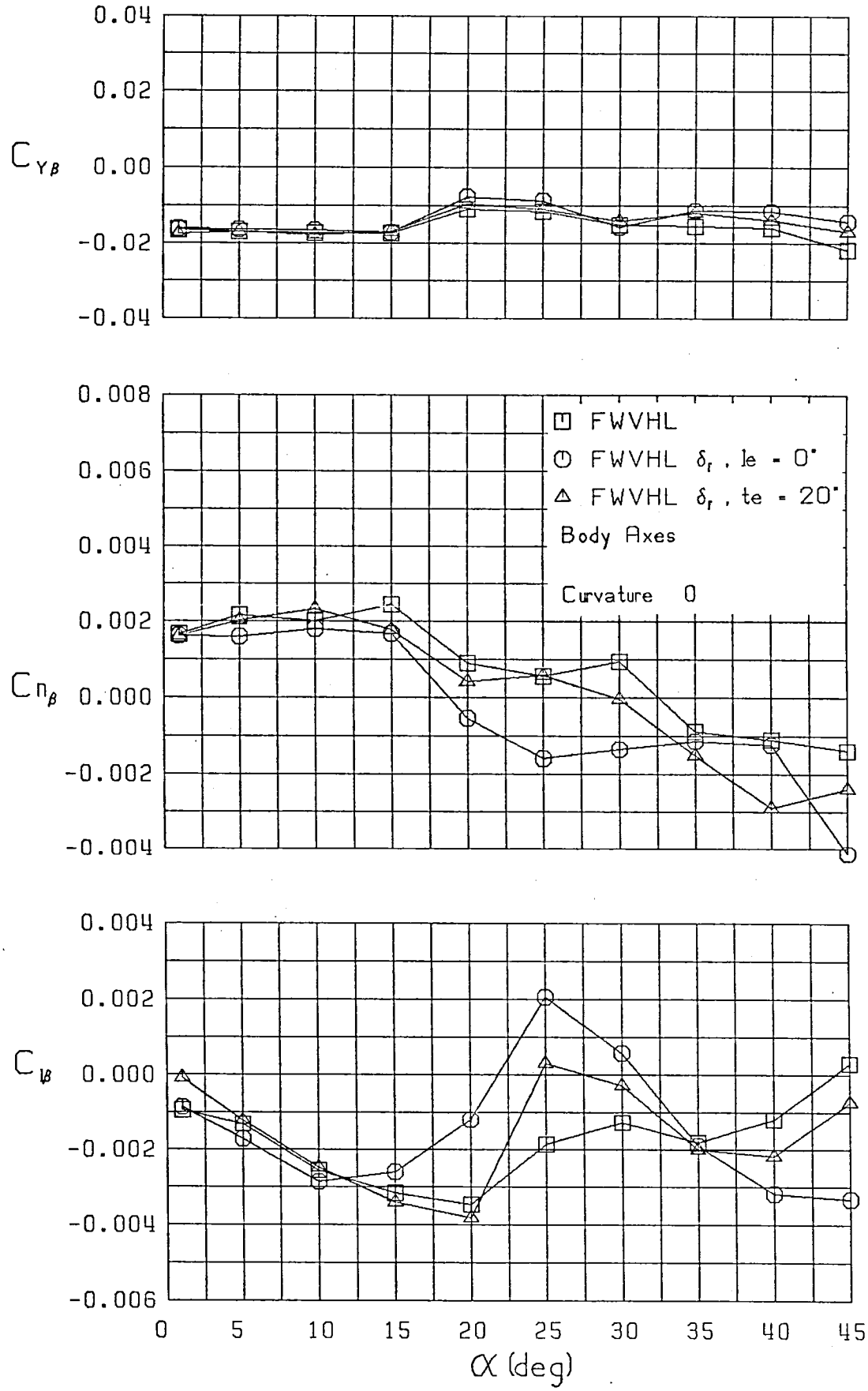

Figure 20 (Continued)

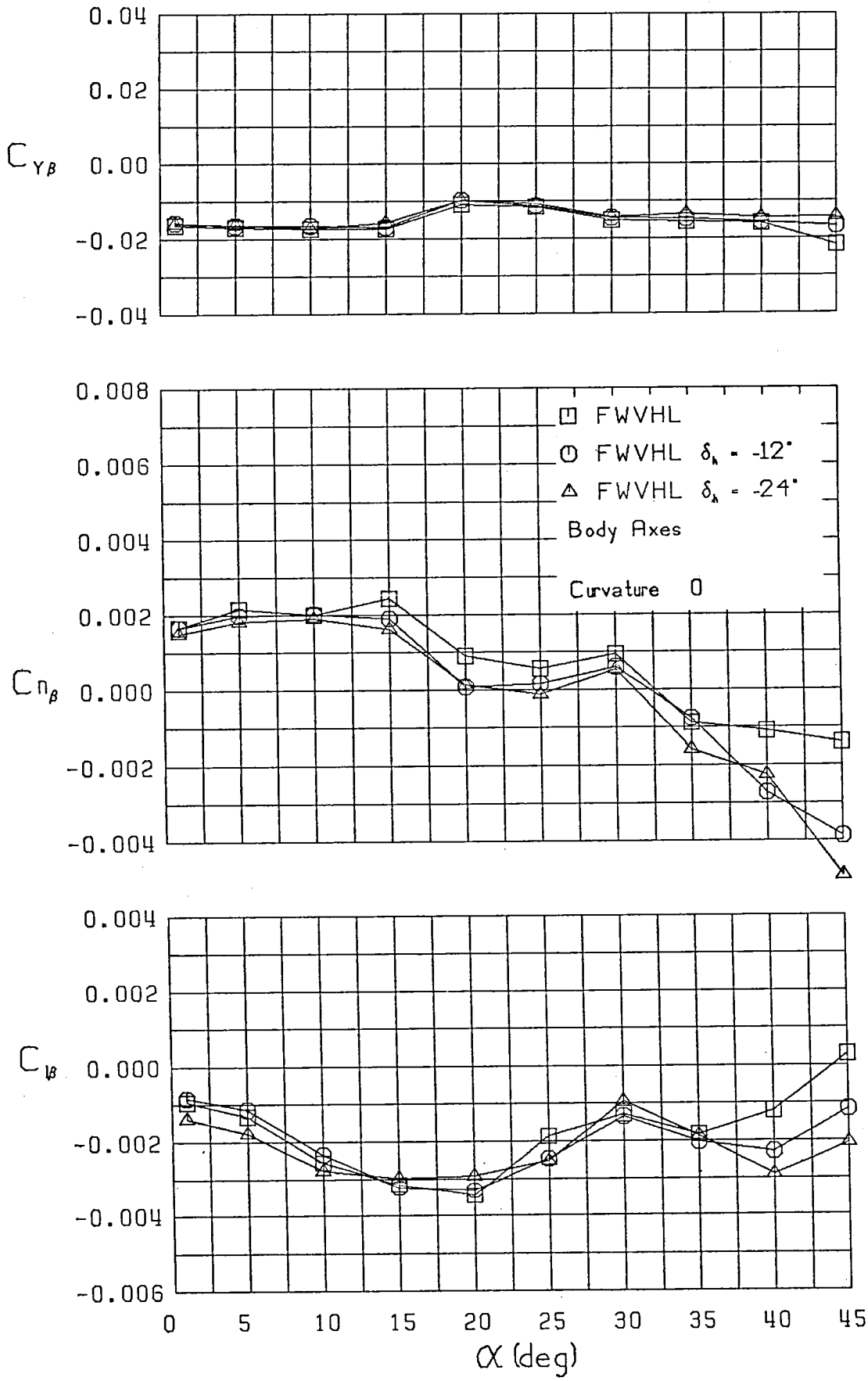

Figure 20 (Continued)

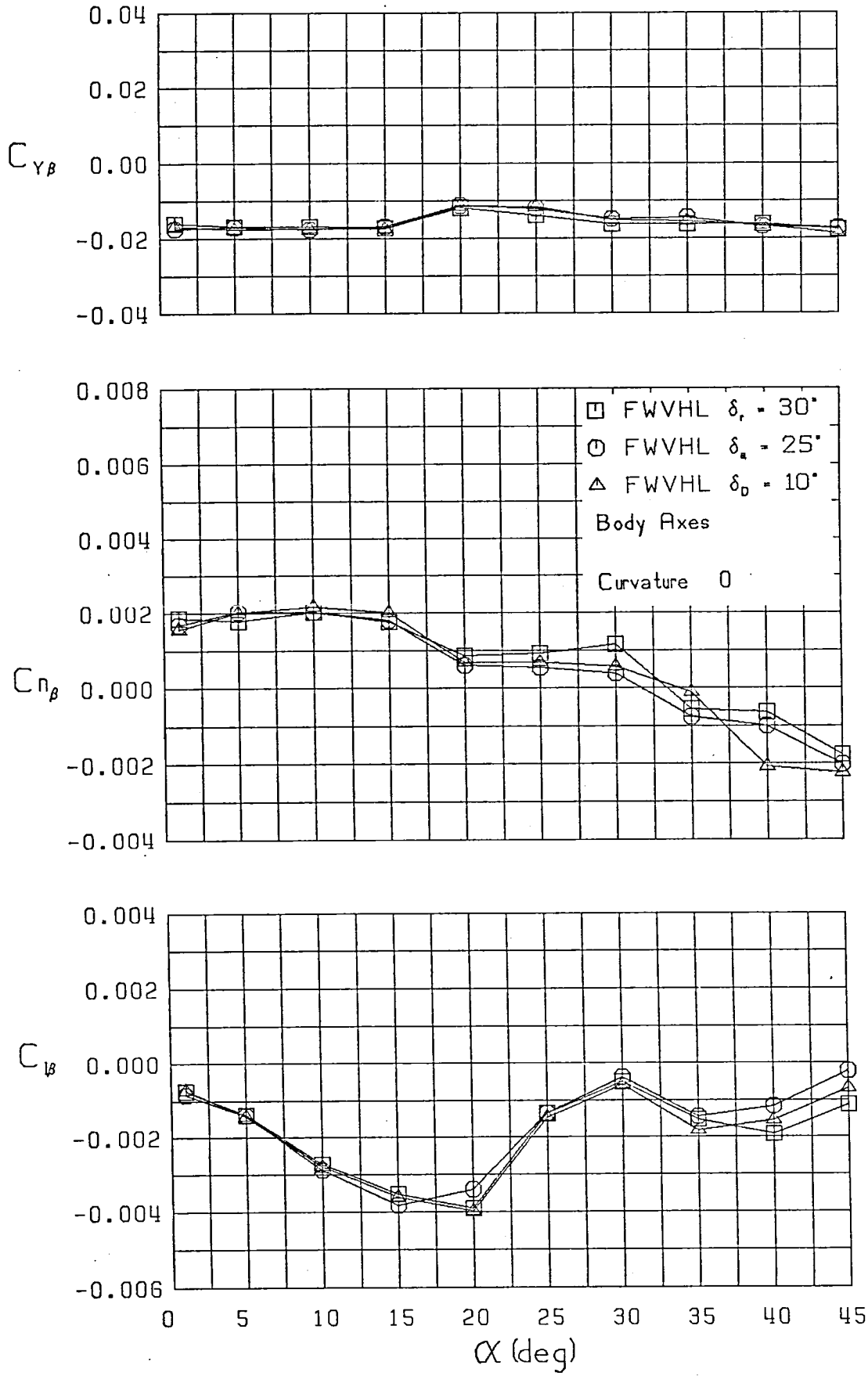

Figure 20 (Continued)

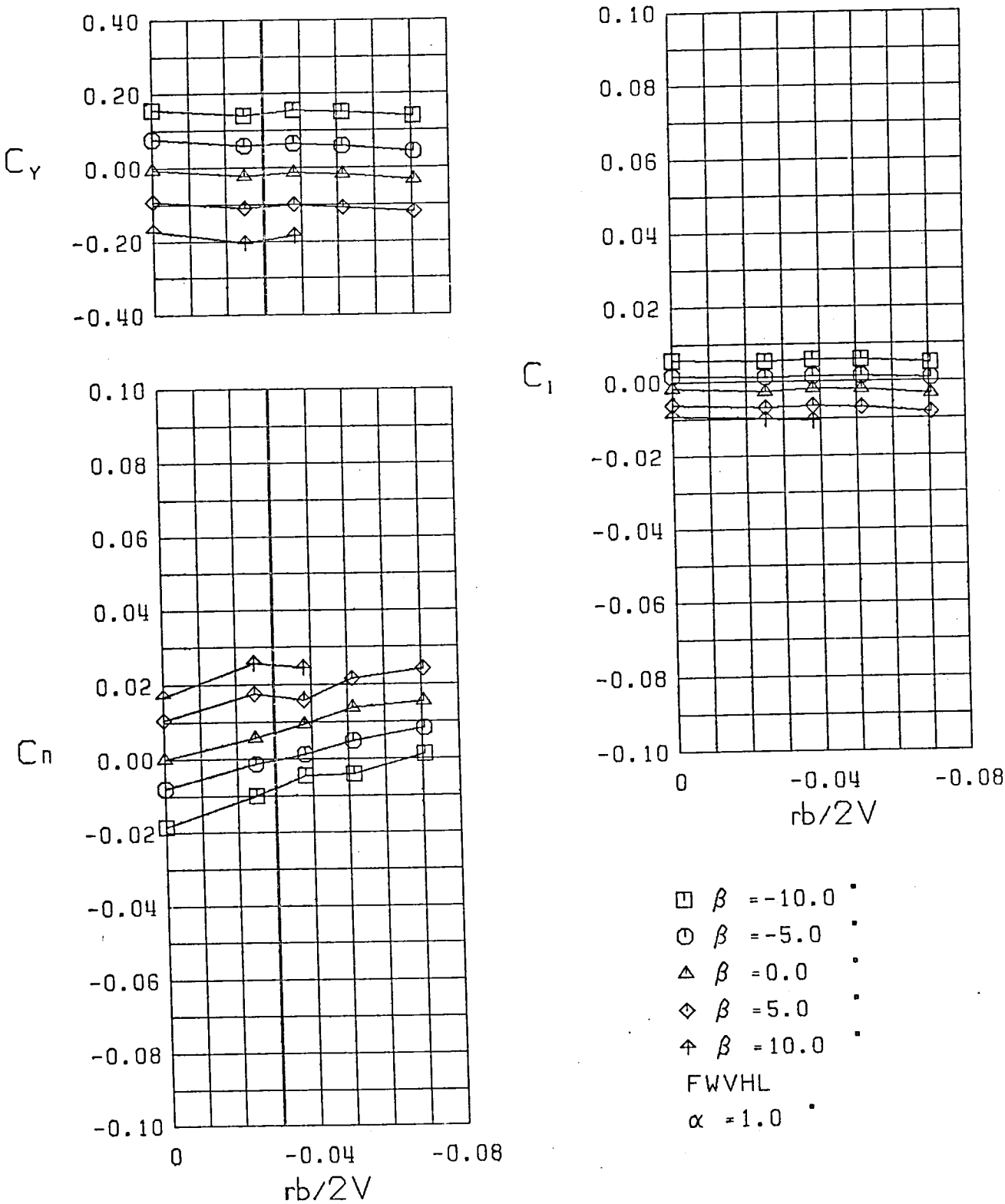

Figure 21 Variation of Static Lateral-Directional Stability Derivatives with Yaw Rates, Configuration 1

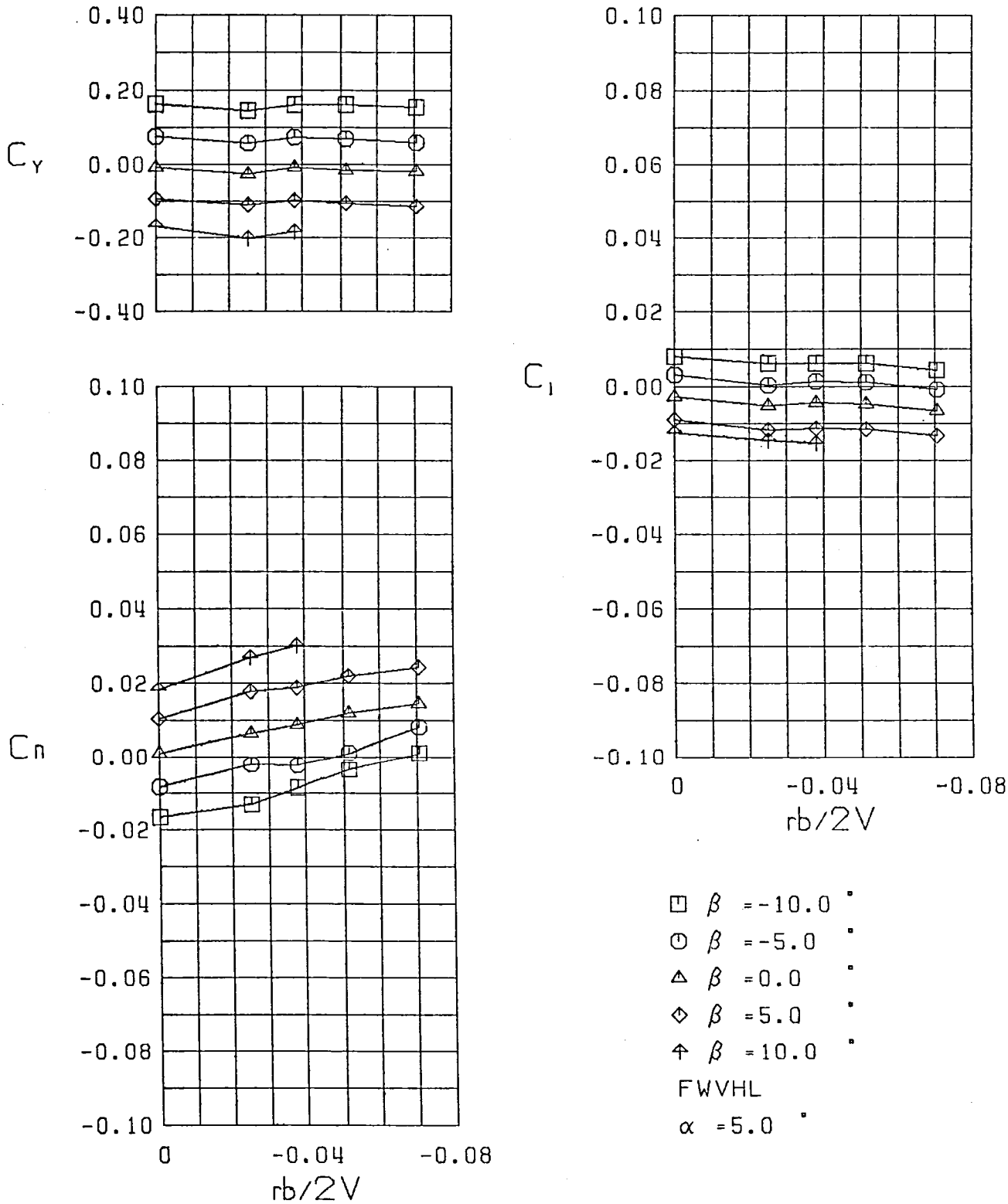

Figure 21 (Continued)

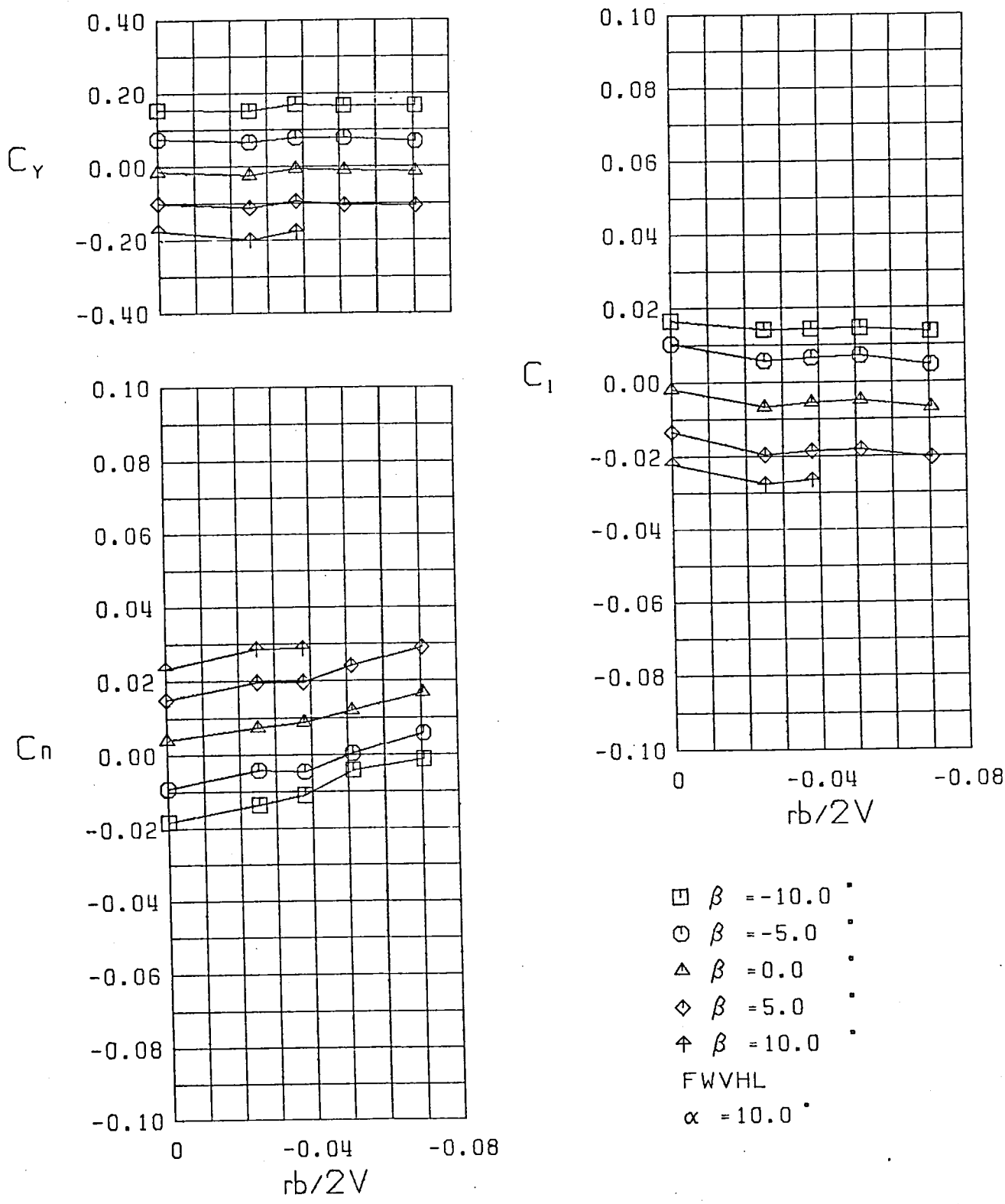

Figure 21 (Continued)

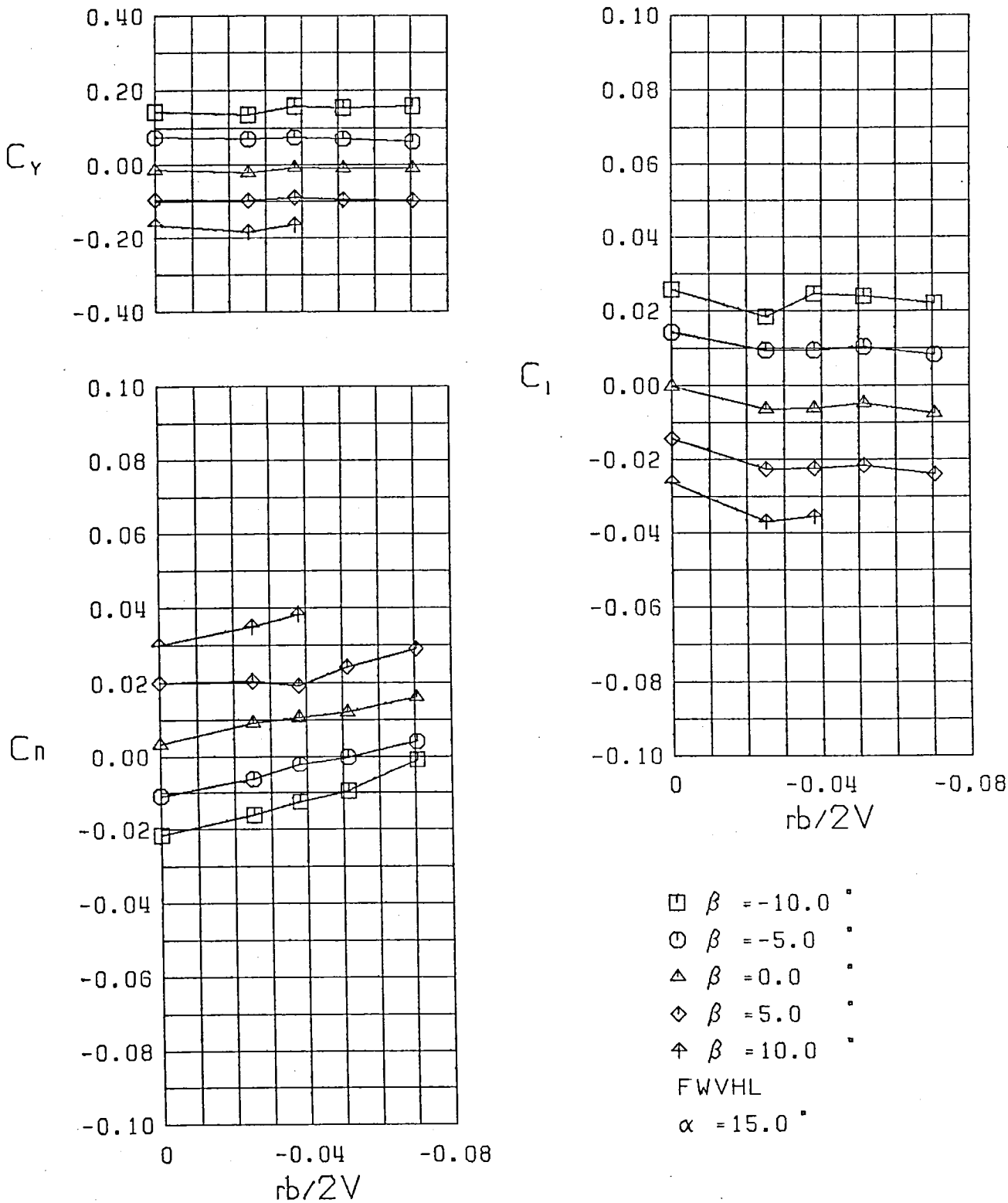

Figure 21 (Continued)

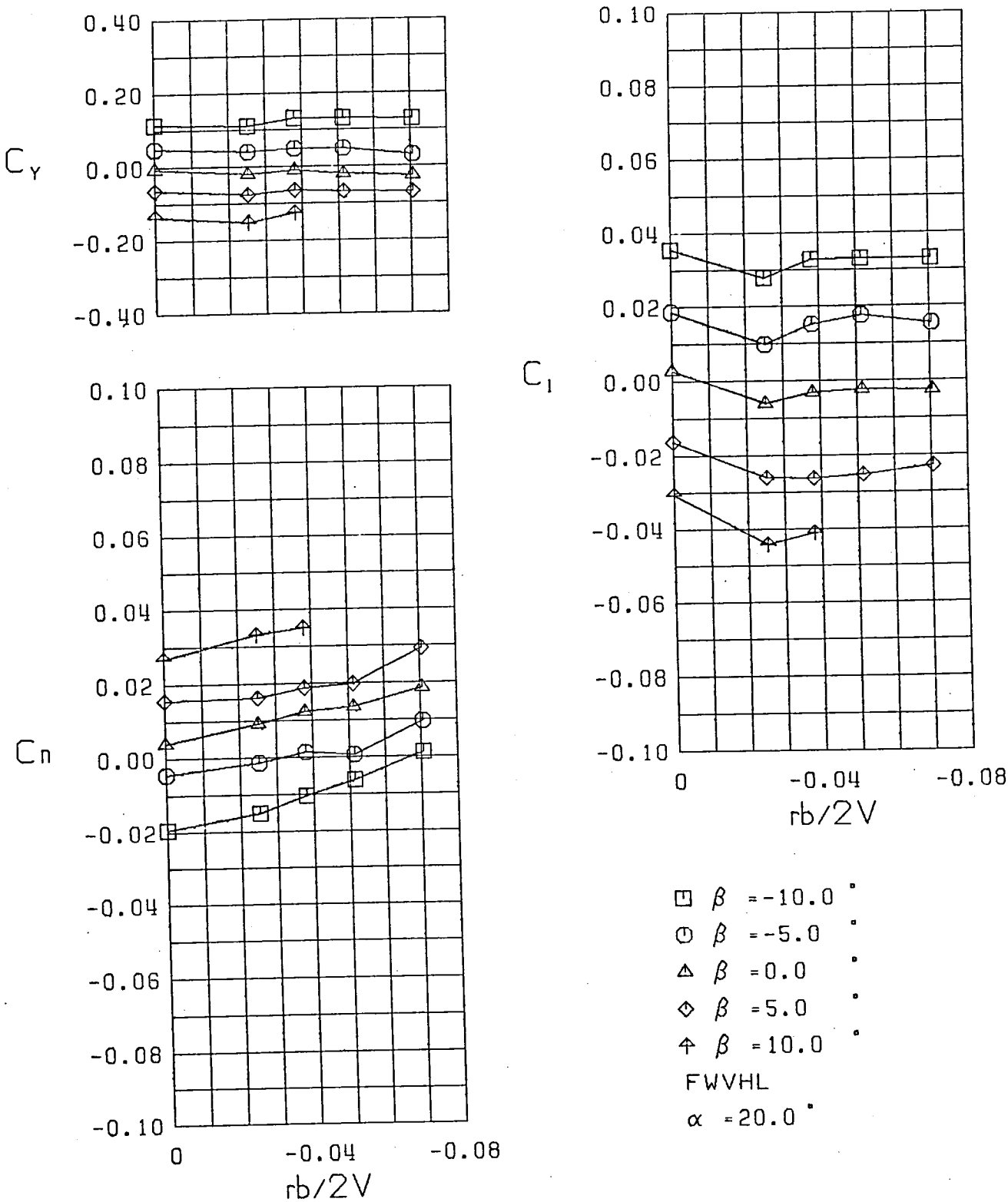

Figure 21 (Continued)

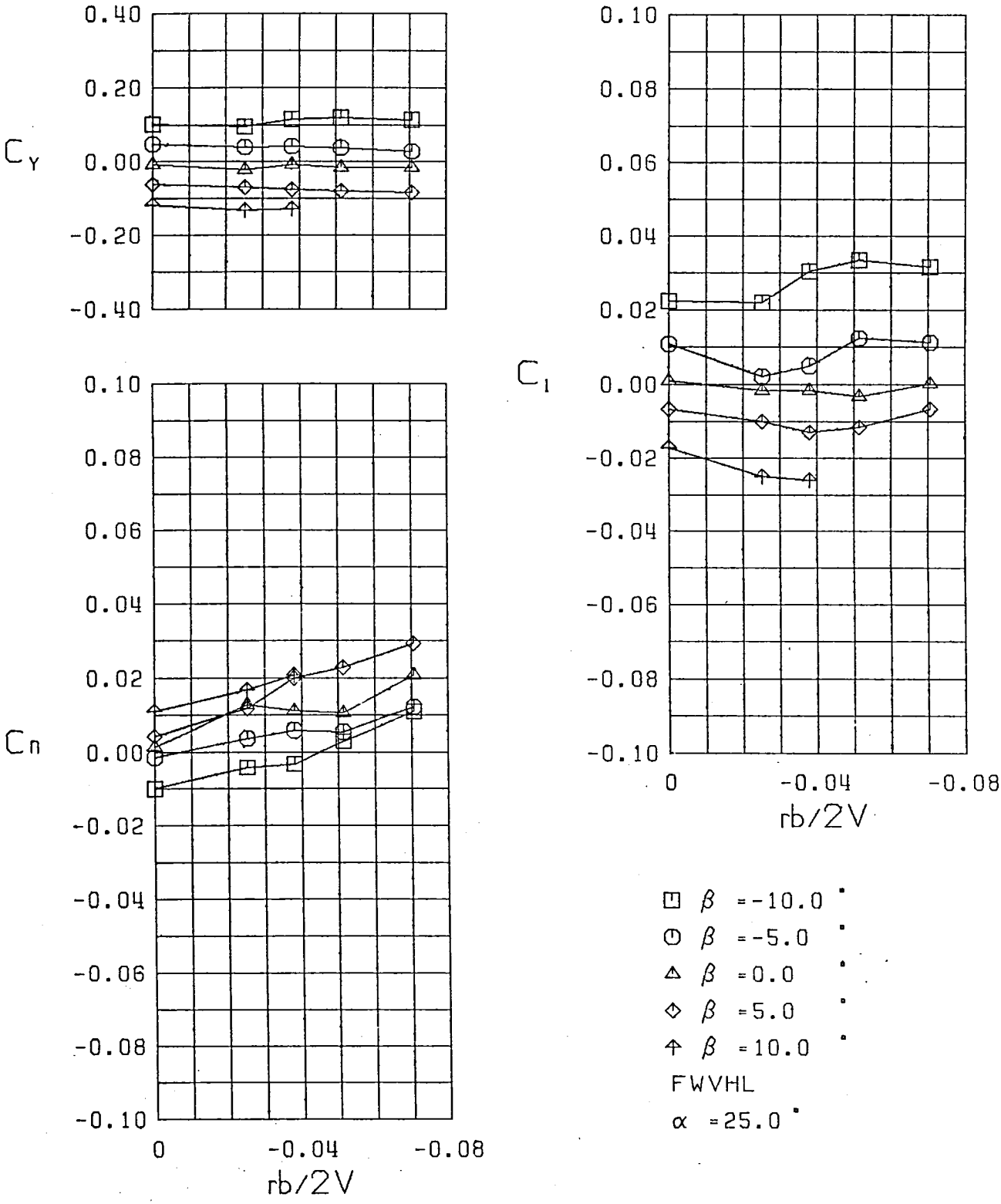

Figure 21 (Continued)

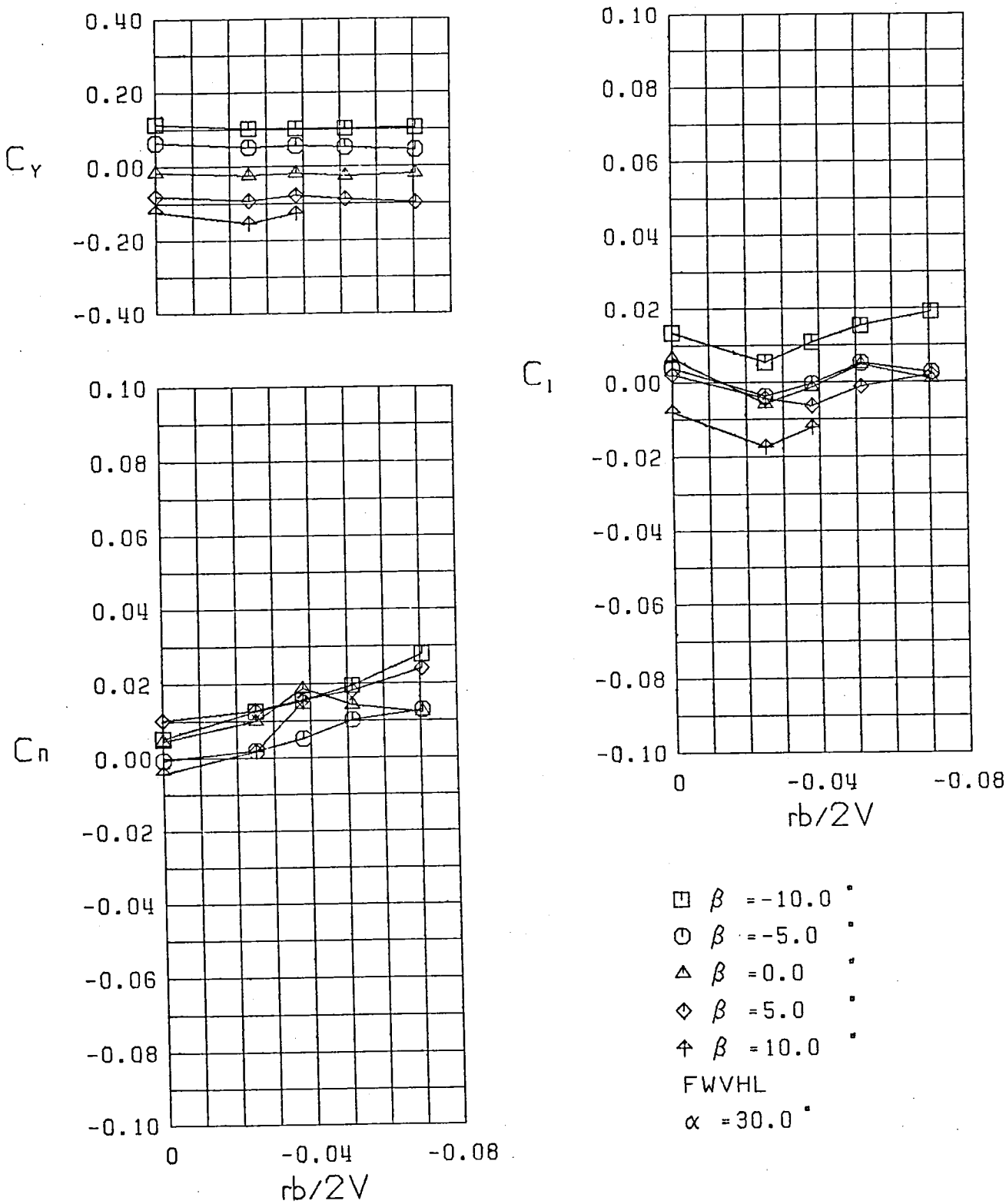

Figure 21 (Continued)

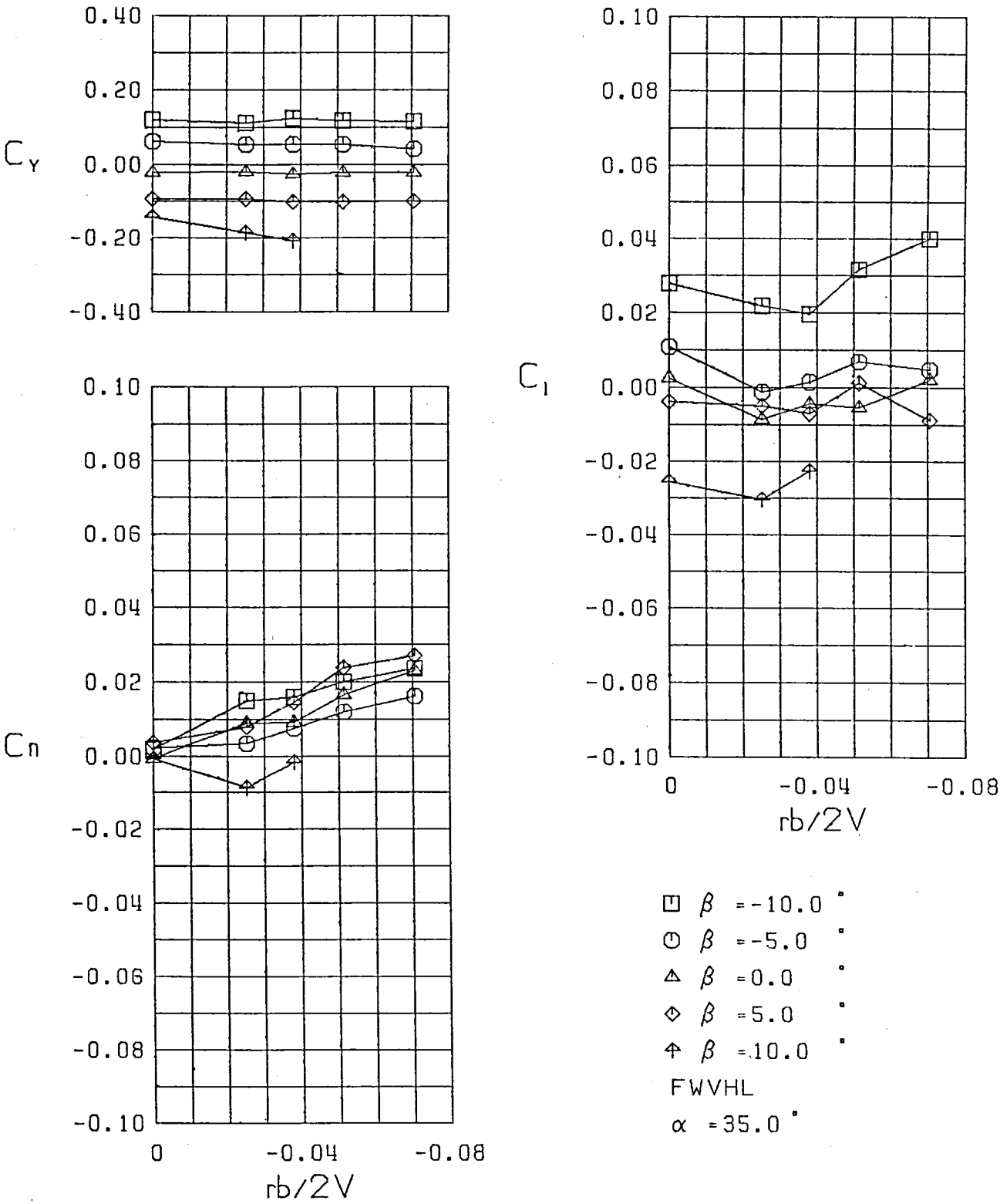

Figure 21 (Continued)

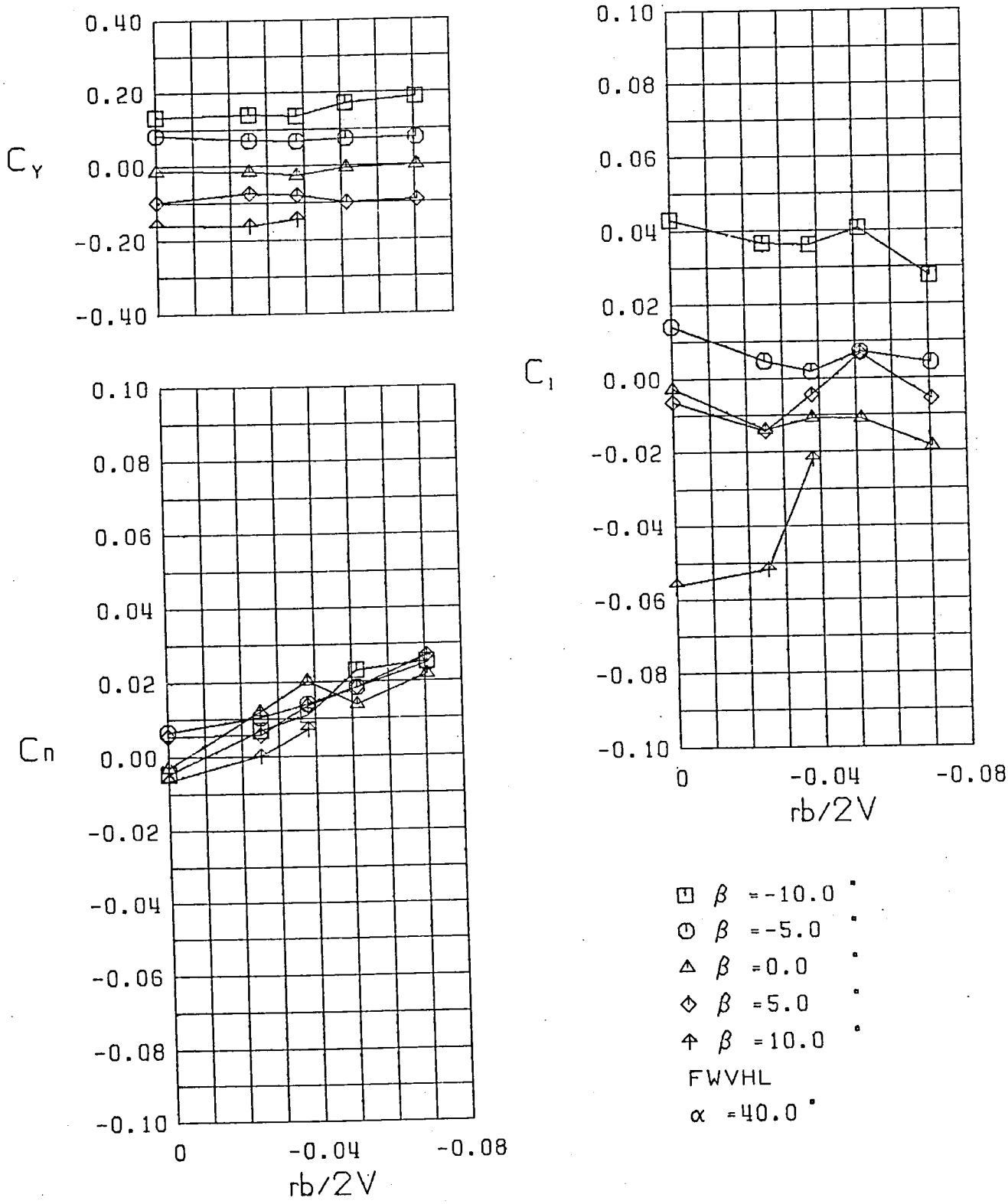

Figure 21 (Continued)

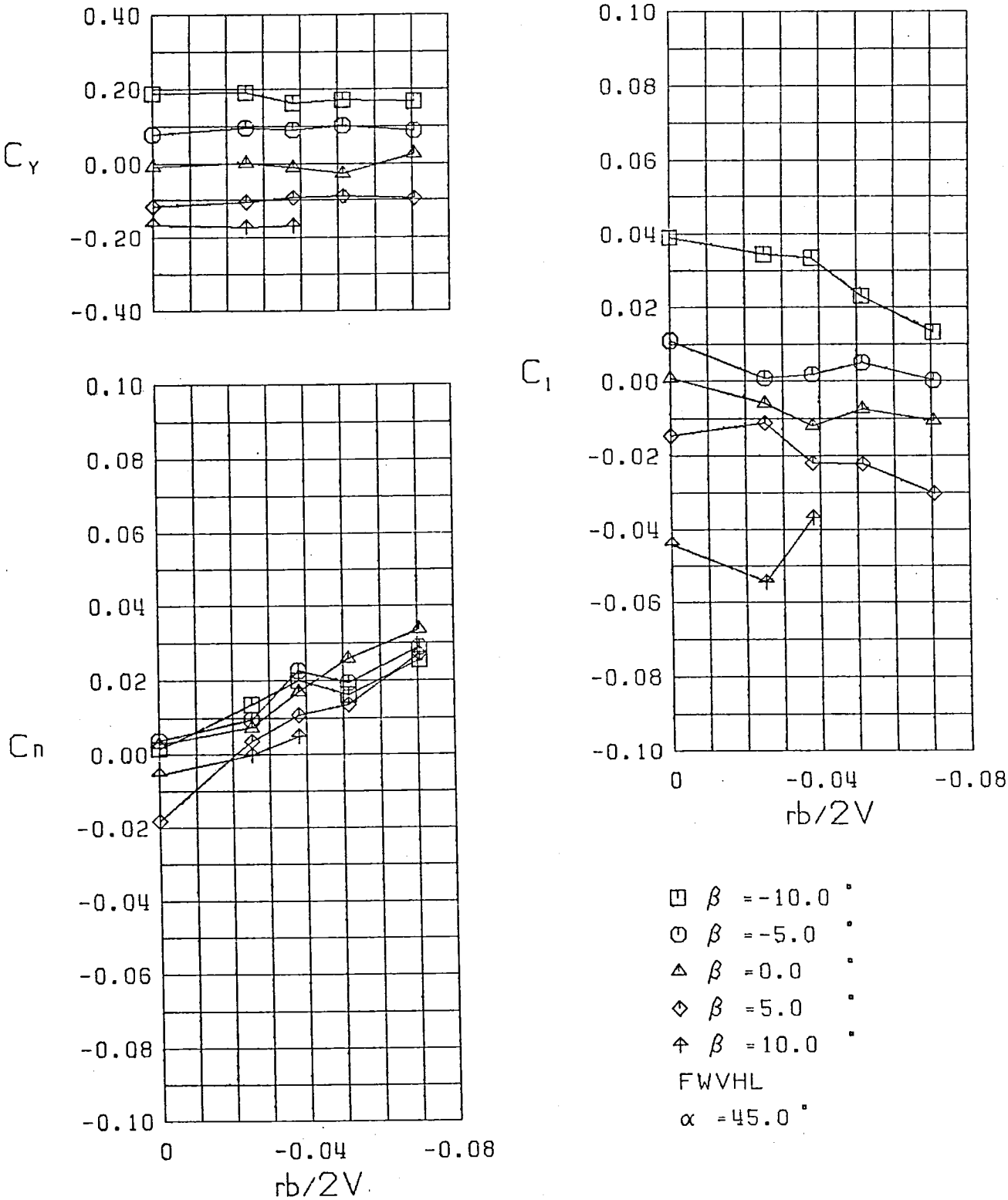

Figure 21 (Continued)

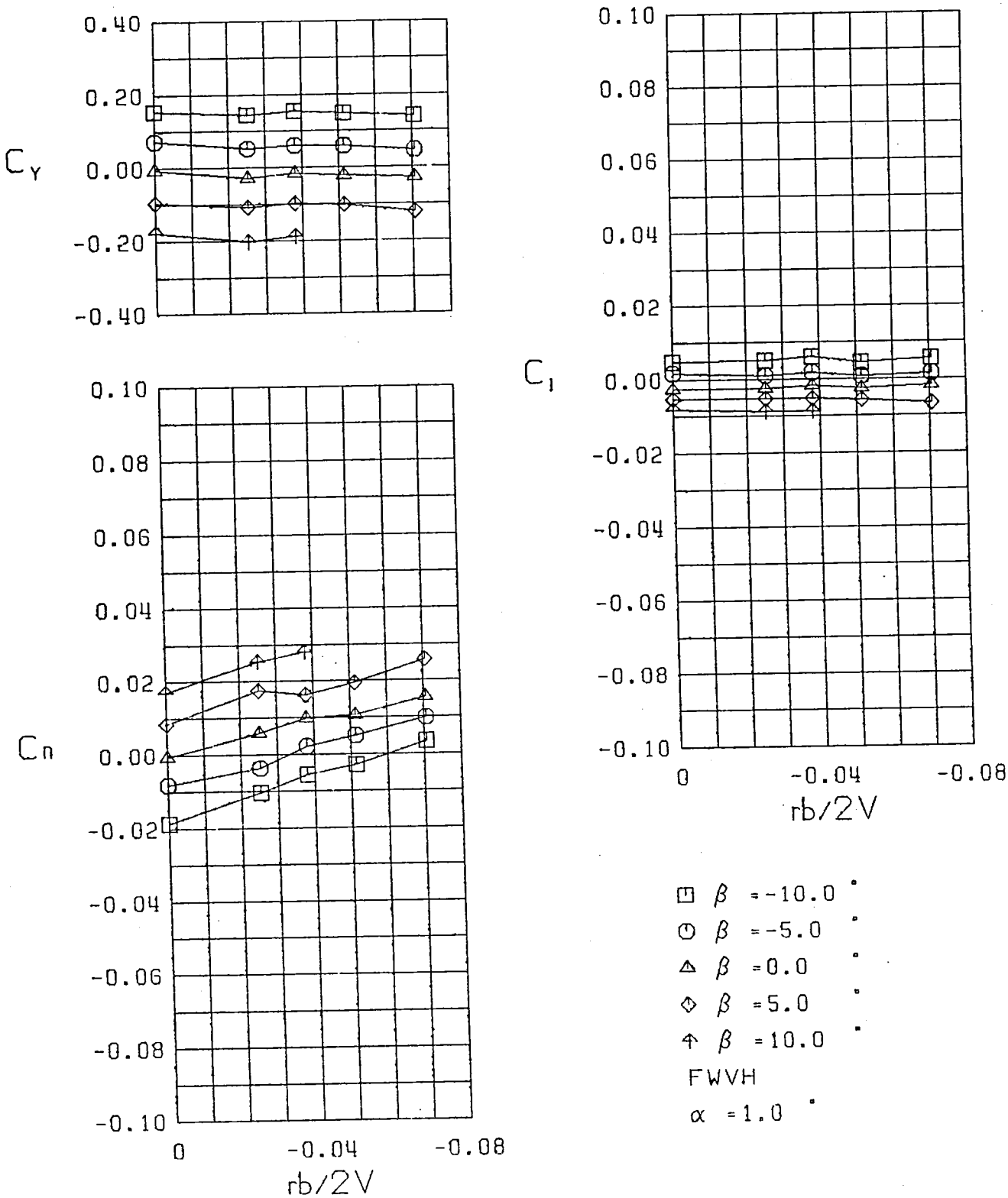

Figure 22 Variation of Static Lateral-Directional Stability Derivatives with Yaw Rate, Configuration 6

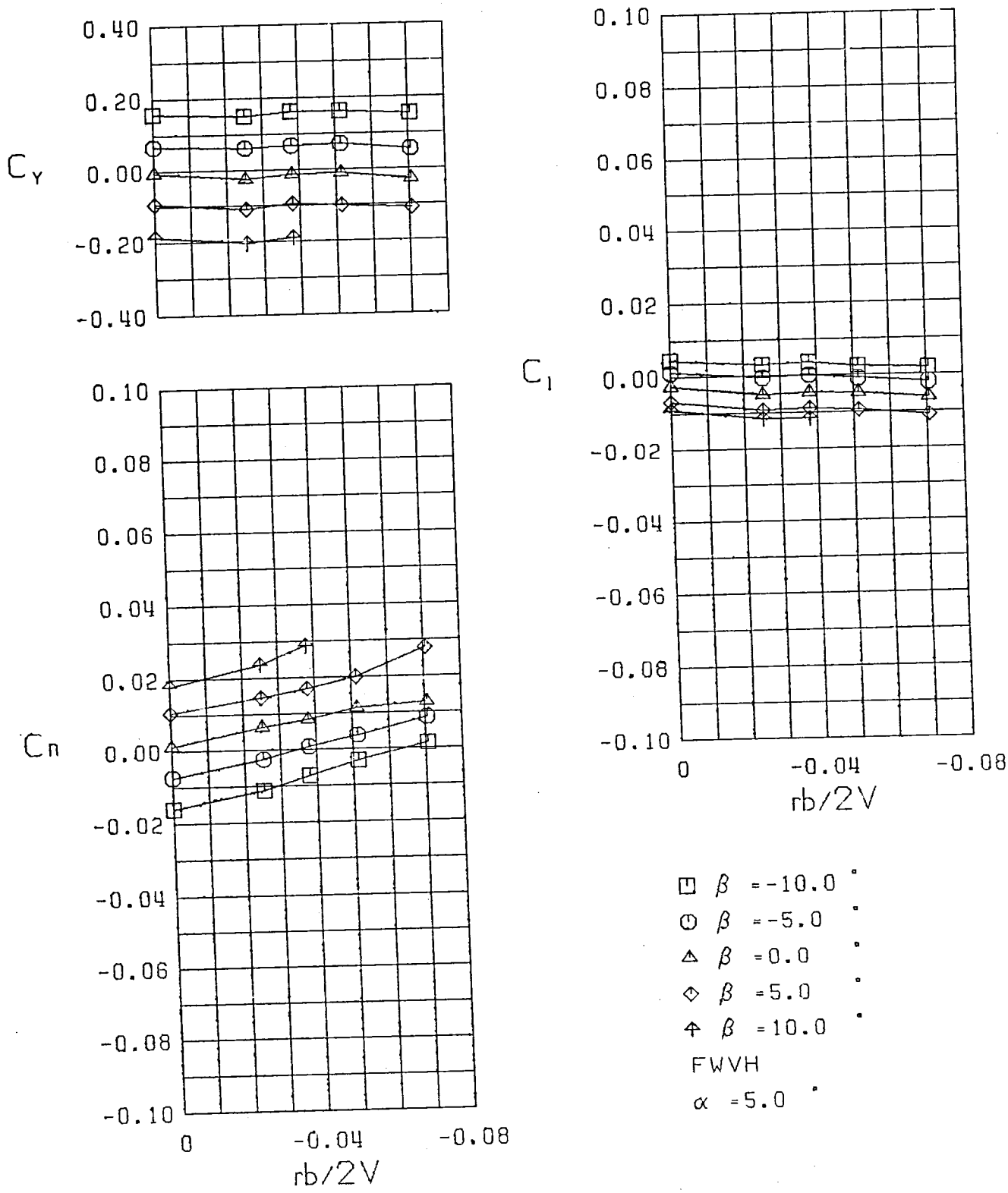

Figure 22 (Continued)

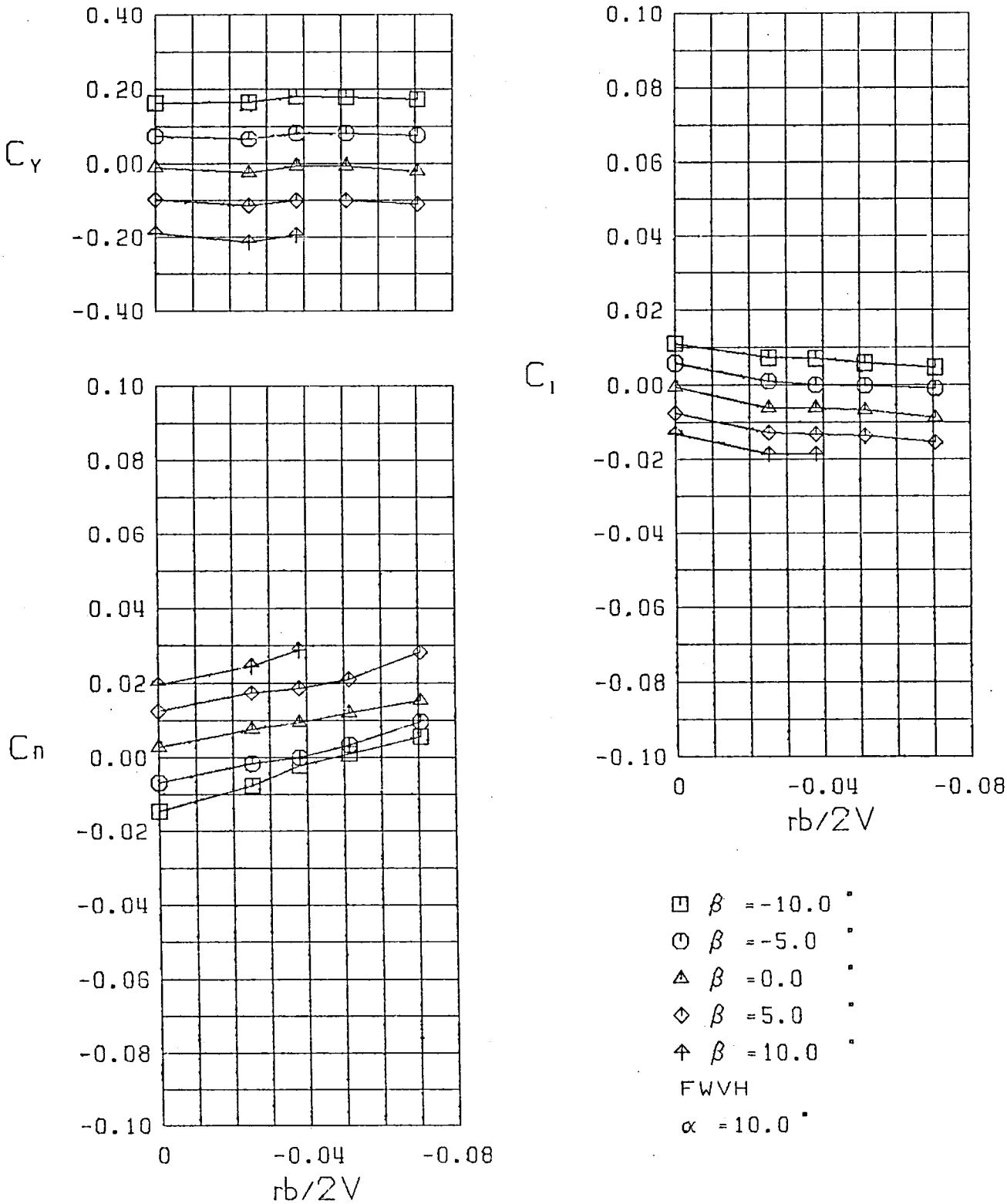

Figure 22 (Continued)

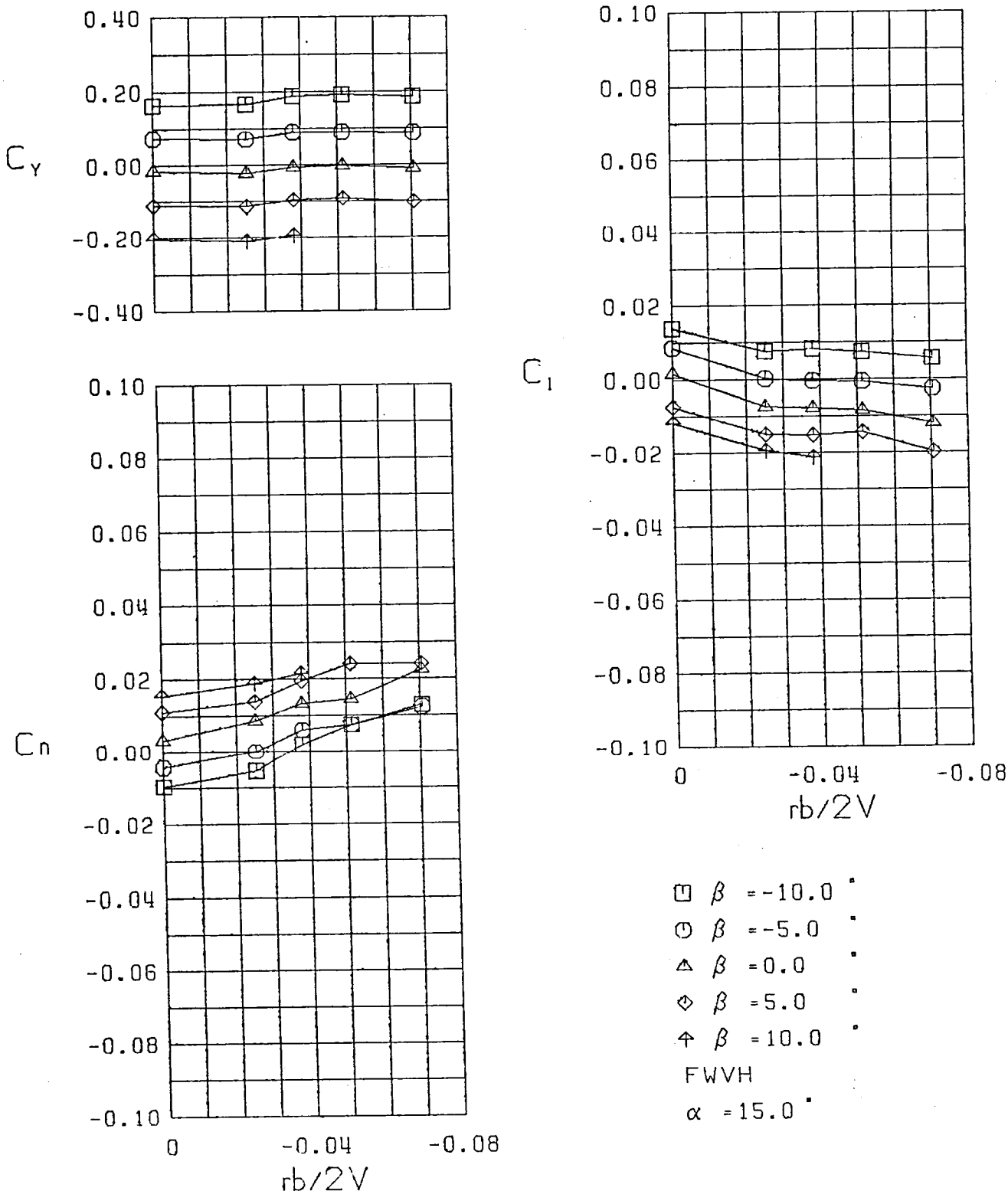

Figure 22 (Continued)

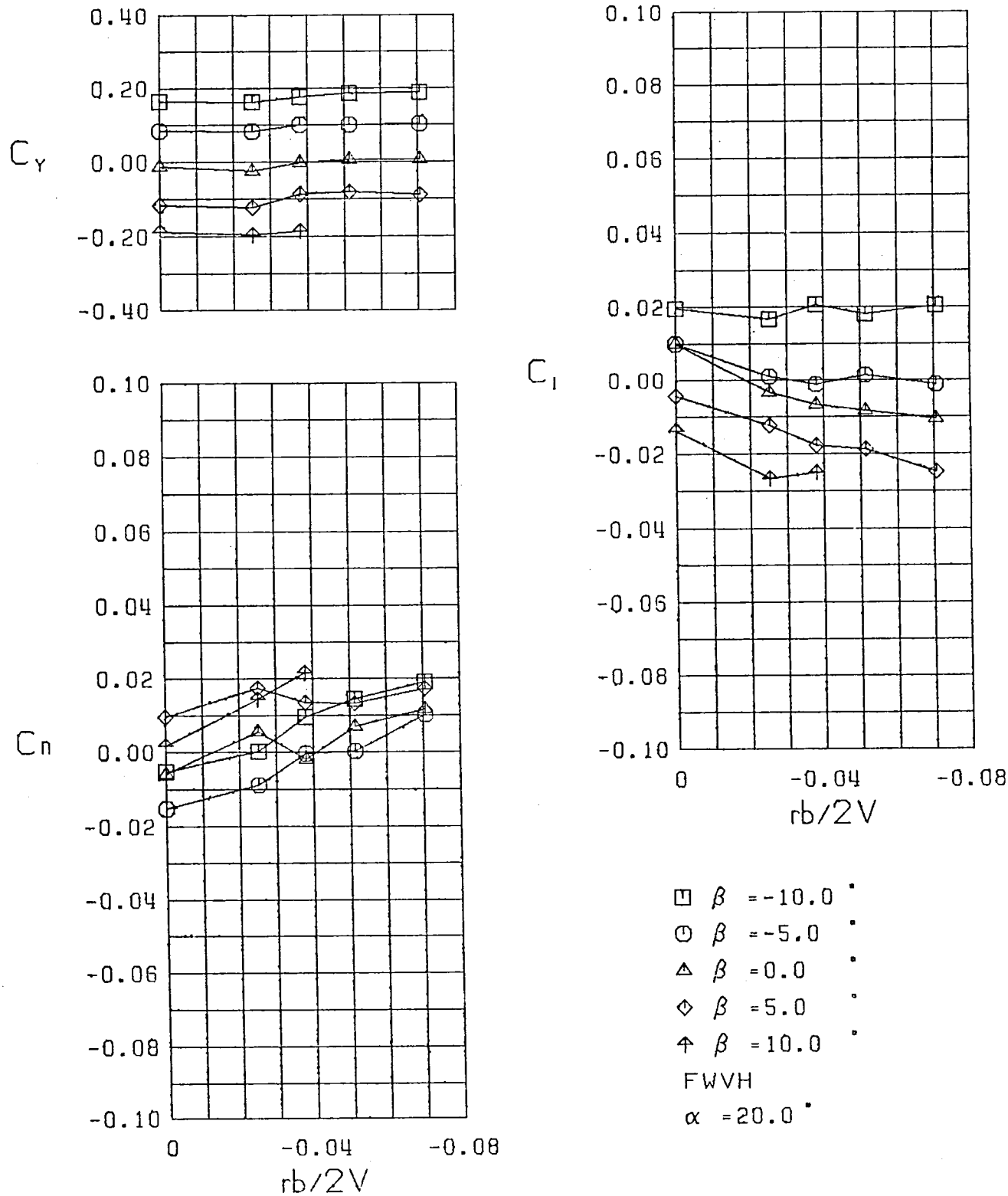

Figure 22 (Continued)

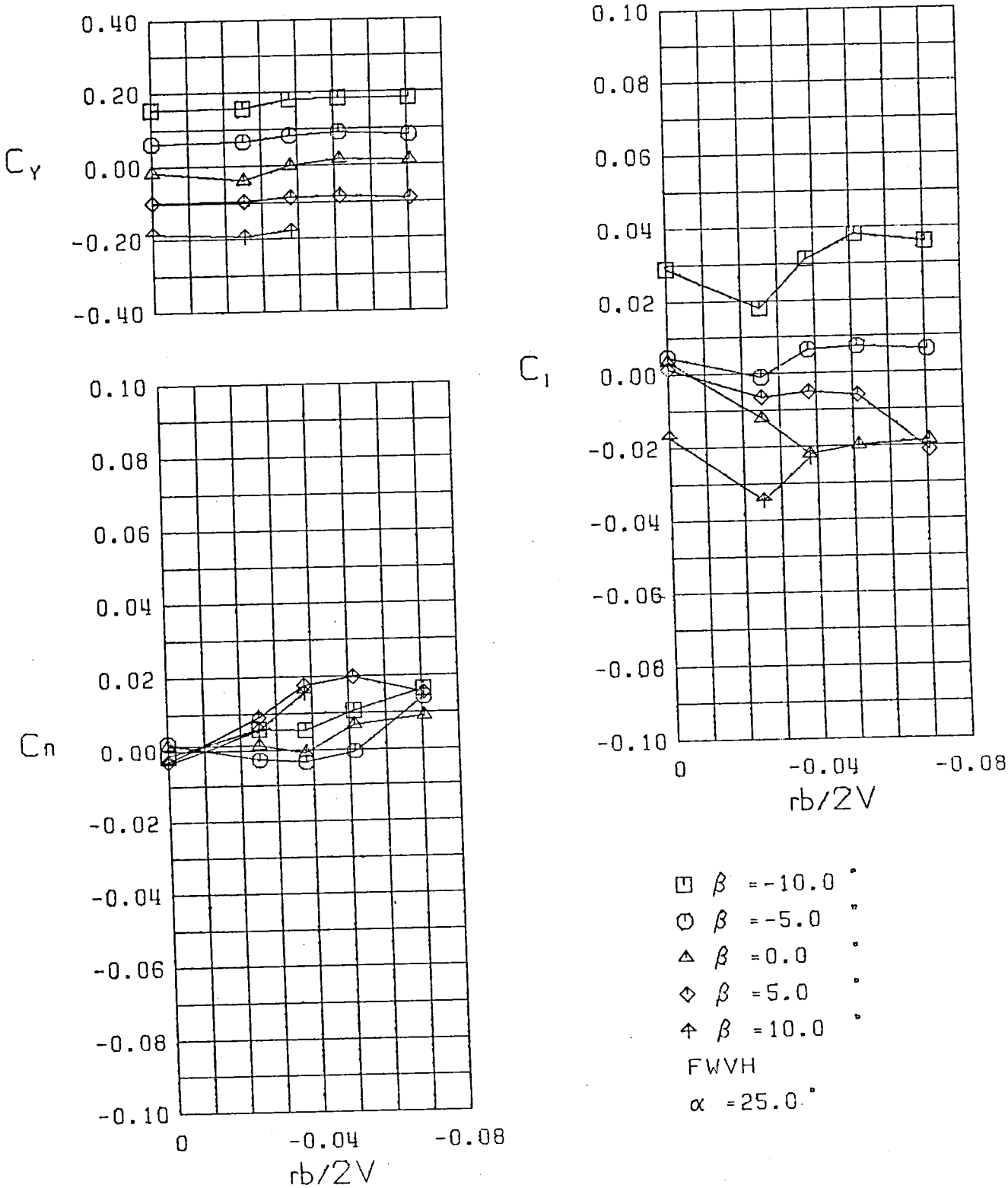

Figure 22 (Continued)

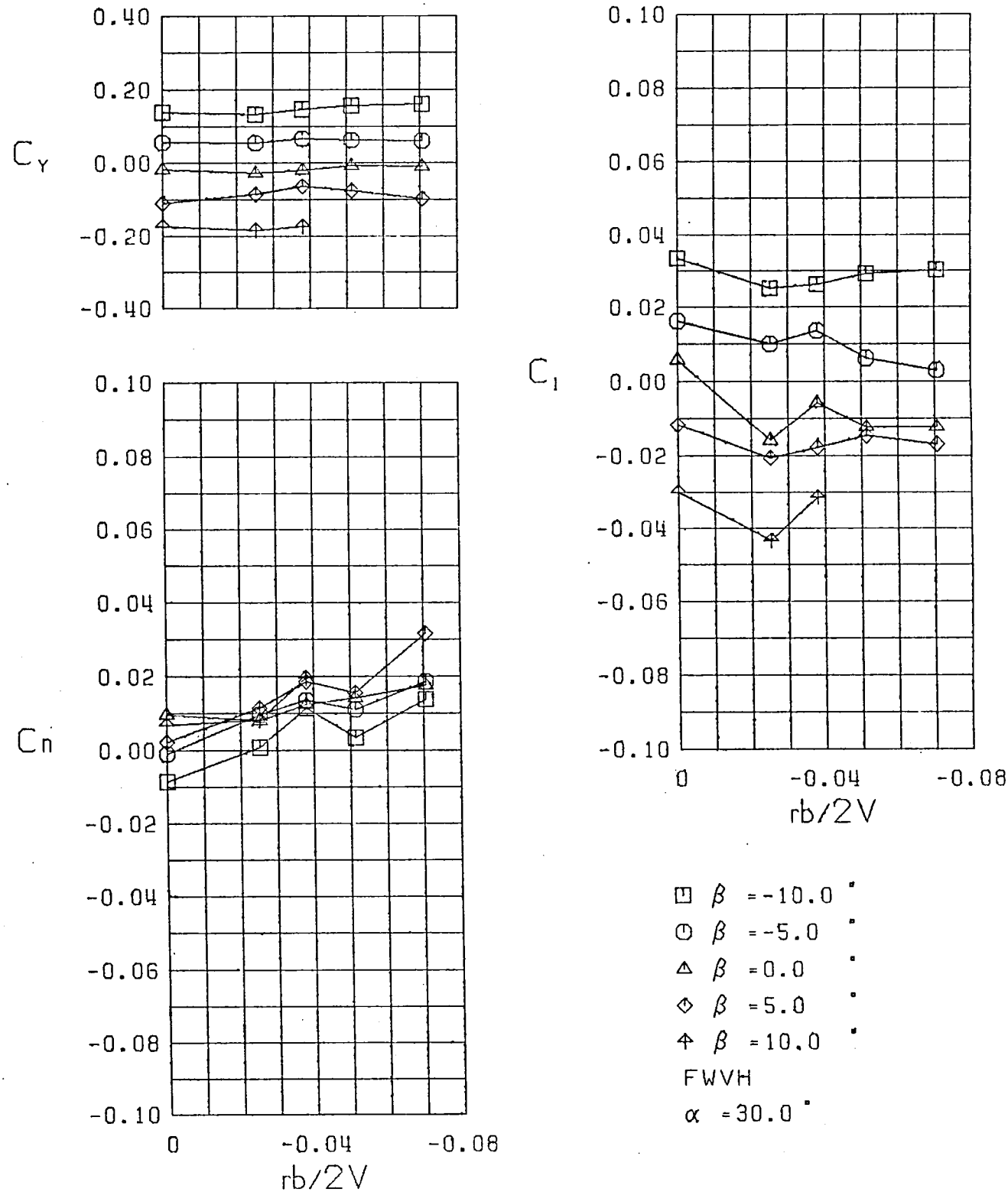

Figure 22 (Continued)

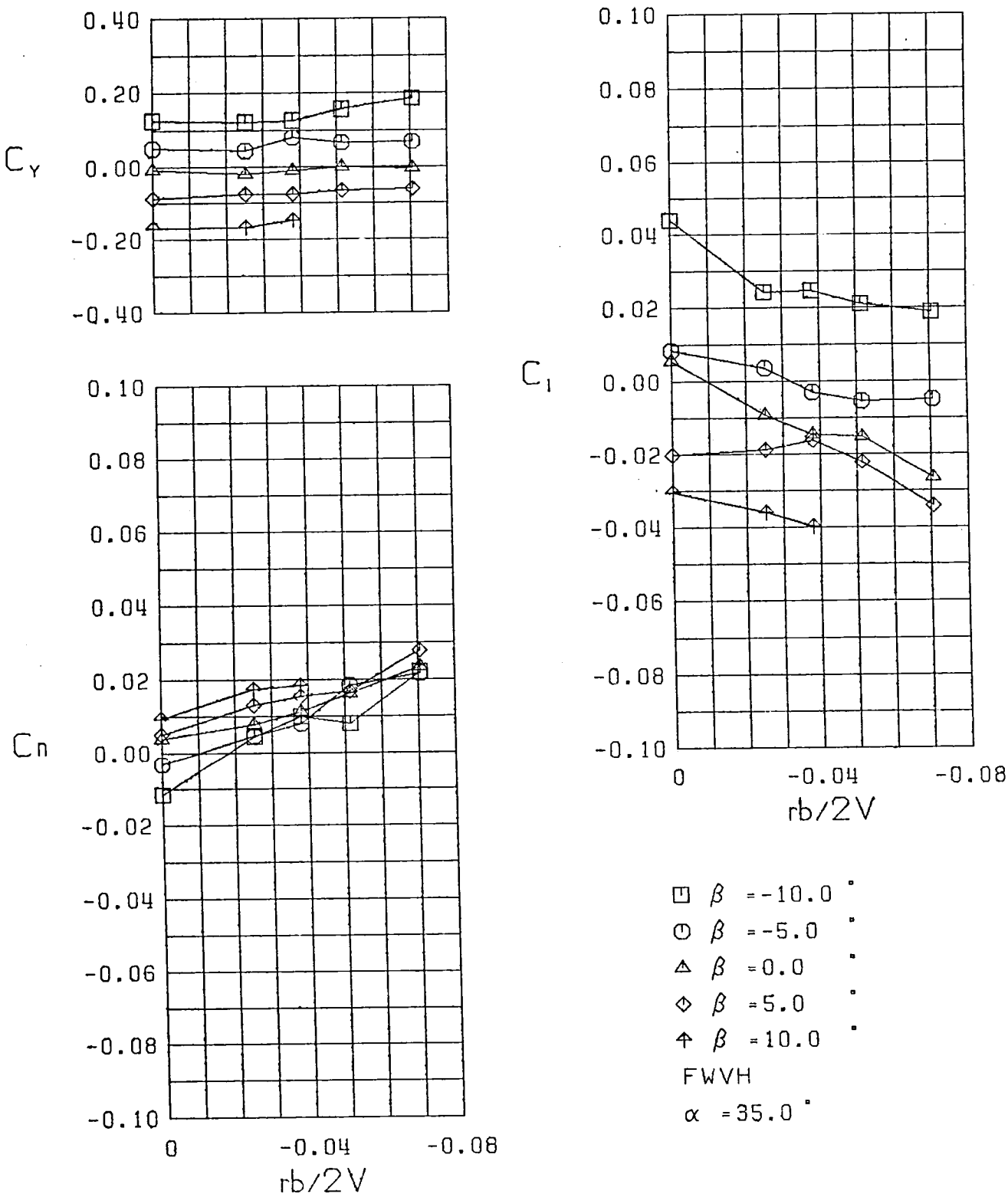

Figure 22 (Continued)

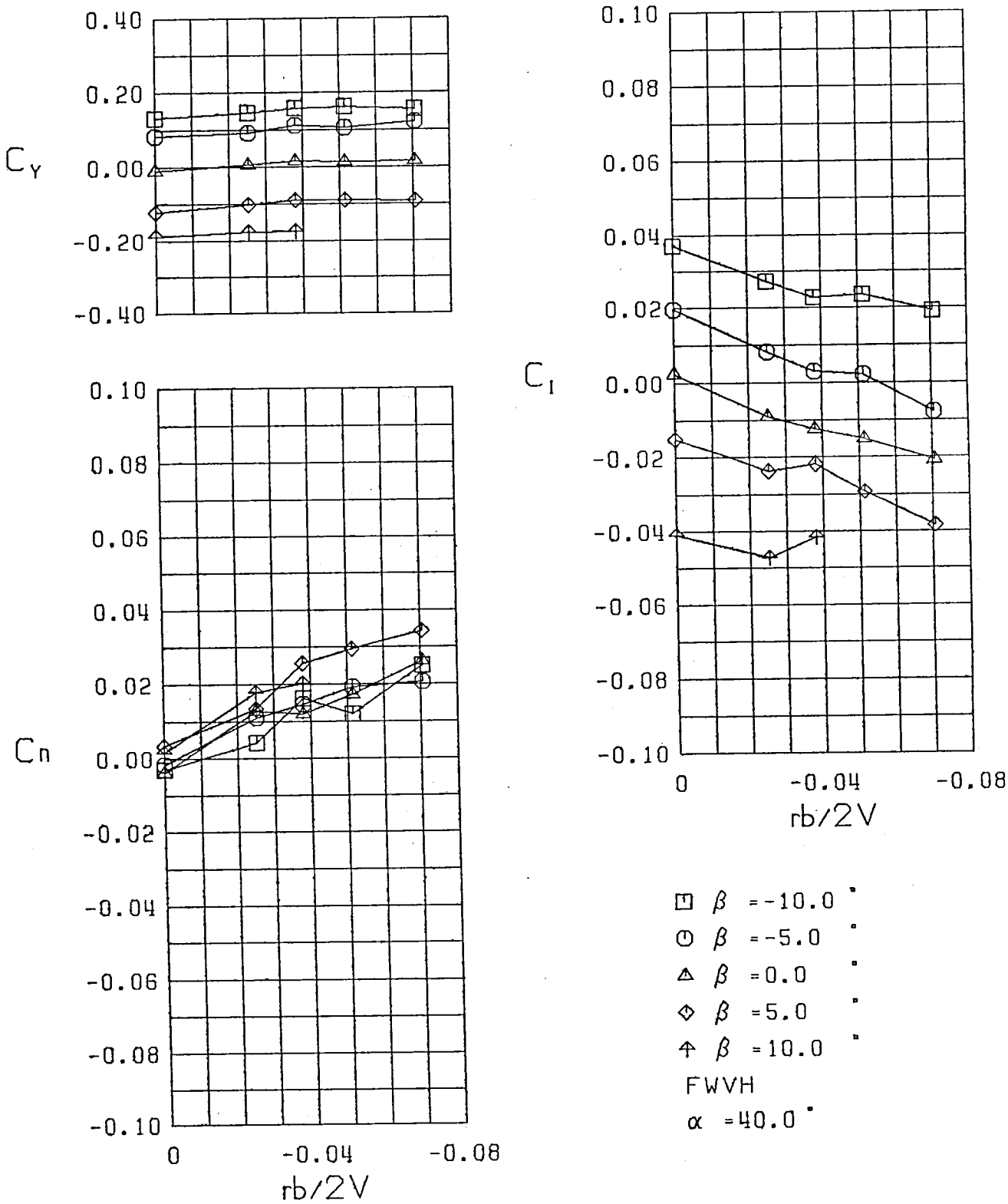

Figure 22 (Continued)

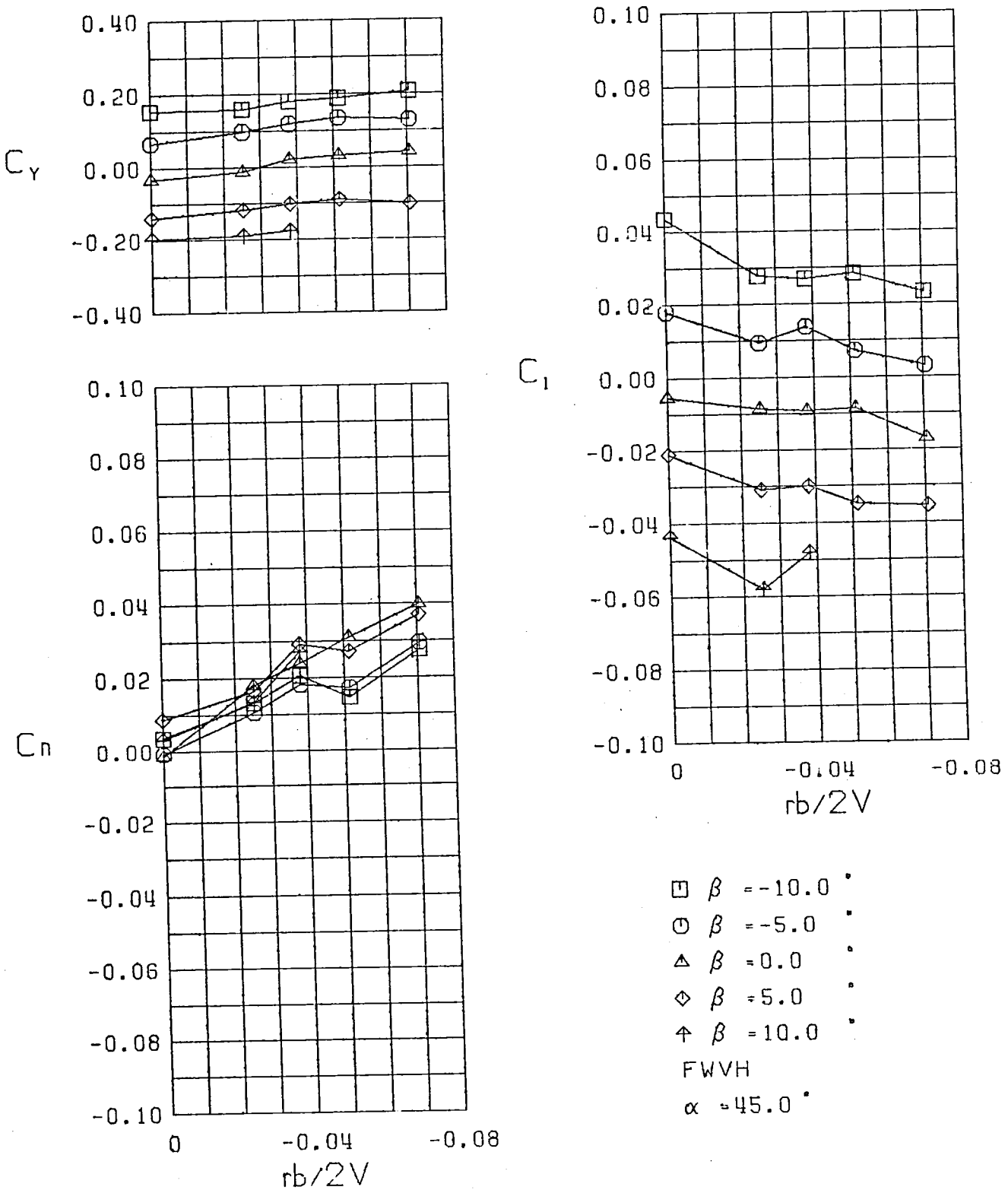

Figure 22 (Continued)

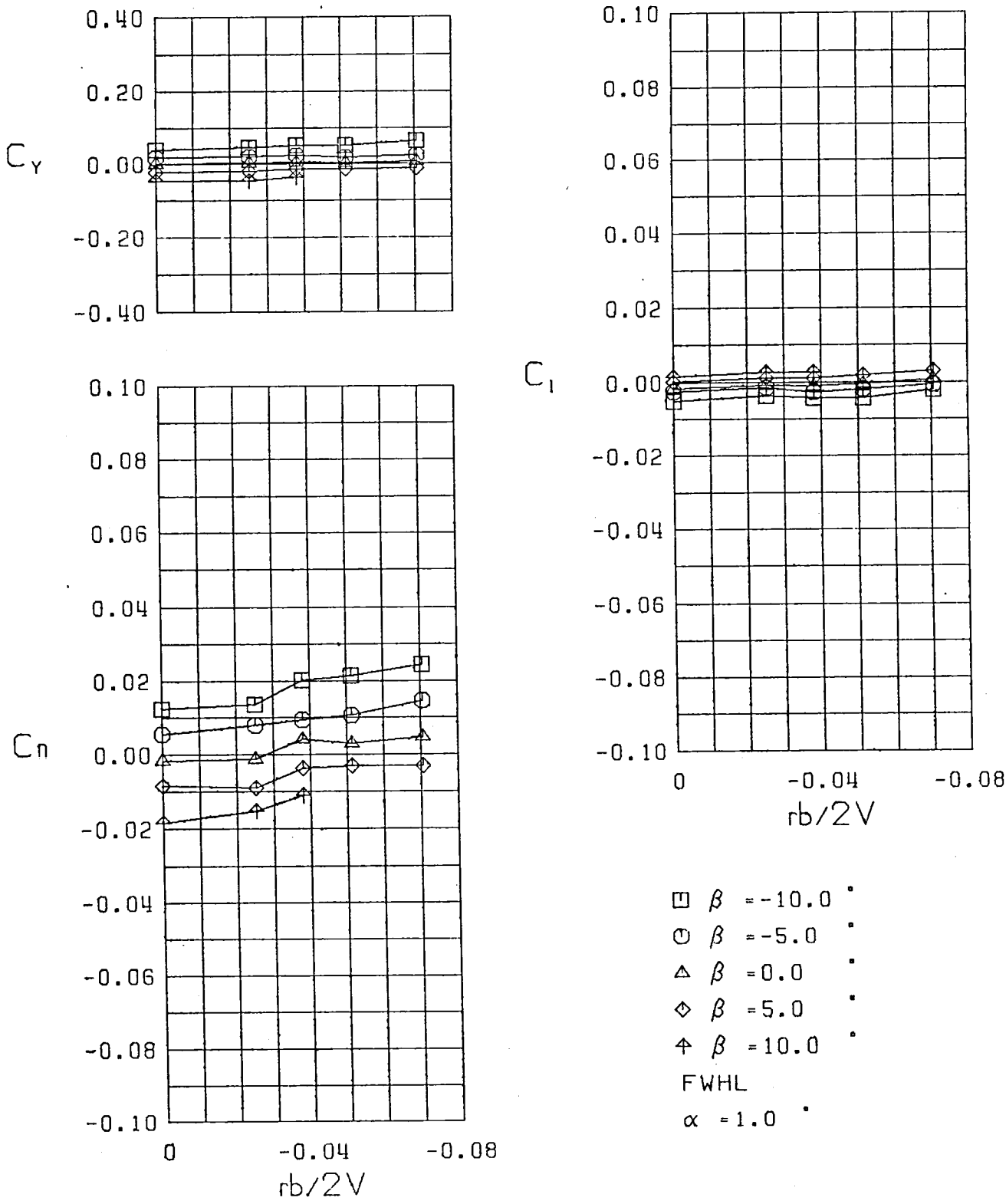

Figure 23 Variation of Static Lateral-Directional Stability Derivatives with Yaw Rate, Configuration 9

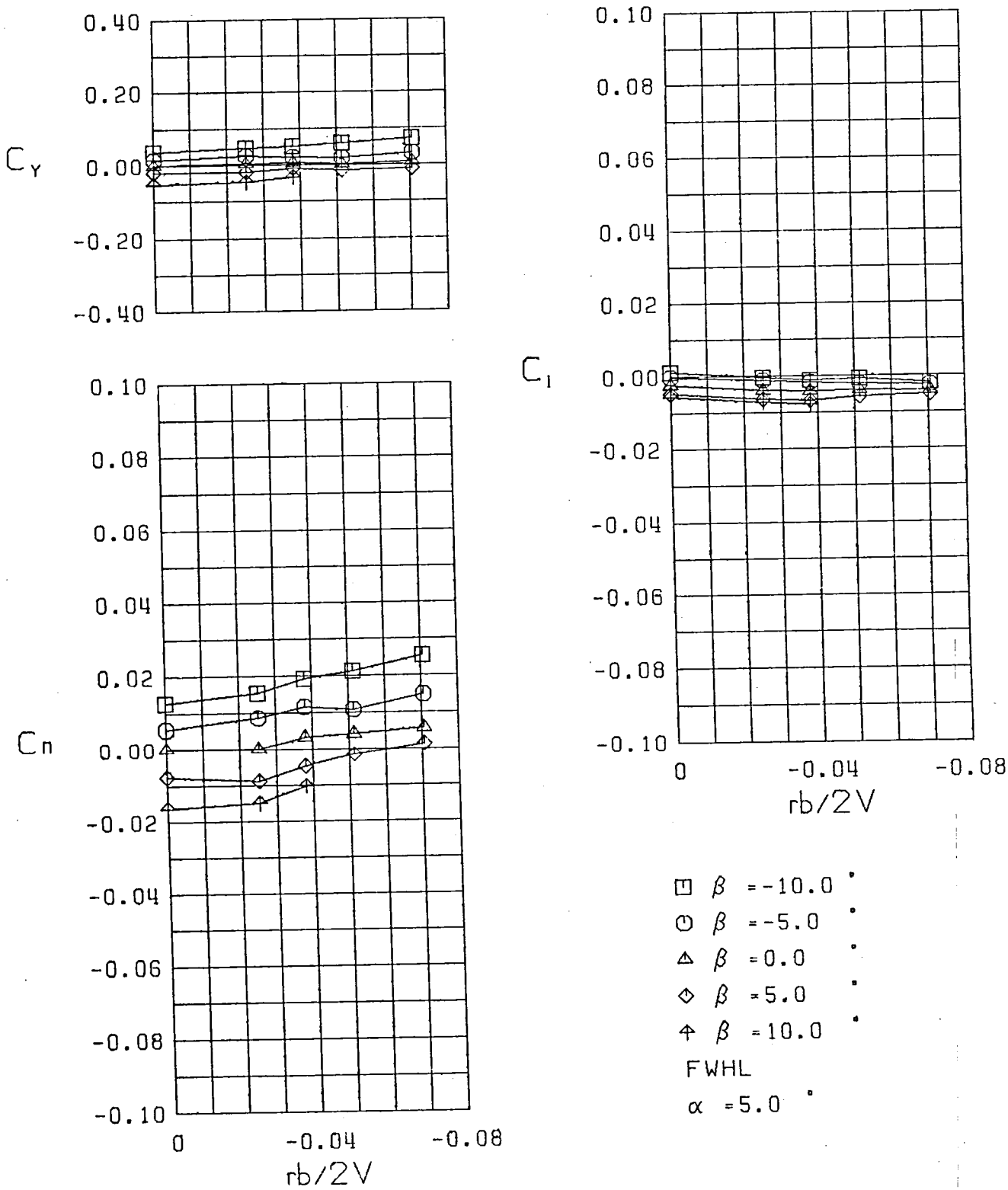

Figure 23 (Continued)

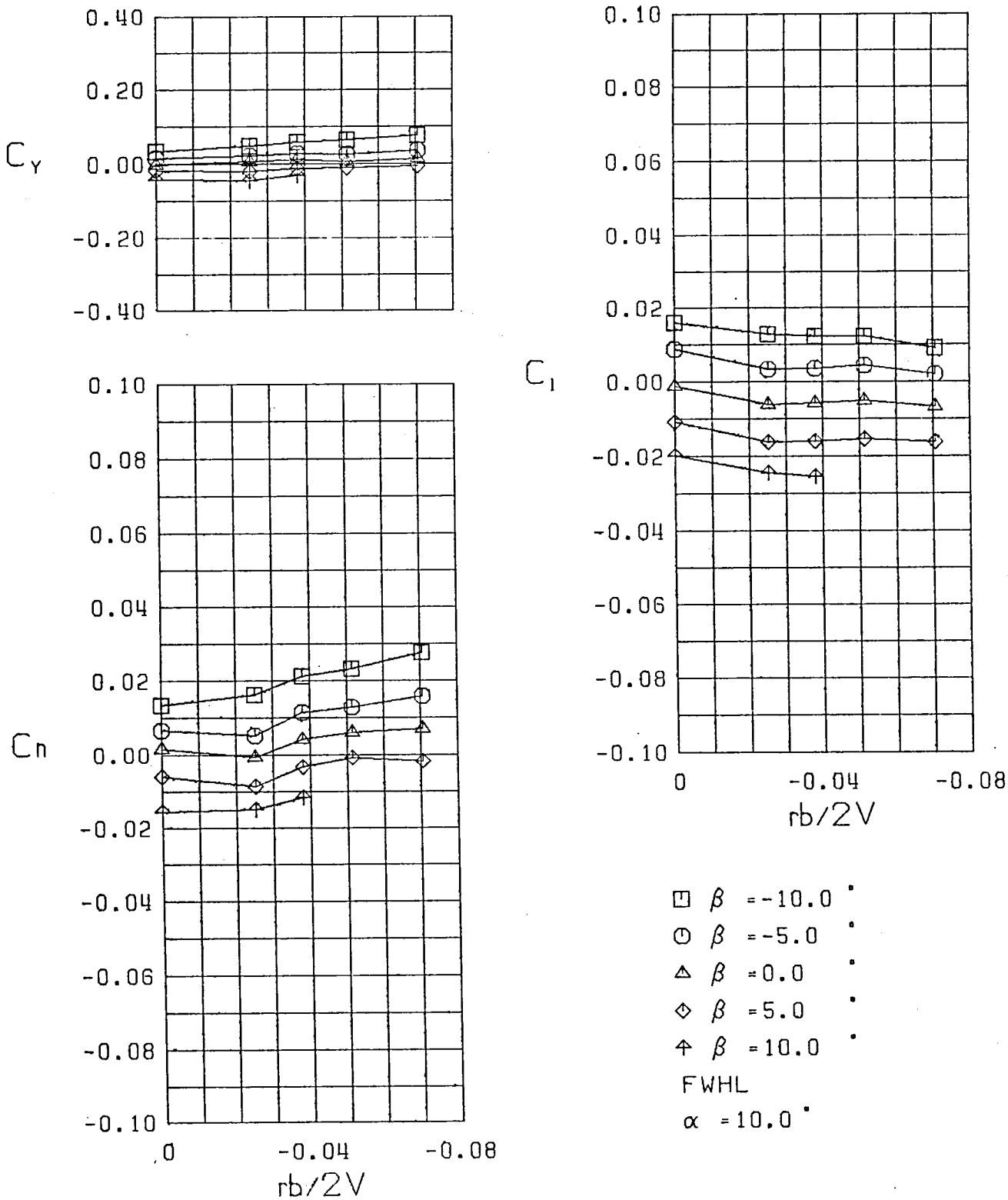

Figure 23 (Continued)

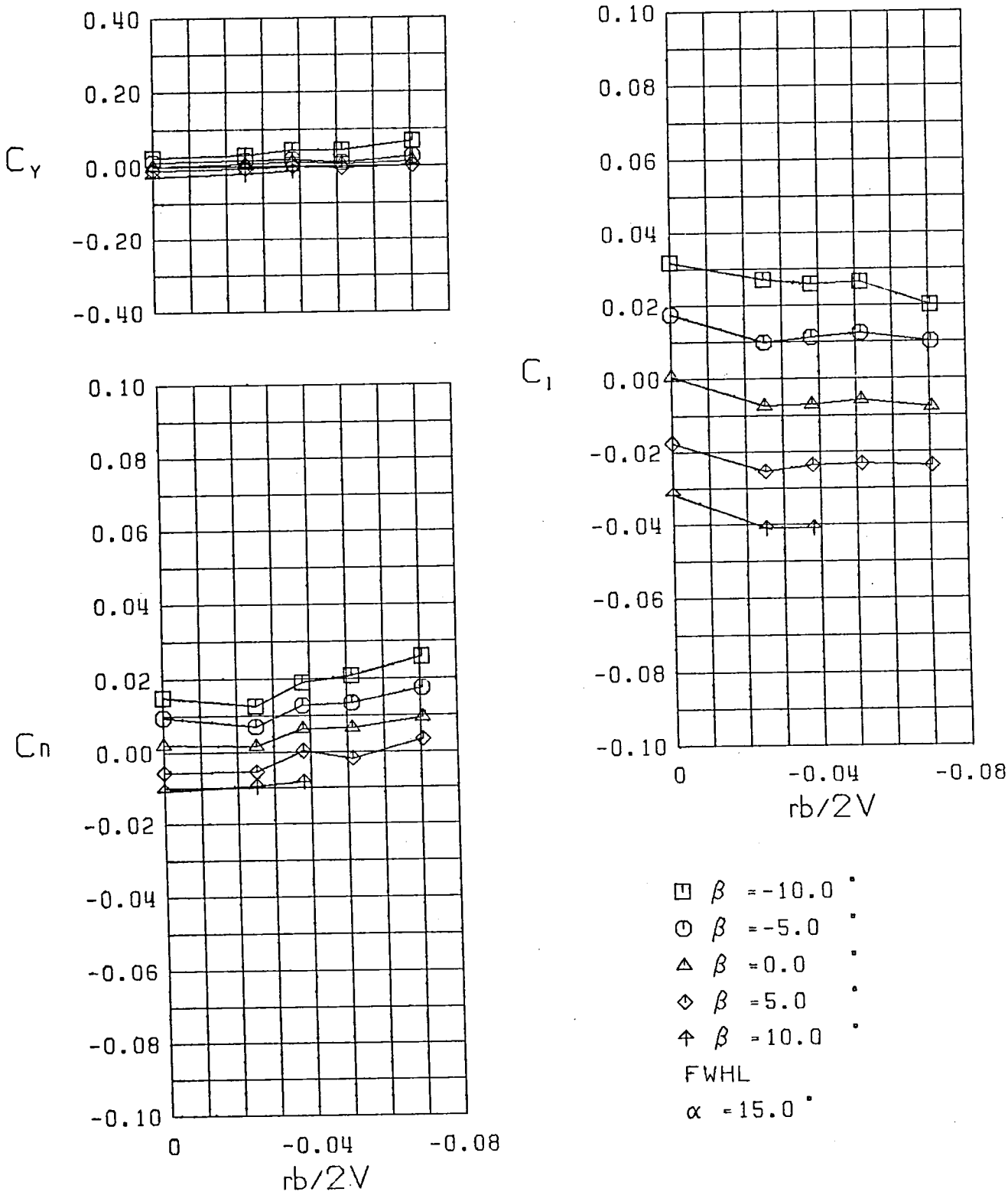

Figure 23 (Continued)

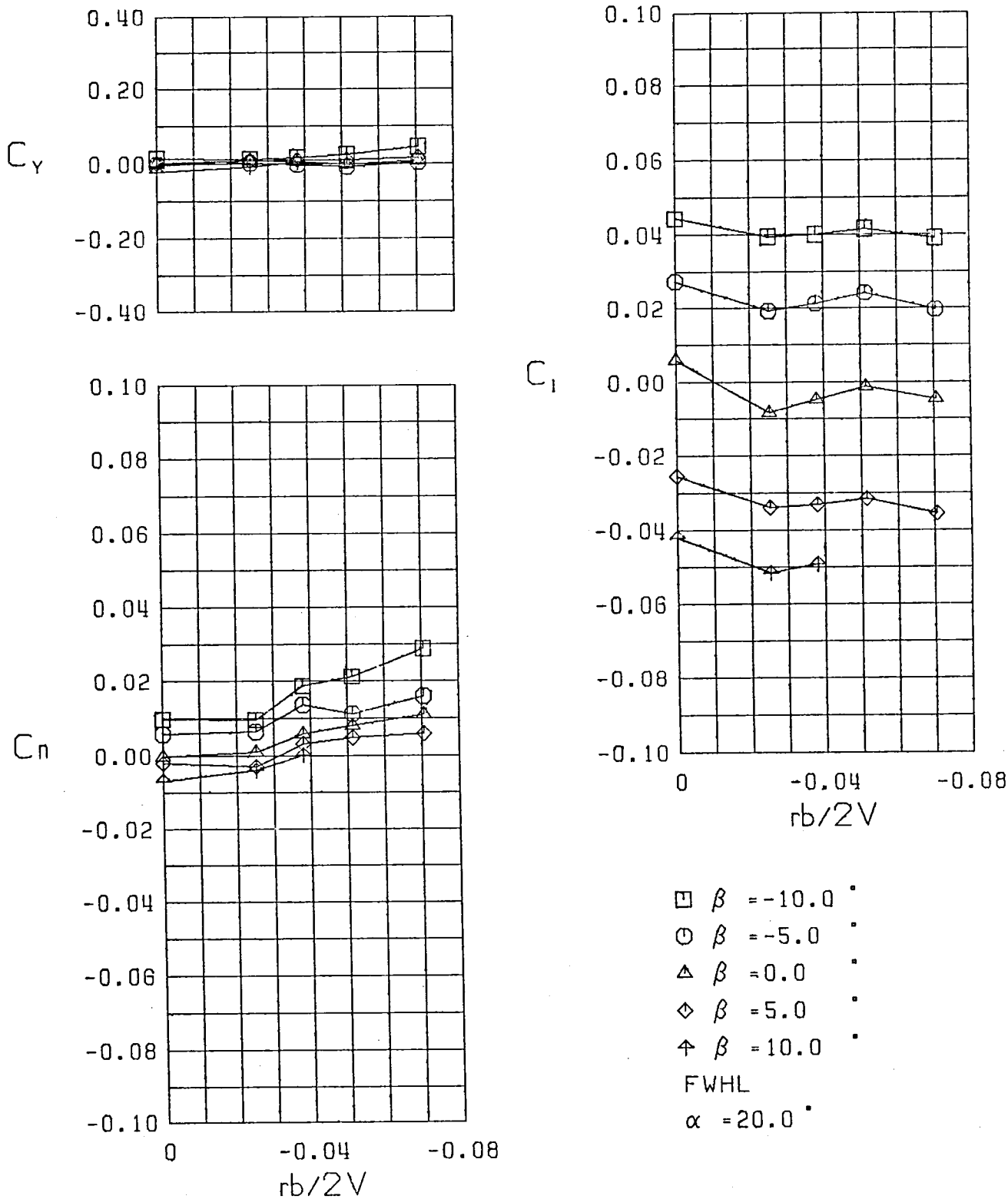

Figure 23 (Continued)

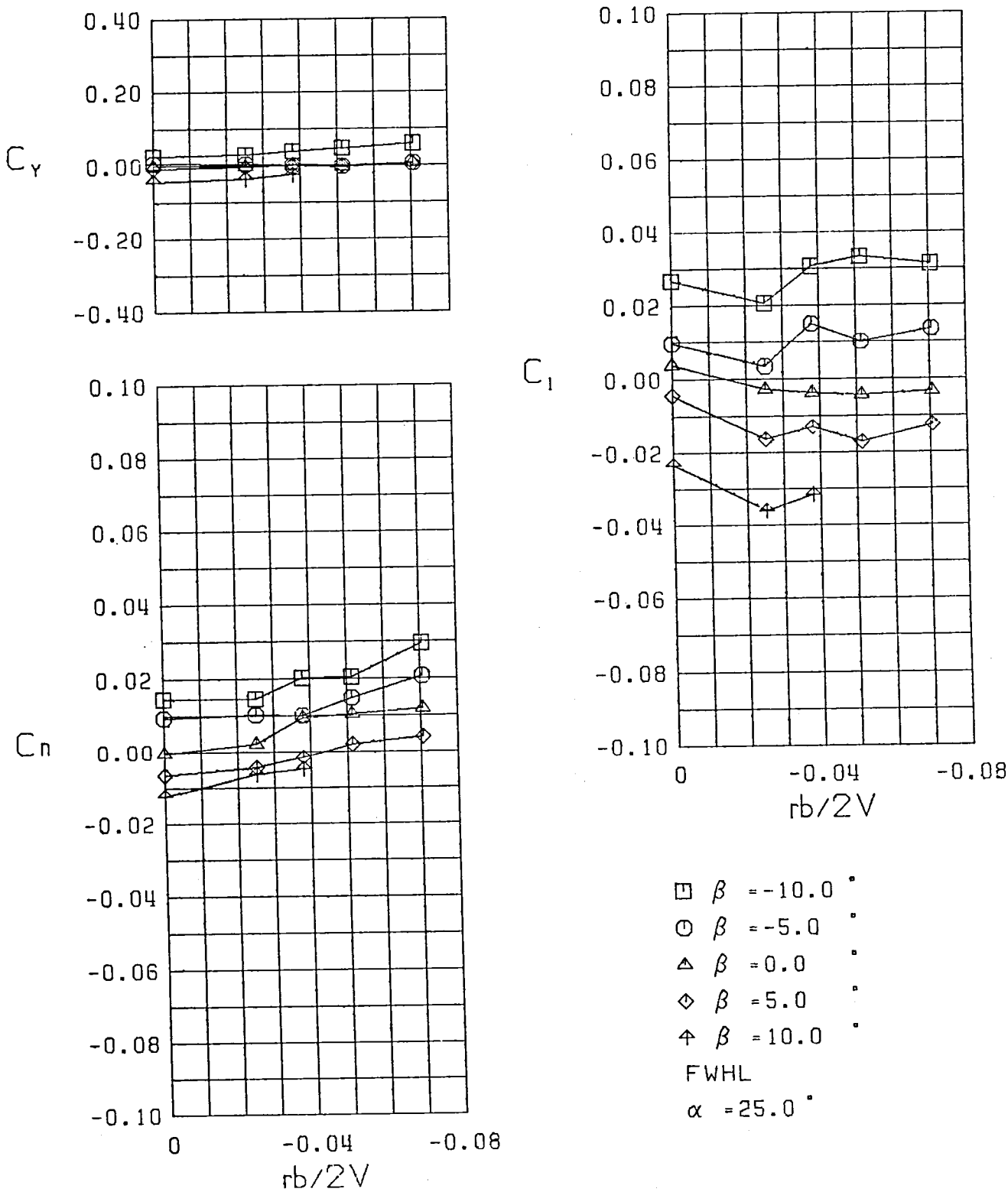

Figure 23 (Continued)

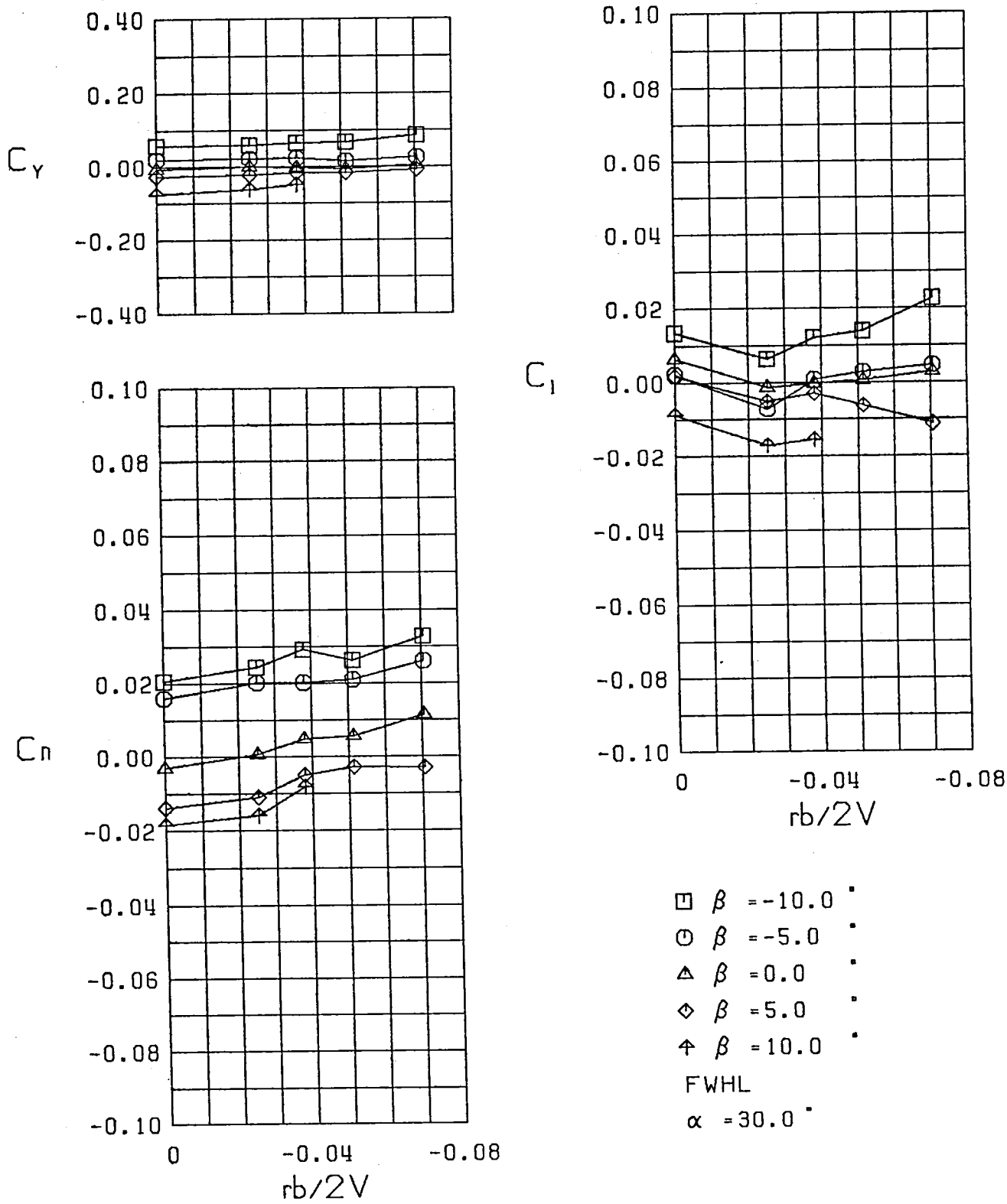

Figure 23 (Continued)

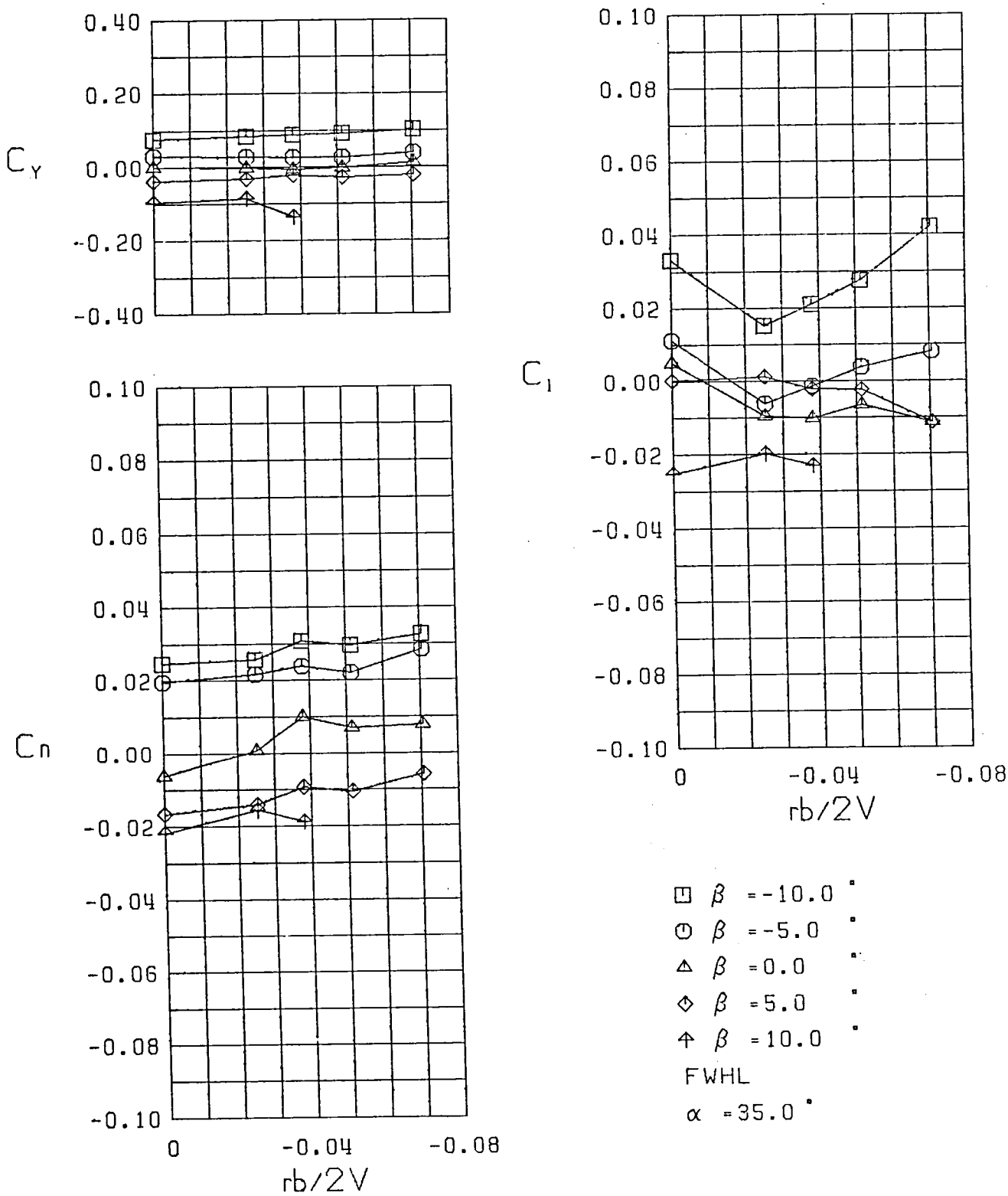

Figure 23 (Continued)

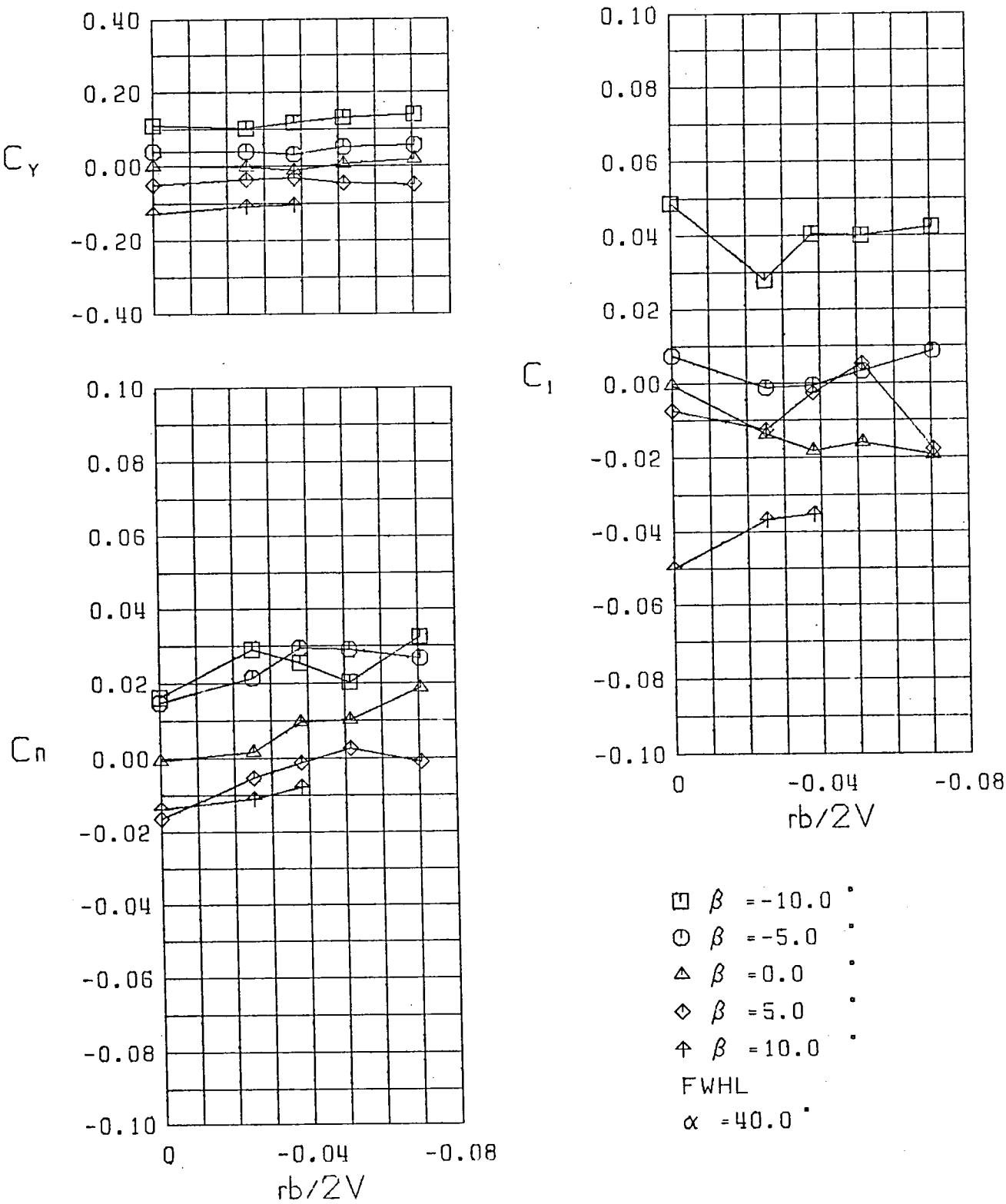

Figure 23 (Continued)

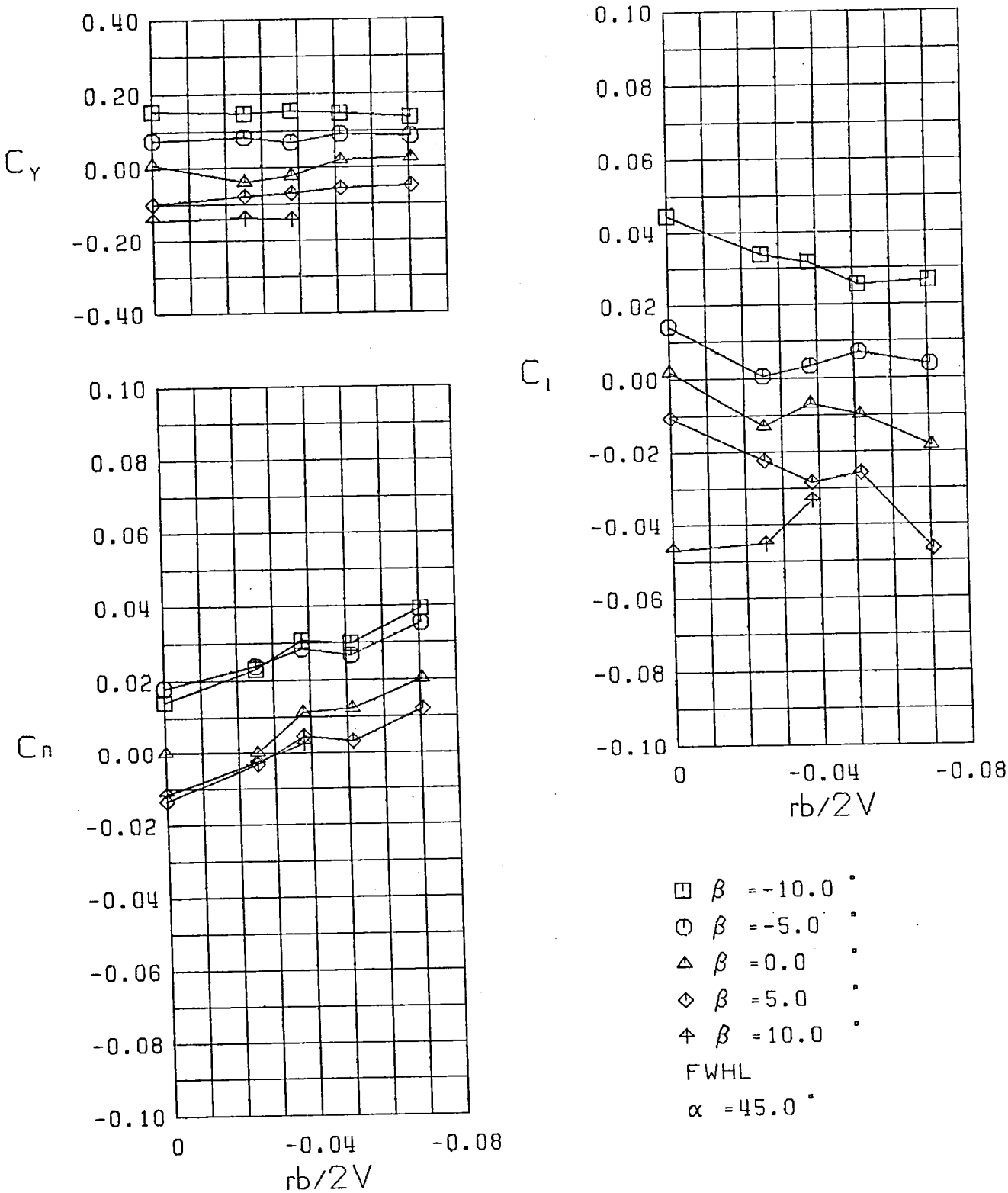

Figure 23 (Continued)

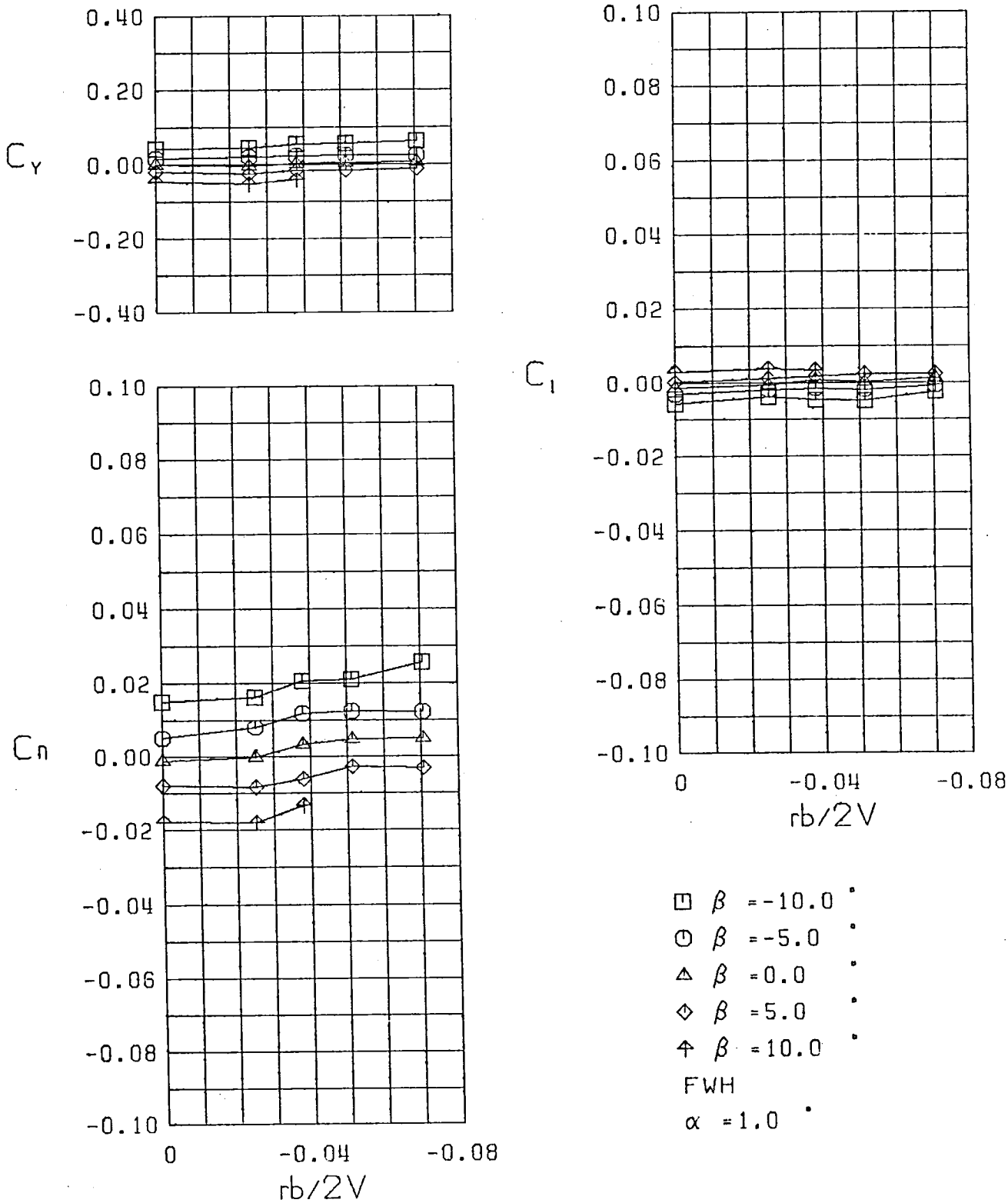

Figure 24 Variation of Static Lateral-Directional Stability Derivatives with Yaw Rate, Configuration 11

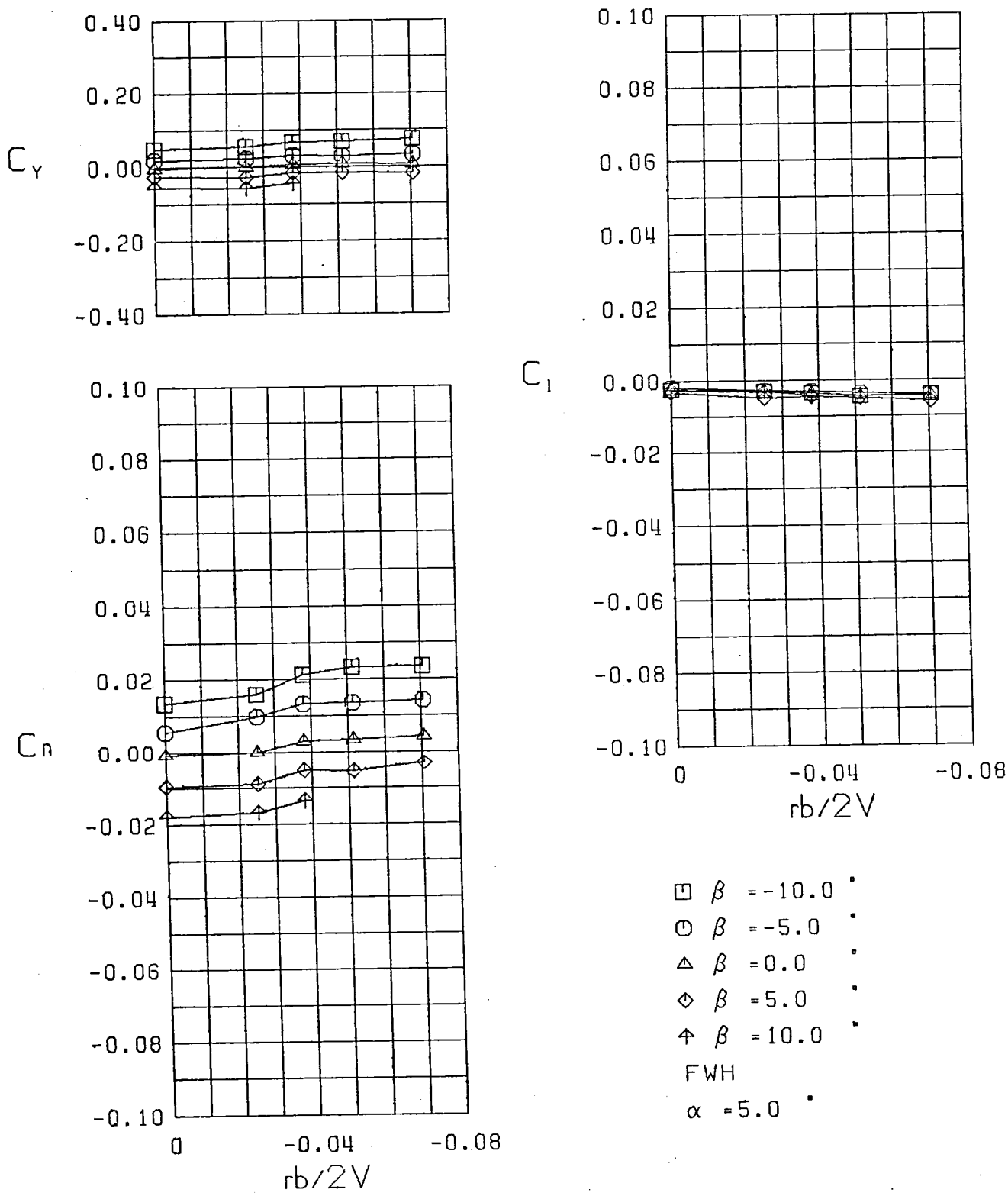

Figure 24 (Continued)

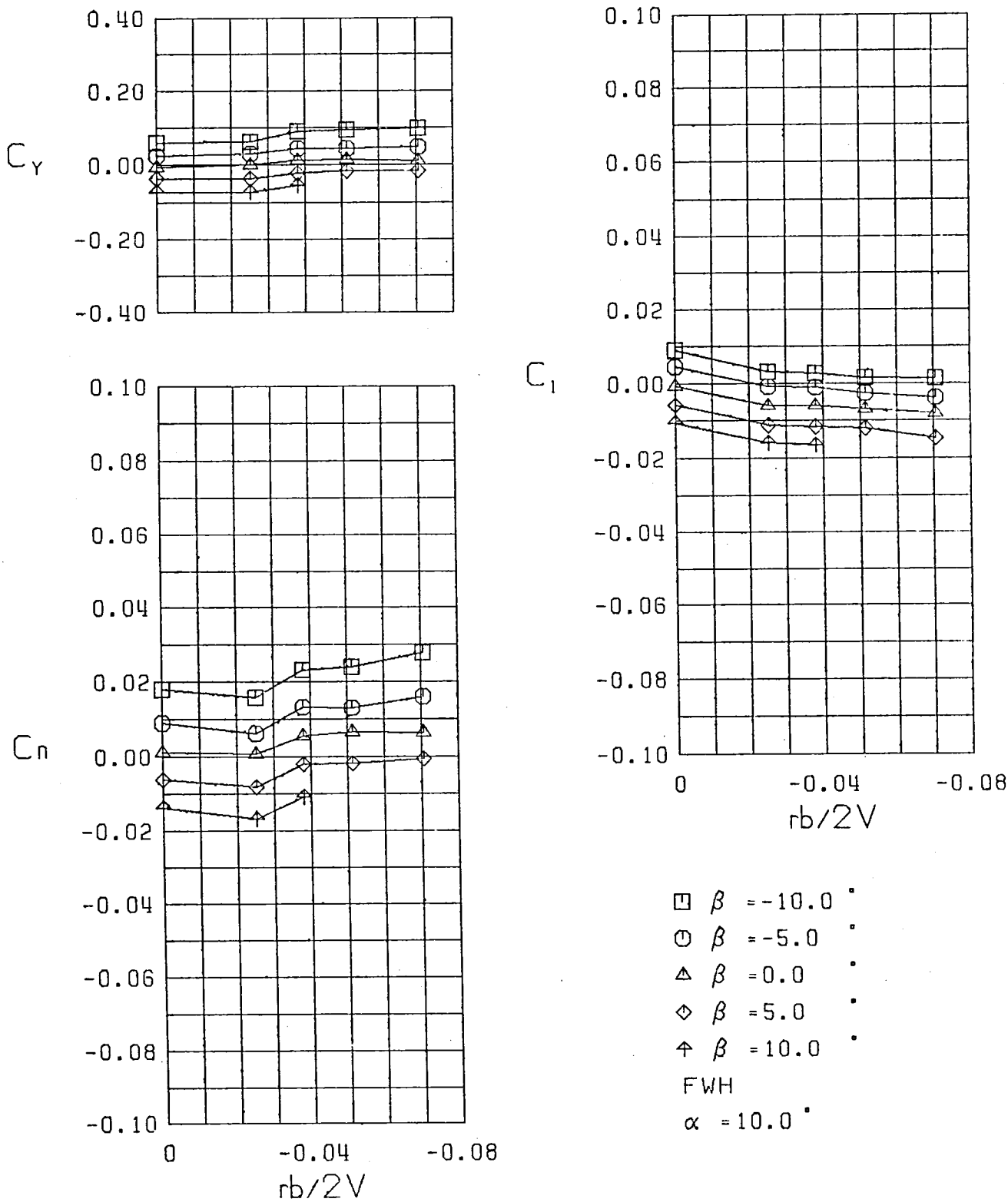

Figure 24 (Continued)

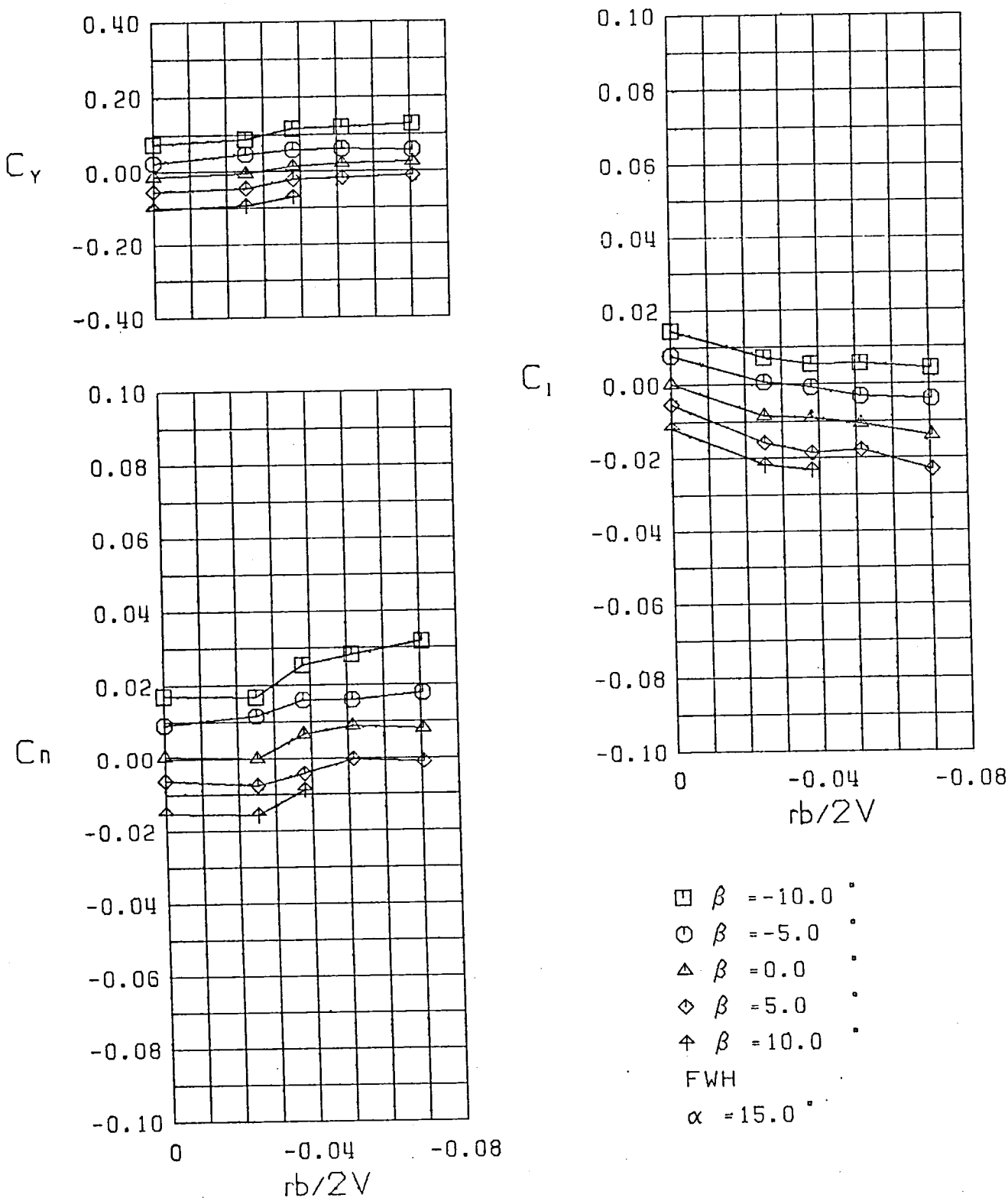

Figure 24 (Continued)

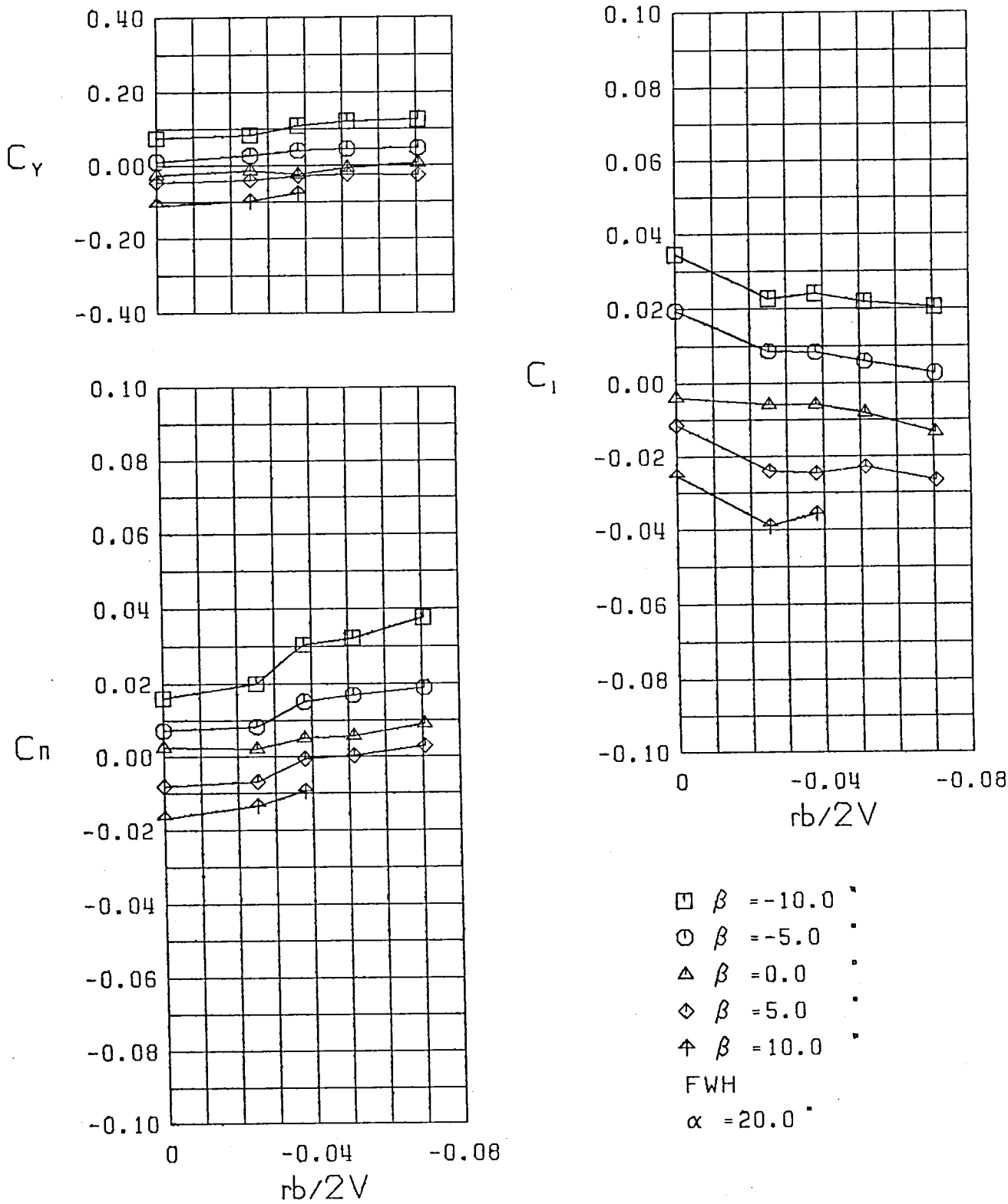

Figure 24 (Continued)

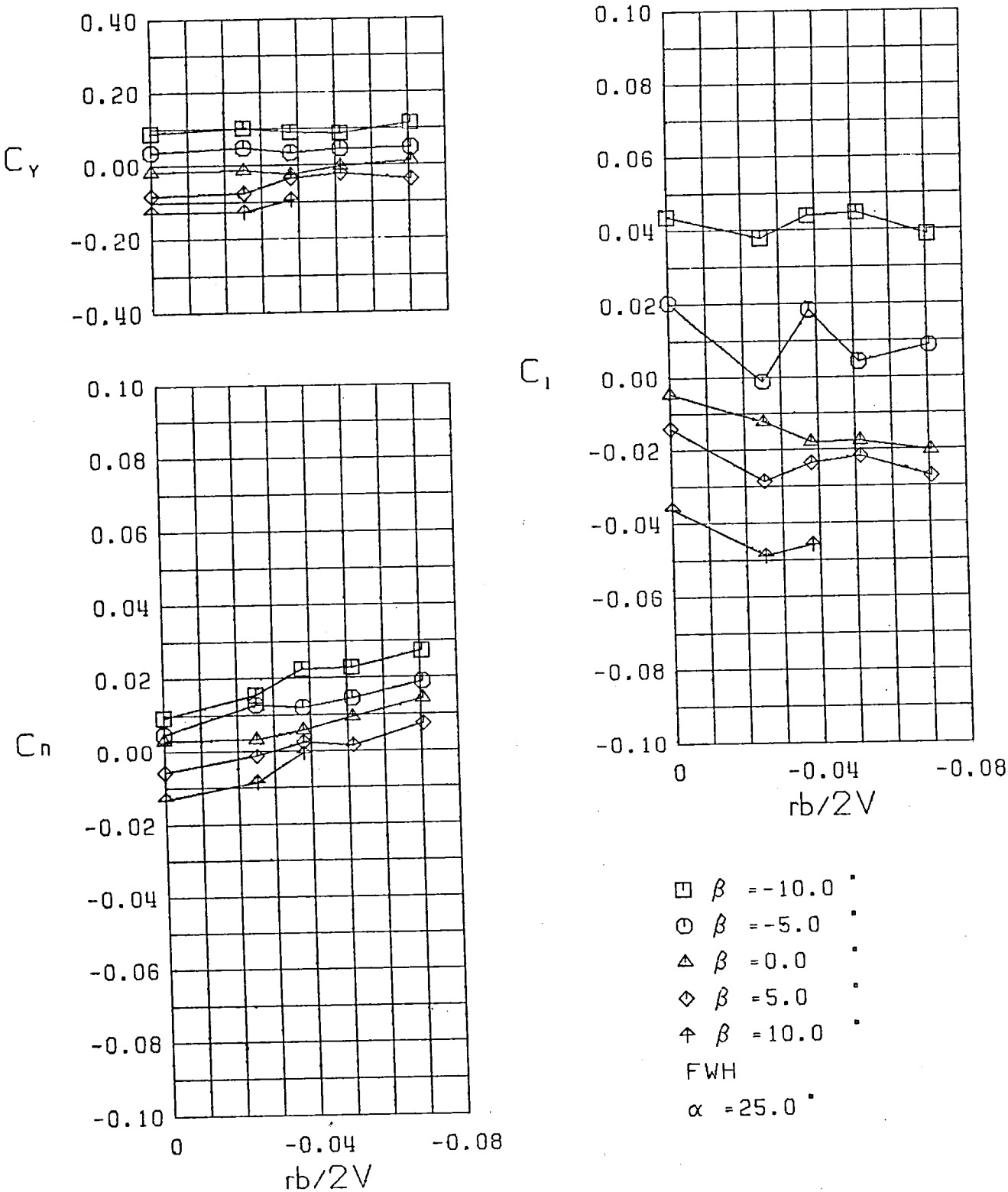

Figure 24 (Continued)

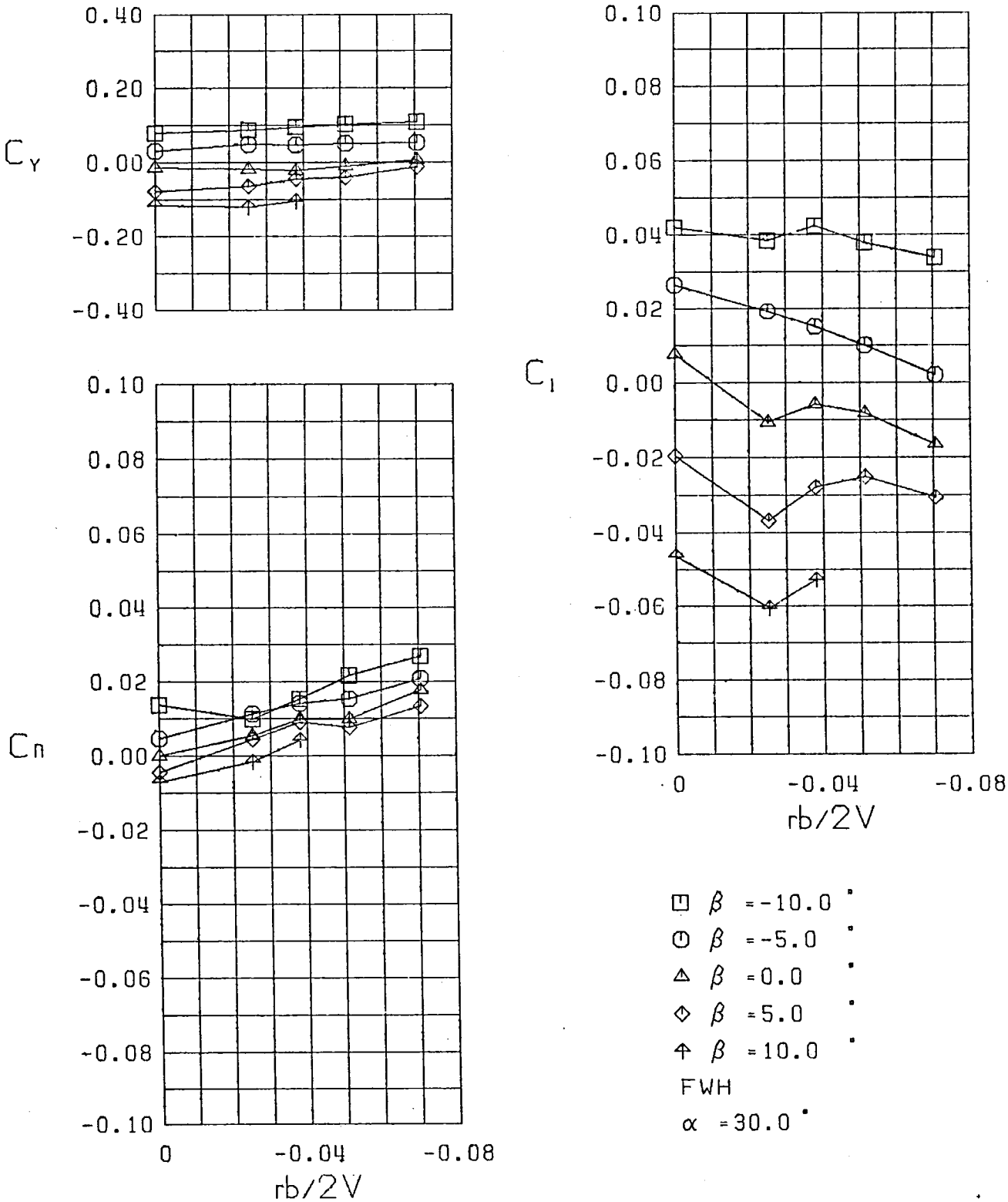

Figure 24 (Continued)

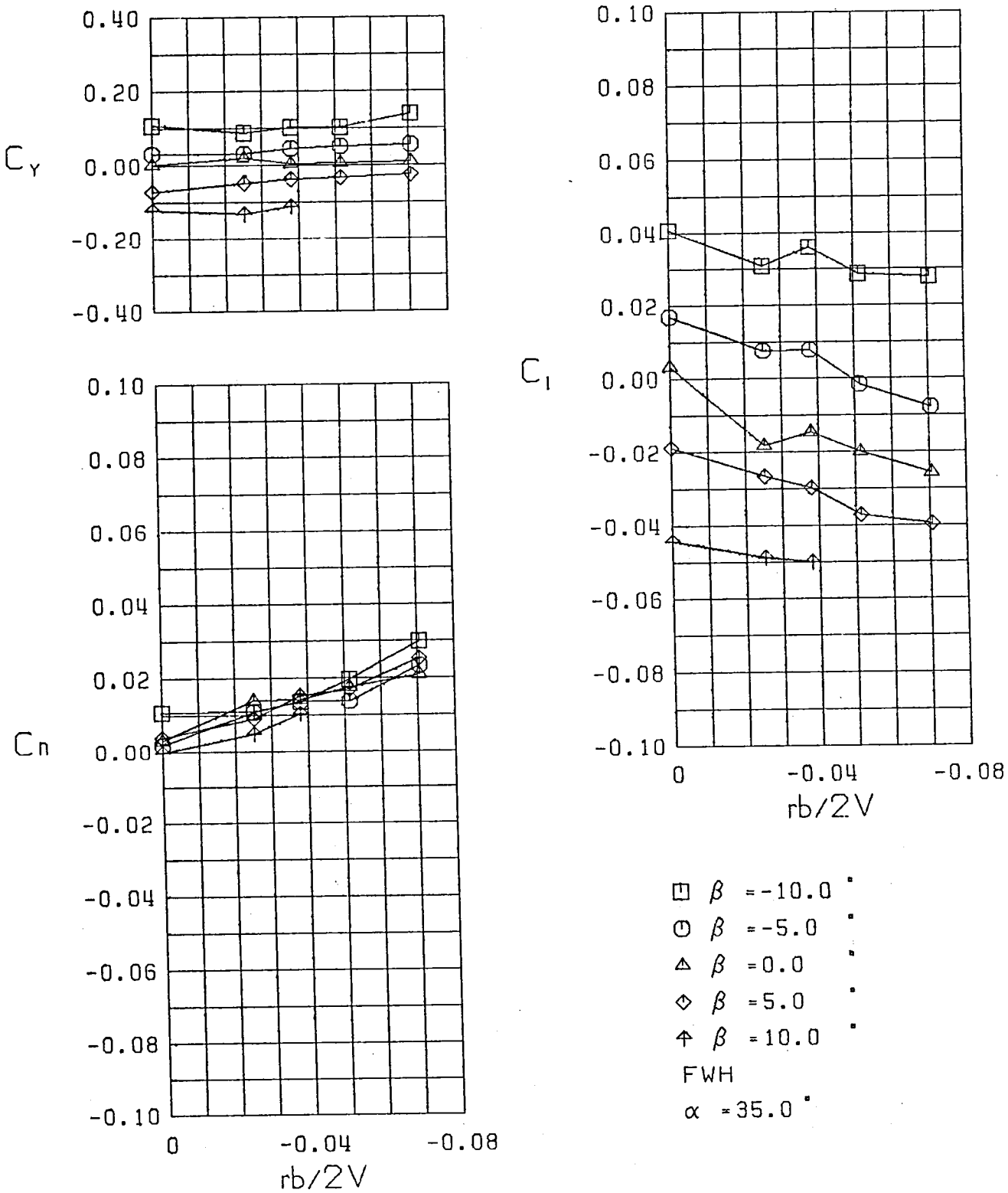

Figure 24 (Continued)

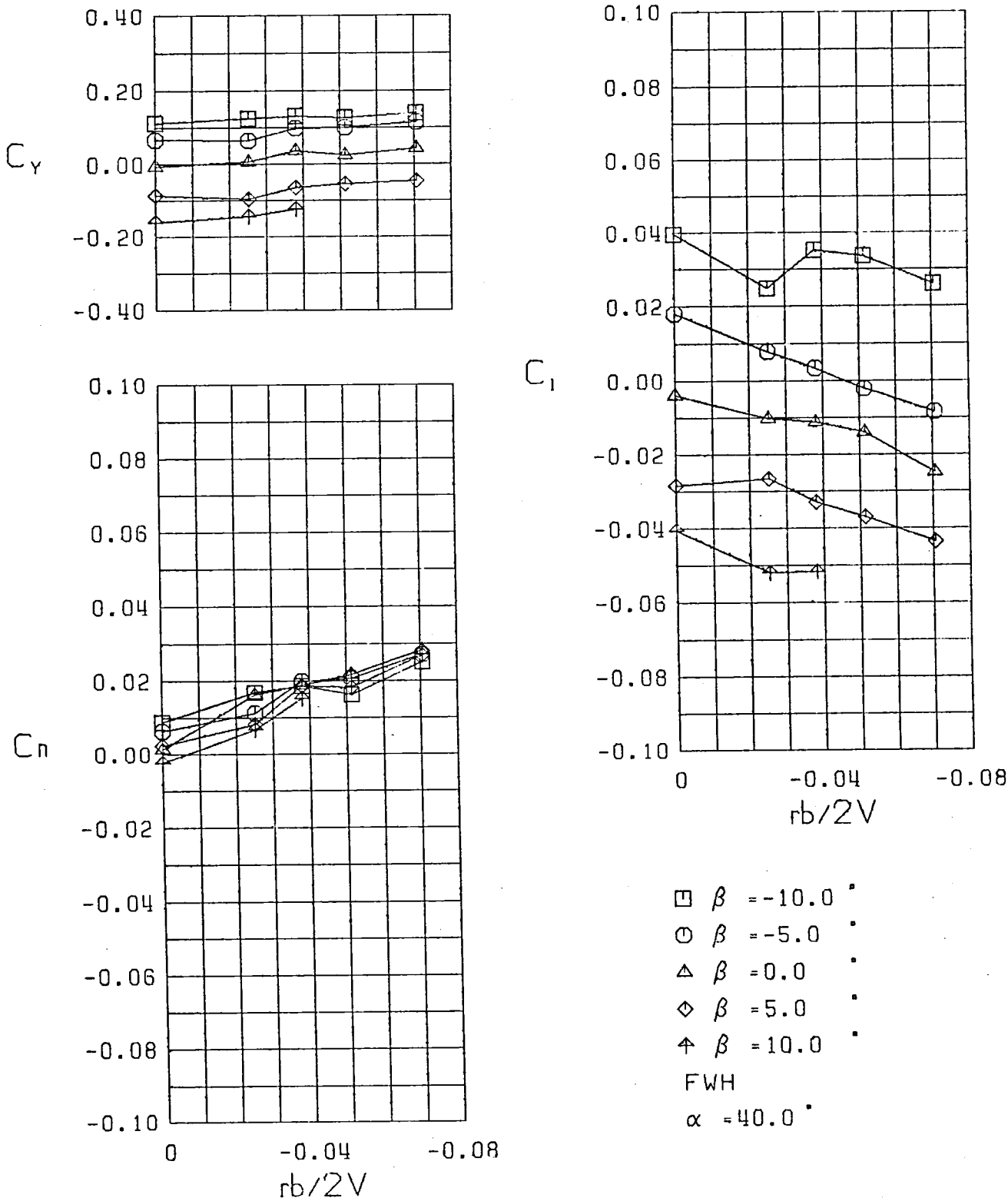

Figure 24 (Continued)

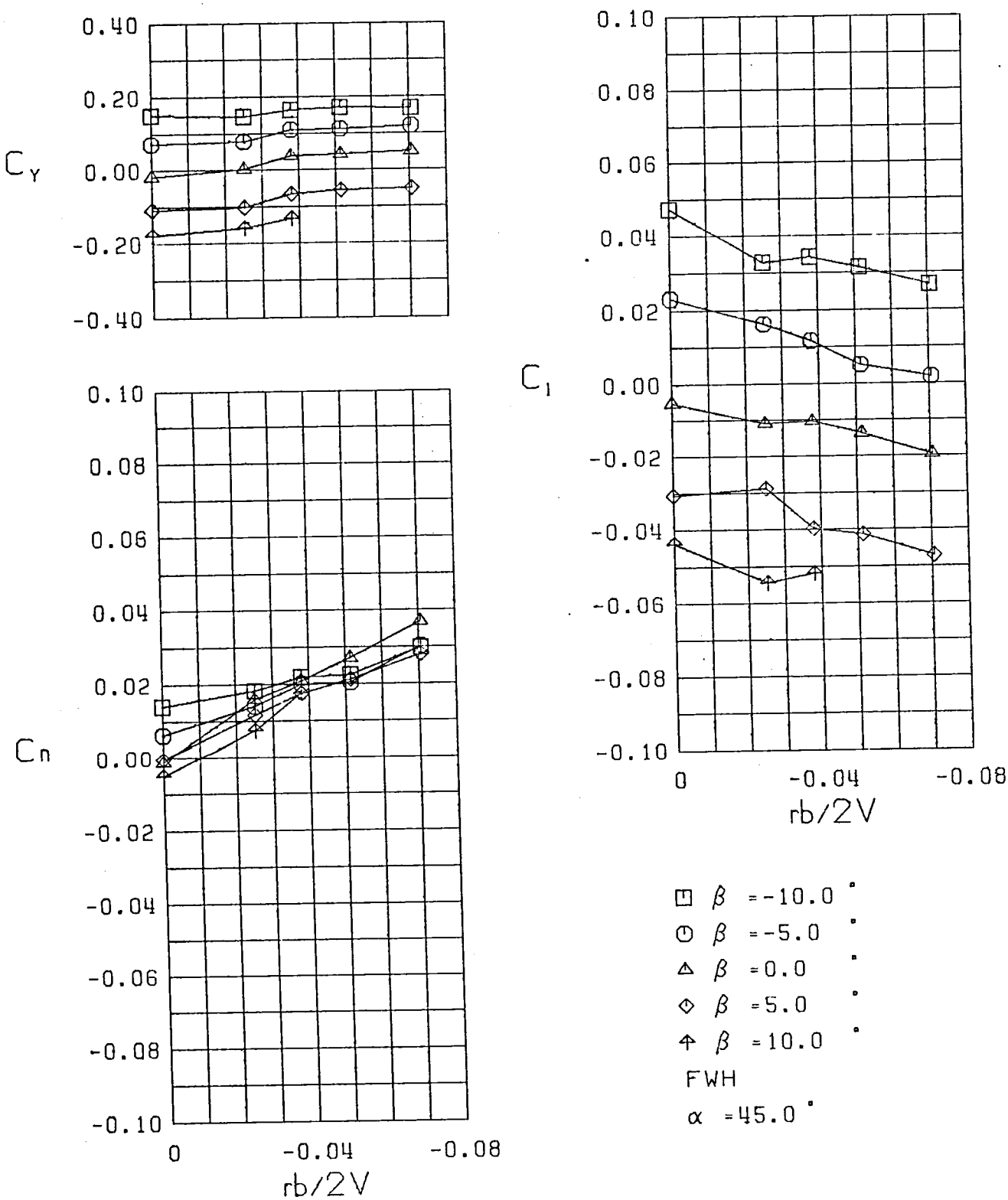

Figure 24 (Continued)

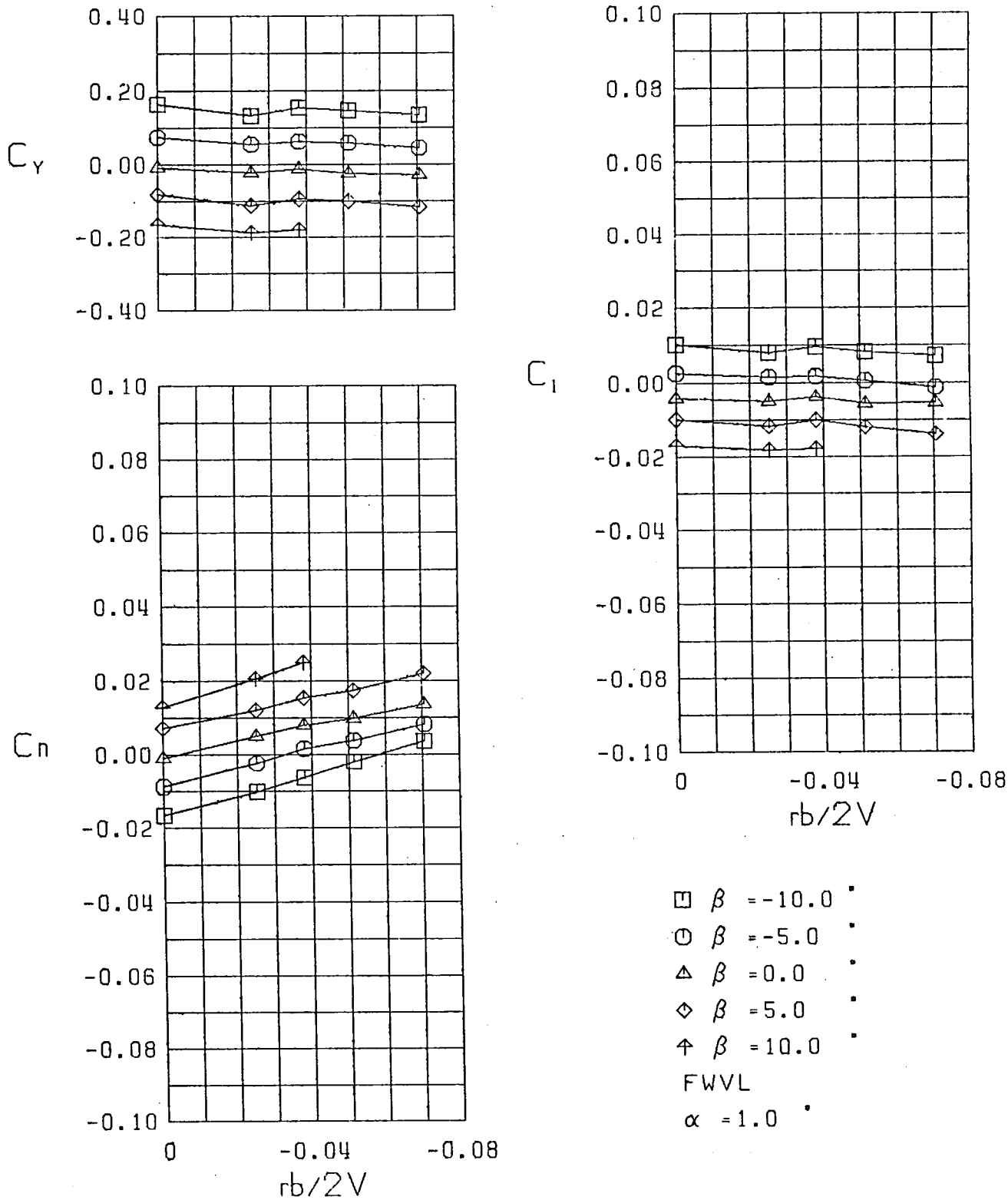

Figure 25 Variation of Static Lateral-Directional Stability Derivatives with Yaw Rate, Configuration 10

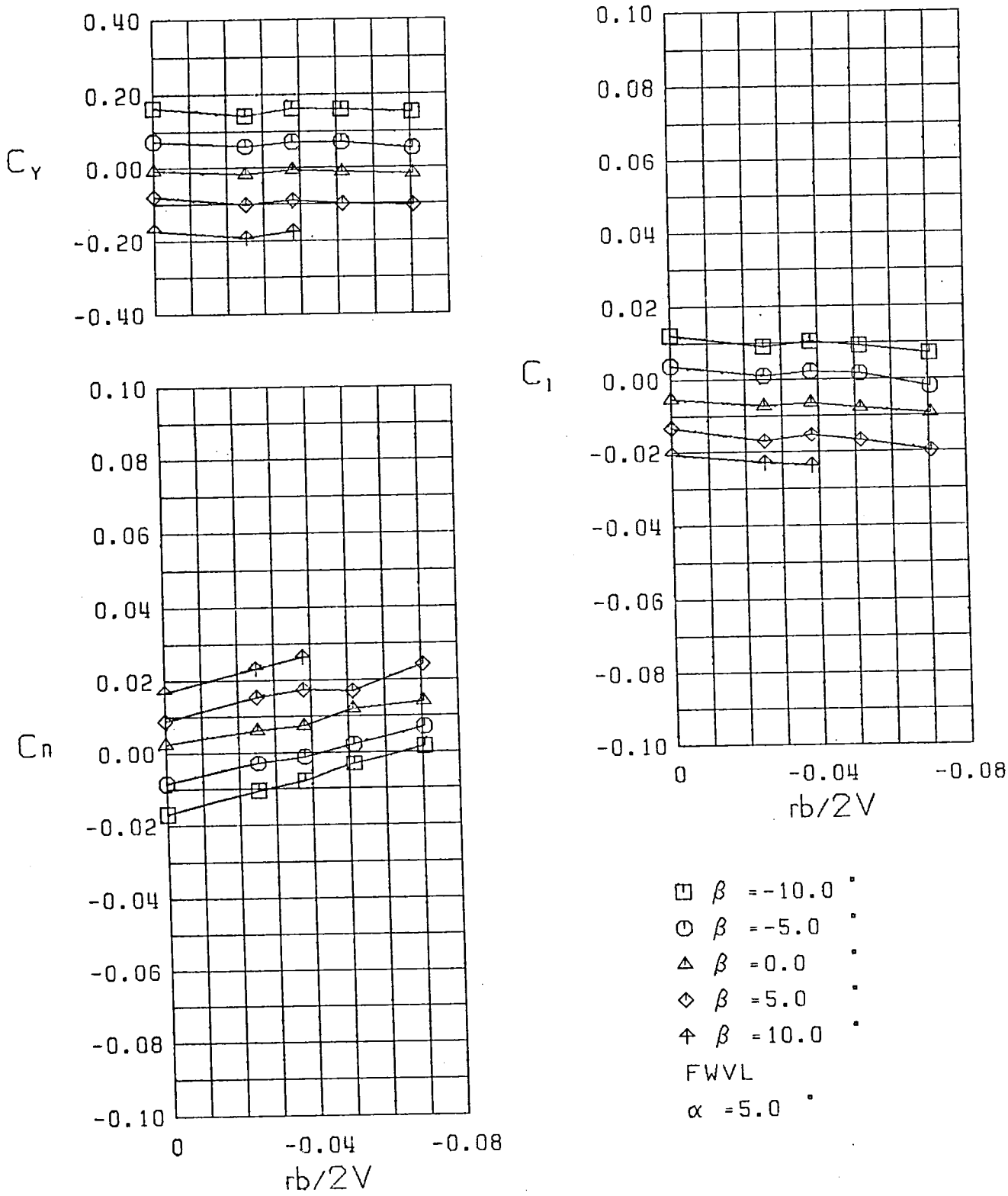

Figure 25 (Continued)

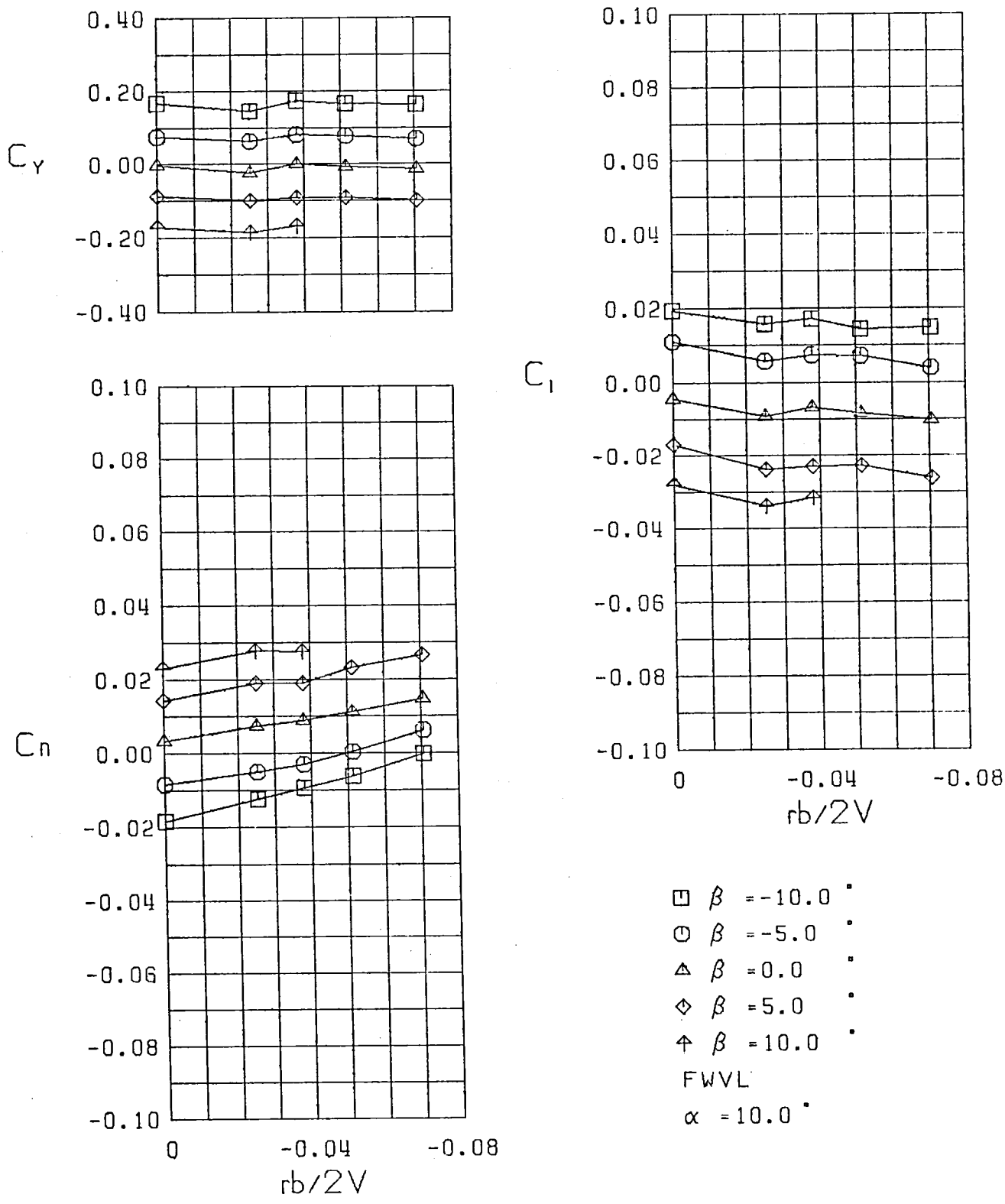

Figure 25 (Continued)

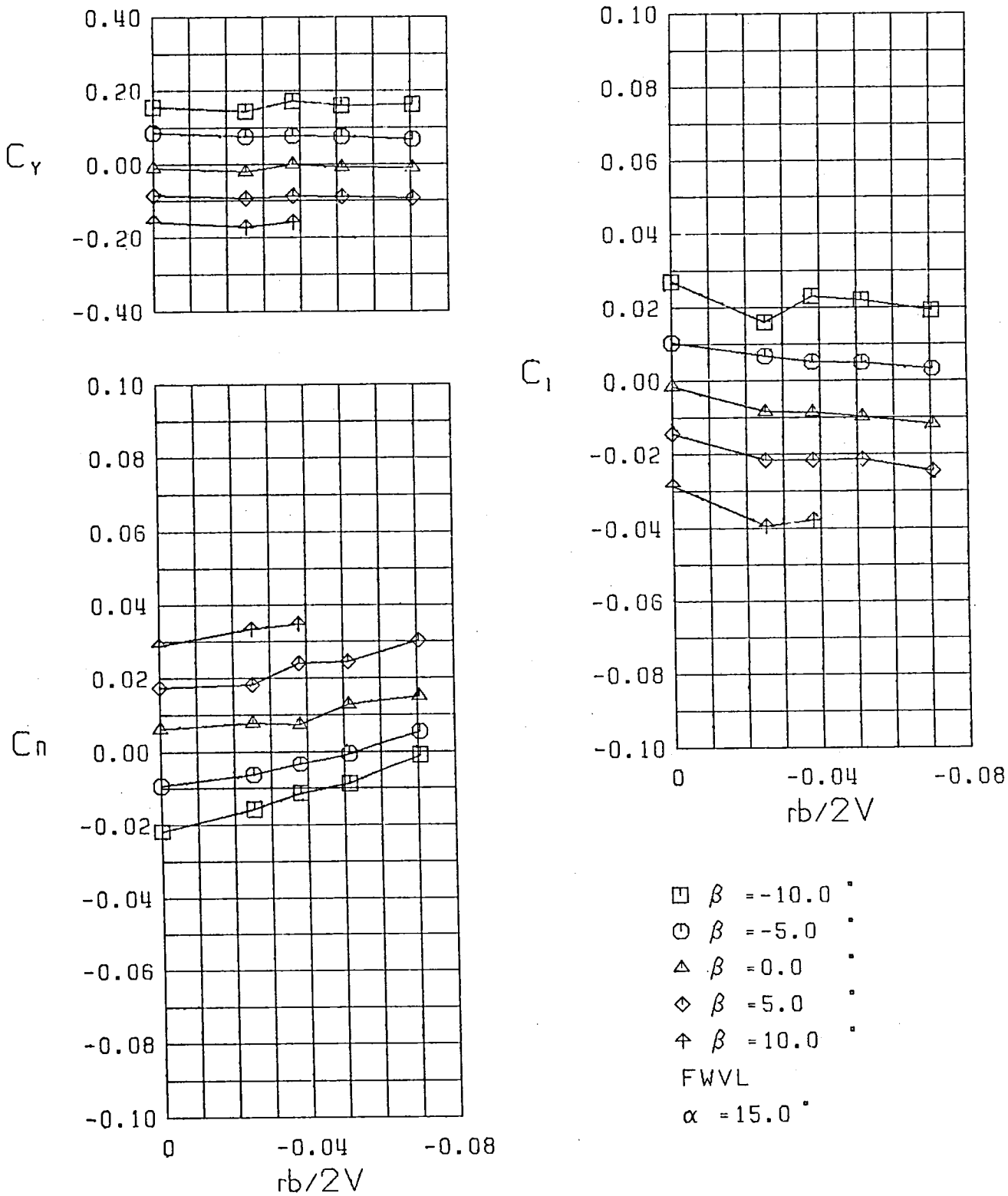

Figure 25 (Continued)

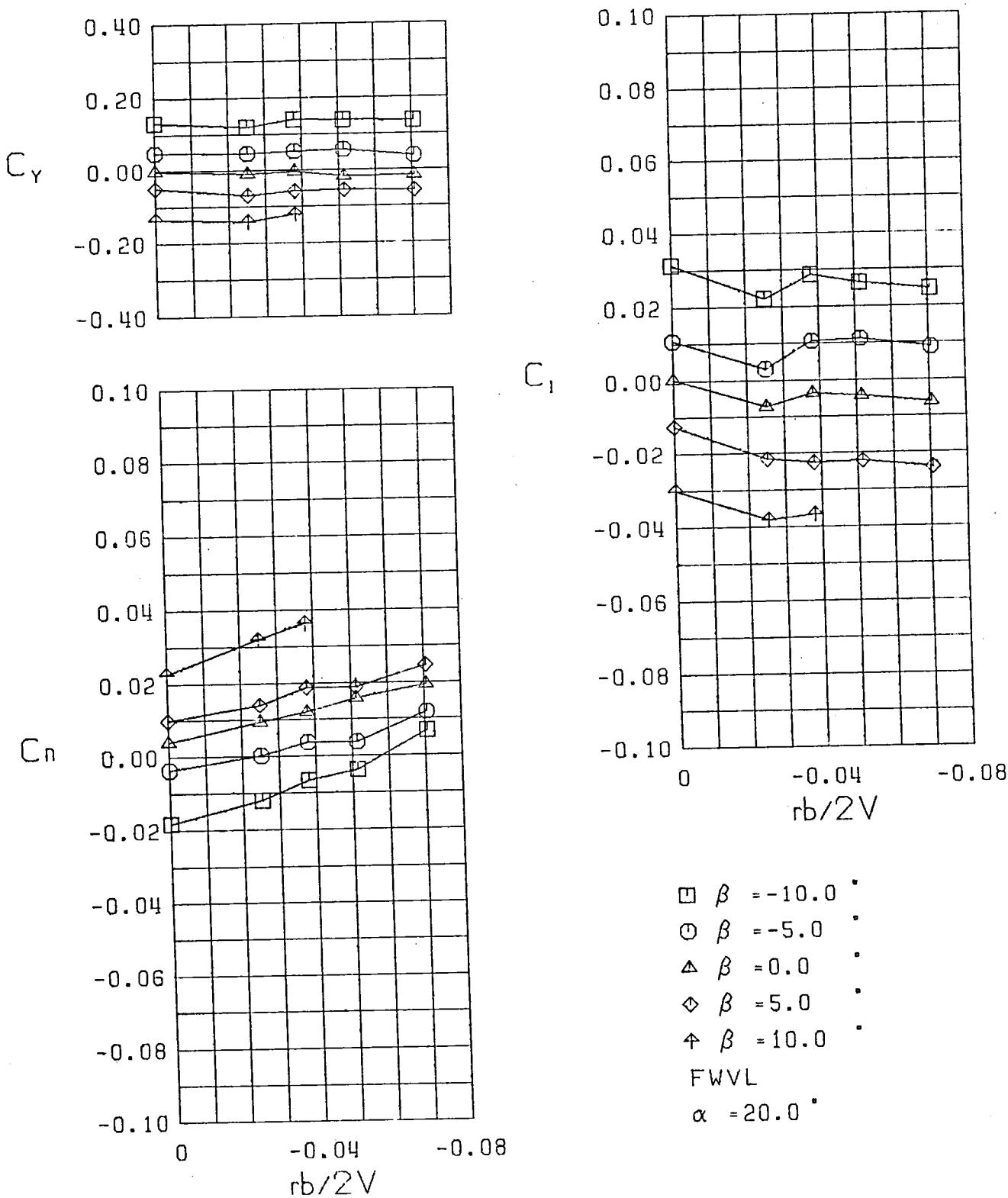

Figure 25 (Continued)

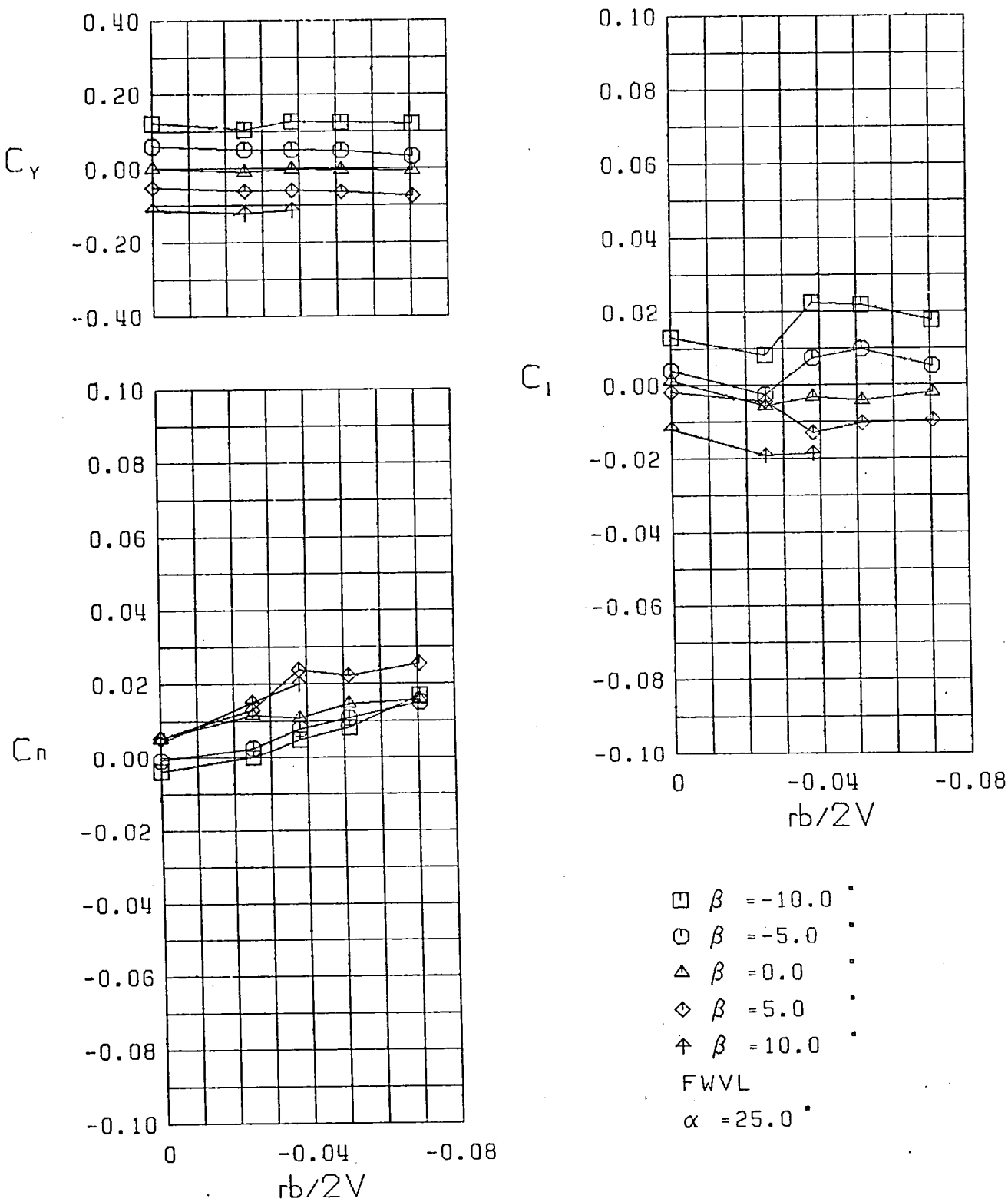

Figure 25 (Continued)

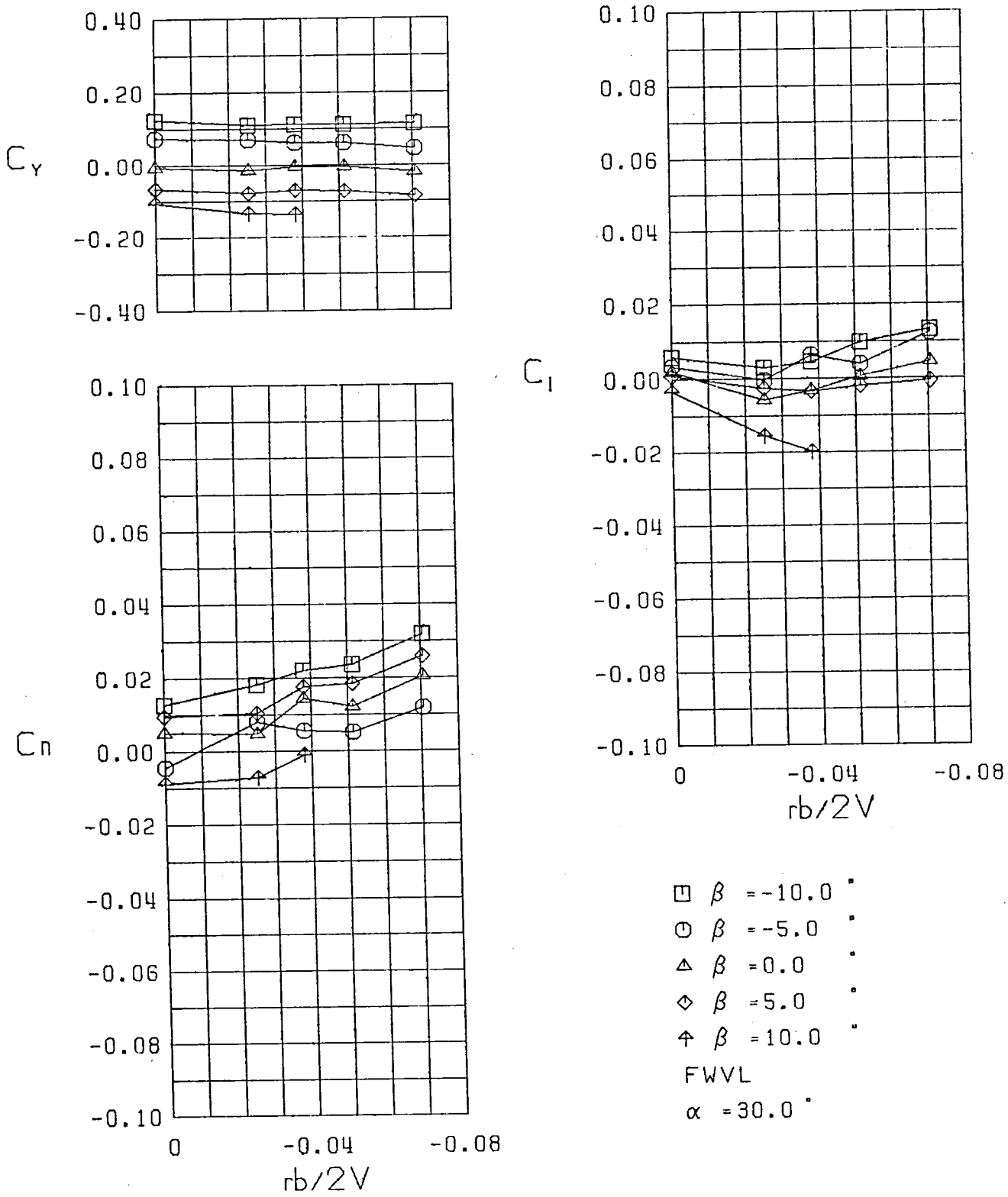

Figure 25 (Continued)

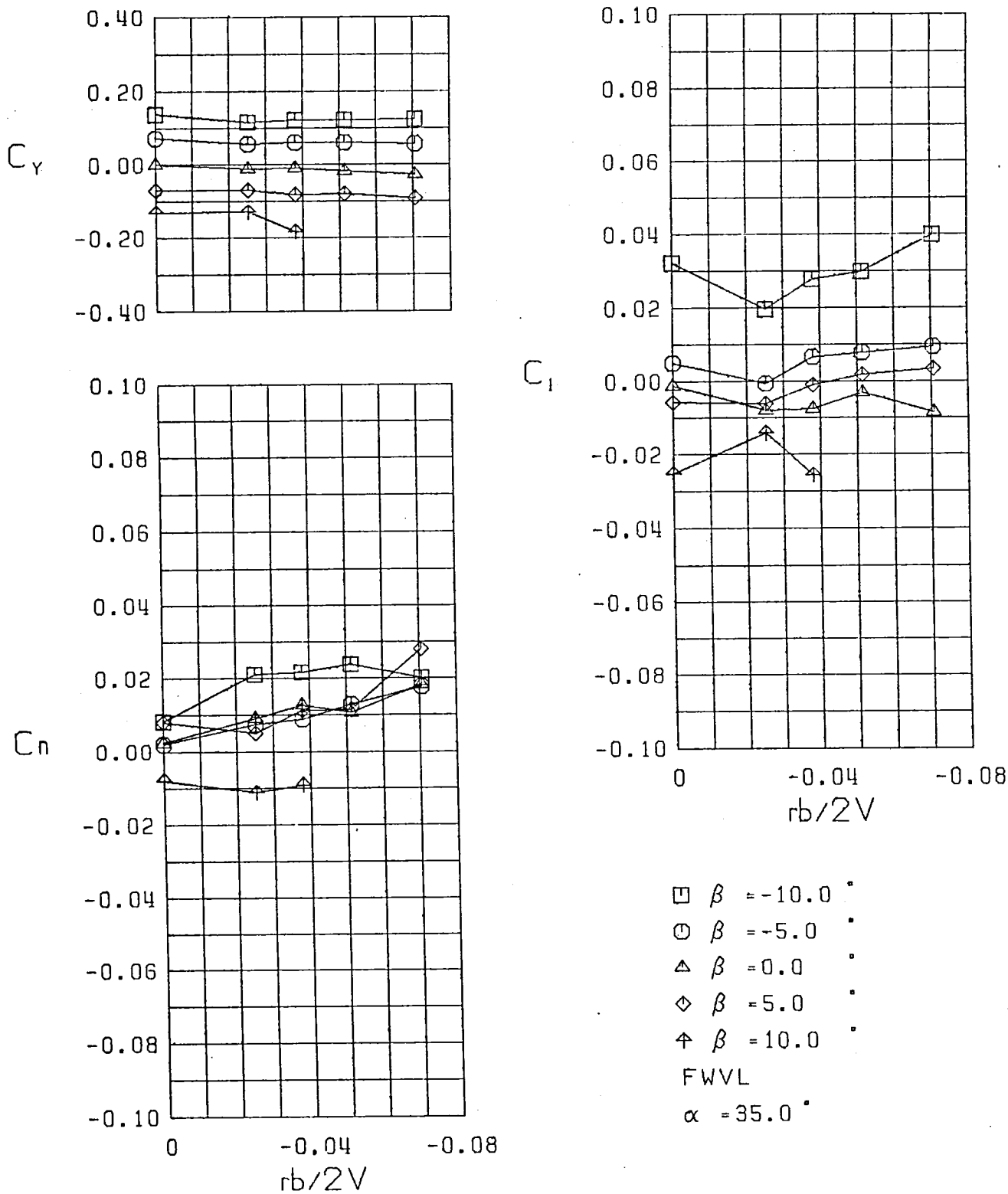

Figure 25 (Continued)

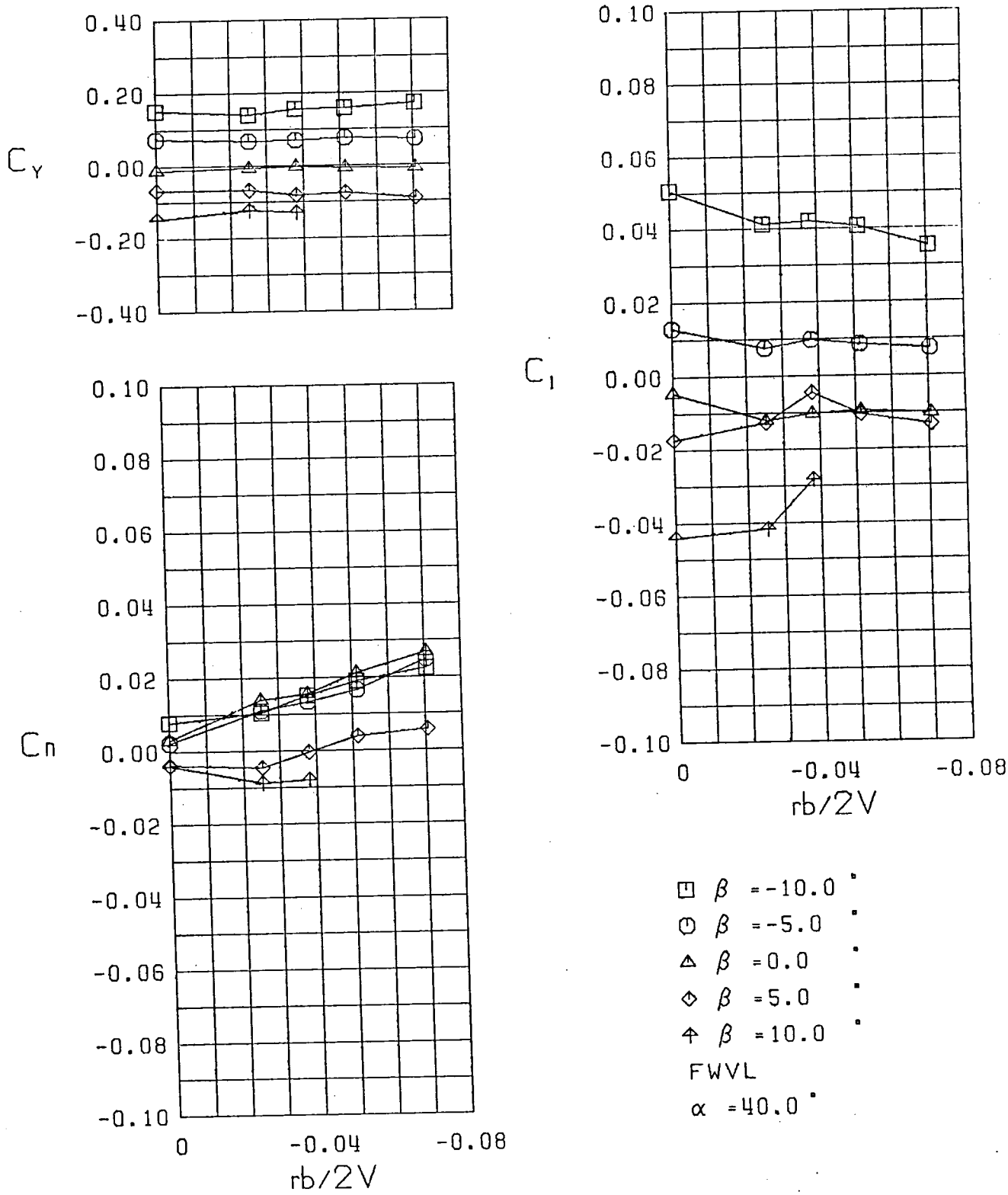

Figure 25 (Continued)

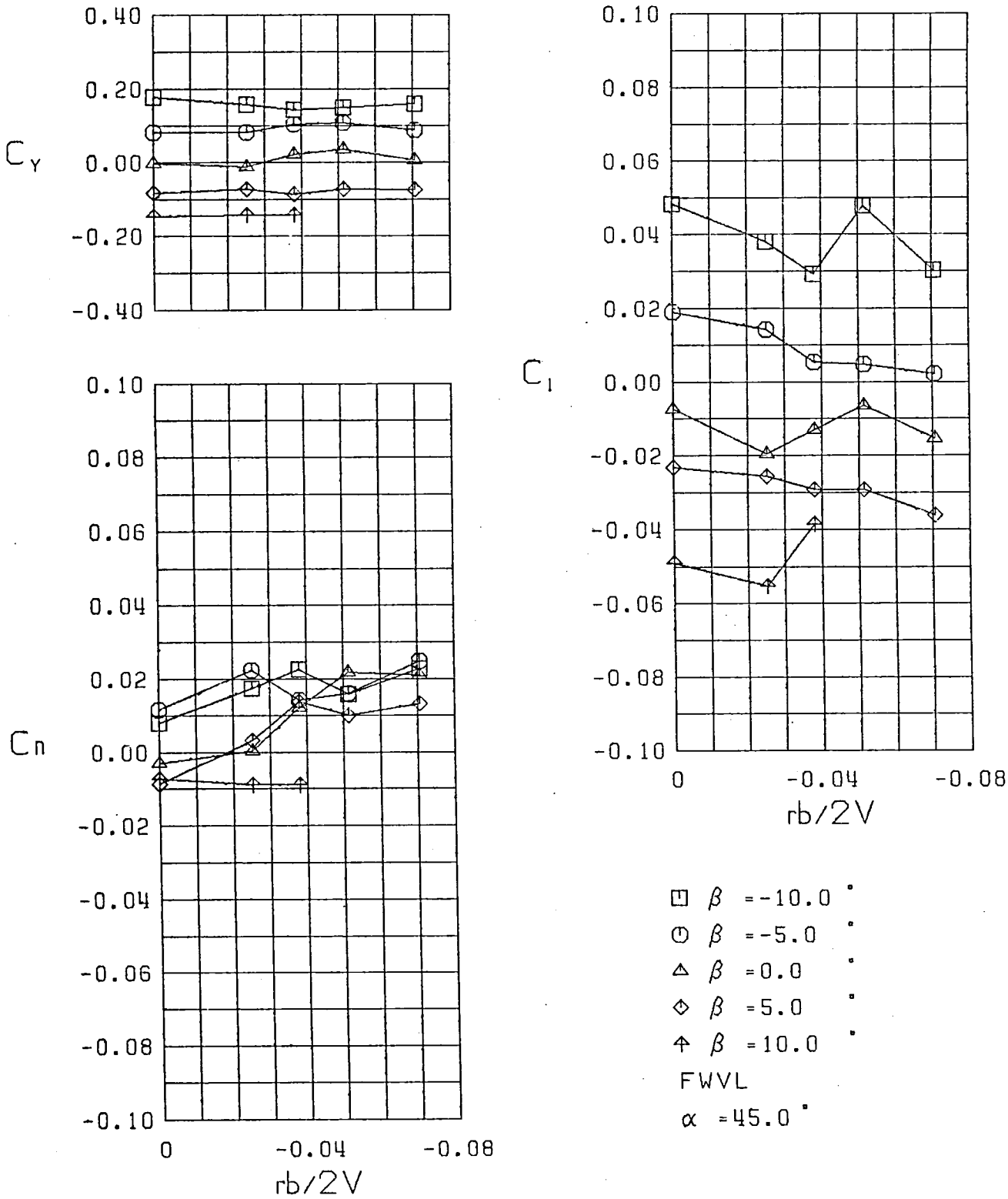

Figure 25 (Continued)

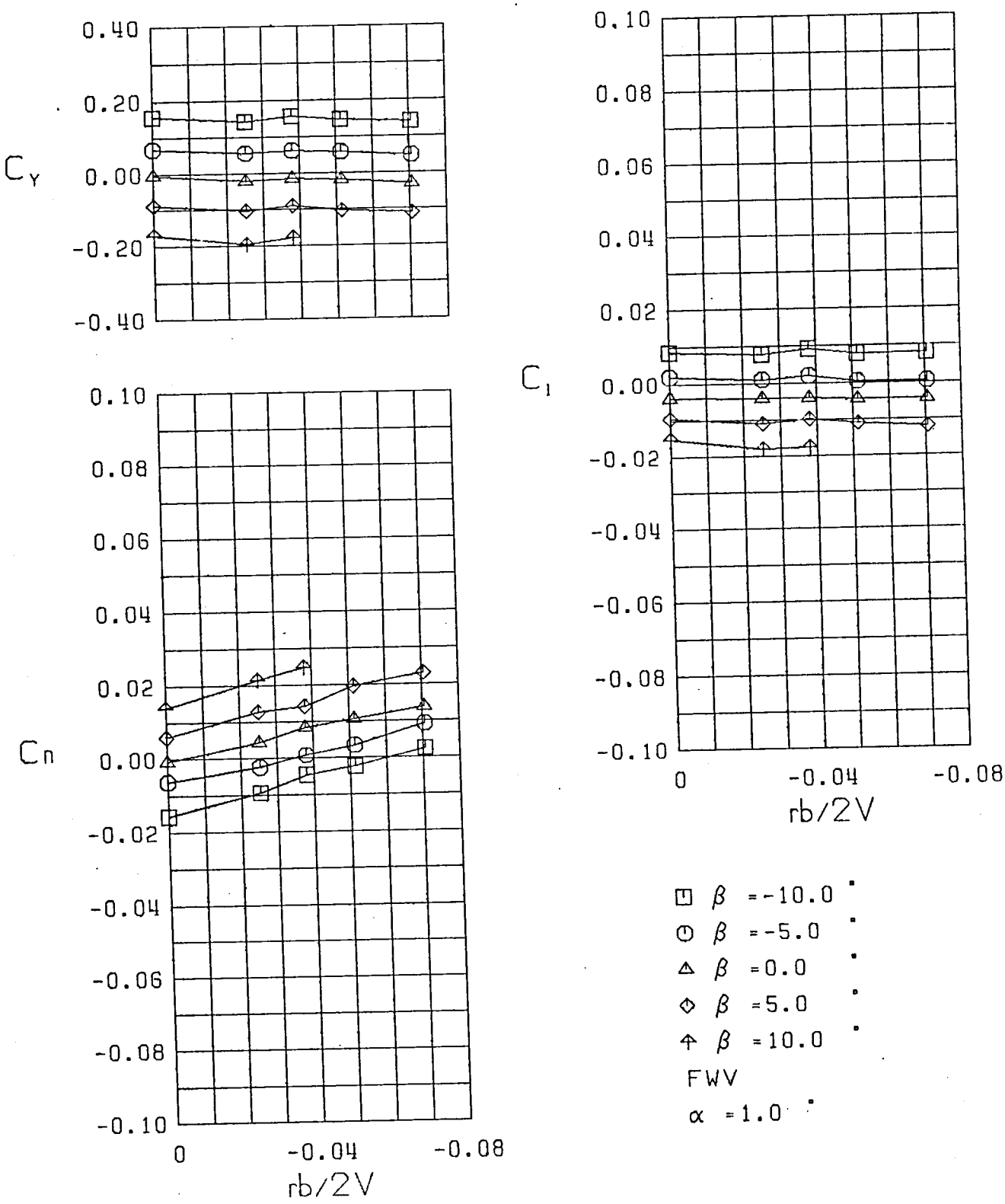

Figure 26 Variation of Static Lateral-Directional Stability Derivatives with Yaw Rate, Configuration 12

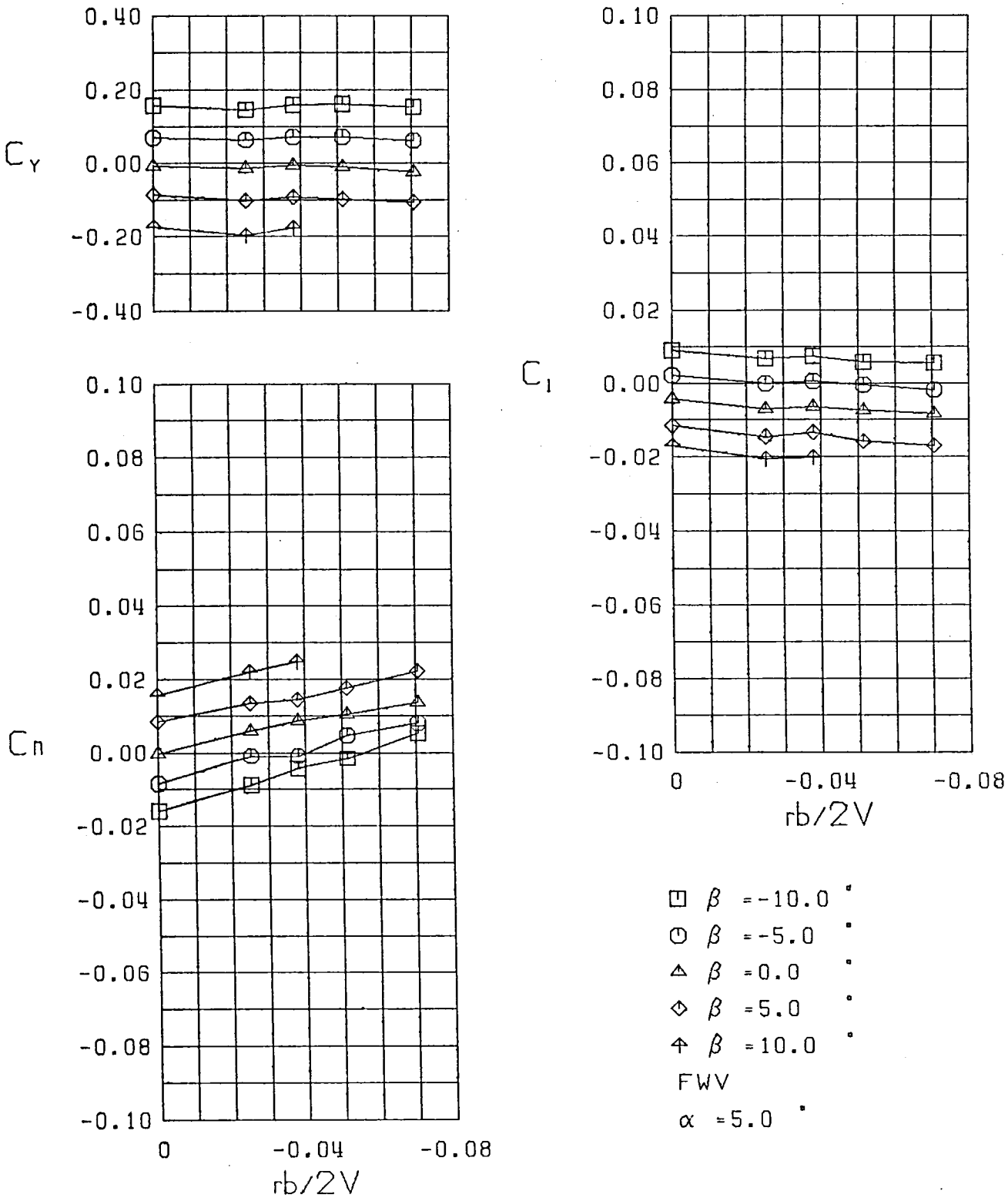

Figure 26 (Continued)

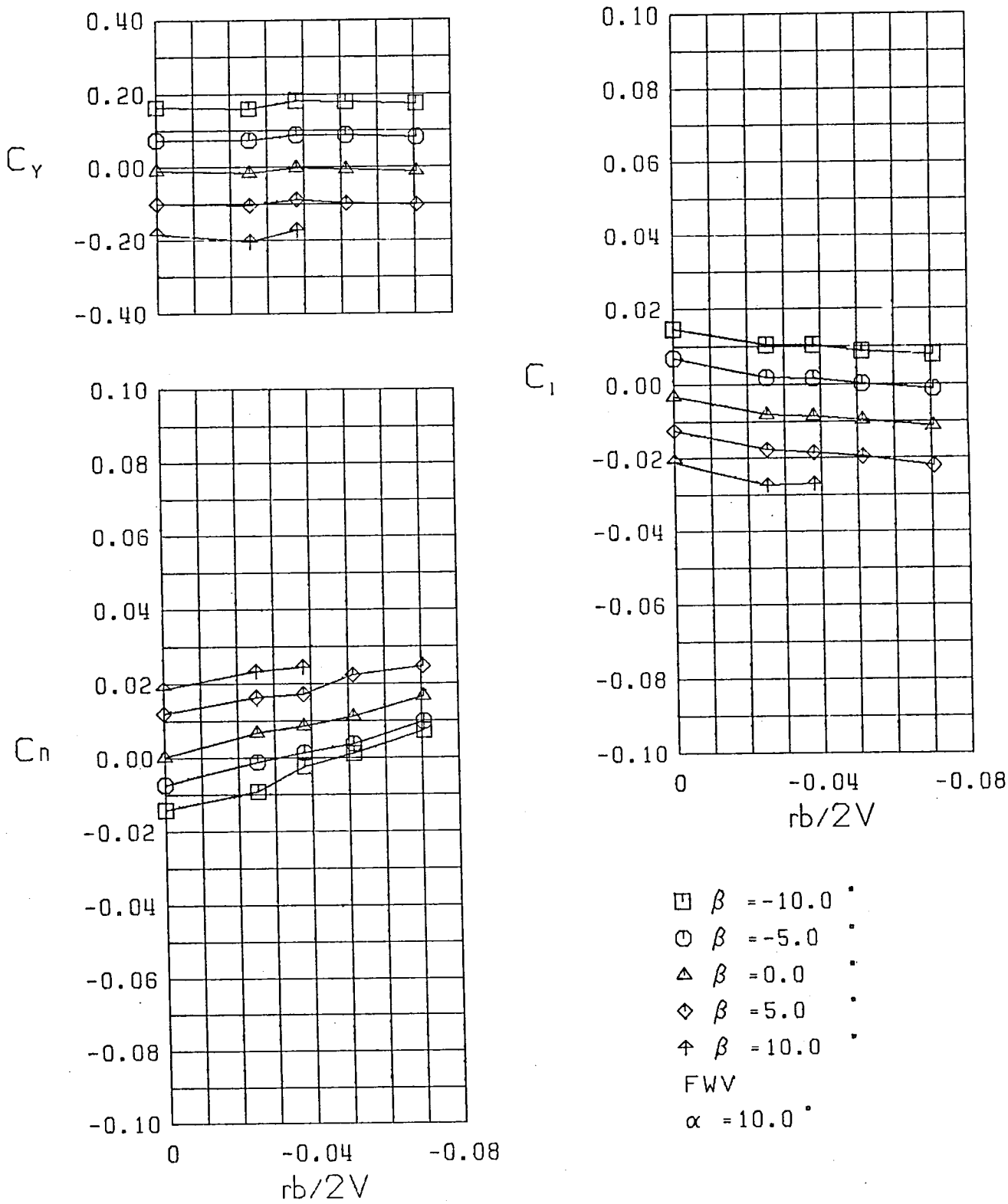

Figure 26 (Continued)

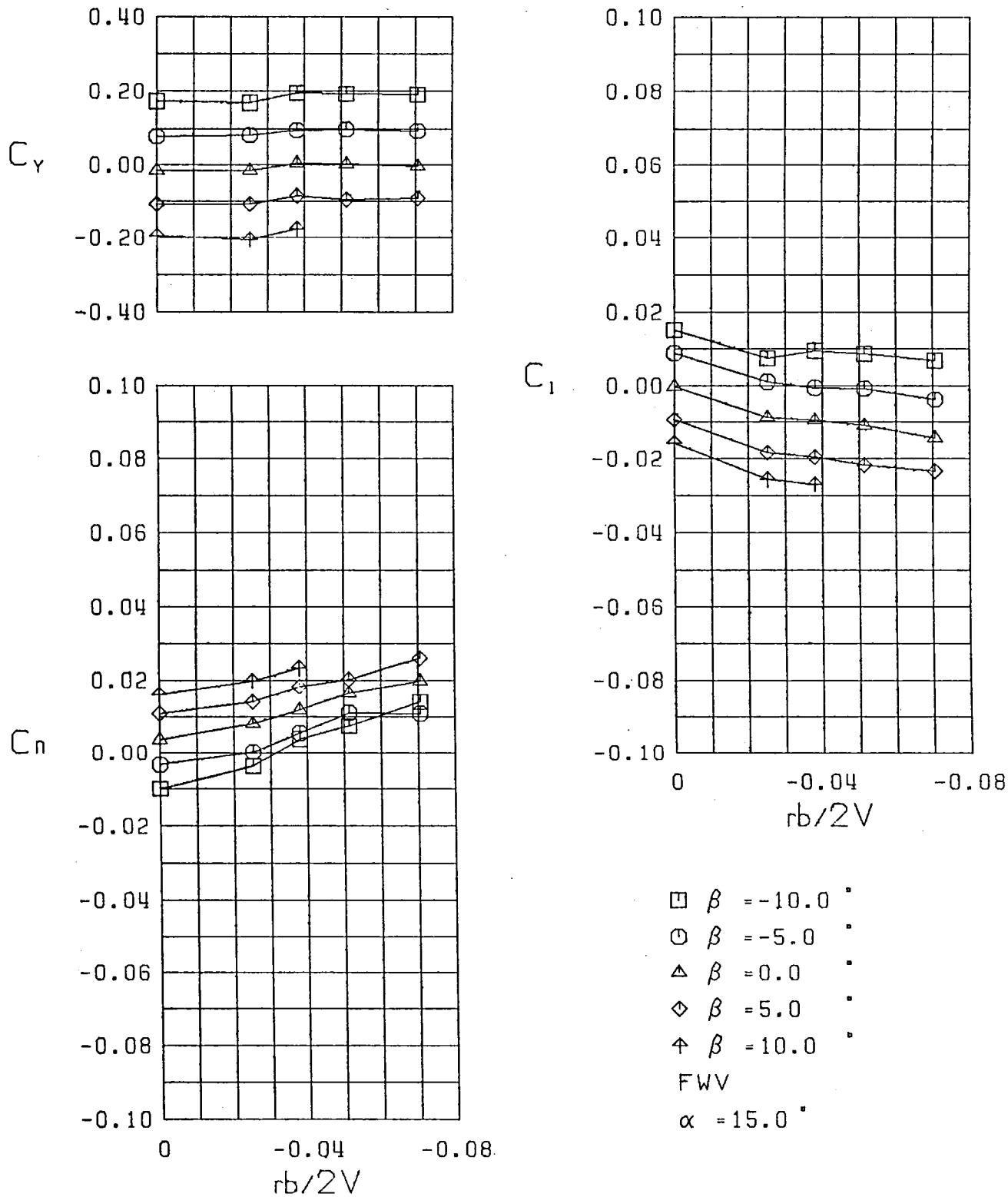

Figure 26 (Continued)

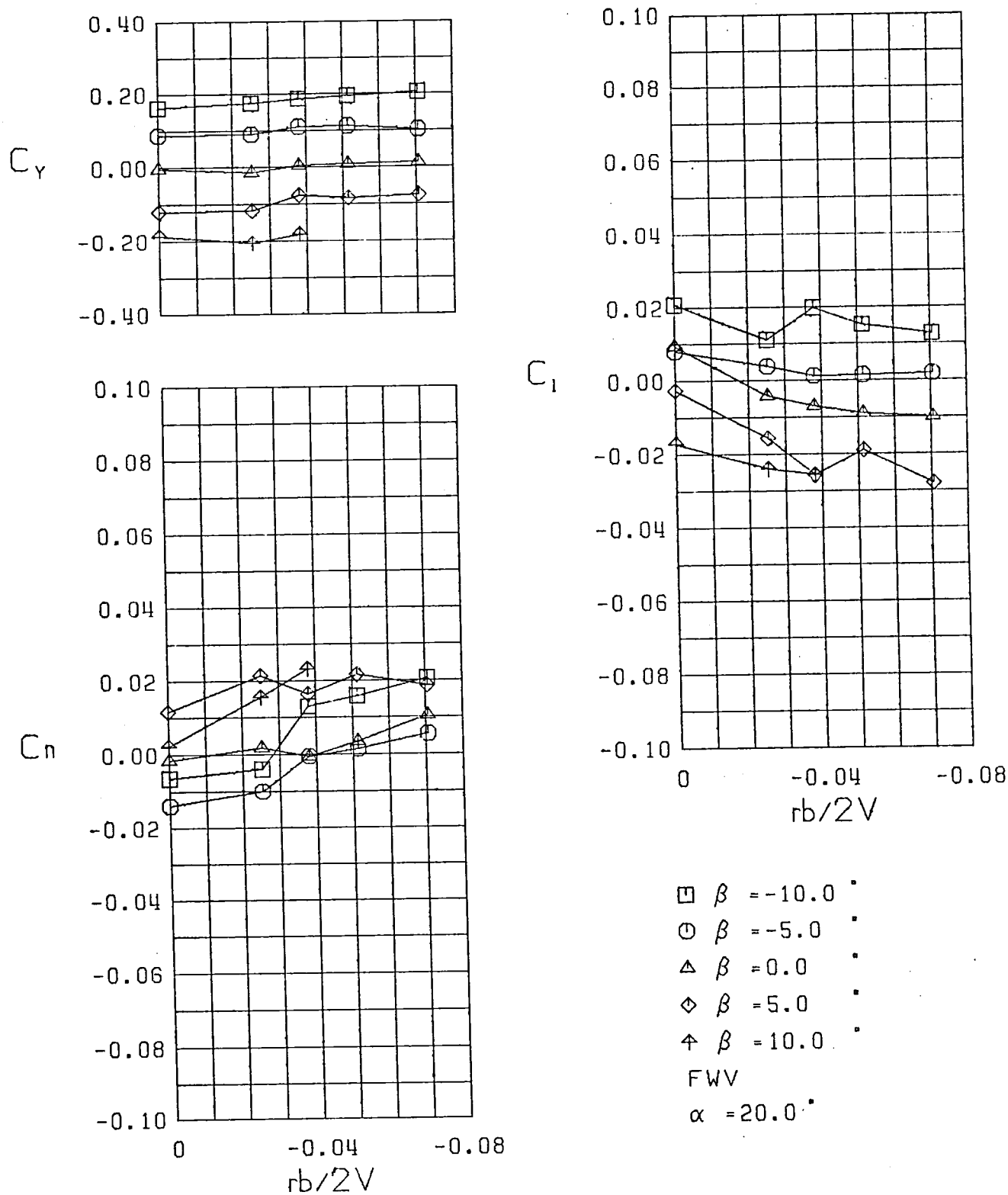

Figure 26 (Continued)

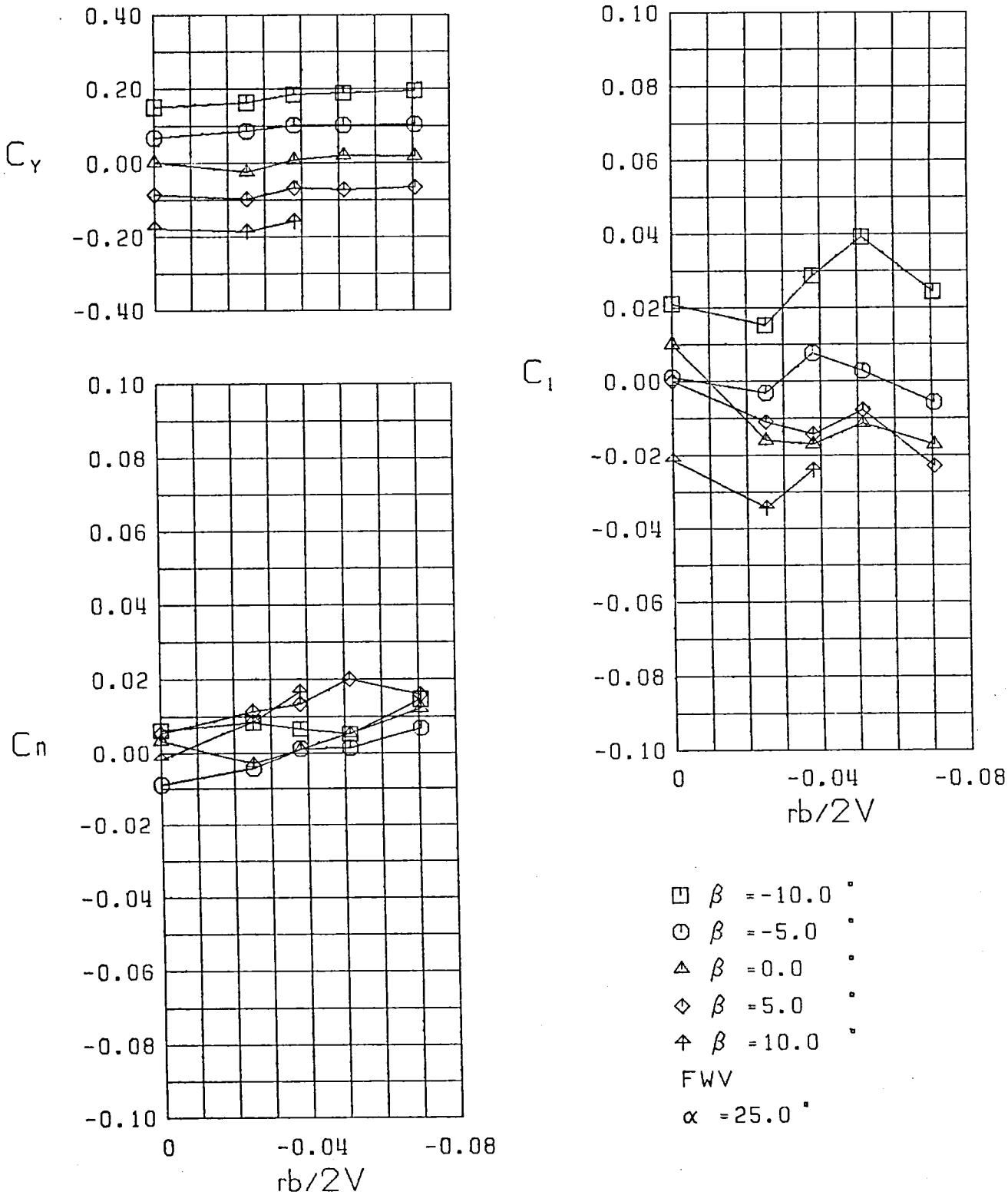

Figure 26 (Continued)

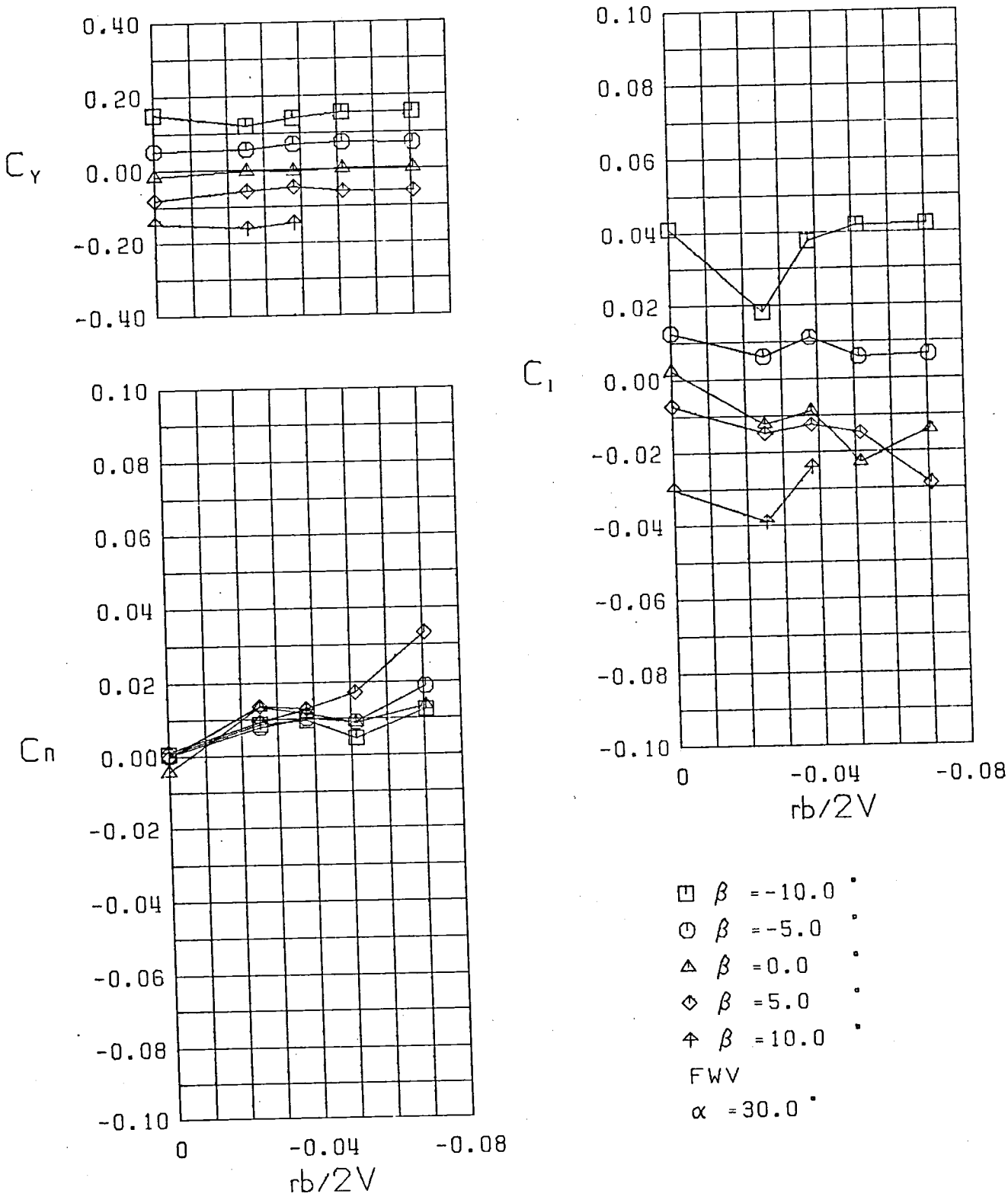

Figure 26 (Continued)

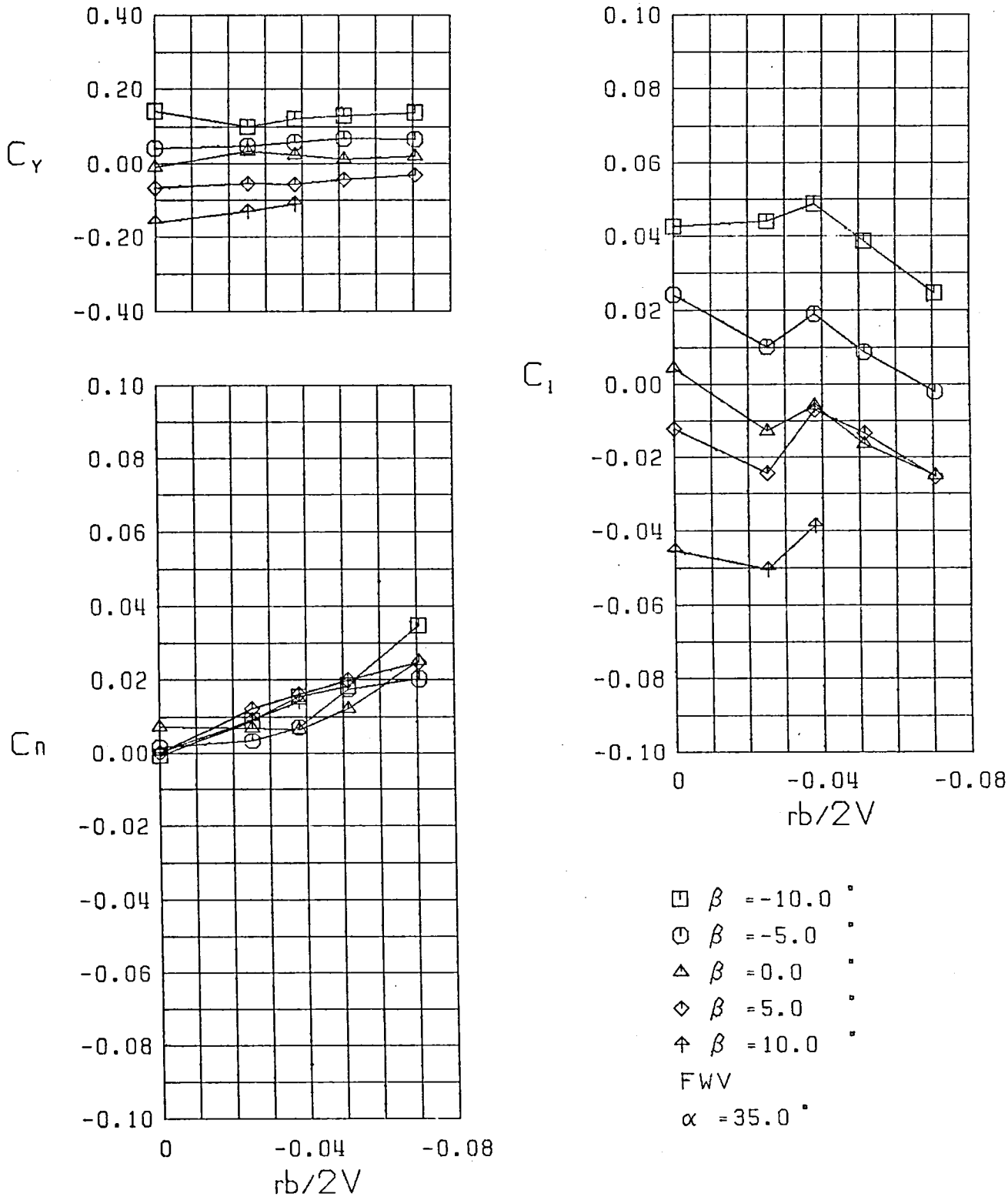

Figure 26 (Continued)

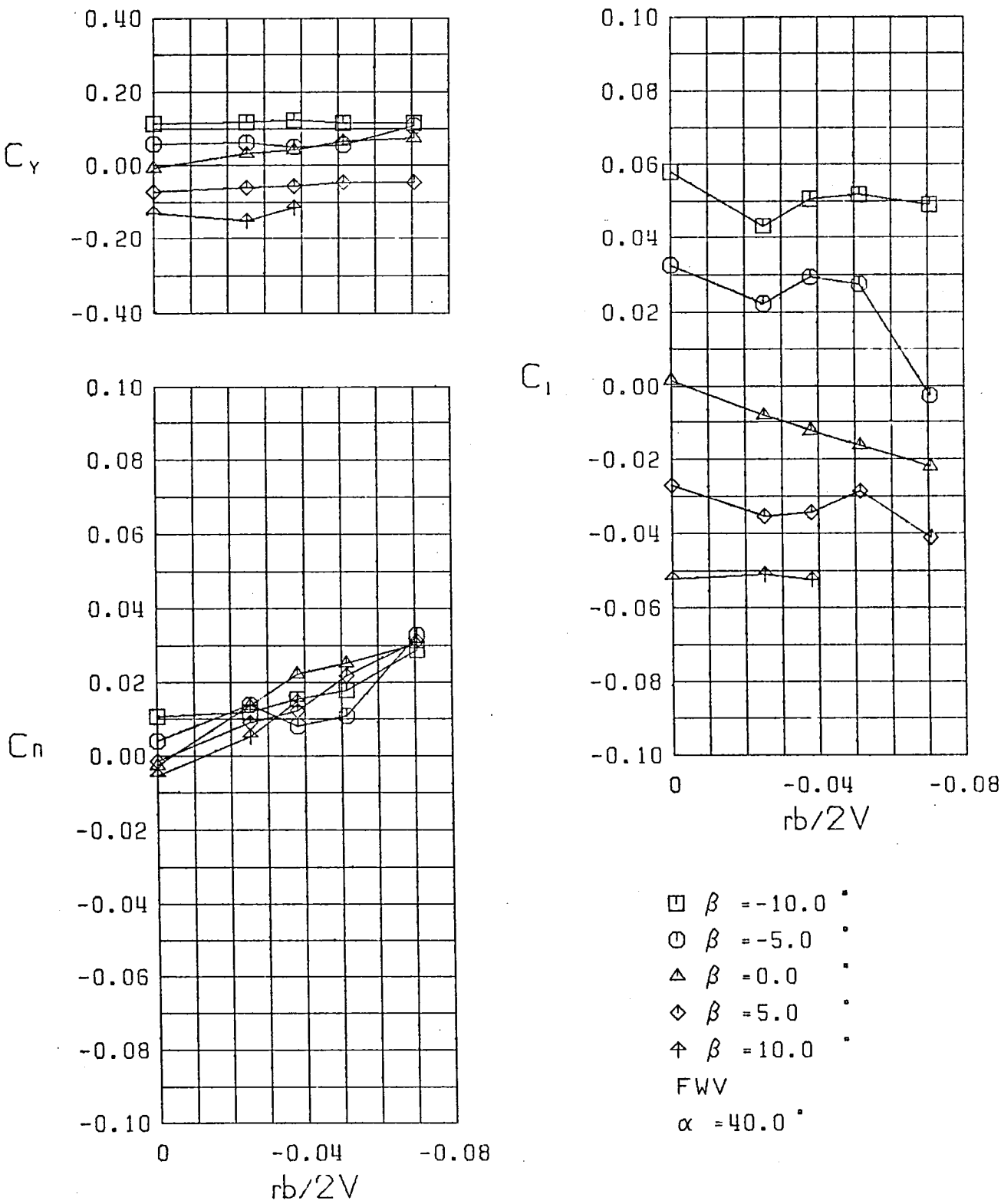

Figure 26 (Continued)

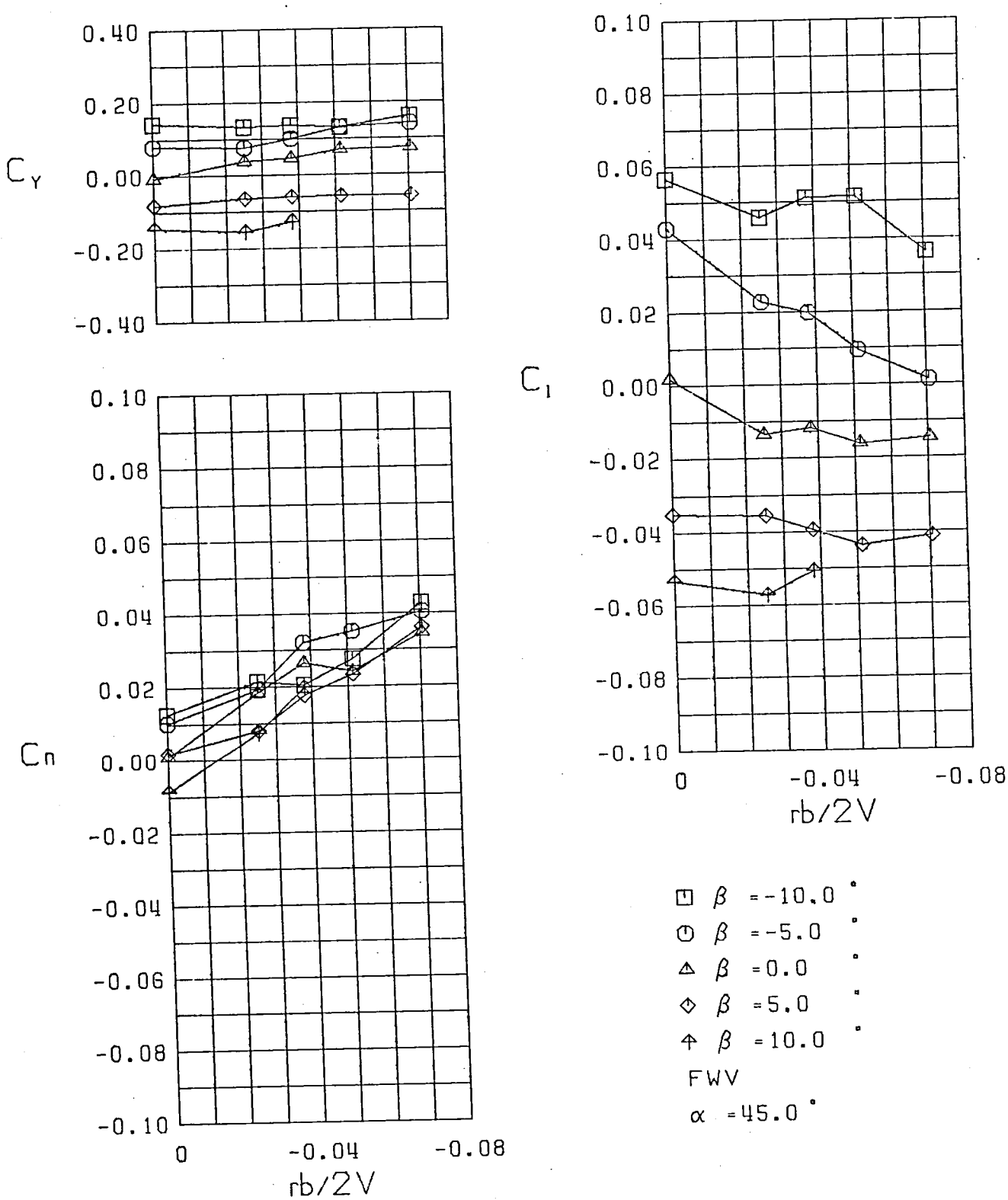

Figure 26 (Continued)

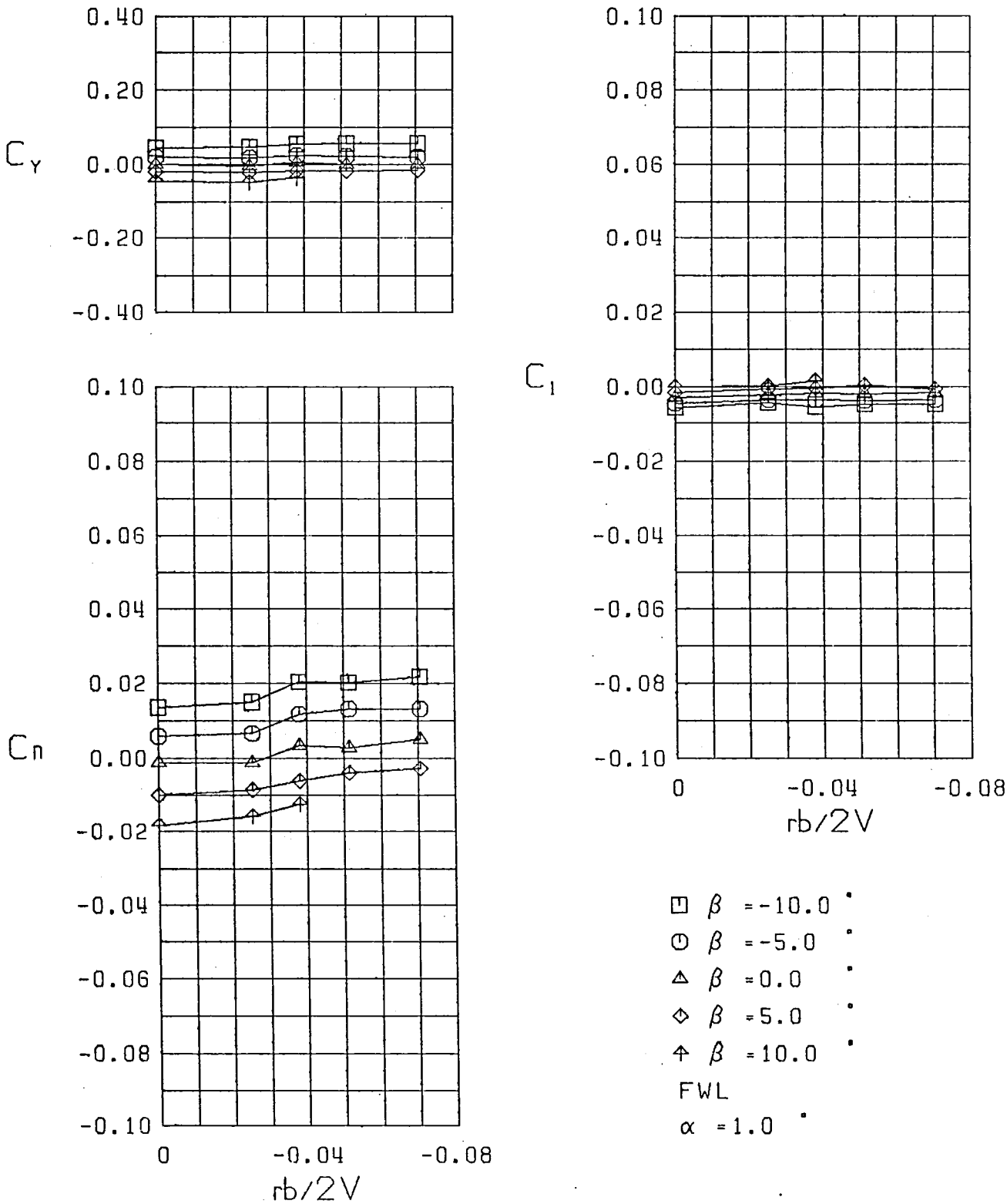

Figure 27 Variation of Static Lateral-Directional Stability Derivatives with Yaw Rate, Configuration 13

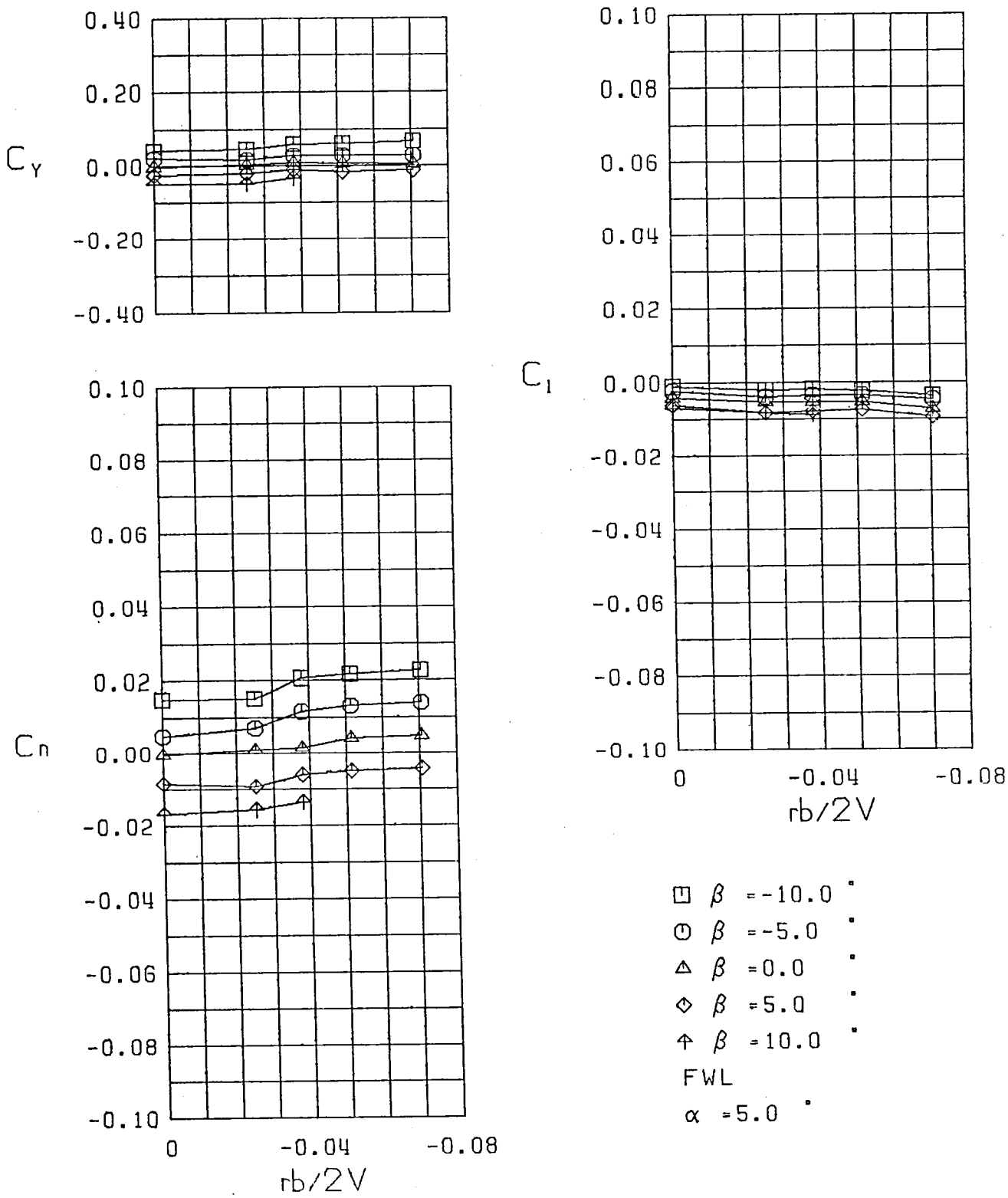

Figure 27 (Continued)

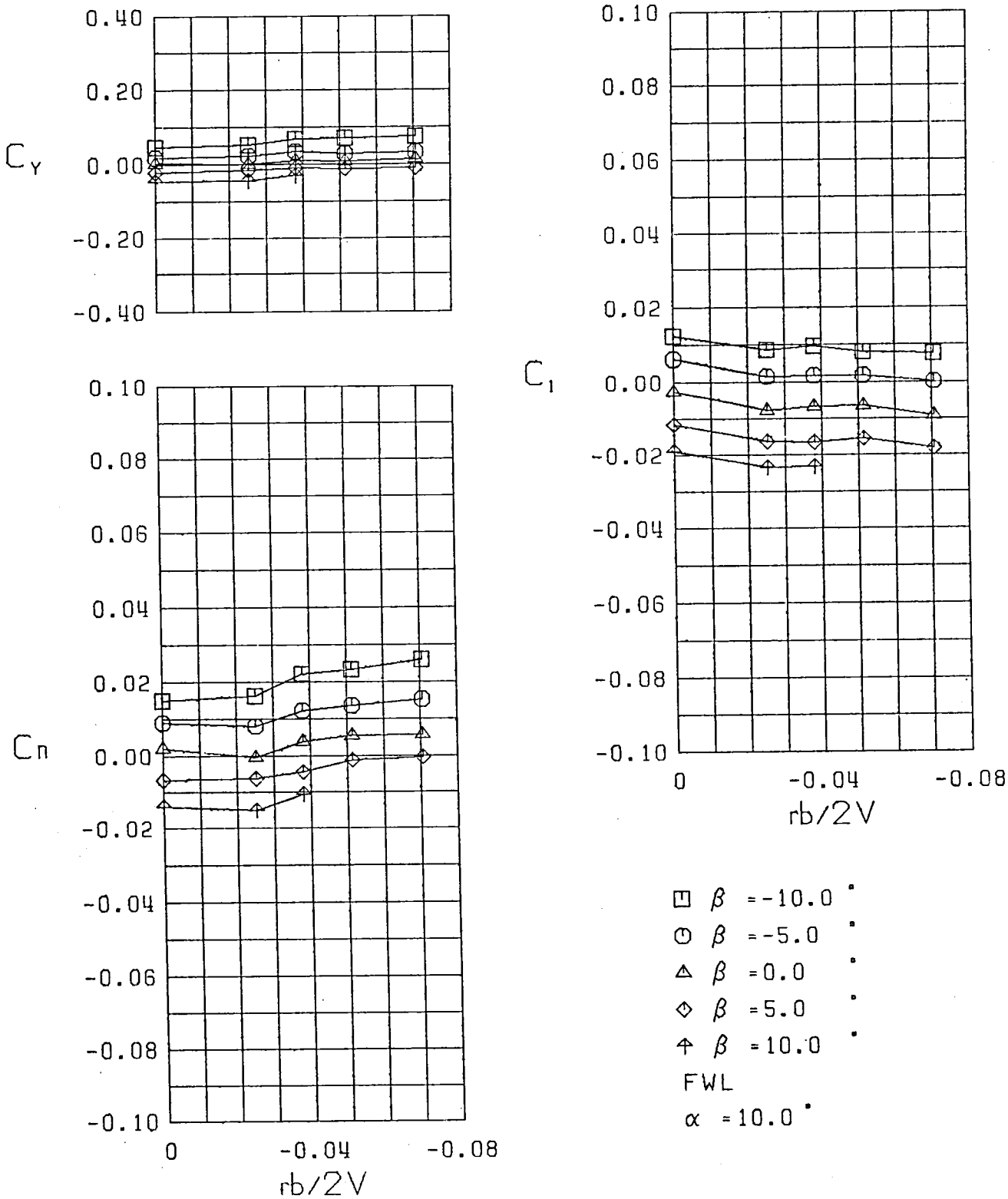

Figure 27 (Continued)

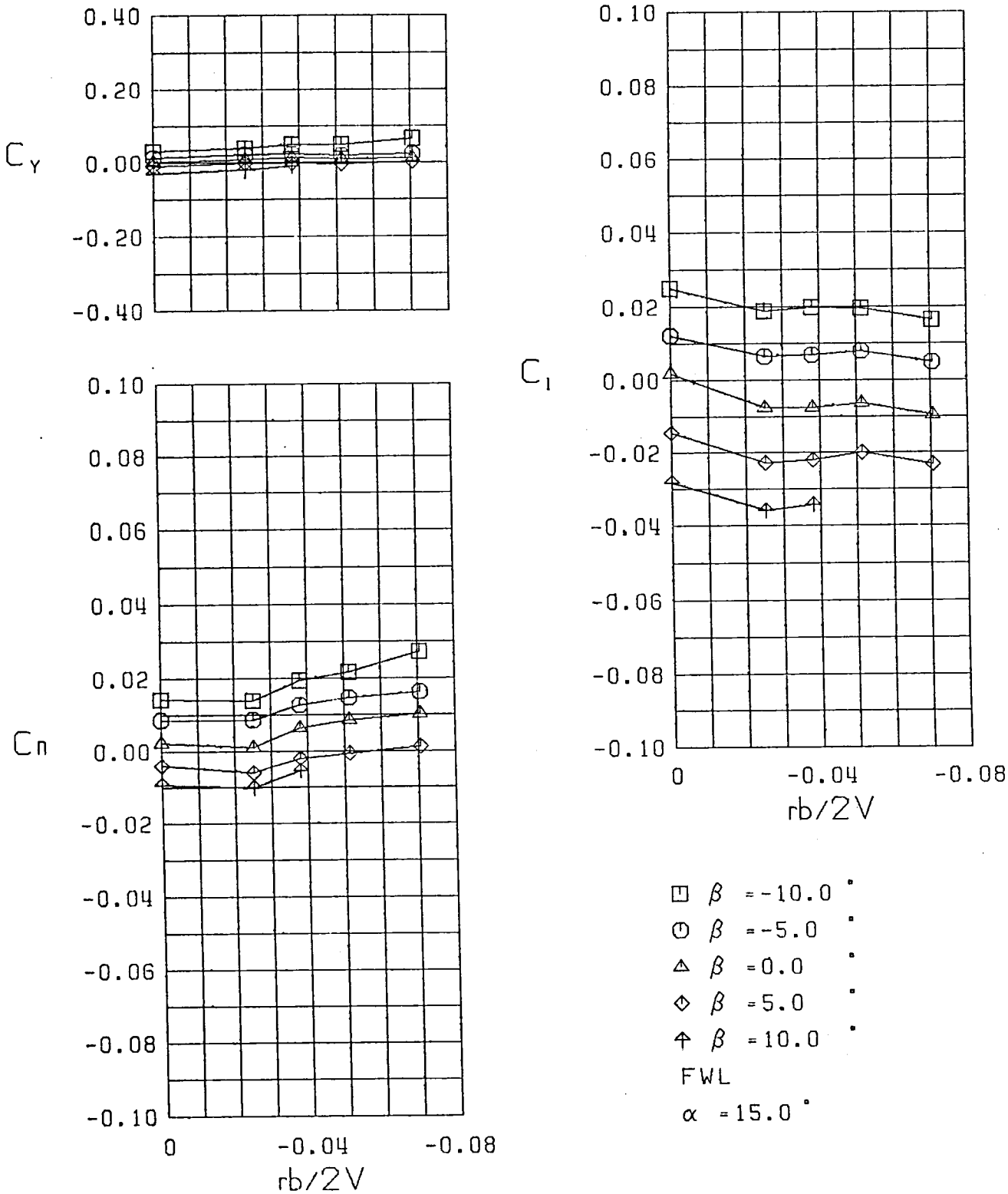

Figure 27 (Continued)

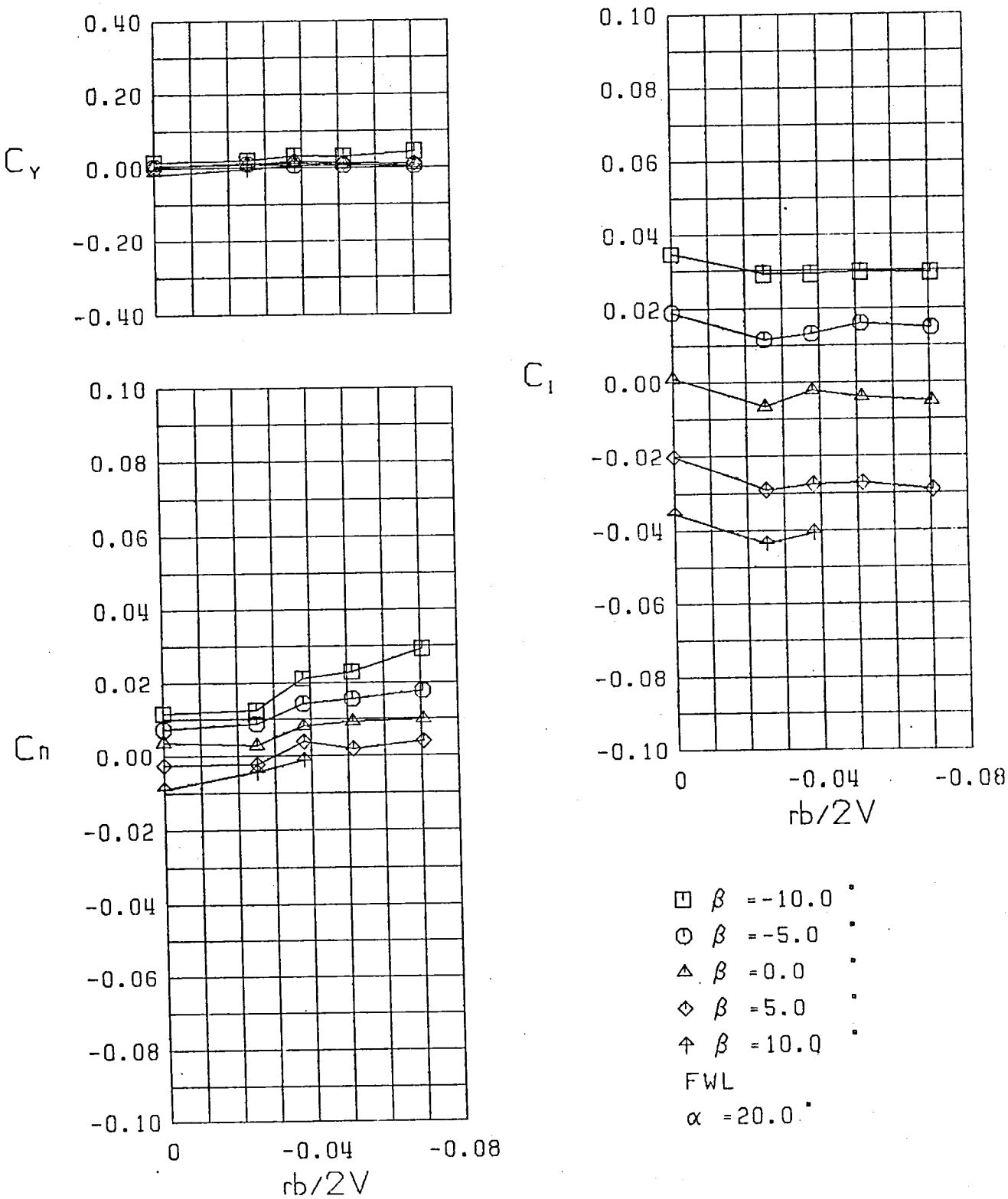

Figure 27 (Continued)

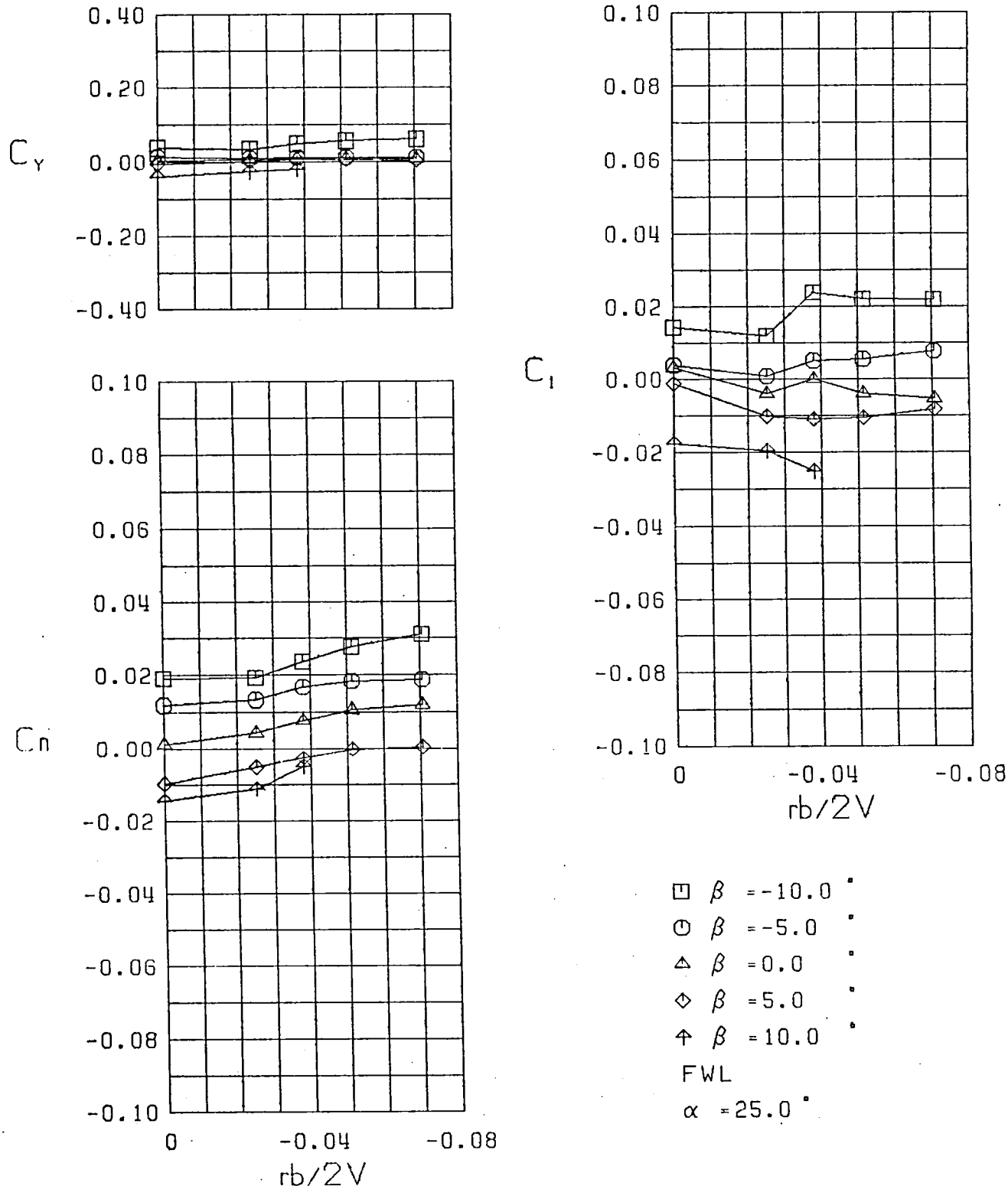

Figure 27 (Continued)

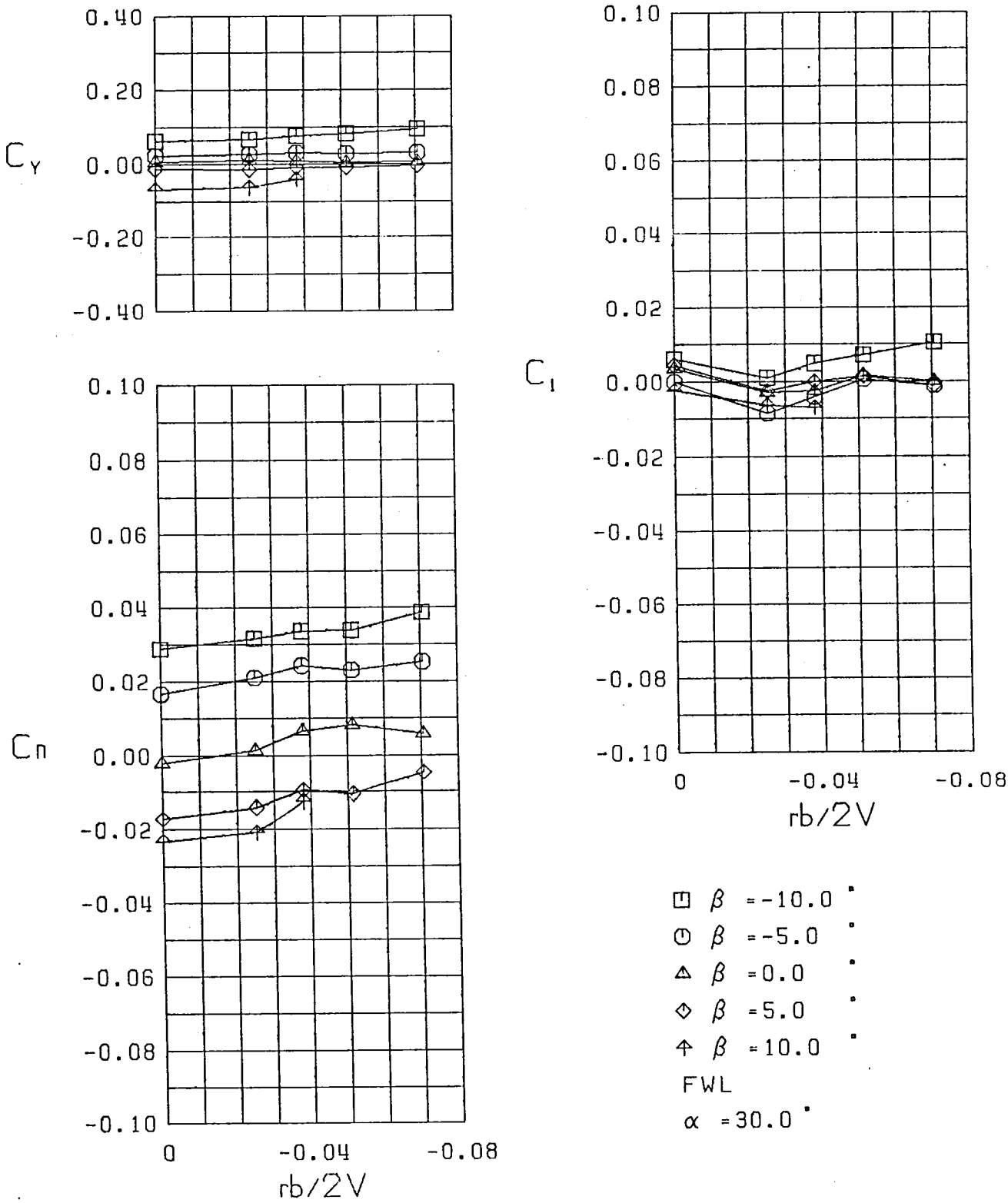

Figure 27 (Continued)

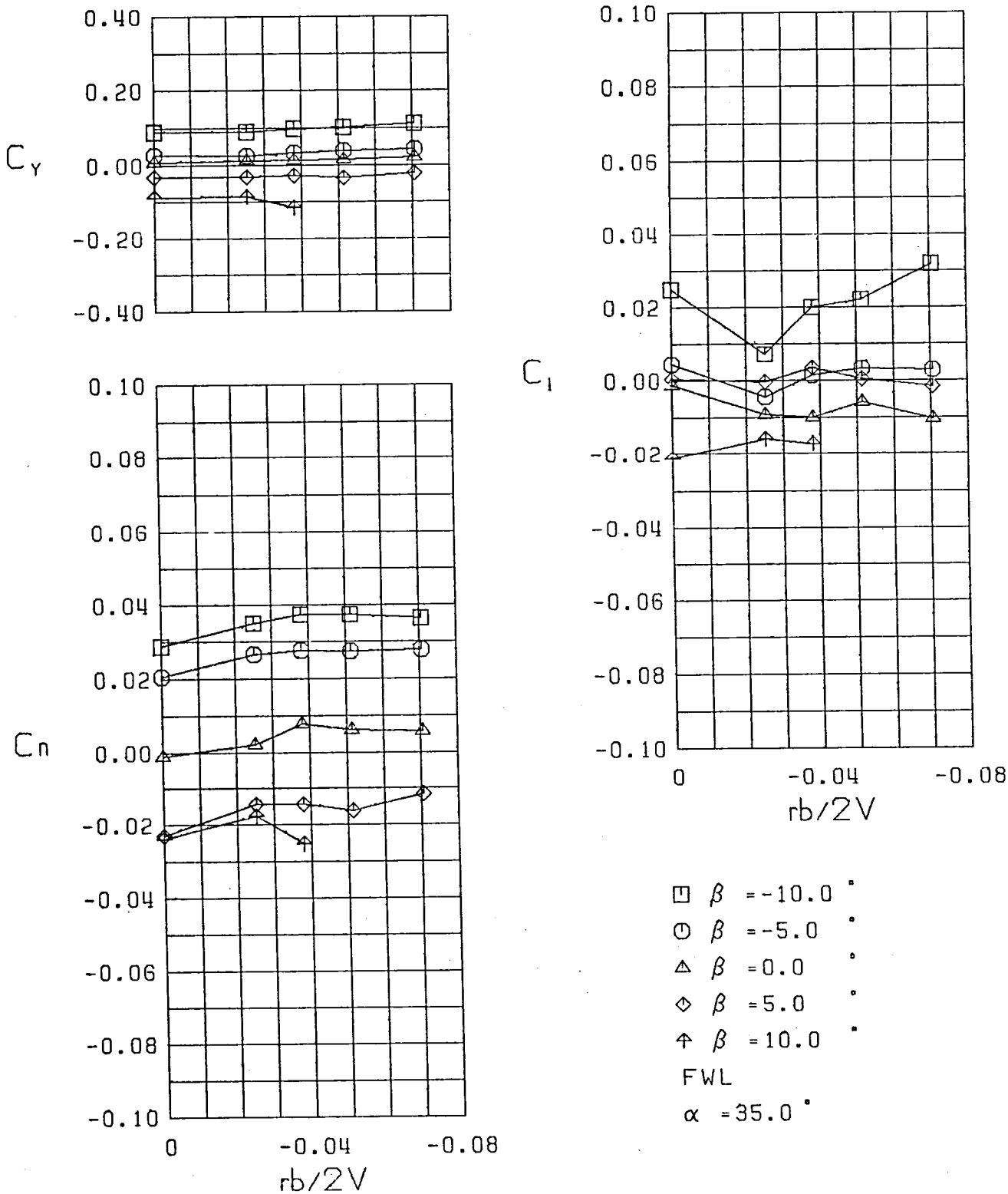

Figure 27 (Continued)

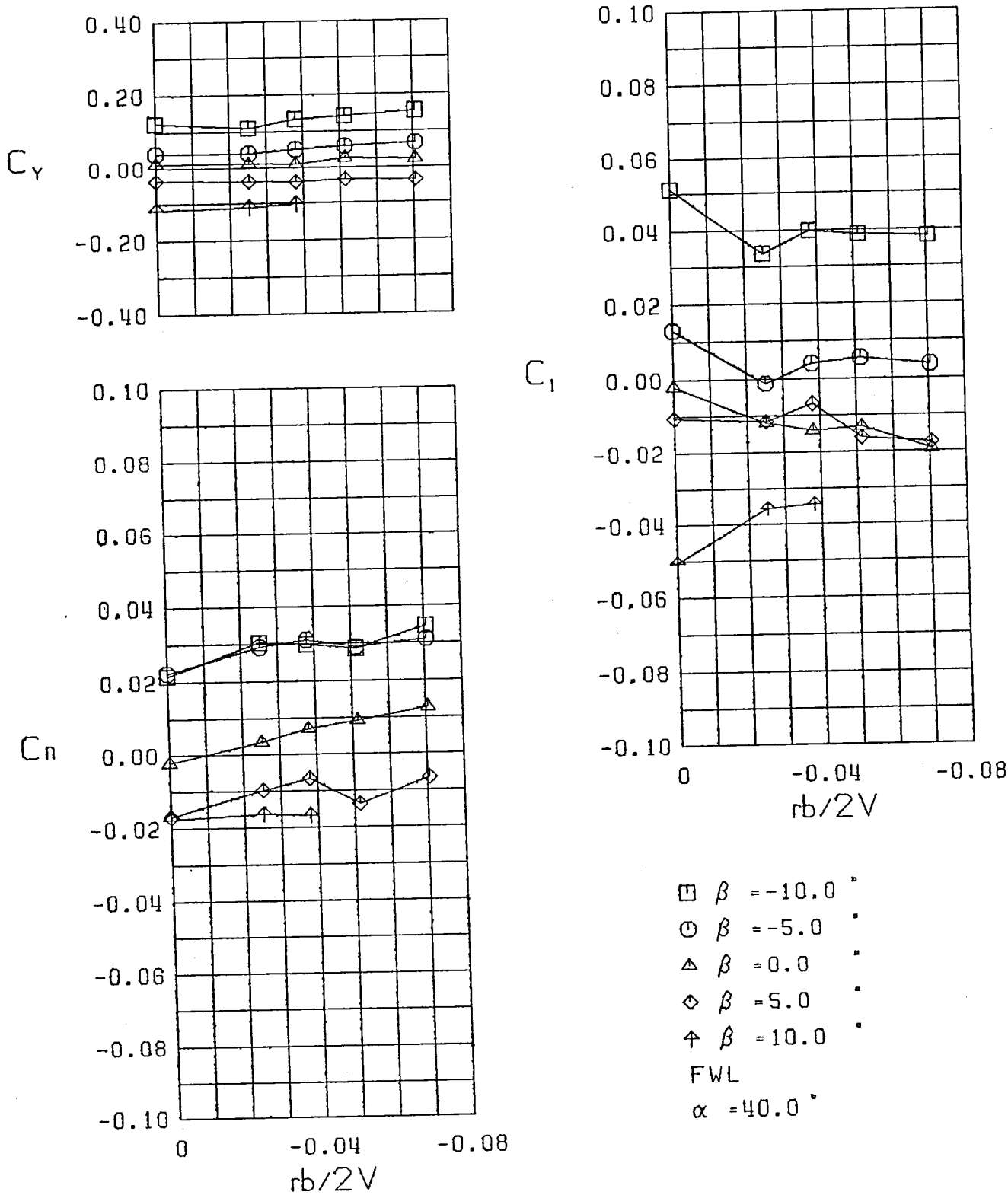

Figure 27 (Continued)

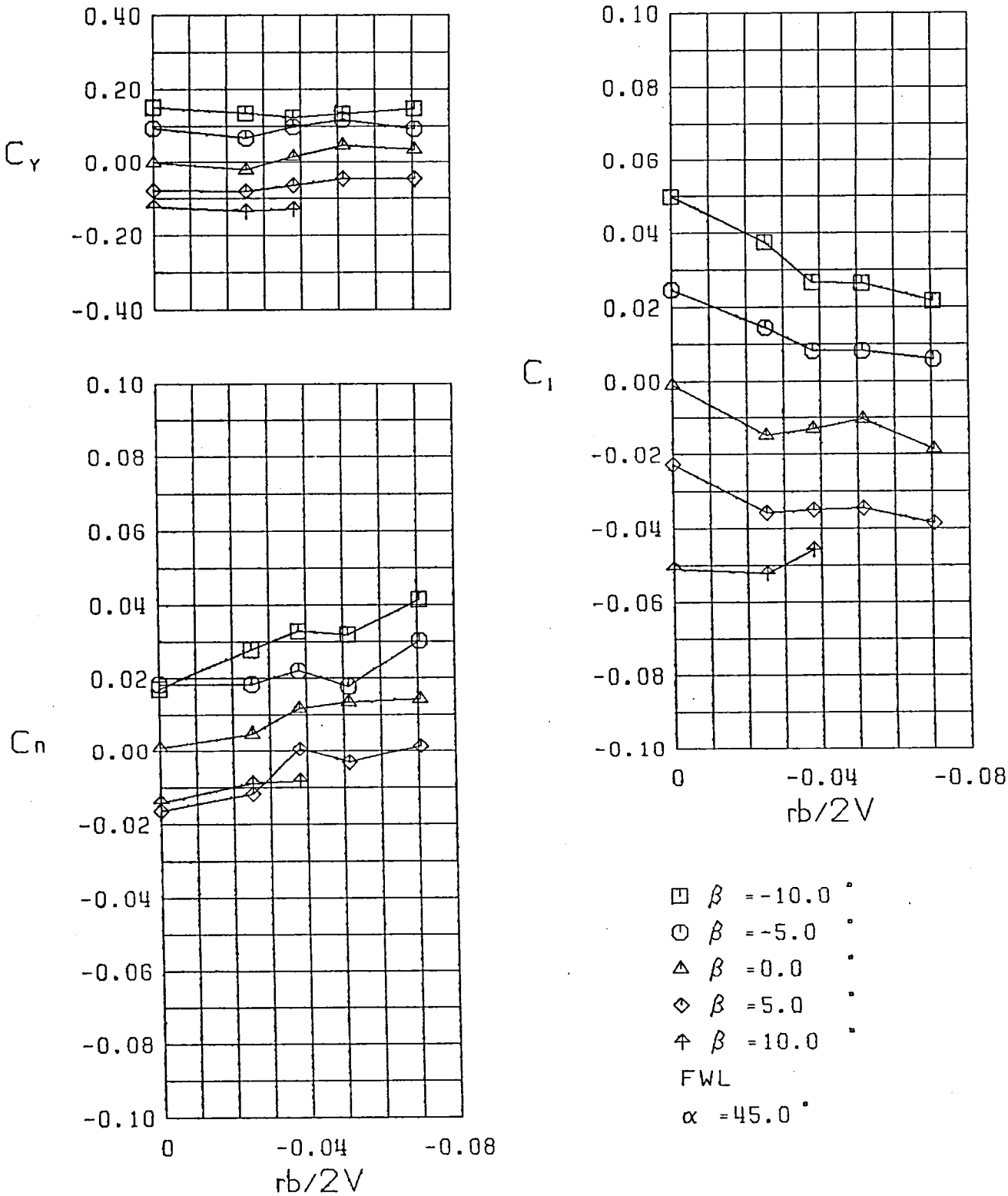

Figure 27 (Continued)

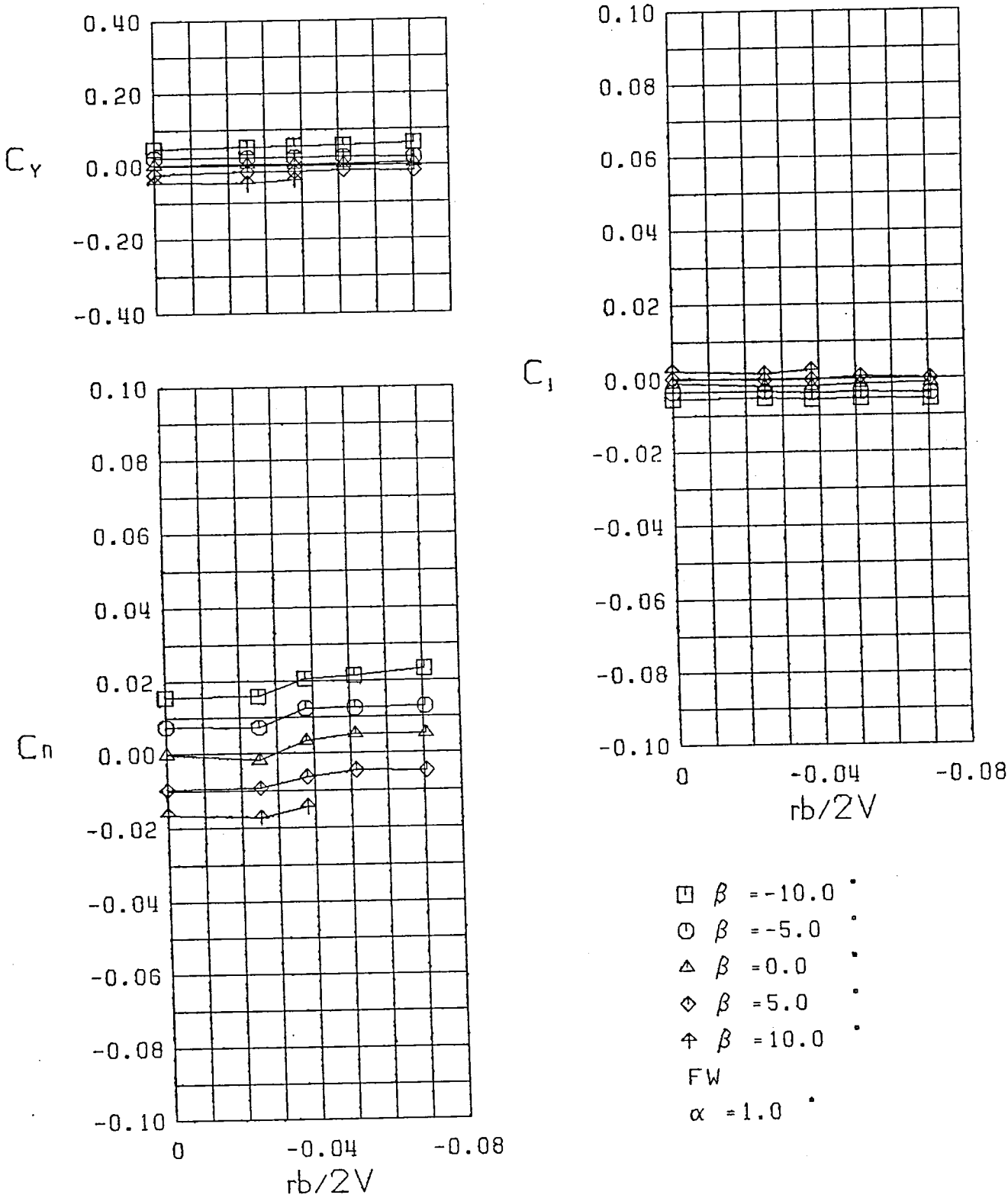

Figure 28 Variations of Static Lateral-Directional Stability Derivatives with Yaw Rate, Configuration 14

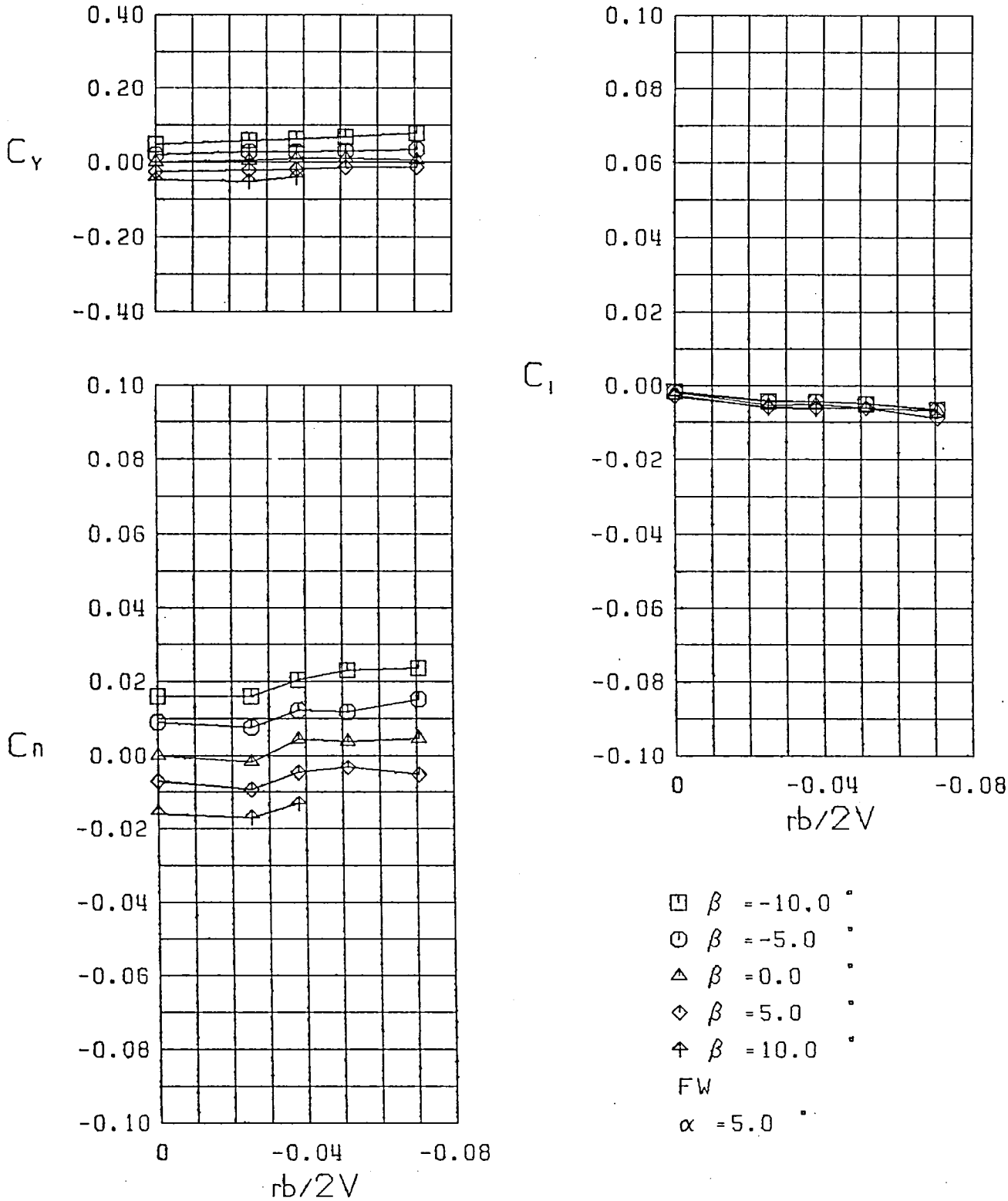

Figure 28 (Continued)

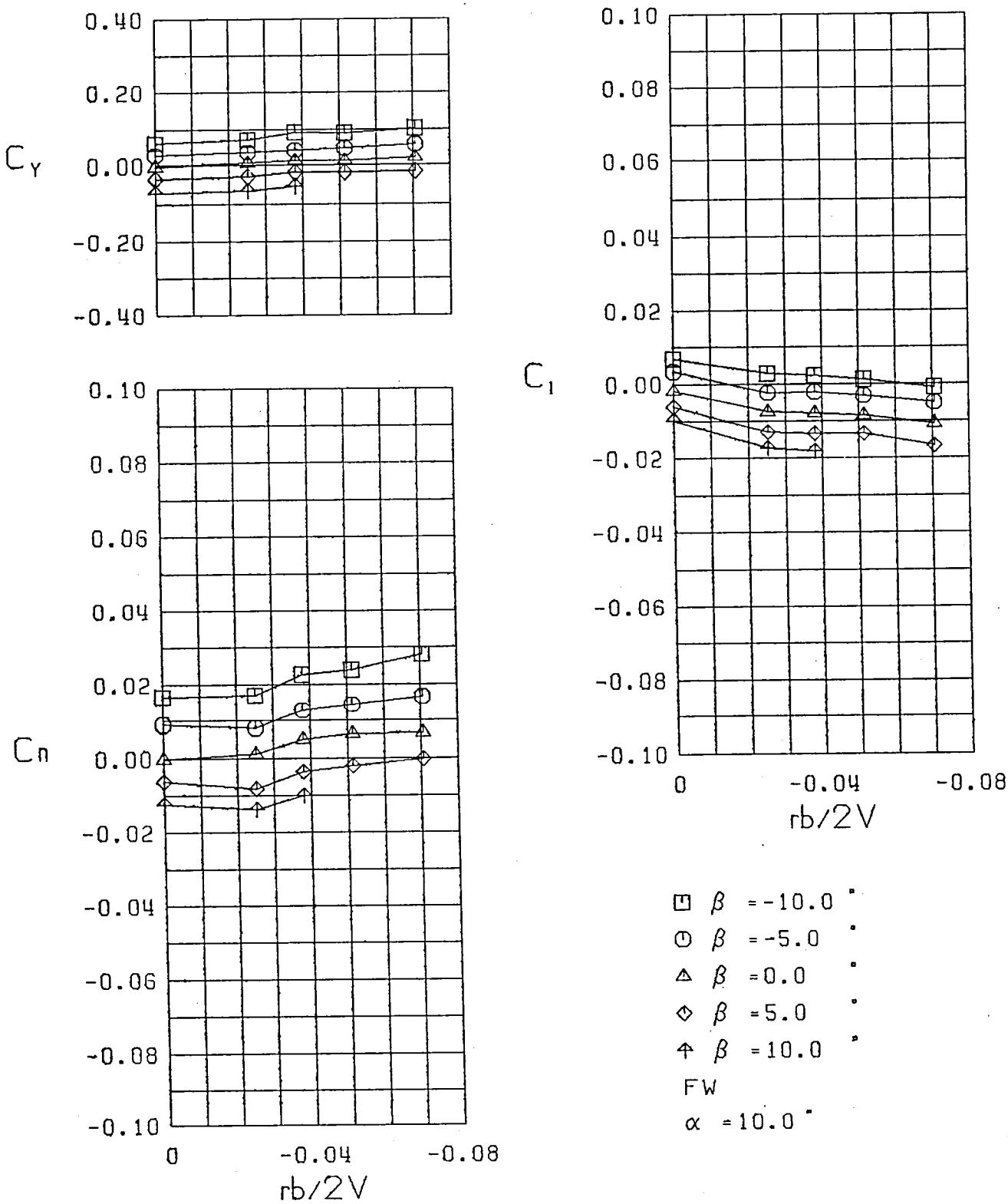

Figure 28 (Continued)

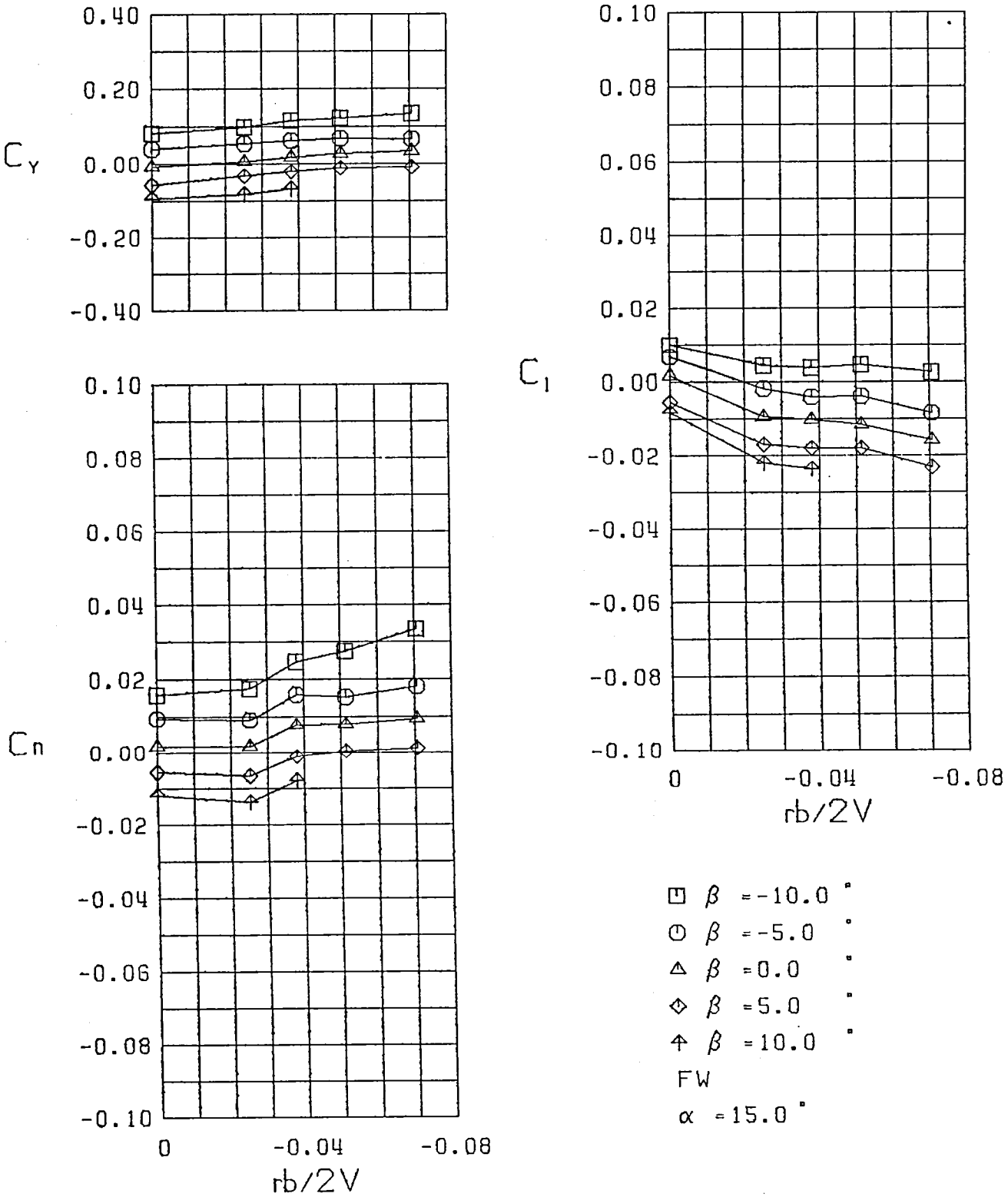

Figure 28 (Continued)

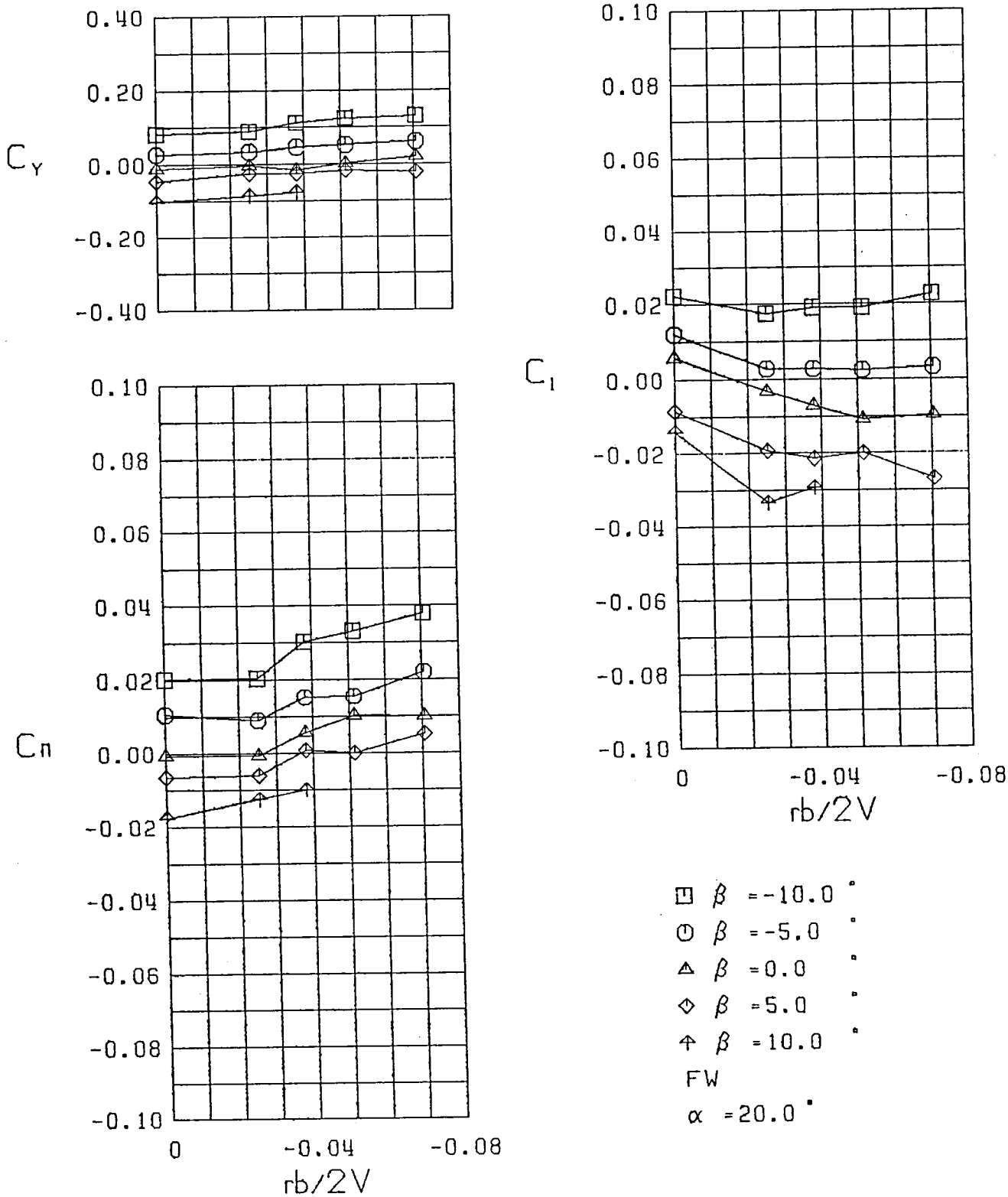

Firgure 28 (Continued)

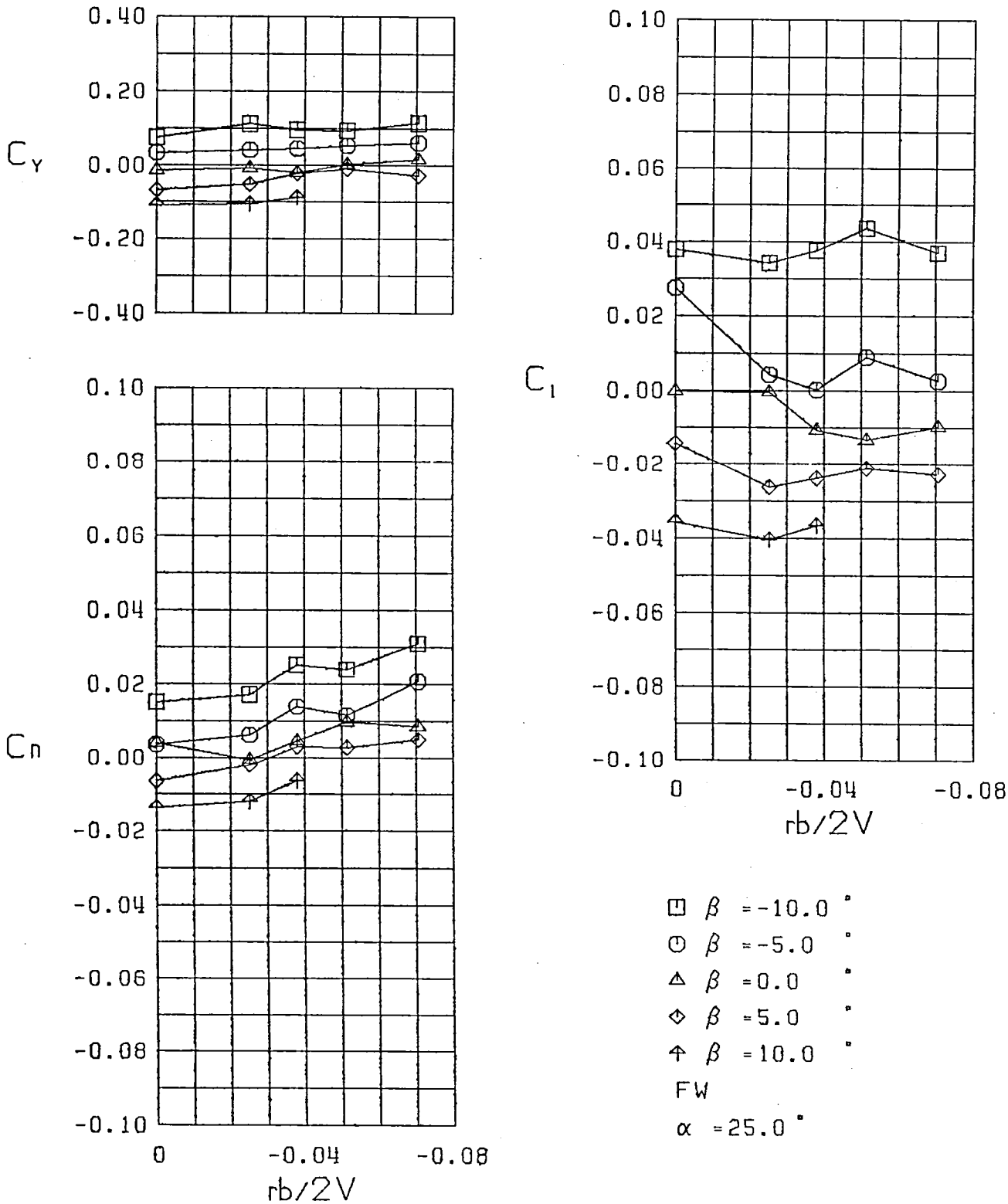

Figure 28 (Continued)

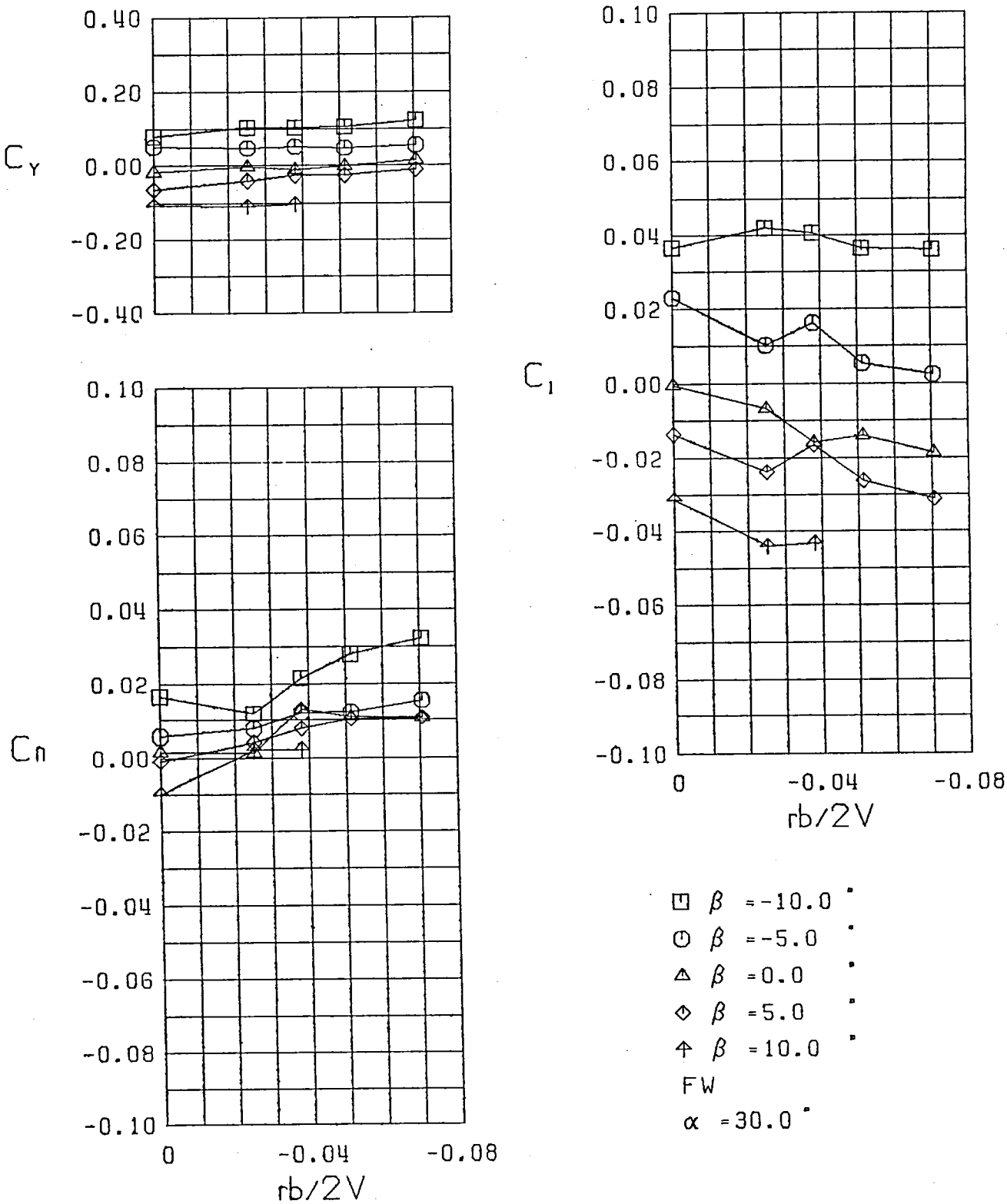

Figure 28 (Continued)

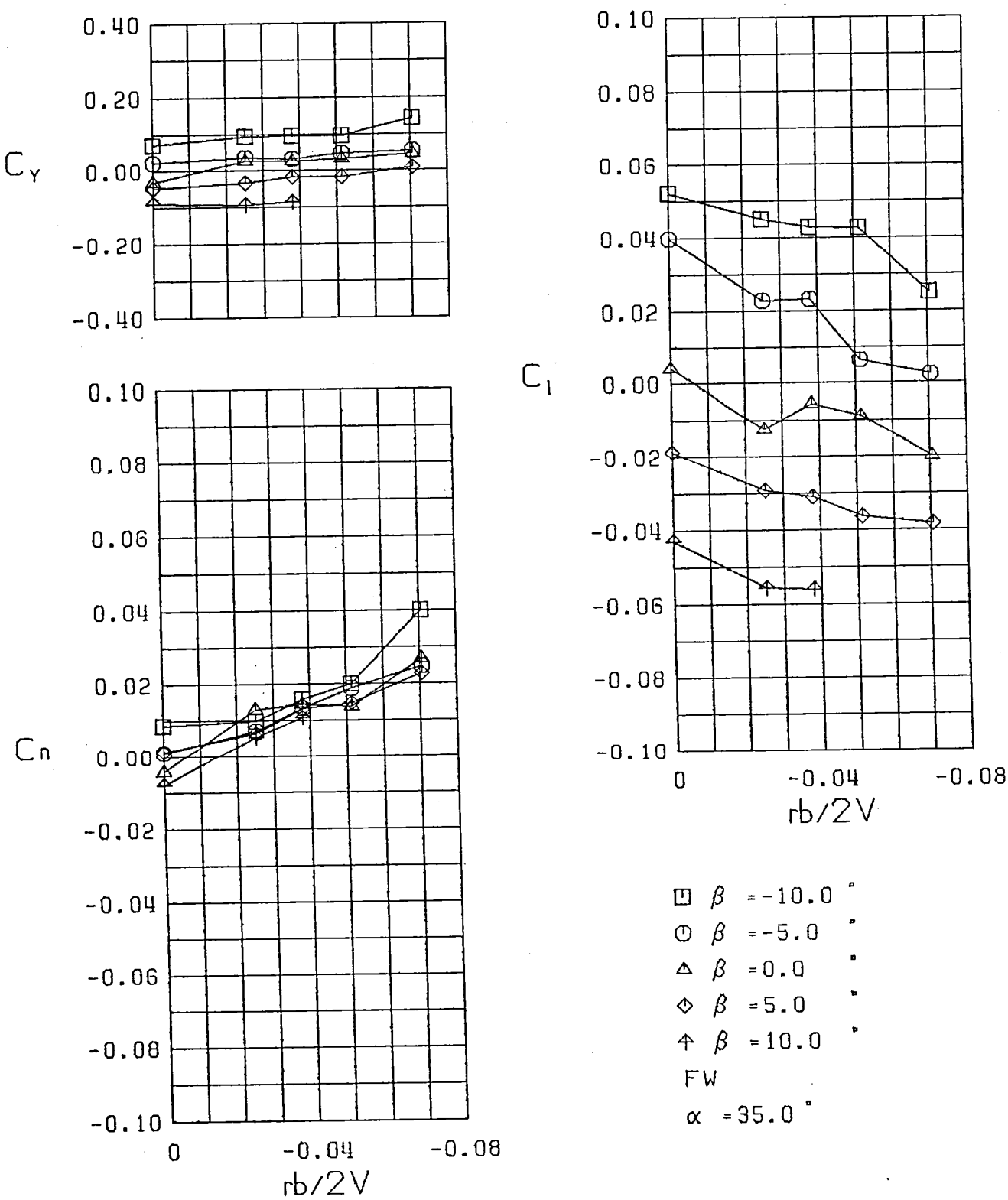

Figure 28 (Continued)

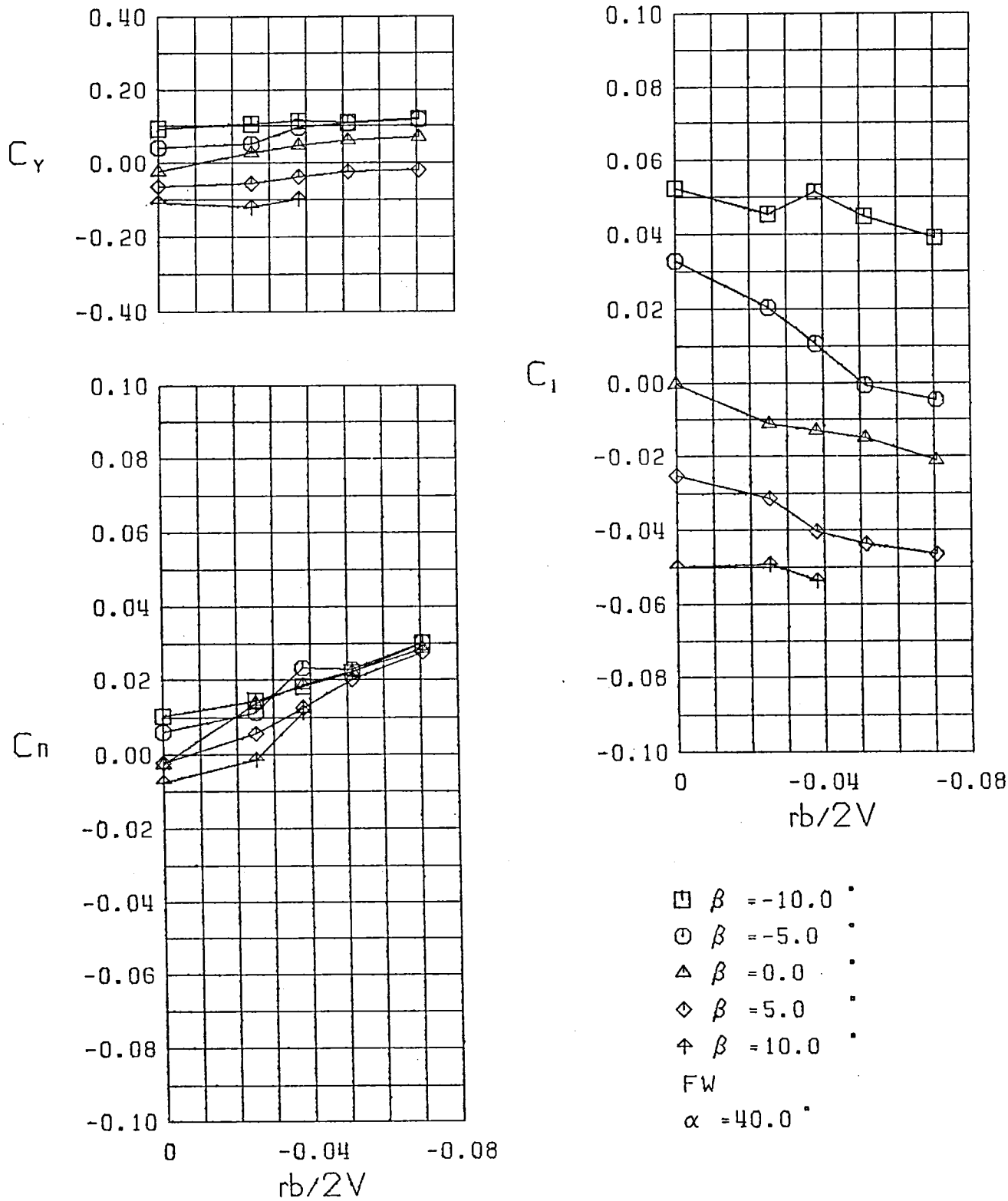

Figure 28 (Continued)

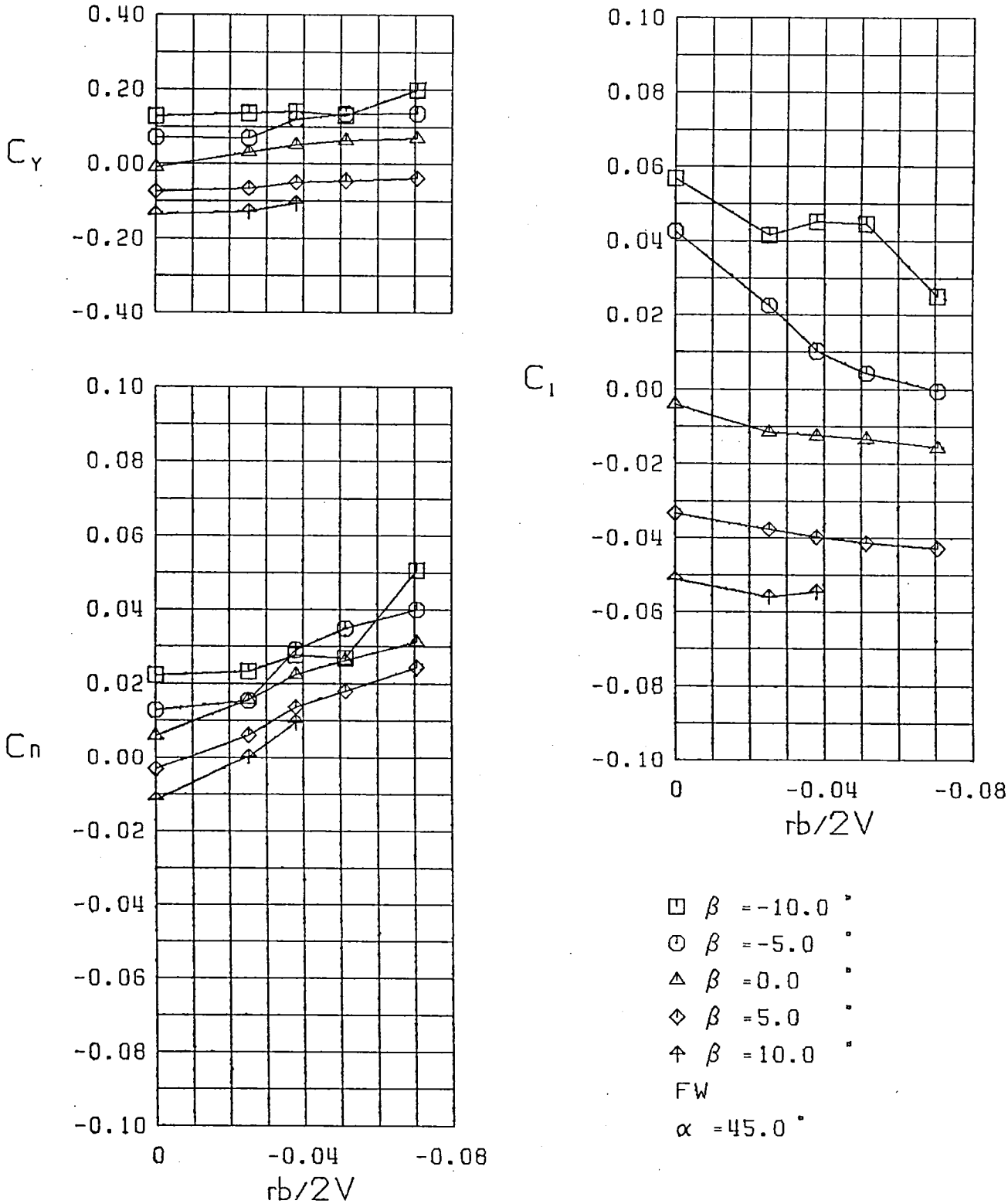

Figure 28 (Continued)

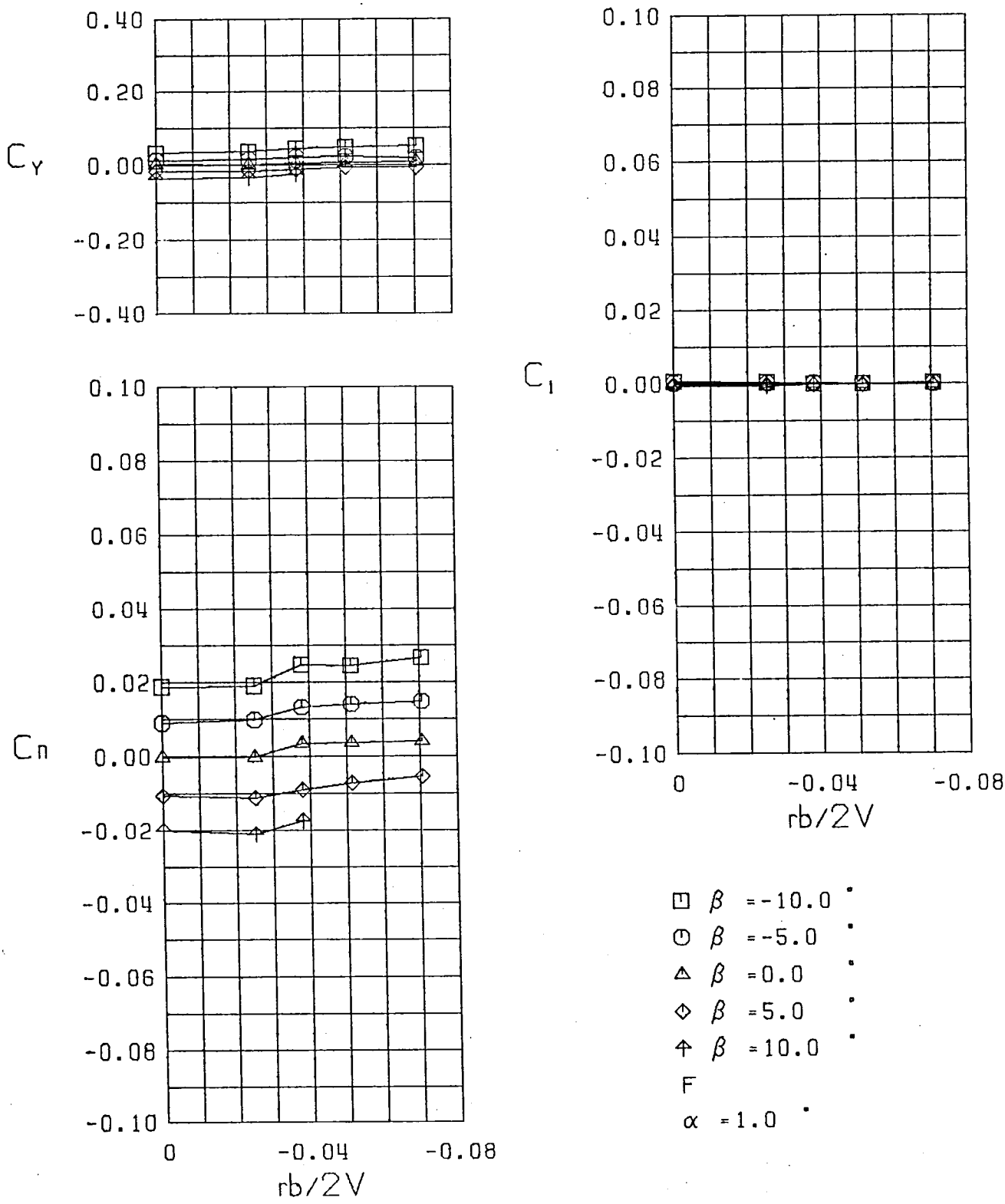

Figure 29 Variation of Static Lateral-Directional Stability Derivatives with Yaw Rate, Configuration 15

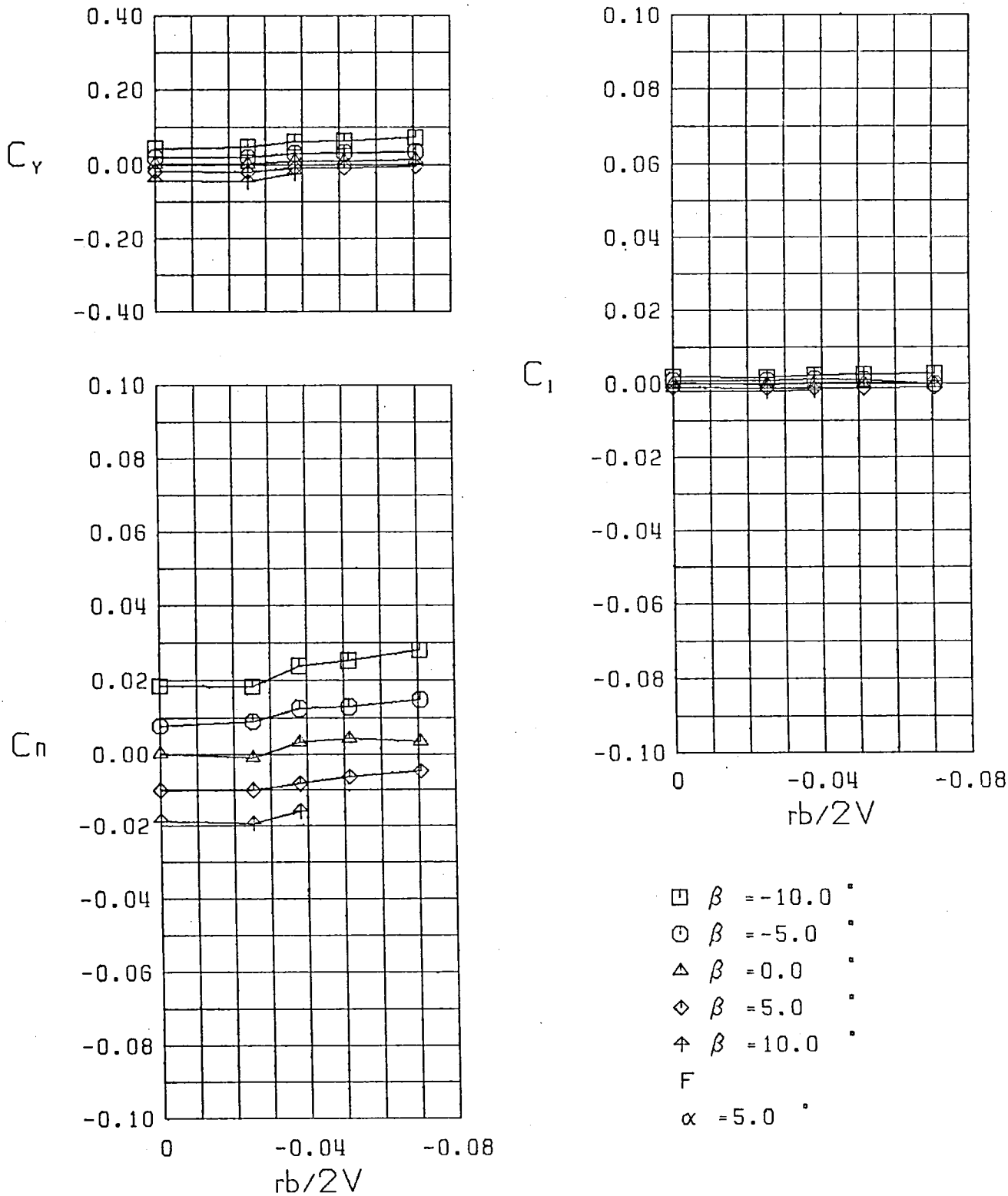

Figure 29 (Continued)

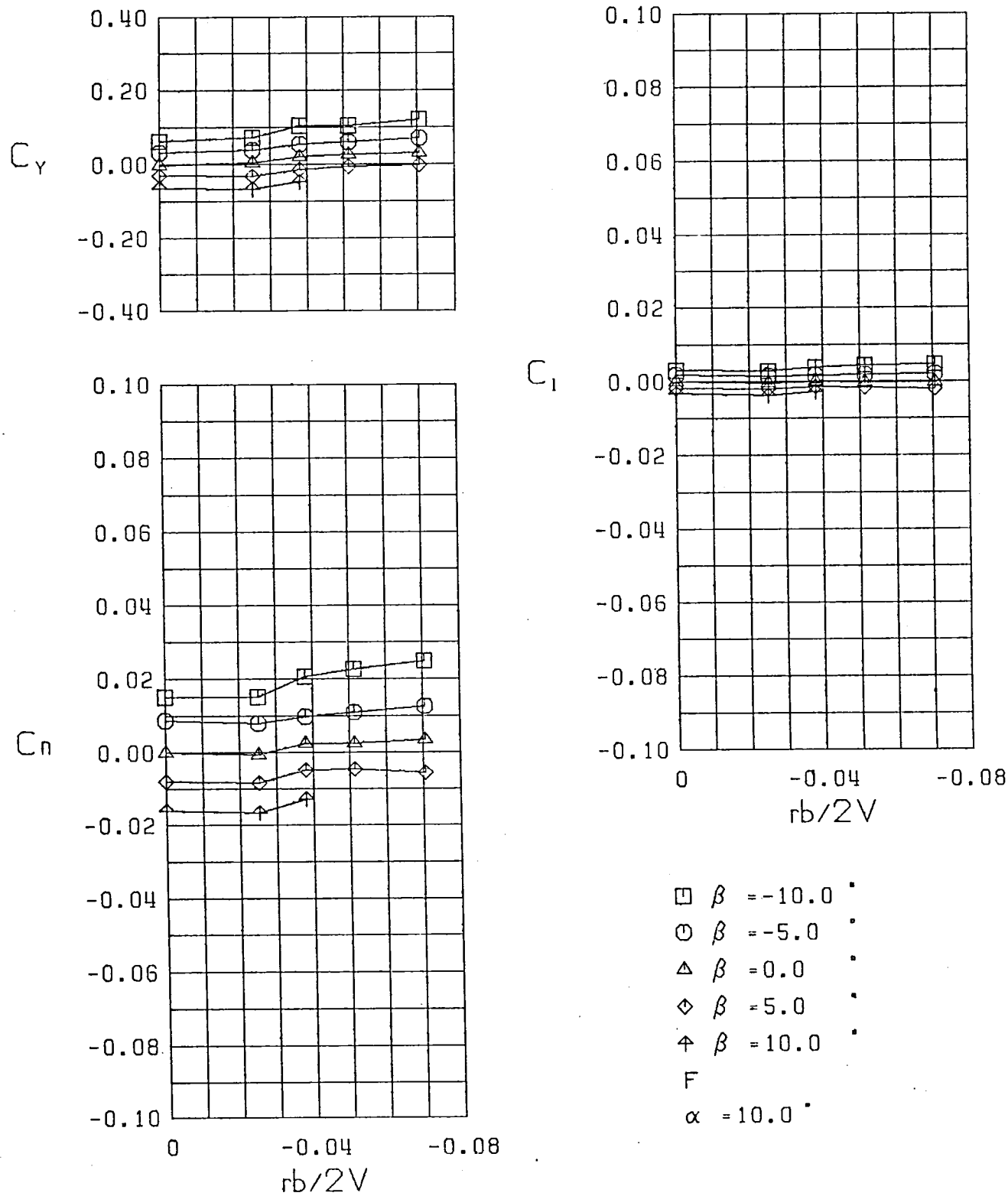

Figure 29 (Continued)

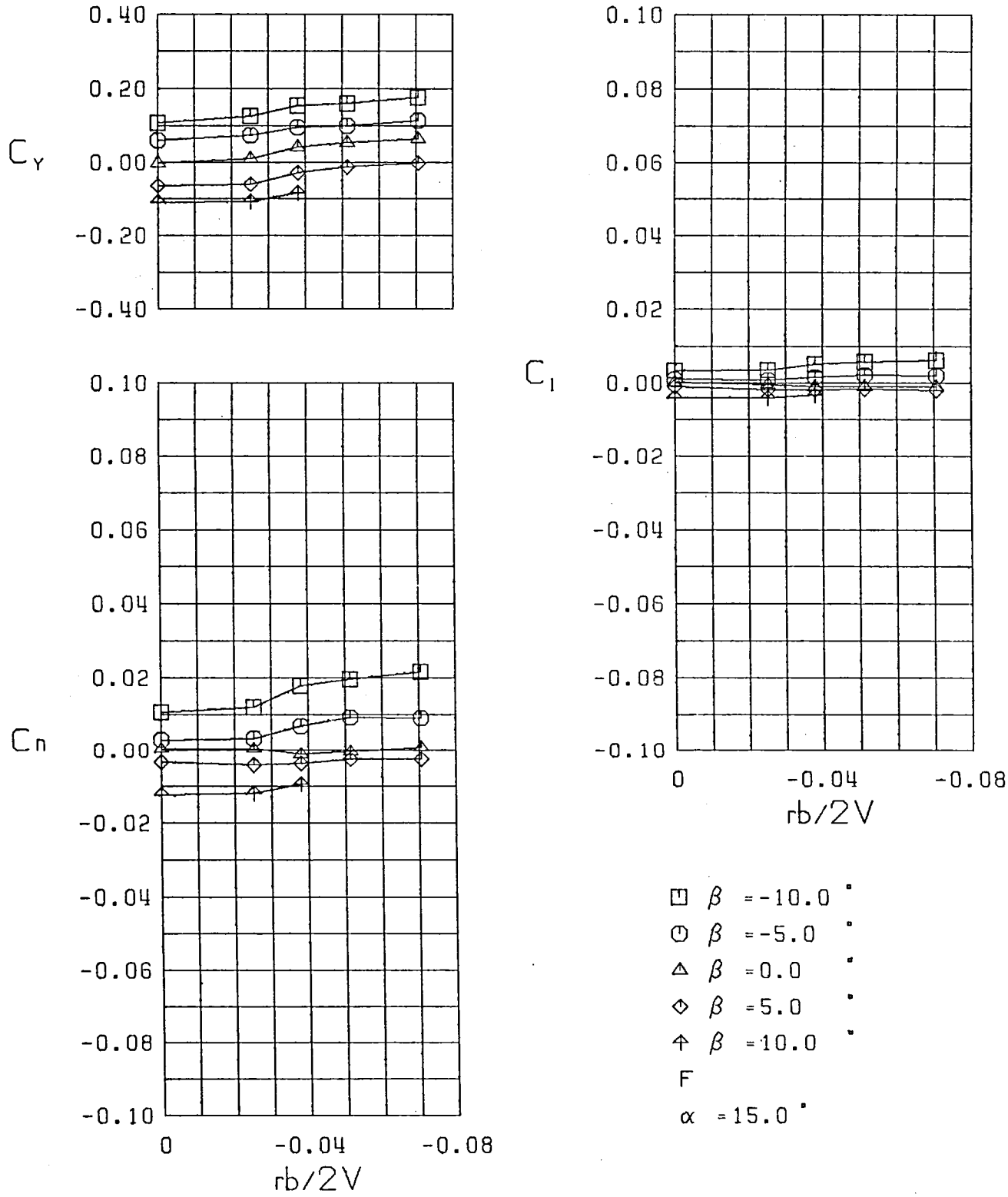

Figure 29 (Continued)

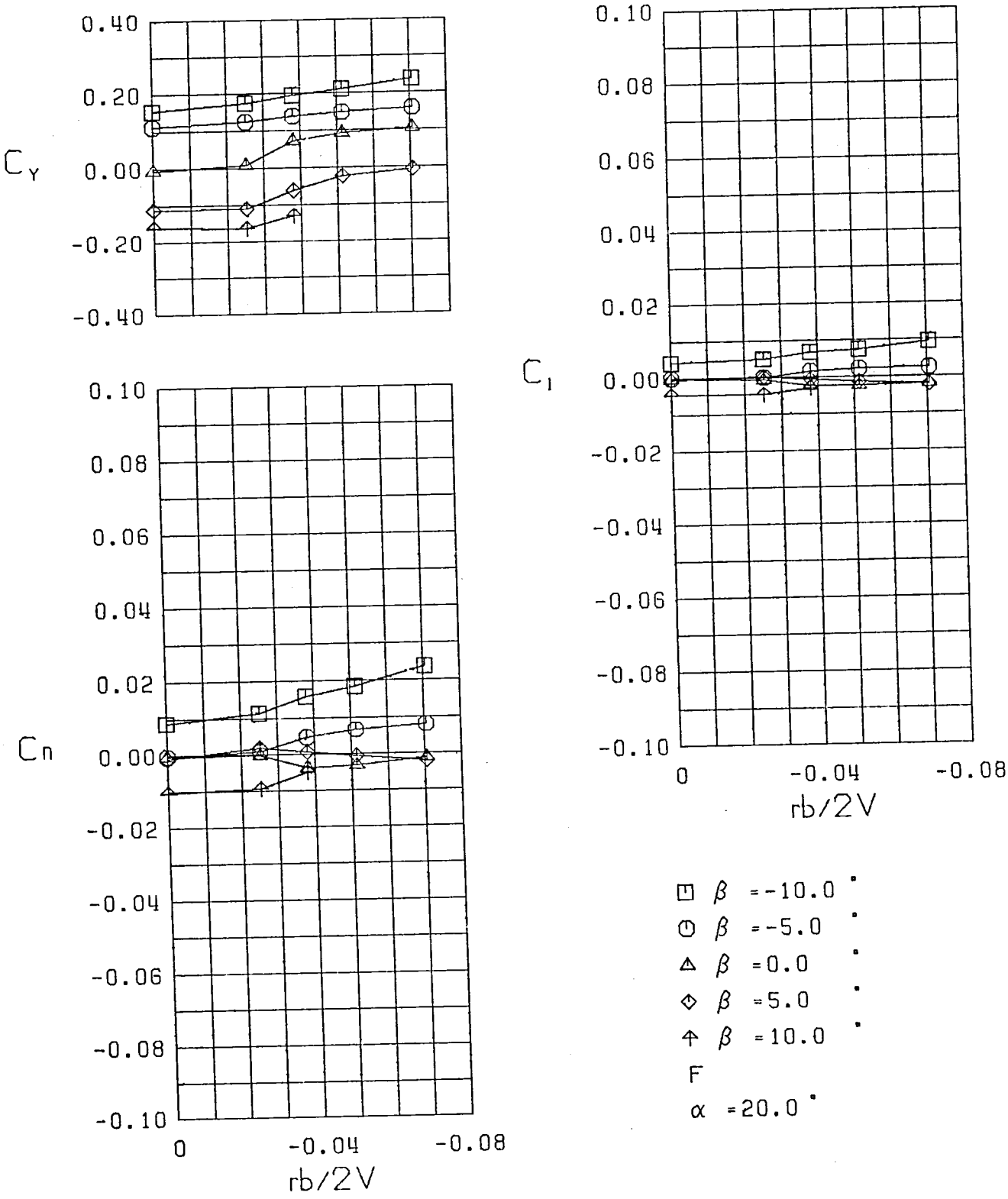

Figure 29 (Continued)

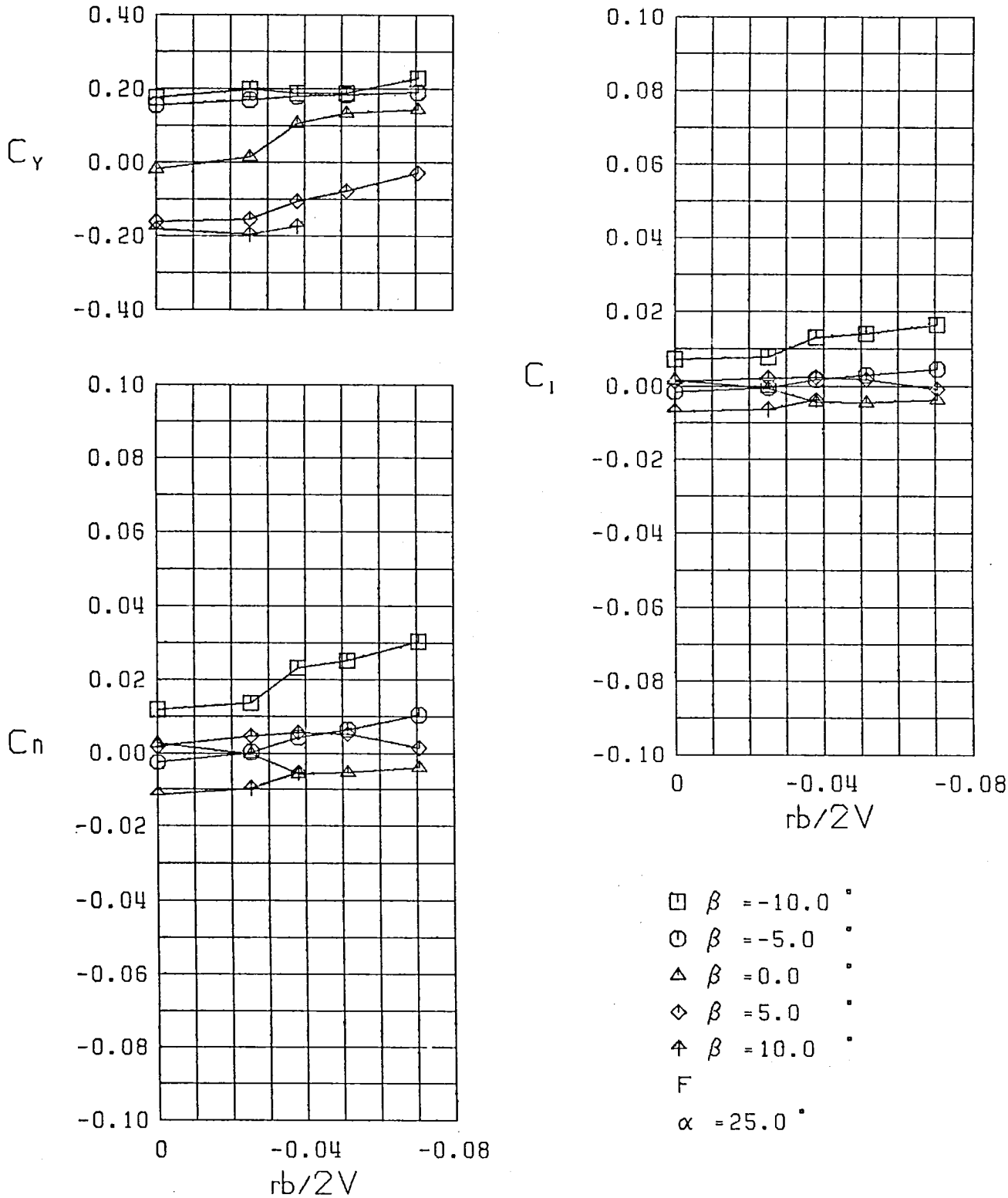

Figure 29 (Continued)

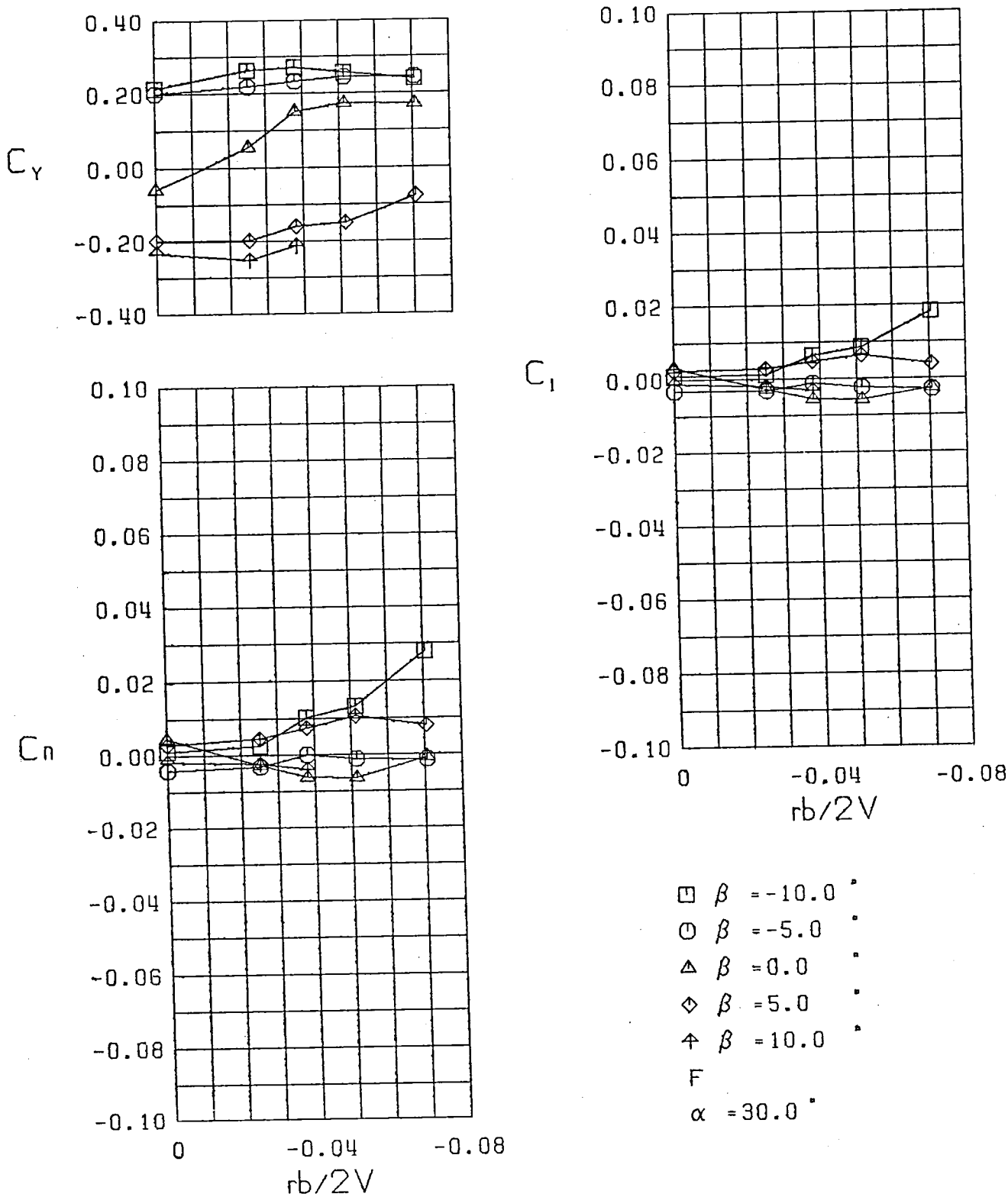

Figure 29 (Continued)

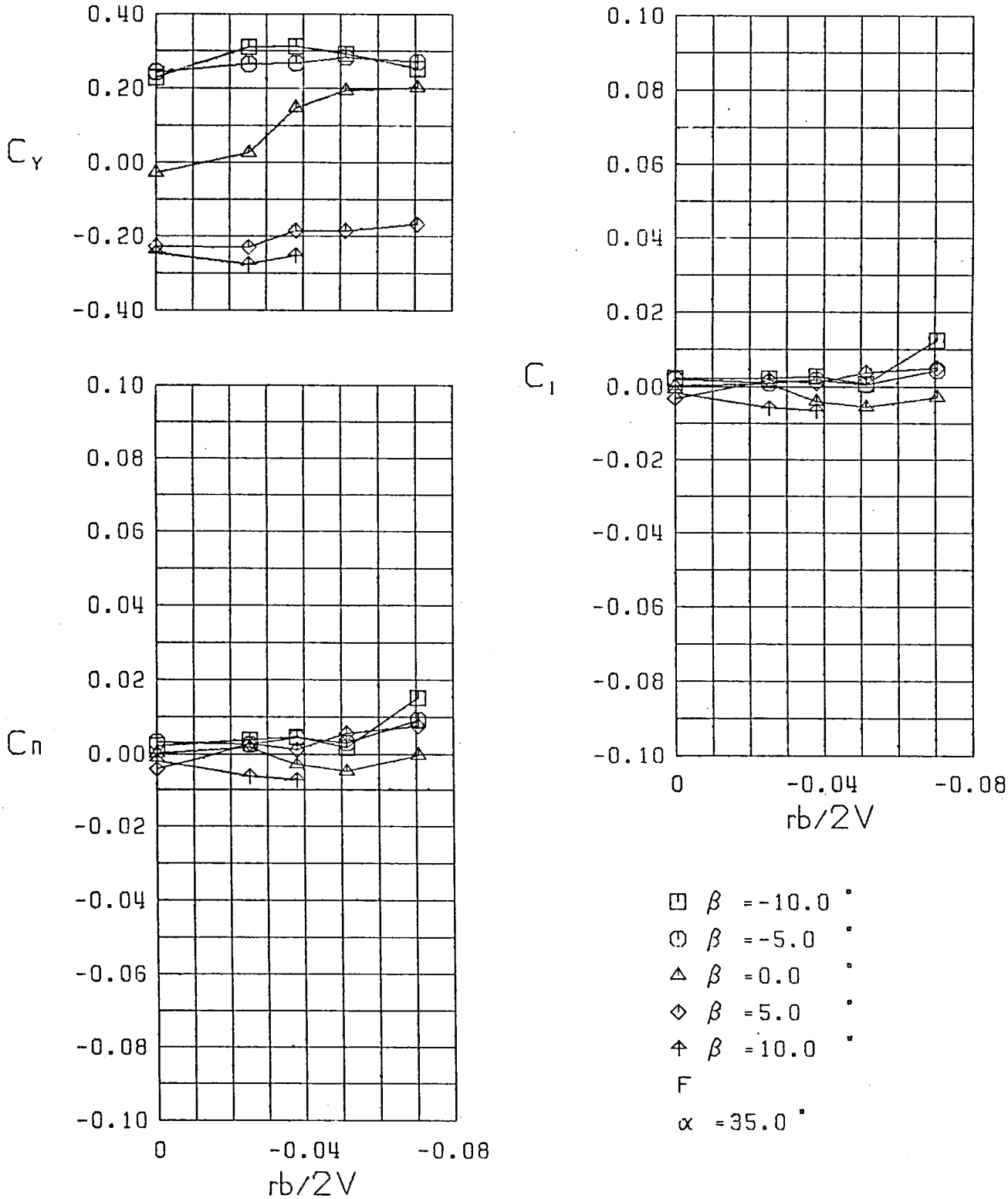

Figure 29 (Continued)

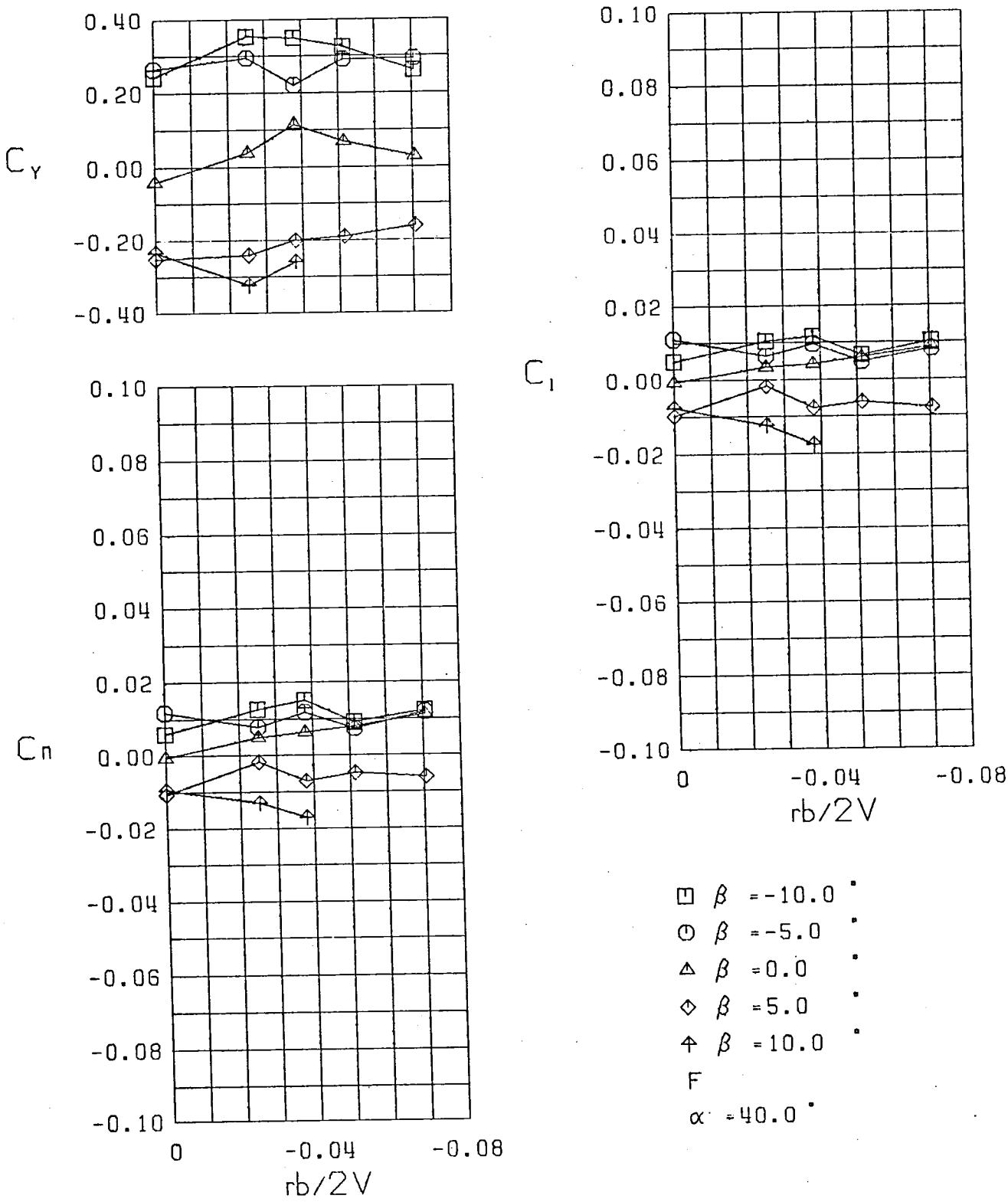

Figure 29 (Continued)

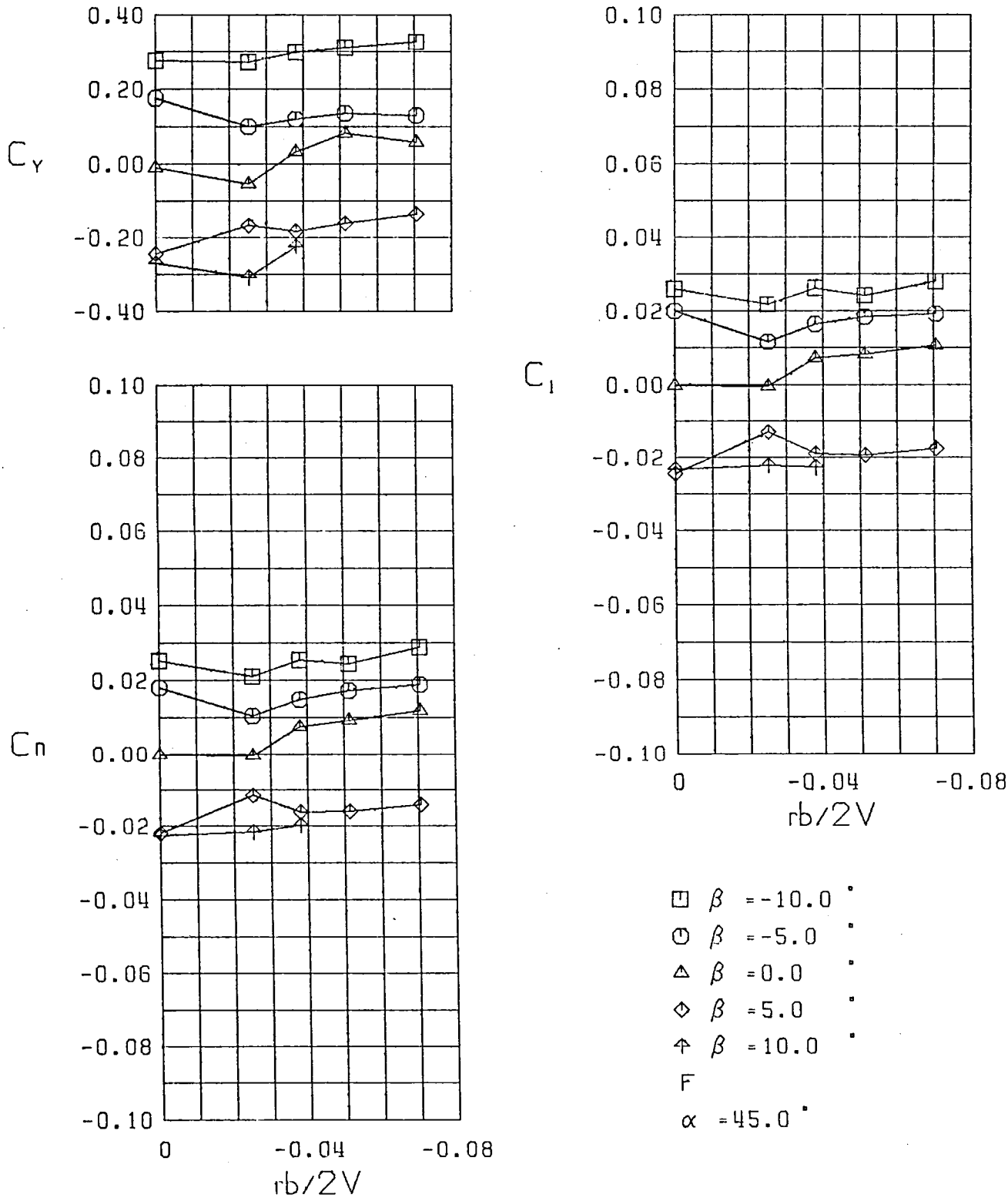

Figure 29 (Continued)

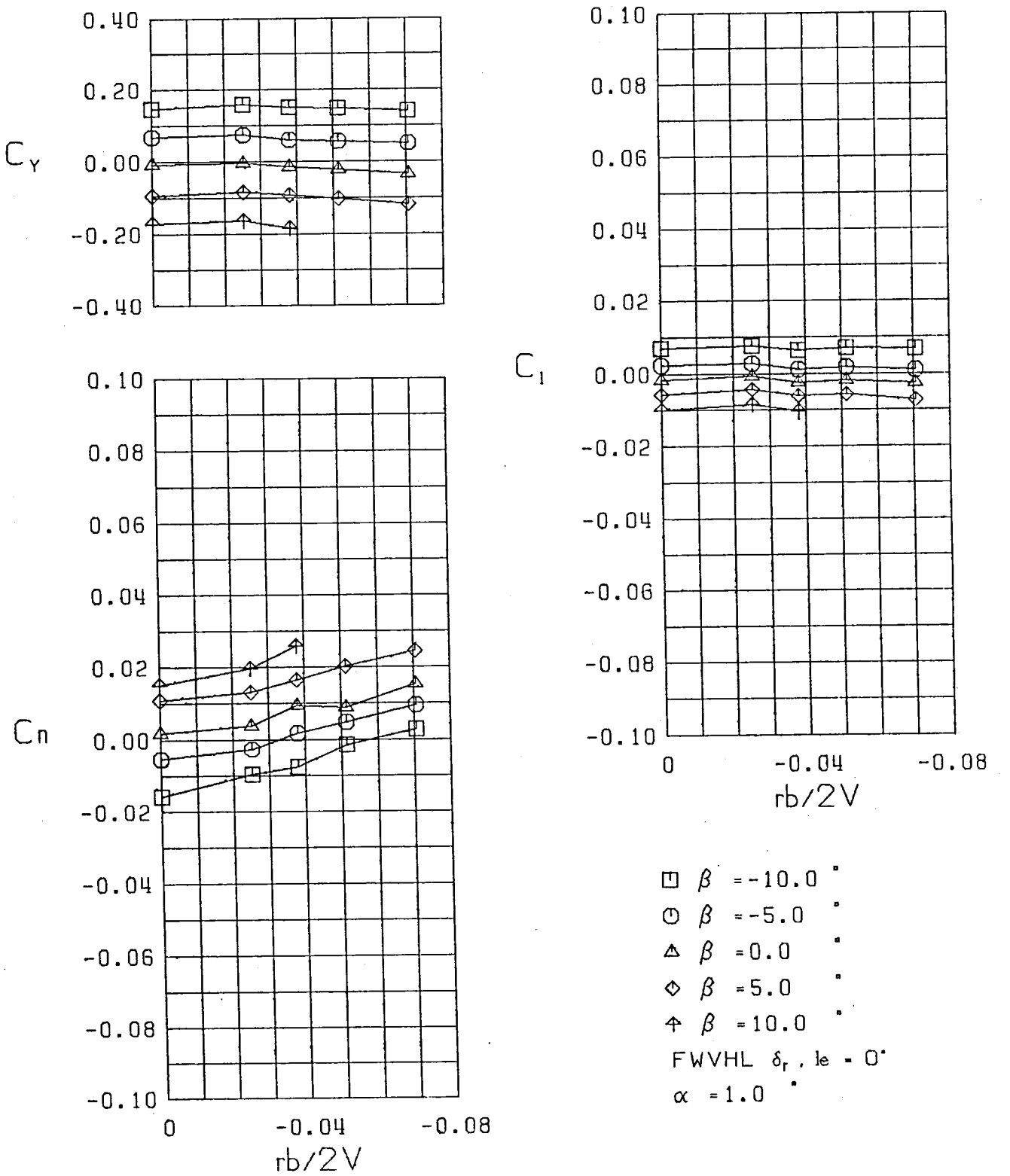

Figure 30 Variation of Static Lateral-Directional Stability Derivatives with Yaw Rate, Configuration 3

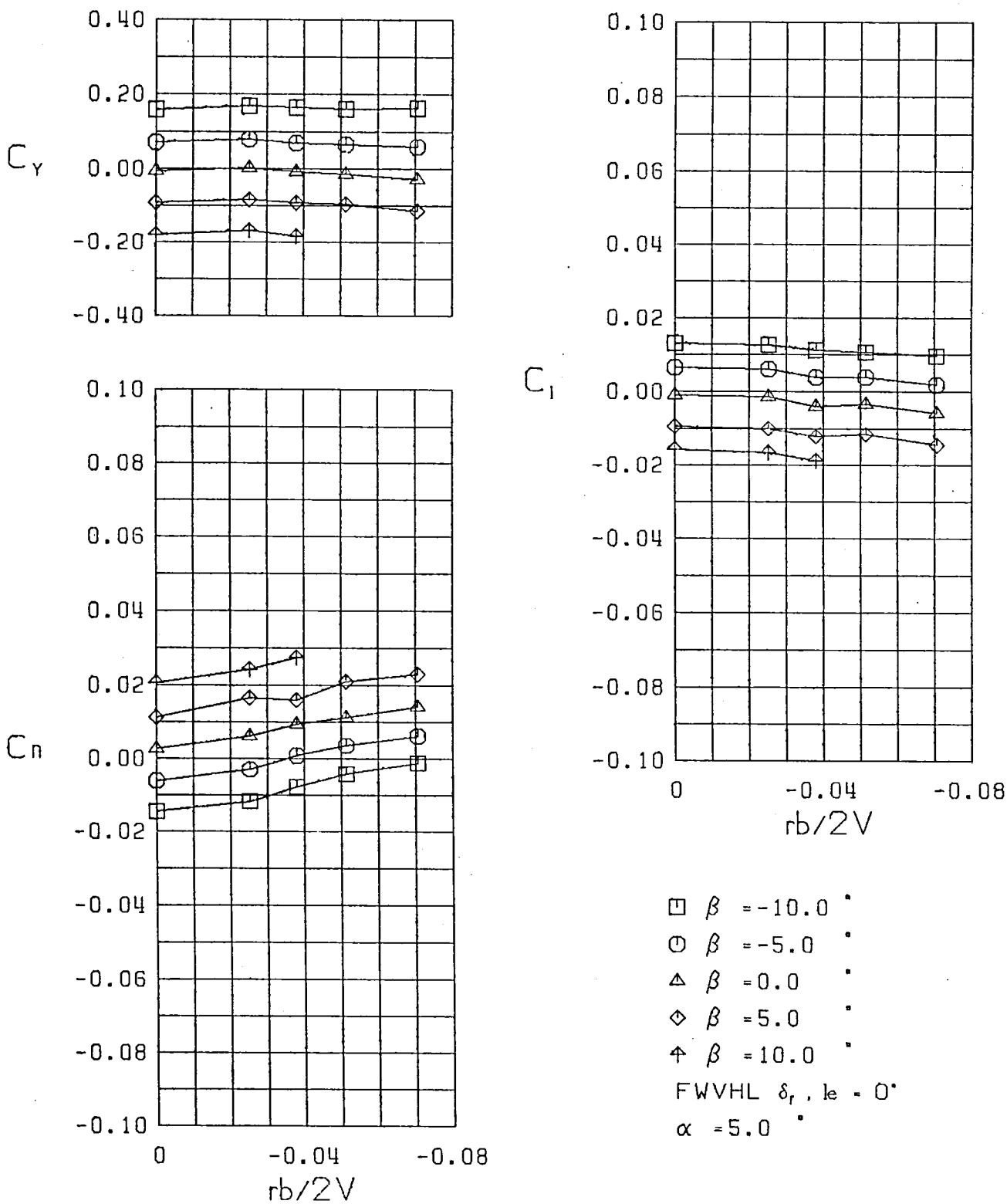

Figure 30 (Continued)

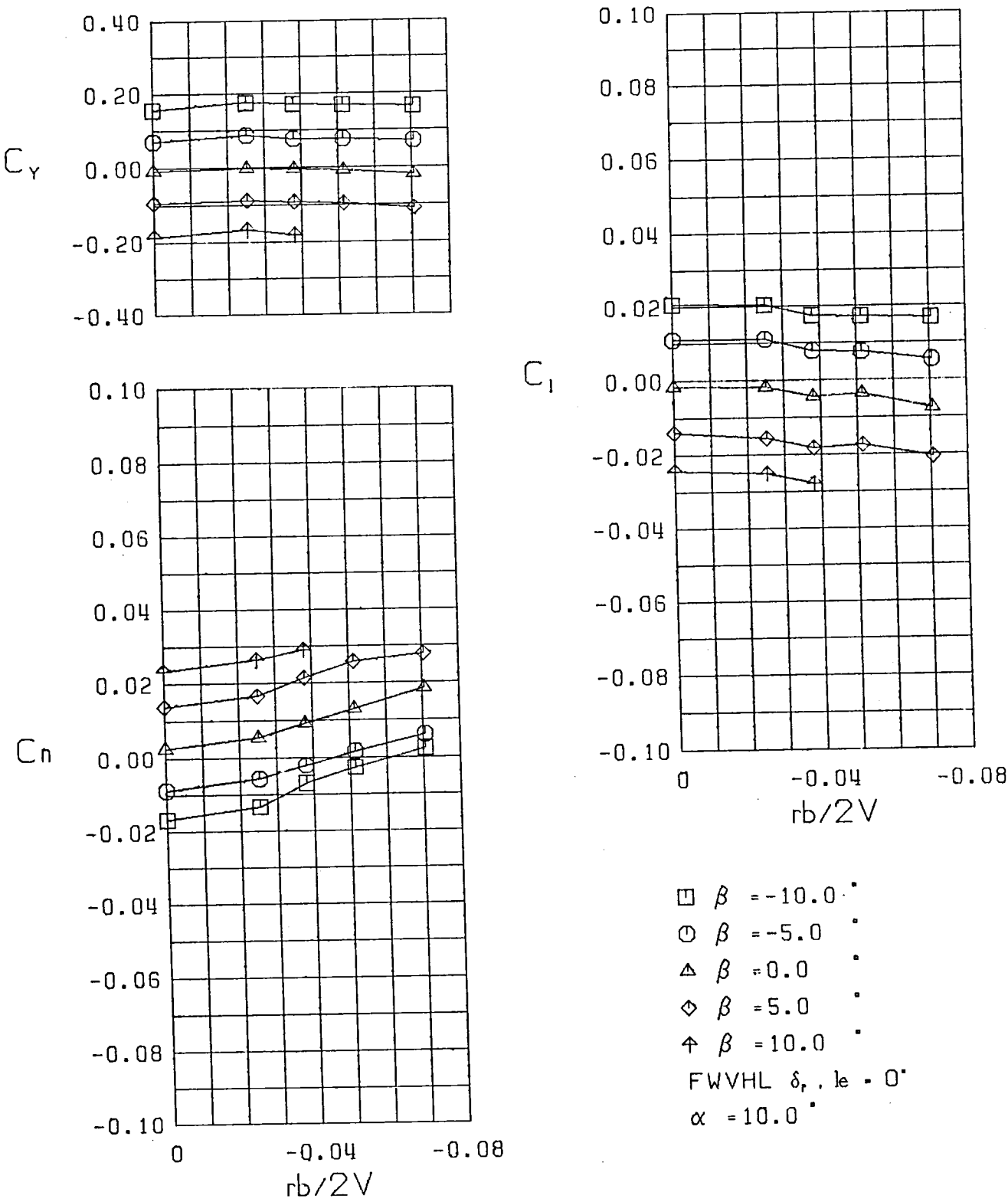

Figure 30 (Continued)

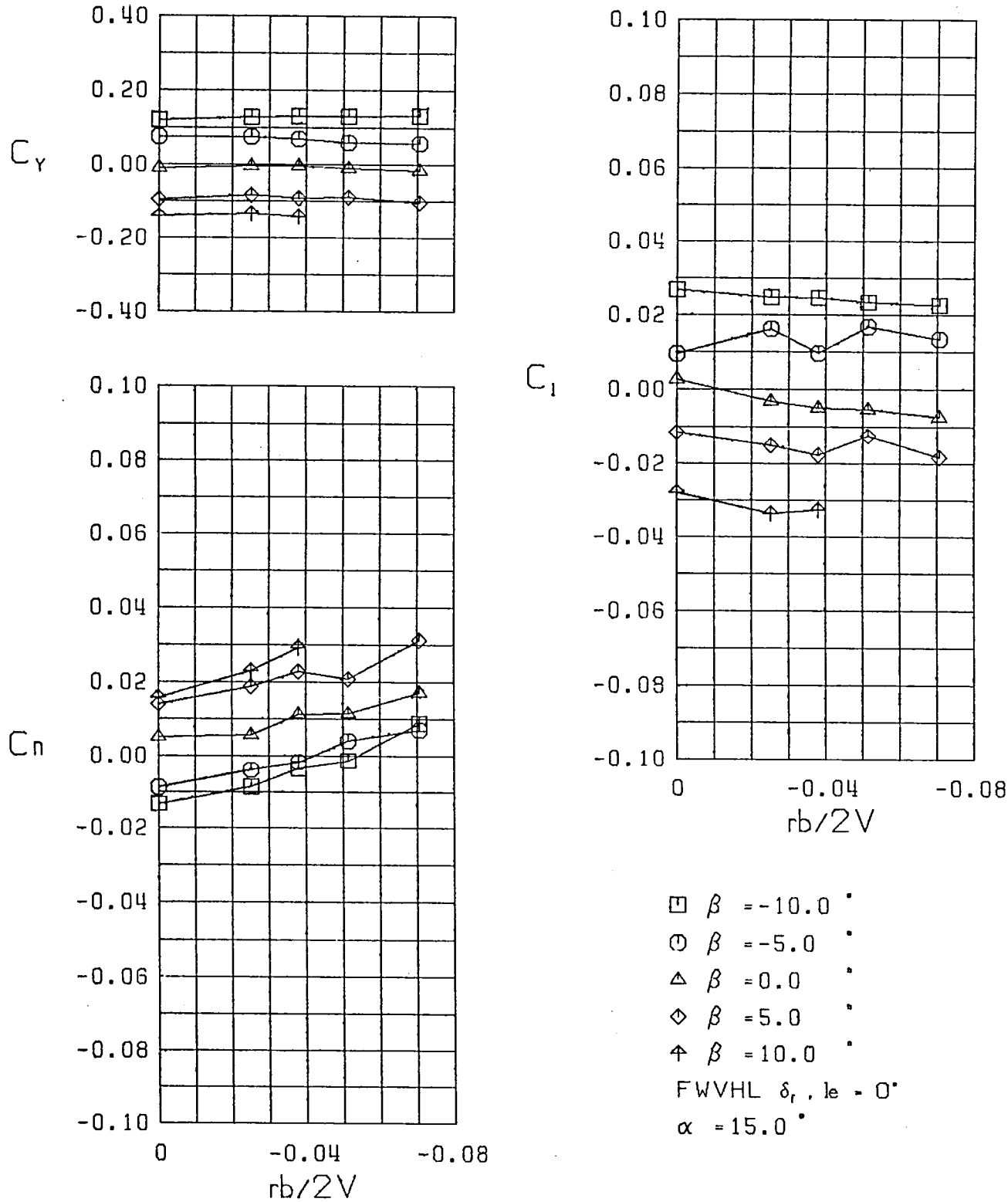

Figure 30 (Continued)

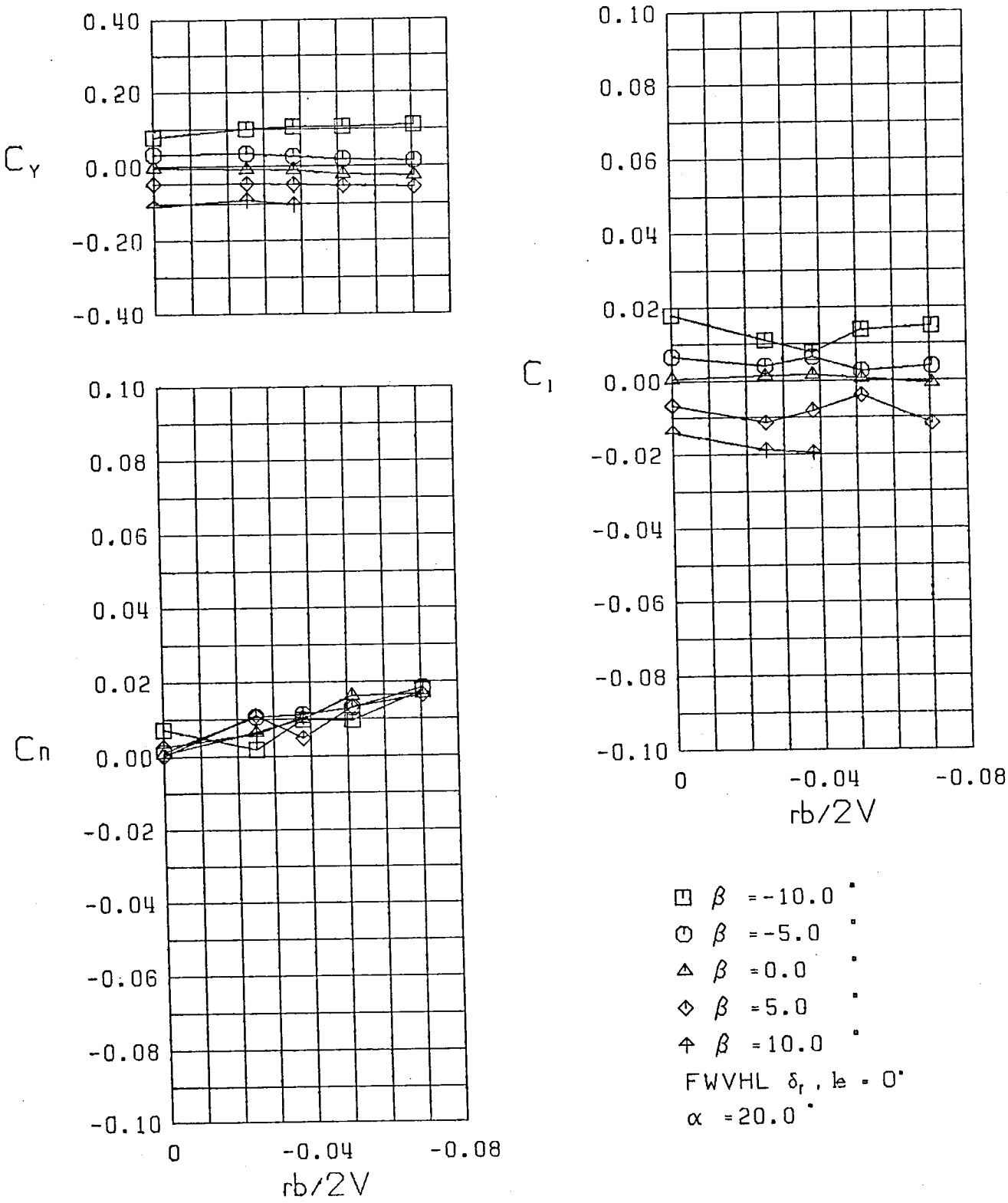

Figure 30 (Continued)

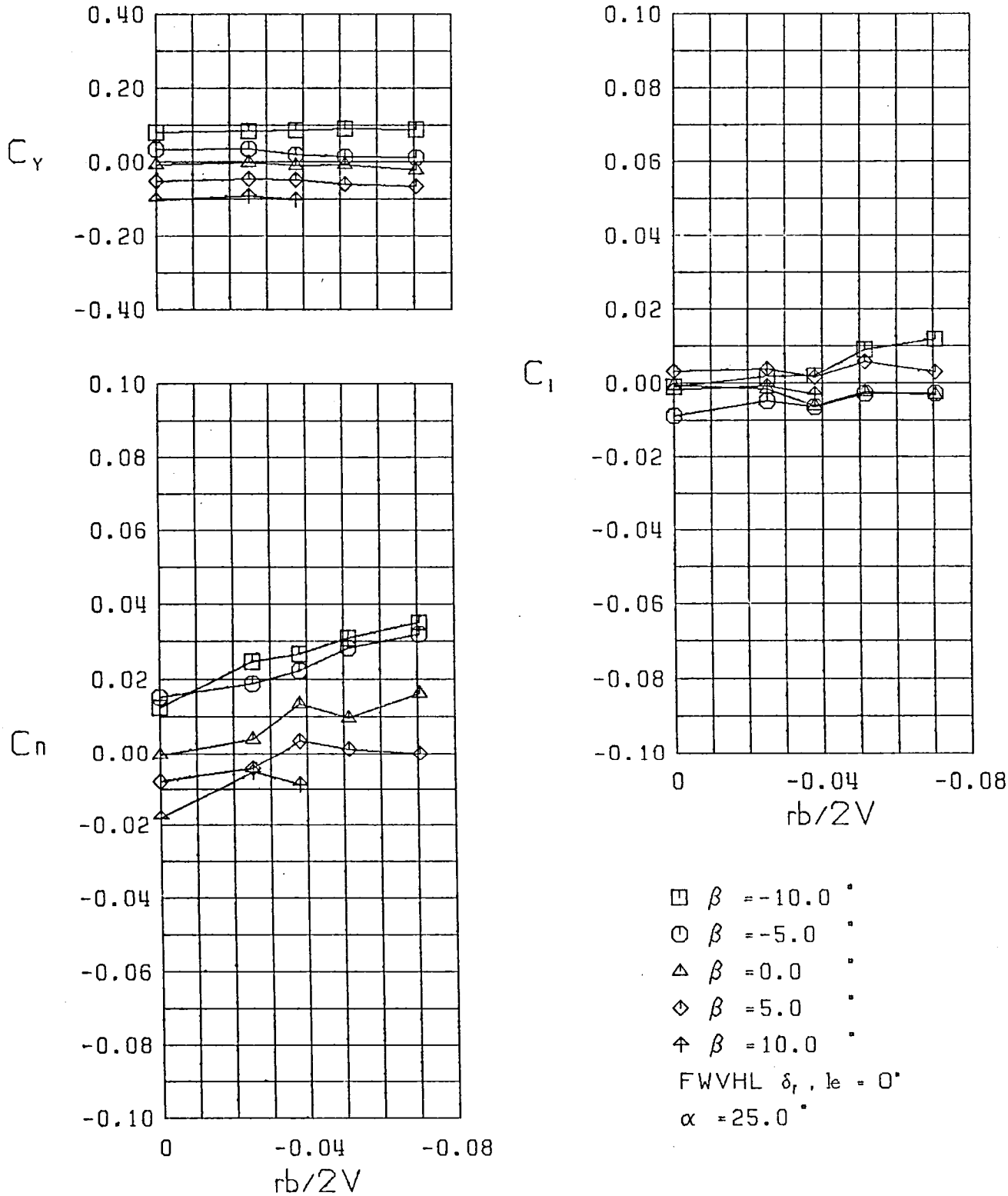

Figure 30 (Continued)

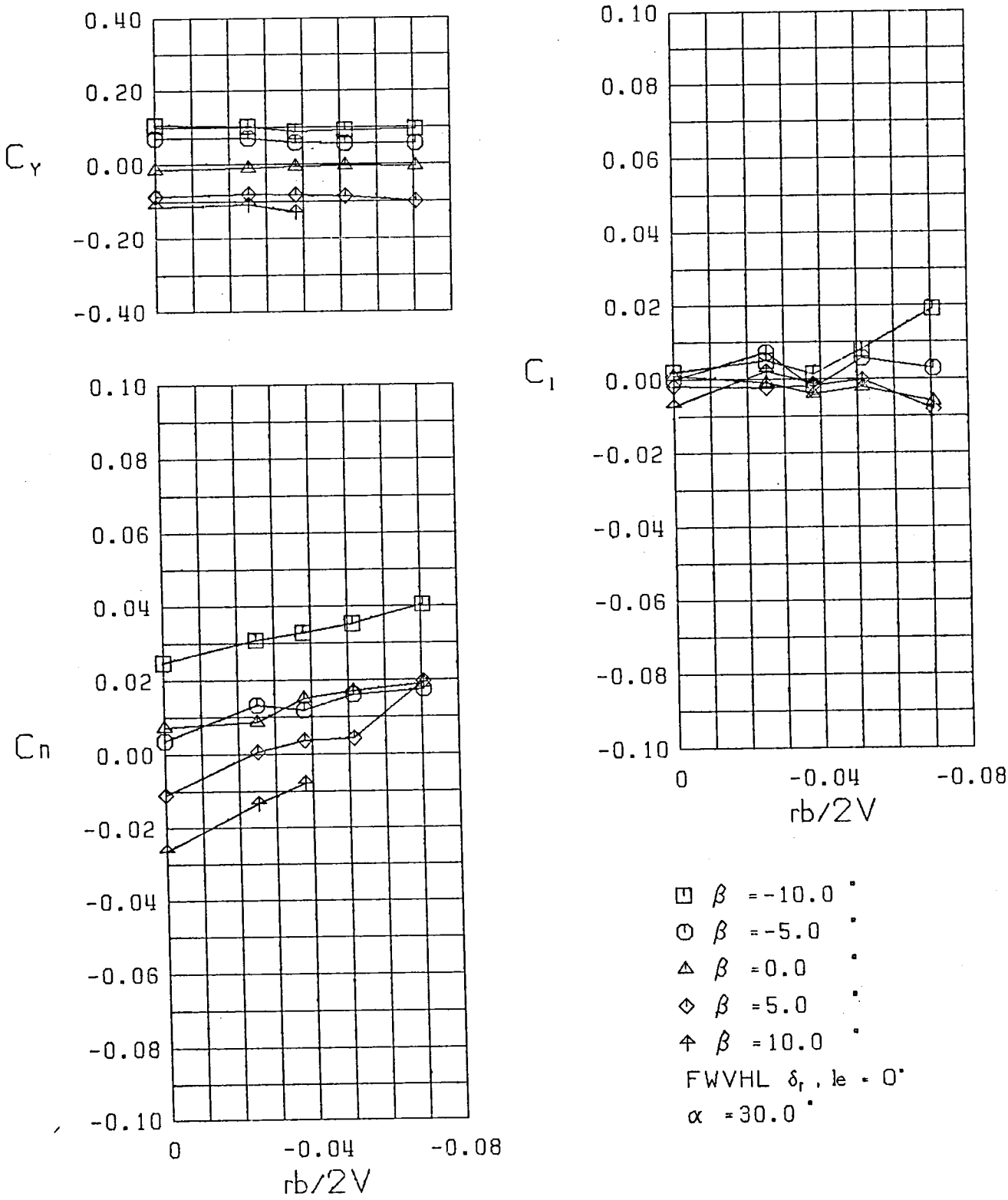

Figure 30 (Continued)

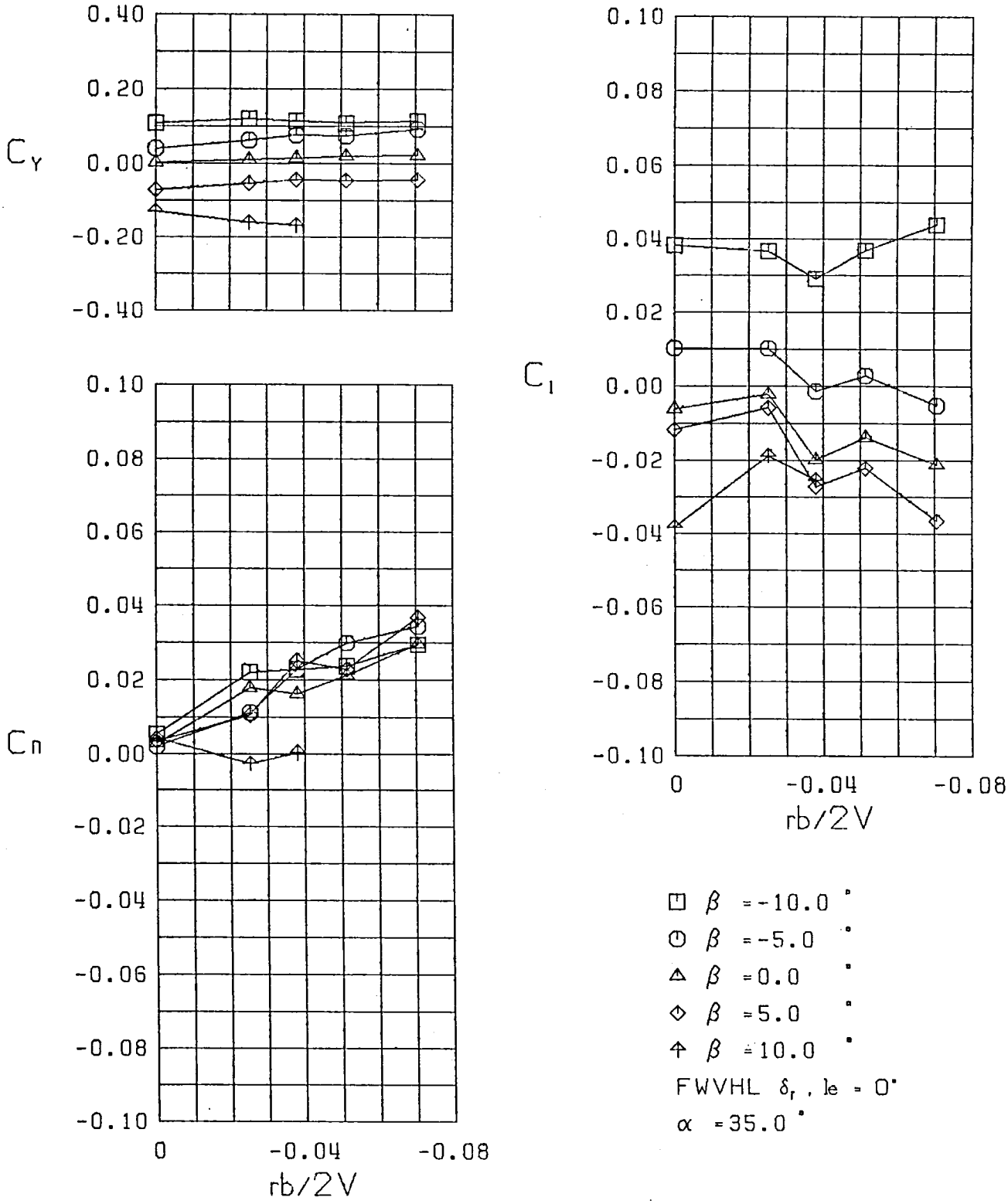

Figure 30 (Continued)

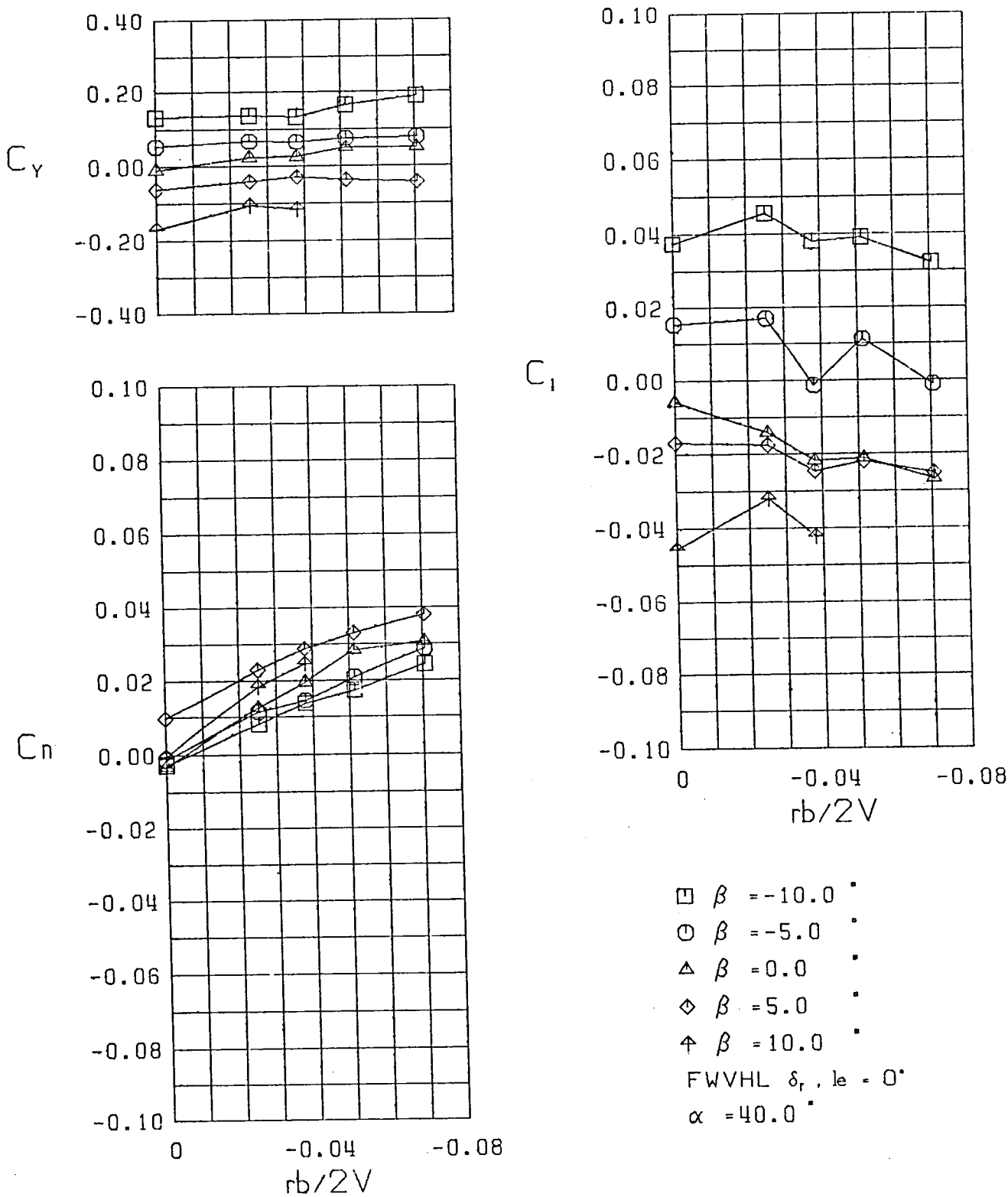

Figure 30 (Continued)

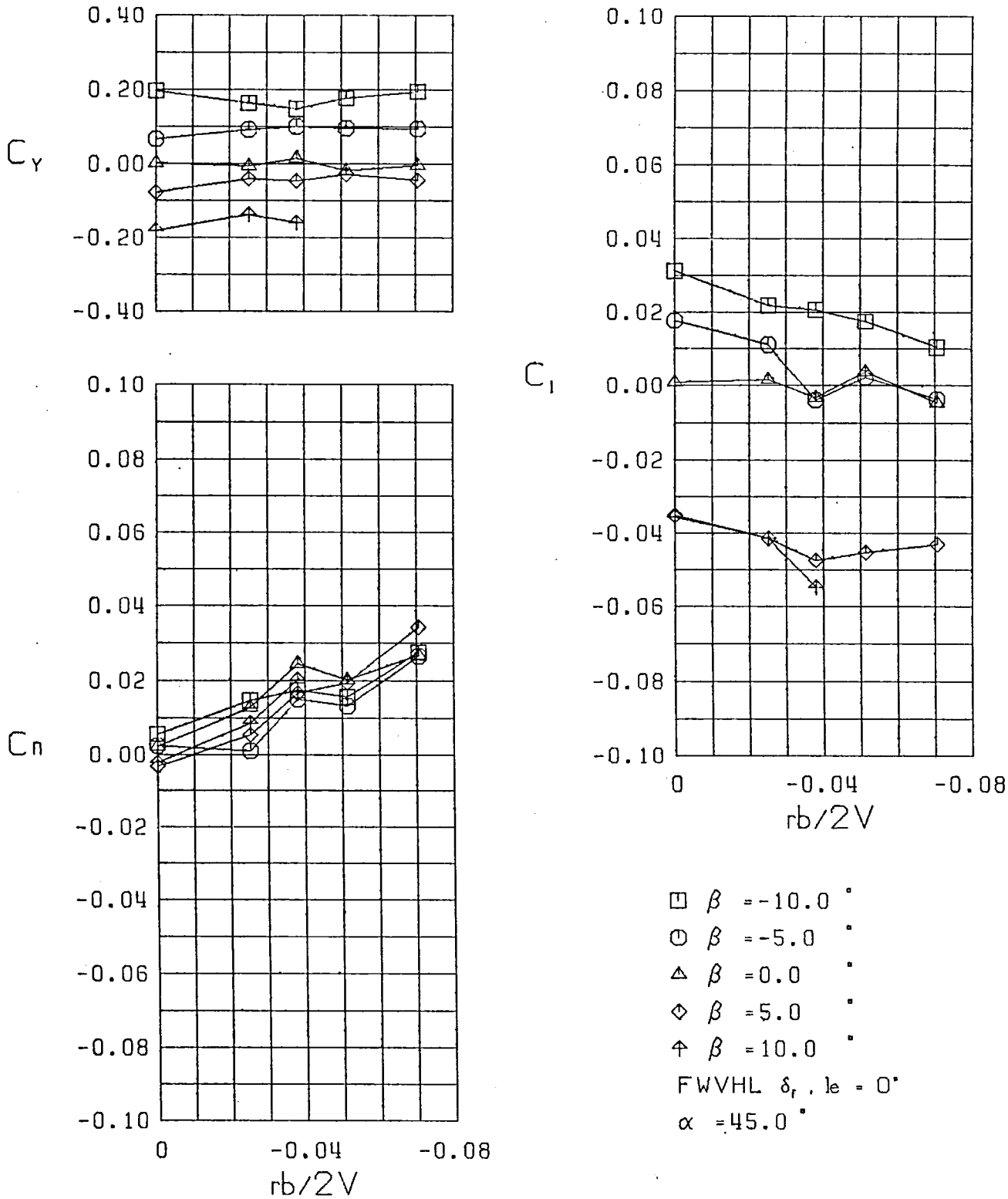

Figure 30 (Continued)

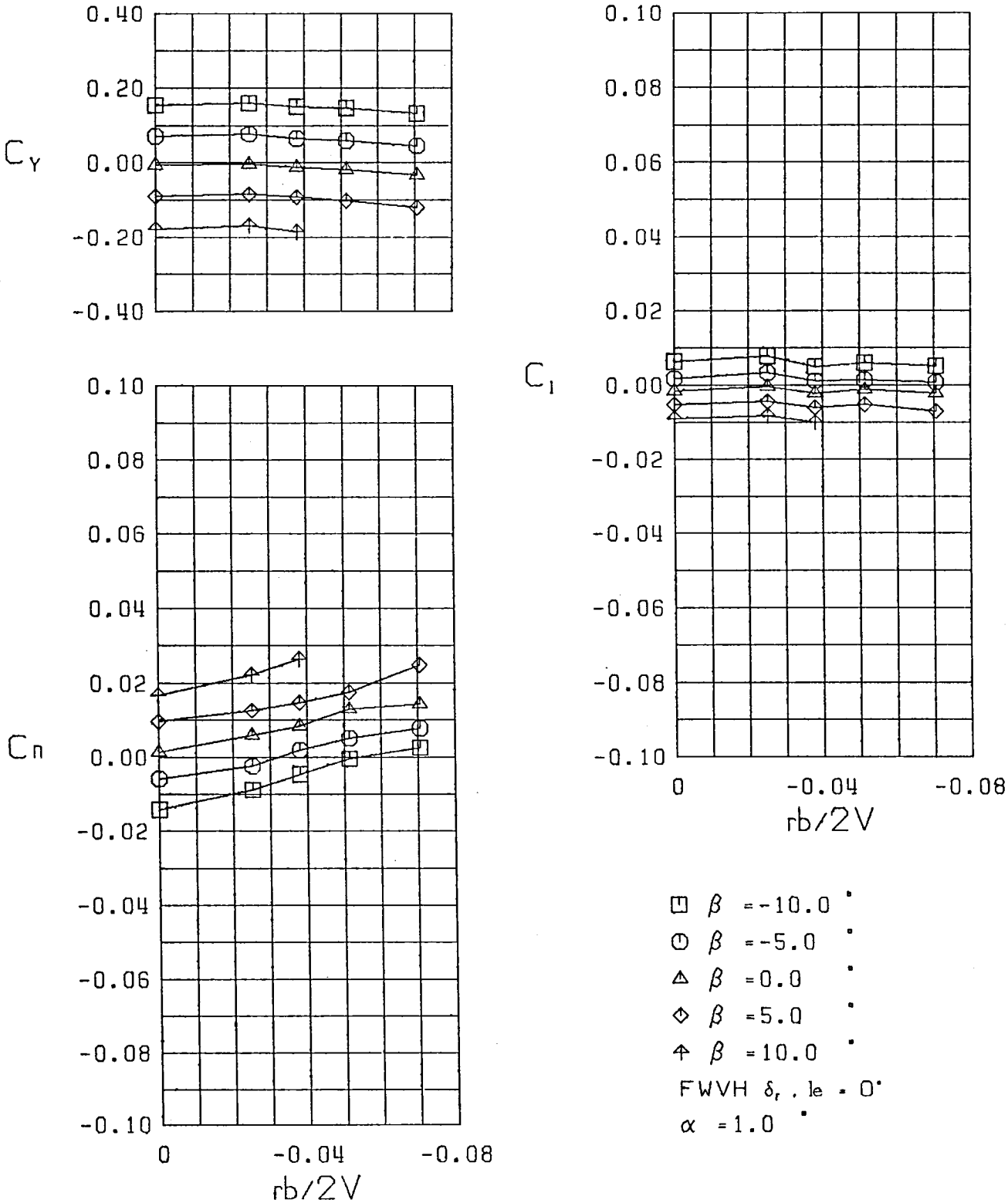

Figure 31 Variation of Static Lateral-Directional Stability Derivatives with Yaw Rate, Configuration 7

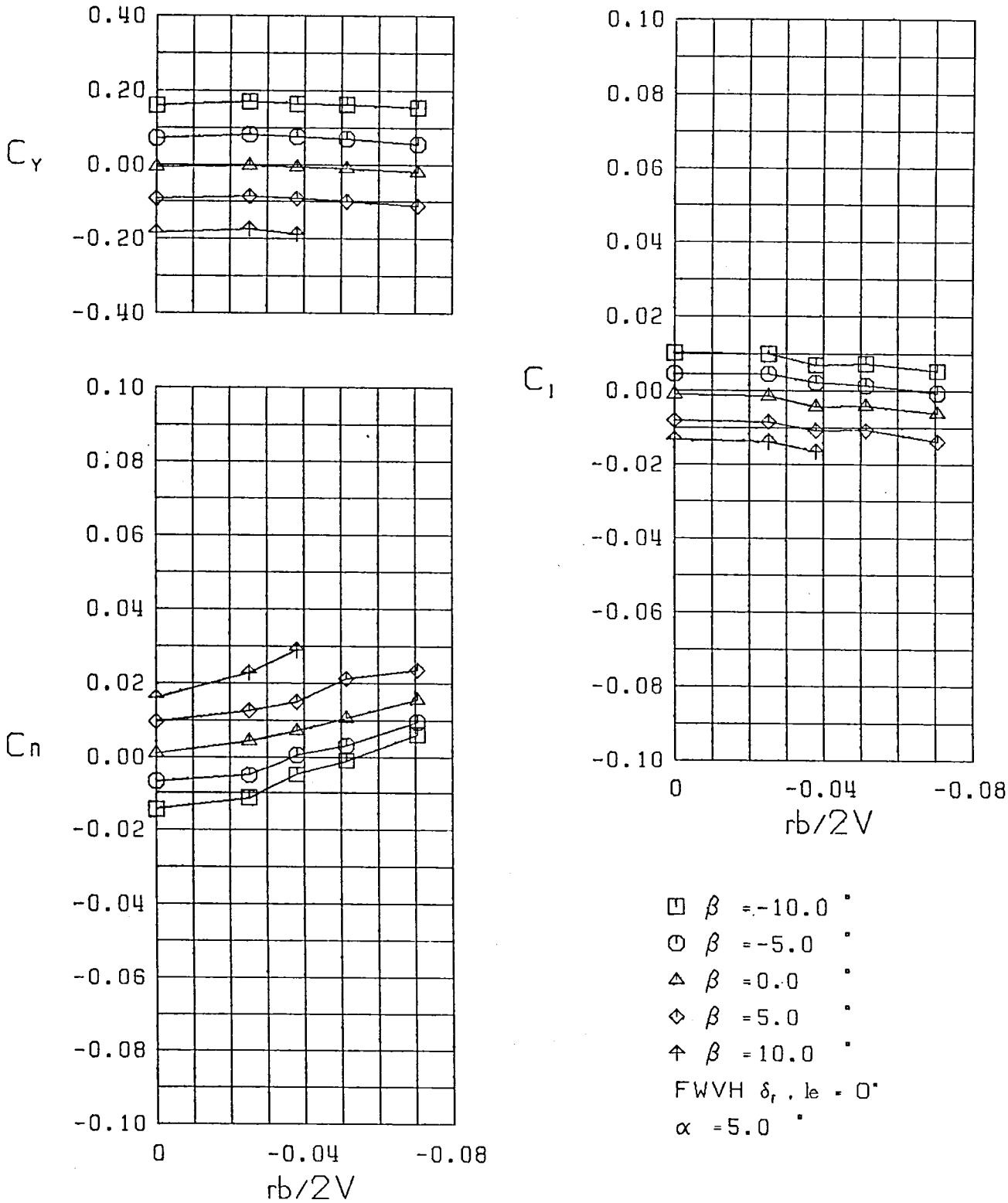

Figure 31 (Continued)

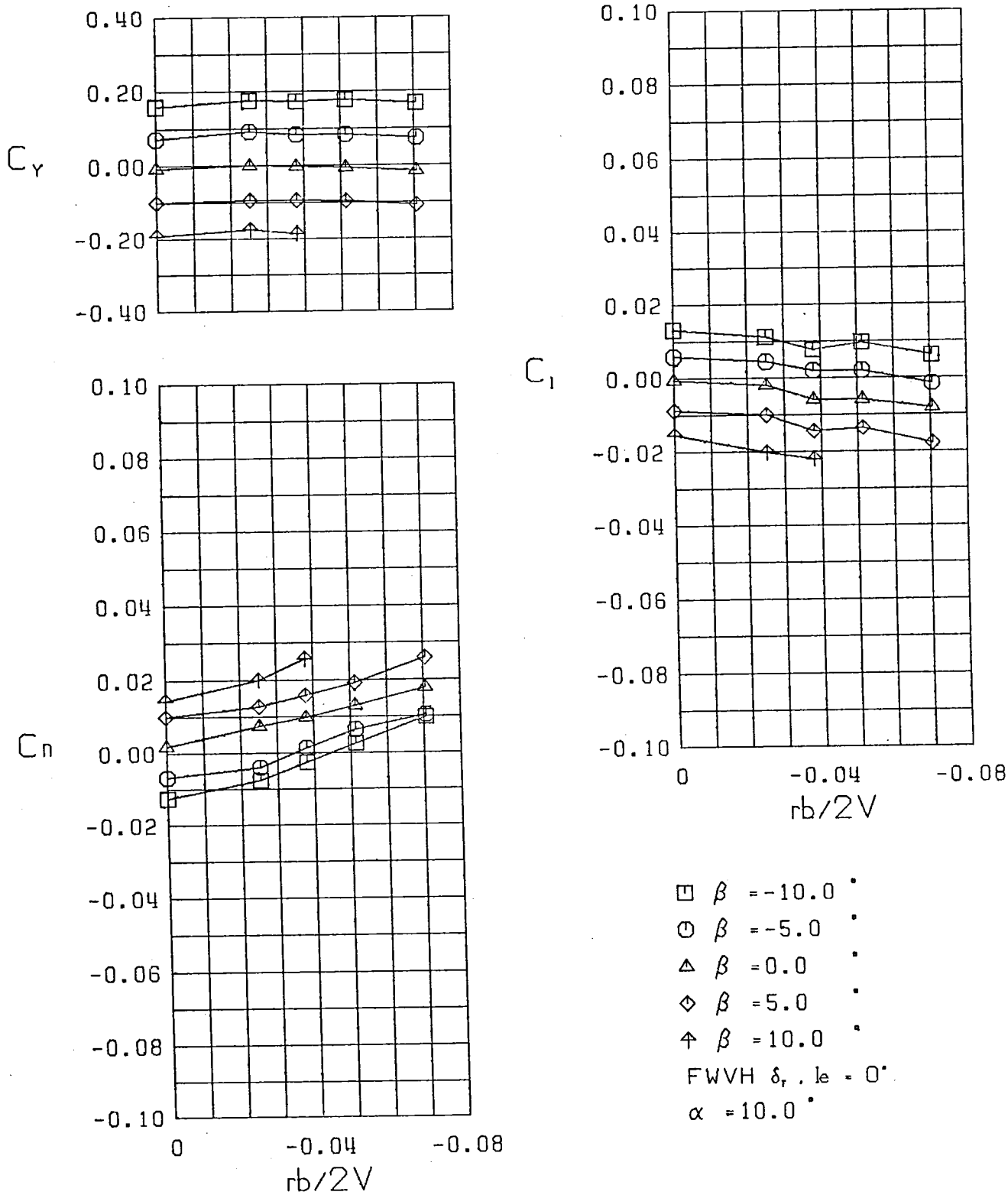

Figure 31 (Continued)

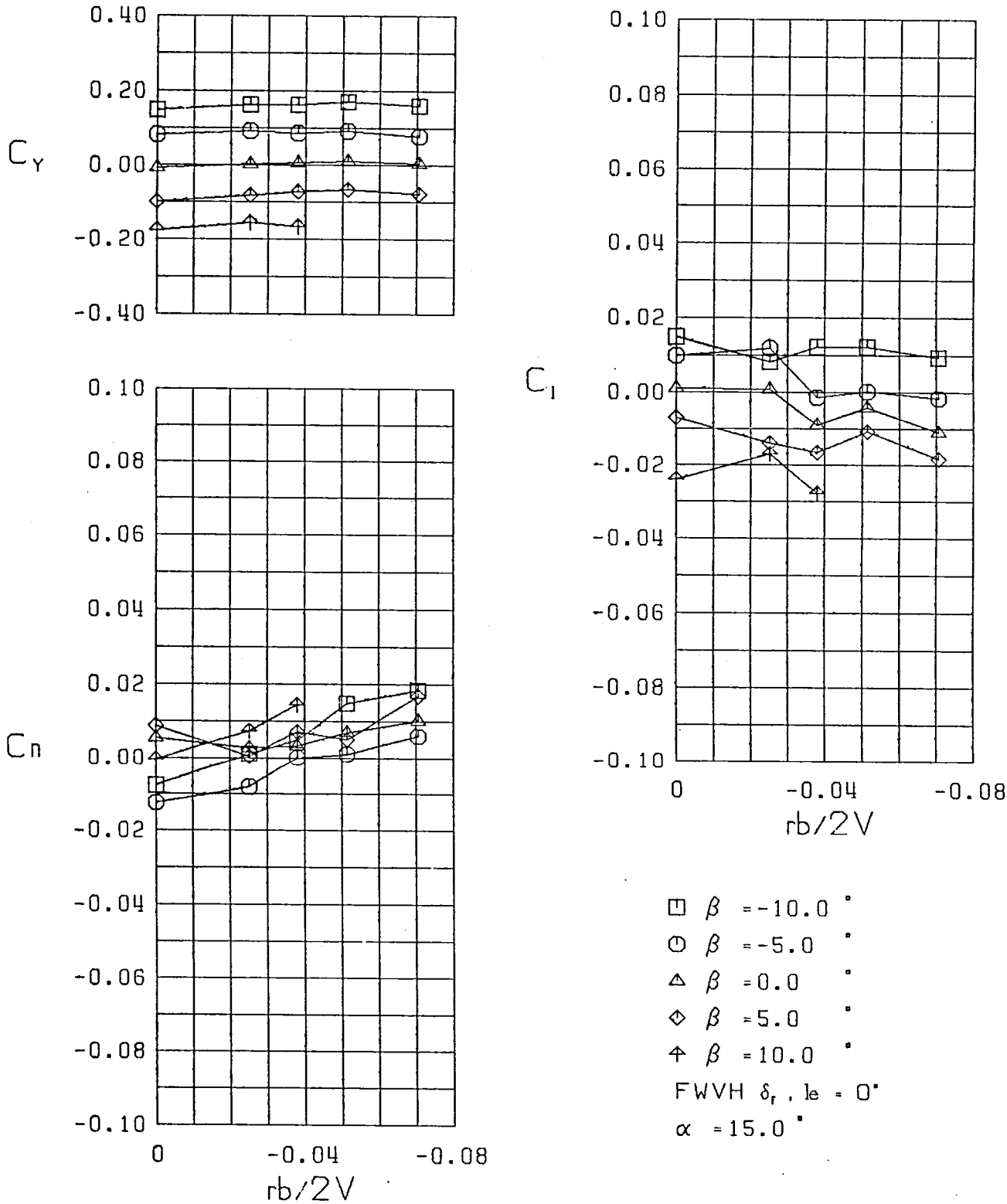

Figure 31 (Continued)

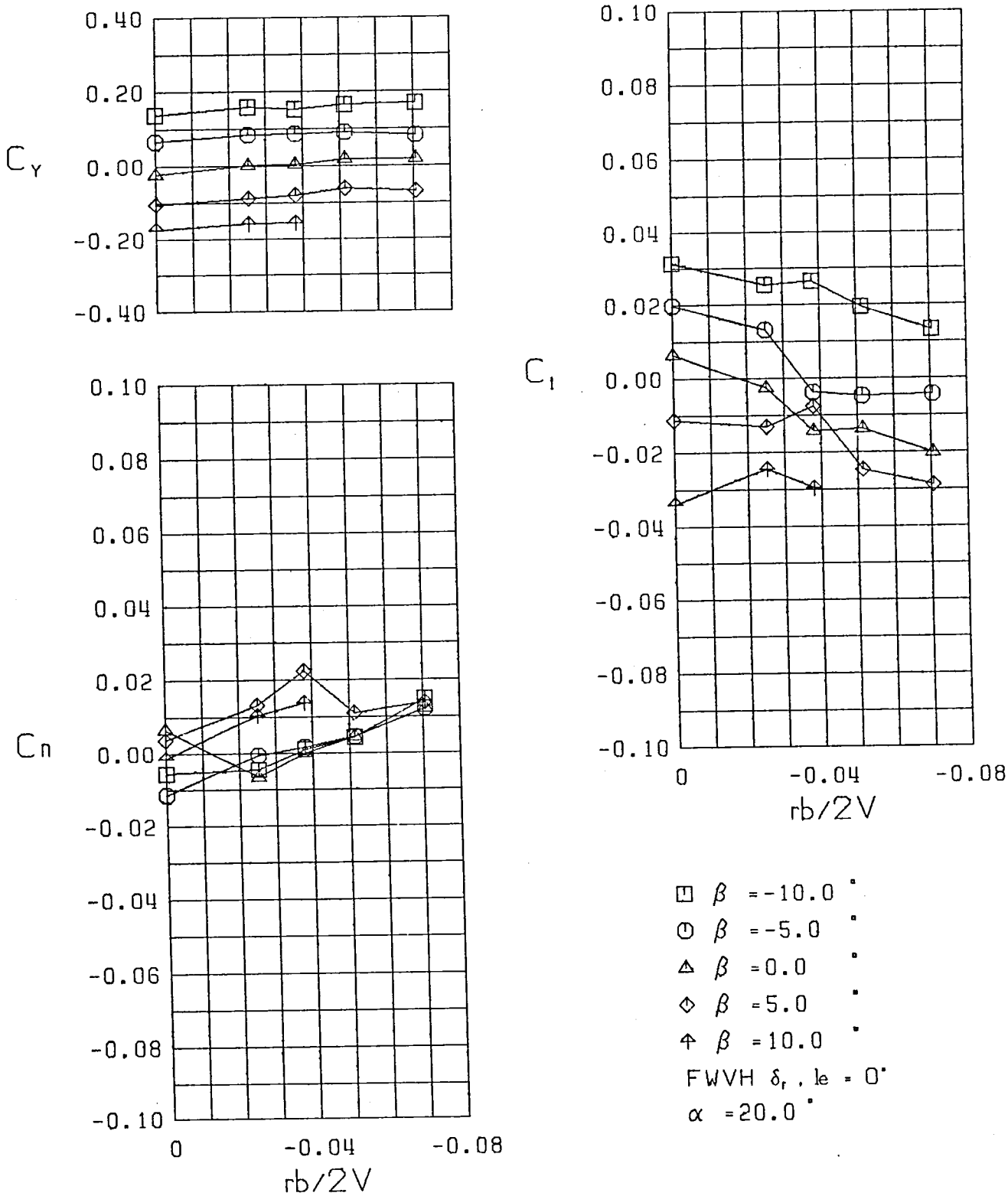

Figure 31 (Continued)

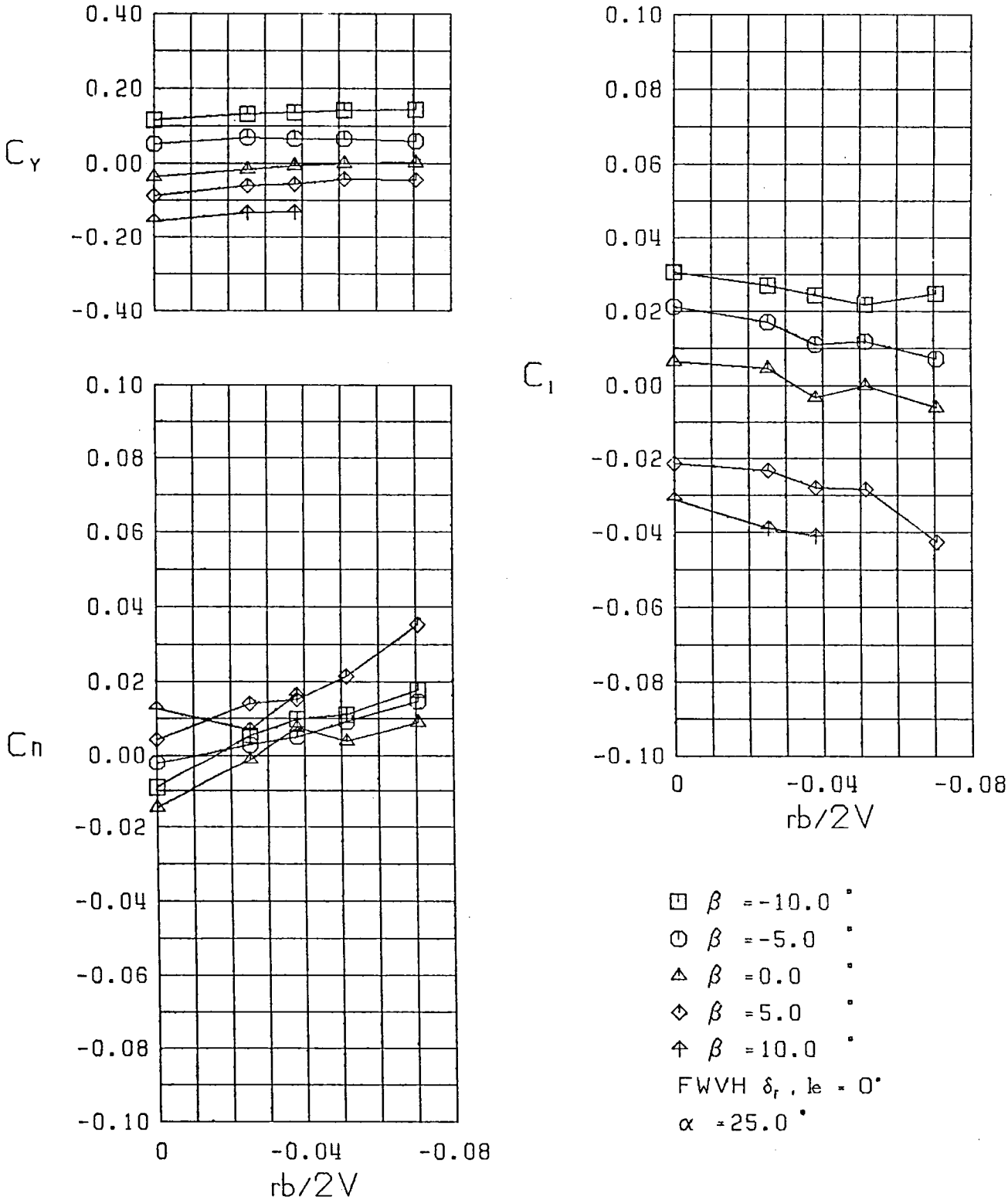

Figure 31 (Continued)

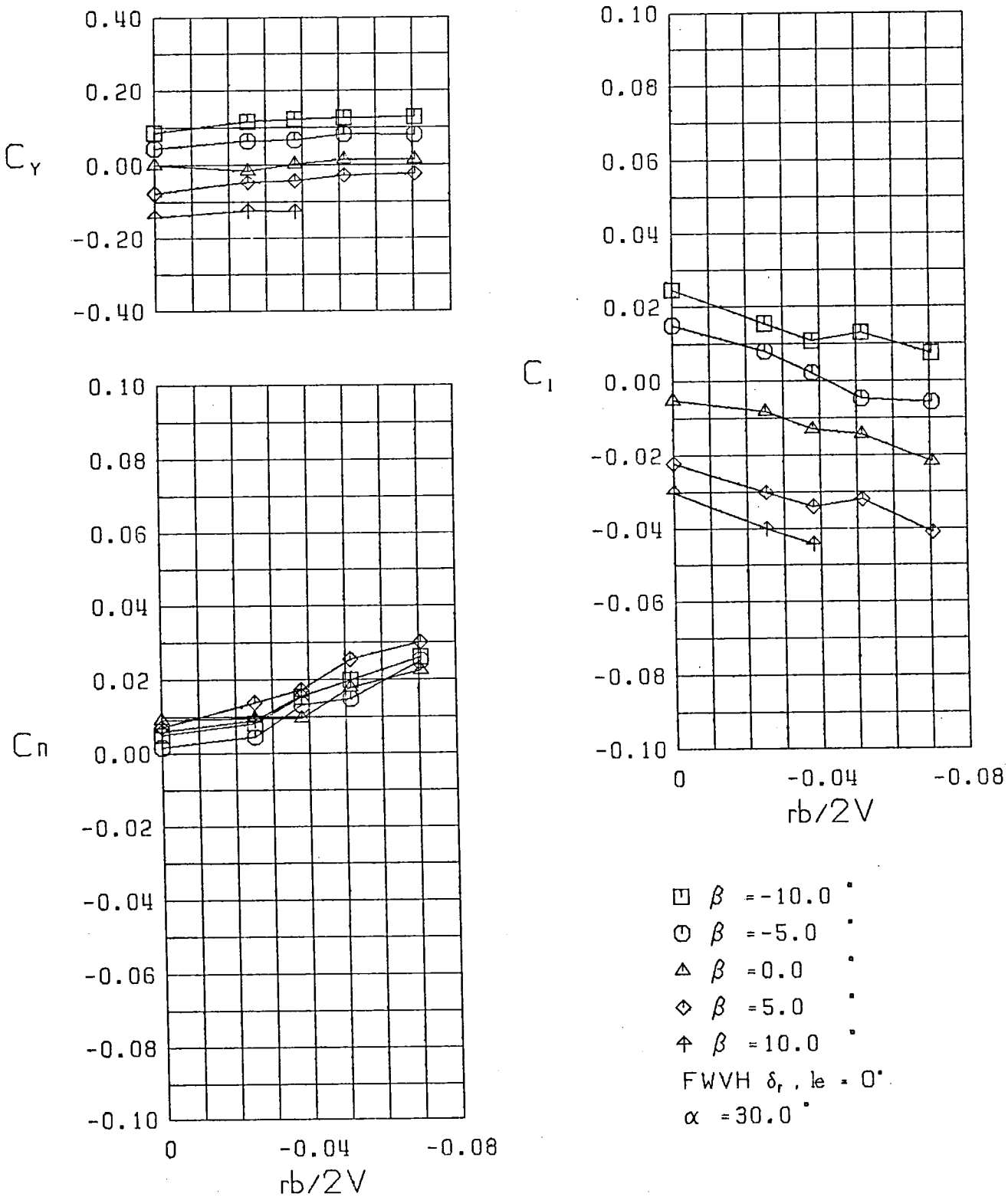

Figure 31 (Continued)

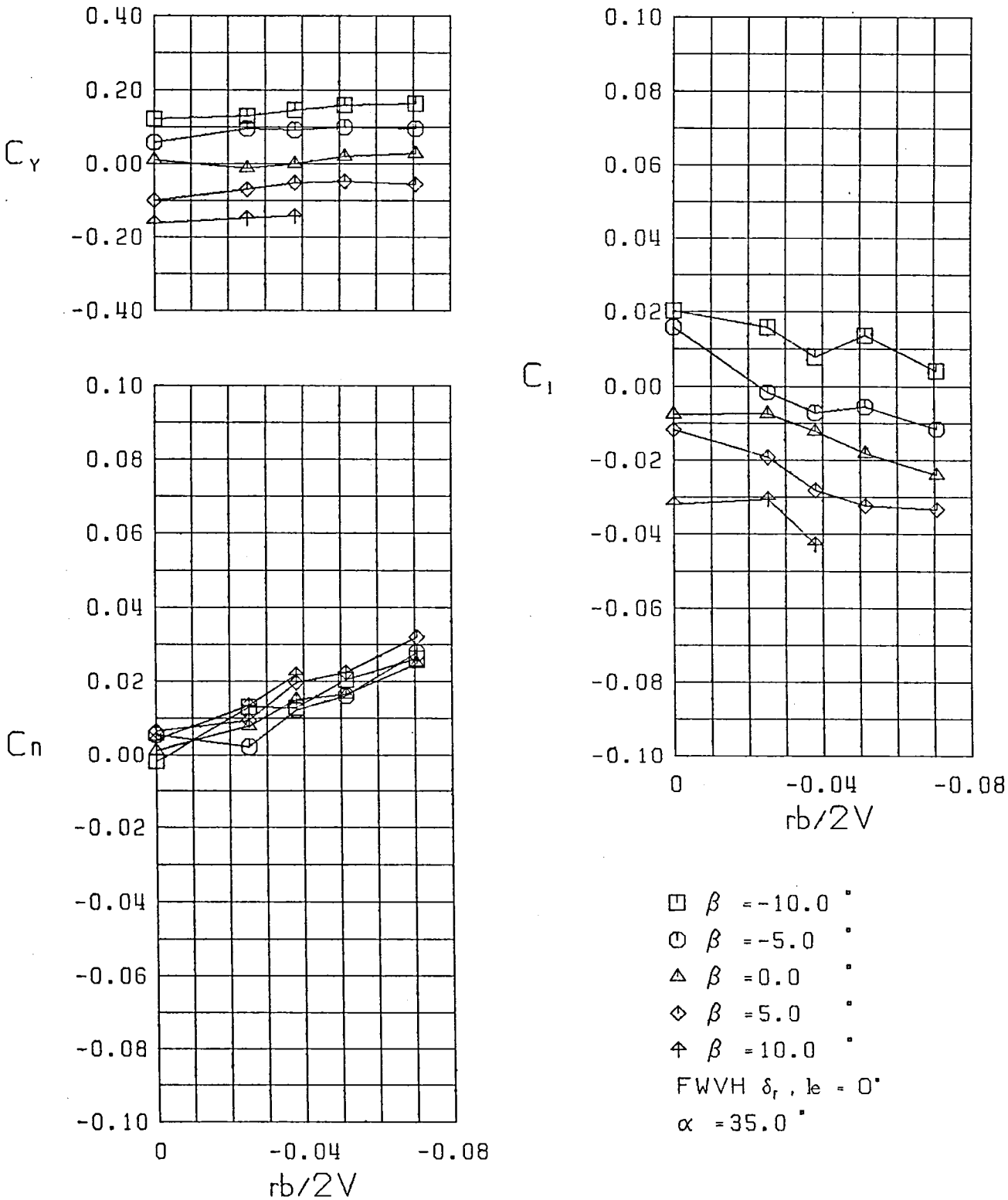

Figure 31 (Continued)

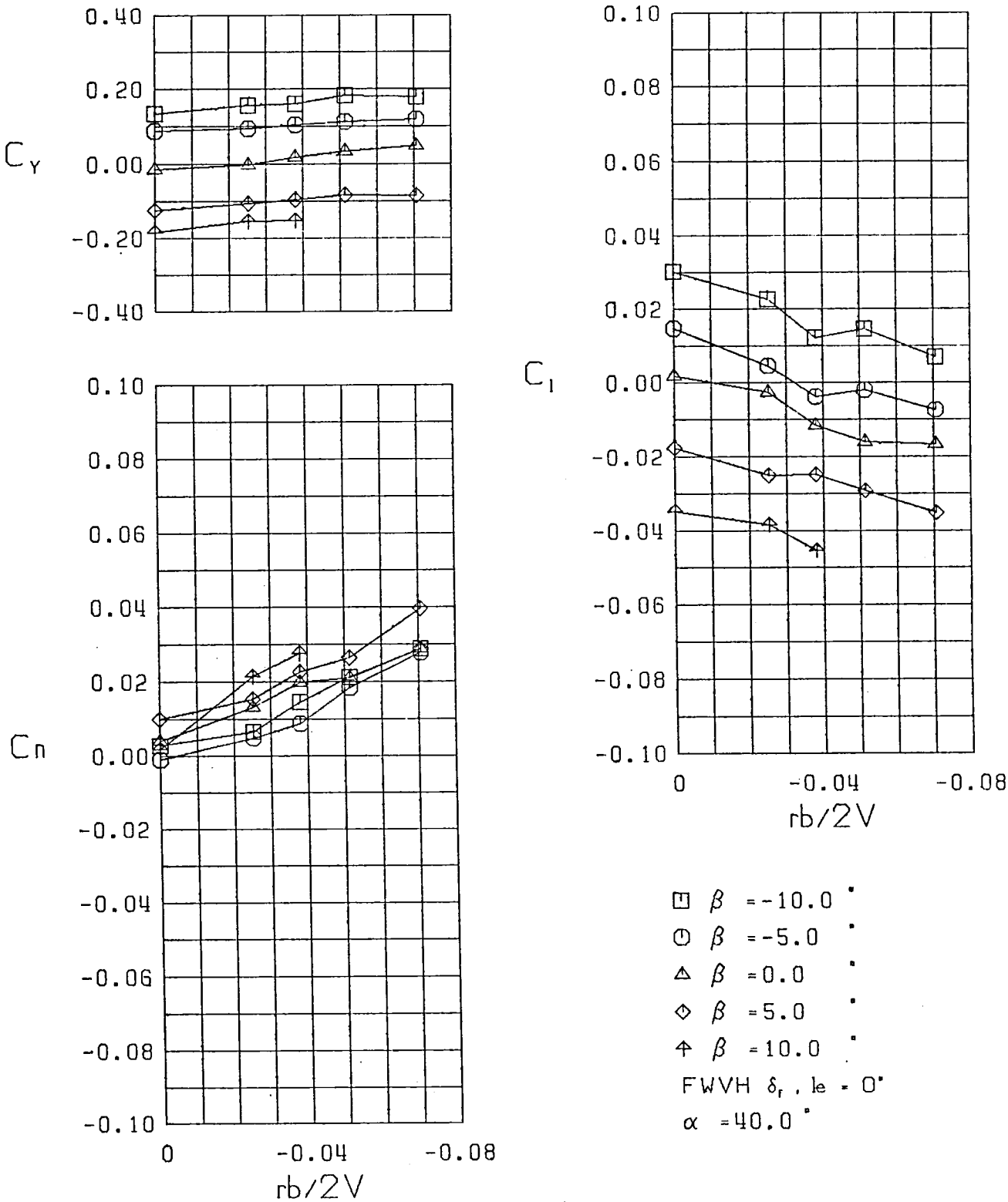

Figure 31 (Continued)

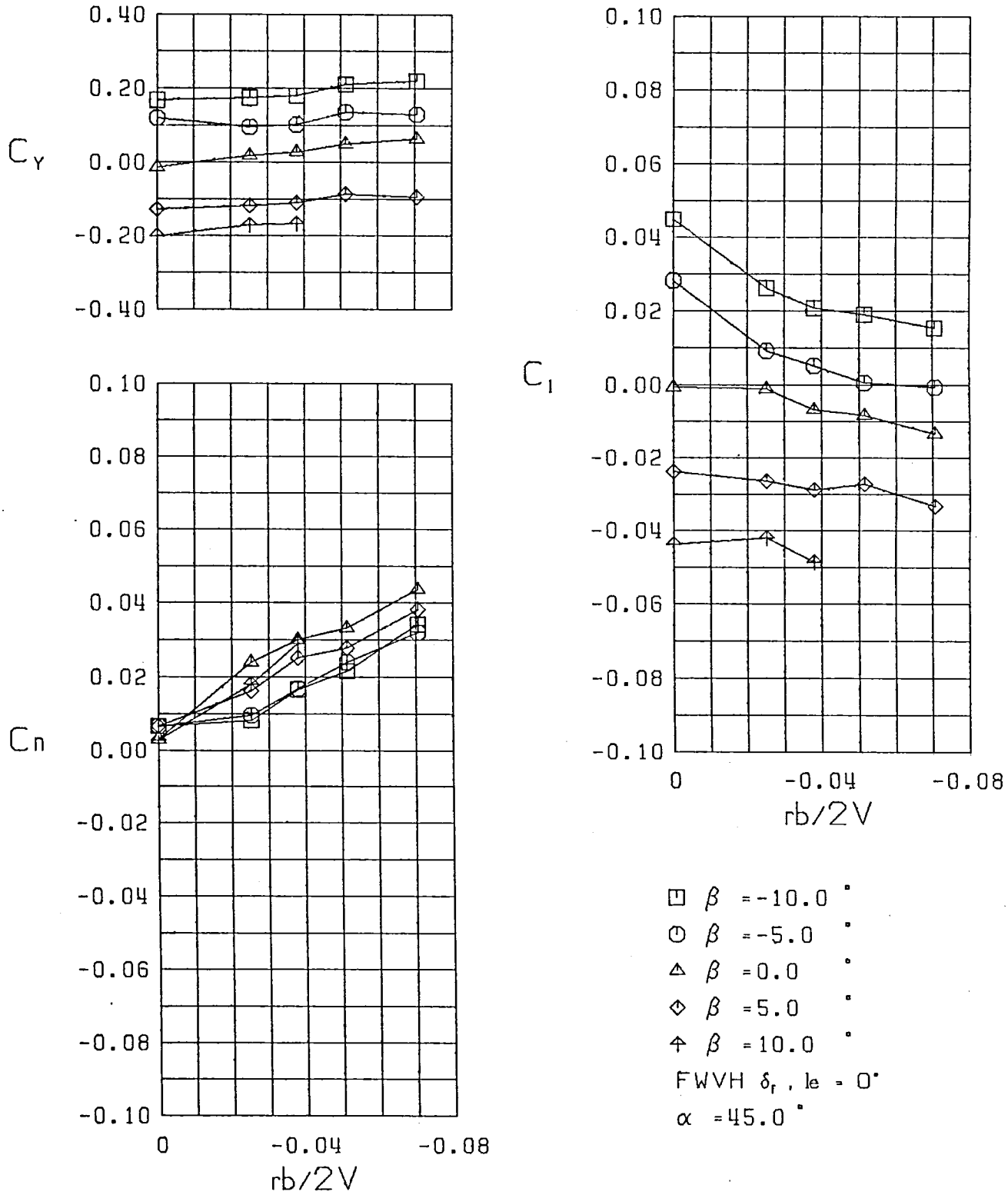

Figure 31 (Continued)

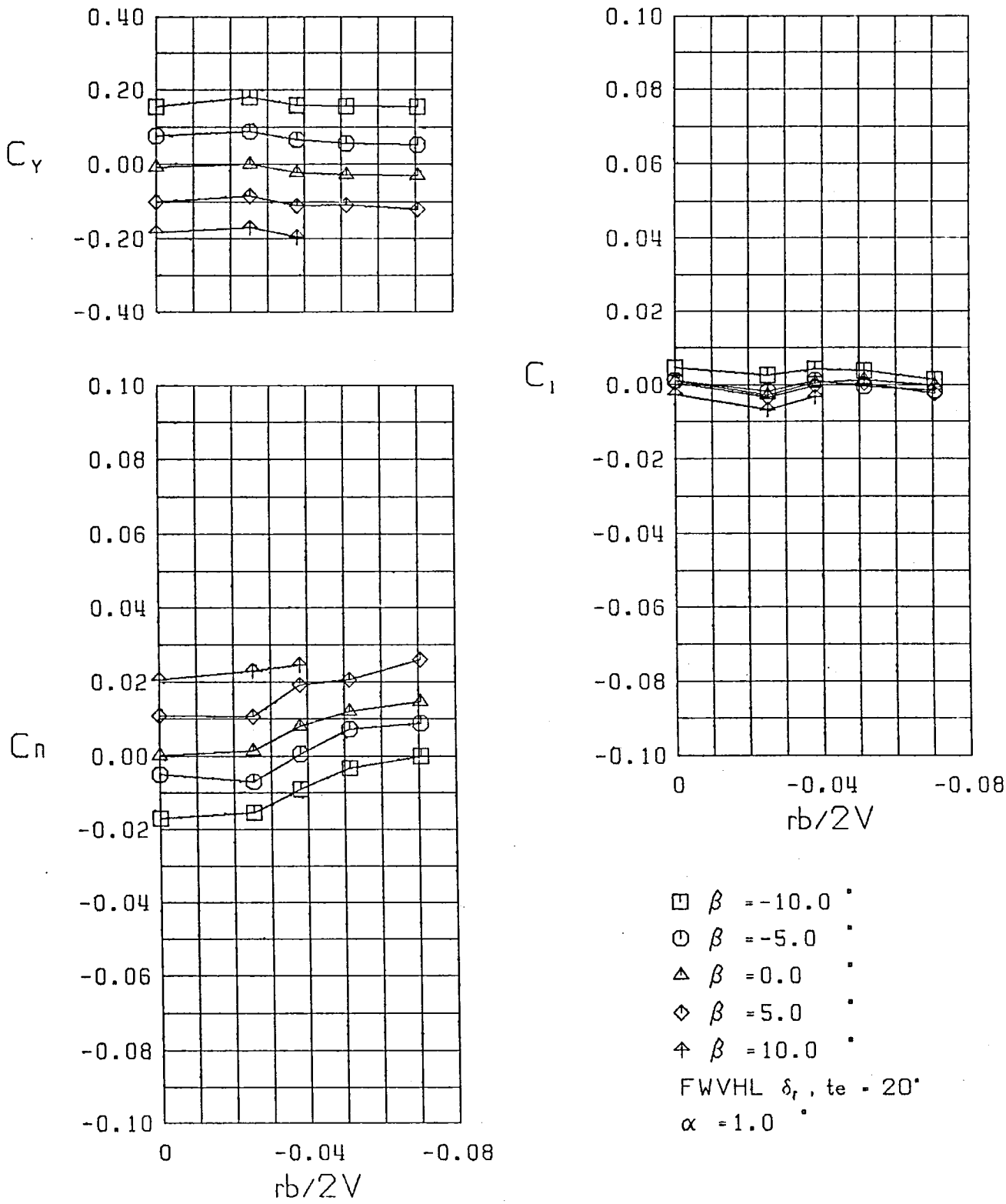

Figure 32 Variation of Static Lateral-Directional Stability Derivatives with Yaw Rate, Configuration 4

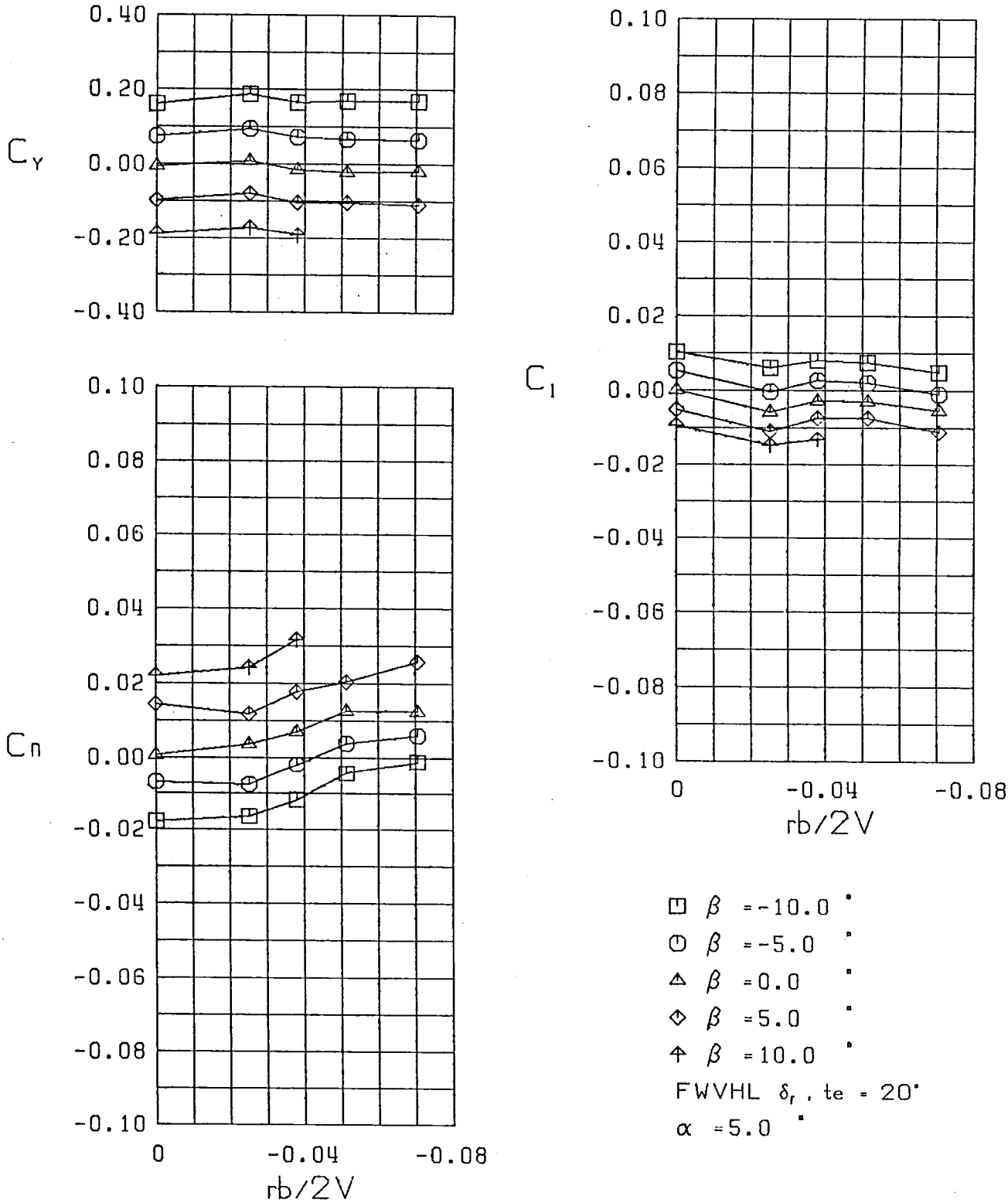

Figure 32 (Continued)

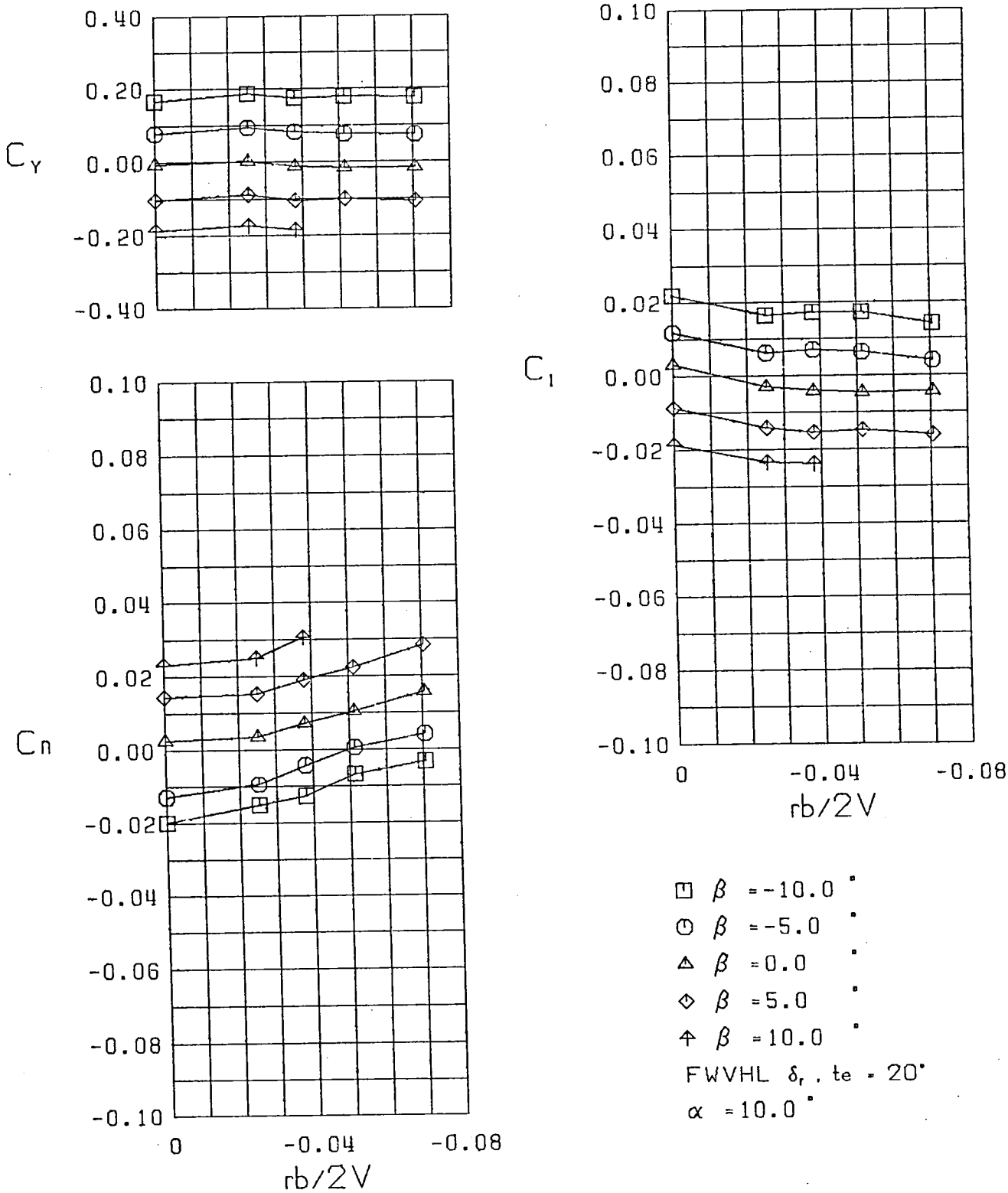

Figure 32 (Continued)

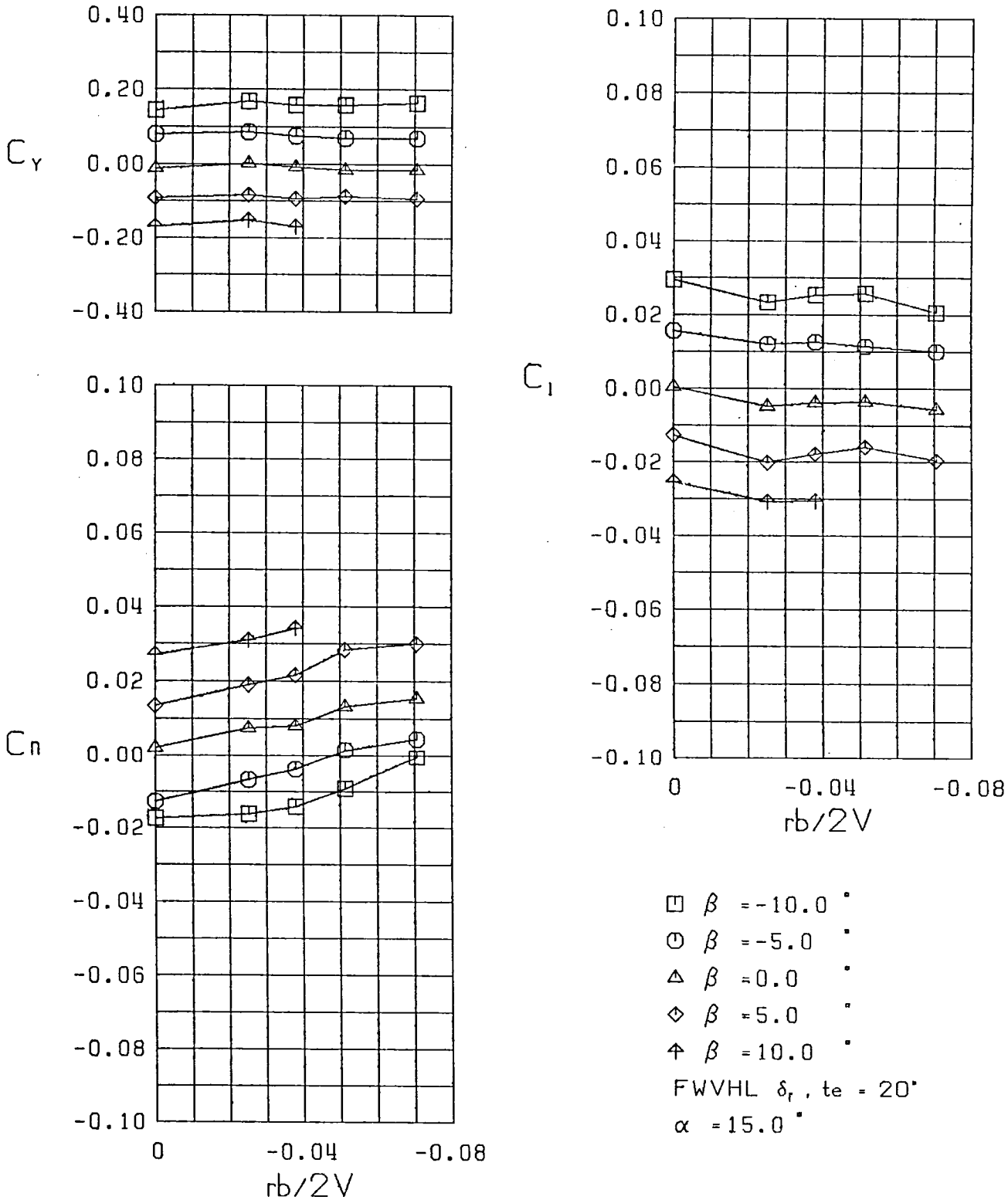

Figure 32 (Continued)

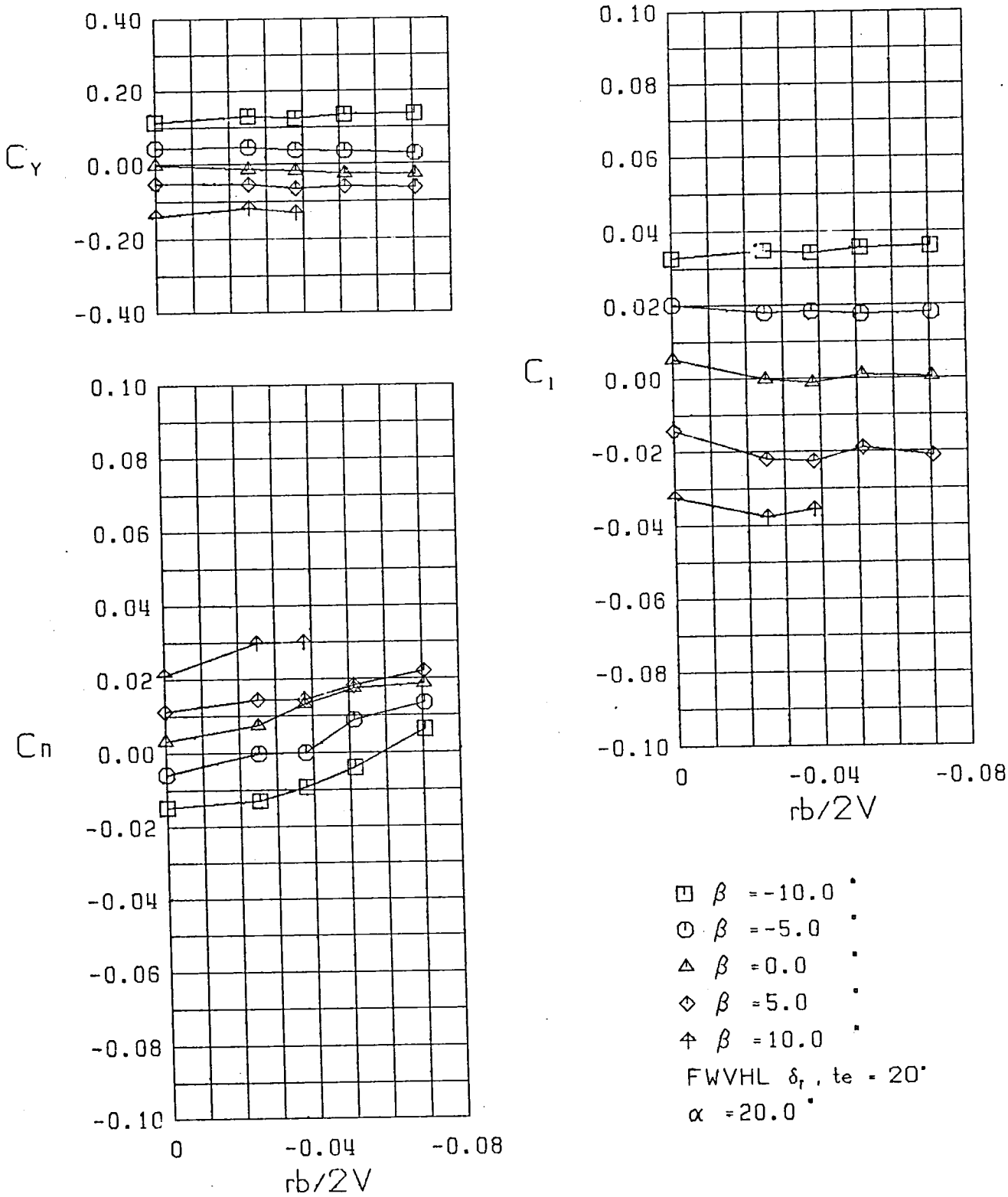

Figure 32 (Continued)

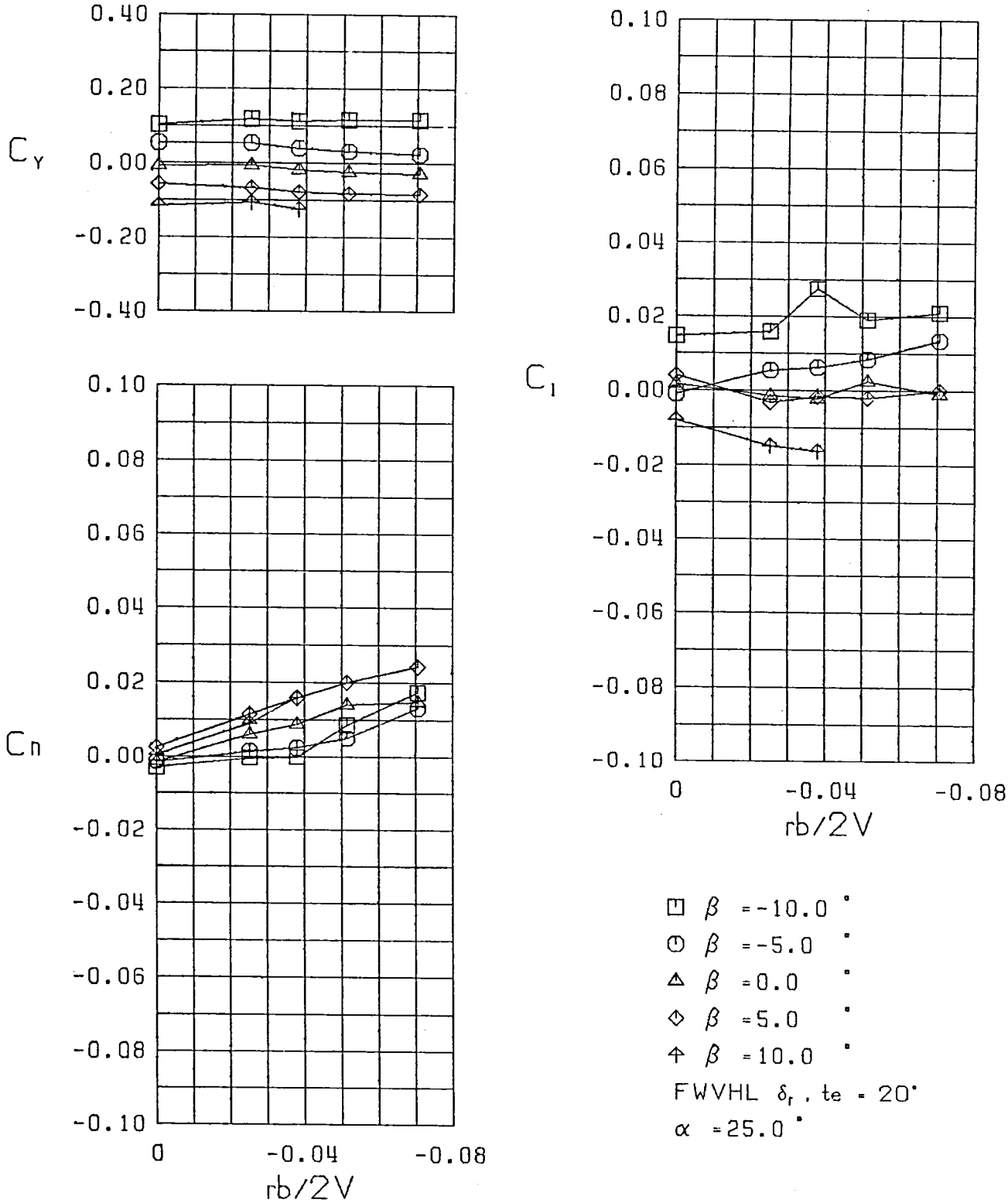

Figure 32 (Continued)

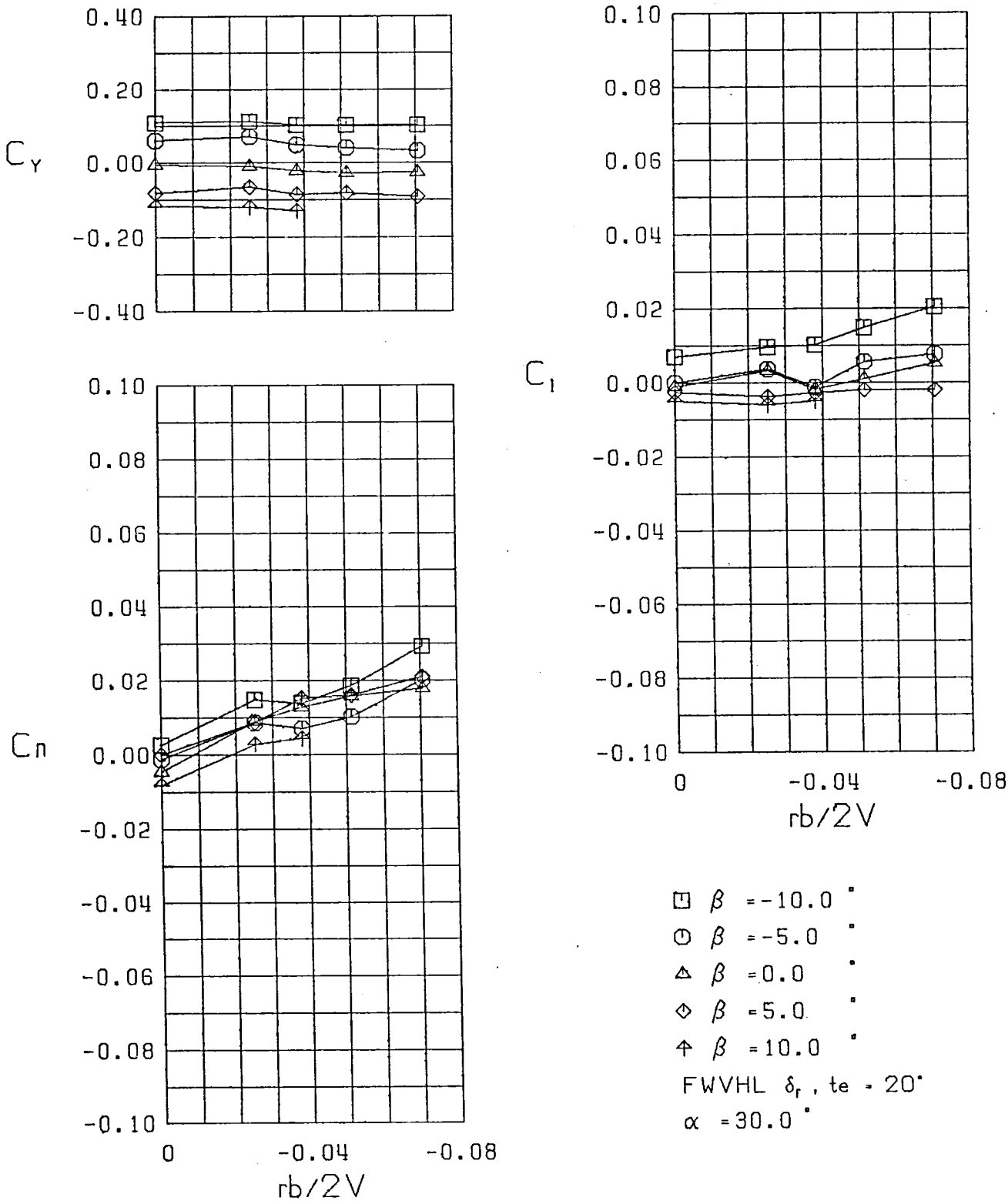

Figure 32 (Continued)

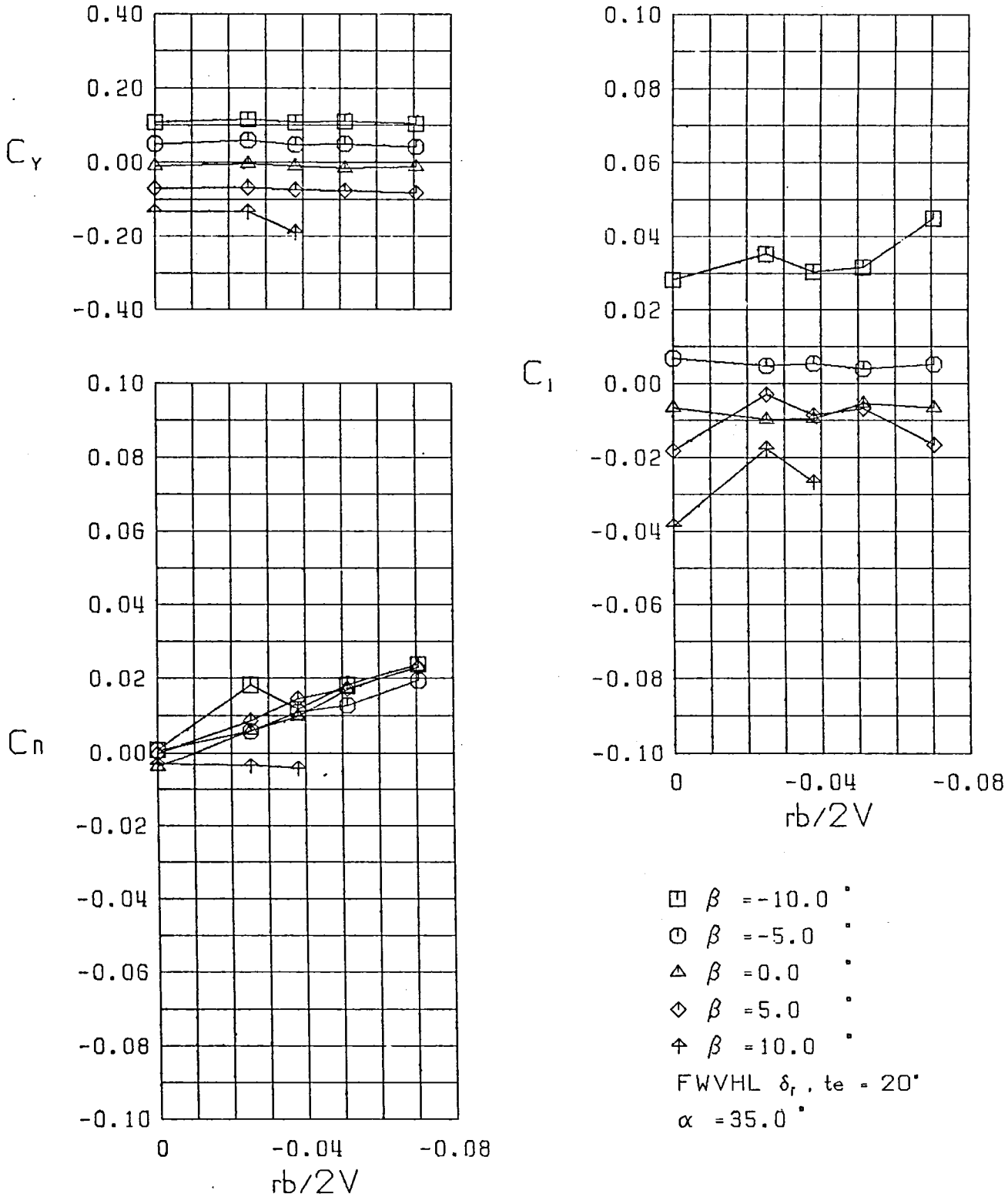

Figure 32 (Continued)

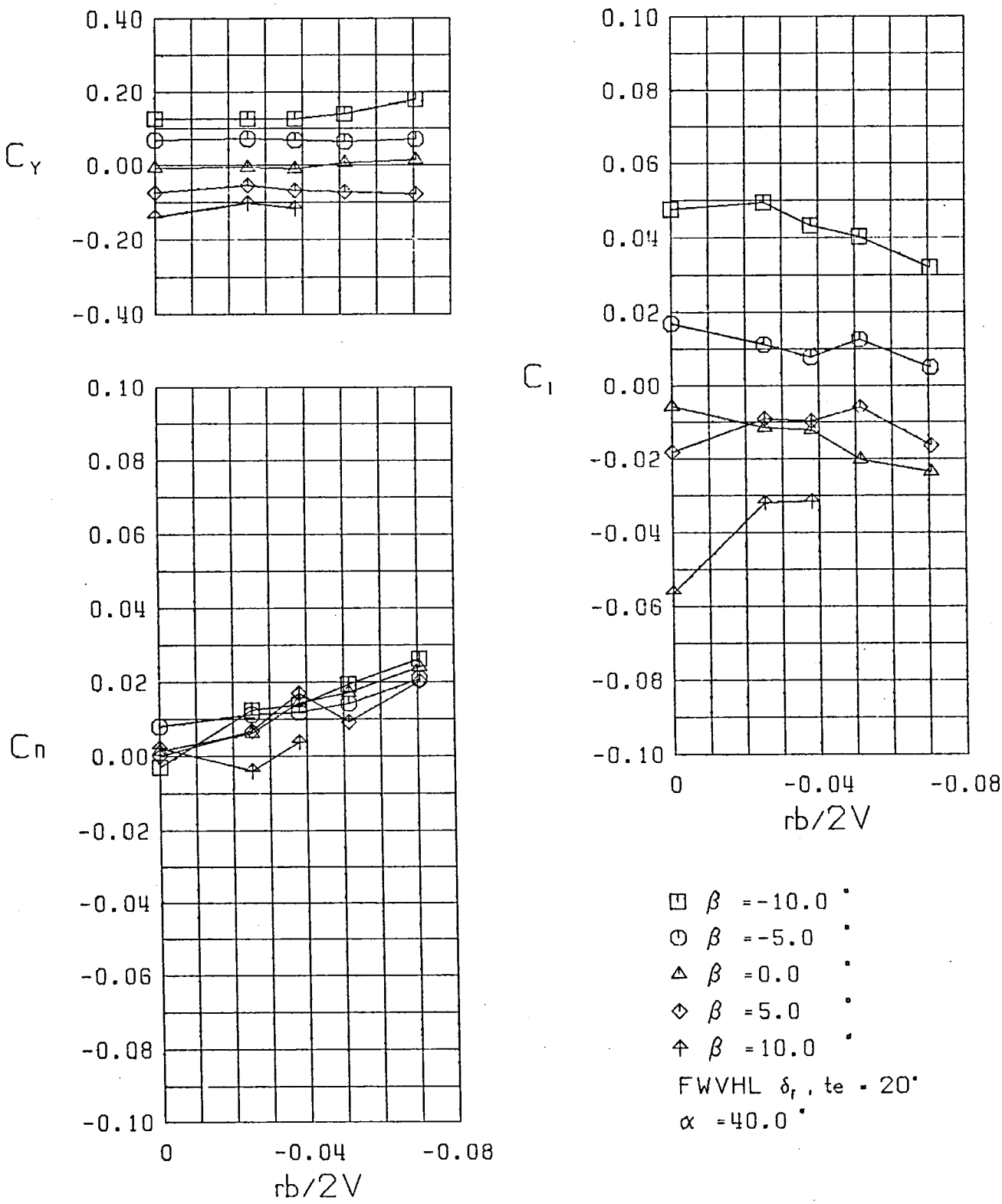

Figure 32 (Continued)

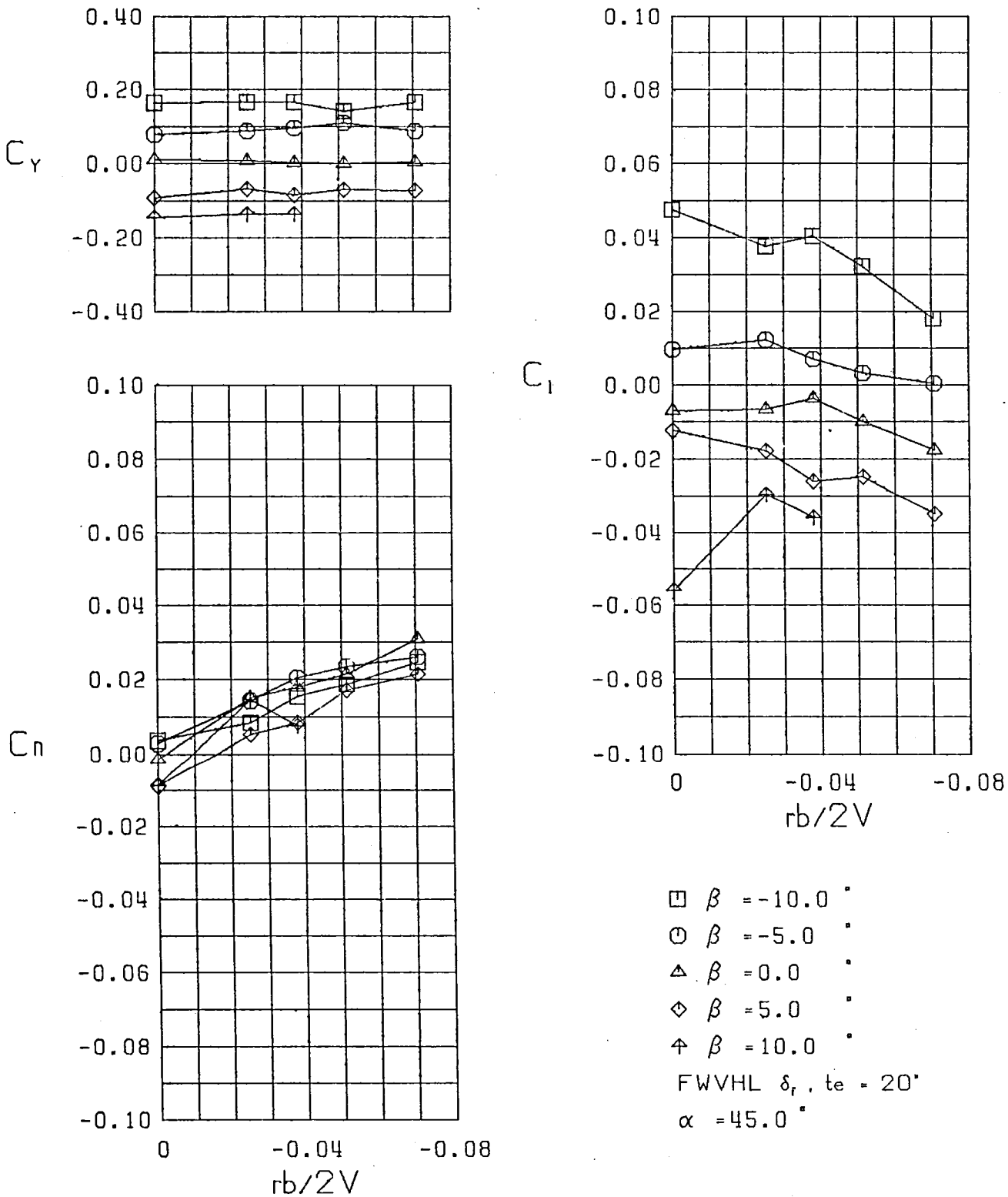

Figure 32 (Continued)

DO NOT REMOVE SLIP FROM MATERIAL

Delete your name from this slip when returning material to the library.

NAME	MS

NASA Langley (Rev. May 1988) RIAD N-75